

Enhanced Convective Heat Transfer in Nongas Generating Nanoparticle Thermites

S. W. Dean

M. L. Pantoya¹

e-mail: michelle.pantoya@ttu.edu

Department of Mechanical Engineering,
Texas Tech University,
Lubbock, TX 79401

A. E. Gash

Lawrence Livermore National Laboratory,
Livermore, CA 94550

S. C. Stacy

Department of Mechanical Engineering,
Texas Tech University,
Lubbock, TX 79401

L. J. Hope-Weeks

Department of Chemistry,
Texas Tech University,
Lubbock, TX 79401

Flame propagation and peak pressure measurements were taken of two nanoscaled thermites using aluminum (Al) fuel and copper oxide (CuO) or nickel oxide (NiO) oxidizers in a confined flame tube apparatus. Thermal equilibrium simulations predict that the Al + CuO reaction exhibits high gas generation and, thus, high convective flame propagation rates while the Al + NiO reaction produces little to no gas and, therefore, should exhibit much lower flame propagation rates. Results show flame propagation rates ranged between 200 m/s and 600 m/s and peak pressures ranged between 1.7 MPa and 3.7 MPa for both composites. These results were significantly higher than expected for the Al + NiO, which generates virtually no gas. For nanometric Al particles, oxidation has recently been described by a melt-dispersion oxidation mechanism that involves a dispersion of high velocity alumina shell fragments and molten Al droplets that promote a pressure build-up by inducing a bulk movement of fluid. This mechanism unique to nanoparticle reaction may promote convection without the need for additional gas generation. [DOI: 10.1115/1.4001933]

Keywords: nanocomposites, enhanced convection, reaction mechanisms, nano-aluminum, thermites, CuO, NiO, peak pressures, flame speeds, DSC, TGA, XRD, gas generation, flame propagation

1 Introduction

Thermites are energetic materials consisting of a metal fuel and a metal oxide [1]. Thermite reactions are generally characterized by high heats of combustion and high adiabatic flame temperatures. As thermites are composites of separate constituent powders, their properties may be adjusted by changing the ratios of their components. Until relatively recently the powders that make up most thermites were only available on the micron scale. With the introduction of powders with average particle sizes on the order of tens of nanometers, new reaction behaviors have been observed. These include enhanced flame propagation rates and increased gas production. This recently developed class of energetic materials, commonly called metastable intermolecular composites, has generated a great deal of interest due to enhanced combustion properties and customization potential.

Two key parameters considered when selecting fuel and oxidizer compositions for a particular application are the amount of gas the reaction will produce and the reaction's propagation rate. In many applications the composite is confined in a tubelike geometry, such that measurements of these parameters taken in a similar geometry are most comparable. This study focuses on measuring the flame propagation rate and peak pressure of two nanoscale aluminum (Al) fueled thermites in order to determine the effects of gas production on flame propagation rate in a confined tubelike geometry.

Energy transport in reacting thermites is generally due to combined convective and advective modes of propagation. Other mechanisms such as radiation can also contribute to the total energy transfer [2]. Advection describes energy transport due to bulk fluid motion and, thus, is directly related to the bulk flow of combustion products. Convection describes energy transport due to

two mechanisms: (1) random molecular motion (diffusion) in the presence of a temperature gradient and (2) bulk fluid motion. Thus, the convective mechanism includes the advection process. Key to the diffusion energy transport contribution is the presence of a temperature gradient. The random molecular motion (zero bulk transport) results in net energy transfer due to motion of high energy molecules relative to the motion of low energy molecules. A temperature gradient is most likely present at two locations: (1) the fluid-flame tube boundary and (2) the flame front—unburned thermite boundary. A thermite reaction propagates through a tube as a series of ignition sites. At the flame front location, convective and conductive heat transport serve to preheat the unburned thermite ahead of the reaction zone, thus, bringing the reactants closer to the ignition temperature as the reaction zone nears. In this way the ignition temperature of the thermite is reached more quickly than in a composite that does not display gas generating properties.

The gas produced by the reaction is composed of reaction products in the vapor phase, so the amount of gas generated in a particular composite is dependent on the physical properties of the reaction products and the thermodynamic properties of the reaction itself. If the reaction reaches a temperature high enough to vaporize the intermediates and products at the pressure inside the tube, then gas will be produced. The two reactions studied here, Al and CuO and Al and NiO, have very different gas generation properties. The Al and CuO reaction is known to produce a large amount of gas (i.e., 0.54 mol of gas/100 g reactants [3]) while the Al and NiO reaction has been predicted to produce very little, if any, gaseous products (i.e., 0.0108 mol of gas/100 g reactants [3]).

Accurate measurements of the temperature inside the reaction zone of a propagating thermite have been elusive thus far. This is largely due to the high propagation rates observed in nanoscaled composites and the tube material used as they preclude the use of many common temperature measuring instruments. As the reaction temperature is unknown the gas production of the thermite cannot be directly measured with any certainty. It must instead be approximated by using thermodynamic equilibrium modeling

¹Corresponding author.

Contributed by the Heat Transfer Division of ASME for publication in the JOURNAL OF HEAT TRANSFER. Manuscript received March 3, 2009; final manuscript received March 26, 2010; published online August 10, 2010. Assoc. Editor: Patrick E. Phelan.

Table 1 Powder properties

Material	Manufacturer	Particle size (nm)	Surface area (m ² /g)	Morphology	Purity (%)
Aluminum	Novacentrix	50	39.8	Spherical	75
Copper (II) oxide	Alfa Aesar	30–50	13	Spherical	98.5
Nickel (II) oxide	LLNL	~11	~55	Spherical	~90.5

software and by measuring the rise in pressure corresponding to the passing of the reaction front. This study uses both of these methods to determine qualitative gas production.

2 Experimental Procedures

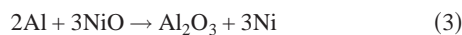
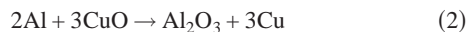
2.1 Sample Preparation. The composites used in this study were synthesized from commercially available powders (Al, CuO) and powder made at Lawrence Livermore National Laboratory (LLNL) using a sol-gel technique (NiO). Table 1 lists the powders used in this study and some of their properties. Properties for the Al and CuO powders were obtained from their respective manufacturers; the particle size and purity of the NiO powder were obtained from X-ray diffraction (XRD) using a Rigaku Ultima III powder XRD. The surface area information was obtained at LLNL by performing Brunauer–Emmett–Teller methods using an ASAP 2000 surface area analyzer (Micromeritics Instrument Corporation, Norcross, GA). The purity of the NiO powder is a measure of its crystallinity and not a measure of impurities in the composite although no impurities were detected in the XRD. The impurities in the Al powder are composed of a nonreactive alumina shell coating the Al particles.

These reactants were chosen due to their anticipated properties based on data from a thermodynamic equilibrium simulation program, REAL code (Timtec, DE), and information from Ref. [3] both applying a constant enthalpy-pressure simulation. Thermal-physical data for stoichiometric conditions are shown below in Table 2 [3].

The Al+CuO composite is predicted to have a high adiabatic flame temperature and high gas production. The Al+NiO reaction was predicted to have a similar flame temperature but much lower gas production. The REAL code data are shown in Fig. 1 as a function of equivalence ratio for reactions in Eqs. (2) and (3). The equivalence ratio (ER) provides a measure of how fuel rich or lean the composition may be and is defined in Eq. (1).

$$ER = \frac{F/O_{act}}{F/O_{sto}} \quad (1)$$

where F/O is the fuel to oxidizer mass ratio and act and sto subscripts represent actual and stoichiometric conditions, respectively. The stoichiometric ratios were calculated from Eqs. (2) and (3).



The reactants were mixed over a range of equivalence ratios in a manner identical to that presented in detail in Refs. [4,5]. Scanning electron micrographs (SEMs) of the mixed reactants are shown in Figs. 2(a) and 2(b).

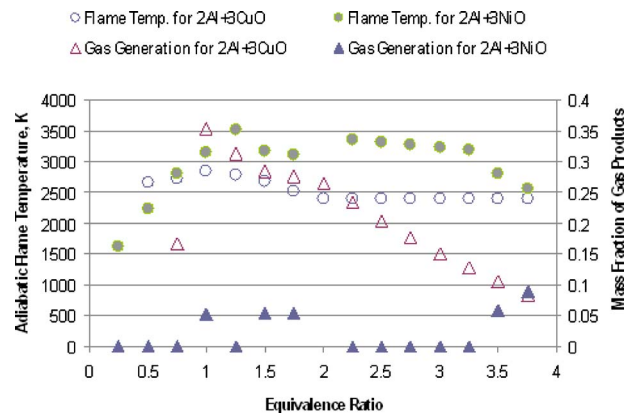
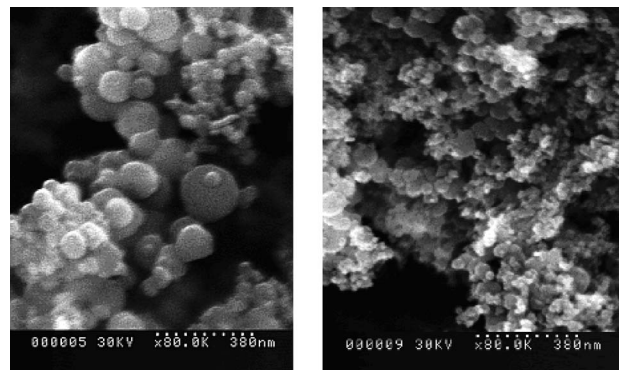
Table 2 Predicted reaction properties [2]

Reaction	Flame temperature (K)	Gas production (mol of gas/100 g)	Heat of reaction (cal/g)
2Al+3CuO	2843	0.5400	974.1
2Al+3NiO	3187	0.0108	822.3

2.2 Confined Burns. An instrumented tube was used to gather data on flame propagation rates and pressures, similar to the “Bockmon tube” reported in Ref. [5]. The tube is machined from 25 mm acrylic rod and 100 mm long with an inner diameter of 3.18 mm. The tube was sealed with vinyl adhesive tape at both ends and Nichrome wire was used as the ignition mechanism. Four 0.19 mm diameter holes were drilled perpendicular to the centerline of the tube to facilitate the acquisition of pressure data.

Once the thermite powder had been prepared; 250 mg was loaded into the tube and placed on a vibrating pad in order to reduce density gradients induced by loading. Time on the vibrating pad was limited to 5–10 s to prevent separation of particle size distributions within the powder mixture. The bulk or tap density for each experiment was approximately 7% of the theoretical maximum density (i.e., loose powder).

After the tube was filled with powder, it was loaded into a steel block with a 25.4 mm diameter hole drilled to accept the tube. The block also had a window milled into its side for the acquisition of flame propagation information by the use of a Phantom 7 (Vision Research) digital high speed camera set to record at 51,000 frames per second. The small holes in the tube were aligned with four PCB Piezotronics model 113A22 piezoelectric pressure sensors

**Fig. 1 REAL code thermochemical simulation for Al+CuO and Al+NiO****Fig. 2 SEM of (a) Al+CuO reactant composite and (b) Al+NiO reactant composite**

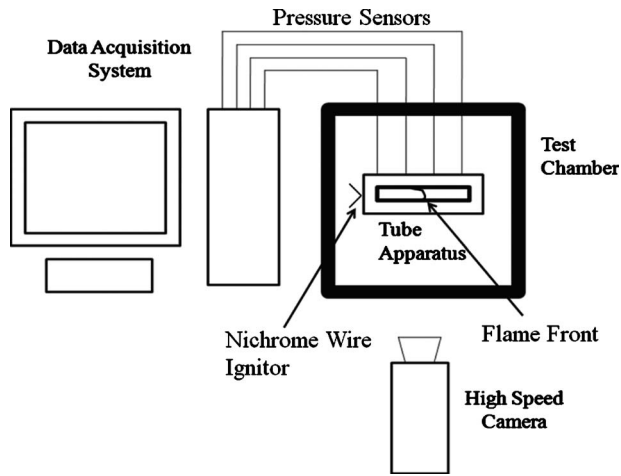


Fig. 3 Schematic showing high speed camera and data acquisition systems

mounted on the block. The steel block was then placed into a steel test chamber for safety purposes, the Nichrome wire in the tube was attached to a power supply, and the chamber was sealed. The pressure in the chamber was then lowered to approximately 63 kPa, the limit of the vacuum system, then backfilled with argon up to atmospheric pressure (approximately 100 kPa). The experimental setup is outlined in Fig. 3.

To initiate a test, first the pressure sensor data acquisition system was engaged through LABVIEW 8.0 (National Instruments, Austin, TX), then the ac transformer attached to the Nichrome wire was turned on which would immediately initiated the reaction. Once the reaction had run to completion the high speed camera was post-triggered to record the previous few seconds of footage.

2.3 Thermal Analysis. In this study a Netzsch STA 409 PC differential scanning calorimeter/thermogravimetric analyzer (DSC/TGA) was used to understand the equilibrium chemical kinetics of the individual reactants. The DSC/TGA was purged with Argon (Ar) during the tests. All samples were run in Platinum (Pt) crucibles with alumina liners. The samples were heated either to 1000 °C or 1400 °C at a rate of 10 deg per minute.

3 Results

3.1 Confined Burn Results. Figure 4 shows a series of still images taken from an Al+CuO test at an ER of 2.5. The vertical

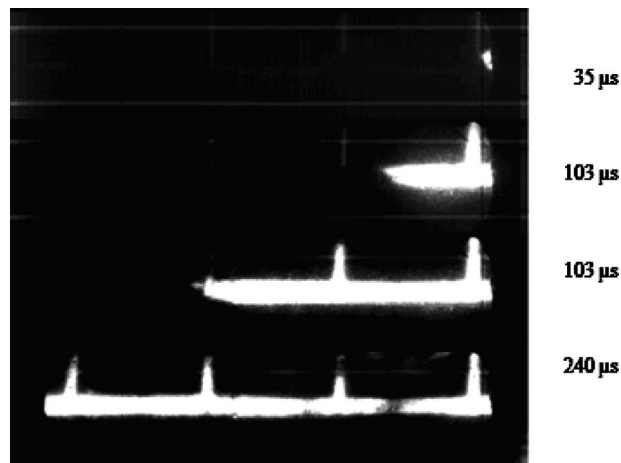


Fig. 4 Still frame images from an Al+CuO test

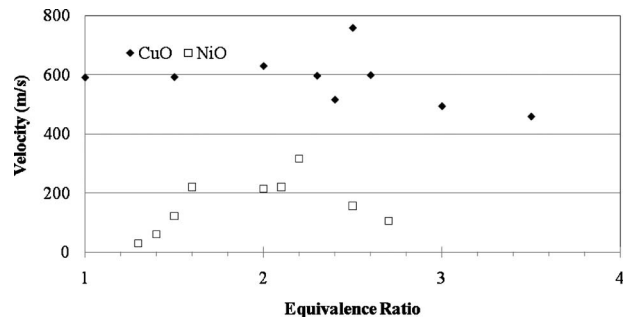


Fig. 5 Flame propagation results for Al+CuO and Al+NiO composites

lines in the image are from hot gasses propagating through the small holes used to collect pressure data. Figures 5 and 6 detail the flame propagation and peak pressure with each data point corresponding to a single test. Multiple tests at each equivalence ratio were not performed due to a lack of raw materials. As a result average trends were identified in the data for the range of equivalence ratios instead of noting peak or specific values at a specified equivalence ratio.

These velocity and pressure results are summarized in Table 3. The uncertainty corresponds to one standard deviation from the average value. Equivalence ratios less than 1.5 were not taken into account for the Al+NiO reaction as these appear to be near the flammability limit of the thermite.

3.2 DSC/TGA Results. Results from DSC/TGA tests are shown in Figs. 7 and 8. Figure 7 shows the reaction of 50 nm Al and NiO. The graph shows what may be a two stage reaction with the first exotherm at 501 °C while the second starts at 645 °C. The reaction between 50 nm Al and CuO is shown in Fig. 8. The exothermic reaction begins at 522 °C.

3.3 XRD Results. The XRD analysis performed on the sol-gel synthesized NiO sample showed that it was largely crystalline with some amorphousness present. The average particle size was between 11 nm and 14 nm. The d-spacing of the NiO was slightly larger than that for bulk NiO. The XRD data show the NiO material possesses crystalline structure and exhibit the characteristic peaks, which correspond to the rock slat NiO. A small deviation of the peak positions compared with the standard is attributed to the

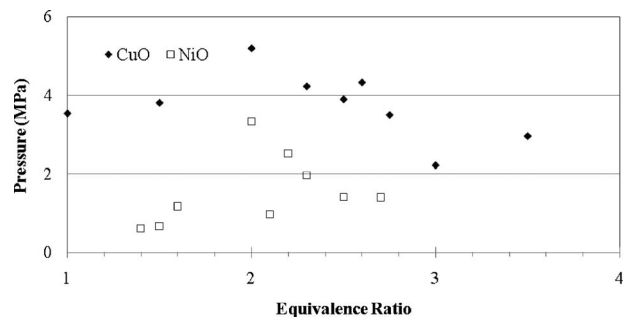


Fig. 6 Peak pressure results for Al+CuO and Al+NiO composites

Table 3 Summary of velocity and peak pressure results

Composite	Velocity (m/s)	Peak pressure (MPa)
Al+CuO	582.9 ± 87.6	3.74 ± 0.85
Al+NiO	193.7 ± 72.2	1.68 ± 0.88

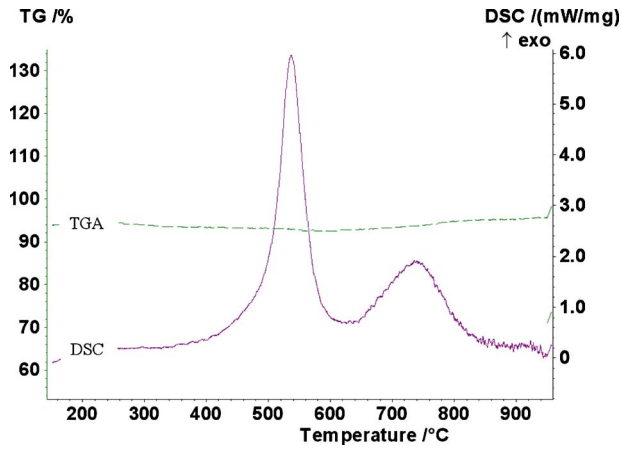


Fig. 7 Heat flow and mass loss curves from the DSC/TGA for Al+NiO at an equivalence ratio of 1.6

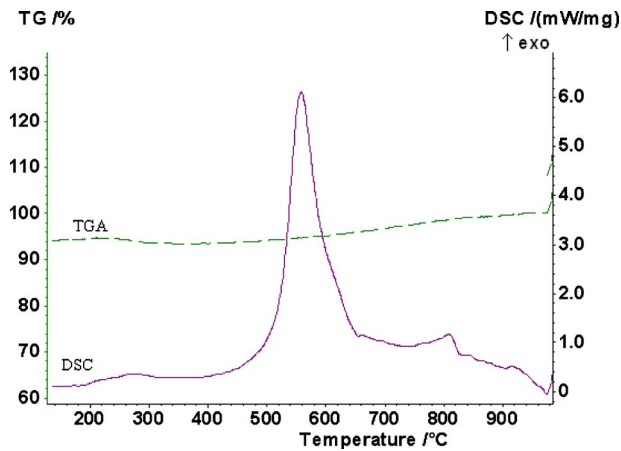


Fig. 8 Heat flow and mass loss curves from the DSC/TGA for Al+CuO at an equivalence ratio of 1.6

method of material preparation and could be due to nonideal stoichiometry. The peak broaden is due to the small crystallite size. No significant contaminates were found in the powder. The intensity- 2θ graph is shown in Fig. 9.

4 Discussion

The instrumented flame tube results show that the Al+CuO reaction produced high peak pressures and flame propagation rates, which were expected. The Al+NiO reaction however, had much higher peak pressures than expected, as well as much faster propagation rates, which were unexpected since the reaction generates virtually no gas. The high peak pressures observed in the Al+NiO reaction are indicative of rapid fluid movement. This fluid movement also enhances convective heat transfer, and this increase in the convective mode of energy propagation leads to higher flame propagation rates. Pressurization rates for both thermites were also comparable: 19.3 GPa/s and 6.04 GPa/s for the Al+CuO and Al+NiO reactions, respectively. There is a relationship between pressurization rate and propagation speed. Bockmon et al. [5], Sanders et al. [6] and Malchi et al. [7] showed that the peak pressure correlates with flame propagation. All of these studies use an instrumented flame tube (similar to the apparatus used here) to simultaneously collect pressure and optical signals. While an explicit correlation may not exist the general trend shows higher pressurization rates are indicative of higher propagation rates. This trend is consistent with the results summarized in Table 3.

The DSC/TGA traces for both thermites in Figs. 7 and 8 show exothermic activity but no mass loss, which corresponds to no gas generation. In these equilibrium DSC/TGA experiments, the temperature is controlled, which prevents thermal runaway of the reaction. Since the reaction does not approach a temperature high enough to boil the products of the reaction, no gaseous products are produced and this result is reflected in the TGA curve showing no sample mass loss. These data confirm that the Al-NiO does not produce gas (Table 4).

The very low heating rate used in the DSC/TGA also prevents the recently proposed melt-dispersion mechanism [8–10] from be-

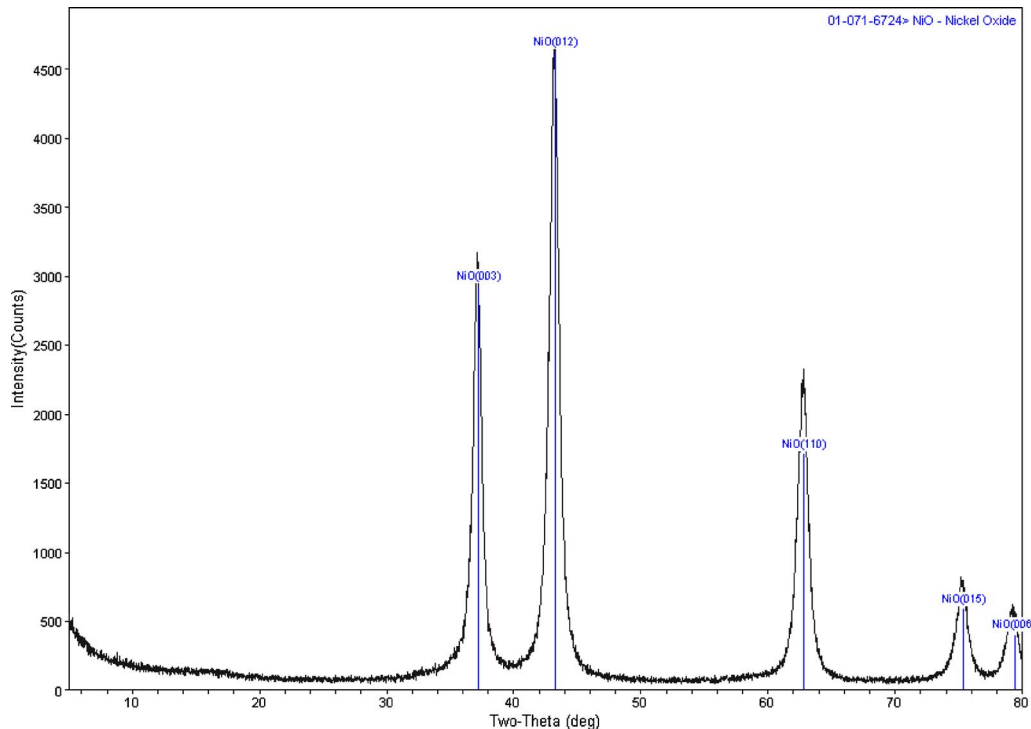


Fig. 9 XRD graph of intensity versus 2θ for the sol-gel synthesized NiO powder

Table 4 Mass losses observed in DSC/TGA tests

Composite	Mass change (%)
CuO	-13.3
NiO	-3.6
Al+CuO	5.45
Al+NiO	0

ing engaged. In this reaction mechanism, which is only applicable to nanoscaled aluminum fueled composites undergoing fast heating, the high strength of the alumina shell and the low thermal inertia of the nanoscaled particles lead to the Al core melting while the alumina shell is still intact. This phase change is accompanied by a 6% volume increase, which causes extremely high stresses to develop in the alumina shell. Once the stress in the shell has reached a critical value, the shell spallates and an unloading pressure wave in the molten Al core causes small liquid Al clusters to be dispersed at high speed [8–10].

One potential explanation for the high peak pressures observed in the Al+NiO instrumented tube tests is that the spallation of the alumina shell and dispersion of molten Al clusters leads to advection of interstitial gasses inside the tube in much the same way that the explosion of a fragmentation grenade leads to the formation of a high pressure shockwave, albeit on a much smaller scale and with much less force. In this way the high observed pressures are not caused by gas generation, a thermodynamic effect but by rapid fluid movement, a physical effect. This explanation is equally valid for the Al+CuO reaction. Here, the thermodynamic and physical effects combine to produce higher peak pressures than those seen in the Al+NiO.

Recently, in Weismiller et al. [11], Al–CuO was examined at pressures between 0–9 MPa (~0 MPa corresponding to vacuum conditions). In an argon environment they observed increased velocities (roughly 200–400 m/s greater than ambient initial pressure conditions). Although they did not examine the nongas generating thermite (i.e., Al–NiO) their results imply that even under vacuum, convective influences from gases produced during reaction can increase flame propagation compared with nonvacuum conditions.

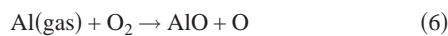
A mathematical model has been developed to assess the reasonableness of the gas phase reaction propagation contributing to enhanced convection. The model assumes that nanometric Al particles react with oxygen from the oxidizer in the gas phase under laminar premixed flame conditions. According to this theory, the flame speed can be calculated from Eq. (4) [12].

$$S_L = \left[-2\alpha(\nu + 1) \frac{\bar{m}_F^m}{\rho_u} \right]^{1/2} \quad (4)$$

where

$$\nu = \left(\frac{m_{\text{air}}}{m_{\text{fuel}}}_{\text{stoic}} \right) \quad (5)$$

Many researchers assume that the solid oxidizer is in the gas phase prior to reaction such that Al oxidation is controlled by Eq. (6) [13–15] and used to determine $\nu=3.8174$.



Equations (7)–(9) are used to calculate reaction kinetics [12].

$$\bar{m}_F^m = \bar{w}_F M W_F \quad (7)$$

$$\bar{w}_F = \frac{d[\text{Al}]}{dt} = -k_g[\text{Al}][\text{O}_2] \quad (8)$$

$$\kappa = A \exp\left(-\frac{E_a}{R_u \bar{T}}\right) \quad (9)$$

The gas phase pre-exponential factor (A) and activation energy (E_a) are obtained from literature [14] and reproduced in Eq. (10) at a combustion temperature $T_g=3200$ K in Ref. [14].

$$\kappa = 9.76 \times 10^{13} \exp(-80/T_g) \text{ cm}^3/(\text{mol s}) \quad (10)$$

where κ is, thus, obtained as $9.52 \times 10^{13} \text{ cm}^3/(\text{mol s})$.

The concentrations of species are determined from Eqs. (11) and (12).

$$[\text{Al}] = x_{\text{Al}} \frac{P}{R_u \bar{T}} \quad (11)$$

$$[\text{O}_2] = x_{\text{O}_2} \frac{P}{R_u \bar{T}} \quad (12)$$

In the above equations, $x_{\text{Al}}=x_{\text{O}_2}=0.5$, $P=1.5 \times 10^6$ Pa, and $R_u=8.315$ J/mol K

$$\bar{T} = \frac{1}{2} \left(\frac{1}{2}(T_b + T_u) + T_b \right) \quad (13)$$

The average temperature is calculated based on the definition in Ref. [12]. The mean temperature \bar{T} is calculated as $\bar{T}=2169$ K from Eq. (13), where $T_b=T_{b,\text{Al}}=2792$ K and $T_u=300$ K. From Eqs. (11) and (12), $[\text{Al}]=[\text{O}_2]=0.0416$ k mol/m³ and from Eqs. (7)–(9) $\bar{w}_F=-1.6473 \times 10^8$ k mol/m³ s and $\bar{m}_F^m=-4.4444 \times 10^9$ kg/m³ s.

The calculated flame speed (S_L) is $S_L=560$ m/s a very good comparison to the measured values reported here (Table 3). However, the reaction kinetics reported for a solid-state diffusion-controlled rate equation does not compare well with the flame speed measurements here. Park et al. [16] reported kinetic parameters $E_a=104.8$ kJ/mol and $A=5.0 \times 10^3$ (1/s) for condensed phase Al reactions. When these Arrhenius parameters are put into the above equations, a flame speed of $S_L=0.1002$ m/s is obtained. These results suggest that modeling reaction propagation as gas phase premixed combustion more accurately describes the experimental results as opposed to a solid, nongas generating reaction. This finding is consistent with the melt-dispersion mechanism, which theorizes that oxidation is accelerated by molten Al droplets that are aerosolized from the original Al particle. While the Al–NiO is a nongas generating reaction, flame propagation can be modeled in the gas phase implying that reaction propagation proceeds according to the melt-dispersion mechanism, which aerosolizes the reactants thereby enhancing convection.

Other possible explanations for the high peak pressures seen in the Al+NiO reaction may involve the composition and phase of the NiO material. The d-spacing results from XRD analysis suggest that the material may be in a metastable phase that could decompose into Ni and O when exposed to high temperatures. Under the slow heating rates of the DSC/TGA, however, no such decomposition was observed. The small amorphous content of the NiO observed in XRD may also contain organic compounds left over from the sol-gel synthesis process although the decomposition and out gassing of these compounds was not observed in the DSC/TGA. The rapid expansion of interstitial gas in the tube due to the high flame temperatures associated with these reactions may also contribute to the observed pressures [17–19].

Figure 10 shows a schematic of some currently known combustion regimes, highlighting the dependence of propagation rate on particle size. The schematic shows the mechanisms for reaction and modes of energy propagation, as well as some examples of composites that exhibit that behavior. The velocity ranges given in the schematic are exclusive to the instrumented tube diagnostic described here with the exception of the monomolecular bond

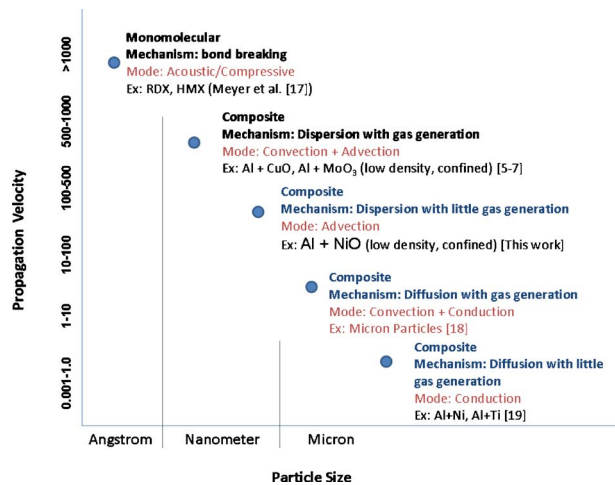


Fig. 10 Schematic of combustion regimes

breaking entry. An entry for nanoscale composites that do not normally exhibit gas generation has been added to the graph between the diffusion regime that controls micron scale reactions and the dispersion with gas generation regime that describes reaction behavior at the nanoscale for gas producing composites. The inclusion of this new dispersion without gas generation regime opens the potential for greater customization toward the thermite applications. Specifically, this study reveals that nongas producing thermites may provide power on par with gas producing thermites if the melt-dispersion mechanism is activated to induce bulk fluid movement and enhance convection. This finding may have implications for applications where noncollateral damage is preferred but high reactivity and exothermicity are desired.

5 Conclusions

A series of tests were conducted on two different nanoscaled thermites, Al+CuO and Al+NiO, at different equivalence ratios. The Al and CuO were obtained from commercial sources; the NiO was synthesized at LLNL using a sol-gel technique. Using an instrumented flame tube apparatus average values for flame propagation rate and peak pressure were determined for a range of equivalence ratios. Average velocities recorded for the Al+CuO and Al+NiO were 582.9 ± 87.6 m/s and 205.5 ± 71.2 m/s, respectively. Average peak pressures recorded were 3.75 ± 0.85 MPa for the Al+CuO and 1.83 ± 0.89 MPa for the Al+NiO. The Al+NiO flame speed and peak pressure were unexpected as it was predicted to evolve almost no gas and have a very low flame propagation rate. Slow heating experiments were also conducted on the thermites and individual reactants using a DSC/TGA. These tests showed that the reactants were pure and that the thermites produce no gas under thermal equilibrium conditions.

The large amount of gas generated by the Al+NiO reaction under high heating rates was potentially explained as a forced convective wave created by the bulk movement of aerosolized molten Al clusters released during the rupture of aluminum particles brought about by the melt-dispersion mechanism.

The gas generation properties for both reactions were determined to be significantly dependant on heating rate. When heated quickly in the instrumented flame tube significant peak pressures were noted in both thermites while slow heating in the DSC/TGA led to no appreciable mass loss.

This is the first study to show that thermites that had previously been predicted to have no significant gas production can in fact produce reactivity (measured in terms of flame speed and peak pressure) on the same order of magnitude as their gas producing counterparts due to new reaction mechanisms possible for nano-

scale particles under high heating rate conditions. As shown in newly presented Fig. 10, this newly proposed reaction mechanism based on dispersion can enhance convection and generate propagation rates comparable to those of gas producing nanoscaled thermites and far in excess of micron scaled thermites. Identifying the propagation modes related to different regimes will enable greater tuneability of reactants to applications.

Acknowledgment

The authors gratefully acknowledge support from the Army Research Office under Contract No. W911NF-04-1-0217 and Dr. Ralph Anthenien. William Bender, a high school student participating in the Clark's Scholar summer research program at Texas Tech University is also acknowledged for his assistance in conducting the Al+NiO instrumented tube tests. Dr. Gash acknowledges that portions of this work were performed under the auspices of the U.S. Department of Energy by Lawrence Livermore National Laboratory under Contract No. DE-AC52-07NA27344.

Nomenclature

α	= thermal diffusivity
κ	= reaction rate constant
k_g	= thermal conductivity of gas
ρ_u	= density of unburned gas
A	= pre-exponential factor
$[Al]$	= aluminum concentration
$[O_2]$	= oxygen concentration
E_a	= activation energy
\bar{m}_F^m	= mass production rate of the fuel
P	= pressure
R_u	= universal gas constant
S_L	= flame speed
\bar{T}	= average temperature
T_b	= boiling temperature of Al
T_u	= temperature of unburned gas
x	= mole fraction

References

- Wang, L. L., Munir, Z. A., and Maximov, Y. M., 1993, "Thermite Reactions: Their Utilization in the Synthesis and Processing of Materials," *J. Mater. Sci.*, **28**, pp. 3693–3708.
- Harrison, J., and Brewster, M. Q., 2009, "Analysis of Thermal Radiation From Burning Aluminum in Solid Propellants," *Combust. Theory Modell.*, **13**(3), pp. 389–411.
- Fischer, S. H., and Grubelich, M. C., 1998, "Theoretical Energy Release of Thermites, Intermetallics and Combustion Metals," 24th International Pyrotechnics Seminar, Monterey, CA.
- Granier, J. J., and Pantoya, M. L., 2004, "Laser Ignition of Nanocomposite Thermites," *Combust. Flame*, **138**, pp. 373–383.
- Bockmon, B. S., Pantoya, M. L., Son, S. F., Asay, B. W., and Mang, J. T., 2005, "Combustion Velocities and Propagation Mechanisms of Metastable Interstitial Composites," *J. Appl. Phys.*, **98**, p. 064903.
- Sanders, V. E., Asay, B. W., Foley, T. J., Tappan, B. C., Pacheco, A. N., and Son, S. F., 2007, "Reaction Propagation of Four Nanoscale Energetic Composites (Al/MoO₃, Al/WO₃, Al/CuO and Al/Bi₂O₃)," *J. Propul. Power*, **23**(4), pp. 707–714.
- Malchi, J. Y., Foley, T. J., Son, S. F., and Yetter, R. A., 2008, "The Effect of Added Al₂O₃ on the Propagation Behavior of an Al/CuO Nano-Scale Thermite," *Combust. Sci. Technol.*, **180**, pp. 1278–1294.
- Levitas, V. I., Asay, B., Son, S. F., and Pantoya, M. L., 2007, "Mechanochemical Mechanism for Fast Reaction of Metastable Intermetallic Composites Based on Dispersion Of Liquid Metal," *J. Appl. Phys.*, **101**, p. 083524.
- Levitas, V. I., Asay, B. W., Son, S. F., and Pantoya, M. L., 2006, "Melt Dispersion Mechanism for Fast Reaction of Nanothermites," *Appl. Phys. Lett.*, **89**, p. 071909.
- Levitas, V. I., Pantoya, M. L., and Dikici, B., 2008, "Melt Dispersion Versus Diffusive Oxidation Mechanism for Aluminum Nanoparticles: Critical Experiments and Controlling Parameters," *Appl. Phys. Lett.*, **92**, p. 011921.
- Weismiller, M. R., Malchi, J. Y., Yetter, R. A., and Foley, T. J., 2009, "Dependence of Flame Propagation on Pressure and Pressurizing Gas for an Al/CuO Nanoscale Thermite," *Proc. Combust. Inst.*, **32**, pp. 1895–1903.
- Turns, S. R., 2000, *An Introduction to Combustion: Concepts and Applications*, 2nd ed., McGraw-Hill, New York.
- Kwon, Y.-S., Gromov, A., Ilyin, A. P., Popenko, E. M., and Rim, G.-H., 2003,

- "The Mechanism of Combustion of Superfine Aluminum Powders," *Combust. Flame*, **133**, pp. 385–391.
- [14] Poletaev, N. I., and Florko, A. V., 2008, "Spectral Studies of the Gas Component of an Aluminum Dust Flame," *Combustion Explos. Shock Waves*, **44**(4), pp. 437–443.
- [15] Law, C. K., 1973, "A Simplified Theoretical Model for the Vapor-Phase Combustion of Metal Particles," *Combust. Sci. Technol.*, **7**, pp. 197–212.
- [16] Park, K., Lee, D., Rai, A., Mukherjee, D., and Zachariah, M. R., 2005, "Size Resolved Kinetic Measurements of Aluminum Nanoparticle Oxidation With Sing Particle Mass Spectrometry," *J. Phys. Chem. B*, **109**(15), pp. 7290–7299.
- [17] Meyer, R., Köhler, J., and Homburg, A., 2002, *Explosives*, 5th ed., Wiley-VCH, Weinheim.
- [18] Watson, K. W., Pantoya, M. L., and Levitas, V. I., 2008, "Fast Reactions With Nano and Micron Aluminum: A Study on Oxidation Versus Fluorination," *Combust. Flame*, **155**(4), pp. 619–634.
- [19] Hunt, E. M., Plantier, K. B., and Pantoya, M. L., 2004, "Nano-Scale Reactants in the Self Propagating High Temperature Synthesis of Nickel Aluminide," *Acta Mater.*, **52**(11), pp. 3183–3191.

Numerical Simulations of the Dynamics and Heat Transfer Associated With a Single Bubble in Subcooled Pool Boiling

Jinfeng Wu

Vijay K. Dhir¹

e-mail: vdhir@seas.ucla.edu

Department of Mechanical and Aerospace
Engineering,
Henry Samueli School of Engineering and
Applied Science,
University of California, Los Angeles,
Los Angeles, CA 90095

In this study, numerical simulations of a vapor bubble in subcooled pool boiling have been performed. The applied numerical procedure coupling level-set function with moving mesh method has been validated by comparing the results of bubble-growth history including bubble departure diameter with data from experiments. The predictions of bubble dynamics and heat transfer for various subcoolings as well as different gravity levels are presented. [DOI: 10.1115/1.4002093]

Keywords: subcooled nucleate boiling, level-set method, moving mesh method, numerical simulation, condensation

1 Introduction

Nucleate boiling is a liquid-vapor phase-change process associated with bubble formation on the heated surface. As it is a very efficient mode of heat transfer, the boiling process has attracted the attention of many researchers in the past. Subcooled nucleate pool boiling exists when the bulk temperature of the liquid pool is below the saturation temperature of the liquid at the given system pressure, and the temperature of the heating surface exceeds the nucleation temperature, which is higher than the saturation temperature.

A key parameter in determining the heat transfer coefficient under subcooled nucleate boiling conditions is the liquid subcooling itself. Gunther and Kreith [1] reported that bubbles ceased to detach as the liquid subcooling was increased. Ramanujapu [2] experimentally studied the dynamics of a single bubble under subcooled boiling conditions up to 5.5°C of subcooling. He observed that a bubble grew to a maximum size and then shrank a little before it detached. In some of the tests, it was observed that the bubble oscillated (expanded and contracted) for a while before departing. Based on those experiments, Ramanujapu and Dhir [3] also reported dynamics of contact angle during bubble growth and departure. Singh [4] numerically confirmed that for certain wall superheats and low liquid subcoolings, a bubble does depart at a size that is smaller than its maximum value during its growth process. However, for high subcoolings, bubbles do not detach from the wall.

Various studies have also been carried out to examine reduced gravity effects on boiling heat transfer. Siegel and Keshock [5] employed a drop tower to study bubble dynamics under gravity fields in the range from 1.4% to 100% of earth-normal gravity. They observed that bubbles became quite large and the growth times were longer in reduced gravity in comparison to those at terrestrial conditions. However, the test duration of about 1 s could not guarantee that test conditions, including the flow field and temperature distribution, were identical to that for time independent low gravity conditions. Straub et al. [6] carried out a series of boiling experiments with heaters of different geometries at low gravity in ballistic rocket flights (TEXUS program, $g/g_e < 10^{-4}$) and in parabolic flights of KC 135 aircraft. The authors

reported several bubble-growth histories for R-113 at $g/g_e < 10^{-4}$ and departure diameters for R-12 bubbles at both earth-normal gravity and $g/g_e \approx 10^{-2}$. The authors proposed that evaporation at the base of a bubble was the primary heat transfer mechanism. Oka et al. [7] reported pool boiling experiments of *n*-pentane at gravity levels of ± 0.005 to $0.05g_e$ during parabolic flights. According to their observation, the bubble size could range from 5 mm to 50 mm after bubble coalescence so as to almost cover the entire heating surface for $\Delta T_w = 19^\circ\text{C}$ and $\Delta T_{\text{sub}} = 9^\circ\text{C}$. The authors also noted that the bubble oscillation enabled continuous supply of the liquid from the bulk to the wall. Qiu and Dhir [8] presented an experimental study on growth and detachment of a single bubble on a heated surface with water as the test fluid for $0.04g_e$. Bubble growth time, bubble size, and shape from nucleation to lift-off were measured under subcooled and saturated conditions. In the limited range of wall superheats and liquid subcoolings, the effects of wall superheat and liquid subcooling on bubble lift-off diameter were found to be small; however, the growth periods were very sensitive to liquid subcooling at a given wall superheat. They also showed that for saturated liquid, bubble departure diameter approximately varied as $g^{-1/2}$ and growth period changed about inversely with the level of gravity. Son et al. [9] presented a bubble-growth model based on the level-set method, which has been proven to be quite effective in correlating the experimental data. The model developed by Son et al. [9] laid a foundation for the current work.

In the present study, a numerical procedure, which is capable of redistributing the mesh and sustains a high node density around the interface as the bubble grows, is used to model the process during subcooled nucleate boiling under various gravity levels. This approach is used to obtain a higher degree of accuracy in calculating the liquid side heat transfer.

2 Numerical Formulation

2.1 Model Description. To analyze the growth of a single bubble in subcooled nucleate boiling, we extend the numerical model originally developed by Son et al. [9]. In that model, the computational domain was divided into two parts: a microregion and a macroregion, as shown in Fig. 1. The microregion is a thin film that lies underneath the bubble, whereas the macroregion consists of the bubble and the liquid surrounding the bubble. In the present work, numerical simulations of fluid flow and heat transfer are carried out in both micro- and macroregions for a

¹Corresponding author.

Contributed by the Heat Transfer Division of ASME for publication in the JOURNAL OF HEAT TRANSFER. Manuscript received June 16, 2009; final manuscript received June 21, 2010; published online August 10, 2010. Assoc. Editor: Satish G. Kandlikar.

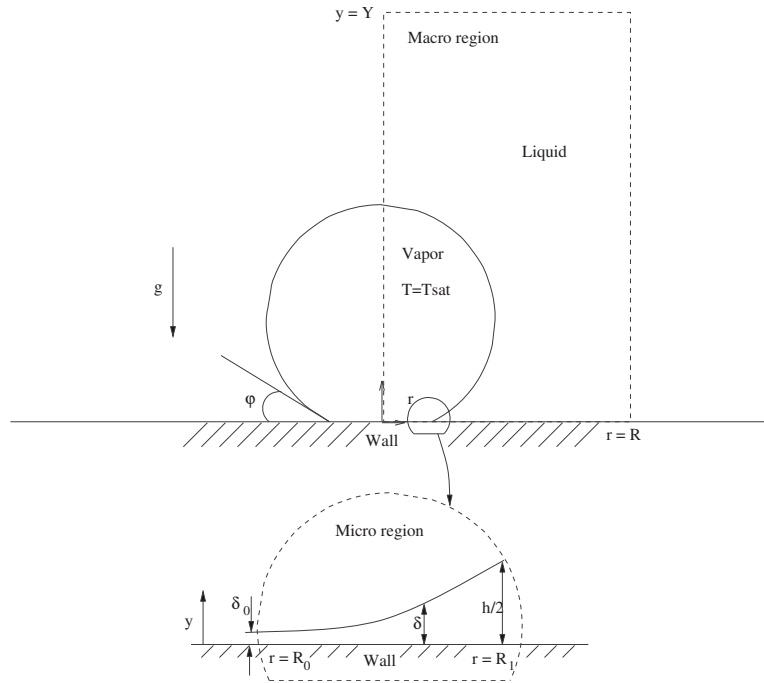


Fig. 1 Macro- and microregions in numerical simulation

given contact angle. The computed shape of the interface in the microregion and the macroregion is matched at the outer edge of the microlayer. In the numerical simulation, a level-set function is used to represent the shape of the interface in the macroregion.

2.2 Assumptions. The following assumptions are made in this study:

- the process is two-dimensional and axis-symmetric;
- the flows are laminar;
- the wall temperature remains constant;
- water at atmospheric pressure is used as the test fluid;
- vapor remains at its saturation temperature;
- the thermodynamic properties of the individual phases are assumed to be insensitive to small changes in temperature and pressure except for surface tension.

For a constant heat flux surface, the temperature of the solid wall will vary because of the spatial and temporal dependences of the liquid side heat transfer coefficient [10]. To resolve the variation in temperature, one must solve conjugate heat transfer problem in the solid. In the present work, the temperature of the solid is assumed to remain constant with the premise that effect of temperature variation on bubble dynamics will be of second order.

2.3 Thermal and Physical Properties. The thermal and physical properties used in carrying out the computation are listed in Table 1. All properties are evaluated for water at atmospheric

Table 1 Thermal and physical properties

Property	Unit	Liquid	Vapor
ρ	kg/m ³	958	0.598
c_p	kJ/kg K	4.212	2.02
k	W/m K	0.68	0.0248
μ	m ² /s	2.85×10^{-4}	1.2×10^{-5}
h_{fg}	kJ/kg	2257	
T_{sat}	K		373.15
β	K ⁻¹	7.5×10^{-4}	
σ	N/m	0.0589	

pressure and saturation temperature of 100°C.

2.4 Governing Equations for the Macroregion. To numerically analyze the macroregion, we use the level-set formulation developed by Son et al. [9] for nucleate boiling of pure liquid. The interface separating the two phases is captured by solving the following equation for the level-set function, ϕ :

$$\frac{\partial \phi}{\partial t} = -\mathbf{u}_{int} \cdot \nabla \phi \quad (1)$$

where

$$\mathbf{u}_{int} = \mathbf{u} + \frac{\mathbf{m}}{\rho} \quad (2)$$

and \mathbf{m} is the evaporation/condensation-rate vector through the bubble interface (see Ref. [9] for details). Reinitialization equation for ϕ is solved until steady state is reached to ensure that $|\nabla \phi| = 1$:

$$\frac{\partial \phi}{\partial t} = \text{sign}(\phi_0)(1 - |\nabla \phi|) \quad (3)$$

In the above equation, ϕ_0 is the solution of Eq. (1). The material properties are assumed to be constant in the individual phases, except near the interface and in a thin region around the interface. To describe such an interface, we define the Heaviside function, H , as follows:

$$H = 1 \quad \text{if } \phi \geq +1.5h$$

$$= 0 \quad \text{if } \phi \leq -1.5h \quad (4)$$

$$= 0.5 + \phi/(3h) + \sin[2\pi\phi/(3h)]/(2\pi) \quad \text{if } |\phi| \leq 1.5h$$

where h is equal to the grid spacing on a uniform grid, and H is 1 in the liquid phase and 0 in the vapor phase. The interface is spread over an interval of $3h$, so that the material properties change continuously at the interface. In terms of H , the properties of interest are defined as follows:

$$\rho = \rho_v + (\rho_l - \rho_v)H \quad (5)$$

$$\mu^{-1} = \mu_v^{-1} + (\mu_l^{-1} - \mu_v^{-1})H \quad (6)$$

$$k^{-1} = k_l^{-1}H \quad (7)$$

where ρ , μ , and k denote the density, the fluid viscosity, and the thermal conductivity, respectively. The subscripts v and l represent the vapor and liquid phases, respectively. Also, Eq. (7) is consistent with the assumption that the vapor temperature remains constant at T_{sat} .

The interfacial curvature is expressed in terms of the level-set function as follows:

$$\kappa = \nabla \cdot \frac{\nabla \phi}{|\nabla \phi|} \quad (8)$$

The governing equations of continuity, momentum, and energy conservation for the macroregion are

$$\frac{\partial \rho}{\partial t} + \nabla \cdot (\rho \mathbf{u}) = 0 \quad (9)$$

$$\rho \left(\frac{\partial \mathbf{u}}{\partial t} + \mathbf{u} \cdot \nabla \mathbf{u} \right) = -\nabla p + \rho \mathbf{g} - \rho \beta_T (T - T_{\text{sat}}) \mathbf{g} - \sigma \kappa \nabla H + \nabla \cdot \mu \nabla \mathbf{u} + \nabla \cdot \mu \nabla \mathbf{u}^T \quad (10)$$

$$\rho c_{pl} \left(\frac{\partial T}{\partial t} + \mathbf{u} \cdot \nabla T \right) = \nabla \cdot k \nabla T \quad \text{for } H > 0$$

$$T = T_{\text{sat}}(p_v) \quad \text{for } H = 0 \quad (11)$$

Since the vapor in the bubble was assumed to remain at the saturation temperature, the energy equation in the vapor is not solved.

The mass conservation equation Eq. (9) can be rewritten, while noting that $\partial \rho / \partial t = -\mathbf{u}_{\text{int}} \cdot \nabla \rho$, as,

$$\nabla \cdot \mathbf{u} = \frac{\dot{m}}{\rho^2} \cdot \nabla \rho + \dot{V}_{\text{micro}} = \frac{k \nabla T}{h_{fg} \rho^2} \cdot \nabla \rho + \dot{V}_{\text{micro}} \quad (12)$$

where \dot{V}_{micro} is the volume addition attributed to the heat transfer from the microlayer, which is

$$\dot{V}_{\text{micro}} = \int_{R_0}^{R_1} \frac{k_l (T_w - T_{\text{int}})}{\rho_v h_{fg} \delta} r dr \quad (13)$$

ΔV_{micro} is a vapor-side control volume near the microregion.

Equations (10)–(12) are nondimensionalized using the characteristic length, time, and velocity scales, l_0 , t_0 , and u_0 , respectively:

$$l_0 = \sqrt{\frac{\sigma}{g(\rho_l - \rho_v)}} \quad (14)$$

$$u_0 = \sqrt{g l_0} = \left[\frac{\sigma g}{(\rho_l - \rho_v)} \right]^{1/4} \quad (15)$$

$$t_0 = \frac{l_0}{u_0} = \left[\frac{\sigma}{g^3 (\rho_l - \rho_v)} \right]^{1/4} \quad (16)$$

The temperature is nondimensionalized such that the wall temperature is 1 and the subcooled liquid temperature is 0, i.e.,

$$\theta = \frac{T - T_l}{T_w - T_l} = \frac{T - T_l}{(T_w - T_{\text{sat}}) + (T_{\text{sat}} - T_l)} = \frac{T - T_l}{\Delta T_w + \Delta T_{\text{sub}}} \quad (17)$$

The governing equations (Eqs. (10)–(12)) are solved throughout the domain to obtain the velocity, temperature, and pressure in each cell. The detailed computational framework is discussed later.

2.5 Governing Equations for the Microregion. This region is illustrated in Fig. 1. The thickness of the microlayer varies from a few molecules at the inner end to a few micrometers near the

outer end, where it joins with the macroregion. Lay and Dhir [11] modeled and numerically solved for the shape of the microlayer underneath a bubble using lubrication theory. In carrying out the analysis, δ is taken to be the thickness of the microlayer measured from the wall, and r is the radial coordinate. The quasistatic mass conservation, momentum, and energy equations in the microlayer are given as

$$q / \rho_l h_{fg} = -\frac{1}{r} \frac{\partial}{\partial r} \int_0^\delta r u dy \quad (18)$$

$$\frac{\partial p_l}{\partial r} = \mu_l \frac{\partial^2 u_l}{\partial y^2} \quad (19)$$

$$q = k_l (T_w - T_{\text{int}}) / \delta = h_{\text{ev}} [T_{\text{int}} - T_v + (p_l - p_v) T_v / \rho_l h_{fg}] \quad (20)$$

where T_w is the wall temperature and T_v is the vapor temperature. T_{int} is the interface temperature, which is approximately T_w at the inner end and T_v at the outer end. A typical profile of T_{int} has been shown in Ref. [9]. Here p_v is the vapor pressure and h_{ev} is the evaporation heat transfer coefficient. The evaporation heat transfer coefficient is obtained from kinetic theory as

$$h_{\text{ev}} = (2M / \pi \bar{R} T_v)^{0.5} \rho_v h_{fg}^2 / T_v, \quad T_v = T_{\text{sat}}(p_v) \quad (21)$$

The pressures in the vapor and liquid phases satisfy the following relation [11]:

$$p_l = p_v - \sigma \kappa - \frac{A}{\delta^3} + \frac{q^2}{\rho_v h_{fg}^2} \quad (22)$$

where surface tension, σ , is a function of temperature, and A is the dispersion constant in the disjoining pressure and its magnitude can be related to the contact angle, which is prespecified for a given liquid-solid combination. In Eq. (22), the second term on the right hand side accounts for the capillary pressure, the third term accounts for the disjoining pressure, and the last term accounts for the recoil pressure. The curvature of the interface is defined as

$$\kappa = \frac{1}{r} \frac{\partial}{\partial r} \left[r \frac{\partial \delta}{\partial r} / \sqrt{1 + \left(\frac{\partial \delta}{\partial r} \right)^2} \right] \quad (23)$$

The combination of the mass, momentum, and energy equations for the microlayer yields

$$\delta''' = f(\delta, \delta', \delta'', \delta''') \quad (24)$$

where ' denotes $\partial / \partial r$.

The boundary conditions for the above equation are imposed as follows:

At $r = R_0$ (inner end of microlayer),

$$\delta = \delta_0, \quad \delta' = \delta'' = 0 \quad (25)$$

where δ_0 is of the order of molecular size and it can be obtained from Ref. [12] at the junction of the evaporating and nonevaporating regions.

At $r = R_1$ (outer end of microlayer),

$$\delta = h/2, \quad \delta' = 0 \quad (26)$$

where h is the grid spacing and $h/2$ is the vertical distance to the first computational node for the level-set function, ϕ , on uniform grids from the wall. In implementing the above boundary conditions, the radius R_1 is determined from the solution of the macroregion. For a given dispersion constant, the microlayer formulation, Eq. (24), and R_0 are solved with the five boundary conditions (Eqs. (25) and (26)). In this work, an apparent contact angle is defined as

$$\tan \varphi = 0.5h / (R_1 - R_0) \quad (27)$$

φ is measurable experimentally and used as boundary conditions in level-set function. Equation (24) is numerically integrated using

a Runge–Kutta method with a separate code. An expression for the rate at which vapor is produced from the microlayer is given in Eq. (13). Within moving meshes, the distance to the first computational node from the wall will no longer be equal to $h/2$ on a uniform grid. It also may vary slightly from time to time. The above equations are still valid when nonuniform grids are used.

3 The Computational Framework

In the current study, a numerical procedure in conjunction with moving mesh method is applied to compute the level-set function. Contravariant velocity components in curvilinear coordinates (ξ, η) are taken as primary variables. For detailed information concerning moving mesh generation and related equations, the reader is referred to Ref. [13]. The resulting equations contain convection terms of the first-order derivatives with respect to ξ, η , and diffusion terms of the second-order derivatives with respect to $\xi\xi, \eta\eta, \xi\eta$, and $\eta\xi$. Taking advantage of the bubble symmetry, we only need to compute one-half of the bubble. We use a staggered-grid finite difference scheme. The scalar parameters are defined at the centers of cells and velocity components are stored at the edges of cells. To easily obtain the discretized forms of various quantities, both Cartesian velocity components and contravariant ones are stored in memory. We use upwind differencing for advection terms and central differencing for diffusion terms. A projection method is used to solve for velocities and pressure. Because the computation for pressure takes most of the computational time, we combine multigrid and conjugate gradient methods so that the numerical solver for pressure converges in less than ten iterations under most circumstances. This in turn results in significant computational savings.

Overall we have the following computational framework:

1. Initialize mesh distribution by solving the mesh equation to steady state. Incorporate level-set function into mesh equation. The resulting mesh would fit well with the initial conditions. It also should be noted that the changes in other variables, such as temperature and temperature gradient, can be easily taken into account in the mesh adaptation process.
2. Update mesh. Using Δt in the mesh equations, solve for one time step to evolve the mesh in forward direction.
3. Solve the level-set advection equation, reinitialize the level-set function, and determine the properties (density, viscosity, and thermal conductivity). The second order essential nonoscillatory (ENO) scheme is applied to discretize ϕ_ξ and ϕ_η . A few iteration steps are used in the reinitialization procedure. We use the interface width of $3h$ to bridge the property difference across the interface.
4. Solve the energy equation for temperature in the liquid. The upwind differencing is used for T_ξ and T_η . The diffusion terms, $T_{\xi\xi}$ and $T_{\eta\eta}$ are implicitly discretized, and $T_{\xi\eta}$ and $T_{\eta\xi}$ are continuously updated by the current iteration until convergence.
5. Solve the momentum equation for intermediate velocities using the pressure at the previous time step.
6. Solve the Poisson equation for pressure. The governing equation for pressure contains \dot{V}_{micro} . Under the assumptions of constant wall temperature and constant contact angle, \dot{V}_{micro} is a function of the distance between the first computational node and the wall. This function is obtained from solution of microlayer beforehand and is incorporated into this numerical procedure. During each time step, the average distance of several first computational nodes along the wall at the interface region is used to retrieve the corresponding microlayer heat transfer.
7. Correct the velocities corresponding to the updated pressure. This ensures that the continuity equation is satisfied.
8. Go to step 2 for the next time step.

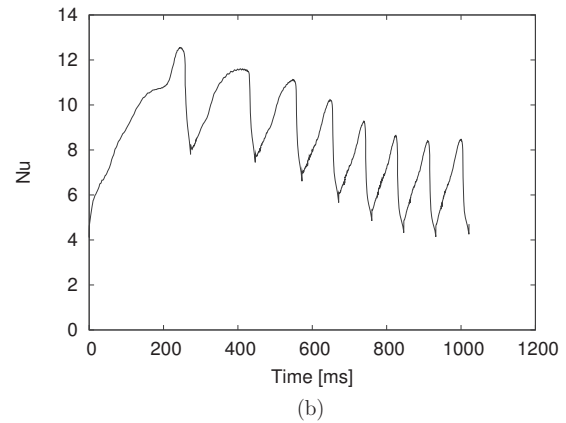
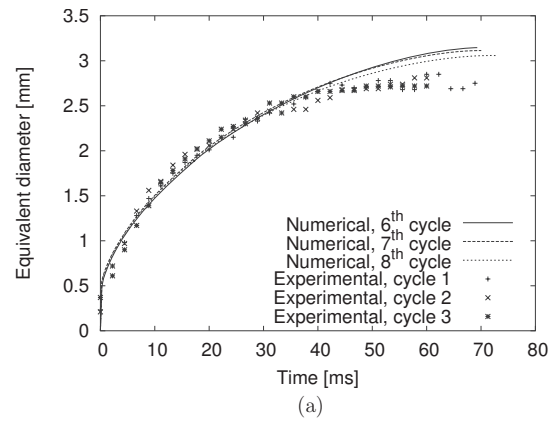


Fig. 2 (a) Growth rate. (b) Nu versus time for wall superheat = 7 °C, liquid subcooling = 1.5 °C, contact angle = 54 deg, pressure = 1.013 × 10⁵ Pa, and g/g₀ = 1.

3.1 Boundary Conditions. At the wall ($y=0$),

$$u = 0, \quad v = 0, \quad \frac{\partial \phi}{\partial y} = -\cos \varphi, \quad T = T_w \quad (28)$$

At the top of computational domain ($y=Y$),

$$\frac{\partial u}{\partial y} = 0, \quad \frac{\partial v}{\partial y} = 0, \quad \frac{\partial \phi}{\partial y} = 0, \quad T = T_l \quad (29)$$

At the planes of symmetry ($r=0, R$),

$$u = 0, \quad \frac{\partial v}{\partial r} = 0, \quad \frac{\partial \phi}{\partial r} = 0, \quad \frac{\partial T}{\partial r} = 0 \quad (30)$$

3.2 Initial Conditions. Initially, the fluid velocity is set to zero. The temperature profile is taken to be linear in the natural convection thermal boundary layer, and its thickness, δ_T , is given by Kays and Crawford [14]:

$$\delta_T = 7.14(v_l \alpha_l / g \beta_T (T_w - T_l))^{1/3} \quad (31)$$

4 Validation

To validate this moving mesh method coupled with level-set function, we studied the case of bubbles rising in a quiescent liquid and compared the results to those given by Ryskin and Leal [15] and Son [16]. A phase-change problem with an analytical solution described in Ref. [17] was also used to test the capability of our method to include heat transfer. The numerical results for these two cases are reported in Ref. [13]. The results of numerical simulations reported here are also validated by comparing the results with the experimental data.

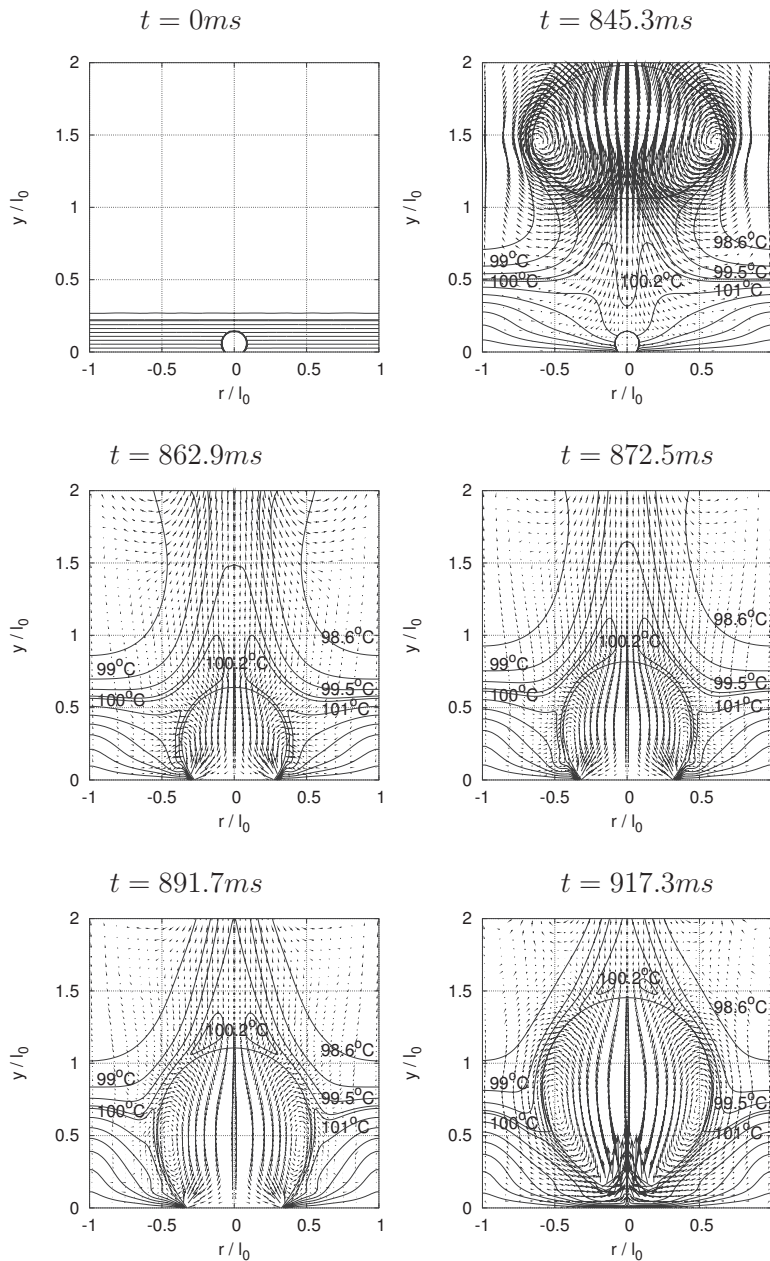


Fig. 3 Flow field and temperature distribution for wall superheat= 7°C , liquid subcooling= 1.5°C , contact angle= 54 deg, pressure= 1.013×10^5 Pa, and $g/g_e=1$

In carrying out numerical simulation, the computational domain is chosen to be $(R/l_0, Y/l_0)=(1,3)$ for a series of bubbles and $(R/l_0, Y/l_0)=(1,2)$ for a single cycle in most cases except for $g/g_e=0.0001$, to minimize the effects of the computational boundary and save computation time. The initial bubble size is determined by the size of grid spacing, which is $D/l_0=0.01$ for normal gravity and $g/g_e=0.01$. The details for $g/g_e=0.0001$ are provided in Sec. 5. Considering the complexity involved in boiling phenomenon, it is impossible to simulate every aspects of bubble dynamics and heat transfer during the process, and some simplifications have to be made. The constant wall temperature is one of them, although in reality it can vary with time and position due to the high evaporation rate near the contact line. In addition, the advancing and receding contact angles differ and depend on the interface velocity. In the present work, a static contact angle is used, as the advancing and receding contact angles are expected to deviate only about 5 deg from the static contact angle [3]. Because

the conjugate heat transfer problem in the solid is not solved, waiting time between successive bubble-growth cycles cannot be predicted and must be specified empirically.

4.1 Case 1: Subcooled Nucleate Boiling Under Earth-Normal Gravity. The prediction from the numerical model was compared with the experimental data of Ramanujapu [2]. The growth of an isolated bubble on a silicon wafer was studied in those experiments. A square cavity, $10 \mu\text{m}$ in width and $20 \mu\text{m}$ in depth, served as the nucleation site. The wafer was heated from below by controlling power through strain gauge heaters while maintaining surface temperature nearly constant. In the experiments, degassed and de-ionized water was used as the test fluid. The heated region around the cavity was much larger than the radius of the computational domain. Further experimental details are given in Ref. [2]. Figure 2(a) shows the comparison for the case where $\Delta T_w=7^{\circ}\text{C}$, $\Delta T_{\text{sub}}=1.5^{\circ}\text{C}$, contact angle of 54 deg,

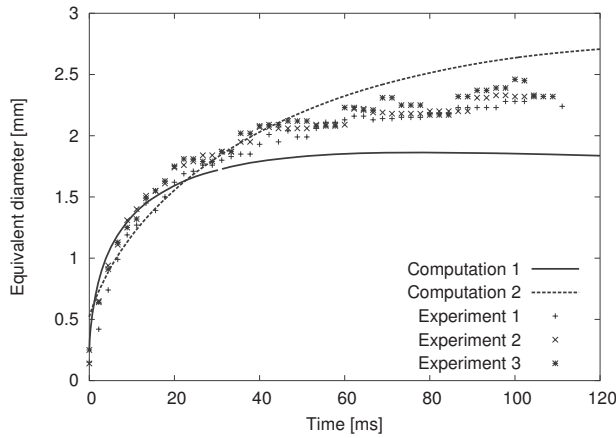


Fig. 4 Growth rate for wall superheat=6.5°C, liquid subcooling=4°C, contact angle=54 deg, pressure=1.013 $\times 10^5$ Pa, and $g/g_e=1$

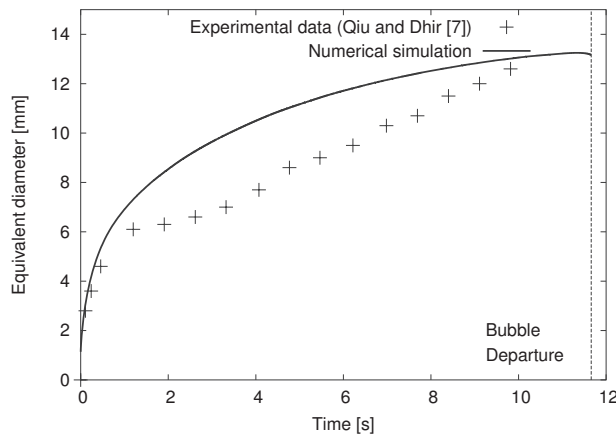


Fig. 5 Growth history for wall superheat=2.5°C, liquid subcooling=0.4°C, contact angle=54 deg, pressure=1.013 $\times 10^5$ Pa, $g/g_e=0.045$, and water as test fluid

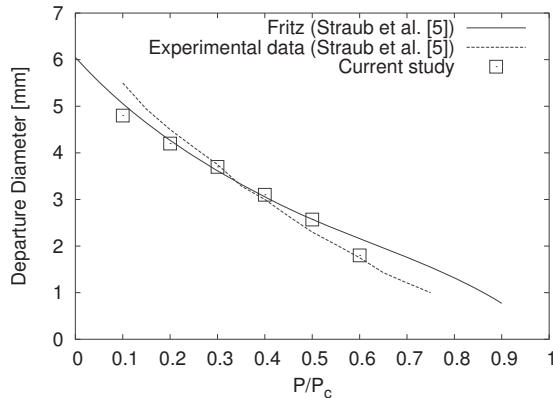


Fig. 6 Comparison of departure diameter of R-12 versus pressure for $g/g_e=0.01$, contact angle=25 deg, wall superheat=8°C, and liquid subcooling=0°C

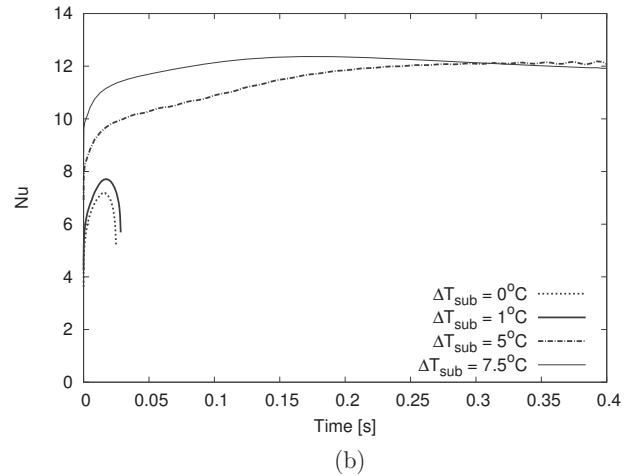
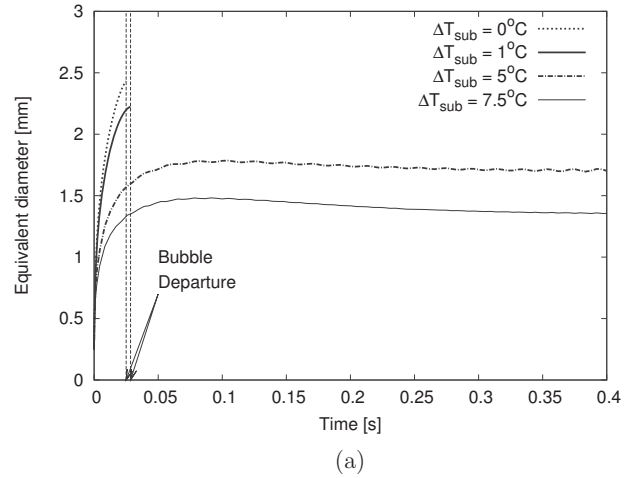


Fig. 7 (a) Growth rate. (b) Nu versus time for wall superheat=8°C, contact angle=38 deg, pressure=1.013 $\times 10^5$ Pa, and $g/g_e=1$

and pressure of 1.013×10^5 Pa. This value of static contact angle has been measured in experiments for water on a clean polished silicon surface.

The data from three different bubble release cycles are compared with the results for three sequential bubbles from simulation. It can be seen that there is a good agreement with the data throughout the growth cycle. Although the model overpredicts the departure diameter by about 10% under these conditions, the predicted growth rate and growth periods match well with those found in the experiments.

Figure 2(b) shows the variation of predicted Nusselt number based on the heater area (19.6 mm^2) averaged heat flux at the wall with time for eight bubble release cycles from the beginning until quasisteady state condition is achieved. In each cycle, the minimum Nusselt number occurs after the bubble lifts off and just prior to the birth of a new bubble. It is fortuitous that, under quasisteady state conditions represented by sixth, seventh, and eighth cycles, the minimum Nusselt numbers in the absence of bubbles comparable to the initial Nu assumed to correspond to steady state natural convection. It should be noted that Nusselt number values higher than the minimum indicate the enhanced heat transfer rate caused by the formation of bubbles. During the first cycle, the thin thermal boundary layer (shown in Fig. 3 at $t = 0$ ms) provides the least heat transfer to the growing bubble. As a result, the first bubble takes much longer time to grow and depart than subsequent bubbles. The thin thermal boundary layer implies a steep temperature gradient close to the wall everywhere

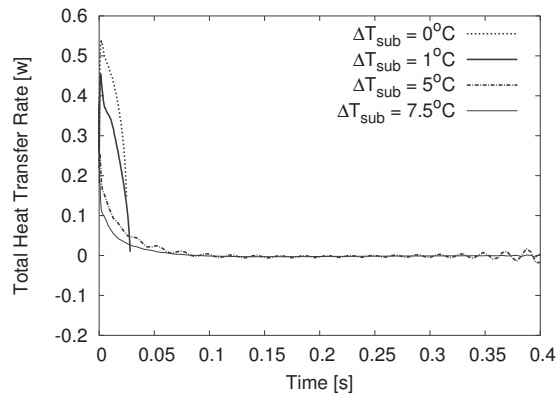


Fig. 8 Total heat transfer rate through the interface and micro-layer for of wall superheat=8°C, contact angle=38 deg, pressure=1.013×10⁵ Pa, and $g/g_e=1$

in the computational domain and yields a larger value of Nu. With time, the flow field that is created causes the thermal layer to thicken around the bubble generation site. As a result, Nu decreases and more heat is stored in the liquid. This leads to a higher rate of evaporation and reduces growth period. When the bubble base shrinks, cold liquid from the sides of the domain flows in and fills the volume. This flow pattern in turn compresses the thermal boundary layer and intensifies the heat transfer. For example, the maximum heat transfer rate in seventh cycle occurs at 910.5 ms as the base radius decreases to 0.57 mm from the maximum value of 0.89 mm prior to departure. Once quasisteady state is achieved, Nu does not alter much from cycle to cycle. This trend is indicated by sixth, seventh, and eighth cycle in Fig. 2(b). The waiting time is not provided with the experiment data. In numerical simulations, too small waiting time will lead to bubble merger in vertical direction and a large waiting time will increase computational time considering many cycles of bubbles. A waiting time of 16.6 ms was empirically used in between successive bubble cycles.

The initial conditions for the first and seventh bubble are shown in Fig. 3 at $t=0$ and 845.3 ms, respectively. The much thicker boundary layer for the seventh cycle, which is similar to sixth and eighth cycled, gives rise to higher growth rate and smaller growth period (≈ 70 ms) in comparison to the first bubble, which has a growth period of 250 ms. Figure 3 provides a sequence of the time-dependent isotherm distributions and velocity fields for the seventh cycle. From Fig. 3, it can be observed that the superheated plume represented by the contour of 100.2°C stays above the top of the bubble throughout this period and the bubble is exposed to the subcooled liquid only during the late portion of the growth period. This process is typical for sixth and eighth cycles as well. It should be noted that as reported in Ref. [9] for saturated case, microlayer contributes about 20% to the total heat transfer rate into the bubble.

The impact of initial conditions on bubble-growth rate is further demonstrated for a higher subcooling case in Fig. 4, which compares the data from experiments with prediction from numerical simulations for $\Delta T_w=6.5^\circ\text{C}$, $\Delta T_{sub}=4^\circ\text{C}$, contact angle of 54° , and pressure of 1.013×10^5 Pa. The data are from Ref. [2]. Numerical computation 1 is based on initial thermal layer thickness given by Eq. (31) and on the assumption that temperature varies linearly in the thermal layer. For this case, bubble reaches a quasistatic size of 1.86 mm and does not depart up to 120 ms. Numerical computation 2 is based on the dimensionless temperature distribution that will exist after several bubble release cycles (e.g. Fig. 3 at $t=845.3$ ms). The prediction from the second set of calculation is in more agreement with the data from experiments, where a bubble of about 2.4 mm in size departs at about 110 ms. Thus the initial condition during subcooled boiling significantly affects the bubble dynamics. Normally initial conditions in the

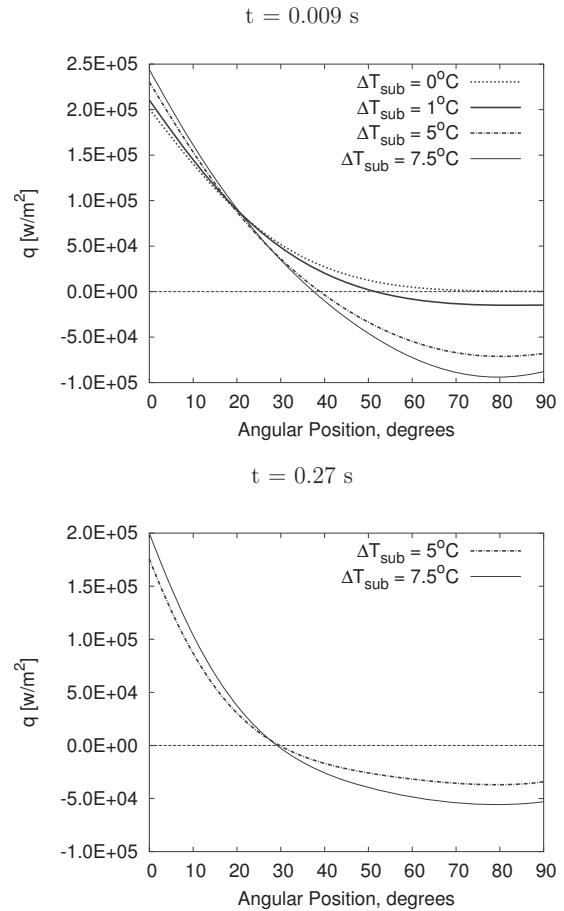


Fig. 9 Heat flux as a function of location along bubble interface for wall superheat=8°C, contact angle=38 deg, pressure=1.013×10⁵ Pa, and $g/g_e=1$

experiments after several bubble nucleation cycles are not known and as a result differences may exist between results of experiments and numerical simulations. To avoid inconsistencies, all the calculations in this work were performed for the first cycle based on the initial linear distribution of temperature in the thermal layer. In carrying out the calculations, the domain size was varied parametrically and little effect on flow field and bubble-growth history was observed for domains larger than those used in the reported work. Also bubbles were allowed to escape from the free surface with liquid, filling the vacated space at the top of the domain.

4.2 Case 2: Subcooled Nucleate Boiling Under Microgravity. This section presents the results for the cases where the gravity levels are much lower than the earth-normal gravity. Under these conditions, not only is the size of the bubble larger but also the growth periods are extended.

The data from the KC-135 flights are used to validate results for the subcooled cases. The detailed information related to the experimental setup is given by Qiu and Dhir [8].

The initial condition is different in the microgravity model, as compared to that at earth-normal gravity in term of the thickness of the thermal layer. The low gravity in the KC-135 flight lasts about 20 s. This relatively short period of time does not allow for the thermal layer to grow and develop over a period of several cycles. Therefore, the conditions at the start of the experiments are a relatively static pool and a growing thermal layer. For the microgravity simulations, we take the results from the first cycle of the bubble growth itself. Assuming heating was started 2 s prior to bubble initiation, the initial thermal boundary layer thickness from

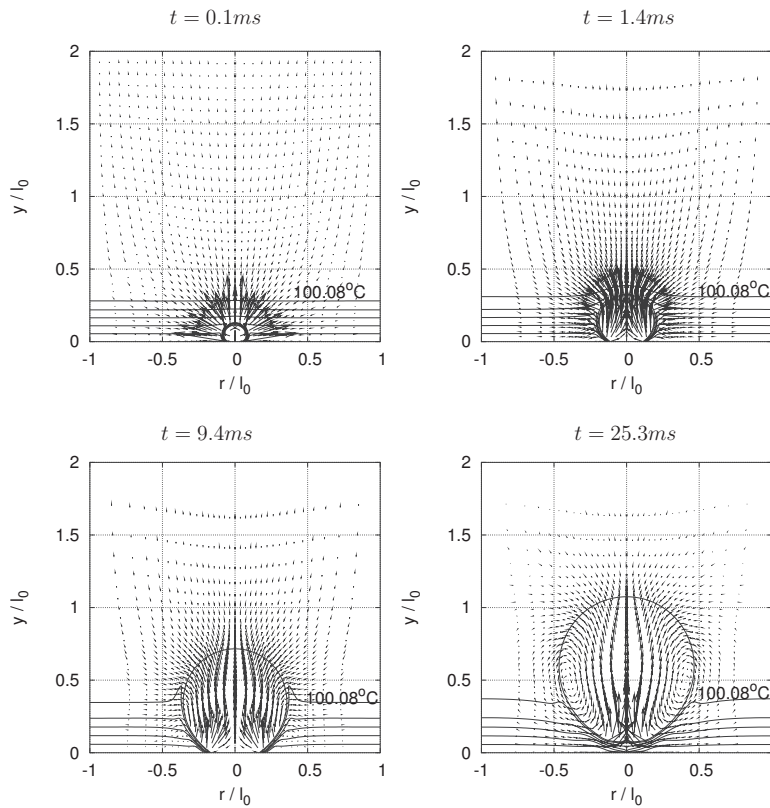


Fig. 10 Temperature distribution and velocity field for wall superheat=8°C, liquid subcooling=0°C, contact angle=38 deg, pressure=1.013×10⁵ Pa, and $g/g_e=1$ (temperature increment between isotherms is 1.58°C)

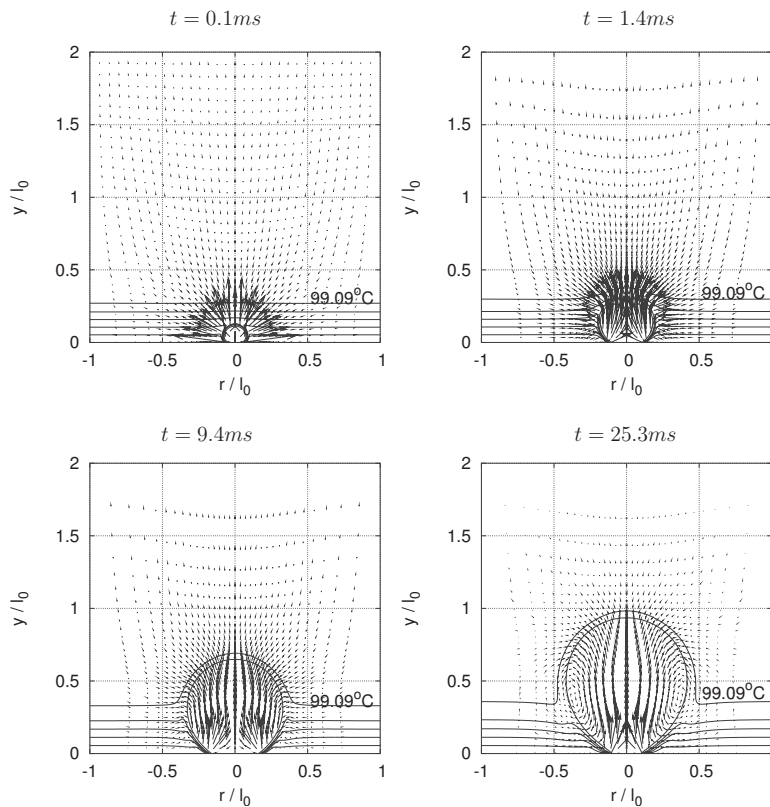


Fig. 11 Temperature distribution and velocity field for wall superheat=8°C, liquid subcooling=1°C, contact angle=38 deg, pressure=1.013×10⁵ Pa, and $g/g_e=1$ (temperature increment between isotherms is 1.78°C)

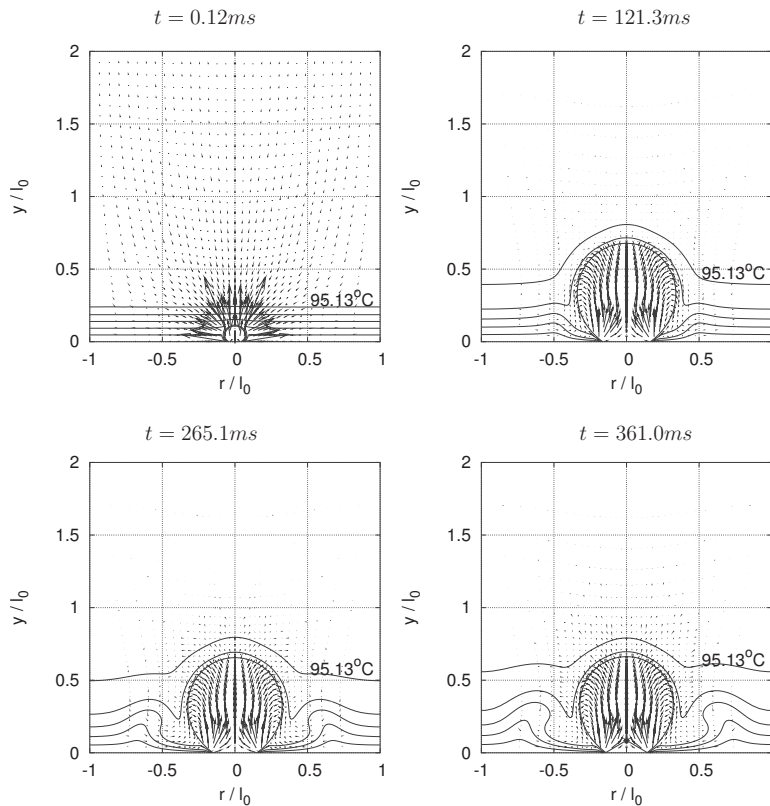


Fig. 12 Temperature distribution and velocity field for wall superheat= 8°C , liquid subcooling= 5°C , contact angle= 38° deg, pressure= 1.013×10^5 Pa, and $g/g_e=1$ (temperature increment between isotherms is 2.57°C)

transient conduction analysis has been set to 1 mm.

Figure 5 displays the comparison of the bubble-growth history between the data and results of simulation for wall superheat $=2.5^{\circ}\text{C}$, liquid subcooling= 0.4°C , contact angle= 54° deg, pressure= 1.013×10^5 Pa, and $g/g_e=0.045$. The predicted departure diameter is in very good agreement with the data, although the predicted time period is longer by about 20%. Model overpredicts the bubble diameter during the midrange of the growth history of the bubble. The reason for this could be that gravitational acceleration in KC-135 is rarely constant. The variation in acceleration in flight affects the thickness of the thermal layer around the bubble and hence the growth rate.

Computed departure diameters for R-12 bubbles at gravity level of $g/g_e=0.01$ are compared with experimental data of Straub et al. [6] in Fig. 6. From the calculated departure sizes by Straub et al.

[6] using Fritz equation and the properties of R-12, contact angles ranging from 18° deg to 30° deg at different p/p_c were expected in their experiments. Therefore, a contact angle of 25° deg was assumed in carrying out the numerical simulation for all p/p_c . Overall the calculated departure diameters agree with the experimental data as p/p_c ranges from 0.1 to 0.6. In the worst case of $p/p_c=0.1$, the numerical simulation underpredicts the departure diameter by 13%.

Based on the above comparisons with the benchmark test cases, we are confident about the validity of our numerical simulations.

5 Results and Discussions

In this section, the numerical results for saturated and subcooled boiling of water as test fluid under various gravity levels are presented. The saturated cases are limiting cases. All the numerical results correspond to the computations of bubble growth and departure for the first cycle.

5.1 Earth-Normal Gravity, $g/g_e=1$. Numerical simulations of single bubble dynamics during saturated and subcooled nucleate boiling of water for a wall superheat of 8°C , a contact angle of 38° deg, and a system pressure of 1.013×10^5 Pa were performed. This contact angle is considered for water on a mildly oxidized copper surface. The growth history of the bubble is used as the primary means of comparing the effect of various parameters. The actual volume of the bubble is first computed; thereafter it is converted into an equivalent diameter of a complete sphere.

Figure 7(a) shows the growth histories of the bubble with four different subcoolings of 0°C , 1°C , 5°C , and 7.5°C , respectively. For the saturated case, the bubble continues to increase in size until it finally departs from the wall after attaining a diameter of 2.43 mm. For liquid subcooling of 1°C , the bubble is predicted to detach from the wall with a diameter of 2.22 mm. For subcoolings of 5°C and 7.5°C , the bubble grows to a maximum size (1.79

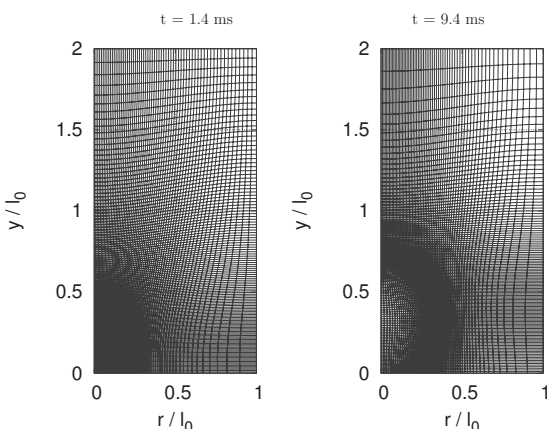


Fig. 13 Evolving grid distribution

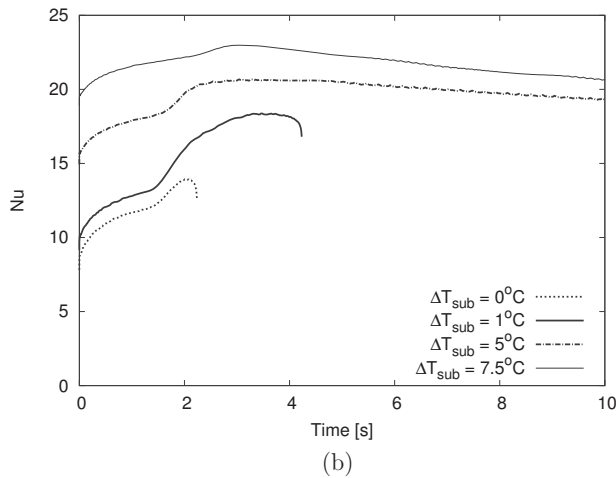
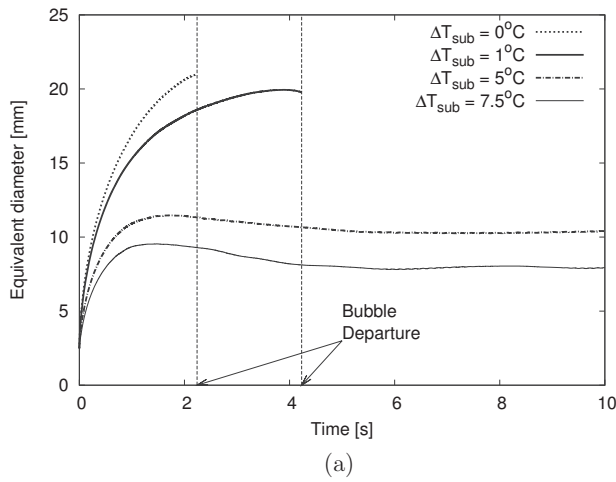


Fig. 14 (a) Growth rate. (b) Nu versus time for wall superheat=8°C, contact angle=38°, pressure=1.013×10⁵ Pa, and g/g_e=0.01

mm for 5°C, 1.49 mm for 7.5°C) and then begins to shrink. This shrinkage is due to the large condensation heat transfer that occurs at the upper portions of the bubble, which becomes larger than the sum of evaporative heat transfer around the bubble and from the microlayer. Eventually a balance is reached between the evaporation and condensation rates, and the bubble acquires a quasistatic diameter while remaining attached to the heated surface (1.70 mm

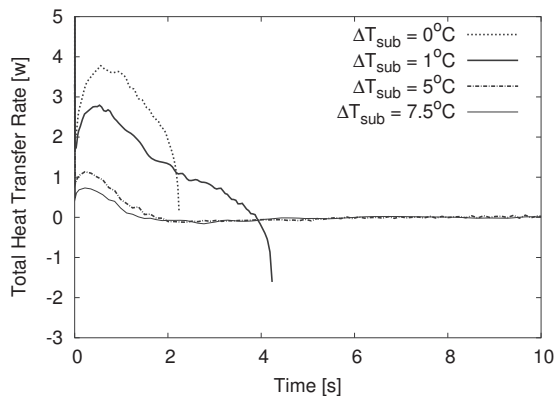


Fig. 15 Total heat transfer rate through the interface and microlayer for wall superheat=8°C, contact angle=38 deg, pressure=1.013×10⁵ Pa, and g/g_e=0.01

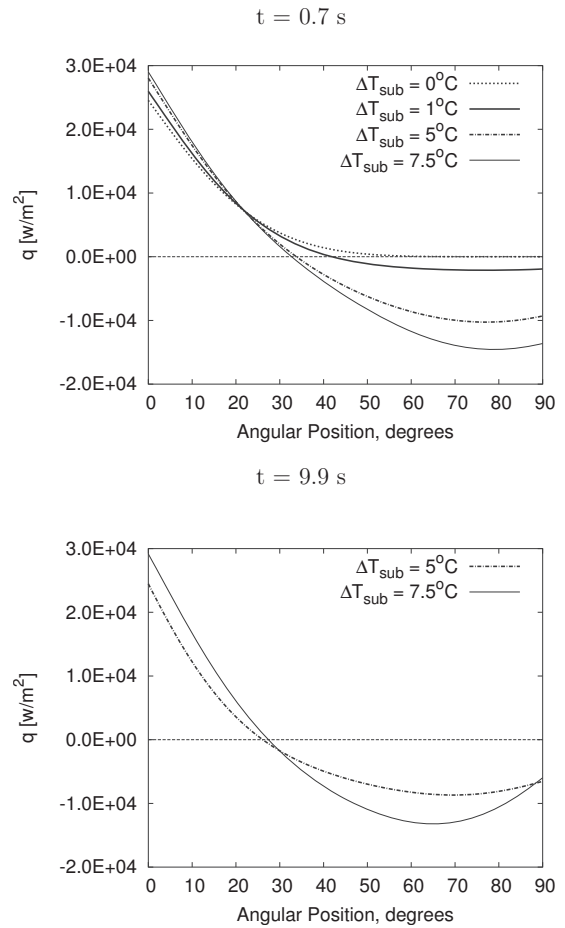


Fig. 16 Heat flux as a function of location along bubble interface for wall superheat=8°C, liquid subcooling=0°C, contact angle=38 deg, pressure=1.013×10⁵ Pa, and g/g_e=0.01

for 5°C subcooling and 1.36 mm for 7.5°C subcooling). The bubble in these cases never achieves the bubble departure size. Nusselt number based on the wall area average heat transfer rate from the wall over the computational domain is shown in Fig. 7(b). The heat transfer coefficient is based on the wall superheat. Initially Nu is higher because of the higher subcooling and the thinner thermal boundary layer. It is found that Nu for 5°C subcooling slightly exceeds that for 7.5°C subcooling after 0.31 s. Possible reason could be the role played by bubble base size: More heat is transmitted into the vapor from the microlayer for the bubble with the larger base area; on the other hand, a larger bubble would have a smaller area through which heat is transferred from the wall to the liquid.

Figure 8 shows the total heat transfer rates into bubble including the contribution from the microlayer and the bubble interface for the four subcoolings. The initial high rate of heat transfer accounts for the rapid bubble growth in the early stages. As the bubble approaches its departure size, the heat transfer rate decreases. For subcoolings of 5°C and 7.5°C, heat transfer rate rapidly approaches zero as condensation balances evaporation and bubble size becomes almost static.

Figure 9 presents the interfacial heat flux as a function of location along the interface at two times during the bubble growth for various subcoolings. The evaporation contribution from microlayer is not considered here. As expected, larger subcooling results in higher condensation rates. At t=0.009 s, the bubbles are in the process of rapid growth. The top of the bubbles are exposed to the subcooled liquid. This yields a steep temperature gradient, which

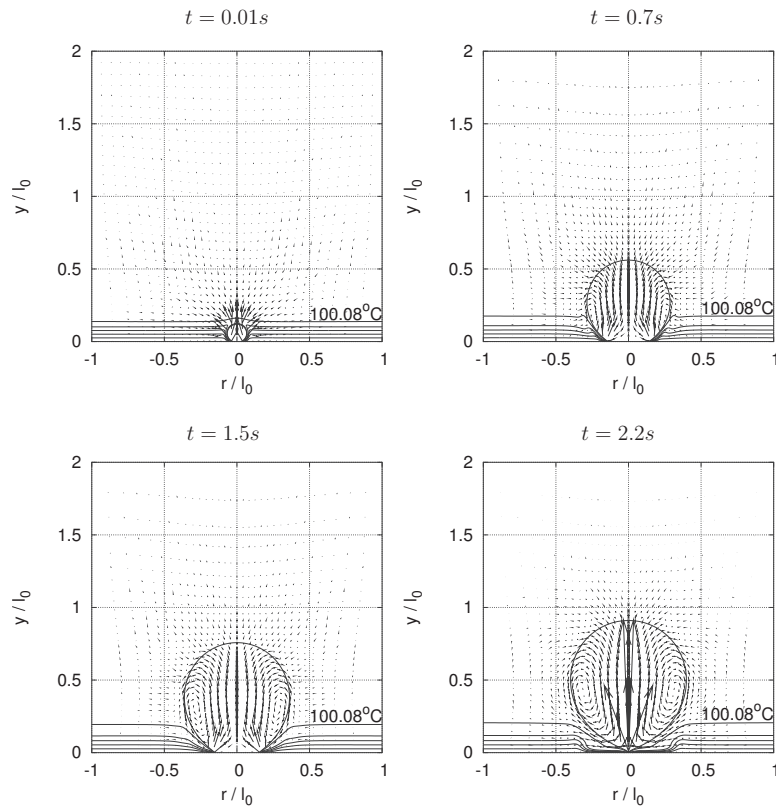


Fig. 17 Temperature distribution and velocity field for wall superheat=8°C, liquid subcooling=0°C, contact angle=38 deg, pressure=1.013×10⁵ Pa, and $g/g_e=0.01$ (temperature increment between isotherms is 1.58°C)

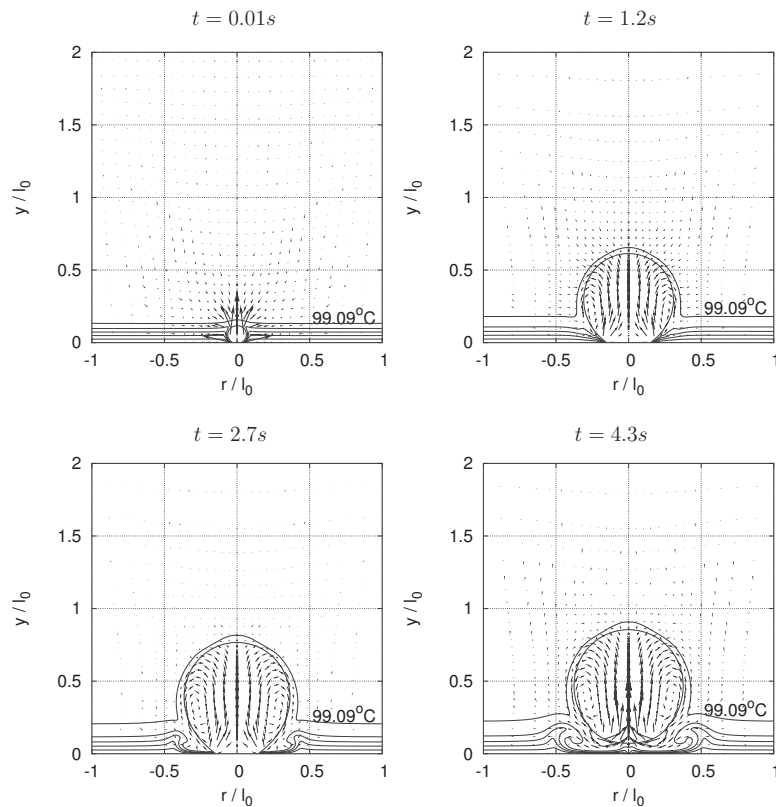


Fig. 18 Temperature distribution and velocity field for wall superheat=8°C, liquid subcooling=1°C, contact angle=38 deg, pressure=1.013×10⁵ Pa, and $g/g_e=0.01$ (temperature increment between isotherms is 1.78°C)

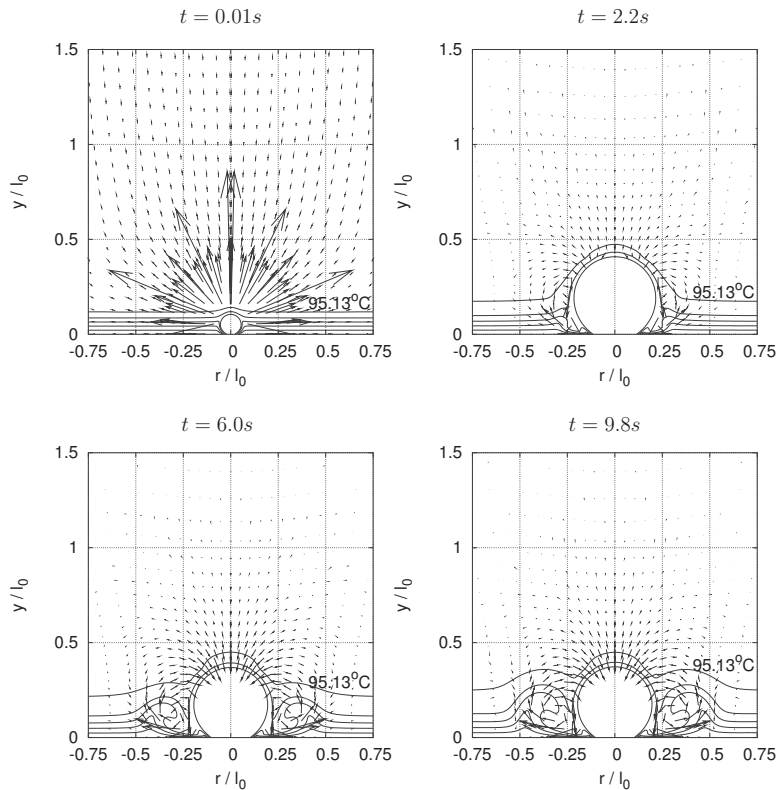


Fig. 19 Temperature distribution and velocity field for wall superheat=8°C, liquid subcooling=5°C, contact angle=38 deg, pressure=1.013×10⁵ Pa, and $g/g_e=0.01$ (temperature increment between isotherms is 2.57°C)

results in high condensation rates. At $t=0.27$ s, the bubble size remains relatively constant and lower condensation rates occur as thermal layer develops on the liquid side.

Figures 10–12 show the calculated flow field and isotherm distribution for subcoolings of 0°C, 1°C, and 5°C, respectively. In each one of those figures, the top isotherm represents a dimensionless temperature of 0.01 and the rest is divided by five equal increments. From Fig. 10, it can be seen that the growing bubble initially pushes the liquid radially out. The location where the vapor-liquid interface contacts the wall is observed to move outward and then inward as the bubble grows and departs. The highest heat transfer rate occurs around the base of the bubble and this is reflected by the packing of isotherms. The nonuniform vapor velocity inside the bubble results in a noticeable clockwise vortex.

For liquid subcoolings of 1°C and 5°C, the isotherm that terminates at the bubble interface represents the saturation temperature. It separates the areas where evaporation takes place from the areas where condensation occurs. We observe that the condensation areas dominate over the evaporation areas during most of the growth period. For 5°C subcooling, vapor flowing upward from the bubble base condenses over most of the interface. The liquid that has just condensed around the interface flows downward toward the wall and thins down the thermal layer near the base of the bubble. This in turn leads to saddle points in the isotherms.

Figure 13 represents the grid structure corresponding to Fig. 10 at $t=1.4$ and 9.4 ms, respectively. For clarity, only every other point is plotted.

5.2 Microgravity. The results for the cases where the gravity level is 1% of earth-normal gravity are included here. At this gravity level, not only is the size of the bubble an order of magnitude larger, but also the growth time periods are much longer.

Figure 14(a) shows the bubble-growth rates for four different liquid subcoolings for a wall superheat of 8°C, a contact angle of 38 deg, and a system pressure of 1.013×10⁵ Pa. The trends of bubble growth are similar to those for earth-normal gravity. At microgravity, subcooling has a more pronounced effect on bubble size. For example, at $g/g_e=1.0$ as quasisteady state is reached, the ratios of $D_{sub}/D_{d,sat}$ are 0.7 and 0.56 for liquid subcoolings of 5°C and 7.5°C, respectively. However, at $g/g_e=0.01$, they are 0.49 and 0.38, respectively. The corresponding area (1963 mm²) averaged heat transfer coefficient from the wall during this process is shown in Fig. 14(b). Although Nu values at 0.01 g_e are higher than those at 1 g_e , the actual heat transfer rate is lower. Here one should note that characteristic length used in defining Nu is ten times larger at 0.01 g_e than at 1 g_e .

Figure 15 depicts the total heat transfer rate across the interface for various liquid subcoolings. At subcooling of 1°C, the maximum heat transfer rate, corresponding to the maximum bubble

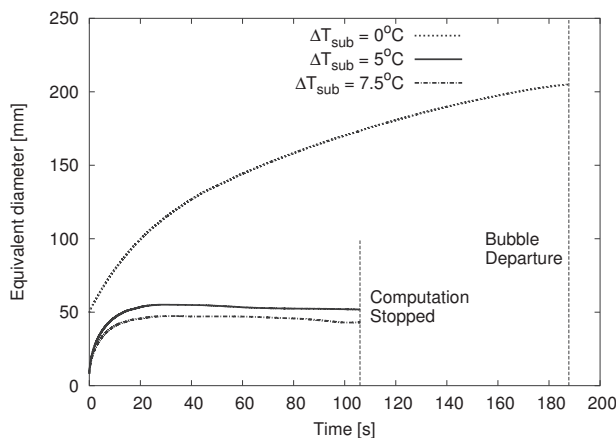


Fig. 20 Growth rate for wall superheat=8°C, contact angle=38 deg, pressure=1.013×10⁵ Pa, and $g/g_e=0.0001$

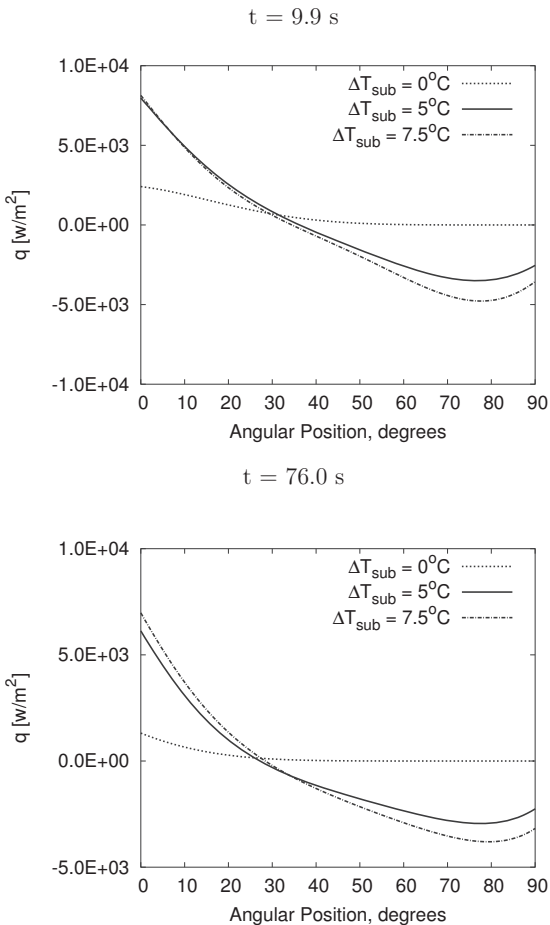


Fig. 21 Heat flux as a function of location along bubble interface for wall superheat=8°C, contact angle=38 deg, pressure =1.013×10⁵ Pa, and g/g_e=0.0001

volume growth rate, is 2.8 W, whereas it is 3.8 W for the saturated case. Therefore, this ratio $Q_{\max, \Delta T_{\text{sub}}=1^\circ\text{C}}/Q_{\max, \text{sat}}$ is 0.74. In contrast, at $g/g_e=1.0$, $Q_{\max, \Delta T_{\text{sub}}=1^\circ\text{C}}/Q_{\max, \text{sat}}$ is 0.85. This observation confirms that the subcooling affects the rate of heat transfer under microgravity more than it does under earth-normal gravity. The reason for this is that interfacial area for the heat transfer is larger in microgravity.

Figure 16 presents the interfacial heat flux along the bubble interface at $t=0.7$ and 9.9 s. The heat transfer from microlayer is not included once again. The trend is similar to that shown in Fig. 9 for $g/g_e=1.0$. However, it must be noted that evaporation and condensation heat fluxes under microgravity conditions are much smaller in magnitude than those for earth-normal gravity. This difference is caused by a thicker thermal layer around the bubble over a longer time scale. A thicker thermal boundary layer results in a smaller temperature gradient, which in turn reduces the heat flux.

Figures 17 and 18 show the flow field and isotherms for liquid subcoolings of 0°C and 1°C, respectively, at $g/g_e=0.01$. Comparing the temperature fields for the two cases, it can be observed that a vortex is caused by condensate flowing down on the liquid side for 1°C subcooling. At the early stage (such as $t=0.01$ s) in Fig. 19 for 5°C subcooling, the larger velocity vectors indicate the rapid bubble growth. Subsequently, condensation begins and the area over which condensation occurs increases rapidly. Finally when the condensation rate is larger than the evaporation rate, the bubble begins to shrink. The condensate flows downward along the bubble interface resulting in the counterclockwise vortex in

the liquid.

Next the numerical results for the cases where the gravity level is 10^{-4} of earth-normal gravity are presented. Here, the computational domain is chosen to be $(R/l_0, Y/l_0)=(0.32, 0.64)$ for the subcooled boiling cases.

Figure 20 shows that for water at saturation temperature, a bubble is predicted to detach from the wall at a size of 205 μm for a wall superheat of 8°C, a contact angle of 38 deg, and a system pressure of 1.013×10^5 Pa. In this study, considering the initial thermal boundary thickness and the eventual bubble size, different initial bubble sizes (50 μm for saturated and 8 μm for subcooled case) and computational domains (250 μm radius for saturated and 80 μm for subcooled case) are used for saturated and subcooled cases. Under subcooled boiling conditions, bubble-growth history similar to that noted earlier for g_e and $0.01g_e$ is observed and bubble continues to remain attached to the heater.

Figure 21 shows the heat flux along the bubble interface at two different times. For both $t=9.9$ s and $t=76.0$ s, the effect of the liquid subcooling is evident. Also consistent with earlier results for $0.01g_e$, the rate of heat transfer is even smaller.

Figure 22 gives the flow field and isotherms for 5°C subcooling. In comparison to earth-normal gravity, a blunt plume appears above the bubble beyond 23.7 s. Upon close inspection, it is observed that the bubble size does not remain absolutely constant and the velocity vectors close to the interface indicate that the bubble oscillates in both horizontal and vertical directions. It is also noted that with time, the plume and wiggle in isotherms near the base are enhanced. It is expected that with reduced viscous forces, the inertia forces and convection terms play a relatively more important role, in view of the increased Re. As a result, the isotherms near the wall begin to appear in a more distorted pattern.

6 Conclusions

A numerical procedure, coupling the level-set function with the moving mesh method, has been employed to simulate subcooled nucleate boiling under various gravity levels. The effect of subcooling on bubble size is more pronounced under microgravity than under earth-normal gravity. At $g/g_e=1.0$, a vortex is generated at higher subcoolings in the liquid side resulting in a saddle point in the temperature profile, but not at low subcooling. Under microgravity conditions, the saddle point in temperature profile develops even for low liquid subcoolings. For a given subcooling, the rate of heat transfer around the bubble decreases with reduction in gravity. This is due to stretching of length and time scales.

Acknowledgment

This work received support from NASA under the Microgravity Physics Program (Glenn Research Center), Contract No. NNX09AN65G.

Nomenclature

- A = dispersion constant
- c_p = specific heat at constant pressure
- \mathbf{g} = gravity vector
- g = gravity
- H = step function
- h = grid spacing for the macro region
- h_{ev} = evaporative heat transfer coefficient
- h_{fg} = latent heat of evaporation
- k = thermal conductivity
- l_0 = characteristic length
- M = molecular weight
- \mathbf{m} = mass flux vector
- Nu = Nusselt number, $ql_0/k_l\Delta T_w$
- p = pressure
- q = heat flux
- R = radius of computational domain or bubble

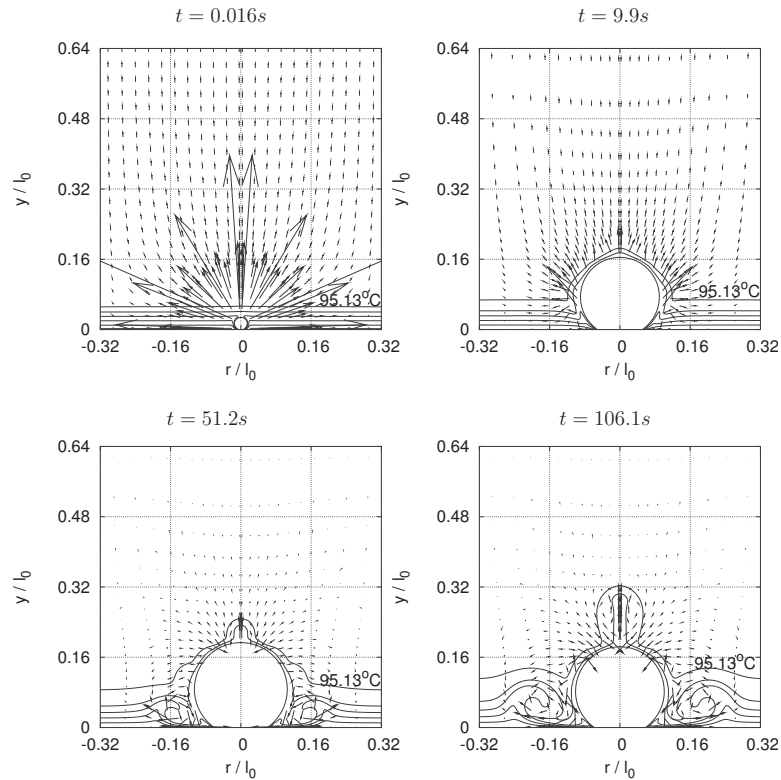


Fig. 22 Temperature distribution and velocity field for wall superheat=8°C, liquid subcooling=5°C, contact angle=38 deg, pressure=1.013×10⁵ Pa, and g/g₀=0.0001 (temperature increment between isotherms is 2.57°C)

R_o = radius of dry region beneath a bubble
 R_1 = radial location of the interface at $y=h/2$
 \bar{R} = universal gas constant
 Re = Reynolds number, $\rho_l u_0 l_0 / \mu_l$
 r = radial coordinate
 T = temperature
 t = time
 t_0 = characteristic time
 ΔT = temperature difference, $T_w - T_l$
 \mathbf{u} = velocity vector, (u, v)
 \mathbf{u}_{int} = interfacial velocity vector
 u_0 = characteristic velocity
 \dot{V}_{micro} = rate of vapor volume production from the microlayer
 ΔV_{micro} = vapor-side control volume
 Y = height of computational domain
 y = vertical coordinate

Greek

α = thermal diffusivity
 β_T = coefficient of thermal expansion
 δ = liquid film thickness
 δ_o = nonevaporating liquid film thickness
 δ_t = thermal layer thickness
 η = curvilinear coordinate
 θ = dimensionless temperature
 κ = interfacial curvature
 μ = dynamic viscosity
 ν = kinematic viscosity
 ξ = curvilinear coordinate
 ρ = density
 σ = surface tension
 ϕ = level-set function
 φ = contact angle

Subscripts

0 = initial condition
 c = critical
 d = departure
 e = earth-normal
 int = interface
 l = liquid
 sat = saturation
 sub = subcooling
 v = vapor
 w = wall
 ξ = partial differentiation with respect to ξ
 η = partial differentiation with respect to η

Superscripts

T = transpose

References

- [1] Gunther, F. G., and Kreith, F., 1954, "Photographic Study of Bubble Formation in Heat Transfer to Subcooled Water," California Institute of Technology Progress Report No. 4-120.
- [2] Ramanujapu, N., 1999, "Study of Growth Rate, Departure Frequency and Shape of a Single Bubble During Saturated and Subcooled Nuclear Boiling," Ph.D. prospectus, University of California, Los Angeles, Los Angeles, CA.
- [3] Ramanujapu, N., and Dhir, V. K., 1999, "Dynamics of Contact Angle During Growth and Detachment of a Vapor Bubble at a Single Nucleation Site," *Proceedings of the Fifth ASME/JSME Joint Thermal Engineering Conference*, San Diego, CA.
- [4] Singh, S., 1999, "Effect of Gravity and Liquid Subcooling on Bubble Dynamics," MS thesis, University of California, Los Angeles, Los Angeles, CA.
- [5] Siegel, R., and Keshock, E. G., 1965, "Effects of Reduced Gravity on Nucleate Boiling Bubble Dynamics in Saturated Water," *AIChE J.*, **10**(4), pp. 509-517.
- [6] Straub, J., Zell, M., and Vogel, B., 1990, "Pool Boiling in Reduced Gravity Field," *Proceedings of the Ninth International Heat Transfer Conference*, pp. 91-112.
- [7] Oka, T., Abe, Y., Tanaka, K., Mori, Y. H., and Nagashima, A., 1992, "Observational Study of Pool Under Microgravity," *JSME Int. J., Ser. II*, **35**(2), pp. 280-286.
- [8] Qiu, D., and Dhir, V. K., 2002, "Single-Bubble Dynamics During Pool Under

- Low Gravity Conditions," *J. Thermophys. Heat Transfer*, **16**(3), pp. 336–345.
- [9] Son, G., Dhir, V. K., and Ramanujapu, N., 1999, "Dynamics and Heat Transfer Associated With a Single Bubble During Nucleate Boiling on a Horizontal Surface," *ASME J. Heat Transfer*, **121**, pp. 623–631.
- [10] Stephan, P., Fuchs, T., Wagner, E., and Schweizer, N., 2009, "Transient Local Heat Fluxes During the Entire Vapor Bubble Life Time," *Proceedings of the ECI International Conference on Boiling Heat Transfer*, Florianópolis, SC, Brazil.
- [11] Lay, J. H., and Dhir, V. K., 1995, "Shape of a Vapor Stem During Nucleate Boiling of Saturated Liquids," *ASME J. Heat Transfer*, **117**, pp. 394–401.
- [12] Wayner, P. C., Jr., 1992, "Evaporation and Stress in the Contact Line Region," *Proceedings of the Engineering Foundation Conference on Pool and External Flow Boiling*, Santa Barbara, CA, pp. 251–256.
- [13] Wu, J., Dhir, V. K., and Qian, J., 2007, "Numerical Simulation of Subcooled Nucleate Boiling by Coupling Level-Set Method With Moving Mesh Method," *Numer. Heat Transfer, Part B*, **51**, pp. 535–563.
- [14] Kays, W. M., and Crawford, M. E., 1980, *Convective Heat and Mass Transfer*, McGraw-Hill, New York, p. 328.
- [15] Ryskin, G., and Leal, L. G., 1984, "Numerical Solution of Free-Boundary Problems in Fluid Mechanics, Part I," *J. Fluid Mech.*, **148**, pp. 1–17.
- [16] Son, G., 2003, "Efficient Implementation of a Coupled Level-Set and Volume-of-Fluid Method for Three-Dimensional Incompressible Two-Phase Flows," *Numer. Heat Transfer, Part B*, **43**, pp. 549–565.
- [17] Son, G., 2001, "A Numerical Method for Bubble Motion With Phase Change," *Numer. Heat Transfer, Part B*, **39**, pp. 509–523.

Wen-Tao Ji

State Key Laboratory of Multiphase Flow in
Power Engineering,
School of Energy and Power Engineering,
Xi'an Jiaotong University,
Xi'an 710049, China

Ding-Cai Zhang

State Key Laboratory of Multiphase Flow in
Power Engineering,
School of Energy and Power Engineering,
Xi'an Jiaotong University,
Xi'an 710049, China;
School of Energy and Environment,
Zhongyuan University of Technology,
Zhengzhou 450007, China

Nan Feng

Jian-Fei Guo

State Key Laboratory of Multiphase Flow in
Power Engineering,
School of Energy and Power Engineering,
Xi'an Jiaotong University,
Xi'an 710049, China

Mitsuharu Numata

Guannan Xi

Environmental Technology Laboratory,
Daikin Industries, Ltd.,
Osaka 591-8511, Japan

Wen-Quan Tao¹

State Key Laboratory of Multiphase Flow in
Power Engineering,
School of Energy and Power Engineering,
Xi'an Jiaotong University,
Xi'an 710049, China
e-mail: wqtao@mail.xjtu.edu.cn

Nucleate Pool Boiling Heat Transfer of R134a and R134a-PVE Lubricant Mixtures on Smooth and Five Enhanced Tubes

Pool boiling heat transfer coefficients of R134a with different lubricant mass fractions for one smooth tube and five enhanced tubes were tested at a saturation temperature of 6 °C. The lubricant used was polyvinyl ether. The lubrication mass fractions were 0.25%, 0.5%, 1.0%, 2.0%, 3.0%, 5.0%, 7.0%, and 10.0%, respectively. Within the tested heat flux range, from 9000 W/m² to 90,000 W/m², the lubricant generally has a different influence on pool boiling heat transfer of these six tubes. [DOI: 10.1115/1.4001931]

Keywords: nucleate pool boiling, enhancement heat transfer, lubricant

1 Introduction

Boiling heat transfer study usually is conducted for pure medium. However, generally, lubricant should be added to the refrigeration systems to lubricate the moving parts. A small amount of lubricant will be carried into the refrigerant circulating system and this small amount of lubricant will be inevitably mixed with the refrigerant, which may influence the boiling heat transfer process.

It has been widely noticed that the lubricant influence on boiling heat transfer is largely dependent on the special interaction of a refrigerant-lubricant pair [1–5], and for this reason, all modified heat transfer correlations [6–8] about refrigerant and lubricant have their own apparent defects in that it is only suitable to the

specific refrigerant-lubricant-surface pairs. No consistent agreement has been reached up to the present. However, from the previous studies, some common understandings may be drawn.

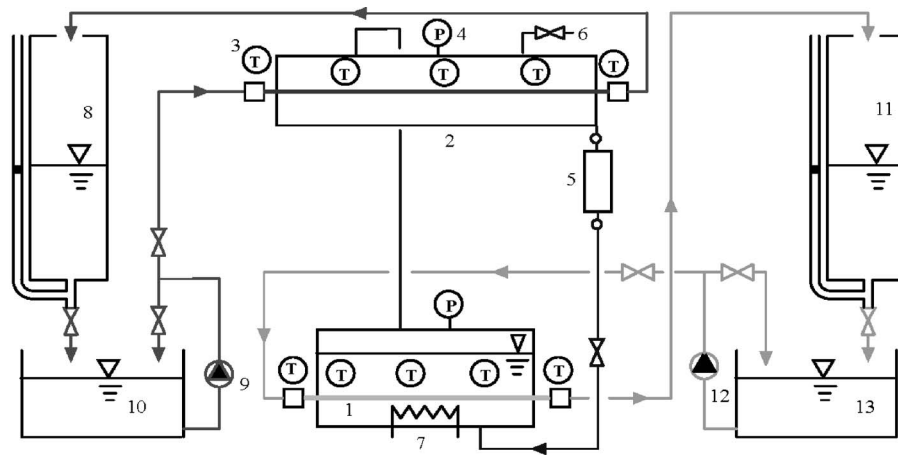
First, lubricant foaming around the heating surface is sometimes beneficial to the pool boiling heat transfer. According to Refs. [9–11], there are three possible reasons. (1) The distance between the wall and the interface of liquid and vapor is drawn closer by the foam; thus, a thinner liquid film exists between the tube's heating surface and foam. (2) The foam provides convenient conditions of secondary nucleation. (3) The foam seems to remove the lubricant from heating surface.

Second, the influence depends on the heating surface structure. For smooth and integral low-fin tubes, an improvement with lubricant is reported several times [11–13]. There are few reports about the heat transfer improvement with small quantities of lubricant for reentrant cavity tubes [14–17].

Third, mass fraction of lubricant is another important factor influencing the refrigerant boiling heat transfer [4,14,16–19]. In

¹Corresponding author.

Contributed by the Heat Transfer Division of ASME for publication in the JOURNAL OF HEAT TRANSFER. Manuscript received December 29, 2009; final manuscript received May 14, 2010; published online August 13, 2010. Assoc. Editor Satish G. Kandlikar.



(1)Boiler; (2)Condenser; (3)Thermocouple; (4)Pressure gauge; (5)Condensate measuring container; (6)Exhausting valve; (7)Subsidiary electric heater; (8)Weight-time flow meter of cooling water; (9)Cooling water pump; (10)Cold water storage tank; (11)Weight-time flow meter of heating water;(12)Heating water pump; (13)Hot water storage tank.

Fig. 1 Schematic diagram of the experimental apparatus

general, various mass fractions of lubricant have different influences on pool boiling heat transfer, and it seems that 3% of lubricant is a kind of threshold beyond which the lubricant effect will be qualitatively different. As far as whether the effect is positive or negative when the mass fraction is less than 3% is, in turn, largely dependent on the heating surface structure.

Fourthly, the type of refrigerant is also a key influencing factor, originated from different thermophysical properties, including liquid viscosity [19], surface tension, miscibility [20], and other pertinent parameters.

Finally, the lubricant type is an influence factor, as well [12,16,17,19,21,22]. Curcio and Somerscales [16] investigated R113/3GS (specially treated naphthene base crude) pool boiling heat transfer on structured surfaces, which showed a general decrease in heat transfer with lubricant mass fraction, and degradation in the performance of all surfaces happened at 10% lubricant. The pool boiling heat transfer data of Kedzierski [4] with lubricant polyol ester (POE) showed that the lubricant excess layer led to an average enhancement of the heat flux between 5 kW/m^2 and 20 kW/m^2 by approximately 24% for the 0.5% lubricant mass fraction, while both 1% and 2% lubricant mass fraction mixtures caused an average deterioration of about 60% in the heat flux range between 4 kW/m^2 and 20 kW/m^2 .

It is commonly recognized that there are three kinds of miscible lubricant of hydro fluoro carbon (HFC) (POE, polyalkylene glycol (PAG), and polyvinyl ether (PVE)) that can provide good lubricant return for better cooling efficiency over a wide range of temperatures [23–25]. The advantages of PVE over POE are better lubricity, no hydrolysis characteristics, better oxidation stability, better solubility with process fluids, and better miscibility with HFCs. In this paper, the effect of the lubricant PVE on the pool boiling heat transfer performances of R134a is investigated, which has not been reported in the literature so far to the authors' knowledge.

The chief objectives of this paper are twofold:

- (1) Provide a more comprehensive database for the pool boiling heat transfer with R134a outside six different tubes; these six tubes include plain, integral-fin, and four enhanced geometries.
- (2) Provide details about the performance of R134a with lubricant additive of polyvinyl ether (PVE) outside the same six enhanced tubes; seven different mass ratios of the lubricant

0.25%, 0.5%, 1.0%, 2.0%, 3.0%, 5.0%, 7.0%, and 10.0% will be studied in this paper; the results will be compared with other lubricants.

2 Experimental Apparatus

The experimental apparatus consists of a measurement system and three circulating systems: circulating systems of refrigerants, and heating and cooling water systems. A schematic figure of the test apparatus is shown in Fig. 1.

The refrigerant circulating system includes the boiler vessel, condenser vessel, and two ducts connecting the two vessels, which are all made of stainless steel. The inner diameter of boiler is 257 mm, with a length of 1100 mm. In the experiment, the heating water is flowing through the inner side of the tube tested, and then, it is going through the weight-time flow meter before it returns to the water tank via a centrifugal pump.

The refrigerant is boiling outside the heating tubes, rising upward to the condenser through the duct between the evaporator and condenser. When reaching the condenser, it is condensed by the cooling water flowing through the condensing tubes fixed in the condenser. The heating water circulates through the tested tube and gets back to the hot water storage tank by another centrifugal pump.

A pressure gauge is used to measure the pressure of the boiler vessel. The range of the measurement is 0 to 2.5 MPa and the precision is $\pm 0.00625 \text{ MPa}$. The temperatures of the refrigerant in different part of the system are measured by platinum resistance temperature transducers (PT100), which have a precision of $\pm (0.15 + 0.002|t|) \text{ K}$ at the test range. The difference between the inlet and outlet water's temperature of heating and cooling is measured by a six-junction copper-constantan thermocouple pile. Thermocouples are used to measure the temperatures of the inlet and outlet of heating and cooling water. The thermocouples and thermocouple piles were calibrated against a temperature calibrator that had a precision of $\pm 0.2 \text{ K}$. A Keithley digital voltmeter having a resolution of $0.1 \mu\text{V}$ is used to measure the electric potential.

The specifications of the test tubes are given in Table 1, d_i listed in Table 1 is the diameter to the root of the inner original embryo tube, and the geometries of the enhanced tubes are given in Fig. 2 in the sequence of Nos. 1–4. The properties of the lubricant, one kind of PVE, are listed in Table 2.

Table 1 Specifications of test tubes

Tubes	Outside diameter d_o (mm)	Inside diameter d_i (mm)	Height of outside fin e (mm)	Outside fin numbers per meter	Number of internal starts	Inner fin helix angle	Height of inside fin H (mm)	Length of test section L (mm)
Plain	19.09	16.41						1100
Integral-fin	19.06	16.28	1.400	786			smooth	1095
No.1	18.78	14.53	0.858 (max)	1435	20	40	0.399	1089
No.2	18.50	15.07	0.628	1561	45	40	0.398	1088
No.3	18.97	16.59	0.567	1696	45	35	0.302	1094
No.4	19.04	16.66	0.755	1761	38	35	0.350	1100

The experimental procedure is basically the same as illustrated in Ref. [26]. For the simplicity of presentation, the details are omitted.

3 Data Reduction and Analysis of Uncertainties

From the quantities measured, the following energy balance is first examined:

Heating power input from heating water

$$\phi_e = m_e c_p (t_{e,1} - t_{e,2}) \tag{1}$$

Cooling power output from cooling water

$$\phi_c = m_c c_p (t_{c,2} - t_{c,1}) \tag{2}$$

In these two equations, $t_{e,1}$ and $t_{e,2}$ are the inlet and outlet temperatures of the heating water (K), respectively, $t_{c,1}$ and $t_{c,2}$ are the inlet and outlet temperatures of the cooling water (K), respectively, c_p is the specific heat capacity of water corresponding to the mean temperature of inlet and outlet water (J/kg K), and \dot{m}_e and \dot{m}_c are the mass flow rates of the heating and cooling waters (kg/s), respectively. The properties of water are taken from Ref. [27].

The allowed maximum difference between these two heat transfer rates was mostly within 3%. Also, the mean value of the two heat transfer rates ϕ was used to determine the overall heat transfer coefficient of the test tube.

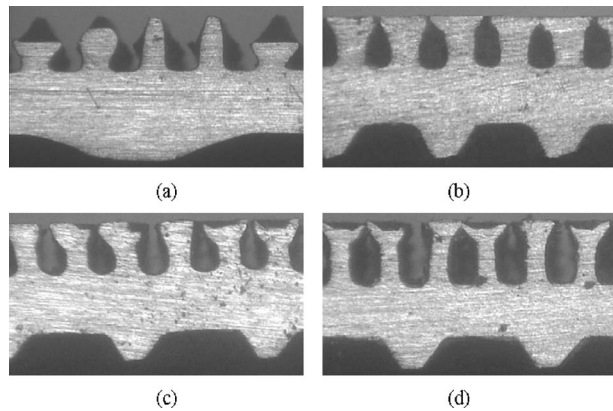


Fig. 2 Sectional view of enhanced tubes

Table 2 Properties of PVE lubricant used

Item	Quantity
Dynamic viscosity at 40°C (mm ² /s)	66.6
Dynamic viscosity at 100°C (mm ² /s)	8.04
Viscosity index	84
Density (g/m ³)	0.9369
Flash point (°C)	204
Pour point (°C)	-37.5
Trace moisture content (parts per million)	100

The overall heat transfer coefficient is determined by the following equation:

$$U = \frac{\phi}{A_o \cdot \Delta t_m} \tag{3}$$

where A_o is the outside area of the embryo test tube.

Δt_m is the log-mean temperature difference, which is defined as follows:

$$\Delta t_m = \frac{|t_{w,in} - t_{w,out}|}{\ln\left(\frac{t_s - t_{w,out}}{t_s - t_{w,in}}\right)} \tag{4}$$

where t_s is the saturation temperature of the refrigerant in the pool, $t_{w,in}$ is the temperature of the inlet water, and $t_{w,out}$ is the temperature of the outlet water.

The heat flux is defined as follows:

$$q = \frac{\phi}{A_o} \tag{5}$$

The boiling heat transfer resistance could be separated from the overall thermal resistance, as follows:

$$\frac{1}{h_o} = \frac{1}{U} - \frac{A_o}{A_i} \frac{1}{h_i} - R_f - R_w \tag{6}$$

In Eq. (6), R_f is the fouling thermal resistance. It was neglected in the present study for that at the beginning of experiment, because the inner and outer surfaces were cleaned using acetone solution, the heating water used was neat enough and the running time of the apparatus was 3 weeks at most. R_w is the thermal resistance of the wall. A_o and A_i are the area of embryo tube's outside and inside surfaces. h_o and h_i are the outside phase change and inside water heat transfer coefficients, respectively.

When the inside of the test tube is smooth, the heat transfer coefficient inside could be calculated using Gnielinski equations [28]

$$h_{ip} = \frac{\lambda}{d_i} \frac{(f/8)(Re - 1000)Pr}{1 + 12.7(f/8)^{1/2}(Pr^{2/3} - 1)} \left[1 + \left(\frac{d_i}{L}\right)^{2/3} \right] \left(\frac{Pr}{Pr_w}\right)^{0.11} \tag{7}$$

(Re = 2300 - 10⁶, Pr = 0.6 - 10⁵)

The above mentioned thermal resistance separation method is also called Wilson plot technique, and the principles and advantages of the Wilson plot technique are described in detail in the literature of Msauda and Rose [29]. If the inside surface is enhanced, the modified Wilson technique can be used to obtain the inside heat transfer coefficients. The basic idea of the modified Wilson plot can be described as follows. Assuming that the heat transfer coefficient of the enhanced inner surface can be represented by $c_i h_{ip}$, where h_{ip} is the heat transfer coefficient determined by the Gnielinski equation at the same fluid velocity and reference temperature. Then, the experiment should first be conducted to determine the appropriate value of the coefficient c_i , which represents the enhancement of the inner surface structure. To proceed, the temperature of refrigeration and the heat flux should be kept constant

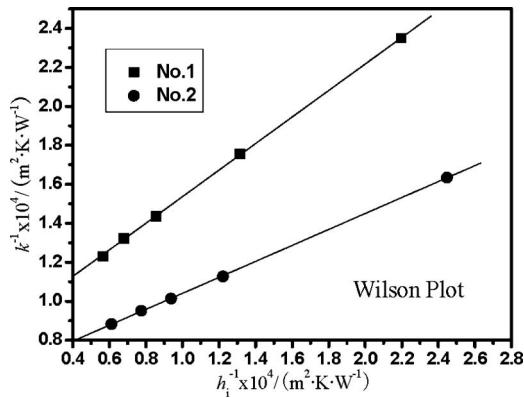


Fig. 3 Wilson plot for enhanced tube Nos.1 and 2

such that h_o is maintained unchanged during the test. Then Eq. (6) can be changed into

$$\frac{1}{U} = a \frac{1}{h_{ip}} + b \quad (8)$$

where

$$a = \frac{d_o}{d_i} \frac{1}{c_i} \quad (9)$$

$$b = \frac{1}{h_o} + R_w \quad (10)$$

A group of the data should be taken by varying the in-tube water velocity, and these data are expressed via the equation of a linear straight line shown by Eq. (8). By using the data regression method, the slope a and the constant term b of the linear straight line can be obtained; hence, the enhancement coefficient of inner side heat transfer c_i can be determined. As an illustration, Fig. 3 shows the reduced test data for the two enhanced tubes Nos. 1 and 2. All other enhanced tubes have the quantitatively same picture. The thus determined values of c_i are 1.885, 3.000, 2.761, and 2.690, respectively, for the four enhanced tubes.

An uncertainty analysis according to the literature [26,30] has been employed to estimate the possible uncertainty of the experimental data and the reduced results. The confidence level for all measurement uncertainties are 95% except indicated individually. The estimated uncertainties of q of the six tubes, plain, integral-fin, and Nos. 1–4, are less than 4.7%, 5.0%, 5.7%, 5.4%, 5.2%, and 4.3%, respectively, and that of U are 8.9%, 7.1%, 8.3%, 9.2%, 9.3%, and 6.6%, respectively. As h_o was not directly measured, the uncertainty of h_o was estimated using the method suggested in Refs. [27,30]. The estimated uncertainties are 18.2–34.3%, 28.7–37.9%, 16.7–29.5%, 22.2–26.8%, 23.5–30.7%, and 22.4–31.7% for the plain, integral-fin, and Nos. 1–4 tubes, respectively.

4 Results and Discussion

4.1 Reliability Validation of the Experimental Apparatus.

In order to test the reliability of the experimental apparatus, we first compared the experimental results with correlations of Cooper [31] and Gorenflo [32] for R134a boiling outside the plain tube at a saturation temperature of 6°C.

Cooper's correlation:

$$h_o = Cq^{0.67} M_r^{0.5} P_r^m (-\log P_r)^{-0.55} \quad (11)$$

where

$$C = 90 \text{ W}^{0.33} / \text{m}^{0.66} \text{ K}$$

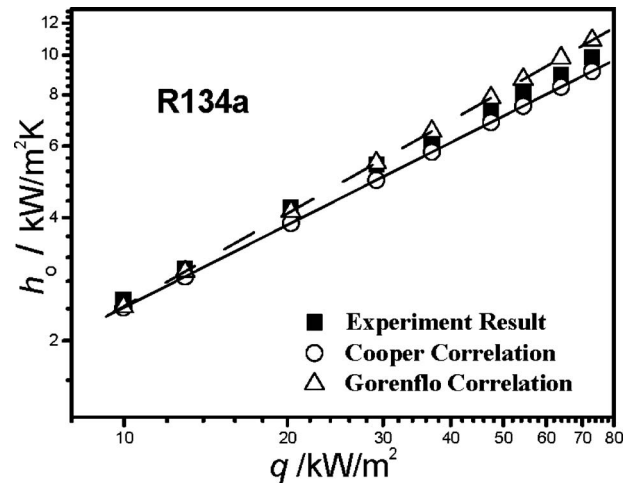


Fig. 4 Comparison of the experiment results with the Cooper and Gorenflo correlation

Gorenflo proposed a method using a reference heat transfer coefficient for each refrigerant at the fixed reference conditions of $P_{ro}=0.1$, $q_o=20 \text{ kW/m}^2$ and $R_{po}=0.4 \mu\text{m}$. The reference heat transfer coefficient h_{ro} of R134a is 4500 $\text{W/m}^2 \text{K}$. At other conditions of pressure, heat flux and roughness, the heat transfer coefficient is computed using the following expressions:

$$h_o = h_{ro} F_{PF} (q/q_o)^{nf} (R_p/R_{po})^{0.133} \quad (12)$$

where

$$F_{PF} = 1.2P_r^{0.27} + 2.5P_r + \left(\frac{P_r}{1 - P_r} \right)$$

$$nf = 0.9 - 0.3P_r^{0.3}$$

In the calculation, the surface roughness $\{R_p\}_{\mu\text{m}}$ was taken as 0.3 μm , as usually suggested of commercial tubes [31]. The relative deviation of the test results from the correlations of Cooper and Gorenflo lies from 4.6% to 9.2% and -5.3% to 10.0%, respectively. Figure 4 shows the comparison of the experimental results with the correlation of Cooper and Gorenflo. These comparisons should confirm the reliability of the experimental data.

4.2 R134a Heat Transfer Coefficients of the Plain and Enhanced Tubes.

The boiling curves of the six tubes at the R134a saturation temperature of 6°C are shown in Fig. 5. From the figure we could observe the following features. First, the boiling heat transfer coefficient of the smooth tube is significantly less than that of the integral and four enhanced tubes, but the differences decrease with an increase in the heat flux. Second for both smooth and integral-fin tubes, the heat transfer coefficients vary with the heat flux linearly in log-log coordinates, while for the four enhanced tubes the $h \sim q$ curves are more or less bent in the high heat flux region. Third, for the four enhanced tubes, tube No. 2 behaves best, tube Nos. 3 and 4 come next, and tube No. 1 is the worst. This order is not corresponding to the outside fin number per unit length. The cross section of the reentrant cavity surface structure of tube No. 2 is almost mouth-closed compared with tube Nos. 3 and 4, which is obviously favorable to the bubble nucleation, leading to its highest heat transfer coefficient in not high heat flux region.

4.3 Heat Transfer Coefficients of the Plain and Enhanced Tubes With Different Lubricant Mass Fractions.

The results shown in Figs. 6(a)–6(f) are the pool boiling heat transfer performances of the plain and five enhanced tubes in the form of h_o

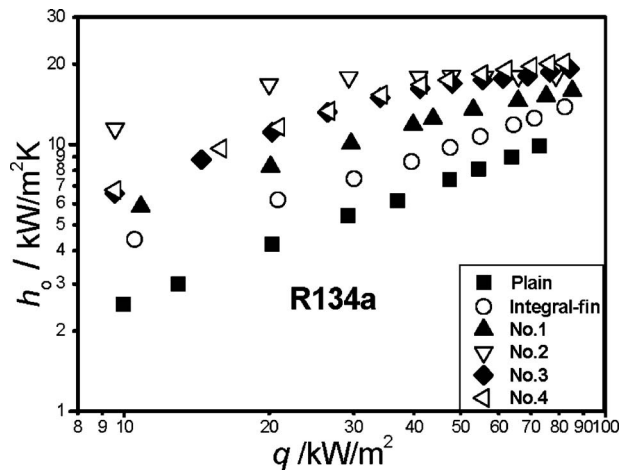


Fig. 5 Boiling heat transfer coefficients of pure R134a for six tubes

versus heat flux q . The parameter ranges are as follows: the lubricant mass fractions are 0.25%, 0.5%, 1.0%, 2.0%, 3.0%, 5.0%, 7.0%, and 10.0%; the heat flux ranges from 9000 W/m^2 to 90,000 W/m^2 ; and the saturation temperature of R134a is 6°C.

From the figure, the major lubricant effects of each tube are described and discussed as follows.

For the plain tube with the increment of lubricant mass fraction, the boiling coefficient first mildly decreases (at mass fraction ratios of 0.25% and 0.5%), then increases (1%), reaches the maximum at a lubricant mass fraction of 3%, and then gradually decreases with further increase in the lubricant mass fraction. With an increase in the ratio, the $h \sim q$ boiling curve gradually becomes mildly bent at higher heat flux. Also, when the ratio increases to as large as 10%, the heat transfer coefficient drastically drops by 30–60%, and the bent of the curve at higher heat flux is very significant.

For the integral-fin tube, the variation trends in the $h \sim q$ boiling curve are basically the same as those of the plain tube with two major differences. First, the mass fraction ratio at which the boiling heat transfer coefficient reduces include 0.25%, 0.5%, and 1%; second, the heat transfer coefficient reduction at a mass fraction ratio of 10% deviates from others not so much and its bent becomes very weak.

For the enhanced tube No. 1, the major features of the variation trends in the plain tube still hold, with two differences. First, the difference between the heat transfer coefficients of the pure R134a and that of ratio 3% decreases; second, the heat transfer coefficient reduction at a mass fraction ratio of 10% becomes more severe at lower heat flux, while the boiling curve bent at higher heat flux becomes mild.

There is one thing in common in the variation trends in the above three tubes: the boiling heat transfer coefficient decreases with a minor mass fraction ratio of oil, then increases, and finally decreases with further increase in the oil mass fraction ratio.

The enhanced tube No. 2 is very special among the six tubes studied in that starting from about $q = 20$ kW/m^2 , further increase in the heat flux has almost no effect on the enhancement of heat transfer. In addition, the reduction effect of oil mass fraction becomes severe from the oil mass fraction ratio of 5%. At a ratio of 10%, the bending of the $h \sim q$ boiling curve is appreciable.

Finally, the enhanced tubes Nos. 3 and 4 have the same trends featured by the following: (1) the boiling heat transfer coefficient of the pure R134a is the highest, and any addition of oil will deteriorate boiling heat transfer; (2) within the heat flux range studied, the boiling curve (h versus q) for any oil mass fraction ratio exhibits a mild bending; the heat transfer coefficient in-

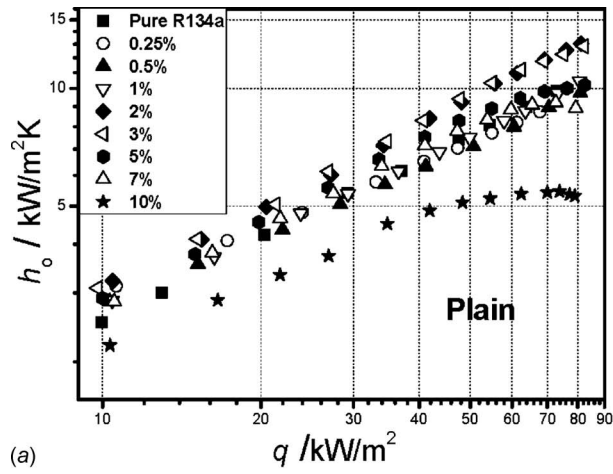
creases with heat flux and the increasing trend gradually becomes mild; and (3) the oil-ratio reduction becomes obvious at a mass fraction of 5%, and becomes severe at 10%.

In order to express clearly the variation trend in the boiling heat transfer coefficient with the oil mass fraction ratio, we proposed a relative method, as shown in Fig. 7. In the figure, the ordinate is the mean ratio of the boiling heat transfer coefficient of the polluted refrigerant over that of pure medium, and the abscissa is the oil mass fraction ratio. From the figure, two groups can be classified. The first group is consisted of the plain tube, integrated tube, and enhanced tube No. 1. For the three tubes, the relative curves show that within a certain region of the ratio, the contamination of oil, broadly speaking, does not deteriorate boiling heat transfer; moreover, it can enhance boiling heat transfer a bit. In the second group, which is composed of three enhanced tubes (Nos. 2–4), oil contamination, generally speaking, tends to deteriorate boiling heat transfer, and the relative curve shows almost monotonic decreasing trend. Such variation trend is mainly dependent on the re-entry structure. The closer the re-entry mouth, the more obvious the monotonic decreasing (see the results of the enhanced tube No. 2). The mouth gaps of Nos. 3 and 4 are not so closed, so the decreasing tendency is not so obvious as that of No. 2.

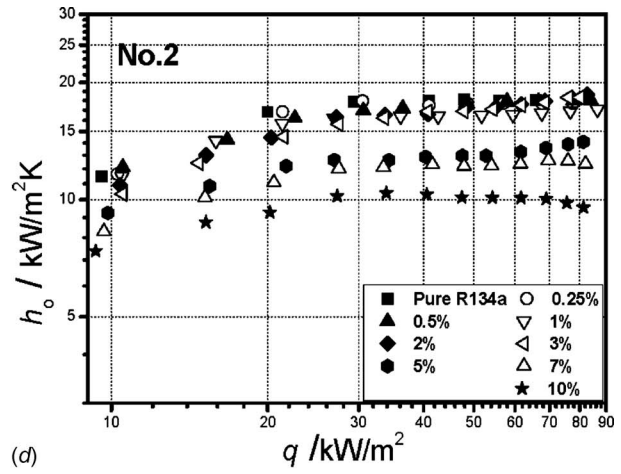
Compared with the results of the effect of other types of lubricant on boiling heat transfer outside horizontal tubes in the literatures, the above experimental results of the lubricant additive of PVE have the following things in common. First, for the plain tube, integral-fin tube, and tube No. 1 within a certain range of mass fraction, the lubricant is beneficial to the pool boiling heat transfer, as reported by many references [9–13]. Second, for the enhanced tubes of the reentrant cavity, the existence of PVE lubricant usually deteriorates the pool boiling heat transfer [14,17]. Third, the 3% threshold of lubricant mass fraction also exists for the plain tube beyond which the pool boiling heat transfer will be drastically reduced [3,11,17]. Fourth, for any tube studied in this paper, the oil mass fraction of 5% and further always reduce the pool boiling heat transfer significantly [3].

Generally speaking, the oil addition has a negligible influence at low weight mass fractions, i.e., below 3% [3]. However, from the point view of mechanism study, it is useful to look after all the way of heat transfer coefficient variation with oil mass fraction from pure refrigerant to a mass fraction of about 5–10%. In this regard, the proposed relative heat transfer coefficient presentation (Fig. 7) is very helpful. It gives the variation in h_{lub}/h_{pur} with oil mass fraction in details. From Fig. 7, it can be clearly observed that for the plain tube, integral-fin tube, and enhanced tube No. 1 within the minor oil mass fraction (0~1%), the pool boiling heat transfer is reduced a bit before it is increased with further increase in the lubricant mass fraction. Even though this reduction is not significant, usually around 1–3%, and not important for engineering design, it may be important for the mechanism study on the oil mass fraction effect. Also, this has been reported in the literature for R134a with POE lubricant by Spinder and Hahne [33]. Their study with one smooth tube and a GEWA-B tube indicated that pool boiling heat transfer decreased drastically even with small amounts of lubricant (0.5%) especially for low heat flux.

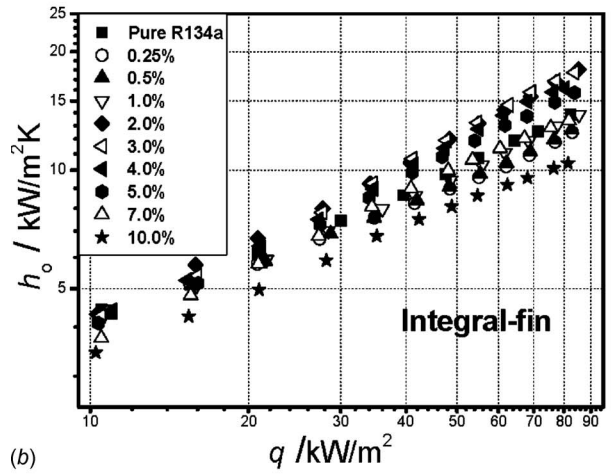
Figure 8 presents the same relative curves from literatures. It can be observed that basically two kinds of curves can be categorized: up-and-down and monotonic down curves. For the single component refrigerant boiling on smooth and integral-fin tubes with POE lubricant, the existence of the lubricant can enhance heat transfer within a certain range of the mass fraction (some case up to 5%; Fig. 8(a)), while no enhancement is obtained outside the reentrant cavity tubes with these lubricants (Fig. 8(b)). The relative curves for the pair of CFC-MO and 507-POE belongs to the second one (Fig. 8(a)). It should be noted that the effect of oil on the boiling heat transfer performance of the tested enhanced tubes is not so severe as that presented in Ref. [33] for GEWA-B. This may be caused by the difference in the cross section geom-



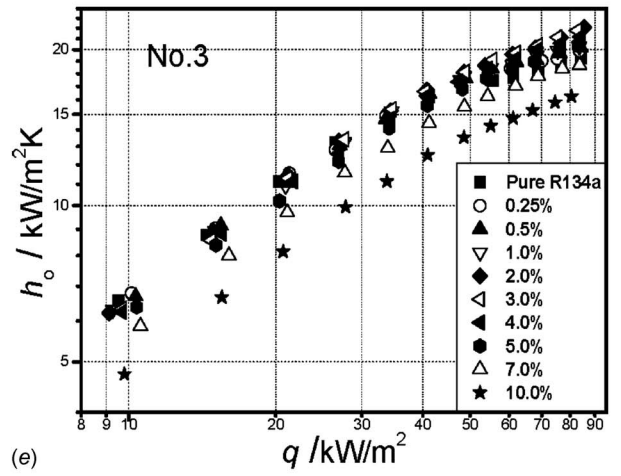
(a)



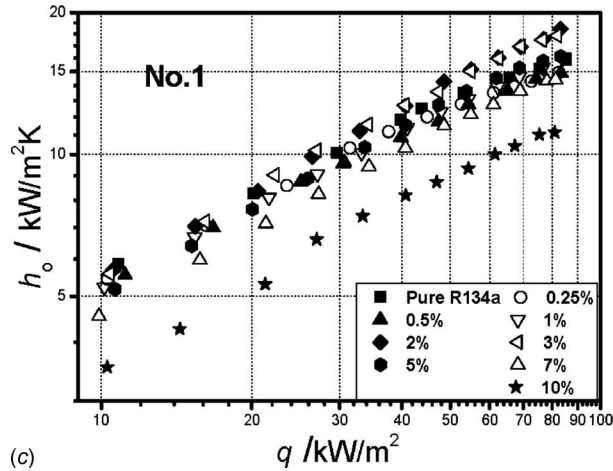
(d)



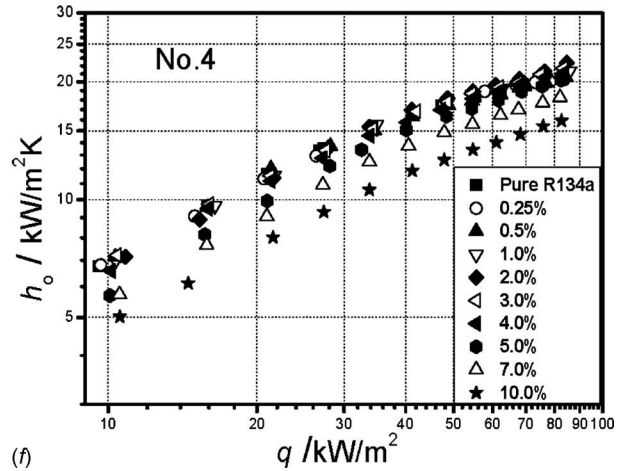
(b)



(e)



(c)



(f)

Fig. 6 Pool boiling heat transfer coefficients of R134a at a saturation temperature of 6°C with different lubrication concentrations

etry; the mouth of GEWA-B is fully closed while in our four tubes only tube No. 2 is a bit closed (but not fully) and all other three tubes are open.

It is interesting to note that the relative presentation method shown in Figs. 7 and 8 is, seemingly, first in the literature for showing the variation trend in boiling heat transfer with oil concentration. Such presentation method has its unique features of simplicity, clearness, and integrity. For integrity we mean that in Figs. 5 and 6, the percentage of heat transfer coefficient variation with oil concentration may more or less vary with heat flux, while

in Figs. 7 and 8, the percentage is an averaged one within the heat flux range tested. Also, it is such an averaged percentage that can represent the effect of oil concentration on the boiling heat transfer performance.

The versatile variation trends in the $h \sim q$ boiling curve with oil ratio come from many factors, and so far, there is no well-accepted understanding in the heat transfer community. Generally speaking, the positive or negative effect of the oil mass fraction depends on two opposite factors. On one side [3], the lubricant presence in the liquid refrigerant causes local oil accumulation.

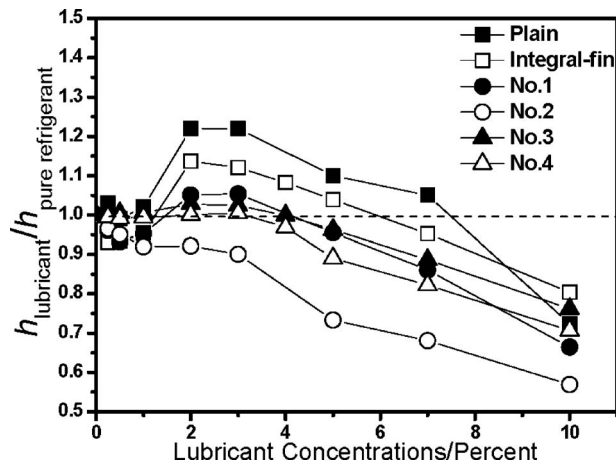


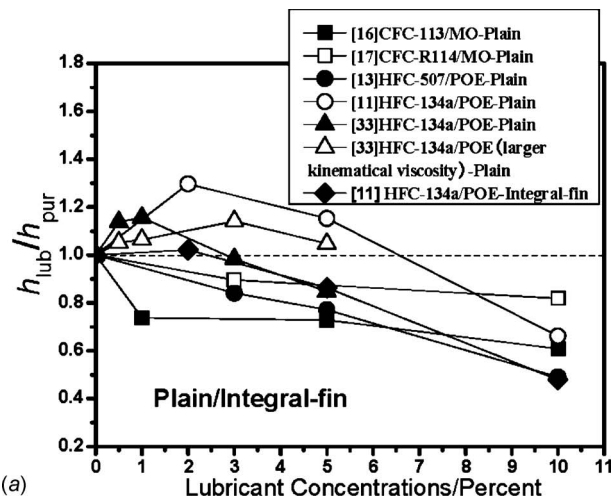
Fig. 7 Variation in the relative boiling heat transfer coefficient of lubricant-mixed refrigerant

Oil-rich layers may form at the solid-liquid and liquid-vapor interfaces. Especially at higher lubricant mass fraction, due to its large viscosity and mass transfer resistance effect, the lubricant tends to decrease the boiling heat transfer. On the other side, the foam caused by the oil may provide some convenient conditions of secondary nucleation, which causes some enhancements. Further studies are highly required to examine at what condition (or combination of conditions) the favorite or the unfavorable factor will be predominant.

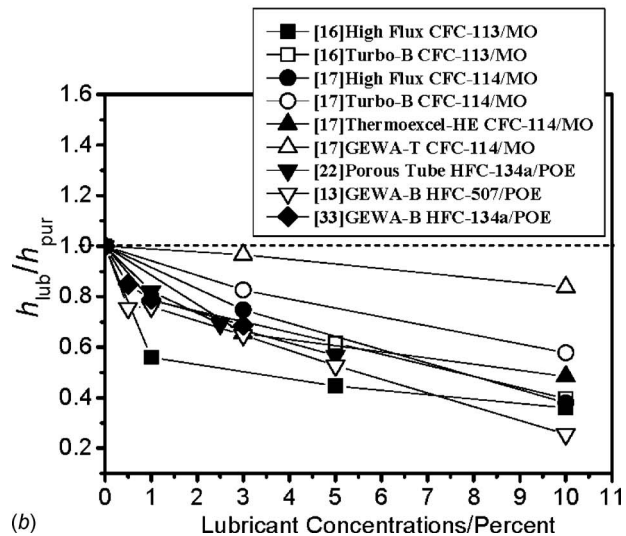
5 Conclusions

The pool boiling heat transfer coefficients of one smooth and five enhanced tubes were measured for R134a mixed with one new type refrigerant-lubricant (PVE). The oil mass fraction varies from 0.25% to 10 %, and the surface heat flux from 9000 W/m² to 90,000 W/m². The following conclusions can be drawn:

- (1) From all three enhanced tubes with re-entry cavity, the performances of tube No. 2 (whose mouth gap of twigs are almost closed) is the best at not high heat flux, and Nos. 3 and 4 are better than No. 2 (whose mouth gap of twigs are quite wide) for heat flux greater than 40 W/m².
- (2) It is found that for the lubricant PVE, the following things are in common with the other lubricants when the effect of its mass fraction on the pool boiling heat transfer is concerned:
 - (a) For the plain tube, integral-fin tube, and enhanced tube No. 1 within a certain range of mass fraction, the lubricant is beneficial to the pool boiling heat transfer.
 - (b) For the enhanced tubes of the reentrant cavity, the existence of the PVE lubricant always deteriorates the pool boiling heat transfer.
 - (c) The 3% threshold of lubricant mass fraction also exists for the plain tube beyond which the pool boiling heat transfer will be drastically reduced.
 - (d) The oil mass fraction of 5% and further always reduce the pool boiling heat transfer significantly.
 - (e) For the plain tube, integral-fin tube, and tube No. 1 within the minor oil mass fraction (0~1%), the pool boiling heat transfer is reduced a bit before it is appreciably increased with further increase in the lubricant mass fraction.
- (3) To present the oil mass fraction effect on the pool boiling heat transfer performance, a relative heat transfer presentation method is proposed in which the heat transfer coefficient of the contaminated medium over that of pure me-



(a)



(b)

Fig. 8 Variation in the relative boiling heat transfer coefficient of lubricant-mixed refrigerant reported in literatures

dium is the ordinate and mass fraction serves as the abscissa. Such presentation can show the oil mass fraction effect very clearly.

Acknowledgment

The supports from the Key Project of NNSFC (Grant No. 50636050), the National Key Projects of Fundamental R/D of China (973), and Daikin Cooperation of Japan are greatly acknowledged.

Nomenclature

- A = area (m²)
- c_i = enhanced ratio of the inside heat transfer coefficient
- c_p = specific heat capacity (J kg⁻¹ K⁻¹)
- C = coefficient of the Cooper correlation
- d = diameter of the tube (mm)
- e = height of the outside fin (mm)
- f = drag coefficient
- F_{PF} = pressure correction factor in Gorenflo's correlation
- h = heat transfer coefficients (W m⁻² K⁻¹)
- h_{ro} = reference heat transfer coefficient in Gorenflo's correlation (W m⁻² K⁻¹)

H = height of the inside fin (mm)
 U = overall heat transfer coefficients ($\text{W m}^{-2} \text{K}^{-1}$)
 L = tube's tested length (m)
 m = mass flow rate (kg s^{-1}); coefficient in Cooper's correlation
 M_r = molecular weight of the refrigerant
 nf = coefficient in Gorenflo's correlation
 Pr = Prandtl number in Gnielinski's correlation
 P_r = reduced pressure in Cooper and Gorenflo's correlation
 P_{ro} = reduced pressure in fixed reference condition of Gorenflo's correlation
 q = heat flux (W m^{-2})
 q_o = fixed reference heat flux in Gorenflo's correlation (W m^{-2})
 Re = Reynolds number
 R_f = thermal resistance of fowl ($\text{m}^2 \text{K W}^{-1}$)
 R_p = average surface roughness of smooth tube (m)
 R_{po} = fixed reference surface roughness in Gorenflo's correlation (μm)
 R_w = thermal resistance of tube wall ($\text{m}^2 \text{K W}^{-1}$)
 t = temperature ($^{\circ}\text{C}$)

Greek Alphabet

ϕ = heat transfer rate (W)
 λ = thermal conductivity ($\text{W m}^{-1} \text{K}^{-1}$)
 Δt_m = logarithmic mean temperature difference $^{\circ}\text{C}$

Subscripts

c = condensing
 e = evaporating
 i = inside of tube
 in = inlet of tube
 ip = inside of the plain tube
 o = outside of tube
 out = outlet of tube
 s = saturation
 w = wall

References

- [1] Stephan, K., 1964, "Influence of Oil on Heat Transfer of Boiling Refrigerant 12 and Refrigerant 22," *Proceedings of the 11th International Congress of Refrigeration*, pp. 369–380.
- [2] Kedzierski, M. A., 2002, "Use of Fluorescence to Measure the Lubricant Excess Surface Density During Pool Boiling," *Int. J. Refrig.*, **25**(8), pp. 1110–1122.
- [3] Shen, B., and Groll, E. A., 2005, "A Critical Review of the Influence of Lubricants on the Heat Transfer and Pressure Drop of Refrigerants. Part I. Lubricant Influence on Pool and Flow Boiling," *HVAC&R Res.*, **11**(3), pp. 341–359.
- [4] Kedzierski, M. A., 2005, "Effect of Bulk Lubricant Concentration on the Excess Surface Density During R134a Pool Boiling," *Int. J. Refrig.*, **28**(4), pp. 526–537.
- [5] Kedzierski, M. A., 2007, "Effect of Refrigerant Oil Additive on R134a and R123 Boiling Heat Transfer Performance," *Int. J. Refrig.*, **30**(1), pp. 144–154.
- [6] Jensen, M. K., and Jackson, D. L., 1984, "Prediction of Nucleate Pool Boiling Heat Transfer Coefficients of Refrigerant-Oil Mixtures," *ASME J. Heat Transfer*, **106**(1), pp. 184–197.
- [7] Kedzierski, M. A., "Improved Thermal Boundary Layer Parameter for Semi-Theoretical Refrigerant/Lubricant Pool Boiling Model," *Proceedings of the International Congress of Refrigeration*, pp. 1–8.
- [8] Kedzierski, M. A., 2003, "A Semi-Theoretical Model for Predicting Refrigerant/Lubricant Mixture Pool Boiling Heat Transfer," *Int. J. Refrig.*, **26**(3), pp. 337–348.
- [9] Stephan, K., 1982, "Heat Transfer in Boiling of Mixtures," *Proceedings of the Seventh International Heat Transfer Conference*, pp. 59–81.
- [10] Udombresuwan, A., and Mesler, R., 1986, "The Enhancement of Nucleate Boiling by Foam," *Proceedings of the Eighth International Heat Transfer Conference*, pp. 2939–2944.
- [11] Hsieh, S. S., and Weng, C. J., 1997, "Nucleate Pool Boiling Heat Transfer Coefficients of Distilled Water (H_2O) and R-134a/Oil Mixtures From Rib-Roughened Surfaces," *ASME J. Heat Transfer*, **119**(1), pp. 142–151.
- [12] Bell, K. I., Hewitt, G. F., and Morris, S. D., 1987, "Nucleate Pool Boiling of Refrigerant/Oil Mixtures," *Exp. Heat Transfer*, **1**(1), pp. 71–86.
- [13] Mohrlok, K., Spindler, K., and Hahne, E., 2001, "The Influence of a Low Viscosity Oil on the Pool Boiling Heat Transfer of the Refrigerant R507," *Int. J. Refrig.*, **24**(1), pp. 25–40.
- [14] Wanniarachchi, A. S., Marto, P. J., and Reilly, J. T., 1986, "The Effect of Oil Contamination on the Nucleate Pool-Boiling Performance of R-114 From a Porous-Coated Surface," *ASHRAE Trans.*, **92**(2B), pp. 525–540.
- [15] Webb, R. L., and McQuade, W. F., 1993, "Pool Boiling of R11 and R123 Oil-Refrigerant Mixtures on Plain and Enhanced Tube Geometries," *ASHRAE Trans.*, **99**(1), pp. 1225–1236.
- [16] Curcio, L. A., and Somerscales, E. F., 1994, *Pool Boiling of Enhanced Heat Transfer Surfaces in Refrigerant-Oil Mixtures and Aqueous Calcium Sulfate Solutions*, U.S. Department of Energy, Washington, DC, pp. 1–149.
- [17] Memory, S. B., Sugiyama, D. C., and Marto, P. J., 1995, "Nucleate Pool Boiling of R-114 and R-114-Oil Mixtures From Smooth and Enhanced Surfaces—I. Single Tubes," *Int. J. Heat Mass Transfer*, **38**(8), pp. 1347–1361.
- [18] Kedzierski, M. A., 2001, "The Effect of Lubricant Concentration, Miscibility, and Viscosity on R134a Pool Boiling," *Int. J. Refrig.*, **24**(4), pp. 348–366.
- [19] Kedzierski, M. A., 2002, "Effect of Bulk Lubricant Concentration on the Excess Surface Density During R123 Pool Boiling," *Int. J. Refrig.*, **25**(8), pp. 1062–1071.
- [20] Youbi-Idrissi, M., Bonjour, J., Marvillet, C., and Meunier, F., 2003, "Impact of Refrigerant-Oil Solubility on an Evaporator Performances Working With R-407C," *Int. J. Refrig.*, **26**(3), pp. 284–292.
- [21] Hughes, D. W., McMullan, J. T., Mawhinney, K. A., and Morgan, R., 1984, "Influence of Oil on Evaporator Heat Transfer (Results for R12 and Shell Clavus 68)," *Int. J. Refrig.*, **7**(3), pp. 150–158.
- [22] Zarnescu, V., Webb, R. L., and Chien, L. H., 2000, "Effect of Oil on the Boiling Performance of Structured and Porous Surfaces," *HVAC&R Res.*, **6**(1), pp. 41–54.
- [23] Kaneko, M., Sakanoue, S., Tazaki, T., Tominaga, S., Takagi, M., and Goodin, M., 1999, "Determination of Properties of PVE Lubricants With HFC Refrigerants [PolyVinylEther]," *ASHRAE Trans.*, **105**(2), pp. 1000–1007.
- [24] Tominaga, S., 1999, "Current Trend of Refrigeration Oil for Alternative Refrigerants," *Refrigeration*, **74**(862), pp. 660–665.
- [25] Fukui, H., Sanechika, K. I., and Ikeda, M., 2000, "Novel Refrigeration Lubricants for Use With HFC Refrigerants," *Tribol. Int.*, **33**(10), pp. 707–713.
- [26] Cheng, B., and Tao, W. Q., 1994, "Experimental Study of R-152a Film Condensation on Single Horizontal Smooth Tube and Enhanced Tubes," *ASME J. Heat Transfer*, **116**(1), pp. 266–270.
- [27] Yang, S. M., and Tao, W. Q., 2006, *Heat Transfer*, Higher Education Press, Beijing, China, pp. 563–564.
- [28] Gnielinski, V., 1976, "New Equations for Heat and Mass Transfer in Turbulent Pipe and Channel Flows," *Int. Chem. Eng.*, **16**, pp. 359–368.
- [29] Masuda, H., and Rose, J. W., 1988, "Condensation of Ethylene Glycol on Horizontal Integral-Fin Tubes," *ASME J. Heat Transfer*, **110**, pp. 1019–1022.
- [30] Kline, S. J., and McClintock, F. A., 1953, "Describing Uncertainties in Single-Sample Experiments," *Mech. Eng.*, **75**(7), pp. 3–9.
- [31] Cooper, M. G., 1984, "Saturation Nucleate Pool Boiling—A Simple Correlation," *International Chemical Engineering Symposium Series*, **86**, pp. 785–792.
- [32] Gorenflo, D., 1993, *Pool Boiling in VDI-Heat Atlas* (English version), VDI-Verlag, Dusseldorf, Germany.
- [33] Spindler, K., and Hahne, E., 2009, "The Influence of Oil on Nucleate Pool Boiling Heat Transfer," *Heat Mass Transfer*, **45**(7), pp. 979–990.

Poiseuille Flow of Reactive Phan–Thien–Tanner Liquids in 1D Channel Flow

T. Chinyoka

Center for Research in Computational and Applied Mechanics,
University of Cape Town,
Private Bag X3,
Rondebosch 7701, South Africa
e-mail: tchinyok@vt.edu

We investigate, using direct numerical simulations, the effects of viscoelasticity on pressure driven flows of thermally decomposable liquids in channels. A numerical algorithm based on the finite difference method is implemented in time and space with the Phan–Thien–Tanner as the model for the viscoelastic liquids. The strong dependence of fluid temperature on the Frank–Kamenetskii parameter is shown for various fluid types and the phenomenon of thermal runaway is demonstrated. It is shown that viscoelastic fluids have in general delayed susceptibility to thermal runaway as compared with corresponding inelastic fluids. This paper demonstrates the efficiency of using semi-implicit finite difference schemes in solving transient problems of coupled nonlinear systems. It also provides an understanding of nonisothermal flows of viscoelastic fluids.

[DOI: 10.1115/1.4002094]

1 Introduction

Investigations of heat transfer in fluid flow have mostly been conducted for Newtonian fluids [1–9]. Similar investigations of boundary layer type flows involving inelastic non-Newtonian fluids have been conducted, see, for example, Ref. [10]. Temperature dependent flows of viscoelastic fluids have been largely limited by the slow development of the relevant universally accepted nonisothermal constitutive models [11–15].

The question of whether solutions of partial differential equations exist globally in time or develop singularities in finite-time remains a focus of attention in the scientific community. The fact that problems of industrial and engineering significance are governed by these equations makes the discussion all the more important. For a comprehensive overview of the typical examples where finite-time blow-up, or at least very rapid growth, occurs in mechanical systems and, in particular, those of thermal-fluid mechanics refer to Ref. [16]. In chemical kinetics, such finite-time blow-up of physical temperatures is commonly referred to as thermal runaway and is closely connected with the so-called Kamenetskii parameter, named after the pioneering work of Frank–Kamenetskii [17]. Experimental investigations and evidence of the thermal runaway problem are provided, for example, in Ref. [3].

The need to understand and control such phenomena as thermal runaway provides the impetus for investigations like the one considered in this work. A similar investigation for reactive lubricants subjected to shear flow was carried out in Ref. [18] where it was demonstrated that viscoelastic Oldroyd-B liquids can withstand higher values of the Frank–Kamenetskii parameter without undergoing thermal runaway as opposed to (inelastic) Newtonian lubricants. For the case of Poiseuille flow in cylindrical pipes, Makinde [2] investigated the steady state one dimensional flow of reactive Newtonian fluids with temperature dependent viscosity. He [2] cited as his primary motivation the pipeline transport of petroleum products in petrochemical industries. However, since most such petroleum products tend to be viscoelastic liquids by nature, it is the objective of this paper to extend the results of Makinde [2] to include such viscoelastic considerations. Also, since the question of global existence of solutions in time is critical to these types of investigations, we found it necessary to also extend the work to

the transient regime; this also helps us capture such time dependent phenomena such as thermal runaway. As in Ref. [2], chemically reacting flows have been considered mostly using Newtonian fluids and the literature on related viscoelastic investigations is quite sparse. For a comprehensive overview of non-Newtonian flows in general and viscoelastic fluid phenomena, in particular, we refer to the excellent treatises [19,20].

As is the commonly accepted approach, see Refs. [7,21,22], we model thermal decomposition of the reactive fluids via Arrhenius kinetics. Following, say, Ref. [7], we will neglect the effects of reactant consumption and thus assume constant fluid concentration. To model the viscoelastic fluids, we will use the PTT constitutive equations with provisions for thermodynamics [12,23].

In Sec. 2, we present the model problem and its governing equations and then proceed to develop the numerical algorithm that we will employ to solve the set of equations. We provide and discuss the graphical results in Secs. 3 and 4 and concluding remarks follow in Sec. 5.

2 Mathematical Modeling

Figure 1 is a sketch of the model problem. The original flow is confined to a two-dimensional channel of width L^* . The flow is driven by a constant pressure gradient $dp^*/dx^* = -G^*$ and we assume no slip conditions at the walls $y^* = 0, L^*$. The walls are maintained at the same constant temperature T_B^* and we also assume that the fluid is initially at this uniform temperature, $T^* = T_B^* > 0$ for time $t^* \leq 0$. We use zero initial velocity and stresses as the initial conditions for the velocity and extra stress components.

The specific heat capacity, density, and thermal conductivity of the fluid will be taken as constant and denoted by c_p^* , ρ^* , and κ^* , respectively. Viscosities and relaxation times tend to be more susceptible to temperature variations and so these will be assumed temperature dependent. We employ a WLF model for the temperature dependency of polymer viscosity (η_p^*) and relaxation time (λ^*); for more details, we refer the reader to Ref. [23]. We will denote the total viscosity by $\eta(T)^* = \eta_s(T)^* + \eta_p(T)^*$, where η_s^* is the solvent viscosity.

The fluid system is governed by the continuity (1), momentum (2), and energy equations (3) for incompressible PTT fluids:

$$\nabla^* \cdot \mathbf{u}^* = 0 \quad (1)$$

$$\rho^* \frac{D}{Dt^*} \mathbf{u}^* = \nabla^* \cdot (-p^* \mathbf{I} + \eta_s(T)^* \underline{\underline{\sigma}}^* + \underline{\underline{\tau}}^*) \quad (2)$$

Contributed by the Heat Transfer Division of ASME for publication in the JOURNAL OF HEAT TRANSFER. Manuscript received June 27, 2009; final manuscript received June 28, 2010; published online August 10, 2010. Assoc. Editor: Walter W. Yuen.

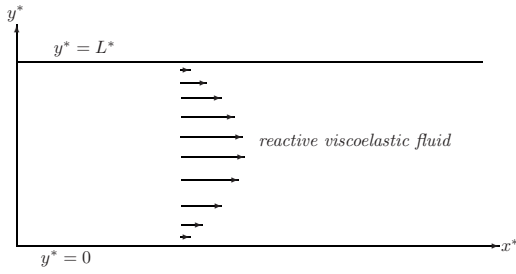


Fig. 1 Schematics of the model problem

$$\rho^* c_p \frac{D}{Dt^*} T^* = \kappa^* \nabla^{*2} T^* + \gamma (\underline{\underline{\tau}}^* : \underline{\underline{\zeta}}^*) + (1 - \gamma) \frac{\text{Tr}(\underline{\underline{\tau}}^*)}{2\lambda(T)^*} + Q^* A^* C^* \times \exp\left(-\frac{E^*}{R^* T^*}\right) \quad (3)$$

where the notation $D/Dt^* := \partial/\partial t^* + \mathbf{u}^* \cdot \nabla^*$ represents the material derivative, $\nabla^* = \partial/\partial x^* + \partial/\partial y^*$ is the gradient operator, $\underline{\underline{\zeta}}^* = [\nabla^* \mathbf{u}^* + (\nabla^* \mathbf{u}^*)^T]$ is the deformation rate tensor, and the extra stress tensor, $\underline{\underline{\tau}}^*$, is modeled by the nonisothermal Phan–Thien–Tanner (PTT) constitutive equation:

$$\underline{\underline{\tau}}^* + \lambda(T)^* \left(\frac{\nabla \cdot \underline{\underline{\tau}}^*}{\eta_p(T)^*} + \frac{\varepsilon}{\eta_p(T)^*} \text{Tr}(\underline{\underline{\tau}}^*) \underline{\underline{\tau}}^* - \underline{\underline{\tau}}^* \frac{D}{Dt^*} \ln[T^*/T_B^*] \right) = \eta_p(T)^* \underline{\underline{\zeta}}^* \quad (4)$$

where the parameter ε determines the elongational behavior of PTT model [11]. The upper convected time derivative $\overset{\nabla}{\underline{\underline{\tau}}}^*$ reads

$$\overset{\nabla}{\underline{\underline{\tau}}}^* = \frac{\partial \underline{\underline{\tau}}^*}{\partial t^*} + (\mathbf{u}^* \cdot \nabla^*) \underline{\underline{\tau}}^* - (\nabla^* \mathbf{u}^*) \underline{\underline{\tau}}^* - \underline{\underline{\tau}}^* (\nabla^* \mathbf{u}^*)^T$$

In the energy equation (3), the parameter γ signifies the ability of viscoelastic fluids to store energy due to their elastic behavior [12,23]. In particular, $0 \leq \gamma \leq 1$, where $\gamma=0$ corresponds to the case of pure energy elasticity and $\gamma=1$ corresponds to pure entropy elasticity. The colon ($:$) denotes the double dot product of two tensors. The last term in Eq. (3) is the source term due to chemical reactions. Here, Q^* is the heat release due to the exothermic reaction, A^* is the Arrhenius prefactor, C^* is the residue concentration, E^* is the activation energy, and R^* is the gas constant, see, for example, Refs. [7,22].

As in Refs. [12,23], we use a Williams-Landel-Ferry (WLF) model for the temperature dependence of the polymer viscosities and relaxation times and a Nahme-type law to model solvent viscosities:

$$\lambda(T)^* = \lambda(T_B)^* \exp\left[-\frac{c_1(T^* - T_B^*)/T_B^*}{c_2 + (T^* - T_B^*)/T_B^*}\right]$$

$$\eta_p(T)^* = \eta_p(T_B)^* \exp\left[-\frac{c_1(T^* - T_B^*)/T_B^*}{c_2 + (T^* - T_B^*)/T_B^*}\right] \quad (5)$$

$$\eta_s(T)^* = \eta_s(T_B)^* \exp(-\varepsilon(T^* - T_B^*)/T_B^*)$$

where the constants λ_B^* , η_{sB}^* , and η_{pB}^* are the dimensional reference quantities, ε is a dimensionless quantity depending on the fluid, and the parameters c_1 and c_2 are, respectively, assigned the values 15 and 50 corresponding to the case where T_B^* is close to the glass transition temperature and hence the polymer viscosity and relaxation times are strongly temperature dependent.

Defining a characteristic velocity U_0^* , say, the centerline velocity for the steady fully developed Poiseuille flow, leads to the dimensionless parameters:

$$\text{Re} = \frac{\rho^* U_0^* L^*}{\eta_B^*}, \quad \text{We} = \frac{\lambda_B^* U_0^*}{L^*}, \quad \text{Pr} = \frac{c_p^* \eta_B^*}{\kappa^*}, \quad \alpha = \frac{R^* T_B^*}{E^*}$$

$$\beta = \frac{\eta_{pB}^*}{\eta_B^*}, \quad \delta_1 = \frac{Q^* A^* E^* C^* L^{*2}}{\kappa^* R^* T_B^{*2}} \exp\left(-\frac{1}{\alpha}\right), \quad \text{Br} = \frac{\eta_B^* U_0^{*2}}{\kappa^* T_B^*} \quad (6)$$

Here Re, We, Pr, and Br are, respectively, the Reynolds, Weissenberg, Prandtl, and Brinkman numbers. α is an activation energy parameter and β is the ratio of the polymer to the total viscosity. The reaction parameter, δ_1 (also called the Frank–Kamenetskii parameter), is described, say, in Refs. [7,17,21,22]. We introduce the following dimensionless variables:

$$t = \frac{U_0^*}{L^*} t^*, \quad y = \frac{y^*}{L^*}, \quad u = \frac{u^*}{U_0^*}, \quad \bar{\lambda}(T) = \frac{\lambda(T)^*}{\lambda_B^*}, \quad \mu(T) = \frac{\eta(T)^*}{\eta_B^*}$$

$$p = \frac{p^*}{\rho^* U_0^{*2}}, \quad T = \frac{(T^* - T_B^*)}{\alpha T_B^*}, \quad \underline{\underline{\tau}} = \frac{L^*}{\eta_B^* U_0^*} \underline{\underline{\tau}}^*, \quad \underline{\underline{\zeta}} = \frac{L^*}{U_0^*} \underline{\underline{\zeta}}^*,$$

$$\nabla = L^* \nabla^* \quad (7)$$

The dimensionless governing equations for the velocity \mathbf{u} , temperature T , and extra stress components $\underline{\underline{\tau}}$ are then

$$\text{Re} \frac{D\mathbf{u}}{Dt} = -\text{Re} \nabla p + \nabla \cdot (\underline{\underline{\tau}} + (1 - \beta)\mu_s \underline{\underline{\zeta}}) \quad (8)$$

$$\text{Re Pr} \frac{DT}{Dt} = \nabla^2 T + \text{Br} \left[\gamma (\underline{\underline{\tau}} : \underline{\underline{\zeta}}) + (1 - \gamma) \frac{\text{Tr}(\underline{\underline{\tau}})}{2 \text{We} \bar{\lambda}} \right] + \delta_1 \exp\left(\frac{T}{1 + \alpha T}\right) \quad (9)$$

$$\underline{\underline{\tau}} + \text{We} \bar{\lambda} \overset{\nabla}{\underline{\underline{\tau}}} + \left(\varepsilon \frac{\text{We}}{\beta} \text{Tr}(\underline{\underline{\tau}}) - \text{We} \bar{\lambda} \frac{D}{Dt} \ln(\alpha T + 1) \right) \underline{\underline{\tau}} = \beta \mu_p \underline{\underline{\zeta}} \quad (10)$$

The dimensionless viscosity and relaxation times, respectively, now read:

$$\mu_p(T) = \exp\left(-\frac{\alpha c_1 T}{c_2 + \alpha T}\right), \quad \mu_s(T) = \exp(-\varepsilon \alpha T)$$

$$\bar{\lambda}(T) = \exp\left(-\frac{\alpha c_1 T}{c_2 + \alpha T}\right)$$

The relevant boundary conditions are now $T(0)=T(1)=0$ and $u(0)=u(1)=0$. The initial condition for the fluid temperature is $T=0$ and as mentioned earlier, the initial conditions for the velocity and extra stress components are taken as zero initial velocity and stresses.

2.1 Numerical Algorithm. Our numerical algorithm is based on the semi-implicit finite difference scheme given in Ref. [24] for the isothermal viscoelastic case. We extend the algorithm to the temperature equation and take the implicit terms at the intermediate time level $(n + \xi)$ where $0 \leq \xi \leq 1$. The algorithm employed in Ref. [18] uses $\xi=1/2$; we will, however, follow the method in Ref. [24] and thus take $\xi=1$ in this paper. The discretization of the governing equations is based on a linear Cartesian mesh and uniform grid on which finite-differences are taken. We approximate both the second and first spatial derivatives with second-order central differences. The equations corresponding to the first and last grid points are modified to incorporate the boundary conditions. The semi-implicit scheme for the velocity component reads

$$\text{Re} \frac{u^{(n+1)} - u^{(n)}}{\Delta t} = \text{Re} G + \frac{\partial}{\partial y} (\tau_{12}^{(n)}) + (1 - \beta)(\mu_s^{(n)} u_{yy}^{(n+\xi)} + u_y^{(n)} \mu_{sy}^{(n)}) \quad (11)$$

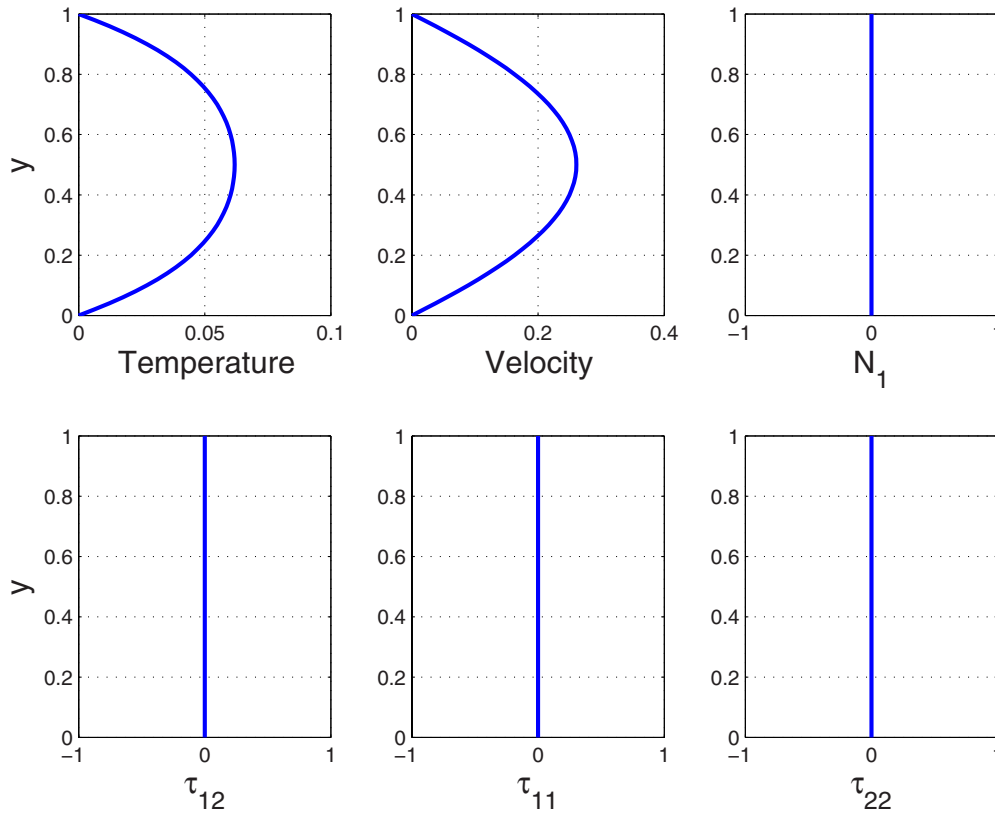


Fig. 2 Newtonian results with zero initial conditions

Here $G=1$ denotes the constant pressure gradient in the x -direction and, as in the Crank–Nicolson scheme, terms given at $(n+\xi)$ are taken as the weighted averages of the corresponding terms at $(n+1)$ and n :

$$u^{(n+\xi)} = \xi u^{(n+1)} + (1-\xi)u^{(n)}$$

The equation for $u^{(n+1)}$ then becomes

$$-r_1 u_{j-1}^{(n+1)} + (\text{Re} + 2r_1)u_j^{(n+1)} - r_1 u_{j+1}^{(n+1)} = \text{explicit terms} \quad (12)$$

where $r_1 = r(1-\beta)\xi\mu^{(n)}$ and $r = \Delta t / (\Delta y)^2$. The solution procedure for $u^{(n+1)}$ thus reduces to the inversion of tridiagonal matrices, which is an advantage over a full implicit scheme. The semi-implicit integration scheme for the temperature equation is similar to that for the velocity component. Unmixed second partial derivatives of the temperature are treated implicitly:

$$\text{Re Pr} \frac{T^{(n+1)} - T^{(n)}}{\Delta t} = T_{yy}^{(n+\xi)} + \delta_1 \exp\left(\frac{T}{1+\alpha T}\right)^{(n)} + \text{Br} \left[2\gamma u_y \tau_{12} + (1 - \gamma) \frac{\text{Tr}(\underline{\tau})}{2 \text{We} \bar{\lambda}} \right]^{(n)} \quad (13)$$

If we define, $\text{Pe} = \text{Re Pr}$ and $r_2 = \xi r$, the equation for $T^{(n+1)}$ then becomes

$$-r_2 T_{j-1}^{(n+1)} + (\text{Pe} + 2r_2)T_j^{(n+1)} - r_2 T_{j+1}^{(n+1)} = \text{explicit terms} \quad (14)$$

and the solution procedure reduces to inversion of a constant tridiagonal matrix. The constitutive equation (10) is treated with an analogous semi-implicit integration scheme. The terms that involve spatial derivatives of the extra stress tensor (which, however, identically vanish in this 1D case) are taken implicitly, as is the linear term in $\underline{\tau}$:

$$\text{We} \bar{\lambda}^{(n)} \left[\frac{\underline{\tau}^{(n+1)} - \underline{\tau}^{(n)}}{\Delta t} \right] + \underline{\tau}^{(n+\xi)} = \text{explicit terms}$$

The equations for the stresses, $\tau_{11}^{(n+1)}$, $\tau_{12}^{(n+1)}$, and $\tau_{22}^{(n+1)}$ are thus of the form

$$(\text{We} \bar{\lambda}^{(n)} + \xi \Delta t) \underline{\tau}^{(n+1)} = \text{explicit terms} \quad (15)$$

The solution procedure is even simpler as it simply entails the direct calculation of the explicit terms. The schemes (12), (14), and (15) were checked for consistency and it was shown that Eqs. (12), (14), and (15) are second-order accurate in space and first-order accurate in time.

3 Results

3.1 Purely Viscous Liquids. By taking zero extra stresses ($\underline{\tau}=0$) and making a slight alteration to the resulting temperature equation (9):

$$\text{Re Pr} \frac{DT}{Dt} = \nabla^2 T + \eta_s \text{Br} \underline{S} : \underline{S} + \delta_1 \exp\left(\frac{T}{1+\alpha T}\right)$$

we recover the case of a purely viscous Newtonian fluid, albeit for variable (temperature dependent) viscosity.

Figure 2 shows the variation of the fluid temperature, velocity, normal stress difference ($N_1 = \tau_{11} - \tau_{22}$), shear stress τ_{12} , and diagonal stress components τ_{11} , τ_{22} with y . The parameter values used in Fig. 2 are $\gamma = \text{We} = \beta = 0$, $t = 100$, $\delta_1 = 0.3$, $\alpha = 1$, $\text{Re} = 10^{-4}$, $\text{Pr} = 10^6$, $\text{Br} = 1$, $\Delta y = 0.02$, and $\Delta t = 0.001$. The notation $\beta=0$ (and/or $\text{We}=0$) in this work should be interpreted as a Newtonian fluid. We recover the expected parabolic velocity profile and temperature profiles and the predictable zero elastic stress field. At the given parameter values, the maximum temperature is $T_{\max} = 0.0619$ and the maximum velocity is $u_{\max} = 0.2608$. For all computations that will follow, the results obtained at time $t=100$ are deep in the convergence zone and practically represent steady state solutions. In fact, the code shows convergence in both space

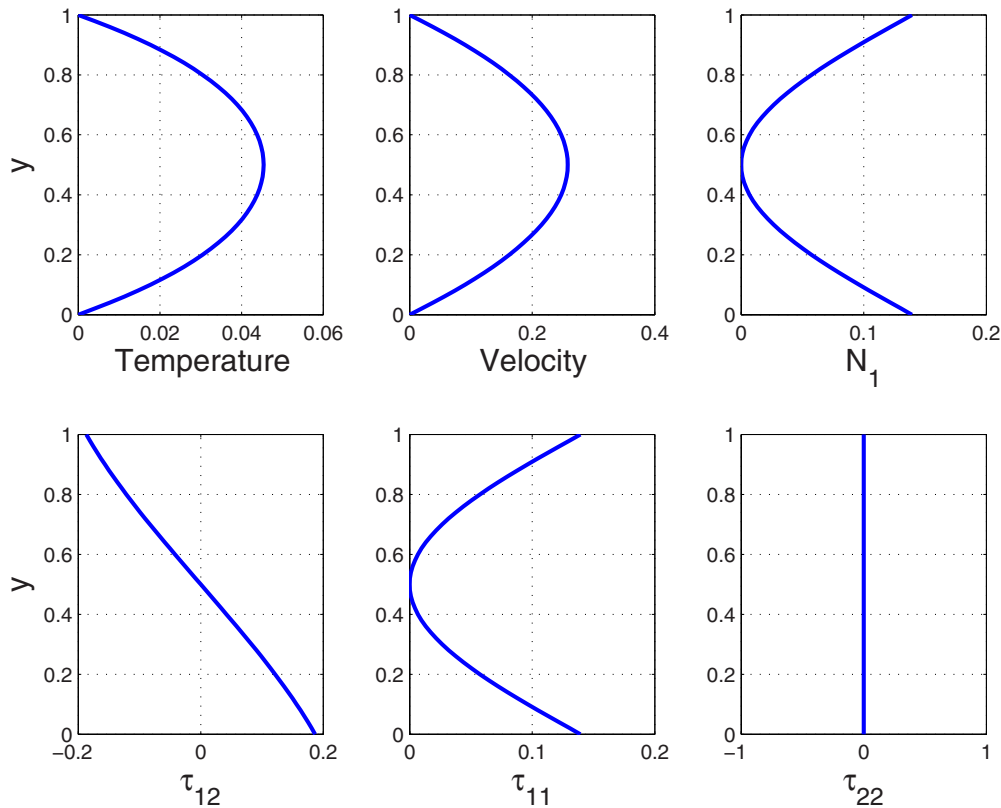


Fig. 3 Viscoelastic results

and time. In this case, the maximum temperature has converged to $T_{\max}=0.0619$ for several mesh sizes and time steps.

3.2 Viscoelastic Effects. If we adjust the parameter values of Fig. 2 to $\gamma=0.5$, $\beta=0.2$, and $We=0.4$ that leads to reduced maximum temperatures and velocities, we now have $T_{\max}=0.0454$ and $v_{\max}=0.2580$.

Figure 3 shows, as expected, that the diagonal stress component remains fixed at zero and that the first and second normal stress differences are non-negative and nonpositive, respectively. The observed reduction in fluid temperature when using the viscoelastic fluid as compared with the Newtonian fluid shows that fluid elasticity can be used to control the growth of fluid temperature and hence delays possible blow-up phenomena such as thermal runaway.

4 Thermal Runaway

Since an increase in the Frank–Kamenetskii parameter (δ_1) would correspondingly increase the strength of the source terms in the temperature equation, it follows that the fluid temperature should increase with increase in δ_1 .

The profiles depicted in Fig. 4 were obtained using the parameter values $t=20$, $\alpha=1$, $Re=10^{-4}$, $Pr=10^6$, $Br=1$, $\gamma=0.5$, $\beta=0.2$, $We=0.2$, $\Delta y=0.02$, and $\Delta t=0.001$. As described earlier, we now show that fluid elasticity can be used to reduce the growth of fluid temperature with increasing reaction parameter.

In Fig. 5, we used $t=20$, $\delta_1=0.1$, $\alpha=1$, $Re=10^{-4}$, $Pr=10^6$, $Br=1$, $\gamma=0.5$, $\beta=0.2$, $We=0.4$, $\Delta y=0.02$, and $\Delta t=0.001$.

In fact, increased fluid elasticity progressively lowers the fluid maximum attainable temperature, albeit only by infinitesimal magnitudes, as shown in Fig. 6.

The results of Fig. 6 were obtained using the same parameter values as those of Fig. 5.

The long term behavior of the fluid maximum temperature with respect to higher values of either δ_1 or time is not directly obvi-

ous. There could be blow-up of the solution (thermal runaway) if δ_1 exceeds certain threshold values as is demonstrated, say, in Refs. [7,18,22] and in related works cited therein. In Ref. [18], maximum temperatures were recorded at finite-time convergence for each value of the reaction parameter until a threshold value of the temperature was reached at which blow-up of the temperature was observed. The results for current work are qualitatively similar to those displayed in Ref. [18] and will not be repeated here. In particular, the threshold value of δ_1 is increased when we use increasingly polymeric liquids. The conclusions are also similar and relate to the ability of viscoelastic fluid to store energy due to their elastic character. Thus while Newtonian fluids would dissipate all the mechanical energy as heat, viscoelastic fluids on the other hand will partially dissipate some of the energy and store some. We conclude by displaying the difference in temperature between the cases of pure entropy elasticity and pure energy elasticity.

In Fig. 5, we used $t=100$, $\delta_1=0.1$, $\alpha=1$, $Re=10^{-4}$, $Pr=10^6$, $Br=1$, $\beta=0.2$, $We=0.4$, $\Delta y=0.02$, and $\Delta t=0.001$. The maximum temperatures corresponding to the profiles of Fig. 7 are recorded in Table 1.

Taking a base temperature of, say, $T_B^*=100^\circ\text{C}$, the maximum physical temperature at the channel centerline for the extreme cases of pure energy elasticity and pure entropy elasticity are 101.68°C and 102.12°C , respectively, a difference of less than 1°C . A similar conclusion regarding the temperature difference between these two cases is reported in Ref. [12] for the nonisothermal flow of a PTT fluid around a cylinder. A Newtonian fluid at these parameter values leads a maximum temperature of 103.46°C . Figure 8 shows a similar computation at a higher reaction parameter, $\delta_1=4$; all other parameter values are the same as for Fig. 7.

The maximum temperature for the Newtonian fluid is 0.7815 and the maximum temperatures for the PTT fluid are recorded in Table 2 for various values of γ .

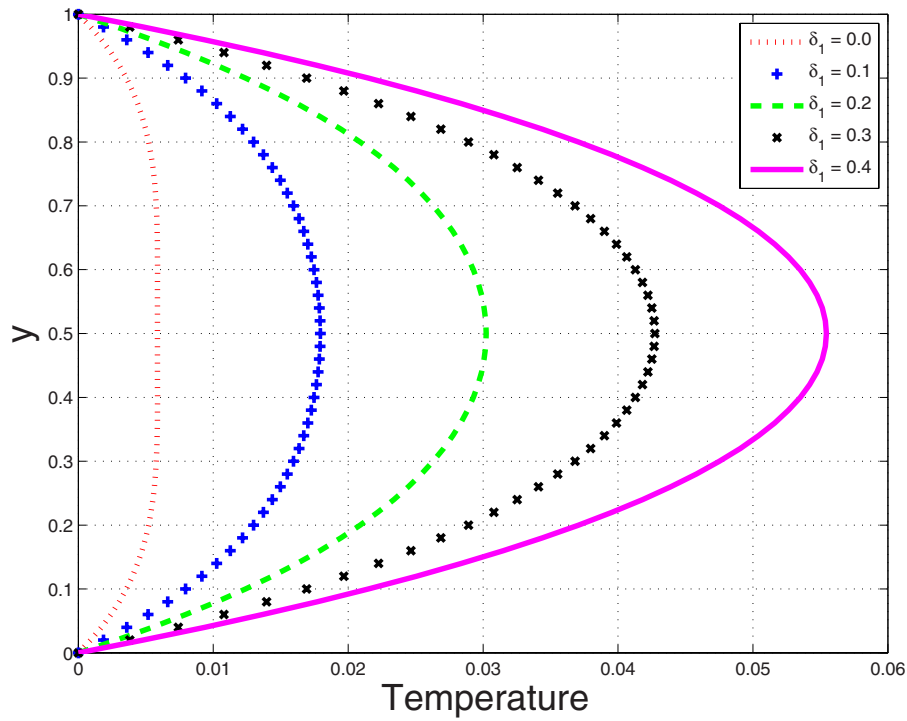


Fig. 4 Effects of We on temperature profiles

If we again take a base temperature of, say, $T_B^* = 100^\circ\text{C}$, the maximum physical temperature at the channel centerline for the extreme cases of pure energy elasticity and pure entropy elasticity are 173.71°C and 175.08°C , respectively. The Newtonian fluid in this case gives a higher maximum temperature of 178.15°C .

5 Conclusion

We investigate the effect of viscoelasticity on the temperature in one dimensional Poiseuille flow of a reactive PTT fluid under Arrhenius kinetics. We demonstrate both a decrease in attainable

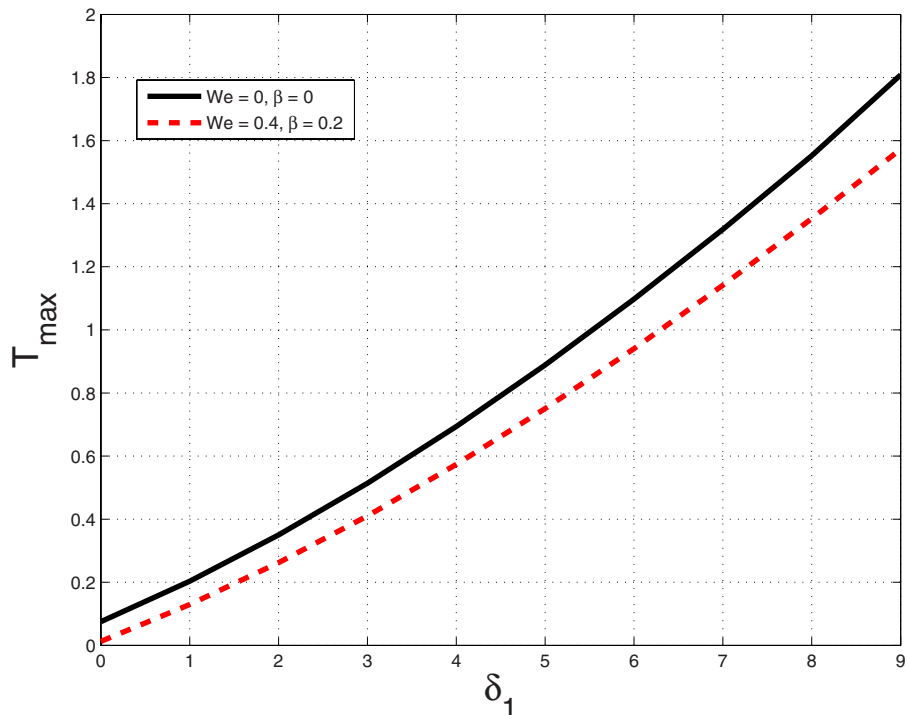


Fig. 5 Effects of viscoelasticity on maximum temperature

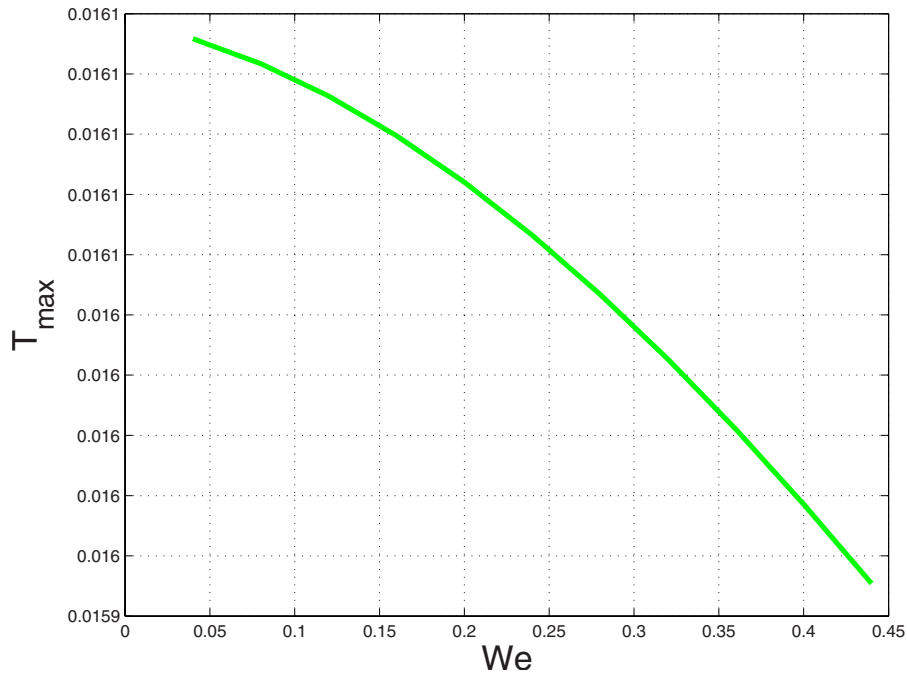


Fig. 6 Variation of maximum temperature with We

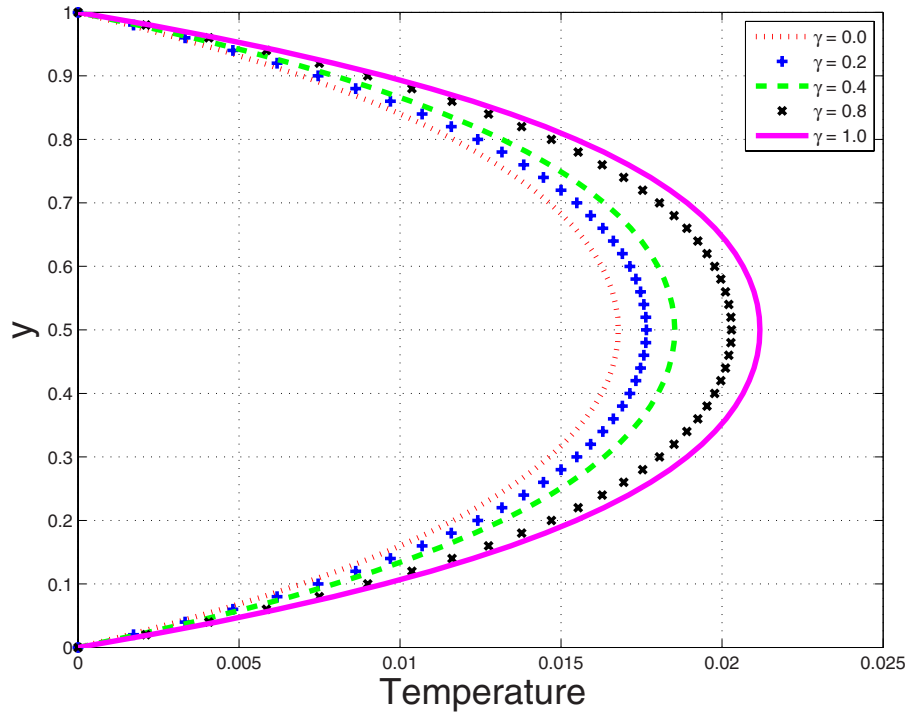


Fig. 7 Temperature profiles for cases ranging from pure entropy to pure energy elasticity

Table 1 Maximum temperatures for various choices of γ

γ	0.0	0.2	0.4	0.8	1.0
T_{\max}	0.0168	0.0177	0.0185	0.0203	0.0212

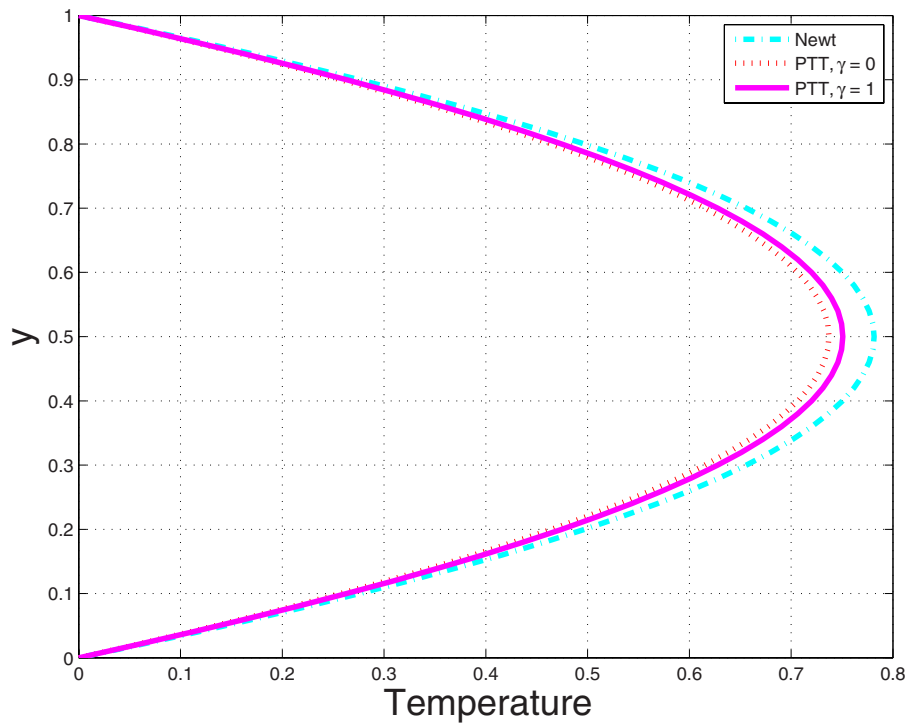


Fig. 8 Temperature profiles for Newtonian, pure entropy to pure energy elasticity

Table 2 Maximum temperatures for various choices of γ

γ	0.0	0.2	0.4	0.8	1.0
T_{\max}	0.7371	0.7399	0.7426	0.7481	0.7508

fluid temperatures and a delay of the thermal runaway phenomenon with increasing fluid elasticity. Hence we have effectively demonstrated the potential of using viscoelastic fluids in controlling the increase of temperature in processes that involve thermally reactive channel flow. We have also checked our code for both temporal and spatial convergence.

Acknowledgment

The author wishes to thank Dr. M.A. Hulsen and Dr. G.W.M. Peters from Eindhoven University of Technology (TU/e) in The Netherlands for discussions and also the staff of TU/e for hosting me while I completed this paper.

References

- [1] Lakshmi Narayana, P. A., and Murthy, P. V. S. N., 2008, "Free Convection Heat and Mass Transfer From a Horizontal Flat Plate With Soret and Dufour Effect in a Darcian Porous Medium," *ASME J. Heat Transfer*, **130**(10), p. 104504.
- [2] Makinde, O. D., 2007, "On Steady Flow of a Reactive Variable Viscosity Fluid in a Cylindrical Pipe With an Isothermal Wall," *Int. J. Numer. Methods Heat Fluid Flow*, **17**(2), pp. 187–194.
- [3] Bair, S., Qureshi, F., and Khonsari, M., 1994, "Adiabatic Shear Localization in a Liquid Lubricant Under Pressure," *ASME J. Tribol.*, **116**, pp. 705–709.
- [4] Ishak, A., Nazar, R., Arifin, N. M., and Pop, I., 2007, "Dual Solutions in Magnetohydrodynamic Mixed Convection Flow Near a Stagnation-Point on a Vertical Surface," *ASME J. Heat Transfer*, **129**, pp. 1212–1216.
- [5] Barletta, A., 1999, "Analysis of Combined Forced and Free Flow in a Vertical Channel With Viscous Dissipation and Isothermal-Isoflux Boundary Conditions," *ASME J. Heat Transfer*, **121**, pp. 349–356.
- [6] Lakshmisha, K. N., Venkateswaran, S., and Nath, G., 1988, "Three-Dimensional Unsteady Flow With Heat and Mass Transfer Over a Continuous Stretching Surface," *ASME J. Heat Transfer*, **110**, pp. 590–595.
- [7] Boddington, T., Gray, P., and Wake, G. C., 1977, "Criteria for Thermal Explosions With and Without Reactant Consumption," *Proc. R. Soc. London, Ser. A*, **357**, pp. 403–422.
- [8] Grubka, L. J., and Bobba, K. M., 1985, "Heat Transfer Characteristics of a Continuous Stretching Surface With Variable Temperature," *ASME J. Heat*

- Transfer*, **107**, pp. 248–250.
- [9] Hasan, M. M., and Eichorn, R., 1982, "Local Nonsimilarity Solution of Free Convection Flow and Heat Transfer From an Inclined Isothermal Horizontal and Inclined Surfaces," *ASME J. Heat Transfer*, **104**, pp. 637–643.
- [10] Chen, H. T., and Chen, C. K., 1988, "Free Convection of Non-Newtonian Fluids Along a Vertical Plate Embedded in a Porous Medium," *ASME J. Heat Transfer*, **110**, pp. 257–260.
- [11] Sugeng, F., Phan-Thien, N., and Tanner, R. I., 1987, "A Study of Non-Isothermal Non-Newtonian Extrudate Swell by a Mixed Boundary Element and Finite Element Method," *J. Rheol.*, **31**(1), pp. 37–58.
- [12] Peters, G. W. M., and Baaijens, F. P. T., 1997, "Modelling of Non-Isothermal Viscoelastic Flows," *J. Non-Newtonian Fluid Mech.*, **68**, pp. 205–224.
- [13] Wapperom, P., and Hulsen, M. A., 1998, "Thermodynamics of Viscoelastic Fluids: The Temperature Equation," *J. Rheol.*, **42**, pp. 999–1019.
- [14] Dressler, M., Edwards, B. J., and Öttinger, H. C., 1999, "Macroscopic Thermodynamics of Flowing Polymeric Liquids," *Rheol. Acta*, **38**, pp. 117–136.
- [15] Hütter, M., Luap, C., and Öttinger, H. C., 2009, "Energy Elastic Effects and the Concept of Temperature in Flowing Polymeric Liquids," *Rheol. Acta*, **48**, pp. 301–316.
- [16] Straughan, B., 1998, *Explosive Instabilities in Mechanics*, Springer, New York.
- [17] Frank-Kamenetskii, D. A., 1969, *Diffusion and Heat Transfer in Chemical Kinetics*, 2nd ed., Plenum, New York.
- [18] Chinyoka, T., 2008, "Computational Dynamics of a Thermally Decomposable Viscoelastic Lubricant Under Shear," *ASME Trans. J. Fluids Eng.*, **130**(12), p. 121201.
- [19] Bird, R. B., Curtiss, C. F., Armstrong, R. C., and Hassager, O., 1987, *Dynamics of Polymeric Liquids* (Fluid Mechanics), 2nd ed., Wiley, New York, Vol. 1.
- [20] Ferry, J. D., 1981, *Viscoelastic Properties of Polymers*, 3rd ed., Wiley, New York.
- [21] Houston, M. H., Hauger, S. A., and Edwards, G., 2002, "Thermal Diffusion and Chemical Kinetics in Laminar Biomaterial Due to Heating by a Free-Electron Laser," *Phys. Rev. E*, **65**, p. 061906.
- [22] Adler, J., 1991, "Thermal Explosion Theory With Arrhenius Kinetics: Homogeneous and Inhomogeneous Media," *Proc. R. Soc. London, Ser. A*, **433**, pp. 329–335.
- [23] Kunisch, K., and Marduel, X., 2000, "Optimal Control of Non-Isothermal Viscoelastic Fluid Flow," *J. Non-Newtonian Fluid Mech.*, **88**, pp. 261–301.
- [24] Chinyoka, T., Renardy, Y. Y., Renardy, M., and Khismatullin, D. B., 2005, "Two-Dimensional Study of Drop Deformation Under Simple Shear for Oldroyd-B liquids," *J. Non-Newtonian Fluid Mech.*, **130**, pp. 45–56.

Y. S. Muzychka
Professor
Mem. ASME
Faculty of Engineering and Applied Science,
Memorial University of Newfoundland,
St. John's, NL, A1B 3X5, Canada

Edmond Walsh
Senior Research Fellow
Mem. ASME

Pat Walsh
Senior Research Fellow
Mem. ASME

Stokes Research Institute,
University of Limerick,
Castletroy, Co. Limerick, Ireland

Simple Models for Laminar Thermally Developing Slug Flow in Noncircular Ducts and Channels

Solutions to the classical Graetz slug flow problem (uniform velocity distribution) in noncircular ducts are examined. These solutions have applications where a constant uniform velocity distribution exists across a channel or duct. These are most often realized in the laminar flow of low Prandtl number liquids, such as liquid metals, and low Reynolds number flows through porous media. Expressions are developed for a number of applications using the asymptotic correlation method of Churchill and Usagi. These expressions vary depending on the definition used for the dimensionless heat transfer coefficient, in the case of constant wall temperature boundary condition (T), and the dimensionless wall temperature for the constant flux boundary conditions (H) and ($H1$). Finally, simple expressions are developed for predicting the thermal entrance length and fully developed flow Nu values for noncircular ducts. [DOI: 10.1115/1.4002095]

Keywords: Graetz flow, plug flow, slug flow, heat transfer coefficient, laminar flow, heat exchangers, heat sinks, porous media, modeling

1 Introduction

Forced convection in slug flows has received considerable attention in the past as a topic of fundamental study [1–7], in part, due to the ease of analytic solution for many problems by analogy with transient conduction. More recently, these solutions have also found applications in liquid and gas flows through porous media [6,8] since on a macroscopic scale, the velocity distribution may be considered flat or uniform with respect to the thermal boundary layer characteristics if the porous media is viewed as a gray medium [6], i.e., one lacking in microscopic detail. More recently, it has been shown that plug flow heat transfer characteristics arise in discrete flows of liquid droplets at large Peclet numbers [9–11]. The present authors have also found plug flow heat transfer characteristics in segmented liquid flows [12,13]. As a result of this recent research activity in published literature, there is a need for simple models, which predict the classic Graetz slug/plug flow heat transfer characteristics in channels of noncircular geometries that are found in practical applications.

In contemporary thermal design, where microchannel and minichannel based systems are frequently proposed, these solutions will assist in the thermal characterization of these devices, which utilize either liquid metals, segmented liquid-gas and liquid-liquid flow, and designed porous media. Furthermore, given that micro-/minichannel shape can vary from the ideal of tube or channel shapes, extension of the classic solutions, such that they may be applied to other less ideal noncircular geometries, is of practical significance.

The present paper re-examines a number of solutions for classic Graetz slug flow, i.e., those problems where no velocity gradient is present in the convective fluid stream. This system, shown in Fig. 1, has been characteristically referred to as slug flow or plug flow with plug flow more appropriately describing the fluid medium moving as a solid in the duct or channel. A number of solutions are considered: these include the plane channel, circular

tube, rectangular duct, and polygonal ducts. Simple models are proposed for simplifying the prediction of mean heat flux or local wall temperature.

Many of the widely available results are found in the various compendiums [1,2], and heat transfer texts [3–7], in addition to several older journal papers. These results will be partly reviewed in order to illustrate the common characteristics required for developing simple models.

2 Problem Statement

The class of internal flow heat transfer problems, which have come to be known as Graetz or Graetz–Nusselt problems, involve solving the energy equation for either fully developed Poiseuille flow or for a uniform velocity distribution.

$$\frac{w}{\alpha} \frac{\partial T}{\partial z} = \nabla^2 T \quad (1)$$

with a constant inlet temperature at $z=0$ and either a constant wall temperature T_w at the duct periphery, or a constant heat flux q_w at the duct periphery. Along the axis of the duct or channel, an adiabatic symmetry condition is prescribed. A number of solutions to these problems for various configurations and boundary conditions are widely available in handbooks with a few exceptions. This paper considers the classic slug flow condition where $w=U$ is constant throughout the cross-section. The slug flow problem has an analog solution in transient conduction when the time variable is transformed using $t=z/U$. Hence, solutions for both isothermal and isoflux boundary conditions are easily obtained in simple geometries such as the tube, channel and flat plate [6].

We will consider three geometries in detail: the one dimensional channel, the tube, and the rectangular duct before considering more complex duct shapes. In these systems much can be learned by considering the heat transfer scales and asymptotic characteristics.

Given the solution for the temperature field in a duct or channel flow we strive to relate the local heat transfer rate to the local wall to fluid temperature difference. We may define this wall to fluid temperature difference in a number of different ways. These include

Contributed by the Heat Transfer Division of ASME for publication in the JOURNAL OF HEAT TRANSFER. Manuscript received September 20, 2009; final manuscript received June 14, 2010; published online August 13, 2010. Assoc. Editor: Ali Ebdian.

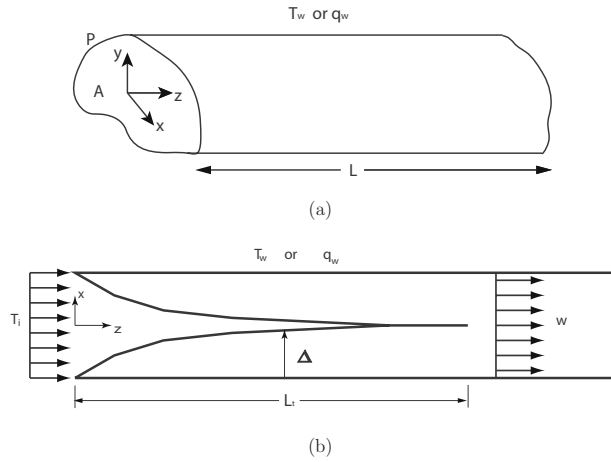


Fig. 1 (a) Graetz slug flow in an arbitrary shaped channel or duct and (b) corresponding thermal boundary layer development

- wall to Inlet $T_w - T_i$
- wall to bulk mean $T_w - T_m$

The correct choice should be based on the application. For example, in single fluid problems, such as heat sinks, the best and easiest approach is to use the wall to inlet temperature difference. However, in two fluid problems such as heat exchangers, the better choice is most often the wall to bulk temperature difference. The most frequently used form for defining the local heat transfer coefficient in an internal flow has traditionally been in terms of the bulk temperature $T_m = T_m(z)$ where

$$T_m = \frac{\int \int \rho c_p w T dA}{\int \int \rho c_p w dA} \quad (2)$$

The local heat flux q_z is often related to a local heat transfer coefficient h_z by means of some defined characteristic temperature difference in the local flow

$$q_z = h_z(T_w - T_m) \quad (3)$$

where $T_w - T_m$ is the local wall to bulk temperature difference. In a duct where the prescribed wall temperature remains constant, the heat flux varies due to changes in the bulk temperature. In a duct where the prescribed wall flux remains constant, the wall temperature varies. In this case the above equation is written as

$$q_w = h_z(T_{w,z} - T_m) \quad (4)$$

and is utilized for determining the local wall temperature $T_{w,z}$.

We may define a dimensionless *local* or *mean* heat transfer coefficient or *Nusselt* number for the two special cases of constant wall temperature and constant wall heat flux. These will be treated separately.

If the duct wall is maintained at a uniform constant temperature T_w , then we define

$$\text{Nu}_{\mathcal{L}} = \frac{q_z \mathcal{L}}{k(T_w - T_m)} \quad (5)$$

which is based on the wall to bulk mean fluid temperature, where \mathcal{L} is an arbitrary length scale related to the channel geometry. Traditionally, the hydraulic diameter is utilized, i.e., $\mathcal{L} = 4A/P$ while more recently [14,15], $\mathcal{L} = \sqrt{A}$ has been utilized with great success in correlating internal flow data.

Alternatively, we could also define

$$\text{Nu}_{\mathcal{L}} = \frac{q_z \mathcal{L}}{k(T_w - T_i)} \quad (6)$$

which is based on the more natural wall to inlet fluid temperature difference. This definition proves useful in the boundary layer region for developing asymptotic solutions where the bulk temperature scales to the inlet fluid temperature, i.e., $T_m \sim T_i$ when the thermal boundary layer is thin. Both forms will be examined, as each has its advantages and disadvantages. If a mean Nusselt number is desired, then we must integrate along the duct length (provided that \mathcal{L} is independent of the flow length).

$$\overline{\text{Nu}}_{\mathcal{L}} = \frac{1}{L} \int_0^L \text{Nu}_{\mathcal{L}} dz \quad (7)$$

The above approach is only useful when the Nusselt number is of the form of Eq. (6). Often it is easier to use simple heat exchanger theory [7] for an isothermal wall to obtain mean Nusselt numbers, which are defined in terms of the wall to bulk temperature difference. This leads to

$$\overline{\text{Nu}}_{D_h} = \frac{1}{4L^*} \ln\left(\frac{1}{\Theta_m}\right) \quad (8)$$

where

$$\Theta_m = \frac{T_m - T_w}{T_i - T_w} \quad (9)$$

when $\mathcal{L} = D_h$ is used as a length scale. The group $L^* = L/D_h \text{Pe}_{D_h}$ is the dimensionless thermal duct length or inverse Graetz number.

However, caution must be exercised when using so called mean heat transfer coefficients in internal flow applications, as the appropriate mean temperature difference must be used. In the case of h defined on the basis of wall to bulk fluid temperature difference, this requires the use of the *log mean temperature difference*

$$\Delta T_{lm} = \frac{(T_w - T_i) - (T_w - T_o)}{\ln \frac{T_w - T_i}{T_w - T_o}} \quad (10)$$

where T_o is the outlet bulk temperature, such that

$$Q = \bar{h} A \Delta T_{lm} \quad (11)$$

or in other words, the mean Nusselt number is then defined as

$$\overline{\text{Nu}}_{\mathcal{L}} = \frac{\bar{q} \mathcal{L}}{k \Delta T_{lm}} \quad (12)$$

where $\bar{q} = Q/A$ is the average heat flux.

In the case of a Nusselt defined on the basis of the wall to inlet temperature difference, this still requires the use of $(T_w - T_i)$. As such, in the case of single fluid systems such as heat sinks, it is more convenient to designate the dimensionless mean wall flux simply as

$$q^* = \frac{\bar{q} \mathcal{L}}{k(T_w - T_i)} \quad (13)$$

since, in these applications, it is the total heat transfer rate related to the wall temperature and duct geometry, which is of interest, not the heat transfer coefficient. This also avoids confusion related to which temperature difference should be used. The definition provided using Eq. (13) can be related to the definition of Eq. (8) by means of

$$q^* = \frac{1}{4L^*} [1 - \exp(-4\overline{\text{Nu}}_{D_h} L^*)] \quad (14)$$

when $\mathcal{L} = D_h$.

Examination of Eqs. (12) and (13) show that two immediate issues are raised. First, in the wall to bulk specification of temperature difference, the log mean temperature difference is re-

quired to obtain the mean heat transfer rate. While the Nusselt number is constant in the fully developed region, the log mean temperature difference decreases with increasing duct length, leading to effectively zero mean heat transfer rate in a very long duct. Second, in the wall to inlet temperature specification while the temperature difference is constant, the mean heat transfer rate approaches zero as a result of an increase in L^* , i.e., Eq. (14), shows $q^* \rightarrow 0$ as $L^* \rightarrow \infty$. The two formulations lead to the same result, but the latter is more physical and more natural when only one fluid is being considered. We will examine the merits of both definitions later when thermally developing and fully developed slug flows are considered in detail.

In other applications where electric resistance heating is used and/or we have a low conductivity duct wall, it may be more realistic to assume a constant heat flux boundary condition. If we maintain a constant flux at the wall q_w , then we may define a Nusselt number as follows:

$$\text{Nu}_{\mathcal{L}} = \frac{q_w \mathcal{L}}{k(T_{w,z} - T_m)} \quad (15)$$

or alternatively as

$$\text{Nu}_{\mathcal{L}} = \frac{q_w \mathcal{L}}{k(T_{w,z} - T_i)} \quad (16)$$

in the thermal boundary layer region, where $T_m \sim T_i$.

It is clear that if a uniform constant heat flux is specified, then the *local* Nusselt number is utilized for the purpose of predicting the *wall to bulk* fluid temperature rise or the wall temperature distribution once T_m is known. Thus, given an expression for the relationship of Nu as a function of dimensionless duct position z^* , one can easily obtain the local wall or wall to bulk temperature difference. In this regard, in single fluid heat exchange systems, where the wall temperature is the parameter of interest, it is more appropriate to consider a dimensionless wall temperature in place of Eq. (16) defined as

$$\Delta T_w^* = \frac{(T_{w,z} - T_i)k}{q_w \mathcal{L}} \quad (17)$$

since the principal solution variable of interest will be the local axial temperature field. This is also the more natural approach when one examines the exact solutions.

Frequently, sources of Nu data and models report a mean Nusselt for the constant flux wall condition defined using Eq. (7). In these cases, the mean heat transfer coefficient is utilized to find the mean wall to bulk temperature difference, which is not as easily defined in the manner of Eq. (10), see Ref. [1]. This approach is only useful in the boundary layer or thermal entrance region where the wall to bulk temperature difference varies, since in a fully developed flow, $T_{w,z} - T_m$ becomes constant.

The formulations involving Eq. (13) and Eq. (17) will prove much more useful in the analysis of single fluid systems since the parameter of interest is defined explicitly in the nondimensional formulation. Concepts, which are lost by the traditional $h\mathcal{L}/k$ interpretation of the Nusselt number.

3 Scaling Analysis

The use of scaling analysis on Eq. (1) proves useful in determining the correct forms of the dimensionless heat transfer coefficient regardless of channel shape and for the development of simple models. The energy equation represents a balance between transverse conduction and axial convection, i.e.,

$$\underbrace{\rho c_p \mathbf{V} \cdot \nabla T}_{\text{convection}} = \underbrace{k \nabla^2 T}_{\text{conduction}} \quad (18)$$

We begin by considering thermally and hydrodynamically fully developed flow in a noncircular duct of constant cross-section. We write the left hand side of Eq. (19) as

$$\rho c_p \mathbf{V} \cdot \nabla T \sim \rho c_p w \frac{(T_m - T_i)}{L} \quad (19)$$

where T_m is the mean axial bulk flow temperature at any point and T_i is the inlet temperature.

Next considering an enthalpy balance on the duct, we write

$$\bar{q}PL = \dot{m}c_p(T_m - T_i) = \dot{m}c_p(T_w - T_i) \quad (20)$$

since $T_m \sim T_w$ for very long ducts, where T_w is the constant wall temperature. Using the above relationship in Eq. (19) we obtain the following result:

$$\rho c_p \mathbf{V} \cdot \nabla T \sim \frac{\bar{q}P}{A} \quad (21)$$

The energy equation, Eq. (18) for fully developed flow now scales according to

$$\frac{\bar{q}P}{A} \sim k \frac{(T_w - T_m)}{\mathcal{L}^2} \quad (22)$$

where \mathcal{L} represents a characteristic transversal length scale of the duct cross-section. Rearranging Eq. (22), we obtain the following result for the Nusselt number:

$$\text{Nu}_{\mathcal{L}} = \frac{\bar{q}\mathcal{L}}{k(T_w - T_m)} \sim \frac{A}{P\mathcal{L}} = B_1 \quad (23)$$

which is a constant and only a function of geometry. This result is valid for both parabolic or uniform velocity distributions, and constant wall temperature or constant wall flux, and is also consistent with analytic results.

In the case of the thermal boundary layer, we now consider the case when the thermal boundary layer is much thicker than the hydrodynamic boundary layer, i.e., $\Delta \gg \delta$, such that $\mathbf{V} \sim U$, and the energy equation scales according to

$$\rho c_p U \frac{(T_w - T_i)}{L} \sim k \frac{(T_w - T_i)}{\Delta^2} \quad (24)$$

which gives

$$\frac{\Delta}{L} \sim \frac{1}{\sqrt{\text{Pe}_L}} \quad (25)$$

Next, considering the heat transfer coefficient, which scales according to

$$h(T_w - T_i) \sim \frac{k(T_w - T_i)}{\Delta} \quad (26)$$

or

$$h \sim \frac{k}{\Delta} \quad (27)$$

and thus Nusselt number becomes

$$\text{Nu}_{\mathcal{L}} \sim \frac{1}{\sqrt{L^*}} = \frac{B_2}{\sqrt{L^*}} \quad (28)$$

where

$$L^* = \frac{L/\mathcal{L}}{\text{Pe}_{\mathcal{L}}} \quad (29)$$

Equations (23) and (28) are universal results, which allow the results for any channel geometry to be modeled simply as a function of these two limits. Simple universal models based on these results will be proposed in a later section.

4 Asymptotic Limits

The Graetz slug flow problem for either constant wall boundary condition or constant heat flux boundary condition contains simple asymptotic behavior that allows the problem to be easily

modeled rather than using the exact eigenvalue series solutions or tabulated data. We consider both the boundary layer region and fully developed flow limit.

4.1 Flat Plate Limit. In the short duct limit, the thermal boundary layer characteristics of slug flows approach those for a flat plate with $Pr \rightarrow 0$. This problem has an analogy to the problem of transient heat conduction into a semi-infinite domain. Solutions for the heat transfer rate are readily available, i.e., Bejan [6]. For a given boundary condition we may write the local Nusselt number based on the downstream coordinate as

$$Nu_z = \frac{0.564}{\sqrt{Pe_z}}, \quad T_w = \text{constant} \quad (30a)$$

$$Nu_z = \frac{0.886}{\sqrt{Pe_z}}, \quad q_w = \text{constant} \quad (30b)$$

If written in terms of a characteristic length scale related to the cross-section \mathcal{L} the above equations become

$$Nu_{\mathcal{L}} = \frac{0.564}{\sqrt{z^*}}, \quad T_w = \text{constant} \quad (31a)$$

$$Nu_{\mathcal{L}} = \frac{0.886}{\sqrt{z^*}}, \quad q_w = \text{constant} \quad (31b)$$

Finally, if the Nusselt is defined on the basis of mean quantities, then the above expressions become after integration over a total flow length L

$$\overline{Nu}_{\mathcal{L}} = \frac{1.128}{\sqrt{L^*}}, \quad T_w = \text{constant} \quad (32a)$$

$$\overline{Nu}_{\mathcal{L}} = \frac{1.772}{\sqrt{L^*}}, \quad q_w = \text{constant} \quad (32b)$$

If the mean Nusselt number for constant flux is defined based on the mean wall temperature, then Eq. (31b) becomes after integration [6].

$$\overline{Nu}_{\mathcal{L}} = \frac{1.329}{\sqrt{L^*}} \quad (33)$$

These equations become universal limits regardless of which temperature difference is specified or which length scale is used when defining Nu.

4.2 Fully Developed Flow. In the limit of very long ducts and channels, the flow eventually becomes thermally and hydrodynamically fully developed. The local Nusselt number approaches a constant value in this case. However, if we use the local wall to inlet temperature scale, a simple universal result follows from an energy balance on the duct. In the case of an isothermal wall, in a very long duct or channel, we may write

$$Q = \dot{m}c_p(T_o - T_i) = \dot{m}c_p(T_w - T_i) \quad (34)$$

where for a long duct, the outlet temperature must asymptotically approach the wall temperature. Introducing the definition of the mass flow rate allows Eq. (34) to be written as

$$Q = \rho U A C_p (T_w - T_i) \quad (35)$$

Next, if we define the heat transfer coefficient on the basis of the wall to inlet temperature difference, we obtain

$$q^* = \frac{Q\mathcal{L}}{kPL(T_w - T_i)} = \frac{\rho U A C_p \mathcal{L}}{kPL} \quad (36)$$

Now introducing the Peclet number we obtain

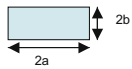
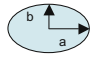

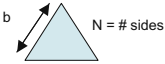
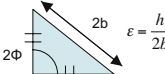
Geometry	Shape	P/A
Rectangle		$\frac{2(\varepsilon + 1)}{\sqrt{\varepsilon}}$
Ellipse		$\frac{4E(\varepsilon')}{\sqrt{\pi\varepsilon}}$
Annulus		$\frac{2\sqrt{\pi}(1+r^*)}{\sqrt{(1-r^{*2})}}$
Polygons		$2\sqrt{N} \left(\tanh\left(\frac{\pi}{N}\right) \right)^{1/2}$
Isosceles Triangle		$\frac{2/\cos\phi + 2\tan\phi}{\sqrt{\tan\phi}}$

Fig. 2 Useful channel and duct shapes

$$q^* = \frac{Pe_{\mathcal{L}} A}{L P} \quad (37)$$

or, after defining the dimensionless duct length one obtains

$$q^* = \frac{1}{L^*} \frac{A/P}{\mathcal{L}} \quad (38)$$

This result is universally applicable to any duct shape for asymptotically large duct lengths. Now the selection of the characteristic length \mathcal{L} is open. We consider two choices, the traditional hydraulic diameter $\mathcal{L} = D_h = 4A/P$ and the square root of the cross-sectional area $\mathcal{L} = \sqrt{A}$. Using these length scales, we obtain

$$q^* = \frac{1}{4L^*} \quad (39)$$

when $\mathcal{L} = D_h$ is used or

$$q^* = \frac{1}{L^*} \frac{\sqrt{A}}{P} \quad (40)$$

when $\mathcal{L} = \sqrt{A}$ is used. The parameter \sqrt{A}/P is an important scaling parameter, which arises quite frequently in transport problems. The above results are simple and have great advantage when determining the heat transfer rates in single fluid systems as the enthalpy balance is fundamental. While Nu is a constant when based on wall to bulk temperature difference, it depends strongly on geometry if D_h is used as a length scale.

4.3 Asymptotic Compact Models. Equations (30a), (30b), (31a), (31b), (32a), (32b), (33), and (39) will be utilized to develop simple accurate expressions for slug flows using the Churchill–Usagi asymptotic correlation method [16]. These models take the form of

$$Nu = [Nu_0^n + Nu_{\infty}^n]^{1/n} \quad (41)$$

where n can be a positive or negative constant depending on the concavity of the curve to be fit. A similar model can be developed for q^* .

5 Exact Solutions for Plug Flow

We will consider three geometries, the one dimensional channel, the tube, and the rectangular channel before considering more complex duct shapes shown in Fig. 2. In these three systems, much can be learned for the more general problem by considering the heat transfer scales and asymptotic characteristics. These asymptotic characteristics may be simple to obtain from the exact full solutions or in most cases are derived from simpler problems,

e.g., the flat plate limit. In either case, they agree nearly exactly with the full series solutions under the limiting cases of large and small dimensionless thermal duct length.

5.1 Plane Channel. The problem of slug flow in a plane channel having a spacing of $2b$ is first considered, as mathematically, it is one of the simplest to solve. The solution is found in Ref. [2] for both isothermal and constant wall flux wall conditions.

5.1.1 Isothermal Wall. The final solution for the temperature profile may be written as

$$\frac{\theta(y, z)}{\theta_i} = \sum_{n=1}^{\infty} \frac{2 \sin(\delta_n) \cos(\delta_n y/b)}{\delta_n} \cdot \exp\left(-\frac{\delta_n^2 \alpha z}{bU b}\right) \quad (42)$$

where

$$\delta_n = \lambda_n b = (2n - 1) \frac{\pi}{2} \quad (43)$$

Using the above solution we may obtain the heat flux distribution along the wall and the mean bulk temperature. By applying Fourier's law at the channel wall, we obtain

$$q_z = \frac{2k(T_w - T_i)}{b} \sum_{n=1}^{\infty} \sin^2(\delta_n) \cdot \exp\left(-\frac{\delta_n^2 \alpha z}{bU b}\right) \quad (44)$$

and integrating the temperature distribution over the cross-section, we obtain

$$\Theta_m = \frac{\theta_m}{\theta_i} = 2 \sum_{n=1}^{\infty} \frac{\sin^2(\delta_n)}{\delta_n^2} \cdot \exp\left(-\frac{\delta_n^2 \alpha z}{bU b}\right) \quad (45)$$

The total heat transfer rate can be obtained by integrating the heat flux distribution along the channel wall in the flow direction. Using the above result, we obtain after integration, the dimensionless heat flux q^* .

$$q^* = \frac{Q'/(2L)D_h}{k(T_w - T_i)} = \frac{1}{2L^*} \sum_{n=1}^{\infty} \frac{\sin^2(\delta_n)}{\delta_n^2} [1 - \exp(-16\delta_n^2 L^*)] \quad (46)$$

where $L^* = L/D_h/\text{Pe}_{D_h}$ is the dimensionless duct length.

The dimensionless heat transfer rate has the following two asymptotes, which can easily be shown from the flat plate limit for $\text{Pr}=0$ since $T_m \sim T_i$ and from the enthalpy balance in fully developed flow. These are

$$q^* = \frac{1.128}{\sqrt{L^*}}, \quad L^* \rightarrow 0 \quad (47)$$

$$q^* = \frac{1}{4L^*}, \quad L^* \rightarrow \infty$$

The flow becomes fully developed when the two limits have roughly the same order of magnitude, i.e., transition from one limit to the other occurs near their intersection, or

$$\frac{1.128}{\sqrt{L^*}} \sim \frac{1}{4L^*} \quad (48)$$

or

$$L_t \sim 0.0491 D_h \text{Pe}_{D_h} \quad (49)$$

A simple model for Eq. (46) can be developed by combining the two asymptotic limits. This simple result takes the form

$$q^* = \left[\left(\frac{1.128}{\sqrt{L^*}} \right)^{-11/2} + \left(\frac{1}{4L^*} \right)^{-11/2} \right]^{-2/11} \quad (50)$$

which has a root mean square (rms) error of approximately 0.8%.

The local Nusselt number is

$$\text{Nu}_{D_h} = \frac{4 \sum_{n=1}^{\infty} \sin^2(\delta_n) \cdot \exp(-16\delta_n^2 z^*)}{\sum_{n=1}^{\infty} \frac{\sin^2(\delta_n)}{\delta_n^2} \cdot \exp(-16\delta_n^2 z^*)} \quad (51)$$

where $z^* = x/D_h/\text{Pe}_{D_h}$. It has the following asymptotic limits:

$$\text{Nu}_{D_h} = \frac{0.564}{\sqrt{z^*}}, \quad z^* \rightarrow 0 \quad (52)$$

$$\text{Nu}_{D_h} = 4\delta_1^2 = 9.87, \quad z^* \rightarrow \infty$$

A simple model for Eq. (51) can be developed by combining the two asymptotic limits. This simple result takes the form

$$\text{Nu}_{D_h} = \left[\left(\frac{0.564}{\sqrt{L^*}} \right)^{5/2} + (9.87)^{5/2} \right]^{2/5} \quad (53)$$

which has a rms error of approximately 4.1%.

The mean Nusselt may be obtained using Eqs. (8) and (45).

$$\overline{\text{Nu}}_{D_h} = \frac{1}{4L^*} \ln \left(\frac{1}{2 \sum_{n=1}^{\infty} \frac{\sin^2(\delta_n)}{\delta_n^2} \cdot \exp(-16\delta_n^2 L^*)} \right) \quad (54)$$

which has the following simple asymptotic limits:

$$\overline{\text{Nu}}_{D_h} = \frac{1.128}{\sqrt{L^*}}, \quad L^* \rightarrow 0 \quad (55)$$

$$\overline{\text{Nu}}_{D_h} = 4\delta_1^2 = 9.87, \quad L^* \rightarrow \infty$$

A simple model for Eq. (54) can be developed by combining the two asymptotic limits. This simple result takes the form

$$\overline{\text{Nu}}_{D_h} = \left[\left(\frac{1.128}{\sqrt{L^*}} \right)^2 + (9.87)^2 \right]^{1/2} \quad (56)$$

which has a rms error of approximately 2.3%.

5.1.2 Constant Heat Flux Wall. In the case of the plane channel with a constant flux boundary on both walls, the solution is also found in Ref. [2]. However, the constant flux boundary makes the problem nonhomogeneous and the solution is a bit more complicated. The important expressions are summarized below [2].

$$\Theta(y, z) = \frac{T(y, z) - T_i}{q_w 4b/k} = \frac{z\alpha}{4b^2 U} + \frac{1}{8} \frac{y^2}{b^2} - \frac{1}{24} - \frac{1}{2} \sum_{n=1}^{\infty} \frac{(-1)^n}{n^2 \pi^2} \cos(n\pi y/b) \exp\left(-\frac{n^2 \pi^2 z\alpha}{b^2 U}\right) \quad (57)$$

The local wall temperature is found when $y=b$.

$$\Theta_w(z) = \frac{T(b, z) - T_i}{q_w 4b/k} = \frac{z\alpha}{4b^2 U} + \frac{1}{12} - \frac{1}{2} \sum_{n=1}^{\infty} \frac{1}{n^2 \pi^2} \exp\left(-\frac{n^2 \pi^2 z\alpha}{b^2 U}\right) \quad (58)$$

The mean bulk temperature found using Eq. (2) is

$$\Theta_m = \frac{T_m(z) - T_i}{q_w 4b/k} = \frac{z\alpha}{4b^2 U} \quad (59)$$

The local Nusselt number based on the wall to bulk temperature difference is

$$\text{Nu}_{D_h} = \frac{12}{1 - 6 \sum_{n=1}^{\infty} \frac{\exp(-16n^2\pi^2 z^*)}{n^2\pi^2}} \quad (60)$$

Equation (60) has the following simple asymptotic limits:

$$\begin{aligned} \text{Nu}_{D_h} &= \frac{0.886}{\sqrt{z^*}}, \quad z^* \rightarrow 0 \\ \text{Nu}_{D_h} &= 12, \quad z^* \rightarrow \infty \end{aligned} \quad (61)$$

The flow becomes fully developed when the two limits have roughly the same order of magnitude, i.e., transition from one limit to the other occurs near their intersection, or

$$\frac{0.886}{\sqrt{z^*}} \sim 12 \quad (62)$$

or

$$L_t \sim 0.00545 D_h \text{Pe}_{D_h} \quad (63)$$

A simple model for Eq. (60) based on the nonlinear superposition of these limits is

$$\text{Nu}_{D_h} = \left[\left(\frac{0.886}{\sqrt{z^*}} \right)^{12/5} + 12^{12/5} \right]^{5/12} \quad (64)$$

which has a rms error of approximately 3.8%.

If the Nusselt number is defined using the more natural *wall to inlet* temperature difference, Eq. (16), then one obtains

$$\text{Nu}_{D_h} = \frac{1}{4z^* + \frac{1}{12} - \frac{1}{2} \sum_{n=1}^{\infty} \frac{\exp(-16n^2\pi^2 z^*)}{n^2\pi^2}} \quad (65)$$

or more appropriately for single fluid systems

$$\Delta T_w^* = 4z^* + \frac{1}{12} - \frac{1}{2} \sum_{n=1}^{\infty} \frac{\exp(-16n^2\pi^2 z^*)}{n^2\pi^2} = \frac{1}{\text{Nu}_{D_h}} \quad (66)$$

Equation (65) has the following asymptotic limits:

$$\begin{aligned} \text{Nu}_{D_h} &= \frac{0.886}{\sqrt{z^*}}, \quad z^* \rightarrow 0 \\ \text{Nu}_{D_h} &= \frac{1}{4z^*}, \quad z^* \rightarrow \infty \end{aligned} \quad (67)$$

An approximate expression for the thermal entrance length obtained from the intersection of the two asymptotes gives

$$\frac{0.886}{\sqrt{z^*}} \sim \frac{1}{4z^*} \quad (68)$$

or

$$L_t \sim 0.0796 D_h \text{Pe}_{D_h} \quad (69)$$

A simple model for Eq. (65) based on the nonlinear superposition of these limits is

$$\text{Nu}_{D_h} = \left[\left(\frac{0.886}{\sqrt{z^*}} \right)^{-3} + \left(\frac{1}{4z^*} \right)^{-3} \right]^{-1/3} \quad (70)$$

which has a rms error of approximately 1.3%.

5.2 Circular Duct. The problem of slug flow in a circular duct of diameter $D=2a$ is now considered. Solutions to this problem are found in Jakob [4], Burmeister [5], and Shah and Bhatti [2].

5.2.1 Isothermal Wall. The final solution for the temperature distribution may be written as

$$\frac{\theta(r, z)}{\theta_i} = 2 \sum_{n=1}^{\infty} \frac{J_0(\delta_n r/a)}{\delta_n J_1(\delta_n)} \exp\left(-\frac{\delta_n^2 \alpha}{a^2 U z}\right) \quad (71)$$

where the eigenvalues are obtained from

$$J_0(\delta) = 0 \quad (72)$$

such that

$$\delta_n = 2.4048, 5.5201, 8.6537, 11.7915, 14.9309, \dots \quad (73)$$

Using the above solution, we may obtain the heat flux distribution along the wall and the total heat transfer Q . By applying Fourier's law at the wall we obtain

$$q_z = \frac{4k(T_w - T_i)}{D} \sum_{n=1}^{\infty} \exp\left(-\frac{\delta_n^2 \alpha}{a^2 U z}\right) \quad (74)$$

for the local flux distribution while the mean bulk temperature along the duct is

$$\Theta_m = \frac{\theta_m}{\theta_i} = 4 \sum_{n=1}^{\infty} \frac{\exp\left(-\frac{\delta_n^2 \alpha}{a^2 U z}\right)}{\delta_n^2} \quad (75)$$

Integrating along the duct wall we obtain the total dimensionless heat transfer rate

$$q^* = \frac{\bar{q}D}{k(T_w - T_i)} = \frac{1}{L^*} \sum_{n=1}^{\infty} \frac{1 - \exp(-4\delta_n^2 L^*)}{\delta_n^2} \quad (76)$$

after introducing $L^* = L/D/\text{Pe}_D$. Equation (76) has the following asymptotic limits:

$$\begin{aligned} q^* &= \frac{1.128}{\sqrt{L^*}}, \quad L^* \rightarrow 0 \\ q^* &= \frac{1}{4L^*}, \quad L^* \rightarrow \infty \end{aligned} \quad (77)$$

The flow becomes fully developed when the two limits have roughly the same order of magnitude, i.e., transition from one limit to the other occurs near their intersection, or

$$\frac{1.128}{\sqrt{L^*}} \sim \frac{1}{4L^*} \quad (78)$$

or

$$L_t \sim 0.0491 D_h \text{Pe}_{D_h} \quad (79)$$

A simple model for Eq. (76) based on the nonlinear superposition of these limits is

$$q^* = \left[\left(\frac{1.128}{\sqrt{L^*}} \right)^{-5/2} + \left(\frac{1}{4L^*} \right)^{-5/2} \right]^{-2/5} \quad (80)$$

which has a rms error of approximately 3.8%.

The local Nusselt number based on the wall to bulk temperature difference is

$$\text{Nu}_D = \frac{\sum_{n=1}^{\infty} \exp(-4\delta_n^2 z^*)}{\sum_{n=1}^{\infty} \frac{\exp(-4\delta_n^2 z^*)}{\delta_n^2}} \quad (81)$$

Equation (81) has the following asymptotic limits:

$$\text{Nu}_D = \frac{0.564}{\sqrt{z^*}}, \quad z^* \rightarrow 0$$

$$\text{Nu}_D = 5.783, \quad z^* \rightarrow \infty \quad (82)$$

A simple model for Eq. (81) based on the nonlinear superposition of these limits is

$$\text{Nu}_D = \left[\left(\frac{0.564}{\sqrt{z^*}} \right)^{11/5} + 5.783^{11/5} \right]^{5/11} \quad (83)$$

which has a rms error of approximately 4.0%.

We may define the mean Nusselt number based on the wall to bulk temperature difference as

$$\overline{\text{Nu}}_D = \frac{1}{4L^*} \ln \left(\frac{1}{4 \sum_{n=1}^{\infty} \frac{\exp(-4\delta_n^2 L^*)}{\delta_n^2}} \right) \quad (84)$$

Equation (84) has the following asymptotic limits:

$$\begin{aligned} \overline{\text{Nu}}_D &= \frac{1.128}{\sqrt{L^*}}, \quad L^* \rightarrow 0 \\ \overline{\text{Nu}}_D &= 5.783, \quad L^* \rightarrow \infty \end{aligned} \quad (85)$$

A simple model for Eq. (84) based on the nonlinear superposition of these limits is

$$\overline{\text{Nu}}_D = \left[\left(\frac{1.128}{\sqrt{L^*}} \right)^2 + 5.783^2 \right]^{1/2} \quad (86)$$

which has a rms error of approximately 2.5%.

5.2.2 Constant Wall Flux. Finally, we consider the case of a tube with a constant flux boundary, the solutions may also be obtained using separation of variables or Laplace transforms. Details of the solution may be found in Burmeister [5]. The important expressions are summarized below.

$$\begin{aligned} \Theta(r, z) &= \frac{T(r, z) - T_i}{q_w 2a/k} = \frac{z\alpha}{a^2 U} + \frac{1}{4} \frac{r^2}{a^2} - \frac{1}{8} - \sum_{n=1}^{\infty} \frac{J_0(\delta_n r/a)}{\delta_n^2 J_0(\delta_n)} \\ &\quad \times \exp\left(-\frac{\delta_n^2 z\alpha}{a^2 U}\right) \end{aligned} \quad (87)$$

where the eigenvalues are roots of

$$J_1(\delta) = 0 \quad (88)$$

such that

$$\delta_n = 3.8317, 7.0156, 10.1735, 13.3237, 16.4706, \dots \quad (89)$$

The local wall temperature is found to be

$$\Theta_w(z) = \frac{z\alpha}{a^2 U} + \frac{1}{8} - \sum_{n=1}^{\infty} \frac{\exp\left(-\frac{\delta_n^2 z\alpha}{a^2 U}\right)}{\delta_n^2} \quad (90)$$

and the mean bulk temperature found using Eq. (2) is

$$\Theta_m = \frac{T_m(z) - T_i}{q_w 2a/k} = \frac{z\alpha}{a^2 U} \quad (91)$$

We may now define a local Nusselt number based on the wall to bulk temperature difference using Eq. (15) to obtain

$$\text{Nu}_D = \frac{8}{1 - 8 \sum_{n=1}^{\infty} \frac{\exp(-4\delta_n^2 z^*)}{\delta_n^2}} \quad (92)$$

Equation (92) has the following asymptotic limits:

$$\text{Nu}_D = \frac{0.886}{\sqrt{z^*}}, \quad z^* \rightarrow 0$$

$$\text{Nu}_D = 8, \quad z^* \rightarrow \infty \quad (93)$$

The flow becomes fully developed when the two limits have roughly the same order of magnitude, i.e., transition from one limit to the other occurs near their intersection, or

$$\frac{0.886}{\sqrt{z^*}} \sim 8 \quad (94)$$

or

$$L_t \sim 0.0123 \text{DPe}_D \quad (95)$$

A simple model for Eq. (92) based on the nonlinear superposition of these limits is

$$\text{Nu}_D = \left[\left(\frac{0.886}{\sqrt{z^*}} \right)^2 + 8^2 \right]^{1/2} \quad (96)$$

which has a rms error of approximately 4.4%.

If the Nusselt number is defined using the more natural wall to inlet temperature difference, Eq. (16), then one obtains

$$\text{Nu}_D = \frac{1}{4z^* + \frac{1}{8} - \sum_{n=1}^{\infty} \frac{\exp(-4\delta_n^2 z^*)}{\delta_n^2}} \quad (97)$$

or for single fluid systems, it is more appropriate to work with

$$\Delta T_w^* = 4z^* + \frac{1}{8} - \sum_{n=1}^{\infty} \frac{\exp(-4\delta_n^2 z^*)}{\delta_n^2} = \frac{1}{\text{Nu}_D} \quad (98)$$

Equation (97) has the following asymptotic limits:

$$\text{Nu}_D = \frac{0.886}{\sqrt{z^*}}, \quad z^* \rightarrow 0 \quad (99)$$

$$\text{Nu}_D = \frac{1}{4z^*}, \quad z^* \rightarrow \infty$$

The flow becomes fully developed when the two limits have roughly the same order of magnitude, i.e., transition from one limit to the other occurs near their intersection, or

$$\frac{0.886}{\sqrt{z^*}} \sim \frac{1}{4z^*} \quad (100)$$

or

$$L_t \sim 0.0833 \text{DPe}_D \quad (101)$$

A simple model for Eq. (97) based on the nonlinear superposition of these limits is

$$\text{Nu}_D = \left[\left(\frac{0.886}{\sqrt{z^*}} \right)^{-2} + \left(\frac{1}{4z^*} \right)^{-2} \right]^{-1/2} \quad (102)$$

which has a rms error of approximately 2.2%.

At this stage it should be seen that the Eqs. (50), (70), (80), and (102) are essentially the same for each boundary condition irrespective of geometry. They only differ in the value of n used to combine the asymptotes. We will use this characteristic to develop universal expressions. Similarly, we see that in the simple models for the Nusselt number, it is only the fully developed flow limit, which varies. We will utilize the observations of Muzychka and Yovanovich [14,15] to develop universal expressions for the case when the wall to bulk temperature difference is preferred.

5.3 Rectangular Duct. Plug flow in a rectangular duct of dimensions $2a$ by $2b$ having an aspect ratio of $0 < b/a < 1$ is now considered. A complete thermal entrance solution is only available for the constant wall temperature condition [17] while solutions for various wall heating conditions are available only for thermally fully developed flows [18].

Table 1 Values of n and the corresponding (rms) error for q^* and \overline{Nu}_{D_h} for the rectangular channel

ϵ	\overline{Nu}_{D_h}		q^*	
	n	rms	n	rms
0.0	2	1.86	-5.6	0.31
0.2	1.9	1.57	-3.3	3.18
0.4	1.9	1.87	-2.7	4.13
0.6	1.9	2.2	-2.4	4.44
0.8	2.0	2.40	-2.3	4.53
1.0	2.0	2.42	-2.3	4.54

5.3.1 *Isothermal Wall.* Thiert [17] obtained a solution for slug flow in a rectangular duct having an isothermal wall. The solution for the dimensionless mean bulk temperature is

$$\Theta_m(z^*) = \frac{\theta_m}{\theta_i} = \frac{64}{\pi^2} \sum_{m=1}^{\infty} \sum_{n=1}^{\infty} \frac{E(z^*)}{(2m-1)^2(2n-1)^2} \quad (103)$$

where

$$E(z^*) = \exp\left(-\frac{4\pi^2 z^* [\epsilon^2(2m-1) + (2n-1)]}{(1+\epsilon)^2}\right) \quad (104)$$

where $z^* = z/D_h/Pe_{D_h}$.

The local and mean Nusselt numbers are

$$\overline{Nu}_{D_h} = \frac{\pi^2 \sum_{m=1}^{\infty} \sum_{n=1}^{\infty} \left(\frac{1}{(2m-1)^2} + \frac{\epsilon^2}{(2n-1)^2} \right) E(z^*)}{(1+\epsilon)^2 \sum_{m=1}^{\infty} \sum_{n=1}^{\infty} \frac{E(z^*)}{(2m-1)^2(2n-1)^2}} \quad (105)$$

and

$$\overline{Nu}_{D_h} = \frac{1}{4L^*} \ln\left(\frac{1}{\Theta_m(L^*)}\right) \quad (106)$$

Finally, the dimensionless mean heat flux based on the wall to inlet temperature can be written simply as

$$q^* = \frac{1}{4L^*} [1 - \exp(-4L^* \overline{Nu}_{D_h})] \quad (107)$$

Equations (105) and (106) have the following characteristic limits:

$$\overline{Nu}_{D_h} = \frac{0.564}{\sqrt{z^*}}, \quad z^* \rightarrow 0 \quad (108)$$

$$\overline{Nu}_{D_h} = \frac{1.128}{\sqrt{L^*}}, \quad L^* \rightarrow 0$$

while, the thermally fully developed flow Nusselt number obtained for large z^* or L^* is

$$\overline{Nu}_{D_h} = \frac{\pi^2(1+\epsilon^2)}{(1+\epsilon)^2} \quad (109)$$

where $\epsilon = b/a$ is the channel aspect ratio. Equation (109) is obtained from the single term representation in Eq. (105) when $z^* \rightarrow \infty$.

Using Eq. (41), expressions can be developed for both \overline{Nu}_{D_h} and q^* . Values of n and the corresponding rms error are given in Table 1. Once again, with the exception of the plane channel $\epsilon = 0$, we see that values for n do not vary considerably. Results are also shown in Figs. 3 and 4 for both q^* and \overline{Nu}_{D_h} for $\epsilon = 0, 0.2, 0.4, 0.6, 0.8, 1$.

5.3.2 *Constant Flux Wall.* Gao and Hartnett [18] and Spiga and Morini [19] obtained solutions for the rectangular duct for the

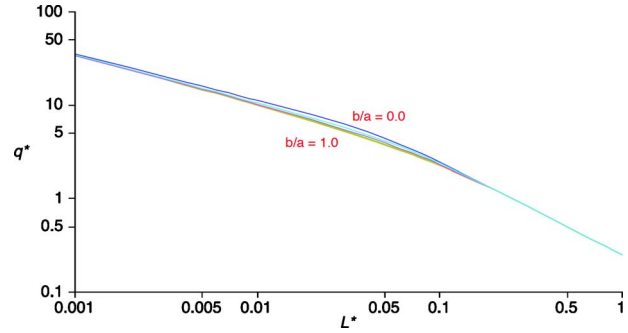


Fig. 3 q^* for the rectangular channel, Eq. (107), for $\epsilon = 0, 0.2, 0.4, 0.6, 0.8, 1$

H1 and H2 conditions, respectively, with Spiga and Morini [19] tabulating thermal entrance data for the H2 condition. In the present study we are mainly concerned with the H1 condition (peripheral mean wall temperature varying axially). Furthermore, it can be easily shown that the Nusselt numbers for fully developed slug flow in a noncircular channel with constant flux condition H1 can be modeled as $f Re_{D_h}/2$ for any duct shape. For the rectangular channel this is given by

$$\overline{Nu}_{D_h} = \frac{12}{(1+\epsilon)^2 \left[1 - \frac{192\epsilon}{\pi^5} \tanh\left(\frac{\pi}{2\epsilon}\right) \right]} \quad (110)$$

The above equation is obtained from the hydrodynamic (friction) solution for a rectangle using only a single term in the series. It is given without proof, as the energy equation for thermally fully developed flow in a rectangular duct can be easily nondimensionalized and transformed into the same dimensionless form as the equation and boundary conditions governing fully developed Poiseuille flow. Thus, the dimensionless mean wall heat flux can be related to the dimensionless mean wall shear stress.

5.4 *Plug Flow in Other Duct Shapes.* Other useful shapes as shown in Fig. 2 are also of interest. Yutaka et al. [20] obtained numerical solutions for flows in polygonal ducts for the limiting case of $Pr=0$, their results are summarized in Table 2. One can see that when the length scale proposed by Muzychka and Yovanovich [14] is used to redefine the thermally fully developed flow Nusselt numbers, there is very little difference in the values for the regular polygons and with the exception of the triangle, they are essentially a constant.

Other shapes, which result in microchannel based systems, include the elliptical channel, trapezoidal channel, and double trapezoidal channel as shown in Fig. 5. Presently, there are no analytical or numerical solutions for these cases for either boundary

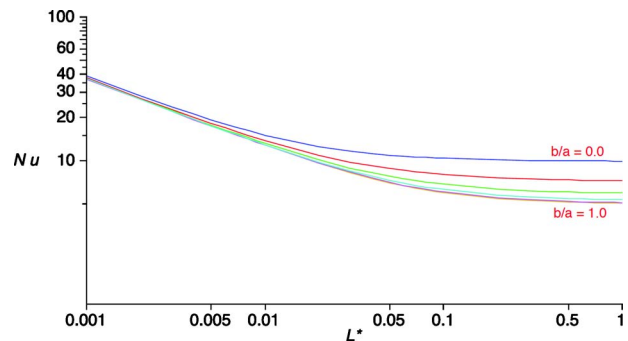


Fig. 4 \overline{Nu}_{D_h} for the rectangular channel, Eq. (106), for $\epsilon = 0, 0.2, 0.4, 0.6, 0.8, 1$

Table 2 Fully developed flow Nusselt numbers in polygonal ducts defined using either $\mathcal{L}=D_h$ or $\mathcal{L}=\sqrt{A}$ as a length scale

	Geometry	Isoflux	Isothermal
Nu_{D_h}	Triangle	6.67	-
	Square	7.08	4.93
	Hexagon	7.53	5.38
	Octagon	7.69	5.53
	Circular	8.00	5.77
$Nu_{\sqrt{A}}$	Triangle	7.60	-
	Square	7.08	4.93
	Hexagon	7.01	5.01
	Octagon	7.00	5.03
	Circular	7.09	5.11

condition T or H1. Approximations for the expected behavior of the Nu of q^* solutions will be developed using the results presented thus far.

Given that the thermal boundary layer region is fully characterized by the flat plate or half space conduction solutions, one only needs the fully developed limit to complete a model for the Nu based on wall to bulk temperature difference. When the data are redefined using the $\mathcal{L}=\sqrt{A}$, one may use $f Re_{\sqrt{A}}$ for the rectangular channel as a very accurate prediction [14,15]. Thus, we obtain using Eq. (110)

$$Nu_{\sqrt{A}}^H = \frac{6}{\sqrt{\epsilon}(1+\epsilon) \left[1 - \frac{192\epsilon}{\pi^5} \tanh\left(\frac{\pi}{2\epsilon}\right) \right]} \quad (111)$$

for the constant wall flux condition Nusselt number in thermally fully developed slug/plug flows. Furthermore, if Eq. (109) is scaled using $\mathcal{L}=\sqrt{A}$ it becomes

$$Nu_{\sqrt{A}}^T = \frac{\pi^2(1+\epsilon^2)}{2(1+\epsilon)\sqrt{\epsilon}} \quad (112)$$

Both Eqs. (111) and (112) will be used to characterize the fully developed flow limit Nusselt numbers based on the wall to bulk temperature in noncircular ducts channels, given that solutions are only a function of channel aspect ratio and are a weak function of channel shape when $\mathcal{L}=\sqrt{A}$ is used as a length scale.

6 Generalized Models for Plug Flows

Using the above results and observations from the channel and tube solutions for the Churchill–Usagi blending parameter, we may now propose a number of universal models. It has been shown that for the wall to inlet temperature specification, that the results are nearly universal for all channel and duct shapes when $\mathcal{L}=D_h$ is used as a characteristic length scale. While for the wall to bulk temperature specification, results are nearly universal and only dependent on aspect ratio when $\mathcal{L}=\sqrt{A}$ is used as a characteristic length scale. Thus it is proposed that the following models be used for all duct shapes:

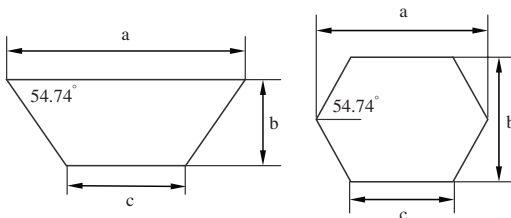


Fig. 5 Microchannels produced in etching processes in Silicon wafers

6.1 Wall to Inlet Temperature Difference T_w-T_i . For a constant wall temperature condition (T) the following is recommended for all duct shapes:

$$q^* = \left[\left(\frac{1.128}{\sqrt{L^*}} \right)^{-5/2} + \left(\frac{1}{4L^*} \right)^{-5/2} \right]^{-2/5} \quad (113)$$

For constant wall flux condition (H,H1) the following is recommended for all duct shapes:

$$\Delta T^* = \left[\left(\frac{0.886}{\sqrt{z^*}} \right)^{-5/2} + \left(\frac{1}{4z^*} \right)^{-5/2} \right]^{2/5} \quad (114)$$

where $\mathcal{L}=D_h$ is used in Eqs. (13) and (17) and to define L^* and z^* .

6.2 Wall to Bulk Temperature Difference T_w-T_m . For a constant wall temperature condition (T) the following is recommended for all duct shapes for the mean Nusselt number:

$$\overline{Nu}_{\sqrt{A}} = \left[\left(\frac{1.128}{\sqrt{L^*}} \right)^2 + (Nu_{\sqrt{A}}^T)^2 \right]^{1/2} \quad (115)$$

For constant wall flux condition (H,H1) the following is recommended for all duct shapes for the local Nusselt number:

$$Nu_{\sqrt{A}} = \left[\left(\frac{0.886}{\sqrt{z^*}} \right)^2 + (Nu_{\sqrt{A}}^H)^2 \right]^{1/2} \quad (116)$$

where $\mathcal{L}=\sqrt{A}$ in Eq. (5) and to define L^* and z^* .

The above formulations can be used for design purposes in channels of any cross-sectional shape for plug flows for either constant wall temperature or constant wall heat flux conditions with very good accuracy. Given that the largest values of n were obtained for the channel, it is found that using the proposed values of $n=-5/2$ in Eqs. (113) and (114), and $n=2$ in Eqs. (115) and (116), yields a rms errors vary between 1.5% and 7% for all shapes considered, making them acceptable for thermal design and analysis.

7 Summary and Conclusions

Classical Graetz plug flow solutions were considered for non-circular channels. It was shown that the full solutions for the tube and channel possess universal asymptotic behavior when the heat transfer characteristics are based on the wall to inlet temperature difference rather than wall to bulk temperature difference, irrespective of thermal boundary condition. This allows simple models to be specified for any channel aspect ratio, which are also verified using the solution for the rectangular channel.

Additionally, simple models were also developed for the case when heat transfer characteristics are based on the wall to bulk temperature difference. In this case the models are based on the characteristic length scale $\mathcal{L}=\sqrt{A}$ proposed by Muzychka and Yovanovich [14,15], which minimize geometry effects. These simple formulations can be used to model heat transfer in simple continuous plug flows, segmented plug flows, and discrete droplets, for channels typically found in microfluidic and other heat exchanger applications.

While the wall to mean bulk temperature scale is more useful in heat exchanger systems. The proposed new models based on the wall to inlet temperature scale are more readily applicable to heat sink design, as only one fluid is present in these applications. The dimensionless heat transfer rate and dimensionless local wall temperature based on this temperature scale are more natural choices, as they appear in the solutions of the temperature field. They are also easily adapted to systems with finite transverse wall resistance using simple resistance network concepts.

Acknowledgment

The authors acknowledge the financial support of the Natural Sciences and Engineering Research Council of Canada (NSERC) and Enterprise Ireland (EI).

Nomenclature

A = flow area, m^2
 C_p = specific heat, $J/kg\ K$
 D = diameter of circular duct, m
 h = heat transfer coefficient, $W/m^2\ K$
 J_0 = Bessel function of the first kind-zero order
 J_1 = Bessel function of the first kind-first order
 k = thermal conductivity, $W/m\ K$
 L = length of tube, m
 L^* = dimensionless length of tube, $\equiv L/DPe_D$
 \dot{m} = liquid mass flow rate, kg/s
 m = summation index
 n = summation index
 n = fitting parameter, Eq. (41)
 Nu_D = Nusselt number, $\equiv hD/k$
 Nu_0 = short duct Nusselt number, $L^* \rightarrow 0$
 Nu_∞ = long duct Nusselt number, $L^* \rightarrow \infty$
 P = perimeter, m
 Pe_D = Peclet number, $\equiv UD/\alpha$
 Pr = Prandtl number, $\equiv \nu/\alpha$
 q = local heat flux, W/m^2
 \bar{q} = mean heat flux, W/m^2
 q^* = dimensionless wall heat flux
 Q = heat transfer, W
 Q' = heat transfer per unit depth, W
 Re_D = Reynolds number, $\equiv UD/\nu$
 T = temperature, K
 T_i = inlet temperature, K
 T_o = outlet temperature, K
 T_m = bulk temperature, K
 T_w = wall temperature, K
 U = uniform velocity, m/s
 ΔT^* = dimensionless temperature
 w = velocity, m/s
 z = local axial coordinate, m

Greek Symbols

α = thermal diffusivity, m^2/s
 δ_n = n th eigenvalue
 Δ = thermal boundary layer thickness, m
 ϵ = channel aspect ratio
 θ = temperature excess, K
 Θ = dimensionless bulk temperature
 ρ = fluid density, kg/m^3

Superscripts

$*$ = dimensionless
 (\cdot) = mean value

Subscripts

D = based on diameter D
 i = inlet

m = mixed mean
 w = wall
 z = local (axial) variation
 0 = denotes $L^* \rightarrow 0$
 ∞ = denotes $L^* \rightarrow \infty$

References

- [1] Shah, R. K., and London, A. L., 1978, *Laminar Flow Forced Convection in Ducts*, Academic, New York.
- [2] Shah, R. K., and Bhatti, M. S., 1987, "Laminar Convective Heat Transfer in Ducts," *Handbook of Single Phase Convective Heat Transfer*, S. Kakac, R. K. Shah, and W. Aung, eds., Wiley, New York, Chap. 3.
- [3] Drew, T. B., 1931, "Mathematical Attacks on Forced Convection Problems: A Review," *Trans. Am. Inst. Chem. Eng.*, **26**, pp. 26–80.
- [4] Jakob, M., 1949, *Heat Transfer*, Vol. 1, Wiley, New York.
- [5] Burmeister, L. C., 1993, *Convective Heat Transfer*, Wiley, New York.
- [6] Bejan, A., 2004, *Convection Heat Transfer*, Wiley, New York.
- [7] Kays, W. M., and Crawford, M. E., 1993, *Convective Heat and Mass Transfer*, McGraw-Hill, New York.
- [8] Bejan, A., and Nield, D., 2001, *Convection in Porous Media*, Springer-Verlag, New York.
- [9] Young, P., and Mohseni, K., 2008, "The Effect of Droplet Length on Nusselt Numbers in Digitized Heat Transfer," *Proceedings of I-THERM, 2008, 11th IEEE Intersociety Conference on Thermal and Thermomechanical Phenomena in Electronic Systems*, pp. 352–359.
- [10] Mohseni, K., and Baird, E. S., 2007, "Digitized Heat Transfer Using Electrowetting on Dielectric," *Nanoscale Microscale Thermophys. Eng.*, **11**, pp. 99–108.
- [11] Baird, E., and Mohseni, K., 2008, "Digitized Heat Transfer: A New Paradigm for Thermal Management of Compact Micro Systems," *IEEE Trans. Compon. Packag. Technol.*, **31**(1), pp. 143–151.
- [12] Muzychka, Y. S., Walsh, E. J., and Walsh, P., 2009, "Heat Transfer Enhancement Using Segmented Gas-Liquid Laminar Fluid Streams," *InterPack 2009*, San Francisco, CA, Jul. 19–23.
- [13] Walsh, P., Walsh, E. J., and Muzychka, Y. S., 2009, "Laminar Slug Flow—Heat Transfer Characteristics With a Constant Flux Boundary," *InterPack 2009*, San Francisco, CA, Jul. 19–23.
- [14] Muzychka, Y. S., and Yovanovich, M. M., 2002, "Laminar Flow Friction and Heat Transfer in Non-Circular Ducts and Channels Part I—Hydrodynamic Problem," *Compact Heat Exchangers: A Festschrift on the 60th Birthday of Ramesh K. Shah*, Grenoble, France, August 24, 2002, G. P. Clelata, B. Thonon, A. Bontemps, and S. Kandlikar, eds., pp. 123–130.
- [15] Muzychka, Y. S., and Yovanovich, M. M., 2002, "Laminar Flow Friction and Heat Transfer in Non-Circular Ducts and Channels Part II—Thermal Problem," *Compact Heat Exchangers: A Festschrift on the 60th Birthday of Ramesh K. Shah*, Grenoble, France, August 24, 2002, G. P. Clelata, B. Thonon, A. Bontemps, and S. Kandlikar, eds., pp. 131–139.
- [16] Churchill, S. W., and Usagi, R., 1972, "A General Expression for the Correlation of Rates of Transfer and Other Phenomena," *AIChE J.*, **18**(6), pp. 1121–1128.
- [17] Thiart, G. D., 1990, "Exact Solution for Slug Flow Laminar Heat Transfer Development in a Rectangular Duct With Isothermal Walls," *ASME J. Heat Transfer*, **112**, pp. 499–501.
- [18] Gao, S. X., and Hartnett, J. P., 1993, "Analytical Nusselt Number Predictions for Slug Flow in Rectangular Duct," *Int. Commun. Heat Mass Transfer*, **20**, pp. 751–760.
- [19] Spiga, M., and Morini, G. L., 1998, "The Developing Nusselt Numbers for Slug Flow in Rectangular Ducts," *Int. J. Heat Mass Transfer*, **41**, pp. 2799–2807.
- [20] Yutaka, A., Hiroshi, N., and Faghri, M., 1988, "Developing Laminar Flow and Heat Transfer in the Entrance Region of Regular Polygonal Ducts," *Int. J. Heat Mass Transfer*, **31**, pp. 2590–2593.

Combined Effects of Temperature and Velocity Jump on the Heat Transfer, Fluid Flow, and Entropy Generation Over a Single Rotating Disk

A. Arikoglu

Department of Aeronautical Engineering,
Faculty of Aeronautics and Astronautics,
Istanbul Technical University,
Maslak, TR-34469 Istanbul, Turkey

G. Komurgoz

Department of Electrical Engineering,
Faculty of Electrical and Electronic Engineering,
Istanbul Technical University,
Maslak, TR-34469 Istanbul, Turkey

I. Ozkol

e-mail: ozkol@itu.edu.tr

A. Y. Gunes

Department of Aeronautical Engineering,
Faculty of Aeronautics and Astronautics,
Istanbul Technical University,
Maslak, TR-34469 Istanbul, Turkey

The present work examines the effects of temperature and velocity jump conditions on heat transfer, fluid flow, and entropy generation. As the physical model, the axially symmetrical steady flow of a Newtonian ambient fluid over a single rotating disk is chosen. The related nonlinear governing equations for flow and thermal fields are reduced to ordinary differential equations by applying so-called classical approach, which was first introduced by von Karman. Instead of a numerical method, a recently developed popular semi numerical-analytical technique; differential transform method is employed to solve the reduced governing equations under the assumptions of velocity and thermal jump conditions on the disk surface. The combined effects of the velocity slip and temperature jump on the thermal and flow fields are investigated in great detail for different values of the nondimensional field parameters. In order to evaluate the efficiency of such rotating fluidic system, the entropy generation equation is derived and nondimensionalized. Additionally, special attention has been given to entropy generation, its characteristic and dependency on various parameters, i.e., group parameter, Kn and Re numbers, etc. It is observed that thermal and velocity jump strongly reduce the magnitude of entropy generation throughout the flow domain. As a result, the efficiency of the related physical system increases. A noticeable objective of this study is to give an open form solution of nonlinear field equations. The reduced recursive form of the governing equations presented gives the reader an opportunity to see the solution in open series form. [DOI: 10.1115/1.4002098]

Keywords: rotating disk flow, temperature jump, velocity slip, entropy generation

1 Introduction

Dramatic consumption of energy sources in the last half-century has caused world countries to reexamine their energy policies. Governments have taken drastic measures to eliminate wasted energy, promote energy-efficiency policy and technology in buildings, appliances, transport, and industry. The scientific environment and researchers have started taking a closer look at energy conversion devices, developing new techniques and analysis methods to better utilize existing resources and protection environment. All these mean is to give an attention to increase the efficiencies all types of energy producing, converting, and consuming systems.

Efficiency calculation of heat exchange systems has been very much restricted to the first law of thermodynamics. However, calculations using the second law of thermodynamics based on entropy generation are more reliable than first law-based calculations. Entropy generation is associated with thermodynamic irreversibility, which is common in all types of heat transfer processes. Different sources are responsible for entropy generation such as heat transfer across finite temperature gradient, characteristic of convective heat transfer, viscous effect, etc. Reduced entropy generation will result in more efficient designing of energy systems since the entropy generation is the measure of the destruction of the available work of the system [1]. Also, entropy

generation results in a decrease in the outputs of power cycles or an increase in the input powers for refrigeration cycles. Therefore, accurate calculation of the entropy generation plays an important role in the design and development of thermofluid components such as heat exchangers, pumps, turbines, pipe networks, energy storage systems, and electronic cooling devices.

The usage of method of second law of thermodynamics as a measure of the system performance was introduced by Bejan [1]. Bejan focused on different reasons behind the entropy generation in applied thermal engineering. Generation of entropy destroys available work of a system. Therefore, it makes a good engineering sense to focus on available work destruction mechanisms, irreversibility of heat transfer, and fluid flow process and try to understand the entropy generation mechanisms. Since then, many studies have been published on the entropy generation and irreversibility of the basic heat exchange systems, having rotating and translating components [2–5].

Rotating disk flow is an important subject in thermal engineering as it appears in many industrial and engineering applications such as gas turbine engines and electronic devices having rotary parts. Mainly, the requirement of high temperatures in the turbine stage to achieve high thermal efficiencies, the cooling of air is essential to ensure long lifetime for turbine disk and blade materials. Thermal efficiency may not only be a function of temperature for such type of rotary systems. The reasons for that are the complexity and the coupling of flow and thermal fields. Since the governing equations, namely, the momentum equations and the energy equation, are highly nonlinear and coupled, obtaining exact-analytical solutions are quite hard. For these reasons, nu-

Contributed by the Heat Transfer Division of ASME for publication in the JOURNAL OF HEAT TRANSFER. Manuscript received February 17, 2010; final manuscript received June 10, 2010; published online August 13, 2010. Assoc. Editor: Wei Tong.

merical solutions are carried out in many cases. For accurate determination of temperature distribution, the flow field must be solved as precisely as possible [6].

The investigations on rotating disk flow and heat transfer have gained considerable attention of researchers in recent years. The steady laminar flow of a viscous incompressible fluid due to a rotating disk of infinite extent in a porous medium was studied by Attia [7]. Sibanda [8] investigated the hydromagnetic steady flow and heat transfer characteristics of an incompressible viscous electrically conducting fluid over a rotating disk in a porous medium with ohmic heating. Osalusi et al. [9] studied ohmic heating, viscous dissipation, and hall and ion-slip currents in MHD flow over a porous rotating disk taking into account the variable fluid properties such as density, viscosity, and thermal conductivity. Results of an exact solution of a laminar heat transfer problem for a rotating disk in a fluid corotating with the disk as a solid body were investigated by Shevchuk and Buschmann [10]. Besides the theoretical studies, considerable work has been carried out on experimental research of convective heat transfer for rotating disk systems [11]. Shevchuk studied on theoretical and empirical relations by using experimental data for mass transfer of a rotating disk in laminar, transitional and turbulent flows for naphthalene sublimation in air [12]. In another study, turbulent heat and mass transfer of a rotating disk for Prandtl and Schmidt numbers much larger than unity were modeled using an integral method validated against empirical equations of different authors for Sherwood numbers [13].

On the other hand, there has been intensive research on microfluidic systems for compact reactor technologies in recent years [14]. Microflow devices, which are widely used in complex systems for medical diagnosis and surgery, chemical analysis, biotechnology, and electronic cooling, are actually downscaled devices such as microchannels, mixers, pumps, and heat pipes. Modeling heat and fluid flow through such small devices is different from the macroscale counterparts in being associated with the inclusion of velocity slip, temperature jump, and other newly developed issues [15,16].

The slip-flow regime has been widely studied, since it leads to quite simple models for further optimization of these microsystems [17]. In the slip-flow regime, standard Navier–Stokes and energy equations can still be employed with modifications to the boundary conditions (BCs) allowing for velocity slip and temperature jump at the walls. The velocity slip effect is very important and should be taken into account for precise prediction of the nature of microflows.

The temperature jump effect is also very important and should be included in the modeling of the slip-flow heat transfer problems. Neglecting this effect leads to a significant over prediction of heat transfer rate. Renksizbulut et al. [18] studied incompressible gas flows and heat transfer in rectangular microchannels of various aspect ratios. Their study is carried out for various Knudsen numbers related to the slip-flow regime by using three-dimensional Navier–Stokes and energy equations together with velocity slip and temperature jump boundary conditions. In another work, Xiao et al. [19] studied microtube gas flows with second-order velocity slip and temperature jump boundary conditions. Meolans [20] studied thermal slip boundary conditions in vibrational nonequilibrium flows. The velocity of the fluid on the surface, where the effect of slip dominates, is related to the slip factor by the boundary conditions given in Ref. [21] and temperature on the surface is related to the jump factor by the boundary conditions given in Ref. [18].

Although there are numerous studies on second law analysis for flow and heat transfer problems [22–24], only a few of them consider the effect of slip and temperature jump on the entropy generation. Yari [25] investigated the entropy generation in a microannulus flow. In the study, the viscous dissipation effect, the velocity slip and the temperature jump at the wall are taken into consideration. Hooman [26] studied forced convection in micro-

electromechanical systems in the slip-flow regime by invoking the temperature jump equation and numerically evaluated entropy generation distribution for fully developed velocity and temperature fields. The entropy generation due to steady laminar forced convection fluid flow through parallel-plates-microchannel is investigated numerically by Haddad et al. [27].

Unfortunately, open literature shows very small number of papers that deal with entropy generation on the rotating disk. Moreover, there are no studies on the entropy generation over rotating disk systems in which, velocity and temperature jump effects are both taken into consideration. The slip dependent velocity results in the reduction in the loss of some part of the mechanical energy into thermal energy. As a consequence, velocity slip reduces the entropy generation and results in the usage of a higher portion of the available energy. Also, relating entropy generation to slip factor on the flow and thermal field solutions gives more accurate results, which help the designer to evaluate the efficiency calculations and geometrical optimization of such rotating system or systems having rotating parts more accurately.

The objective of the present paper is to analyze the combined effects of velocity and temperature jump on the entropy generation over a rotating disk. The similarity variables introduced by von Karman are used to reduce heat and flow field equations to a set of nonlinear ordinary differential equations. The resulting equations are solved by using differential transform model (DTM). Analytical, fast converging series solutions are obtained for the flow and thermal field equations. To determine the physical characteristics of the flow field, the Knudsen number based classification is chosen. That is, the slip and no-slip regimes that lie in the range $0 < Kn < 0.1$ are considered. The entropy generation distribution is obtained by solving the related entropy generation equation by taking velocity and temperature jump conditions into consideration. The effects of Knudsen number, Reynolds number, and group parameter (ψ) on velocity, temperature, entropy generation, and Bejan number (Be) are discussed.

2 Mathematical Modeling

Slip over a moving surface is mainly caused by two effects, which are surface roughness and rarefaction of the fluid. Rarefied flow is commonly encountered in many engineering aspects such as high-altitude flight, micromachines, vacuum technology, aerosol reactors, etc. An important dimensionless parameter in rarefied flow is Knudsen number (Kn). Knudsen number is a measure of rarefaction, which is the ratio of the mean free path to a characteristic length in the fluid domain. The macro Navier–Stokes and energy equations with classical no-slip and no-temperature jump boundary conditions are applicable for flows with $Kn < 0.001$. In first-order slip approach, temperature-slip jump conditions should be applied to the Navier–Stokes equations for the Knudsen number that lies between the range of $0.001 < Kn < 0.1$, which correspond to the slip-flow regime. For $Kn > 0.1$, the flow field cannot be assumed to be continuum and the Navier–Stokes equations are not valid, which correspond to the transition regime. This flow regime should be simulated on the base of the Boltzman kinetic equation. For larger Knudsen numbers, where $Kn > 10$, the flow is defined as free molecular regime and the molecular approach is used to model the microfluidic systems [17]. Due to its great occurrence in gas microsystems, the slip-flow regime has been widely studied since it leads to quite simple models, which can be used for further optimization.

In this study, the disk surface has uniform temperature T_w , while the fluid flow satisfies the velocity slip and heat transfer satisfies the temperature jump conditions on the surface of the rotating disk. The velocity slip on the disk surface is considered as a result of rarefaction of the fluid; however, the solution obtained here can also be applied to the case where slip is a result of surface roughness.

2.1 Boundary Conditions

2.1.1 Velocity Slip Boundary Condition. For the more accurate prediction of a flow field, considering the effect of velocity slip is very important and should be included in the modeling. According to the slip-flow theory, the fluid velocity at the surface is different from the wall velocity in proportion to the local velocity gradient in normal direction. The following form has been proposed by Karniadakis and Beskok [28]:

$$U_s - U_w = \frac{2 - \sigma_v}{\sigma_v} \lambda \frac{\partial u}{\partial z} + \frac{3}{2\pi} \frac{\beta - 1}{\beta} \frac{\text{Kn}^2 \text{Re}}{\text{Ec}} \frac{\partial T}{\partial r} \quad (1)$$

where U_s is the velocity of the fluid adjacent to the disk surface, U_w is the wall velocity, and σ_v is the tangential momentum accommodation coefficient, which is defined as the fraction of molecules reflected diffusively and depends on fluid and surface finish and it is usually determined experimentally [18]. Tangential momentum accommodation coefficient is equal to unity for diffuse molecular collision and slip velocity is unbounded if $\sigma_v = 0$.

The second term on the right-hand side of Eq. (1) is responsible for the thermal creep effect, which induces velocity slip along the wall due to the temperature gradient adjacent to the wall along the surface. Thermal creep effects can be powerful enough to drive the flow without even having an inflow velocity field. It can be shown through a dimensional analysis that this thermal creep term is of second-order in terms of Knudsen number. Thus, it is negligible in the slip-flow regime comparing to the first term, which is of first-order. Therefore, as a reasonable approximation, only the first terms in the slip/jump boundary conditions will be retained in the present work as in Refs. [18,29].

2.1.2 Temperature Jump Condition. The fluid temperature over the disk differs from the wall temperature in proportion to the local normal temperature gradient. The original form of the temperature jump condition was derived by von Smoluchowski [28]. Smolochowski's temperature jump relation can be derived by considering the kinetic approach to conductive energy balance between fluid and solid surface. Accurate calculation of temperature jump is necessary in many engineering fields such as aerothermodynamics of space vehicles, vacuum system, and microelectromechanical systems. By assuming the impinging molecular stream is in equilibrium, the corresponding temperature jump condition can be given by [28]

$$T_s - T_w = \frac{2 - \sigma_t}{\sigma_t} \frac{2\beta}{1 + \beta \text{Pr}} \frac{\lambda}{\partial z} \frac{\partial T_s}{\partial z} \quad (2)$$

where T_s is the temperature of the fluid adjacent to the disk surface, T_w is the disk wall temperature, and σ_t is the energy accommodation coefficient, which represents a fraction of molecules that experience diffusive reflection at the solid surface. The energy accommodation coefficient has the value between the range of $0 < \sigma_t < 1$. In typical engineering applications, σ_t is close to 0.9 [28]. Another important point is that σ_t is a value determined experimentally that depends on the surface finish, the fluid temperature, and the pressure.

2.2 Flow Field. Considering the steady and incompressible flow over a single free disk in a Newtonian fluid, the equations of conservation of momentum and mass can be given as [6,11]

$$u \frac{\partial u}{\partial r} + w \frac{\partial u}{\partial z} - \frac{v^2}{r} + \frac{1}{\rho} \frac{\partial p}{\partial r} = \frac{\mu}{\rho} \left(\frac{\partial^2 u}{\partial r^2} + \frac{1}{r} \frac{\partial u}{\partial r} - \frac{u}{r^2} + \frac{\partial^2 u}{\partial z^2} \right) \quad (3)$$

$$u \frac{\partial v}{\partial r} + w \frac{\partial v}{\partial z} + \frac{uv}{r} = \frac{\mu}{\rho} \left(\frac{\partial^2 v}{\partial r^2} + \frac{1}{r} \frac{\partial v}{\partial r} - \frac{v}{r^2} + \frac{\partial^2 v}{\partial z^2} \right) \quad (4)$$

$$u \frac{\partial w}{\partial r} + w \frac{\partial w}{\partial z} + \frac{1}{\rho} \frac{\partial p}{\partial z} = \frac{\mu}{\rho} \left(\frac{\partial^2 w}{\partial r^2} + \frac{1}{r} \frac{\partial w}{\partial r} + \frac{\partial^2 w}{\partial z^2} \right) \quad (5)$$

$$\frac{\partial(ru)}{\partial r} + \frac{\partial(rw)}{\partial z} = 0 \quad (6)$$

The slip boundary conditions for the problem considered are introduced as follows:

$$u = \frac{2 - \sigma_v}{\sigma_v} \lambda \frac{\partial u}{\partial z}, \quad v = r\Omega + \frac{2 - \sigma_v}{\sigma_v} \lambda \frac{\partial v}{\partial z}, \quad w = 0 \quad \text{at } z = 0 \quad (7)$$

$$u \rightarrow 0, \quad v \rightarrow 0 \quad \text{as } z \rightarrow \infty \quad (8)$$

where Ω is the angular velocity of the rotating disk. Following von Karman, a dimensionless axial coordinate $\zeta = z\sqrt{\Omega/\nu}$ is introduced together with the following velocity components and the pressure [30]:

$$u = \Omega r F(\zeta), \quad v = \Omega r G(\zeta), \quad w = \sqrt{\Omega\nu} H(\zeta), \quad p = -\rho\Omega\nu P(\zeta) \quad (9)$$

The following system of ordinary differential equations is obtained by using the dimensionless axial coordinate, the velocity components and the pressure:

$$F'' = HF' + F^2 - G^2 \quad (10)$$

$$G'' = HG' + 2FG \quad (11)$$

$$H' = -2F \quad (12)$$

$$P'' = HH' - H'' \quad (13)$$

The BCs in Eqs. (7) and (8) can be written as follows [31]:

$$F(0) = \gamma F'(0), \quad G(0) = 1 + \gamma G'(0), \quad H(0) = 0 \quad (14)$$

$$F(\infty) = 0, \quad G(\infty) = 0 \quad (15)$$

where $\gamma = [(2 - \sigma_v)\lambda\sqrt{\Omega/\nu}]/\sigma_v$ is defined as the slip factor. By using the rotational Reynolds number and the value of tangential momentum accommodation number for air as 0.9 [28], the slip factor can be written as follows:

$$\gamma = 1.22 \times \text{Kn} \sqrt{\text{Re}} \quad (16)$$

In order to transform the infinite ζ range to a finite ξ range, the following dependent and independent variables are used, which were introduced by Benton [32]:

$$\xi = e^{-c\zeta} \quad (17)$$

$$F(\zeta) = c^2 f(\xi), \quad G(\zeta) = c^2 g(\xi), \quad H(\zeta) = -c[1 - h(\xi)] \quad (18)$$

By using the variables in Eqs. (17) and (18), Eqs. (10)–(12) are rewritten as follows:

$$\xi^2 f''(\xi) = f^2(\xi) - g^2(\xi) - \xi f'(\xi) h(\xi) \quad (19)$$

$$\xi^2 g''(\xi) = 2f(\xi)g(\xi) - \xi g'(\xi)h(\xi) \quad (20)$$

$$\xi h'(\xi) = 2f(\xi) \quad (21)$$

The boundary conditions in Eqs. (14) and (15) become

$$f(1) = \gamma f'(1), \quad g(1) = c^{-2} - \gamma c g'(1), \quad h(1) = 1 \quad (22)$$

$$f(0) = 0, \quad g(0) = 0, \quad h(0) = 0 \quad (23)$$

2.3 Thermal Field. The energy equation by neglecting dissipation terms can be written as follows [6,33]:

$$\rho c_p \left(u \frac{\partial T}{\partial r} + w \frac{\partial T}{\partial z} \right) - k \left(\frac{\partial^2 T}{\partial z^2} + \frac{\partial^2 T}{\partial r^2} + \frac{1}{r} \frac{\partial T}{\partial r} \right) = 0 \quad (24)$$

It is assumed that heat transfer is only in the z direction and then Eq. (24) becomes [31,33]:

$$\rho c_p \left(w \frac{dT}{dz} \right) - k \frac{d^2 T}{dz^2} = 0 \quad (25)$$

Dimensionless temperature is defined as follows:

$$\theta = \frac{T - T_\infty}{T_w - T_\infty} \quad (26)$$

Then, Eq. (25) can be evaluated in the following dimensionless form:

$$\theta' = Pr H \theta' \quad (27)$$

where Pr is the Prandtl number. By using Eq. (26), the BCs given in Eq. (2) become

$$\theta(\infty) = 0, \quad \theta(0) = 1 + \phi \theta'(0) \quad (28)$$

where ϕ is the temperature jump factor and it can be explicitly written as follows:

$$\phi = \left(\frac{2 - \sigma_t}{\sigma_t} \right) \left(\frac{2\beta}{1 + \beta} \right) \frac{Kn}{Pr} \sqrt{Re} \quad (29)$$

By using the value of energy accommodation coefficient as 0.9 [28], Prandtl number as 0.72 and the specific heat ratio as 1.4, ϕ takes the following form:

$$\phi = 1.43 \times \frac{Kn}{Pr} \sqrt{Re} \quad (30)$$

Then, integrating Eq. (27) and applying the second boundary condition in Eq. (28), dimensionless temperature can be evaluated in terms of the axial component of the velocity field as follows:

$$\theta(\zeta) = \theta'(0) \left(\int_0^\zeta e^{Pr \int_0^\alpha H(\alpha) d\alpha} d\chi + \phi \right) + 1 \quad (31)$$

and the missing BC $\theta'(0)$ is evaluated by Eq. (31) together with the far field BC given in Eq. (28) as follows:

$$\theta'(0) = -1 / \left(\int_0^\infty e^{Pr \int_0^\alpha H(\alpha) d\alpha} d\chi + \phi \right) \quad (32)$$

Once flow field is obtained, the thermal field is acquired from Eqs. (31) and (32) by using numerical integration.

To solve the equation system (19)–(21) with the BCs given in Eqs. (22) and (23), DTM is applied at $\xi=0$. For the solutions carried out, MATHEMATICA, a powerful symbolic calculation software, is utilized. DTM is a semi-analytical technique depending on Taylor series that is promising for various types of differential equations. It is possible to obtain highly accurate results or exact solutions for differential or integrodifferential equations considered. By using the theorems in Refs. [34,35], the differential transform of Eqs. (19)–(21) can be evaluated as given in Appendix.

3 Entropy Generation

The entropy generation rate can be expressed for the steady and axially symmetrical flow in a Newtonian fluid as follows [1,36]:

$$\begin{aligned} \dot{S}_G^m = & \frac{k}{T_w^2} \left(\frac{\partial T}{\partial z} \right)^2 + \frac{\mu}{T_w} \left\{ 2 \left[\left(\frac{\partial u}{\partial r} \right)^2 + \frac{1}{r^2} u^2 + \left(\frac{\partial w}{\partial z} \right)^2 \right] + \left(\frac{\partial v}{\partial z} \right)^2 \right. \\ & \left. + \left(\frac{\partial u}{\partial z} \right)^2 + \left[r \frac{\partial}{\partial r} \left(\frac{v}{r} \right)^2 \right] \right\} \quad (33) \end{aligned}$$

Using the dimensionless variables in Eq. (9), together with the dimensionless temperature, Eq. (33) can be written in the following simple form, which is already given in our previous study [36].

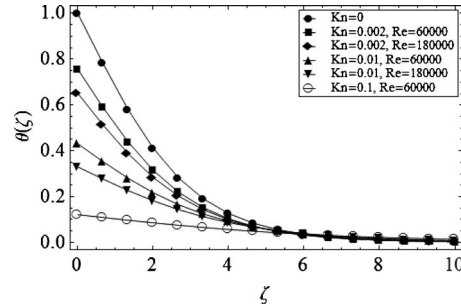


Fig. 1 Variation in $\theta(\zeta)$ with respect to ζ for different values of Re and Kn

$$N_g = Re \theta'(\zeta)^2 + \psi \{ 3 Re^2 H'(\zeta)^2 + Re^3 \bar{r}^2 [G'(\zeta)^2 + F'(\zeta)^2] \} \quad (34)$$

The ratio $\psi = Br / \alpha Re^2$ is called the group parameter, which shows the relative importance of viscous effects to heat transfer irreversibility. The effects of ψ and Re on the entropy generation rate are explicitly seen from Eq. (34).

An increase in ψ is to increase the entropy generation due to viscous effects. The effect of increasing Reynolds number, which is the ratio of inertial and viscous forces, is to increase the effect of viscous dissipation caused by the velocity components in all directions and the finite temperature difference irreversibilities caused by heat transfer.

4 Result and Discussion

Figures 1–4 illustrate the dimensionless velocity and temperature profiles obtained from Eqs. (19)–(21) together with Eq. (27) for different values of Re and Knudsen number. As seen from Fig. 1, the increase in Knudsen number results in a decrease in the dimensionless temperature and the temperature jump is greater at the higher Kn. Temperature jump at the wall for nonzero Kn reduces the amount of heat transfer from the wall. Therefore, less amount of heat is transferred from the wall to the adjacent fluid.

The temperature of the adjacent fluid over the disk surface (T_s) is lower than the disk wall temperature (T_w) for nonzero Kn number because of the temperature jump. An important point is that, the temperature does not change with Re number for Kn=0. The temperature of the adjacent fluid over the disk surface reduces with both increasing Kn and Re since the temperature jump is directly related to these two parameters as seen from Eq. (30).

Similarly, Figs. 2–4 show the dimensionless radial, circumferential and axial velocity profiles at different values of Kn and Re numbers. Figures demonstrate that the velocities strongly depend

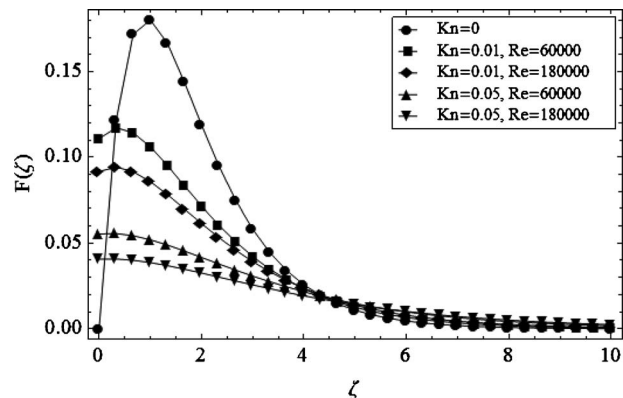


Fig. 2 Variation in $F(\zeta)$ with respect to ζ for different Re and Kn

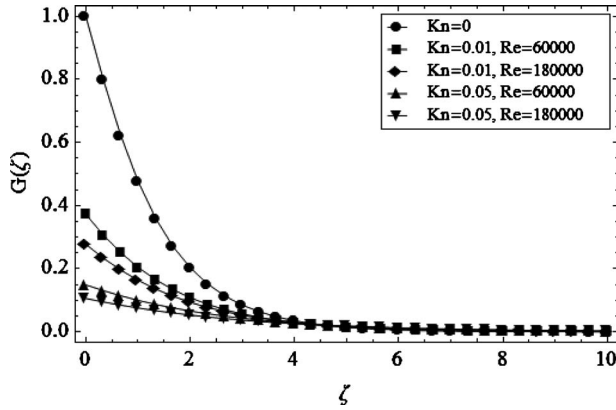


Fig. 3 Variation in $G(\zeta)$ with respect to ζ for different Re and Kn

on the Knudsen number. It is observed that the circumferential velocity on the wall decreases with an increase in Kn.

The numerical values for the velocity gradients and the Nusselt number on the disk surface for $Kn=0$ is presented in Table 1. The results show very good agreement with the already existing ones.

Figure 5 shows the spatial distribution of the local entropy generation through out the flow domain for different values of Kn and Re. As the Knudsen number increases the local entropy generation decreases especially on the disk surface. The local entropy generation is higher near the wall because of the higher local velocity and temperature gradients. As Knudsen number increases, both the temperature and the velocity gradients decrease. This results in a decrease in the local entropy generation. When the first-order slip/jump conditions are considered, both the velocity slip and temperature jump are proportional to Kn as seen in Eqs. (16) and (30).

Figure 6 shows the variation in entropy generation with Kn for different values of Re and ψ . The increase in velocity slip and

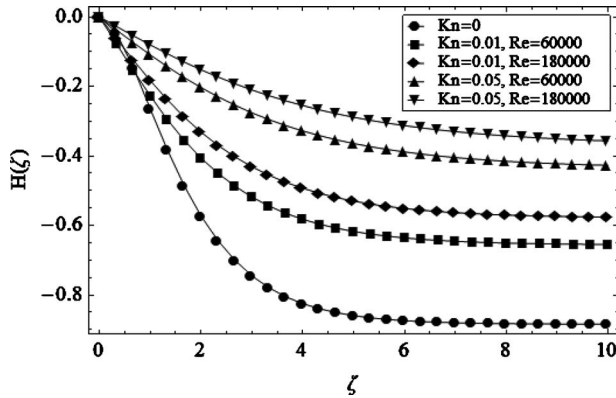


Fig. 4 Variation in $H(\zeta)$ with respect to ζ for different Re and Kn

Table 1 Comparison of results for F' , G' , and Nu at $\zeta=0$ (Pr = 0.72 and $Kn=0$)

	$F'(0)$	$G'(0)$	Nu
Proposed	0.510215	-0.615923	0.328573
Owen [6]	0.5102	-0.6159	-
Miklavcic [37]	0.51023262	-0.61592201	-
Shevchuk [11]	-	-	0.3286
Lin [38]	-	-	0.32857
Oehlbeck [39]	-	-	0.341

temperature jump at the wall brings about reducing heat transfer and momentum transfer from the wall to the fluid and this also causes the reduction in the local entropy generation.

Figure 7 shows the variation in the entropy generation along the radial coordinate on the disk surface for different values of the group parameter and Reynolds number. The group parameter determines the relative importance of the viscous effects to heat transfer irreversibility. As seen from the figure, increasing ψ results in increasing local entropy generation due to viscous dissipation. Moreover, entropy generation increases with increasing Re. As a result of higher angular velocities and the velocity gradients while closer to the outer region of the disk ($\bar{r} \rightarrow 1$), the entropy generation by viscous dissipation increases. Also this effect is intensified for higher values of ψ .

The average values are considered since they give an idea for the total performance of the system. Reducing the entropy generation on the surface leads to the case of minimization of the entropy generation that maintains the maximum usage of available energy. Apparently, Kn has effect on the loss of mechanical energy since it is directly related to slip on the surface.

The dimensionless volumetric entropy generation rate, which is an important measure of the total entropy generation, can be defined as follows:

$$N_{g,av} = \frac{1}{\nabla} \int_0^m \int_0^1 2\pi\bar{r}N_g d\bar{r}d\zeta \quad (35)$$

where ∇ is the volume considered. Since the gradients in flow and thermal fields exponentially decay with increasing ζ , zero volumetric entropy generation is obtained if the complete flow domain is considered. Therefore, the volumetric entropy generation is calculated inside of a sufficiently large finite domain, which includes the boundary layer effects of both flow and thermal fields. Therefore, the integration in Eq. (35) is obtained in the domain $0 \leq \bar{r} \leq 1$ and $0 \leq \zeta \leq m$, where m is a sufficiently large number.

The change in $N_{g,av}$ with respect to Kn, ψ , and Re is shown in Fig. 8. One can observe that the effect of increasing Re also increases the entropy generation due to the intensified fluid friction and heat transfer irreversibilities especially for the smaller Knudsen number. The effect of Kn is to reduce the velocity gradients in radial, circumferential, and axial directions as well as the temperature gradient in the entire flow field. This brings about a reduction in the volumetric entropy generation rate.

The total local entropy generation in Eq. (34) can be written as the summation of local entropy generation due to heat transfer irreversibility (N_H), which is the first term, and the local entropy generation due to fluid friction irreversibility (N_F), which is the second term on the right-hand side as follows:

$$N_g = N_H + N_F \quad (36)$$

During the calculations it may be possible to evaluate these terms separately then compare them to see the dominance of one term on the other. Local entropy generation due to heat transfer contains only the entropy generation by heat transfer due to axial conduction from the rotating disk. Local entropy generation due to fluid friction includes velocity gradients in axial, radial, and circumferential directions.

Another irreversibility distribution parameter is the Bejan number (Be), which is the ratio of entropy generation due to the heat transfer to the total entropy generation. This number is given in dimensionless form for the problem considered in this study as follows [1,36]:

$$Be = \frac{N_H}{N_g} = \frac{\theta'(\zeta)^2}{\theta'(\zeta)^2 + \psi[3 \text{Re} H'(\zeta)^2 + \text{Re}^2 \bar{r}^2 [G'(\zeta)^2 + F'(\zeta)^2]]} \quad (37)$$

Bejan number has values in the range of $0 < Be < 1$ and the specific value of $Be=1$ corresponds to a case, where the heat transfer

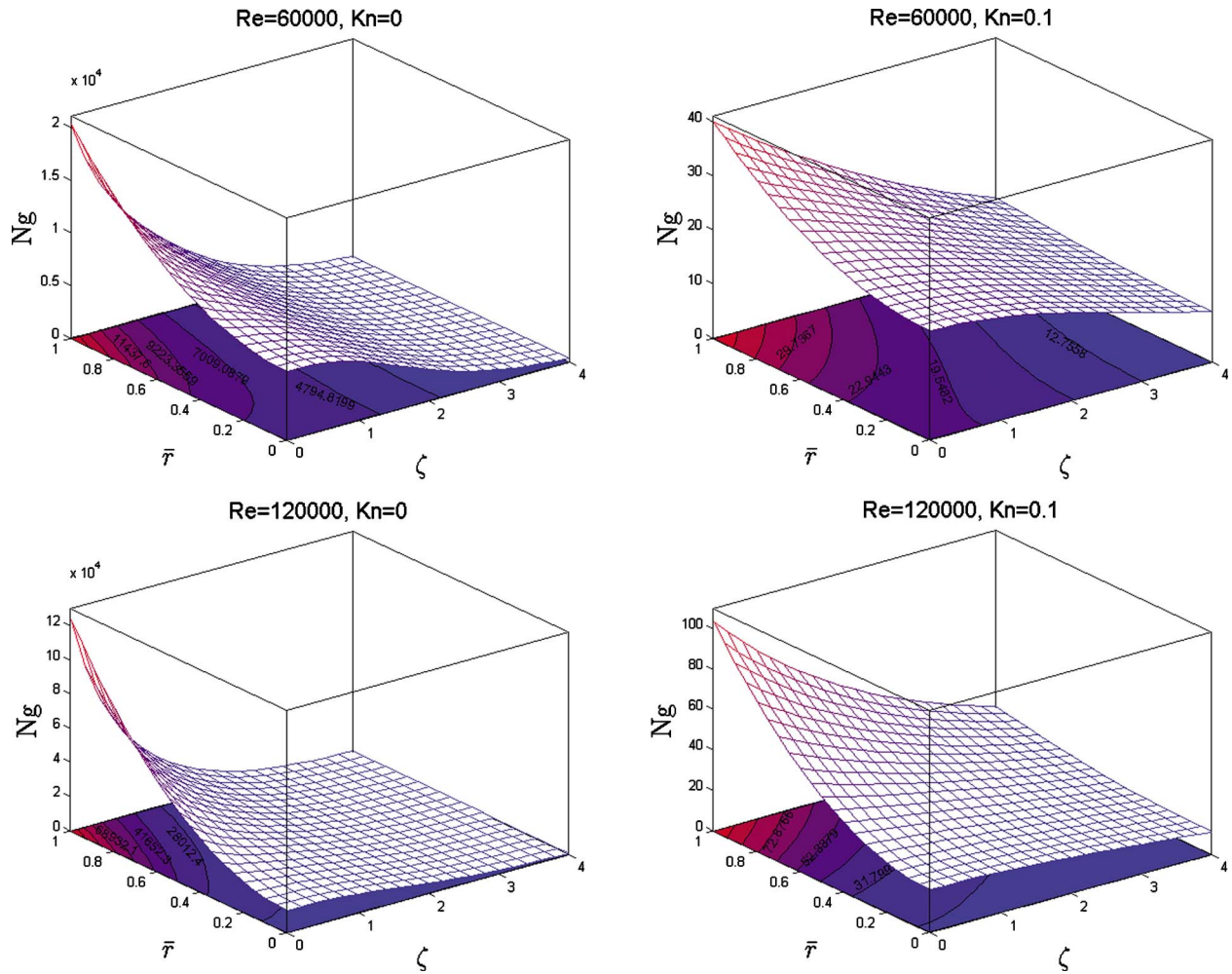


Fig. 5 Variation in N_g with respect to \bar{r} and ζ ($\psi=10^{-10}$)

irreversibility totally dominates. For $Be=0$ the fluid friction effects totally dominate on the entropy generation. For $Be=0.5$, the irreversibility caused by viscous effects dominates and for $Be \geq 0.5$, the irreversibility caused by heat transfer dominates. When $Be=0.5$, the heat transfer and the fluid friction entropy generation rates are equal.

Figure 9 shows the effects of Kn on the Bejan number for different values of the Reynolds number. The spatial distribution of Bejan number shows that the viscous contribution increases with radial coordinate due to the increasing velocities, as ex-

pected. The effect of the axial coordinate is vice versa, since the velocity gradients decay faster than the temperature gradient. Also, figure shows that the Bejan number increases on the surface and the variation along the axial coordinate is reduced with an increase in Kn .

The effect of Kn on the Bejan number over the disk surface for different values of the group parameter and Reynolds number is shown in Fig. 10. An increase in ψ decreases Be due to the increasing viscous effects. Another fact is that, Be converges to

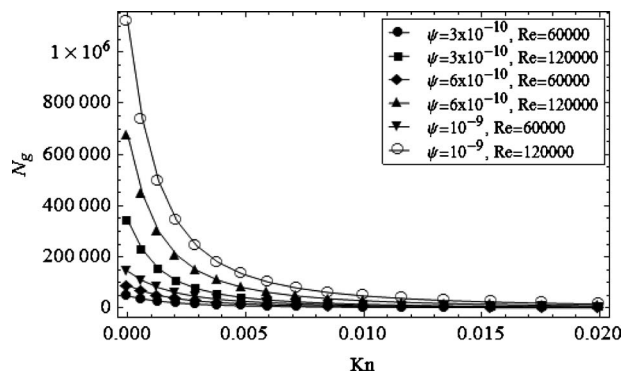


Fig. 6 Variation in N_g with respect to Kn for different ψ and Re ($\zeta=0$ and $\bar{r}=1$)

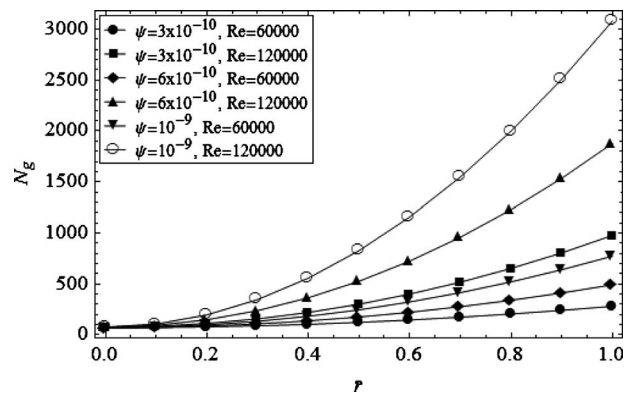


Fig. 7 Variation in N_g with \bar{r} for different ψ and Re ($\zeta=0$ and $Kn=0.05$)

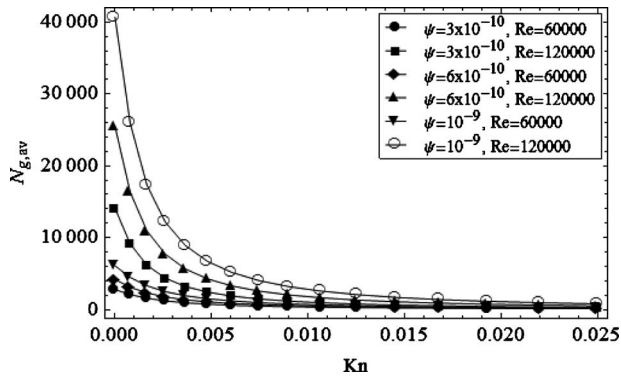


Fig. 8 Variation in $N_{g,av}$ with respect to Kn for different ψ and Re

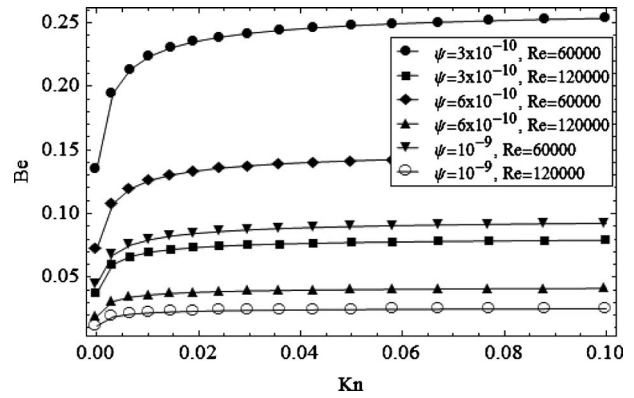


Fig. 10 Variation in Be with respect to Kn for different ψ and Re ($\zeta=0$ and $\bar{r}=1$)

constant values with increasing Kn . Also, the Bejan number decreases with Reynolds due to an increase in viscous effects.

Figure 11 shows the change in Be with respect to Kn for various values of Re at different radial locations. It is observed that, the Bejan number decreases as \bar{r} increases. The entropy generation by viscous dissipation increases as a result of higher velocities and the velocity gradients closer to the outer region of the disk ($\bar{r} \rightarrow 1$). Bejan number converges to 1 where the thermal effects dominate the entropy generation [40].

The average Bejan number can be defined similar to the definition of average entropy generation.

$$Be_{av} = \frac{1}{V} \int_0^m \int_0^1 2\pi\bar{r} Be d\bar{r}d\zeta \quad (38)$$

The change in average Bejan number with respect to the Knudsen number, Reynolds number, and group parameter are investigated and depicted in Fig. 12. The increase in ψ and Re bring about

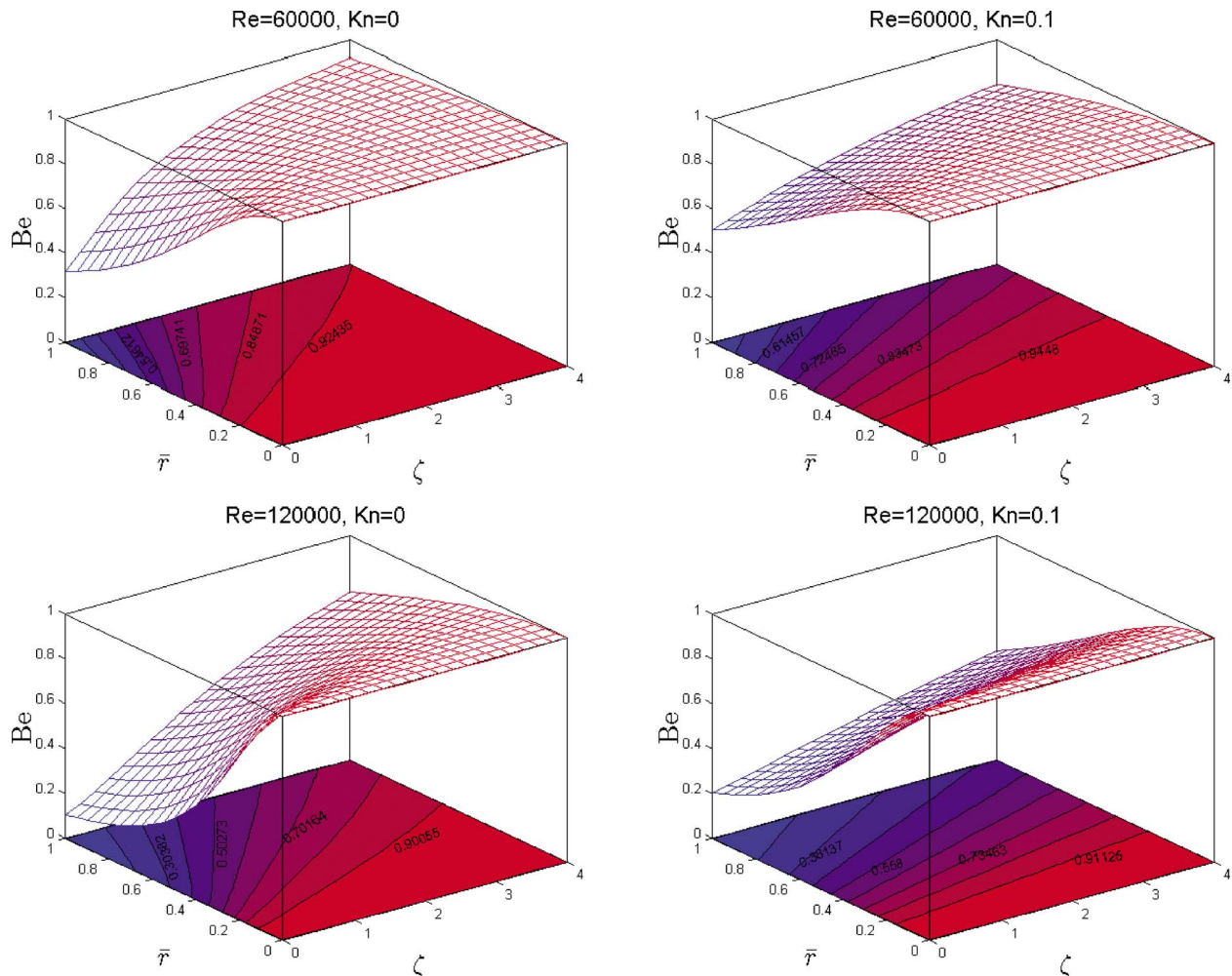


Fig. 9 Variation in Be with respect to \bar{r} and ζ ($\psi=10^{-10}$)

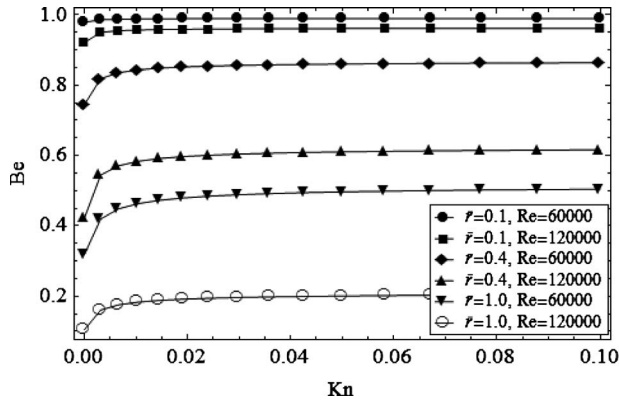


Fig. 11 Variation in Be with respect to Kn for different Re and \bar{r} ($\psi=10^{-10}$ and $\zeta=0$)

decrease in average Be due to the increasing viscous effects.

Nusselt Number, which is the ratio of convective heat transfer to the conductive heat transfer, can be given as follows [41]:

$$Nu = - \frac{\partial \theta(\zeta)}{\partial \zeta} \quad (39)$$

The variations in the heat transfer rate along the main flow direction (ζ) for a rotating disk at several Knudsen and Reynolds numbers are shown in Fig. 13. It is clear that the temperature jump at the wall for nonzero Kn cases reduces the amount of heat transfer from the wall. Despite the constant wall temperature, the heat

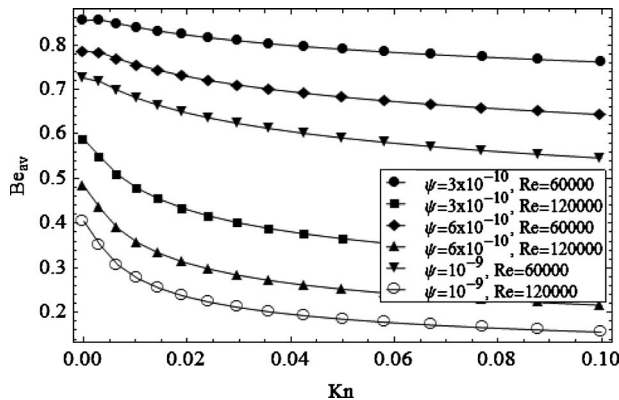


Fig. 12 Variation in Be_{av} with respect to Kn for different ψ and Re

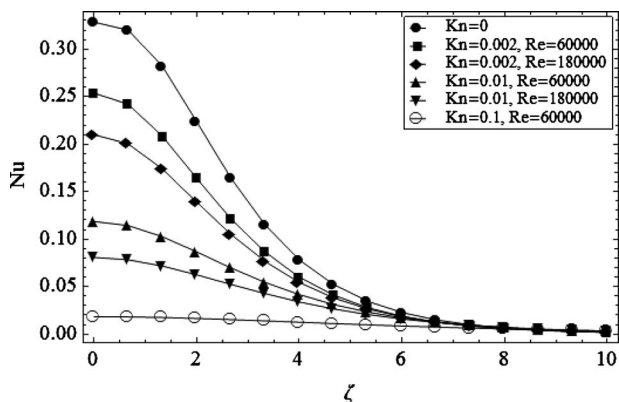


Fig. 13 Variation in Nu with respect to ζ for different Kn and Re

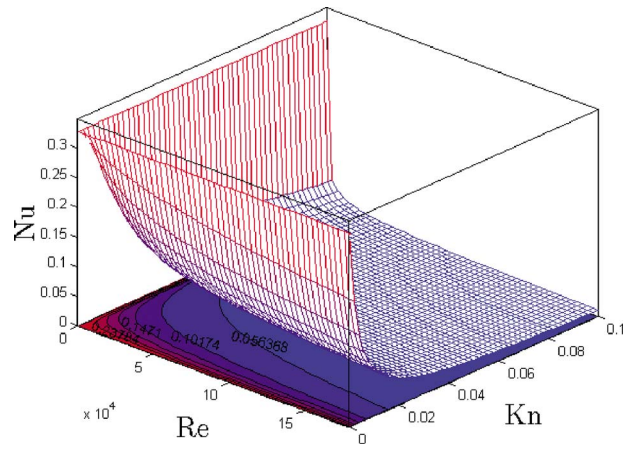


Fig. 14 Variation in Nu with respect to Kn and Re on the disk surface ($\zeta=0$)

transfer rate is not constant. It is possible to deduce from Fig. 13 that velocity slip together with temperature jump dramatically reduces the heat transfer rates. While the Knudsen number increases, the heat transfer rate diminishes since the temperature jump and velocity slip effects increase due to the rarefaction. The Nusselt number approaches to zero for increasing ζ . The variation of Nusselt number with Kn and Re on the disk surface ($\zeta=0$) is presented in three-dimensional form in order to better visualize the effect of system parameters on the heat transfer from the disk surface in Fig. 14.

Since the significant velocity and temperature gradients in the fluid are confined into the layers in the region adjacent to the disk surface, the thickness of these layers can be defined by certain standard measures [41]. For the tangential direction, the displacement thickness can be defined as follows:

$$\delta_{dis} = \int_0^{\infty} G(\zeta) d\zeta \quad (40)$$

where δ_{dis} is defined as a fictitious fluid-layer thickness. This layer is rotating at uniform tangential velocity and this layer is also capable to carry a tangential mass flow equal to that carried by the actual tangential velocity distribution. Similarly it is possible to define, as a measure of the extent of the thermal layer, a thermal thickness based on the temperature excess above the ambient is introduced as

$$\delta_t = \int_0^{\infty} \theta(\zeta) d\zeta \quad (41)$$

Figure 15 shows the change in δ_{dis} and δ_t with respect to ζ for different values of Re and Kn. The thicknesses of both fictitious layers increase with Kn and Re. The results for Kn=0 are in good agreement with the results of Attia for the steady state case [41].

5 Conclusion

In this study, the equation of entropy generation for the flow over a rotating free disk for steady and axially symmetrical case in a Newtonian fluid is derived. DTM based numerical-analytical method is used to solve the Navier-Stokes and energy equations with velocity slip and temperature jump conditions at the disk surface. Although similar procedure is followed as in our previous studies [29,30,36], this time temperature jump conditions are included. Graphical representations for local and volumetric values of entropy generation and Bejan number are presented for different values of the flow parameters. The common property observed in these figures is that the effect of Kn number is to reduce the

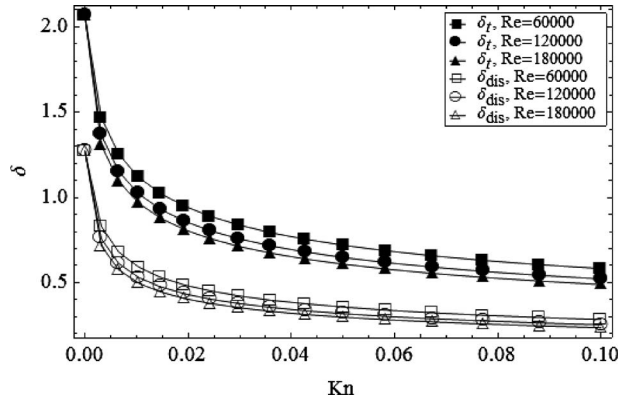


Fig. 15 Variation in δ_{dis} and δ_t with respect to Kn for different Re

magnitude of entropy generation. It is noticed that the entropy generation over the disk is directly related to Reynolds number and Group parameter.

Furthermore, in this study, the Nusselt number is calculated to show the variation in the heat transfer rate between the ambient fluid and the rotating disk surface. Velocity slip together with temperature jump at the wall reduces the amount of heat transfer from the rotating disk. Variations in displacement and thermal thicknesses are obtained for different field parameters.

The results of this study give an opportunity to the designer to use the second law of thermodynamics in efficiency calculations of rotating fluidic systems, since second law-based calculations for many engineering systems are more reliable than first law-based calculations. This study could be used to optimize the design of such systems by following the same procedure to minimize the entropy generation rate.

Nomenclature

- Be = Bejan number, N_H/N_g
- Be_{av} = average Bejan number
- Br = rotational Brinkman number, $\mu\Omega^2 R^2/k\Delta T$
- c_p = constant temperature specific heat, $\text{kJ kg}^{-1} \text{K}^{-1}$
- Ec = Eckert number, $(\Omega R)^2/c_p\Delta T$
- F, f = dimensionless radial velocities
- G, g = dimensionless circumferential velocities
- H, h = dimensionless axial velocity
- \tilde{F} = differential transform of f
- \tilde{G} = differential transform of g
- \tilde{H} = differential transform of h
- k = thermal conductivity, $\text{W m}^{-1} \text{K}^{-1}$
- Kn = Knudsen number, λ/R
- n = number of terms considered in DTM calculation
- N_g = dimensionless entropy generation rate, $\dot{S}_G'''/(k\Omega\rho\Delta T/\mu T_w)$
- $N_{g,av}$ = average entropy generation rate
- N_H = entropy generation due to heat transfer irreversibility
- N_F = entropy generation due to fluid friction irreversibility
- Nu = Nusselt number, $-\partial\theta(\zeta)/\partial\zeta$
- p = pressure, N/m^2
- P = dimensionless pressure
- Pr = Prandtl number, $\mu c_p/k$
- r = radial coordinate, m
- \bar{r} = dimensionless radial coordinate, $\bar{r}=r/R$
- R = radius of the disk, m

Re = rotational Reynolds number, $\text{Re}=\Omega R^2/\nu$

- \dot{S}_G''' = entropy generation rate
- T = temperature, K
- T_w = temperature on the disk, K
- T_s = surface temperature, K
- T_∞ = temperature at infinity, K
- u = radial velocity, m/s
- U_s = slip-flow velocity, m/s
- U_w = velocity of the disk, m/s
- v = circumferential velocity, m/s
- w = axial velocity, m/s
- z = axial coordinate, m

Greek Letters

- α = dimensionless temperature difference, $\alpha=\Delta T/T_w$
- β = specific heat ratio
- ΔT = temperature difference, T_w-T_∞
- γ = slip factor, $[(2-\sigma_v)\lambda\Omega^{1/2}]/\sigma_v\nu^{1/2}$
- δ_{dis} = displacement thickness
- δ_t = thermal thickness
- ζ = dimensionless axial coordinate, $z\sqrt{\Omega/\nu}$
- θ = dimensionless temperature, $\theta=(T-T_\infty)/(T_w-T_\infty)$
- λ = mean free path, m
- μ = dynamic viscosity, $\text{Nm}^{-2} \text{s}$
- ν = kinematic viscosity, m^2/s
- ξ = stretched dimensionless axial coordinate, $e^{-c\xi}$
- ρ = density, kg/m^3
- σ_v = tangential momentum accommodation coefficient
- σ_t = energy accommodation coefficient
- ϕ = temperature jump factor $((2-\sigma_t)/\sigma_t)(2\beta/(1+\beta))(\text{Kn}/\text{Pr})\sqrt{\text{Re}}$
- ψ = group parameter, $\psi=\text{Br}/\alpha \text{Re}^2$
- Ω = angular velocity of the rotating disk, rad/s
- ∇ = dimensionless volume

Appendix

The differential transform of Eqs. (19)–(21) is evaluated as below.

$$\tilde{F}(k) = \frac{1}{k(k-1)} \sum_{l=0}^k [\tilde{F}(l)\tilde{F}(k-l) - \tilde{G}(l)\tilde{G}(k-l) - l\tilde{F}(l)\tilde{H}(k-l)] \quad (\text{A1})$$

$$\tilde{G}(k) = \frac{1}{k(k-1)} \sum_{l=0}^k [2\tilde{F}(l)\tilde{G}(k-l) - l\tilde{G}(l)\tilde{H}(k-l)] \quad (\text{A2})$$

$$\tilde{H}(k) = \frac{2}{k}\tilde{F}(k) \quad (\text{A3})$$

where $k \geq 2$ and $\tilde{F}(k)$, $\tilde{G}(k)$, and $\tilde{H}(k)$ correspond to the differential transform of $f(\xi)$, $g(\xi)$, and $h(\xi)$, respectively. To evaluate the dependent variables, it is necessary to know the missing BCs $f'(0)$, $g'(0)$, and $h'(0)$. First, the values of $\tilde{F}(k)$, $\tilde{G}(k)$, and $\tilde{H}(k)$ in terms of $f'(0)=f_1$, $g'(0)=g_1$ are obtained. Then, by using the BCs given in Eqs. (22) and (23) for $\xi=1$, f_1 , g_1 , and c are evaluated. This approach is cost efficient and works much faster than the numerical techniques since it is not iterative, i.e., the boundary conditions are not evaluated by using a shooting technique, instead they are evaluated at once. Then, the BCs given in Eqs. (22) and (23) for $\xi=0$ are transformed as follows:

$$\tilde{F}(0) = 0, \quad \tilde{G}(0) = 0, \quad \tilde{H}(0) = 0, \quad \text{and} \quad \tilde{F}(1) = f_1, \quad \tilde{G}(1) = g_1 \quad (\text{A4})$$

By using the recurrence relations in Eqs. (A1)–(A3) and the transformed boundary conditions in Eq. (A3), $\tilde{F}(k)$, $\tilde{G}(k)$, and $\tilde{H}(k)$ for $k=2, 3, \dots, N$ are evaluated. Then, invoking the inverse transformation rule in Ref. [34], the series solutions are obtained.

$$f(\xi) = \sum_{k=0}^N \tilde{F}(k) \xi^k, \quad g(\xi) = \sum_{k=0}^N \tilde{G}(k) \xi^k, \quad h(\xi) = \sum_{k=0}^N \tilde{H}(k) \xi^k \quad (\text{A5})$$

where N is the number of terms to be considered. By calculating up to $N=6$, it gives

$$\begin{aligned} f(\xi) = & f_1 \xi - \frac{1}{2}(f_1^2 + g_1^2) \xi^2 + \frac{1}{4} f_1 (f_1^2 + g_1^2) \xi^3 - \frac{1}{144} (f_1^2 + g_1^2) (17f_1^2 \\ & + g_1^2) \xi^4 + \frac{f_1 (f_1^2 + g_1^2) (61f_1^2 + 13g_1^2)}{1152} \xi^5 \\ & - \frac{(f_1^2 + g_1^2) (1971f_1^4 + 854f_1^2 g_1^2 + 35g_1^4)}{86400} \xi^6 + \dots \end{aligned} \quad (\text{A6})$$

$$\begin{aligned} g(\xi) = & g_1 \xi - \frac{1}{12} g_1 (f_1^2 + g_1^2) \xi^3 + \frac{1}{18} f_1 g_1 (f_1^2 + g_1^2) \xi^4 \\ & - \frac{g_1 (f_1^2 + g_1^2) (53f_1^2 + 5g_1^2)}{1920} \xi^5 + \frac{f_1 g_1 (f_1^2 + g_1^2) (65f_1^2 + 17g_1^2)}{5400} \xi^6 \\ & + \dots \end{aligned} \quad (\text{A7})$$

$$\begin{aligned} h(\xi) = & 2f_1 \xi - \frac{1}{2}(f_1^2 + g_1^2) \xi^2 + \frac{1}{6} f_1 (f_1^2 + g_1^2) \xi^3 - \frac{1}{288} (f_1^2 + g_1^2) (17f_1^2 \\ & + g_1^2) \xi^4 + \frac{f_1 (f_1^2 + g_1^2) (61f_1^2 + 13g_1^2)}{2880} \xi^5 \\ & - \frac{(f_1^2 + g_1^2) (1971f_1^4 + 854f_1^2 g_1^2 + 35g_1^4)}{259200} \xi^6 + \dots \end{aligned} \quad (\text{A8})$$

The solutions are given here up to $O(\xi^6)$, however, one can easily evaluate higher-ordered terms. After evaluating $f(\xi)$, $g(\xi)$, and $h(\xi)$, the original dependent variables $F(\zeta)$, $G(\zeta)$, and $H(\zeta)$ are obtained by using Eqs. (17) and (18). Also, in the case of necessity, one can obtain $P(\zeta)$ from the following equation:

$$P(\zeta) - P_0 = H(\zeta)^2/2 - H'(\zeta) \quad (\text{A9})$$

References

- Bejan, A., 1980, "Second Law Analysis in Heat Transfer," *Energy*, **5**, pp. 720–732.
- Erbay, L. B., Ercan, M. S., Sulus, B., and Yalcin, M. M., 2003, "Entropy Generation During Fluid Flow Between Two Parallel Plates With Moving Bottom Plate," *Entropy*, **5**(5), pp. 506–518.
- Mahmud, S., and Fraser, R. A., 2003, "The Second Law Analysis in Fundamental Convective Heat Transfer Problems," *Int. J. Therm. Sci.*, **42**(2), pp. 177–186.
- Yilbas, B. S., 2001, "Entropy Analysis of Concentric Annuli With Rotating Outer Cylinder," *Int. J. Exergy*, **1**(1), pp. 60–66.
- Abu-Hijleh, B. A. K., and Heilen, W. N., 1999, "Entropy Generation Due to Laminar Natural Convection Over a Heated Rotating Cylinder," *Int. J. Heat Mass Transfer*, **42**(22), pp. 4225–4233.
- Owen, J. M., and Roger, R. H., 1989, *Flow and Heat Transfer in Rotating-Disk Systems*, Research Studies Press, Wiley, New York.
- Attia, H. A., 2009, "Steady Flow over a Rotating Disk in Porous Medium With Heat Transfer," *Nonlinear Analysis: Modelling and Control*, **14**(1), pp. 21–26.
- Sibanda, P., 2010, "On steady MHD flow and Heat Transfer Past a Rotating Disk in a Porous Medium With Ohmic heating and Viscous Dissipation," *Int. J. Numer. Methods Heat Fluid Flow*, **20**(3), pp. 269–285.
- Osalusi, E., Side, J., and Harris, R., 2007, "The Effects of Ohmic Heating and Viscous Dissipation on Unsteady MHD and Slip Flow over a Porous Rotating Disk With Variable Properties in the Presence of Hall and Ion-Slip Currents," *Int. Commun. Heat Mass Transfer*, **34**, pp. 1017–1029.
- Shevchuk, I. V., and Buschmann, M. H., 2005, "Rotating Disk Heat Transfer in a Fluid Swirling as a Forced Vortex," *Heat Mass Transfer*, **41**, pp. 1112–1121.
- Shevchuk, I. V., 2009, *Convective Heat and Mass Transfer in Rotating Disk Systems*, Springer, Berlin.
- Shevchuk, I. V., 2008, "A New Evaluation Method for Nusselt Numbers in Naphthalene Sublimation Experiments in Rotating-Disk Systems," *Heat Mass Transfer*, **44**, pp. 1409–1415.
- Shevchuk, I. V., 2009, "Turbulent Heat and Mass Transfer Over a Rotating Disk for the Prandtl or Schmidt Numbers Much Larger Than Unity: An Integral Method," *Heat Mass Transfer*, **45**, pp. 1313–1321.
- Hooman, K., Hooman, F., and Famouri, M., 2009, "Scaling Effects for Flow in Micro-Channels: Variable Property, Viscous Heating, Velocity Slip, and Temperature Jump," *Int. Commun. Heat Mass Transfer*, **36**, pp. 192–196.
- Sparrow, E. M., and Haji-Sheikh, A., 1964, "Velocity Profile and Other Local Quantities in Free-Molecule Tube Flow," *Phys. Fluids*, **7**, pp. 1256–1251.
- Hooman, K., 2007, "Entropy Generation for Microscale Convection: Effects of Different Thermal Boundary Conditions, Velocity Slip, Temperature Jump, Viscous Dissipation, and Duct Geometry," *Int. Commun. Heat Mass Transfer*, **34**, pp. 945–957.
- Colin, S., 2005, "Rarefaction and Compressibility Effects on Steady and Transient Gas Flows in Microchannels," *Microfluid. Nanofluid.*, **1**, pp. 268–279.
- Reksizbulut, M., Niazmand, H., and Tercan, G., 2006, "Slip-Flow and Heat Transfer in Rectangular Microchannels With Constant Wall Temperature," *Int. J. Therm. Sci.*, **45**, pp. 870–881.
- Xiao, N., Elsnab, J., and Ameal, T., 2009, "Microtube Gas Flows With Second-Order Slip Flow and Temperature Jump Boundary Conditions," *Int. J. Therm. Sci.*, **48**, pp. 243–251.
- Meolans, J. G., 2003, "Thermal Slip Boundary Conditions in Vibrational Non-equilibrium Flows," *Mech. Res. Commun.*, **30**, pp. 629–637.
- Gad-el-Hak, M., 1999, "The Fluid Mechanics of Microdevices—The Freeman Scholar Lecture," *ASME J. Fluids Eng.*, **121**(1), pp. 5–33.
- Ozkol, I., Komurgoz, G., and Arikoglu, A., 2007, "Entropy Generation in the Laminar Natural Convection From a Constant Temperature Vertical Plate in an Infinite Fluid," *Proc. Inst. Mech. Eng., Part A*, **221**, (A5), pp. 609–616.
- Baytas, A. C., 1997, "Optimisation in an Inclined Enclosure for Minimum Entropy Generation in Natural Convection," *J. Non-Equil. Thermodyn.*, **22**(2), pp. 145–155.
- Ogulata, R. T., Doba, F., and Yilmaz, T., 1999, "Second-Law and Experimental Analysis of a Cross-Flow Heat Exchanger," *J. Heat Transfer Eng.*, **20**(2), pp. 20–27.
- Yari, M., 2009, "Second-Law Analysis of Flow and Heat Transfer Inside a Microannulus," *Int. Commun. Heat Mass Transfer*, **36**(1), pp. 78–87.
- Hooman, K., 2008, "Heat Transfer and Entropy Generation for Forced Convection Through a Microduct of Rectangular Cross-Section: Effects of Velocity Slip, Temperature Jump, and Duct Geometry," *Int. Commun. Heat Mass Transfer*, **35**(9), pp. 1065–1068.
- Haddad, O., Abuzzaid, M., and Al-Nimr, M., 2004, "Entropy Generation Due to Laminar Incompressible Forced Convection Flow Through Parallel-Plates Microchannel," *Entropy*, **6**(5), pp. 413–426.
- Karniadakis, G. E., and Beskok, A., 2002, *Microflows: Fundamentals and Simulation*, Springer-Verlag, New York, p. 56.
- Arikoglu, A., and Ozkol, I., 2005, "Analysis for Slip Flow Over a Single Free Disk With Heat Transfer," *ASME J. Fluids Eng.*, **127**(3), pp. 624–627.
- Karman, T., 1921, "Über Laminare und Turbulente Reibung," *Z. Angew. Math. Mech.*, **1**, pp. 233–252.
- Arikoglu, A., and Ozkol, I., 2006, "On the MHD and Slip Flow Over a Rotating Disk With Heat Transfer," *Int. J. Numer. Methods Heat Fluid Flow*, **16**(2), pp. 172–184.
- Benton, E. R., 1966, "On the Flow Due to a Rotating Disk," *J. Fluid Mech.*, **24**, pp. 781–800.
- Attia, H. A., 2008, "Rotating Disk Flow and Heat Transfer Through a Porous Medium of a Non-Newtonian Fluid With Suction and Injection," *Commun. Nonlinear Sci. Numer. Simul.*, **13**(8), pp. 1571–1580.
- Arikoglu, A., and Ozkol, I., 2005, "Solution of Boundary Value Problems for Integro-Differential Equations by Using Differential Transform Method," *Appl. Math. Comput.*, **168**(2), pp. 1145–1158.
- Arikoglu, A., and Ozkol, I., 2006, "Solution of Difference Equations by Using Differential Transform Method," *Appl. Math. Comput.*, **174**(2), pp. 1216–1228.
- Arikoglu, A., Komurgoz, G., and Ozkol, I., 2008, "Effect of Slip on the Entropy Generation From a Single Rotating Disk," *ASME J. Fluids Eng.*, **130**(10), p. 101202.
- Miklavcic, M., and Wang, C. Y., 2004, "The Flow Due to a Rough Rotating Disk," *Z. Angew. Math. Phys.*, **55**, pp. 235–46.
- Lin, H. T., and Lin, L. K., 1987, "Heat-Transfer From a Rotating Cone or Disk to Fluids of Any Prandtl Number," *Int. Commun. Heat Mass Transfer*, **14**(3), pp. 323–332.
- Oehlbek, D. L., and Erian, F. F., 1979, "Heat-Transfer From Axisymmetric Sources at the Surface of a Rotating-Disk," *Int. J. Heat Mass Transfer*, **22**(4), pp. 601–610.
- Komurgoz, G., Arikoglu, A., Turker, E., and Ozkol, I., 2010, "Second-Law Analysis for an Inclined Channel Containing Porous-Clear Fluid Layers by Using the Differential Transform Method," *Numer. Heat Transfer, Part A*, **57**(8), pp. 603–623.
- Attia, H. A., 2001, "Transient Flow a Conducting Fluid With Heat Transfer Due to an Infinite Rotating Disk," *Heat Mass Transfer*, **28**(3), pp. 439–448.

An Experimental Study on Heat Transfer Around Two Side-by-Side Closely Arranged Circular Cylinders

Takayuki Tsutsui

Department of Mechanical Engineering,
National Defense Academy,
1-10-20 Hashirimizu,
Yokosuka, Kanagawa 239-8686, Japan
e-mail: tsutsui@nda.ac.jp

The present paper describes heat transfer around two side-by-side closely arranged circular cylinders. The flows around two circular cylinders in a side-by-side arrangement can be classified into three flow patterns according to the gap between the two cylinders. The heat transfer characteristics of the cylinders in each flow regime were experimentally investigated. The diameter of the circular cylinders was 40 mm and the gap between the two cylinders varied from 4 mm to 40 mm. The free stream velocity ranged from 4 m/s to 24 m/s, resulting in Reynolds nos. ranging from 1.1×10^4 to 6.2×10^4 . The local heat transfer coefficient of both cylinders was measured. The overall Nusselt no. of the two cylinders was found to be minimum at $G/D (= \text{gap}/\text{diameter}) = 0.4$, which is the minimum drag coefficient condition of the two cylinders, too. [DOI: 10.1115/1.4002147]

Keywords: two circular cylinders, side-by-side arrangement, heat transfer, flow visualization

1 Introduction

Flows around buildings in close proximity to each other and in tube bundles in heat exchangers depend on the configurations of the buildings or the tubes. Tandem and side-by-side arrangements of two circular cylinders are among the most basic configurations. As such, several studies have investigated flows around two circular cylinders in side-by-side closely spaced arrangements (e.g., Refs. [1–4]). Previous studies have examined, for example, the pressure distribution, fluid force, and vortex structure [5,6].

According to Zdravkovich [4], three distinct interference flow regimes were observed and these regimes depend on the gap between the cylinders. The Strouhal no. shows the flow characteristics of the two closely spaced cylinders in a side-by-side arrangement. Figure 1 shows the relationship between the Strouhal no. St and the gap ratio G/D and the photographs of three typical flow patterns. Three distinct interference flow regimes have been observed as follows. (1) The single eddy street regime ($G/D < 0.2-0.3$) in which the flow through the gap adheres to the upper cylinder and forms a large eddy behind the two cylinders as a single bluff body. (2) The biased flow regime ($0.3 \leq G/D \leq 1$) in which the gap flow forms a narrow wake and exhibits higher frequency vortex shedding while lower cylinder has a wider wake and exhibits lower frequency vortex shedding. In the biased flow regime, the gap flow intermittently switches from one side to the other side of cylinders. (3) The coupled wake regime ($1 < G/D$) in which both wakes have the same size and frequency.

The flow patterns and fluid forces acting on the cylinders change drastically according to the gap size. The heat transfer around each cylinder can be changed by varying this gap size. The present study investigates the heat transfer characteristics of two cylinders in a side-by-side closely spaced arrangement. The local and average heat transfers around the cylinders are measured for various gap sizes and Reynolds nos.

2 Experimental Apparatus and Method

The coordinate system and notation used in this study are presented in Fig. 2. The experiments were performed in a low-speed wind tunnel with a working section having a height of 400 mm, a width of 300 mm, and a length of 800 mm. We refer to the upper and lower cylinders as cylinder nos. 1 and 2, respectively. The diameter D of the two circular cylinders was 40 mm and the gap G between the cylinders varied from 4 mm to 40 mm. The free stream velocity U varied from 4 m/s to 24 m/s and the turbulent intensity was approximately 0.4% in this velocity range. The Reynolds no. based on D ranged from 1.1×10^4 to 6.2×10^4 . Spontaneous intermittent gap flow switching from one side to the other was suppressed by setting the cylinders slightly staggered by 2.0 deg from the side-by-side arrangement except for $G/D=1.0$ because the switching rarely occur for $G/D=1.0$. About the staggering effect on flow field, we previously confirmed that few differences between with and without stagger by comparing pressure distribution around two cylinders for both cases. According to a previous paper [5], the flow around the slightly staggered cylinders was almost the same as that around the side-by-side cylinders.

Figures 3(a) and 3(b) show a constant-heat-flux model and the measurement system used in the present study, respectively. The model was used for the local heat transfer measurements and was fabricated from a 3 mm thick acrylic resin pipe, which was covered with 8 μm thick stainless steel sheet. The sheets were electrically connected in series and were heated by applying a direct current to produce a constant-heat-flux condition. The temperature difference between the heated face and the free stream was approximately 10°C. Copper-constantan thermocouples having diameters of 0.1 mm were attached to the underside of the stainless steel sheets in a spiral arrangement at 10 deg intervals.

The local temperatures on the surfaces of the two cylinders were measured, simultaneously, with respect to the free stream velocity and gap parameters. The local heat transfer coefficient h was obtained as follows:

$$h = I^2 R / \{A(t - t_0)\} \quad (1)$$

where I and R are the current and resistance of the stainless sheet, A is the active surface area, and t and t_0 are the local temperature

Contributed by the Heat Transfer Division of ASME for publication in the JOURNAL OF HEAT TRANSFER. Manuscript received December 16, 2009; final manuscript received July 6, 2010; published online August 16, 2010. Assoc. Editor: Ali Ebadian.

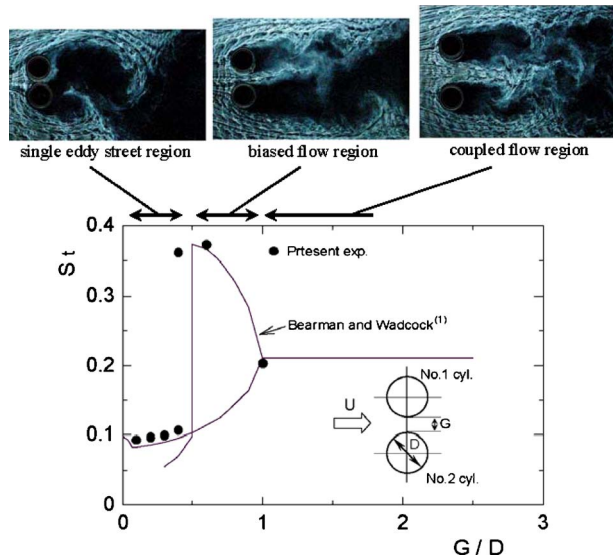


Fig. 1 Strouhal no. and three typical flow patterns

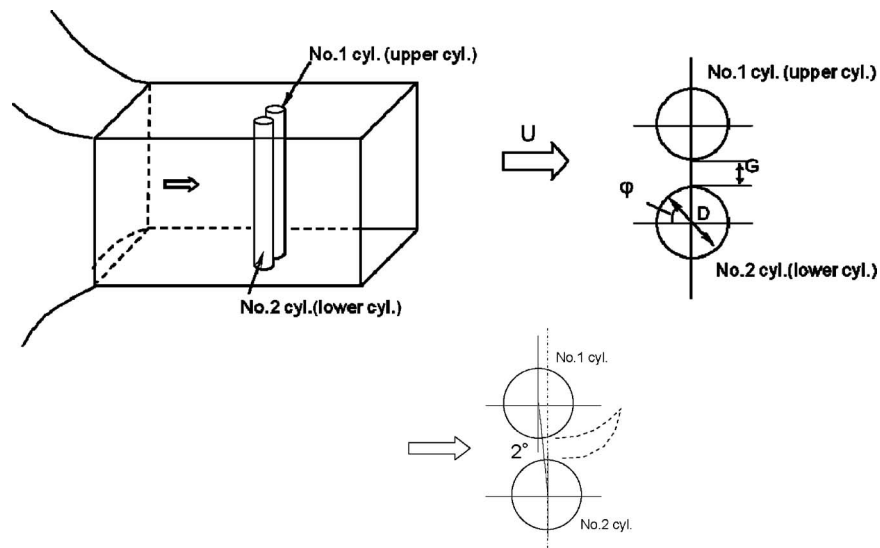


Fig. 2 Coordinate system and notation

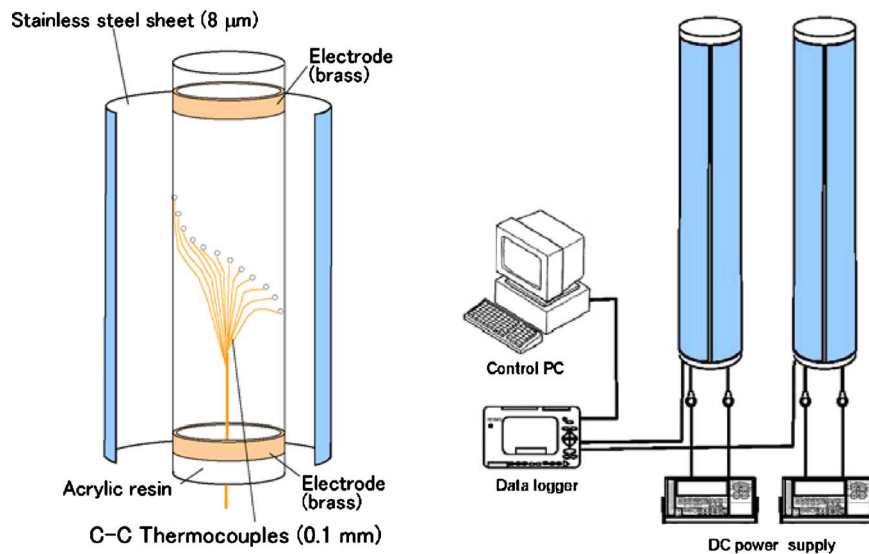


Fig. 3 Experimental model and measurement system: (a) constant-heat-flux model and (b) heat transfer measurement system

on the surface of the cylinder and the local temperature of the free stream, respectively.

The experimental uncertainties were calculated using standard uncertainty analysis methods proposed by Kline [7]. The total uncertainty for the heat transfer coefficient $\Delta h/h$ is obtained using the following equation:

$$\frac{\Delta h}{h} = \sqrt{\left(\frac{\Delta t}{t}\right)^2 + \left(\frac{\Delta q_{in}}{q_{in}}\right)^2 + \left(\frac{\Delta q_{loss}}{q_{loss}}\right)^2} \quad (2)$$

where $\Delta t/t$, $\Delta q_{in}/q_{in}$, and $\Delta q_{loss}/q_{loss}$ are the uncertainties of the measured temperature, the heat input, and the heat loss, respectively. The constant-heat-flux model yielded the following values: $\Delta t/t=2\%$, $\Delta q_{in}/q_{in}=1\%$, and $\Delta q_{loss}/q_{loss}=5\%$. Therefore, the total uncertainty for the heat transfer coefficient is within 5.5%.

The flow visualization was performed using the smoke wire method. Two I-type hot wire probes were used to measure the vortex shedding frequencies behind the two cylinders. The hot wires were set up at $1D$ outside and $2.5D-3.0D$ downstream from the center of the cylinders. The I-type hot wire probe was used for measurement of time averaged velocity and fluctuating velocity of the wake, too.

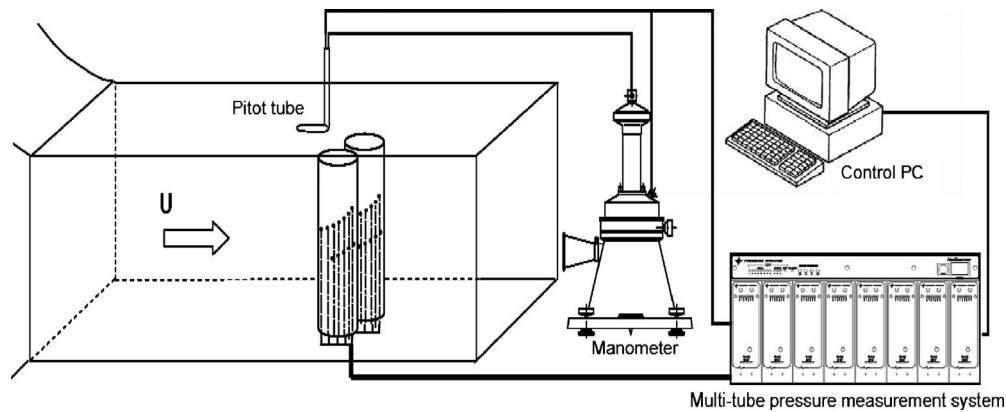


Fig. 4 Pressure measurement system

The surface pressure on the two cylinders was measured by a multitube pressure measurement system connected to 0.6 mm diameter pressure taps in a spiral arrangement at 10 deg intervals on the surfaces of the cylinders. Figure 4 shows the pressure measurement system.

3 Results and Discussion

3.1 Flow Visualization. Figures 5(a)–5(g) are photographs of the flow visualizations around the two cylinders obtained using the smoke wire method. The smoke reveals the streamlines, which describe the behavior of the flow around the cylinders. Figure 5(a) shows the flow around a single cylinder. Figure 5(b) shows the flow for $G/D=0.1$ in which a single vortex street is formed behind the cylinders. The gap flow adheres to the rear face of cylinder no. 1. The shear layer that separates from the lower side of cylinder no. 2 rolls up and reattaches itself. The front stagnation points of both cylinders shift toward the center of the gap. In Figs. 5(c)–5(f), for $G/D=0.2$ –0.6, the gap flow becomes biased toward the upper cylinder and rolls up behind it. The upper and lower cylinders have narrow and wide wakes, respectively. As the gap increases, the narrower wake widens. In addition, the separated shear layers extend and the front stagnation points move gradually

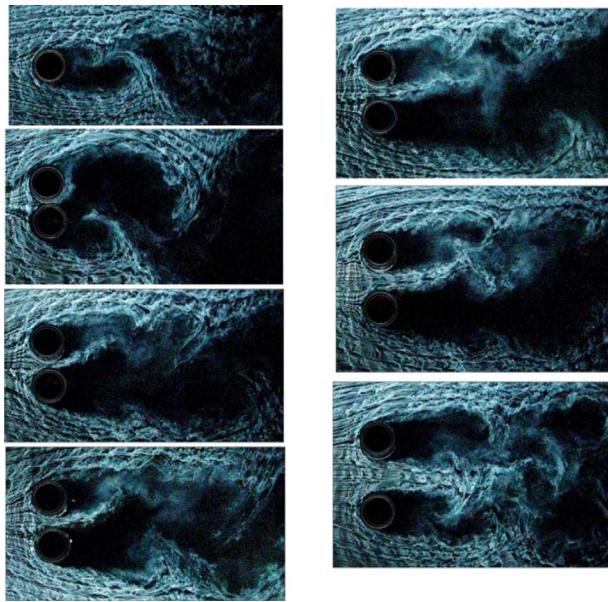


Fig. 5 Flow visualization around the two cylinders ($Re=3.1 \times 10^4$): (a) single cylinder, (b) $G/D=0.1$, (c) $G/D=0.2$, (d) $G/D=0.3$, (e) $G/D=0.4$, (f) $G/D=0.6$, and (g) $G/D=1.0$

from the direction of the center of the gap between the cylinders toward the front of the cylinders. In Fig. 5(g), for $G/D=1.0$, coupled wakes are formed and antiphase vortex shedding occurs.

3.2 Local Heat Transfer. The local Nusselt no. distributions of the two cylinders for various gap ratios are shown in Figs. 6(a)–6(g), which are the same conditions as in Fig. 5. Generally, as the gap increases, the points at which the Nusselt nos. are maximum, near the front of the cylinder, moves from the direction of the center of the gap between the cylinders to the front of the cylinders. The Nusselt no. at the rear of cylinder no. 2 is lower than that of cylinder no. 1 and that of the single cylinder. Figure 6(b) shows the distribution for $G/D=0.1$ where cylinder no. 2 has two Nusselt no. peaks at $\phi=30$ deg and 120 deg, which are, respectively, the front stagnation point and the rear reattachment point of the separated shear layer, as shown by the flow visualization photograph in Fig. 5(b). Figures 6(c)–6(f) show the distributions for $G/D=0.2$ –0.6; the Nusselt nos. near the front of both cylinders are higher than those near the rear, because different width wakes are formed behind the cylinders. Figure 6(g) shows almost the same Nusselt no. distribution as that for the single cylinder.

Figure 7 shows the variations in the average Nusselt nos. on the front face \overline{Nu}_f ($\phi=-90$ –90 deg) and rear face \overline{Nu}_r ($\phi=90$ –90 deg) as a function of the gap ratio in order to assess the influence of the gap. The Nusselt nos. at the front and rear areas of a single circular cylinder can be expressed as follows [8]:

$$\overline{Nu}_f = 0.746 Re^{0.5} \quad (3)$$

$$\overline{Nu}_r = 0.114 Re^{0.67} \quad (4)$$

$$\text{for } 10^3 \leq Re \leq 10^5$$

The front face is covered with a laminar boundary layer and the correlation between the Nusselt no. and the Reynolds no. in the laminar flow is $Nu \propto Re^{0.5}$. For the rear face in the separated region, the correlation is $Nu \propto Re^{0.67}$ [8]. Therefore, we divided \overline{Nu}_f and \overline{Nu}_r by $Re^{0.5}$ and $Re^{0.67}$, respectively. The gap ratio has little effect on \overline{Nu}_f of both cylinders but affects \overline{Nu}_r , especially for the lower cylinder. Here, \overline{Nu}_r has a minimum value at $G/D=0.3$ –0.4.

3.3 Average Heat Transfer. Figures 8(a)–8(f) show the average Nusselt no. of cylinder nos. 1 and 2, Num_1 and Num_2 , respectively, as a function of the Reynolds no. for the gap ratios. Figure 8(a) shows the average Nusselt no. for the single eddy street regime. Figures 8(b)–8(e) show the average Nusselt nos. for the bias flow regime and Fig. 8(f) shows the average Nusselt no. for the coupled wake regime. For Figs. 8(a)–8(e), the values of

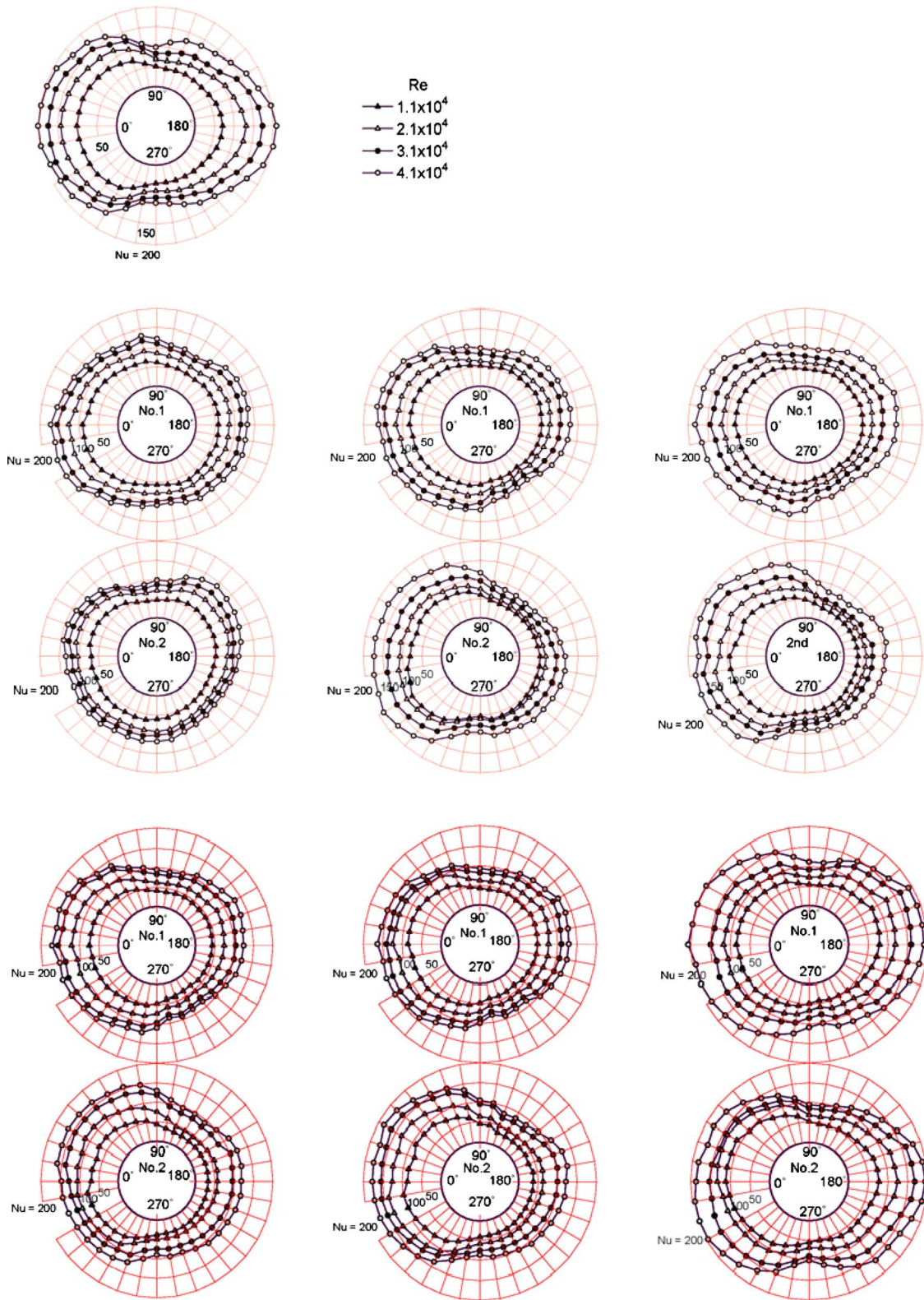


Fig. 6 Local Nusselt no. distributions: (a) single cylinder, (b) $G/D=0.1$, (c) $G/D=0.2$, (d) $G/D=0.3$, (e) $G/D=0.4$, (f) $G/D=0.6$, and (g) $G/D=1.0$

Num_1 and Num_2 are less than that of Nu for the single circular cylinder and the value of Num_1 is higher than that of Num_2 . For Fig. 8(f), the values of Num_1 and Num_2 agree well with Nu of the single cylinder and the value of Num_1 is identical to the value of Num_2 . The variation between Num_1 and Num_2 gradually de-

creases as the gap becomes larger.

The average Nusselt no. of the two cylinders $Num = \{(Num_1 + Num_2)/2\}$ is shown in Fig. 9. Num has a minimum value at $G/D=0.4$ ($Re < 1.8 \times 10^4$) and $G/D=0.3$ ($Re \geq 1.8 \times 10^4$). Figure

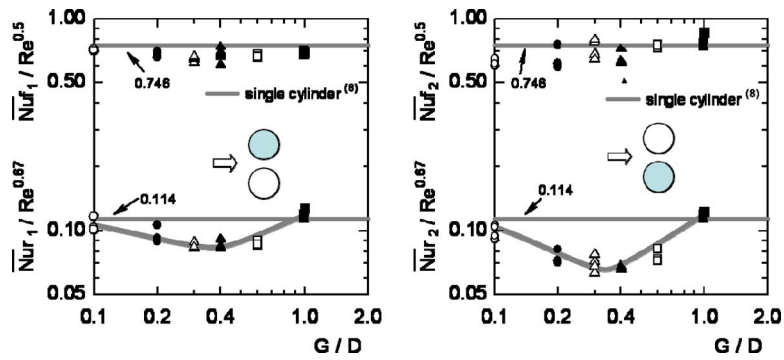


Fig. 7 Correlation among Nu_r , Nu_s , and the gap ratio: (a) cylinder no. 1 and (b) cylinder no. 2

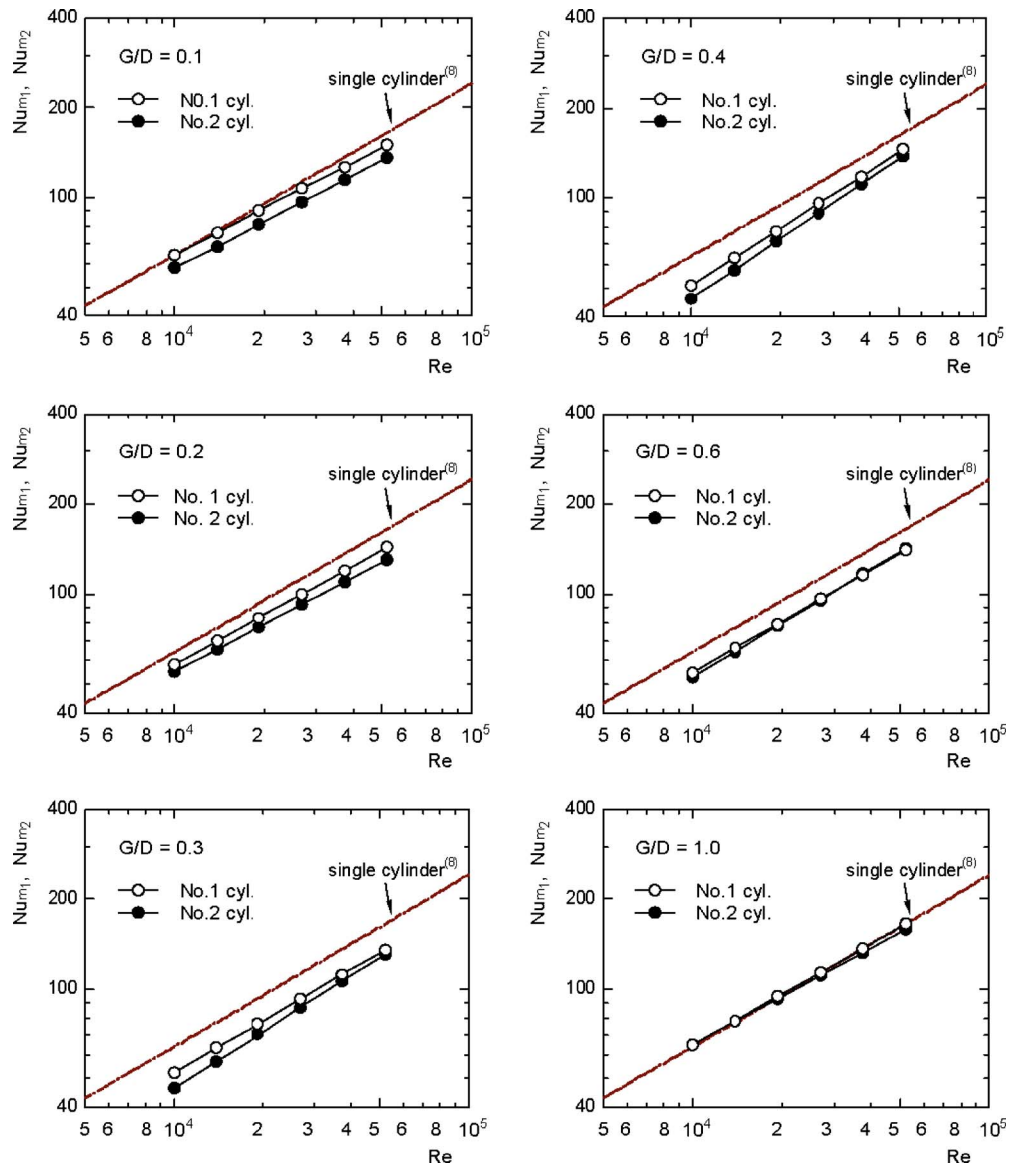


Fig. 8 Average Nusselt no. of cylinder nos. 1 and 2: (a) $G/D=0.1$, (b) $G/D=0.2$, (c) $G/D=0.3$, (d) $G/D=0.4$, (e) $G/D=0.6$, and (f) $G/D=1.0$

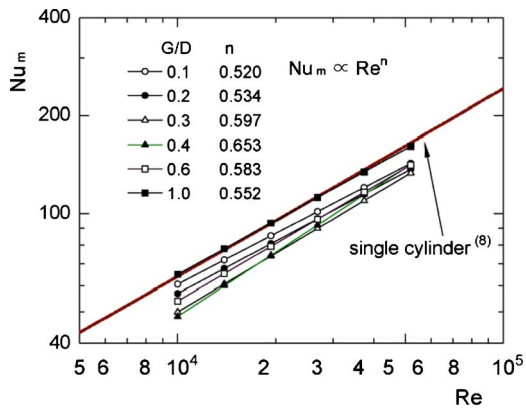


Fig. 9 Average Nusselt no. of the two cylinders

10 shows the correlation between Nu_m and the gap ratio. The gap ratio of the minimum Nu_m shifts 0.4–0.3 with increasing Reynolds no.

3.4 Pressure Field and Wake. We measured the pressure distribution around the two cylinders to determine the pressure field. The pressure coefficient distributions C_p around the cylinders for $G/D=0.3$ and $G/D=0.4$ are shown in Fig. 11. In both cases, the value of C_p on the rear face of cylinder no. 2 is lower than that of cylinder no. 1 and that of a single cylinder because cylinder nos. 1 and 2 have narrow and wide wakes, respectively. Figure 12 shows the drag coefficients C_D of the two cylinders, which are obtained by integrating the surface pressure distribution. The drag coefficients C_D of both cylinders have minimum values at $G/D=0.3$ –0.4. This indicates that the shear layers that separated from both cylinders elongated downstream and rolled up and formed vortex in the far distance from the cylinders. Therefore, the drag decreases and the Nusselt no. at the rear face also decreases.

To discuss further on the hypothesis, we measured velocity distribution behind the two cylinders. Figure 13 shows the velocity

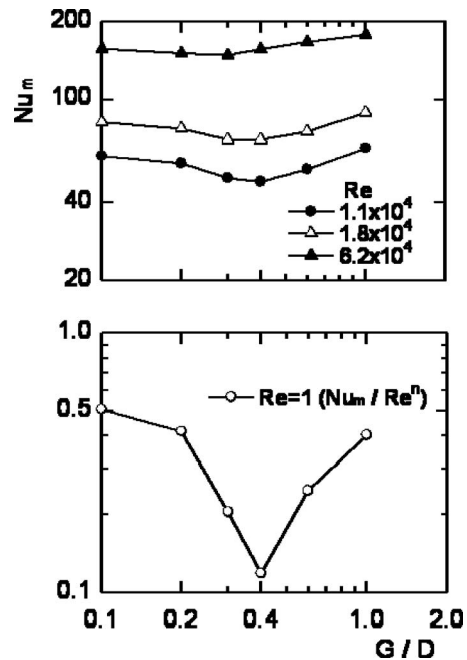


Fig. 10 Correlation between average Nu_m and the gap ratio

u/U and turbulence intensity $\Delta u/U$ behind the two cylinders where Δu is the RMS value of the fluctuating velocity. Figure 13(a) shows the distributions for $G/D=0.1$ in which a single vortex street is formed behind the cylinders. In Figs. 13(b) and 13(c), the gap flow becomes biased. The difference between Figs. 13(b) and 13(c) is shown clearly in the distributions in $x/D=3.0$. For $G/D=0.2$ in $x/D=3.0$ and $Y/D=\pm 2-3$, the velocity and turbulence intensity change suddenly. Same position for $G/D=0.3$, these change gently. In $x/D=5.0$ and 8.5, slight differences between $G/D=0.2$ and $G/D=0.3$ appeared. Sudden change in ve-

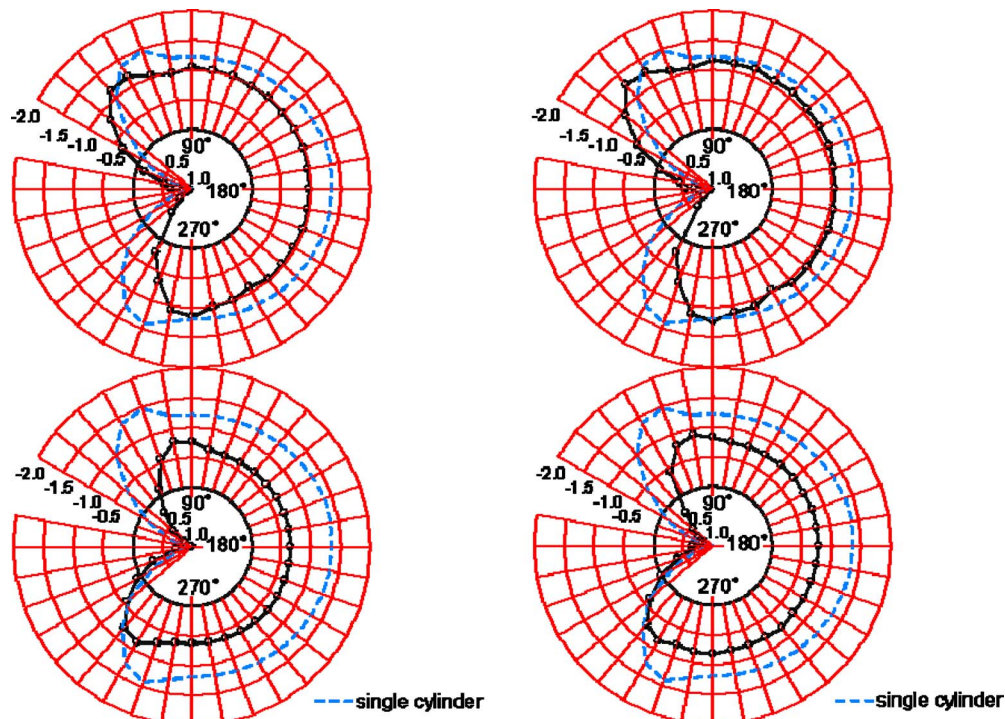


Fig. 11 Pressure coefficient distribution ($G/D=0.4$ and $Re=4.2 \times 10^4$)

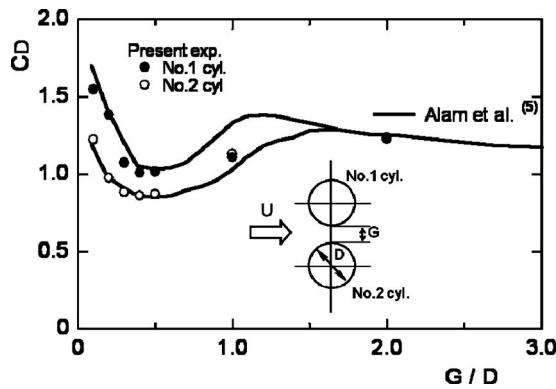


Fig. 12 Drag coefficient ($Re=4.2 \times 10^4$)

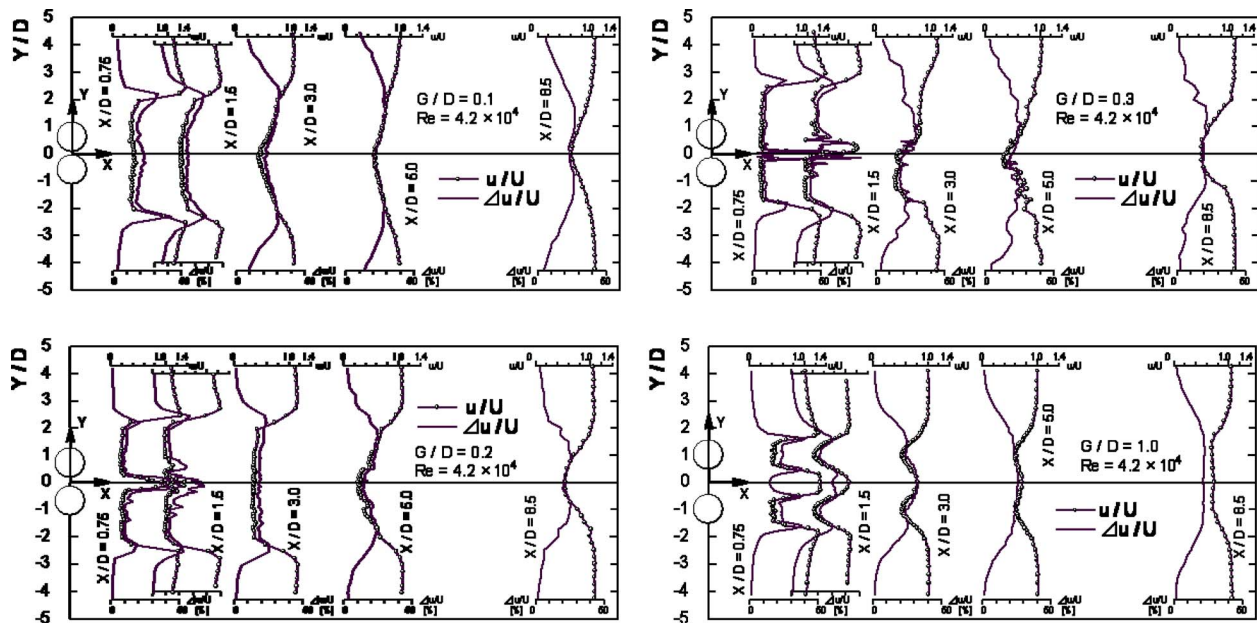


Fig. 13 Velocity and turbulence intensity distributions behind two cylinders: (a) $G/D=0.1$, (b) $G/D=0.2$, (c) $G/D=0.3$, and (d) $G/D=1.0$

locity generates a strong vorticity, therefore, the separated shear layers elongate longer and roll up weaker for $G/D=0.3$ than that for $G/D=0.2$. Figure 13(d) shows the coupled wakes for $G/D=1.0$.

4 Conclusions

Experimental studies were conducted on the heat transfer around two circular cylinders in a side-by-side arrangement using a low-speed wind tunnel. Intermittent gap flow switching was suppressed by setting the cylinders to be slightly staggered from the side-by-side arrangement.

The experimental results revealed the following. Cylinder nos. 1 and 2 have narrow and wide wakes, respectively. The gap ratio strongly affects the heat transfer at the rear face of the two cylinders. The overall Nusselt no. of the two cylinders has a minimum at $G/D=0.4$ ($Re < 1.8 \times 10^4$) and $G/D=0.3$ ($Re \geq 1.8 \times 10^4$), which is the condition for minimum drag coefficient of both cylinders. These findings indicate that the shear layers that separated from both cylinders elongated downstream and rolled up and formed vortex in the far distance from the cylinders. As a result, the drag decreased and the Nusselt no. of rear face decreased, simultaneously.

Nomenclature

- C_D = pressure drag coefficient of the circular cylinder
- C_p = pressure coefficient = $(p - p_0) / 0.5 \rho U_0^2$
- D = diameter of the circular cylinder
- f = vortex shedding frequency from the circular cylinder
- G = gap between the two circular cylinders
- h = local heat transfer coefficient
- h_m = overall heat transfer coefficient
- Nu = local Nusselt no. = hD / λ
- Nu_m = average Nusselt no. = $(Nu_1 + Nu_2) / 2$
- p and p_0 = pressure and static pressure
- St = Strouhal no. = fD / U
- Re = Reynolds no. = UD / ν
- U and u = free stream velocity and velocity
- Δu = RMS value of fluctuating velocity
- θ = angle
- ν and ρ = kinematic viscosity and density of the fluid

Subscripts

- f and r = front and rear parts of the cylinders

1 and 2 = cylinder nos. 1 and 2

References

- [1] Bearman, P. W., and Wadcock, A. J., 1973, "The Interaction Between a Pair of Circular Cylinders Normal to a Stream," *J. Fluid Mech.*, **61**, pp. 499–511.
- [2] Zdravkovich, M. M., 1977, "Review of Flow Interference Between Two Circular Cylinders in Various Arrangement," *ASME J. Fluids Eng.*, **199**, pp. 618–633.
- [3] Williamson, C. H. K., 1985, "Evolution of a Single Wake Behind a Pair of Bluff Bodies," *J. Fluid Mech.*, **159**, pp. 1–18.
- [4] Zdravkovich, M. M., 2003, *Flow Around Circular Cylinders*, Vol. 2, Oxford University Press, New York, p. 997.
- [5] Mahbub, A., Moriya, M., and Sakamoto, H., 2003, "Aerodynamic Characteristics of Two Side-by-Side Circular Cylinders and Application of Wavelet Analysis on the Switching Phenomenon," *J. Fluids Struct.*, **18**, pp. 325–346.
- [6] Alam, M. M., and Zhou, Y., 2007, "Flow Around Two Side-by-Side Closely Spaced Circular Cylinders," *J. Fluids Struct.*, **23**, pp. 799–805.
- [7] Kline, S. J., 1985, "The Purposes of Uncertainty Analysis," *ASME Trans. J. Fluids Eng.*, **107**, pp. 153–160.
- [8] Igarashi, T., and Hirata, M., 1977, "Heat Transfer in Separated Flows, Part 2: Theoretical Analysis," *Heat Transfer-Jpn. Res.*, **6**(3), pp. 60–78.

An Experimentally Validated Numerical Modeling Technique for Perforated Plate Heat Exchangers

M. J. White¹

Accelerator Division/Cryogenic Systems,
Fermi National Accelerator Laboratory,
Batavia, IL 60510

G. F. Nellis

S. A. Klein

Department of Mechanical Engineering,
University of Wisconsin-Madison,
Madison, WI 53703

W. Zhu

Y. Gianchandani

Department of Mechanical Engineering,
University of Michigan-Ann Arbor,
Ann Arbor, MI 48109

Cryogenic and high-temperature systems often require compact heat exchangers with a high resistance to axial conduction in order to control the heat transfer induced by axial temperature differences. One attractive design for such applications is a perforated plate heat exchanger that utilizes high conductivity perforated plates to provide the stream-to-stream heat transfer and low conductivity spacers to prevent axial conduction between the perforated plates. This paper presents a numerical model of a perforated plate heat exchanger that accounts for axial conduction, external parasitic heat loads, variable fluid and material properties, and conduction to and from the ends of the heat exchanger. The numerical model is validated by experimentally testing several perforated plate heat exchangers that are fabricated using microelectromechanical systems based manufacturing methods. This type of heat exchanger was investigated for potential use in a cryosurgical probe. One of these heat exchangers included perforated plates with integrated platinum resistance thermometers. These plates provided in situ measurements of the internal temperature distribution in addition to the temperature, pressure, and flow rate measured at the inlet and exit ports of the device. The platinum wires were deposited between the fluid passages on the perforated plate and are used to measure the temperature at the interface between the wall material and the flowing fluid. The experimental testing demonstrates the ability of the numerical model to accurately predict both the overall performance and the internal temperature distribution of perforated plate heat exchangers over a range of geometry and operating conditions. The parameters that were varied include the axial length, temperature range, mass flow rate, and working fluid. [DOI: 10.1115/1.4000673]

Keywords: perforated plate, heat exchanger, axial conduction, cryogenic, MEMS

1 Introduction

Perforated plate heat exchangers were invented in the 1940s by McMahan et al. [1] and are often used to provide a compact design for a recuperative heat exchanger in applications where high effectiveness is required in the presence of a large operating temperature span. A perforated plate heat exchanger is constructed of many plates that are oriented perpendicular to the flow. Two different types of plates are used in an alternating sequence. Low conductivity spacers provide a high axial resistance and the perforated plates provide a high stream-to-stream conductance to create a compact heat exchanger. The plates are hermetically sealed to prevent fluid leakage between the streams and to the external environment. Figure 1 illustrates, qualitatively, the temperature distribution expected in the fluids and the spacer/heat transfer plate material [2].

The perforated plates are composed of high conductivity material and include many small flow passages. Therefore, the stream-to-stream thermal resistance within the heat exchanger plate is low. The spacer is made of low conductivity material and the cross-sectional area available for axial conduction in each spacer is small. Therefore, the temperature gradient across each spacer is approximately linear. The fluid passing through the spacer does

not change temperature significantly because there is very little surface area for heat transfer and therefore the stream-to-stream thermal communication is poor.

Perforated plate heat exchangers have been used as the recuperative heat exchanger for cryogenic refrigerators. For example, perforated plate heat exchanger consisting of copper heat transfer plates interspersed with stainless steel spacers have been used in turbo-Brayton cryocooler for space applications [3]. Jeheon and Jeong [4] discussed a perforated plate heat exchanger fabricated from copper plates separated by Kapton spacers. Venkatarathnam and Sarangi [5] presented a review of perforated plate heat exchangers and their manufacture and application.

Modeling of perforated plate heat exchangers is often accomplished by ignoring the discrete nature of the plate-spacer structure of the heat exchanger in order to treat the plates as a series of fins. This approach ignores the impact of the discrete plates that is clearly evident in Fig. 1 as well as the effect of axial conduction. For high effectiveness applications, these effects can dominate the performance of the heat exchanger. Venkatarathnam [6] derived the closed form effectiveness-*NTU* solution for a perforated plate heat exchanger. However, the use of this solution necessarily neglects the effect of temperature-dependent properties and does not explicitly include the effect of axial conduction. Several researchers have examined the impact of axial conduction on continuous heat exchangers, for example, Refs. [7–10]. More detailed numerical models of perforated plate heat exchanger models simulate each plate-spacer pair individually and integrate these solutions using energy balances. Examples of this approach include Refs. [11–13].

¹Corresponding author.

Contributed by the Heat Transfer Division of ASME for publication in the JOURNAL OF HEAT TRANSFER. Manuscript received February 4, 2009; final manuscript received October 1, 2009; published online August 10, 2010. Assoc. Editor: Srinivas Garimella.

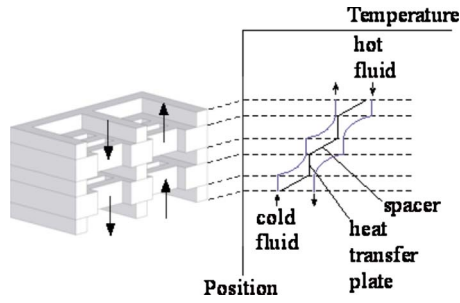


Fig. 1 Qualitative temperature distribution in a spacer/heat transfer plate unit [2]

The numerical model presented in this paper is an example of this approach. The detailed heat exchanger numerical model previously published by Nellis [8] in order to understand the impact of axial conduction and parasitic heat load is used to simulate each individual plate. The model was expanded in order to allow a specified heat transfer rate at each end. The models of individual plates are integrated via energy balances in order to develop a detailed numerical model of the entire perforated plate heat exchanger.

The model was specifically applied to a perforated plate heat exchanger with silicon heat transfer plates and borosilicate glass spacers that was manufactured using microelectromechanical systems (MEMS)-based processes. The heat exchanger was instrumented and installed in a vacuum test facility for performance testing. One advantage of MEMS-based manufacturing is that it is possible to integrate various types of sensors with the plates. Some of the tested perforated plate heat exchangers included platinum resistance thermometers (PRTs) integrated with individual plates, allowing the resolution of the internal details of the heat exchanger processes. These integrated PRTs provide the only direct and internal verification of a perforated plate heat exchanger model that the authors are aware of and clearly show interesting behavior such as the temperature-jump phenomena that is expected for heat exchangers experiencing a large amount of axial conduction. Other researchers (for example, Refs. [13,14]) have compared the overall performance (e.g., heat transfer rate or effectiveness) with model prediction but have not measured and compared the internal temperature distribution.

Section 1 describes the numerical model of a single plate. Section 2 describes the energy balances that are necessary to integrate the single-plate models and models of the spacers in order to develop a set of equations that describe the thermal behavior of the entire heat exchanger. The implementation of these equations in the iterative equation solver EES [15] is discussed. Section 5 presents the experimental measurements that are used to validate the numerical model, including in situ measurements of the temperature distribution within the heat exchanger.

2 Single-Plate Heat Exchanger Model

The model of a single heat exchanger plate is based on the numerical simulation technique developed by Nellis [8]. Figure 2 illustrates a schematic of a single plate, which experiences a flow of hot fluid on one side (entering at $T_{h,in}$ with total capacitance rate \dot{C}_h) and cold fluid on the other (entering at $T_{c,in}$ with total capacitance rate \dot{C}_c) as well as an external and parasitic heat transfer to the hot fluid (\dot{q}_h) and the cold fluid (\dot{q}_c) along the length of the plate and into either end of the plate ($\dot{q}_{w,h}$ and $\dot{q}_{w,c}$). Within any single plate, the properties of the working fluid and material are assumed to be temperature independent, but they may vary from plate to plate.

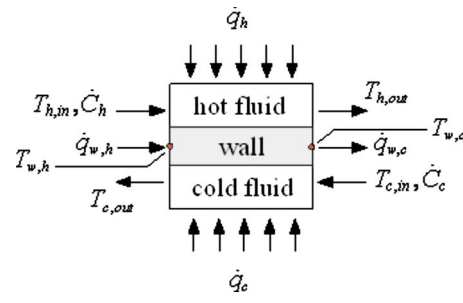


Fig. 2 Schematic of a single plate

The model is developed in dimensionless form in order to maximize its utility and modularity. The dimensionless temperatures of the hot fluid (θ_h), cold fluid (θ_c), and wall (θ_w) are defined according to

$$\theta = \frac{T - T_{c,in}}{T_{h,in} - T_{c,in}} \quad (1)$$

The axial conduction parameter λ is the dimensionless parameter that captures the relative importance of axial conduction within the plate (not across the entire heat exchanger). The axial conduction parameter is approximately equal to the ratio of the heat conducted axially to the heat conducted stream-to-stream and it is defined according to [7]

$$\lambda = \frac{1}{R_{ac} \dot{C}_{min}} \quad (2)$$

where R_{ac} is the thermal resistance to axial conduction through the plate and \dot{C}_{min} is the minimum capacitance rate. The dimensionless parasitic heat loads along the length of the plate (χ_h and χ_c) and into the ends of the plate ($\chi_{w,h}$ and $\chi_{w,c}$) are defined by normalizing against the maximum possible rate of heat transfer:

$$\chi = \frac{\dot{q}}{\dot{C}_{min}(T_{h,in} - T_{c,in})} \quad (3)$$

The dimensionless capacitance rates of the hot and cold fluid are defined as

$$\mu = \frac{\dot{C}_h}{\dot{C}_{min}} \quad (4)$$

$$\nu = \frac{\dot{C}_c}{\dot{C}_{min}} \quad (5)$$

The total number of transfer units on either side of the plate (NTU_h and NTU_c) is defined as the ratio of the conductance between the stream and the plate (UA_h and UA_c) to the minimum capacity rate (\dot{C}_{min}).

$$NTU_h = \frac{UA_h}{\dot{C}_{min}} \quad (6)$$

$$NTU_c = \frac{UA_c}{\dot{C}_{min}} \quad (7)$$

The conductance must include the convective heat transfer between the fluid and the surface as well as conduction resistance within the plate.

Each plate is modeled using a numerical model based on a finite difference technique. Figure 3 illustrates the distribution of the nodes within the plate.

The dimensionless axial distance from the hot end of the plate (Z) is defined according to

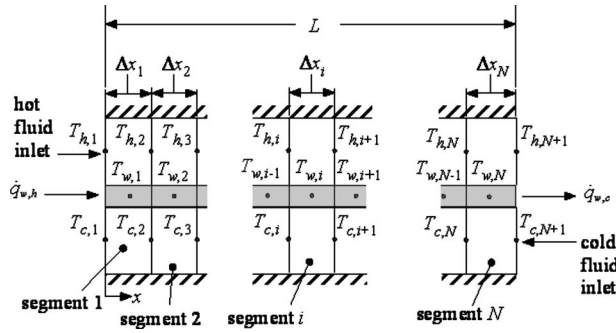


Fig. 3 Distribution of the nodes used to simulate a single plate

$$Z = \frac{x}{L} \quad (8)$$

where x is the axial distance from the hot end of the plate and L is the total thickness of the plate. The dimensionless width of an individual element is

$$\Delta Z = \frac{\Delta x}{L} \quad (9)$$

where Δx is the dimensional width of the element. The computational efficiency of the numerical model is increased by using an exponentially distributed grid of nodes in order to allow the elements to be concentrated toward the ends of the plate. The width of an individual element ΔZ_i is calculated using

$$\Delta Z_i = \frac{\exp(-\gamma(1-2i/N))}{2\sum_{i=1}^{N/2} \exp(-\gamma(1-2i/N))} \quad (10)$$

where N is the number of elements and γ is the grid concentration factor. If the grid concentration factor γ is equal to 0, then the grid is equally distributed across the length of the heat exchanger. Positive values of γ result in the elements being concentrated near the heat exchanger ends and negative values result in the elements being concentrated in the middle of the heat exchanger.

The dimensionless hot side energy balance for an arbitrary i th segment is given by

$$\mu_h \theta_{h,i-1} + \chi_h \Delta Z_i = \mu_h \theta_{h,i} + NTU_h \Delta Z_i \left(\frac{\theta_{h,i} + \theta_{h,i-1}}{2} - \theta_{w,i} \right) \quad \text{for } i = 1, \dots, N \quad (11)$$

The dimensionless cold side energy balance for an arbitrary i th segment is

$$\chi_c \Delta Z_i + \nu_c \theta_{c,i} + NTU_c \Delta Z_i \left(\theta_{w,i} - \frac{\theta_{c,i} + \theta_{c,i-1}}{2} \right) = \nu_c \theta_{c,i-1} \quad \text{for } i = 1, \dots, N \quad (12)$$

The dimensionless wall energy balance for an arbitrary i th segment is

$$\begin{aligned} & \chi_w \Delta Z_i + NTU_h \Delta Z_i \left(\frac{\theta_{h,i} + \theta_{h,i-1}}{2} - \theta_{w,i} \right) + \frac{2\lambda}{\Delta Z_i + \Delta Z_{i-1}} (\theta_{w,i-1} - \theta_{w,i}) \\ & = NTU_c \Delta Z_i \left(\theta_{w,i} - \frac{\theta_{c,i} + \theta_{c,i-1}}{2} \right) + \frac{2\lambda}{\Delta Z_i + \Delta Z_{i+1}} (\theta_{w,i} \\ & - \theta_{w,i+1}) \quad \text{for } i = 2 \dots (N-1) \end{aligned} \quad (13)$$

The wall elements at the ends of the heat exchanger must be treated separately. The energy balances on the first and last segments are

$$\begin{aligned} & \chi_w \Delta Z_1 + NTU_h \Delta Z_1 \left(\frac{\theta_{h,1} + \theta_{h,0}}{2} - \theta_{w,1} \right) + \frac{\lambda}{\Delta Z_0} (\theta_{w,0} - \theta_{w,1}) \\ & = NTU_c \Delta Z_1 \left(\theta_{w,1} - \frac{\theta_{c,1} + \theta_{c,0}}{2} \right) + \frac{2\lambda}{\Delta Z_1 + \Delta Z_2} (\theta_{w,1} - \theta_{w,2}) \end{aligned} \quad (14)$$

$$\begin{aligned} & NTU_h \Delta Z_N \left(\frac{\theta_{h,N} + \theta_{h,N-1}}{2} - \theta_{w,N} \right) + \chi_w \Delta Z_N + \frac{2\lambda}{\Delta Z_N + \Delta Z_{N-1}} (\theta_{w,N-1} \\ & - \theta_{w,N}) = NTU_c \Delta Z_N \left(\theta_{w,N} - \frac{\theta_{c,N} + \theta_{c,N-1}}{2} \right) + \frac{\lambda}{\Delta Z_{N+1}} (\theta_{w,N} \\ & - \theta_{w,N+1}) \end{aligned} \quad (15)$$

Four boundary conditions are required to complete the set of algebraic equations. Two boundary conditions are defined by the fluid inlet temperatures:

$$\theta_{h,i=0} = 1 \quad (16)$$

$$\theta_{c,i=N} = 0 \quad (17)$$

The wall end conduction boundary equations are

$$\theta_{w,i=0} = \frac{\chi_{w,h} \Delta Z_0}{\lambda} + \theta_{w,i=1} \quad (18)$$

$$\theta_{w,i=N} = \frac{\chi_{w,c} \Delta Z_{N+1}}{\lambda} + \theta_{w,i=N+1} \quad (19)$$

The numerical model is implemented as a subprogram in EES [15]. The subprogram requires the dimensionless characteristics of the plate and inlet conditions; it returns the dimensionless outlet fluid temperatures ($\theta_{h,out}$ and $\theta_{c,out}$) as well as the dimensionless temperature of the wall material at the hot and cold ends ($\theta_{w,h}$ and $\theta_{w,c}$). These values can be used to compute the outlet fluid temperatures ($T_{h,out}$ and $T_{c,out}$) and hot and cold end wall temperatures ($T_{w,h}$ and $T_{w,c}$).

3 Integration of the Single-Plate Heat Exchanger Models

The perforated plate heat exchanger is modeled as a series of constant property heat exchangers (one per plate) using the single-plate heat exchanger model described in Sec. 2. The plates and spacers are integrated, as shown in Fig. 4.

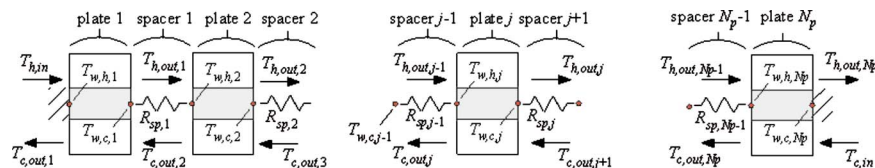


Fig. 4 Integration of plates and spacers in order to simulate a perforated plate heat exchanger

The thermodynamic and transport properties of the fluid and material are evaluated using the temperatures and pressures at the axial midpoint of each perforated plate. The numerical model described with an exponentially distributed grid (the concentration factor is set to $\gamma=1.5$) provides the temperature distribution within each plate and the outlet temperatures. This approach of separately simulating each plate using a detailed numerical model allows for accurate estimates of the temperature distribution with modest computational effort.

The surface area of the spacers is so small (28 mm² versus 430 mm²) and the thermal conductivity is so small relative to the perforated plates (less than 1.3 W/m K for glass versus greater than 150 W/m K for silicon) that the stream-to-stream heat transfer in the spacers can be neglected. This is a conservative assumption as any small additional heat transfer that occurs between the plates will improve the heat exchanger performance. However, the quantity of heat that is conducted axially through each spacer into the adjacent heat exchanger plate cannot be neglected. Figure 4 shows the numbering system used to integrate the plate and spacer models.

The plate and spacer models are integrated as follows. For an arbitrary plate j , the hot fluid inlet temperature is taken to be the hot fluid outlet temperature of plate $j-1$ (i.e., no energy transfer occurs as the fluid passes through the spacer). Similarly, the cold fluid inlet temperature is taken to be the cold fluid outlet temperature of plate $j+1$. The hot fluid inlet temperature for the first plate (plate 1) is the temperature of the hot fluid entering the device. The cold fluid inlet temperature for the last plate (plate N_p) is the temperature of the cold fluid entering the device. The ends of the perforated plate heat exchanger are assumed to be insulated. Therefore, $\dot{q}_{w,h,1}$ and \dot{q}_{w,c,N_p} are both zero. The rates of heat transfer into the ends of each plate are related to the end temperatures according to the resistance of the spacers:

$$\dot{q}_{w,c,j} = \dot{q}_{w,h,j+1} = \frac{(T_{w,c,j} - T_{w,h,j+1})}{R_{sp,j}} \quad \text{for } j = 1, \dots, N_p \quad (20)$$

where R_{sp} is the thermal resistance of the spacer, also computed at the average temperature of the spacer.

The calculation of the plate conductance and plate and spacer thermal resistances as well as the parasitic heat loads all depend on the specific geometry and materials used to construct the perforated plate heat exchanger and the fluid properties. In general, user-specific functions must be written in order to account for the geometry, materials, and working fluids for the particular heat exchanger being studied. Further details about the numerical model as well as a discussion of the specific calculations used to model the experimental perforated plate heat exchanger that is presented in this paper are presented in Ref. [16].

The solution to the set of implicit nonlinear equations required to simulate the perforated plate heat exchanger is facilitated by the use of the iterative equation solver EES [15] and a set of reasonable initial guess values. Because of the nonlinear character of the equations related to the temperature-dependent properties, the model has a low probability of convergence unless a systematic approach is used to provide reasonable guess values for the iteration process. The following guidelines are used to develop a set of guess values that will allow the equation solver to reliably converge on a solution.

A linear temperature distribution is assumed and used as guess values for the wall and fluid streams and a constant fluid pressure is assumed for each stream. In addition, all thermophysical properties should initially be set by the user to constant values consistent with the average value of these quantities. If parasitic heat loads exist, they should initially be set to zero. If a small number of plates are chosen, the model should converge on a solution very quickly in this limit. The number of plates (N_p) should be gradually increased (after the guess values are updated) until the desired number of plates is reached. The number of segments used to simulate each perforated plate (N) should be kept low (between 4

and 8) during this step in order to reduce computational time. The results from the previous solution should always be used as the guess values for the next solution in order to optimize convergence time and reliability. The next step is to adjust the number of segments used to simulate each perforated plate. The number of segments required is dependent on the accuracy required and the temperature differences (stream-to-stream and axial). As a general rule, the number of nodes should be increased until the stream outlet temperatures remain constant to within a desired accuracy. The user-specific material and fluid property functions with the largest impact on the temperature distribution and the most variability across the entire heat exchanger should be included into the numerical model first, after updating guess values based on the constant property solution. In refrigeration applications, the working fluid is generally at or near the liquefaction temperature near the cold end of the heat exchanger and therefore the fluid properties are often more important and more temperature dependent than the material properties. Usually, it is best to activate temperature-dependent fluid heat capacity first, followed by the axial and stream-to-stream thermal resistances and then the pressure drop, and parasitic heat load calculations.

These guidelines were found to be useful in the process of modeling the cryogenic heat exchanger discussed in Sec. 4. Different applications may require a re-ordering of the sequence in which variables are switched from constant to temperature dependent. In addition, some applications may allow some of the above steps to be performed in parallel, while other applications may require the activation of temperature-dependent properties one stream at a time.

The effectiveness of the heat exchanger is the primary output of the model as is defined as the ratio of the actual rate of heat transfer to the maximum possible rate of heat transfer. Due to the presence of parasitic heat transfer, the effectiveness may be defined using either the rate of heat transfer from the hot fluid or to the cold fluid:

$$\varepsilon_h = \frac{\dot{m}_h(i_{h,T=h,in} - i_{h,T=h,out})}{\dot{q}_{max}} \quad (21)$$

$$\varepsilon_c = \frac{\dot{m}_c(i_{c,T=c,out} - i_{c,T=c,in})}{\dot{q}_{max}} \quad (22)$$

where i is the mass specific enthalpy, \dot{m} is the mass flow rate, and \dot{q}_{max} is the maximum possible rate of heat transfer. The maximum possible rate of heat transfer is defined as the minimum of the rate of heat transfer required to bring the hot fluid to the cold fluid inlet temperature and the rate of heat transfer required bring the cold fluid to the hot fluid inlet temperature:

$$\dot{q}_{max} = \min[\dot{m}_c(i_{c,T=h,out} - i_{c,T=c,in}), \dot{m}_h(i_{h,T=h,in} - i_{h,T=c,in})] \quad (23)$$

4 Experimental Validation

An experimental test facility was constructed with commercially calibrated PRTs in order to measure the performance of small perforated plate heat exchangers for cryogenic applications. A schematic of the facility is shown in Fig. 5.

The warm inlet temperature to the heat exchanger was maintained near room temperature (295 K) and the cold inlet temperature to the heat exchanger was controlled by the use of a cryocooler and heater. The heat exchanger was tested inside a large vacuum insulated container with multilayer insulation (MLI) so that parasitic heat loads could be minimized. The hot side inlet pressure was kept at approximately 2 bar absolute or lower and the cold side outlet pressure was kept slightly above 1 bar absolute. The numerical model results showed a low sensitivity to

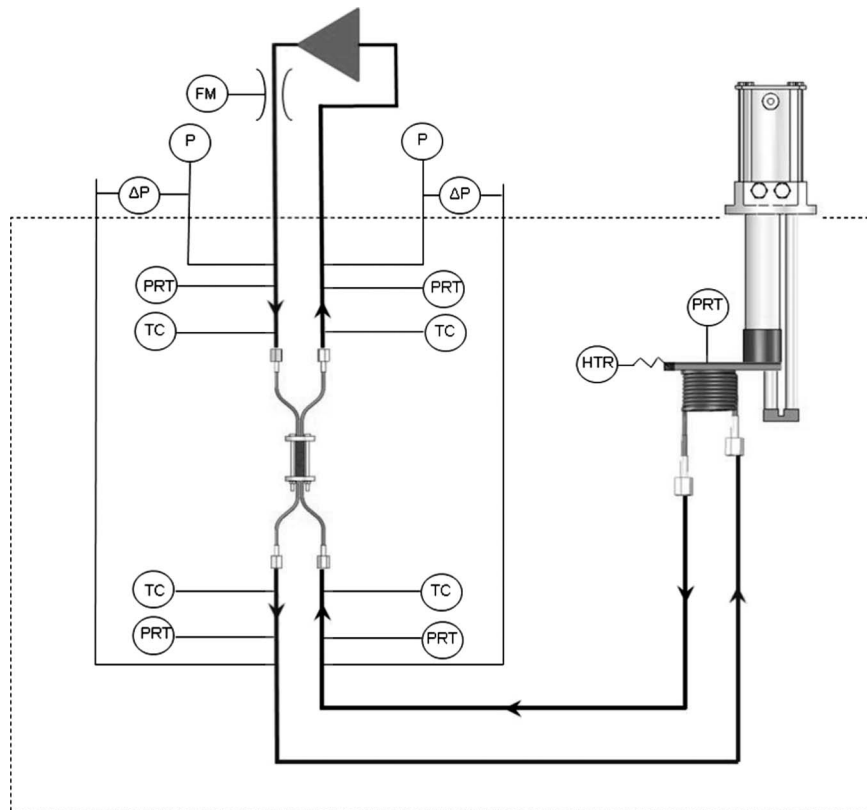


Fig. 5 Simplified flow schematic of the cryogenic test facility used for testing the MEMS heat exchangers. The temperature at each port was measured using a platinum resistor (PRT) and a type E thermocouple (TC). The absolute pressure (P) was measured at the warm end ports of the heat exchanger and the differential pressure drop (ΔP) was measured on each side of the heat exchanger. A heater (HTR) was used to control the cryocooler temperature and a flow meter (FM) was used to measure the mass flow rate.

pressure drop. Further information on the calculated and experimental pressure profiles, which are unique for each heat exchanger, can be found in Ref. [16].

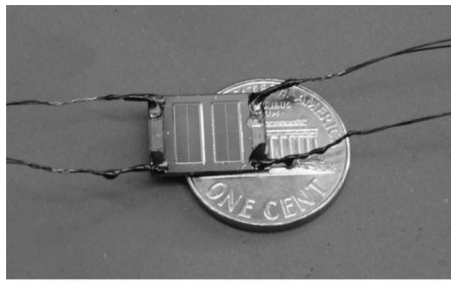
The heat exchangers that were tested were designed for a cryosurgical application. The objective was to create a lightweight and compact heat exchanger that could be installed in the part of a cryoprobe that is held in a surgeon's hand. The perforated plates were fabricated from silicon, which has a high thermal conductivity (similar to that of copper). The spacers were fabricated from borosilicate glass, which has a low thermal conductivity (less than that of stainless steel). Silicon and borosilicate glass were selected not only because of their desirable material properties but also because they are nonmagnetic (and therefore MRI compatible) and can be manufactured using existing MEMS equipment and procedures. A MRI compatible cryoprobe has the potential to provide the surgeon with real-time feedback related to the size and shape of the frozen tissue, which will allow complete ablation of the malignant tissue to be verified. Utilizing MEMS-fabrication technology may allow the use of many, small-scale, highly engineered flow passages in the heat exchanger plate.

The silicon and borosilicate glass were anodically bonded at the wafer level and diced in order to form "dies," which consist of one perforated plate and one glass spacer. The outer dimensions of the die are $10 \times 10 \text{ mm}^2$. For each stream there are two columns of 74 flow passages installed in the perforated plate. The flow passages each have a cross section of $1.4 \times 0.05 \text{ mm}^2$ and the thickness of the silicon plate is 0.5 mm. The glass spacers had a thickness of 0.3 mm. The dies were stacked and bonded using a common cryogenic epoxy. Stainless steel headers are attached

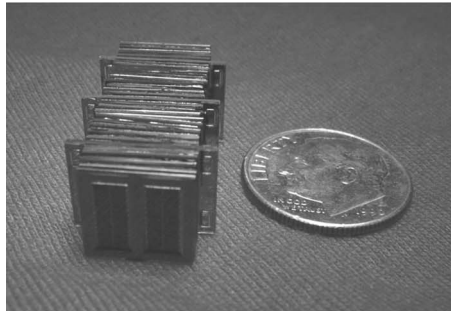
with epoxy to the heat exchanger stack in order to provide the interface between the heat exchanger and the experimental test facility.

One of the prototype heat exchangers contained perforated plates with platinum wires deposited on the surface to provide integrated temperature sensors [17]. The platinum wires were deposited on the fin material that was between the micromachined ducts. Because of the low contact resistance between the PRT and the wall, the temperature measured by the PRTs is biased toward the duct wall temperature rather than the actual fluid temperature. Thus the hot side integrated PRT measurements will be biased slightly lower and the cold side PRT measurements will be biased slightly higher than the actual fluid temperature. Figure 6(a) illustrates a single die with an integrated PRT with measurement leads. Figure 6(b) illustrates a perforated plate heat exchanger composed of several plate/spacer dies. Figure 6(c) illustrates the perforated plate heat exchanger integrated with headers. More information regarding the design and fabrication of the heat exchanger and the experimental test facility can be found in the literature [16,18–21].

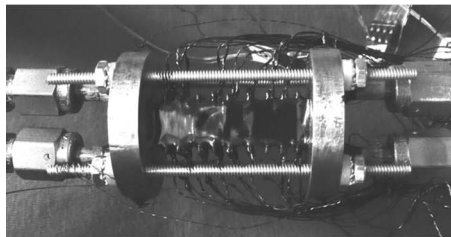
The first prototype heat exchanger that was tested consisted of 16 dies and contained no integrated PRTs. The heat exchanger was tested using helium gas over a range of mass flow rate. The warm inlet temperature was maintained between 299 K and 301 K, while the cold inlet temperature was maintained between 196 K and 207 K. All heat exchanger inlet and outlet temperatures were measured using commercially calibrated PRTs with a rated absolute uncertainty of $\pm 0.25 \text{ K}$. Figure 7 illustrates the measured effectiveness based on the hot and cold streams as well as the



(a)



(b)



(c)

Fig. 6 (a) Single die with integrated PRT, (b) perforated plate heat exchanger, and (c) perforated plate heat exchanger integrated with headers

predicted values of these quantities as a function of mass flow rate. The details related to the calculation of the experimental uncertainty can be found in Ref. [16].

The numerical model predictions are within the experimental uncertainty over the entire range of flow rates measured. The numerical model was always solved starting with two elements for each plate. The number of elements per plate was increased by

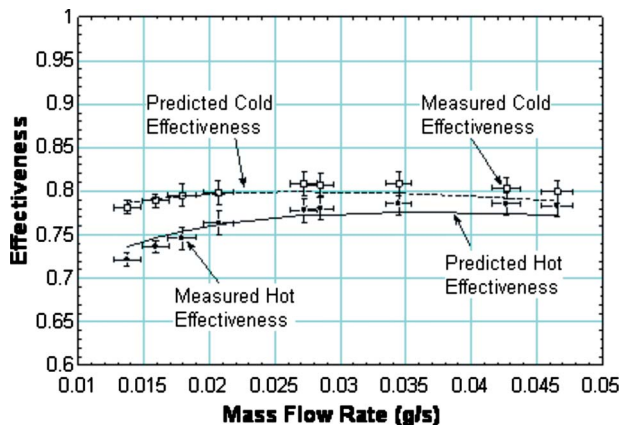


Fig. 7 Measured and predicted effectiveness based on the hot and cold streams as a function of the mass flow rate for the 16 die heat exchanger tested with helium

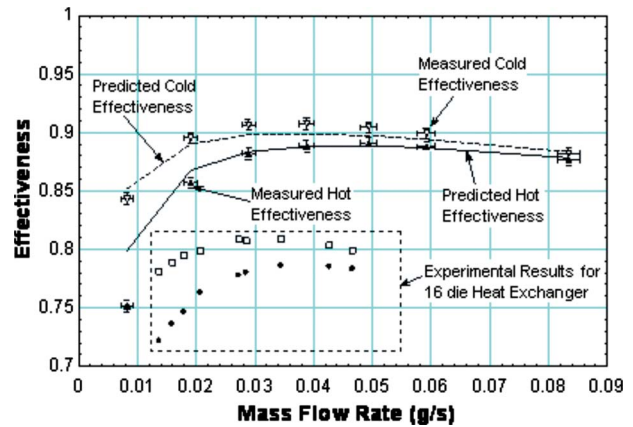


Fig. 8 Measured and predicted effectiveness based on the hot and cold streams as a function of the mass flow rate for the 43 die heat exchanger tested with helium. Also shown are the test results for the 16 die heat exchanger, shown in Fig. 7.

two until two consecutive solutions had outlet temperatures identical to within ± 0.01 K, which generally was eight elements per plate for the plots shown in this paper.

A similar test was performed on a heat exchanger that consists of 43 dies and these results are shown in Fig. 8. The warm inlet temperature was maintained between 295 K and 303 K and the cold inlet temperature was maintained between 237 K and 252 K for these tests. The predicted effectiveness lies slightly out of the range of experimental uncertainty range for a few data points but is within the experimental uncertainty for the majority of the points. Also overlaid onto Fig. 8 are the 16 die effectiveness test results from Fig. 7. The 43 die heat exchanger exhibited a significantly higher effectiveness over the entire range of flow rates tested. This is expected as the 43 die heat exchanger has both a significantly larger stream-to-stream heat transfer area as well as increased resistance to axial heat transfer.

As shown in Figs. 7 and 8, the numerical model predicted effectiveness was within the experimentally measured effectiveness uncertainty range for almost all of the data points. The data obtained at the lowest flow rates disagree with the model predictions. At low flow rates, the effectiveness is very sensitive to parasitic heat loads due to the low capacity rates of the two fluid streams. The model is in good agreement with the experimental data when the heat exchanger is being operated at design conditions (i.e., peak effectiveness).

The 43 die heat exchanger contains 5 dies with at least one functional integrated PRT (note that some plates were capable of measuring the temperature on only one fluid). Prior to testing but after assembly, the integrated PRTs were calibrated against commercially calibrated PRTs that were installed in the heat exchanger headers at each fluid inlet and outlet. The estimated uncertainty of the integrated PRTs is ± 1.0 K [16]. The integrated PRTs provide a measurement of the temperature distribution associated with each test point. The measured temperature distribution (the hot and cold fluid temperatures as a function of axial position, expressed in terms of the plate number) associated with the lowest mass flow rate data point in Fig. 8 is shown in Fig. 9. Also shown in Fig. 9 are the hot and cold temperatures predicted by the numerical model for the same inlet conditions.

The measured heat exchanger temperature distribution for the highest mass flow rate data point shown in Fig. 8 is presented in Fig. 10. Also presented in Fig. 10 is the temperature distribution predicted by the numerical model for the same inlet conditions.

The fidelity of the model was verified by carrying out an additional set of tests using ethane as the working fluid with the 43 die heat exchanger. The measured and predicted effectiveness based on the hot and cold fluids is shown in Fig. 11 as a function of mass flow rate. The warm inlet temperature was maintained be-

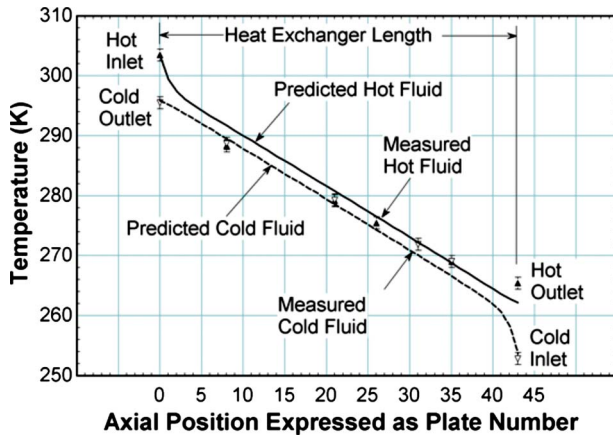


Fig. 9 Measured and predicted hot and cold fluid temperatures as a function of position (expressed in terms of plate number) for the lowest mass flow rate data point taken with helium, shown in Fig. 8

tween 295 K and 298 K while the cold inlet temperature was maintained between 242 K and 255 K. The numerical model slightly overpredicts the effectiveness but does correctly predict the mass flow rate at which the peak effectiveness is observed.

The temperature distributions for the lowest and highest ethane mass flow rate data points test are presented in Figs. 12 and 13,

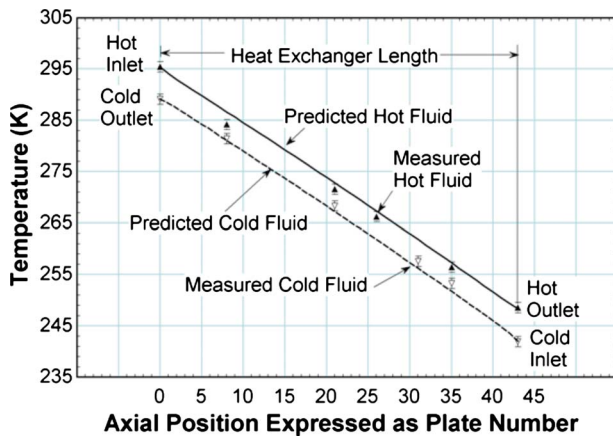


Fig. 10 Measured and predicted hot and cold fluid temperatures as a function of position (expressed in terms of plate number) for the highest mass flow rate data point taken with helium, shown in Fig. 8

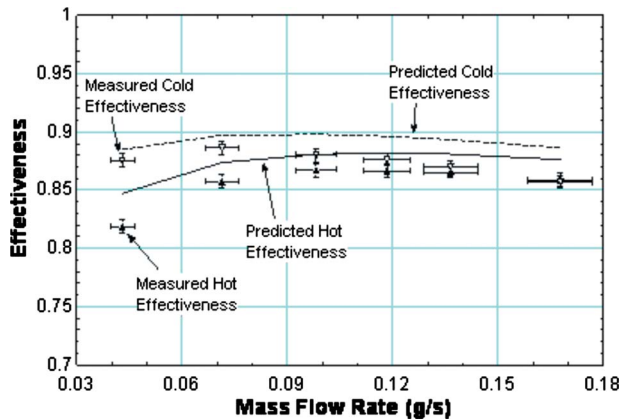


Fig. 11 Measured and predicted effectiveness based on the hot and cold streams as a function of the mass flow rate for the 43 die heat exchanger tested with ethane

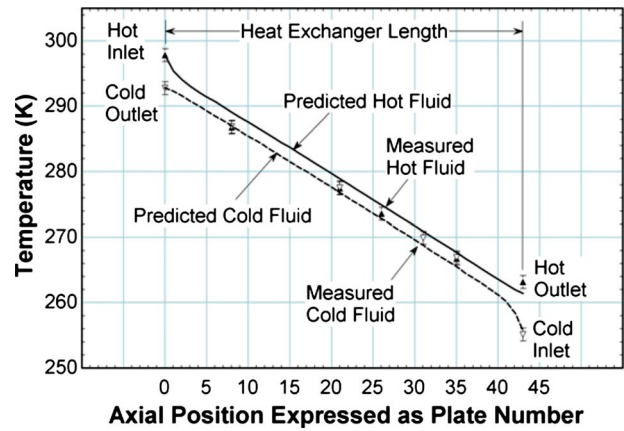


Fig. 12 Measured and predicted hot and cold fluid temperatures as a function of position (expressed in terms of plate number) for the lowest mass flow rate data point taken with ethane, shown in Fig. 11

respectively. The temperature distribution measured using ethane exhibits the same behaviors observed using helium and discussed previously.

Examining Figs. 7–13 shows that the perforated plate heat exchanger model presented in this paper is in good agreement with the experimental data. This agreement is not only evident in the overall performance but also in the predicted and measured temperature distribution within the heat exchanger.

Axial conduction is the dominant effectiveness penalty at low mass flow rate operating conditions (i.e., high NTU and high λ conditions) and causes “temperature jumps” at the inlets to the heat exchanger [2]. This behavior is predicted by analytical and numerical models and causes the wall temperature at the ends of the heat exchanger to be strongly biased toward the outlet stream temperature. The stream-to-stream temperature difference is small (because the NTU is large) and the only thing preventing the heat exchanger from achieving an effectiveness near unity is the presence of the sharp temperature “jumps” at either end of the device. This behavior is shown clearly in Figs. 9 and 12 for the smallest helium and ethane mass flow rates, respectively.

When the mass flow rate is high, the dominant effectiveness penalty is related to the thermal resistance to heat transfer between the streams. This is consistent with a low NTU , low λ operating condition. The temperature difference between the streams becomes large and the temperature “jumps” at either end of the heat

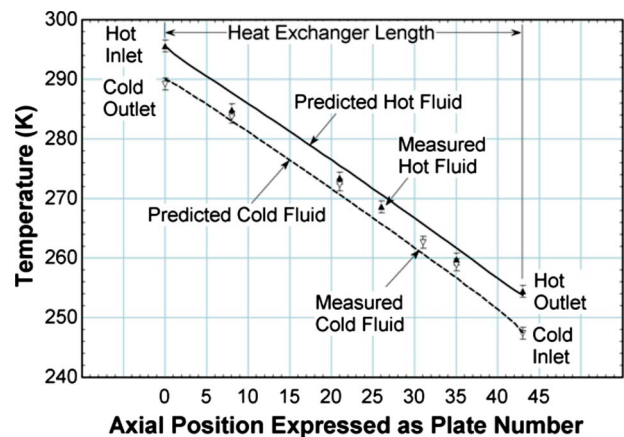


Fig. 13 Measured and predicted hot and cold fluid temperatures as a function of position (expressed in terms of plate number) for the highest mass flow rate data point taken with ethane, shown in Fig. 11

exchanger disappear. This behavior is shown clearly in Figs. 10 and 13 for the largest helium and ethane mass flow rates, respectively.

The effectiveness measurements shown in Figs. 8 and 11 also show the behavior expected for a heat exchanger experiencing an externally applied parasitic heat transfer. The parasitic heat transfer causes the heat transfer rate from the hot stream to be different than the heat transfer rate to the cold stream. In refrigeration applications, the parasitic heat transfer resulted in additional heating of the cold stream and reduced cooling of the hot stream. The parasitic heat loads associated with this experimental setup, radiation and conduction from the vacuum vessel, are strongly dependent on the cold end temperature of the heat exchanger but are almost completely independent of the mass flow rate through the heat exchanger. Thus the difference between the effectiveness associated with the hot and cold fluids is high when mass flow rate is small but becomes small as the mass flow rate increases.

Comparing the experimental and numerical model results for the two working fluids shows a trend. The helium results match each other within experimental uncertainty in almost all cases but the ethane experimental results are consistently slightly lower than the model results. The cause of this discrepancy is not understood.

5 Conclusion

A numerical modeling technique for perforated plate heat exchangers was presented. This numerical model allows each perforated plate to be modeled in detail but retains computational efficiency by using nodes that are exponentially concentrated near the edges of each perforated plate. The individual plate and spacer models are integrated using energy balances and solved using a commercial equation solving program. The numerical model was applied to a specific perforated plate/spacer geometry that was fabricated from silicon heat exchanger plates and glass spacers. The model predictions were validated against experimental measurements in a cryogenic, vacuum insulated test facility using two different working fluids. Although the numerical model was experimentally validated using only cryogenic temperature gases, the same approach could be used to model heat exchangers operating at higher temperatures or with liquids as the working fluid provided that suitable thermophysical property data and flow correlations are available.

Several of the perforated plates within the heat exchanger included integrated platinum resistance temperature detectors and therefore it was possible to resolve the internal temperature distribution. The numerical model predictions were in good agreement with both the measured effectiveness based on the heat transfer to either stream as well as the temperature distribution measured within the heat exchanger.

Acknowledgment

This work was funded through the University of Michigan by a grant from the National Institute of Health, Grant No. NIH/NINBS R33 EB003349-05.

Nomenclature

\dot{C}	= fluid capacitance rate
Δx	= dimensional element width
ΔZ	= dimensionless element width
i	= fluid enthalpy
L	= axial length
\dot{m}	= mass flow rate
N	= number of elements
NTU	= number of transfer units
\dot{q}	= heat transfer rate
R	= thermal resistance
T	= temperature
UA	= stream-to-stream conductance
x	= axial distance

Z = dimensionless axial distance

Greek Symbols

χ	= dimensionless heat load
ε	= heat exchanger effectiveness
γ	= grid concentration factor
λ	= axial conduction parameter
μ	= dimensionless hot stream capacitance rate
ν	= dimensionless cold stream capacitance rate
θ	= dimensionless temperature

Subscripts

ac	= axial conduction
c	= cold stream
h	= hot stream
i	= element number
in	= inlet
J	= plate number
max	= maximum
min	= minimum
p	= plate
sp	= spacer
out	= outlet
w	= wall

References

- [1] McMahon, H. O., Bowen, R. J., and Bleyle, G. A., 1950, "A Perforated Plate Heat Exchanger," *Trans. ASME*, **72**, pp. 623–632.
- [2] Nellis, G. F., and Klein, S. A., 2009, *Heat Transfer*, Cambridge University Press, New York.
- [3] Swift, W. L., Zagarola, M. V., Nellis, G. F., McCormick, J. A., Sixsmith, H., and Gibbon, J. A., 1999, "Development of Turbo-Brayton technology for Low Temperature Applications," *Cryogenics*, **39**, pp. 989–995.
- [4] Jeheon, J., and Jeong, S., 2007, "Cryogenic Heat Exchanger With Photo-Etched Mini-Perforated Plates Allowing Flow By-Pass," *Proceedings of the ASME/JSME Summer Heat Transfer Conference*, pp. 503–508.
- [5] Venkatarathnam, G., and Sarangi, G., 1990, "Matrix Heat Exchangers and Their Application in Cryogenic Systems," *Cryogenics*, **30**, pp. 907–918.
- [6] Venkatarathnam, G., 1996, "Effectiveness-NTU Relationship in Perforated Plate Heat Exchangers," *Cryogenics*, **36**, pp. 235–241.
- [7] Kroeger, P. G., 1967, "Performance Degradation in High Effectiveness Heat Exchanger Due to Axial Conduction Effects," *Advances in Cryogenic Engineering*, Vol. 31, R. W. Fast, ed., Plenum, New York, pp. 363–372.
- [8] Nellis, G. F., 2003, "A Heat Exchanger Model That Includes Axial Conduction, Parasitic Heat Loads, and Property Variations," *Cryogenics*, **43**, pp. 523–538.
- [9] Barron, R. F., 1984, "Effect of Heat Transfer From Ambient on Cryogenic Heat Exchanger Performance," *Adv. Cryog. Eng.*, **29**, pp. 265–272.
- [10] Chowdhury, K., and Sarangi, S., 1984, "Performance of Cryogenic Heat Exchangers With Heat Leak From the Surroundings," *Adv. Cryog. Eng.*, **29**, pp. 273–280.
- [11] Sarangi, S., and Barclay, J. A., 1984, "An Analysis of Compact Heat Exchanger Performance," *Cryogenic Process Equipment*, ASME, New York, pp. 37–44.
- [12] Venkatarathnam, G., and Sarangi, G., 1991, "Analysis of Matrix Heat Exchanger Performance," *ASME J. Heat Transfer*, **113**, pp. 830–837.
- [13] Ahuja, V., and Green, R., 1998, "Application of Matrix Heat Exchangers to Thermomechanical Exergy Recovery From Liquid Hydrogen," *Cryogenics*, **38**(9), pp. 857–867.
- [14] Hoch, D. W., Nellis, G. F., Meagher, N. L., Maddocks, J. R., and Stephens, S., 2007, "Development and Testing of a Multi-Plate Recuperative Heat Exchanger for Use in a Hybrid Cryocooler," *Cryocoolers*, Vol. 14, S. D. Miller and R. G. Ross, Jr., eds., ICC Press, Annapolis, MA, pp. 515–524.
- [15] Klein, S. A., 2008, *Engineering Equation Solver (EES)*, www.fchart.com, Version 8.120.
- [16] White, M. J., 2008, "Performance of a MEMS Heat Exchanger for a Cryosurgical Probe," MS thesis, University of Wisconsin-Madison, Madison, WI.
- [17] Zhu, W., White, M. J., Nellis, G. F., Klein, S. A., and Gianchandani, Y. B., 2010, "A Si/Glass Bulk Micromachined Cryogenic Heat Exchanger for High Heat Loads: Fabrication, Test, and Application Results," *J. Microelectromech. Syst.*, **19**(1), pp. 38–47.
- [18] White, M. J., Zhu, W., Nellis, G. F., Klein, S. A., and Gianchandani, Y. B., 2008, "Performance of a MEMS Heat Exchanger for a Cryosurgical Probe," *Cryocoolers 15*, ICC Press, Long Beach, CA.
- [19] Zhu, W., White, M. J., Hoch, D. W., Nellis, G. F., Klein, S. A., and Gianchandani, Y. B., 2007, "Two Approaches to Micromachining Si Heat Exchangers for Joule-Thomson Cryosurgical Probes," *Proceedings of the IEEE MEMS*, Kobe, Japan, pp. 317–320.

[20] Zhu, W., White, M. J., Hoch, D. W., Nellis, G. F., Klein, S. A., and Gianchandani, Y. B., 2008, "A Perforated Plated Stacked Si/Glass Heat Exchanger With In-Situ Temperature Sensing for Joule-Thomson Coolers," *Proceedings of the IEEE MEMS*, Tuscon, AZ, pp. 844–847.

[21] Hoch, D. W., Zhu, W., Nellis, G. F., Schuetter, S. D., Klein, S. A., and Gianchandani, Y. B., 2006, "Progress Towards a Micromachined Heat Exchanger for a Cryosurgical Probe," *Cryocoolers 14*, ICC Press, Annapolis, MD, pp. 505–514.

Second Law Analysis of Heat Exchangers

Ahmad Fakhri

Professor
Fellow ASME
Bradley University,
Peoria, IL 61625
e-mail: ahmad@bradley.edu

This paper further explores the topic of an ideal heat exchanger, which is still an open question. It is shown that the minimization of entropy production or exergy destruction should not be an objective in heat exchanger design. It is further proven that heat exchanger effectiveness does not correlate with irreversibility. A new performance measure, entropy flux, is introduced and a general expression for its evaluation is presented. It is shown that entropy flux captures many desirable attributes of heat exchangers. For a given effectiveness, a single stream heat exchanger has the absolute maximum entropy flux, and for capacity ratios greater than zero, counterflow has the highest entropy flux, parallel flow the lowest, and the shell and tube heat exchangers are somewhere in between. [DOI: 10.1115/1.4002097]

Keywords: heat exchangers, efficiency, heat exchanger efficiency, entropy minimization, exergy, exergy maximization

1 Introduction

The concept of efficiency is used to assess the performance of components and systems. Efficiency is a comparison between the actual (real) and ideal (best) performances. The ideal behavior is generally known from modeling and the limitations dictated by physical laws, particularly, the second law of thermodynamics. Knowing the efficiency and the ideal performance, the actual performance can be determined. Efficiency provides a clear and intuitive measure of a system's performance by showing how close an actual system comes to the best that it can be and if further improvements are feasible and justified. The definition of an ideal heat exchanger is still an open question, as no general definition exists to characterize what constitutes an ideal heat exchanger. This paper attempts to clarify some of the confusion surrounding this issue and proposes a new approach that may help in clarification of this question.

The second law of thermodynamics leads to the inequality of Clausius

$$\oint \frac{\delta q}{T} \leq 0 \quad (1)$$

stating that the most efficient cycles are the reversible ones in which the integral is zero, or the net rate of entropy production around the cycle is zero. Since the ideal cycles produce no entropy, ideal processes are generally assumed to also operate reversibly, producing no entropy. This makes the isentropic process the ideal process for many components and is used to define the component efficiency based on the second law.

Despite much effort, the application of second law to the actual heat transfer processes has not yielded a consistent method for assessing the performance of heat transfer processes. The function of a heat exchanger is to transfer heat, thus, produce entropy (notwithstanding the unrealistic case of an infinitely large heat exchanger) therefore; the concept of isentropic efficiency cannot be extended to heat exchangers. A reversible heat transfer process happens isothermally and across an infinitesimally small temperature difference, requiring an infinitely large heat exchanger. This, too, is unrealistic.

The performance of heat exchangers is assessed by a number of measures, which have been developed independent of efforts to define an ideal heat exchanger. Relating the performance measures to the ideal behavior has also been studied extensively but with little success so far.

One of the most widely used methods for characterizing the performance of heat exchangers (HX) is the log mean temperature difference (LMTD) correction factor F . Relating F to the heat exchanger irreversibility has not been pursued much, primarily because most correlations for correction factors are implicit and rather complicated. Another measure of assessing the performance of heat exchangers is the heat exchanger effectiveness. The efforts in linking the effectiveness of a heat exchanger to its rate of entropy production have not been successful. The minimum irreversibility condition does not appear to correlate with the effectiveness of the heat exchanger. Shah and Skiepko [1], for example, showed that the heat exchanger effectiveness could be maximum or minimum at the minimum irreversibility operating point [1].

Fakhri [2–5] recently introduced another measure for determining the performance of heat exchangers, the heat exchanger efficiency. The actual rate of heat transfer in a heat exchanger is given by

$$q = \eta UA(\bar{T} - \bar{t}) \quad (2)$$

This approach proposes that the driving temperature difference in the heat exchanger is the arithmetic mean temperature difference (AMTD), which is the difference between the average temperatures of hot and cold fluids. The actual rate of heat transfer in any heat exchanger is always less than the product of its UA and AMTD or $\eta \leq 1$ [3]. The efficiency of a number of commonly used heat exchangers is given by the general expression

$$\eta = \frac{\text{Tanh}(Fa)}{(Fa)} \quad (3)$$

where Fa , the fin analogy number, is the nondimensional group that characterizes the performance of different heat exchangers. This is a remarkable outcome in that the efficiency of a wide variety of heat exchangers has the same functional form as the efficiency of a constant area insulated tip fin. The expressions for Fa for some of the commonly used heat exchangers are given in Table 1.

The efficiency expressions for cross flow heat exchangers are more complex than Eq. (3), however, for some cross flow heat exchangers Eq. (3) can still be used with high degree of accuracy by generalizing the fin analogy number [5]. It is also important to

Contributed by the Heat Transfer Division of ASME for publication in the JOURNAL OF HEAT TRANSFER. Manuscript received February 7, 2010; final manuscript received June 13, 2010; published online August 13, 2010. Assoc. Editor: Giulio Lorenzini.

Table 1 Fin analogy number of various heat exchangers

Counter	Parallel	Single stream	Single shell
$Fa = NTU \frac{(1 - C_r)}{2}$	$Fa = NTU \frac{(1 + C_r)}{2}$	$Fa = \frac{NTU}{2}$	$Fa = \frac{NTU \sqrt{1 + C_r^2}}{2}$

note that the parallel flow and counterflow heat exchangers represent the low and high limits of efficiency for a given NTU and C_r , respectively. The efforts to find a basis for the concept of heat exchanger efficiency is underway by the author and this paper is an effort in that direction.

In an attempt to define an ideal process for heat transfer in heat exchangers or to define the ideal heat exchanger, the idea of minimization of entropy has been proposed. This approach, the irreversibility minimization in heat exchangers, was first proposed by MacClintock [6]. Bejan [7] introduced a nondimensional parameter, the number of entropy generation units as a measure of heat exchanger irreversibility. The number of entropy generation units N_s is the ratio of the total amount of entropy generated in the heat exchanger and the maximum capacity rate. Aceves-Saborio, et al. [8] extended the irreversibility minimization method by including a term to account for the exergy of the heat exchanger material. Badescu [9] used two optimization approaches, the minimum entropy generation, and the minimum lost available work. His results show that regardless of optimization criterion, parallel flow heat exchangers cannot be optimal but counterflow devices can be. Johannessen et al. [10] showed that the entropy production, as a result of heat transfer alone, is minimum when the local entropy production is constant in all parts of the system and the minimum is independent of the value of the heat transfer coefficient. Guo et al. [11] studied entropy generation minimization due to the heat conduction under finite temperature difference and fluid friction under finite pressure drop. They showed that there is a trade-off between the pumping power and heat exchanger effectiveness. Additional insights can be gained from Refs. [12,13] and the an extensive review of the works in this area is given by Shah and Skiepko [14].

The entropy minimization method has found limited application in heat exchanger design due to its shortcomings as a useful design tool. For example, the global optimum often leads to a heat exchanger with infinite area [8]. In applying the concept of entropy minimization to heat exchangers, a number of assumptions are invoked either implicitly or explicitly whose validity have not been questioned much or systematically investigated. These assumptions are as follows.

1. It is possible to minimize entropy production (exergy destruction) in a heat exchanger.
2. It is desirable to minimize entropy production (exergy destruction) in a heat exchanger.
3. Similar to isentropic efficiency, heat exchanger effectiveness is related to irreversibility.

In this paper, it is shown that the above three assumptions are indeed incorrect and in fact the entropy minimization approach is not an appropriate tool for analysis of heat exchangers and should not be an objective in heat exchanger design. A new performance measure, entropy flux is introduced and it is argued that the maximization of the entropy flux, provides useful insight in heat exchanger design.

2 Analysis

There are two types of heat exchanger problems, one where the inlet and the exit temperatures are known and the size of the heat exchanger is to be determined (sizing problems). The reverse problem is called the rating problem where the size of the heat

exchanger and the inlet temperatures are known and the heat transfer rate and the fluid exit temperatures are sought. For both types of problems, the flow rates are also typically known and, therefore, the exit temperatures are known or can be determined. These are important constraints, in that the designer does not have much control over the operating conditions and, thus, cannot arbitrarily change them.

Consider a typical heat exchanger sizing problem in which a cold fluid with capacity C_c at t_1 is to be heated to t_2 using a hot fluid available at T_1 . Usually, the capacity of the hot fluid C_h is also known. The amount of heat transfer is, therefore, known and determined from

$$q = C_c(t_2 - t_1) \quad (4)$$

which can then be used to determine the exit temperature of the hot fluid from

$$T_2 = T_1 - \frac{q}{C_h} \quad (5)$$

Assuming heat transfer from the surroundings to be zero, the rate of entropy generation for a heat exchanger, is given by

$$\dot{S}_{gen} = \dot{m}_h(s_{2,h} - s_{1,h}) + \dot{m}_c(s_{2,c} - s_{1,c}) \quad (6)$$

In general, entropy production is due to two effects, finite temperature difference causing heat transfer and friction leading to pressure drop. The function of a heat exchanger is to transfer heat and, therefore, in defining an ideal heat transfer process based on the second law, only irreversibility caused by heat transfer need to be considered. The goal of this work is to clarify some issues dealing with the application of the second law to heat exchangers. Therefore, to isolate the different factors, the entropy production as a result of friction needs to be considered separately. In addition, in most cases, the irreversibility due to heat transfer accounts for most of entropy produced and as describe below separating the two effects will not impact the outcome much. For incompressible substances (liquids), the entropy change is only a function of temperature and therefore pressure change does not appear in Eq. (6). For gases, although entropy is a function of temperature and pressure, the pressure change across the heat exchangers is typically small and the entropy generated as a result of pressure drop is much smaller than that generated as a result of temperature change. Mohamed [15] showed that the entropy generation due to pressure is too low compared with that due to temperature and can be neglected. Therefore, for liquids as well as gases, considering constant specific heats, the amount of entropy generated becomes

$$\dot{S} = C_h \ln \frac{T_2}{T_1} + C_c \ln \frac{t_2}{t_1} \quad (7)$$

Note that the rate of exergy destruction is related to the entropy production through

$$\dot{\Xi} = T_0 \dot{S} = \dot{m}_c(\xi_{c1} - \xi_{c2}) + \dot{m}_h(\xi_{h1} - \xi_{h2}) \quad (8)$$

and, therefore, the minimization of entropy production, maximization of exergy, or minimization of exergy destruction are equivalent.

As shown above, for a typical sizing problem, the flow rates, the inlet and exit temperatures, and the rate of heat transfer are known, thus, from Eqs. (7) and (8), the amount of entropy generated or exergy destroyed is fixed regardless of the heat exchanger type. Therefore, the designer does not have the option of optimizing them. The only decision left to make is what type of heat exchanger to use that meets the design specifications. Generally, the designer will have many options in the selection of a heat exchanger that will meet the heat transfer design criteria. The final choice will be based on other factors like size, weight, cost, durability, pressure drop, maximum pressure, etc., but not on how reversible the heat exchanger is.

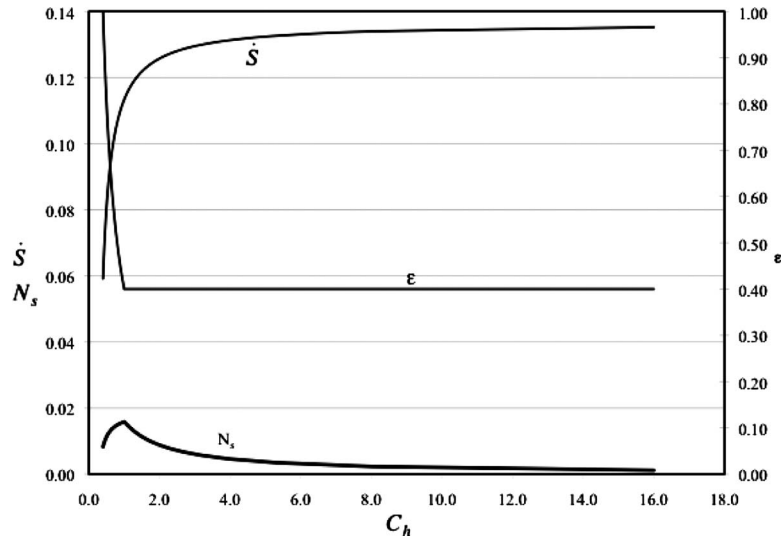


Fig. 1 Entropy, effectiveness, and N_s change with capacity

In a typical rating problem, the inlet temperatures and the flow rates of both fluids are known and the heat exchanger is also specified. Again, the heat transfer and exit temperatures can be determined, which in turn fix the rate of entropy production, or the degree of the irreversibility of the process. These discussions show that the designer does not have the option of changing the amount of entropy generated or the first assumption is not valid. It is also important to note that for these problems, the number of entropy generation units N_s is also independent of the heat exchanger used and therefore, it too cannot be used for characterizing a heat exchanger.

Let us consider a generalization of the sizing problem in which one has control over the amount of hot fluid used, i.e., C_h , is taken to be a variable. Consider a cold fluid with a capacity of 1 W/K is to be heated from 300 K to 420 K using a hot fluid at 600 K available at any flow rate (capacity).

Figure 1 is a plot of the amount of entropy generated, the heat exchanger effectiveness, and N_s as a function of the capacity of the hot fluid. As the mass flow rate of the hot fluid increases, the amount of entropy generated also increases, at the same time; the heat exchanger effectiveness decreases rapidly first and then stays constant over a large portion of the flow rate.

Therefore, the third assumption, that heat exchanger effectiveness is related to irreversibility, is also invalid. The variation in the N_s with respect to the hot fluid capacity also shows a peak even though the actual amount of entropy generated is an increasing function of the hot fluid capacity. Initially, the hot fluid capacity is less than the cold fluid capacity ($C_c=1$) and, therefore, as the amount of entropy generated increases, the number of entropy generation units also increases initially. Once the capacity of the hot fluid exceeds that of the cold fluid, N_s starts to decrease. Again note that the value of N_s only depends on the operating conditions and not on the heat exchanger type used.

The above observations are now proven mathematically. Solving for C_h in terms of t_2 from Eqs. (4) and (5)

$$C_h = C_c \frac{(t_2 - t_1)}{(T_1 - T_2)} \quad (9)$$

which when substituted in Eq. (7) results in

$$\dot{S} = C_c \frac{(t_2 - t_1)}{(T_1 - T_2)} \ln \frac{T_2}{T_1} + C_c \ln \frac{t_2}{t_1} \quad (10)$$

In this equation, everything is fixed except T_2 , which changes as a result of changing C_h . Differentiating Eq. (10) with respect to T_2 to determine if it has an optimum,

$$\frac{d\dot{S}}{dT_2} = C_c \frac{(t_2 - t_1)}{(T_1 - T_2)^2} \left[\frac{T_1}{T_2} - \ln \frac{T_1}{T_2} - 1 \right] \quad (11)$$

The term outside of the bracket is positive, assuming

$$\alpha = \ln \frac{T_1}{T_2} \quad (12)$$

then the term inside the bracket can be written as

$$\left[\frac{T_1}{T_2} - \ln \frac{T_1}{T_2} - 1 \right] = [e^\alpha - (\alpha + 1)] = \left[1 + \alpha + \frac{\alpha^2}{2} + \frac{\alpha^3}{6} + \dots - (\alpha + 1) \right] \\ = \left[\frac{\alpha^2}{2} + \frac{\alpha^3}{6} + \dots \right] \quad (13)$$

The term inside the bracket in Eq. (13) is also positive or the entropy production rate is an increasing function of the exit temperature of the hot fluid (T_2) or the equation does not have an optimum solution. From Eq. (9), since C_h is proportional to T_2 , then entropy production rate is also an increasing function of C_h , confirming the trend seen in Fig. 1.

The absolute minimum amount of entropy generation occurs at the left boundary when $T_2=t_1$. From Eq. (7), the minimum amount of entropy generated becomes

$$\dot{S}_{\min} = C_h \ln \frac{t_1}{T_1} + C_c \ln \frac{t_2}{t_1} \quad (14)$$

In this case, the hot fluid goes through the maximum theoretically possible temperature change (T_1-t_1), therefore, must have minimum capacity and thus the heat transfer in the heat exchanger will be the maximum theoretically possible or the heat exchanger will have an effectiveness of one, which requires an infinitely large heat exchanger and is not of practical interest. This is the well-known result that minimizing entropy results in an unrealistic heat exchanger. The fact that the minimum entropy generation criterion results in an infinitely large heat exchanger is an indication that the objective should not be to minimize entropy.

The maximum amount of entropy generated occurs at the right boundary when $T_2=T_1$ or for the case when the hot fluid goes through an isothermal process. This means that the hot fluid has a capacity of infinity ($C_r=0$) or we are dealing with a single stream heat exchanger, one requiring phase change. The maximum amount of entropy generated is

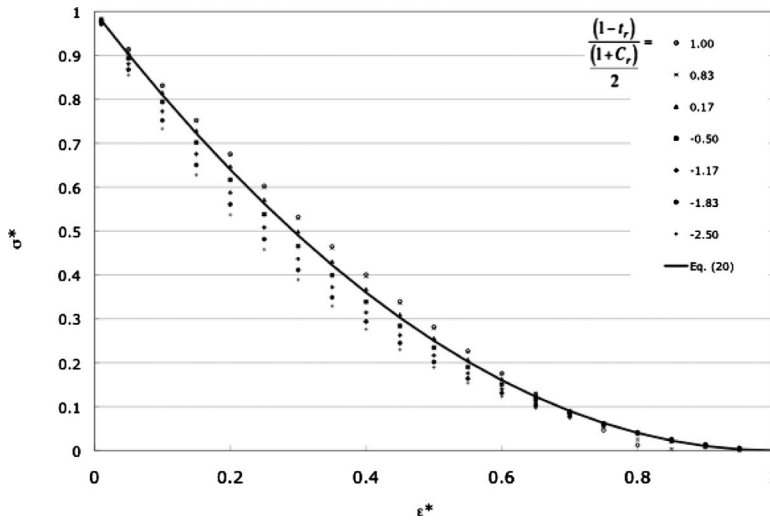


Fig. 2 Comparison of exact and approximate solution

$$\dot{S}_{\max} = -\frac{C_c(t_2 - t_1)}{T_1} + C_c \ln \frac{t_2}{t_1} \quad (15)$$

Therefore, the minimum amount of entropy is generated in an infinitely large heat exchanger and the maximum in a single stream heat exchanger. In practice, single stream heat exchangers (condensers and evaporators) are widely used, when there is a need to transfer large amounts of heat even though they generate the maximum amount of entropy and conversely, large heat exchangers that generate minimum amount of entropy (for the same heat transfer) are rarely used.

These show that minimizing entropy should not be an objective and it is not even desirable in the design of heat exchangers. The least irreversible heat exchanger is avoided for its impracticality. Therefore, the first two assumptions are not valid, i.e., in practical heat exchanger problems, the designer does not generally have the option of reducing the entropy and even when that option is available, the smallest heat exchanger is the opposite alternative, one that maximizes the amount of entropy.

We now consider the third assumption that heat exchanger effectiveness is related to irreversibility. As was shown above, the minimum entropy generation rate happens when effectiveness is 1, not withstanding the fact that it occurs at an infinitely large heat exchanger. Also, the maximum amount of entropy is generated in a single stream heat exchanger, which also has the highest effectiveness at a given NTU. Shah and Skiepo [14] point out that depending on the heat exchanger type, the heat exchanger effectiveness can attain any value at the maximum or minimum entropy generation point. Below we will prove that the effectiveness is not a measure of irreversibility. To show the incorrectness of the third assumption, we need to come up with a correlation relating entropy to effectiveness. Bejan [7] showed that the amount of entropy generated as a result of heat transfer alone could be expressed by

$$\dot{S} = C_{\min} \ln \left[1 + \varepsilon \frac{1 - T_r}{T_r} \right] + C_{\max} \ln [1 + C_r \varepsilon (T_r - 1)] \quad (16)$$

where $T_r = t_1/T_1$ or T_1/t_1 depending on whether the cold or the hot fluid has the minimum capacity, respectively. Equation (16) can be rearranged as

$$\dot{S} = C_{\min} \ln [1 + \varepsilon (T_r^{-1} - 1)] [1 + C_r \varepsilon (T_r - 1)]^{1/C_r} \quad (17)$$

and if we define two new variables, one a scaled effectiveness

$$\varepsilon^* = \varepsilon \frac{(1 + C_r)}{2} \quad (18)$$

and the second, a scaled entropy generation rate

$$\sigma^* = \frac{(1 - \varepsilon^*)}{\varepsilon^*} \frac{\dot{S}}{C_{\min}} \frac{(1 + C_r)}{2} \frac{T_r}{(1 - T_r)^2} \quad (19)$$

Then in terms of these new variables, Eq. (17) can be written as

$$\sigma^* = \frac{T_r}{(1 - T_r)^2} \frac{(1 + C_r)}{2} \left[\frac{1}{\varepsilon^*} - 1 \right] \ln \left[1 - \varepsilon^* \frac{(1 - T_r)}{(1 + C_r)} \right] \times \left[1 + \frac{C_r}{T_r} \varepsilon^* \frac{(1 - T_r)}{(1 + C_r)} \right]^{1/C_r} \quad (20)$$

Equation (20) is a scaled version of the general Eq. (16) and can be used to determine the amount of entropy generated in a heat exchanger. The advantage Eq. (20) is that it is almost independent of C_r and T_r and after much algebra and taking the limits, it can be shown that σ^* is approximately

$$\sigma^* \approx [1 - \varepsilon^*]^2 = \left[1 - \frac{\varepsilon(1 + C_r)}{2} \right]^2 \quad (21)$$

This is a much simpler form compared with Eq. (20) and can be used to examine the salient feature of the problem. Figure 2 compares Eq. (20) with Eq. (21) for several values of C_r and T_r and as can be seen Eq. (21) represents a reasonable approximation to the exact solution. Note that for all heat exchangers, ε^* and σ^* vary between zero and one.

Solving for the amount of entropy generated from Eq. (21)

$$\dot{S} = \frac{(1 - T_r)^2}{T_r} C_{\min} \varepsilon \left[1 - \frac{\varepsilon}{2} (1 + C_r) \right] \quad (22)$$

since

$$\varepsilon = \frac{q}{C_{\min}(T_1 - t_1)} \quad (23)$$

then Eq. (22) can also be written as

$$\dot{S} = \frac{(1 - T_r)^2}{T_r} \frac{q}{(T_1 - t_1)} \left[1 - \frac{q}{2(T_1 - t_1)} \left(\frac{1}{C_{\min}} + \frac{1}{C_{\max}} \right) \right] \quad (24)$$

This is an approximation to Eq. (16). Going back to a typical rating problem, the inlet temperatures of the hot and cold fluids are known, so is the amount of heat transfer. Equation (24) is an increasing function of C_{\min} and C_{\max} , therefore, as the capacity of either fluid is increased, the amount of entropy generation also increases. The same is not true for effectiveness. If C_{\max} is reduced from infinity to C_{\min} , the effectiveness stays the same since all the terms on the right hand side of Eq. (23) are constant. Even though effectiveness is constant, Eq. (24) shows that decreasing C_{\max} results in a decrease in the amount of entropy generated. As the capacity of the fluid, which originally had the higher capacity, is further reduced, the higher capacity and lower capacity fluids switch. Past this point, q_{\max} begins to decrease and since the amount of heat transfer is constant, the effectiveness starts to increase. This proves the trend seen in Fig. 1 with respect to effectiveness.

As shown above, entropy minimization should not be an objective in heat exchanger design, and effectiveness is not a measure of irreversibility, therefore if and how the second law can advantageously be used in heat exchanger design is still an open question. One possibility is presented below by developing a measure that captures the desirable features of heat exchangers, allowing the comparison of different heat exchangers under varying operating conditions by applying the second law. A new measure to characterize the performance of heat exchangers can be defined as

$$\Gamma = \frac{\dot{S}}{UA} \quad (25)$$

which is termed the entropy flux. Entropy flux incorporates three main features of heat exchangers, namely, entropy generated, which so far is only a result of heat transfer, overall heat transfer coefficient and the area of the heat exchanger. In heat exchanger design, the goal is to increase the heat transfer while reducing the size. This means that higher values of entropy flux are desirable. Ogiso [16] defined the same parameter as a measure of the irreversibility index for a balanced counterflow heat exchanger. From Eq. (17),

$$\Gamma = \frac{1}{NTU} \ln[(1 + \varepsilon(T_r^{-1} - 1))(1 + C_r \varepsilon(T_r - 1))^{1/C_r}] \quad (26)$$

If we define a scaled entropy flux as

$$\Gamma^* = \frac{\Gamma T_r}{(1 - T_r)^2} \quad (27)$$

From Eq. (24), an approximate expression for the scaled entropy flux can be obtained

$$\Gamma^* = \frac{\varepsilon}{NTU} \left[1 - \frac{\varepsilon}{2}(1 + C_r) \right] \quad (28)$$

The exact expression for scaled entropy flux is

$$\Gamma^* = \frac{T_r}{(1 - T_r)^2} \frac{1}{NTU} \ln[(1 + \varepsilon(T_r^{-1} - 1))(1 + C_r \varepsilon(T_r - 1))^{1/C_r}] \quad (29)$$

Equation (28) is simpler and is not a function of temperature ratio, however, it is an approximate solution. Note that for Ogiso's case of balanced counterflow heat exchanger, Eq. (28) becomes

$$\Gamma^* = (1 - \varepsilon)^2 \quad (30)$$

and the results of this expression match closely those of Ref. [16].

For various heat exchangers, expressions relating NTU to effectiveness and capacity ratio can be substituted in Eq. (28) or (29) to eliminate NTU and arrive at an expression for the deter-

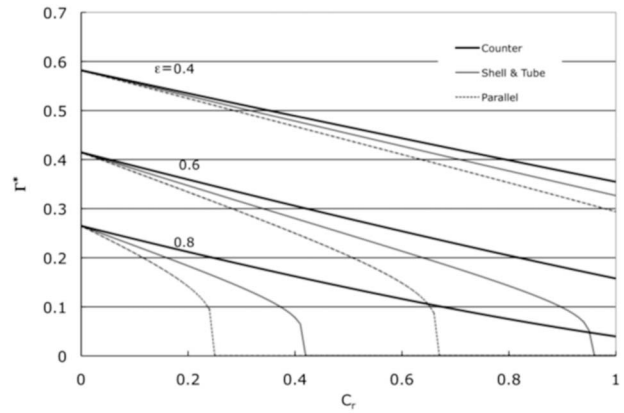


Fig. 3 Scaled entropy flux

mination of the entropy flux in terms of effectiveness and capacity ratio. For example, for a counterflow heat exchanger

$$NTU_{\text{counter}} = - \frac{1}{(1 - C_r)} \ln \frac{1 - \varepsilon}{[1 - \varepsilon C_r]} \quad (31)$$

and similar expressions are available for other heat exchangers. Figure 3 is a plot of Eq. (29) as a function of the capacity ratio, for three types of heat exchangers. For a given effectiveness, a single stream heat exchanger has the highest entropy flux or it will provide the smallest area. The entropy flux for a single stream heat exchanger is given approximately by

$$\Gamma_{\text{max}}^* = - \frac{\varepsilon}{\ln(1 - \varepsilon)} \left| \frac{2 - \varepsilon}{2} \right| \quad (32)$$

and it is exactly given by

$$\Gamma^* = \frac{T_r}{(1 - T_r)^2} \frac{1}{\ln(1 - \varepsilon)} \{ \ln(1 + \varepsilon(T_r^{-1} - 1)) + \varepsilon(T_r - 1) \} \quad (33)$$

Also, for a given capacity, the counterflow heat exchanger has a higher entropy flux followed by shell and tube and parallel flow heat exchangers. For a given set of operating conditions, i.e., flow rates and inlet and exit temperatures, the amount of entropy generated is fixed, therefore the heat exchanger with maximum entropy flux will have the minimum area or the entropy flux will correlate inversely with the area. Figure 3 also shows that at low C_r or low effectiveness the size of the heat exchanger is independent of the type used. At higher values of the capacity ratios, some heat exchangers are not viable options.

The utility of the approach is further demonstrated through two examples. Consider the example discussed in Fig. 1 where a cold fluid with a capacity of 1 W/K is to be heated from 300 K to 420 K using a hot fluid at 600 K available at any flow rate (capacity), assuming $U = 1$ W/m² K. Table 2 shows the result for different values of the hot fluid exit temperature.

For a given exit temperature of the hot fluid, the rate of entropy production is the same regardless of the heat exchanger type selected. As the exit temperature of the hot fluid decreases, the rate of entropy production decreases even after the capacity of the hot fluid is reduced below that of the cold fluid. Also, for each of the heat exchangers, the size monotonically increases while the entropy flux decreases. Figure 3 shows that the most compact heat exchanger is a single stream one that has the highest entropy flux. For other cases, the entropy flux of a counterflow is the highest, corresponding to the least area followed by the shell and tube and parallel flow heat exchanger.

Consider a specific case of the above example, where the hot fluid exits at 500 K. Let us explore the possibility of accomplish-

Table 2 Effect of hot fluid exit temperature on heat exchanger area and entropy flux

T_2	C_r	ε	\dot{s}	Counter flow		Single Shell and tube		Parallel flow	
				A	Γ^*	A	Γ^*	A	Γ^*
600	0.00	0.40	0.13646	0.51	0.534	0.51	0.534	0.51	0.534
550	0.42	0.40	0.12764	0.56	0.453	0.58	0.443	0.59	0.432
500	0.83	0.40	0.11769	0.63	0.372	0.67	0.351	0.72	0.326
480	1.00	0.40	0.11333	0.67	0.340	0.72	0.313	0.80	0.282
450	0.80	0.50	0.10633	0.73	0.292	0.83	0.256	1.02	0.208
440	0.75	0.53	0.10386	0.75	0.276	0.88	0.236	1.16	0.179
430	0.71	0.57	0.10131	0.78	0.259	0.94	0.216	1.41	0.144
301	0.40	1.00	0.05962	3.48	0.034	-	-	-	-

ing this by using two counterflow heat exchangers connected in series, as shown in Fig. 4. Table 3 shows the results for different values of T' .

As can be seen in Table 3, for all cases, the total heat exchanger area is the same, therefore, as far as the area is concerned, it does not matter which alternative is picked. The total amount of entropy generated is also constant for all cases, however, the first case, i.e., having a single heat exchanger, has the highest total entropy flux and, thus, the preferred option. This also is the actual case typically selected in practice.

It appears that the entropy flux is a criterion by which the performance of different heat exchangers can be directly and quantitatively compared, under various operating conditions. None of the other measures used for evaluating the performance of heat exchangers has yielded consistent results. For example, the first three cases in Table 2 have the same effectiveness. It is also important to note that entropy flux is the ratio of entropy production to UA. For the same flow rate and inlet and exit temperatures, different heat exchangers will not necessarily have the same overall heat transfer coefficient.

3 Conclusions

In this paper, it is shown that it is neither possible nor desirable to minimize entropy generation in typical heat exchanger design problems. It is also shown that heat exchanger effectiveness does not consistently correlate with irreversibility and should not be viewed as having the same connotation for heat exchangers as the isentropic efficiency has for many components. Furthermore, it is shown that entropy minimization should not be a design objective in heat exchanger design. A new performance measure, entropy flux, is introduced and it is shown that maximization of the en-

ropy flux provides a useful criterion by which different heat exchangers under different operating conditions can directly and objectively be compared.

Nomenclature

- A = heat exchanger surface area, m²
- C_c = heat capacity rate of the cold fluid $C_c = (\dot{m}c_p)_c$
- C_h = heat capacity rate of the hot fluid $C_h = (\dot{m}c_p)_h$
- C_{\min} = minimum heat capacity rate = $\min(C_c, C_h)$
- C_{\max} = maximum heat capacity rate = $\max(C_c, C_h)$
- c_p = constant pressure specific heat
- C_r = capacity ratio $C_r = C_{\min}/C_{\max}$
- N_s = number of entropy generation units
- $N_s = \dot{S}/C_{\max}$
- NTU = number of transfer units $NTU = UA/C_{\min}$
- q = rate of heat transfer
- s = specific entropy
- \dot{S} = rate of entropy production
- t_1 = hot fluid temperature
- $T_r = T_r = t_1/T_1$ or T_1/t_1 inlet temperature of the fluid with minimum capacity divided by inlet temperature of the fluid with maximum capacity
- t = cold fluid temperature
- U = overall heat transfer coefficient, W/m² K
- ε = HX effectiveness $\varepsilon = q/C_{\min}(T_1 - t_1)$
- ε^* = scaled effectiveness
- σ^* = scaled nondimensional entropy generation rate
- ξ = flow availability or exergy per unit mass
- Γ = entropy flux $\Gamma = \dot{S}/UA$

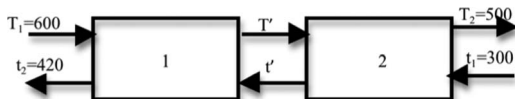


Fig. 4 Heat exchangers in series

Subscripts and Superscripts

- 1 = inlet
- 2 = outlet
- * = nondimensional

Table 3 Entropy flux of two counter flow heat exchangers in series

T'	t'	ε_1	\dot{s}_1	Γ_1	A_1	ε_2	\dot{s}_2	Γ_2	A_2	\dot{s}_T	Γ_T	A_T
500	300	0.40	0.118	0.19	0.63	0.00	0.000	0.27	0.00	0.1177	0.45	0.63
510	312	0.38	0.102	0.18	0.57	0.06	0.015	0.26	0.06	0.1177	0.44	0.63
520	324	0.35	0.088	0.17	0.51	0.11	0.030	0.25	0.12	0.1177	0.42	0.63
530	336	0.32	0.074	0.17	0.45	0.16	0.043	0.24	0.18	0.1177	0.40	0.63
540	348	0.29	0.062	0.16	0.39	0.20	0.056	0.23	0.24	0.1177	0.39	0.63
550	360	0.25	0.050	0.15	0.32	0.24	0.068	0.22	0.31	0.1177	0.37	0.63
560	372	0.21	0.039	0.15	0.26	0.28	0.079	0.21	0.37	0.1177	0.36	0.63
570	384	0.17	0.028	0.14	0.20	0.31	0.090	0.21	0.44	0.1177	0.35	0.63
580	396	0.12	0.018	0.14	0.13	0.34	0.100	0.20	0.50	0.1177	0.34	0.63
590	408	0.06	0.009	0.13	0.07	0.37	0.109	0.19	0.57	0.1177	0.33	0.63
600	420	0.00	0.000	0.13	0.00	0.40	0.118	0.19	0.63	0.1177	0.31	0.63

References

- [1] Shah, R. K., and T. Skiepko, 2004, "Entropy Generation Extrema and Their Relationship With Heat Exchanger Effectiveness—Number of Transfer Unit Behavior for Complex Flow Arrangements," *ASME J. Heat Transfer*, **126**(6), pp. 994–1002.
- [2] Fakheri, A., 2003, "The Shell and Tube Heat Exchanger Efficiency and Its Relation to Effectiveness," *Proceedings of the 2003 American Society of Mechanical Engineers (ASME) International Mechanical Engineering Congress and Exposition (IMECE)*, Washington, DC, Nov. 16–21.
- [3] Fakheri, A., 2008, "Efficiency and Effectiveness of Heat Exchanger Series," *ASME J. Heat Transfer*, **130**(8), p. 084502.
- [4] Fakheri, A., 2007, "Heat Exchanger Efficiency," *ASME J. Heat Transfer*, **129**(9), pp. 1268–1276.
- [5] Fakheri, A., 2006, "Thermal Efficiency of the Cross Flow Heat Exchangers," *Proceedings of the 2006 ASME International Mechanical Engineering Conference and Exposition*, Chicago, IL, Nov. 5–10.
- [6] McClintock, F. A., 1951, "The Design of Heat Exchangers for Minimum Irreversibility," ASME Paper No. 51-A-108.
- [7] Bejan, A., 1977, "Concept of Irreversibility in Heat Exchanger Design: Counterflow Heat Exchangers for Gas-to-Gas Applications," *ASME J. Heat Transfer*, **99**(3), pp. 374–380.
- [8] Aceves-Saborio, S., Ranasinghe, J., and Reistad, G. M., 1989, "Extension to the Irreversibility Minimization Analysis Applied to Heat Exchangers," *ASME J. Heat Transfer*, **111**(1), pp. 29–36.
- [9] Badescu, V., 2004, "Optimal Strategies for Steady State Heat Exchanger Operation," *J. Phys. D*, **37**, pp. 2298–2304.
- [10] Johannessen, E., Nummedal, L., and Kjelstrup, S., 2002, "Minimizing the Entropy Production in Heat Exchange," *Int. J. Heat Mass Transfer*, **45**, pp. 2649–2654.
- [11] Guo, J., Cheng, L., and Xu, M., 2010, "Multi-Objective Optimization of Heat Exchanger Design by Entropy Generation Minimization," *ASME J. Heat Transfer*, **132**, p. 081801.
- [12] Naterer, G. F., and Camberos, J. A., 2008, *Entropy-Based Design and Analysis of Fluid Engineering Systems*, CRC Press, Boca Raton, FL.
- [13] Bejan, A., 1996, *Entropy Generation Minimization. The Method of Thermodynamic Optimization of Finite-size Systems and Finite-Time Processes*, CRC Press, New York.
- [14] Shah, R. K., and T. Skiepko, 2005, "Exchanger Performance Behavior Through Irreversibility Analysis for 1–2 TEMA G Heat Exchangers," *ASME J. Heat Transfer*, **127**, pp. 1296–1304.
- [15] Mohamed, H. A., 2006, "Entropy Generation in Counter Flow Heat Exchangers," *ASME J. Heat Transfer*, **128**, pp. 87–92.
- [16] Ogiso, K., 2003, "Duality of Heat Exchanger Performance in Balanced Counter-Flow Systems," *ASME J. Heat Transfer*, **125**, pp. 530–532.

On Variance-Reduced Simulations of the Boltzmann Transport Equation for Small-Scale Heat Transfer Applications

Nicolas G. Hadjiconstantinou

Gregg A. Radtke

Lowell L. Baker

Department of Mechanical Engineering,
Massachusetts Institute of Technology,
Cambridge, MA 02139

We present and discuss a variance-reduced stochastic particle simulation method for solving the relaxation-time model of the Boltzmann transport equation. The variance reduction, achieved by simulating only the deviation from equilibrium, results in a significant computational efficiency advantage compared with traditional stochastic particle methods in the limit of small deviation from equilibrium. More specifically, the proposed method can efficiently simulate arbitrarily small deviations from equilibrium at a computational cost that is independent of the deviation from equilibrium, which is in sharp contrast to traditional particle methods. The proposed method is developed and validated in the context of dilute gases; despite this, it is expected to directly extend to all fields (carriers) for which the relaxation-time approximation is applicable.

[DOI: 10.1115/1.4002028]

1 Introduction and Motivation

Particle-mediated energy transport in the transition regime between the ballistic and diffusive limits has recently received significant attention in connection to micro- and nanoscale science and technology [1]. Applications can be found in a variety of diverse fields such as thin semiconductor films [2,3] and superlattices [1], ultrafast processes [4,5], convective heat transfer [6,7], and gas-phase damping [8,10].

For a considerable number of applications, a classical description using the Boltzmann transport equation represents a good compromise between fidelity and complexity [1]. However, a numerical solution of the Boltzmann equation remains a formidable task due to the complexity associated with the collision operator and the high dimensionality of the distribution function. Both these features have contributed to the prevalence of particle solution methods, which are typically able to simulate the collision operator through simple and physically intuitive stochastic processes while employing importance sampling, which reduces computational cost and memory usage [11]. Another contributing factor to the wide usage of particle schemes is their natural treatment of the advection operator, which results in a numerical method that can easily handle and accurately capture traveling discontinuities in the distribution function [11]. An example of such a particle method is direct simulation Monte Carlo (DSMC) [12], which has become the standard simulation method for dilute gas flow. Methods that are similar in spirit have also been used for simulating phonon transport in solid state devices [13,14].

One of the most important disadvantages of particle methods for solving the Boltzmann equation derives from their reliance on statistical averaging for extracting field quantities from particle data [13,15]. In simulations of processes close to equilibrium, thermal noise typically exceeds the available signal. When coupled with the slow convergence of statistical sampling (statis-

tical error decreases with the square root of the number of samples), this often leads to computationally intractable problems [15].

The present paper describes a particle simulation framework that alleviates the above disadvantages to a considerable extent while retaining the basic (and desirable) features of particle methods. This is achieved by simulating only the deviation from equilibrium, as originally proposed in Ref. [11]. Subsequent work [16] has shown that deviational methods (particle methods simulating the deviation from equilibrium) using the original Boltzmann (hard-sphere) collision operator require particle cancellation to prevent the number of simulated particles from growing in an unbounded manner. A stable deviational method (that does not require particle cancellation) for the hard-sphere gas was first developed in Refs. [17,18]; in that work, it was shown that the growth in the number of simulated particles observed in the collision-dominated regime when using the traditional hard-sphere collision operator [16] can be overcome using a special (but equivalent) form of the hard-sphere collision operator first derived by Hilbert [19]. In this paper, we exploit this observation to develop a deviational method for simulating the Boltzmann equation in the relaxation-time approximation. The method presented here considers the deviation from a suitably defined *global* equilibrium distribution and appears to be stable (does not require particle cancellation) for typical deviations from equilibrium.

2 Background

The Boltzmann transport equation is used to describe (under appropriate conditions) transport processes in a wide variety of fields [1], including dilute gas flow [20], phonon [21], electron [22], neutron [23], and photon transport [24]. It may be written as

$$\frac{\partial f}{\partial t} + \mathbf{c} \cdot \frac{\partial f}{\partial \mathbf{r}} + \mathbf{a} \cdot \frac{\partial f}{\partial \mathbf{c}} = \left[\frac{df}{dt} \right]_{\text{coll}} \quad (1)$$

where $f(\mathbf{r}, \mathbf{c}, t)$ is the single-particle distribution function [20], $[df/dt]_{\text{coll}}(\mathbf{r}, \mathbf{c}, t)$ denotes the collision operator, $\mathbf{r}=(x, y, z)$ is the position vector in physical space, $\mathbf{c}=(c_x, c_y, c_z)$ is the molecular velocity vector, $\mathbf{a}=(a_x, a_y, a_z)$ is the acceleration due to an exter-

Contributed by the Heat Transfer Division of ASME for publication in the JOURNAL OF HEAT TRANSFER. Manuscript received January 21, 2009; final manuscript received April 12, 2010; published online August 13, 2010. Assoc. Editor: Kenneth Goodson.

nal field, and t is time. In this paper, we focus on the relaxation-time approximation [20,1]

$$\left[\frac{df}{dt} \right]_{\text{coll}} = -\frac{1}{\tau}(f - f^{\text{loc}}) \quad (2)$$

where $f^{\text{loc}}(\mathbf{r}, \mathbf{c}, t)$ is the *local equilibrium* distribution function and τ is the relaxation time.

To focus the discussion, we specialize our treatment to the dilute gas case;¹ however, we hope that this exposition can serve as a prototype for the development of similar techniques in all fields where the relaxation-time approximation is applicable. In the interest of simplicity, in the present paper we assume $\tau \neq \tau(\mathbf{c})$ and that no external forces are present. The first assumption can be easily relaxed, as discussed in Sec. 3.1. External fields also require only relatively straightforward modifications to the algorithm presented below.

A dilute gas in equilibrium is described by a Maxwell-Boltzmann distribution, leading to a local equilibrium distribution

$$f^{\text{loc}} = \frac{n_{\text{loc}}}{\pi^{3/2} c_{\text{loc}}^3} \exp\left(-\frac{\|\mathbf{c} - \mathbf{u}_{\text{loc}}\|^2}{c_{\text{loc}}^2}\right) \quad (3)$$

which is parametrized by the local number density $n_{\text{loc}} = n_{\text{loc}}(\mathbf{r}, t)$, the local flow velocity $\mathbf{u}_{\text{loc}} = \mathbf{u}_{\text{loc}}(\mathbf{r}, t)$, and the most probable speed $c_{\text{loc}}(\mathbf{r}, t) = \sqrt{2k_B T_{\text{loc}}/m}$ based on the local temperature $T_{\text{loc}} = T_{\text{loc}}(\mathbf{r}, t)$. Here, k_B is Boltzmann's constant, and m is the molecular mass.

3 Variance Reduction Formulation

In a recent paper [11], Baker and Hadjiconstantinou showed that significant variance reduction can be achieved by simulating only the deviation $f^d(\mathbf{r}, \mathbf{c}, t) \equiv f - f^e$ from an *arbitrary*, but judiciously chosen, underlying equilibrium distribution $f^e(\mathbf{r}, \mathbf{c}, t)$. By adopting this approach, it is possible to construct Monte Carlo simulation methods [11,16,17,25] that can capture arbitrarily small deviations from equilibrium at a computational cost that is *small* and independent of the magnitude of this deviation. This is in sharp contrast to regular Monte Carlo methods, such as DSMC, whose computational cost for the same signal-to-noise ratio increases *sharply* [15] as the deviation from equilibrium decreases.

In the work that follows, the underlying equilibrium distribution (f^e) will be identified with absolute equilibrium,

$$f^e \equiv F(\mathbf{c}) = \frac{n_0}{\pi^{3/2} c_0^3} \exp\left[-\frac{\mathbf{c}^2}{c_0^2}\right] \quad (4)$$

where n_0 is a reference (equilibrium) number density and $c_0 = \sqrt{2k_B T_0/m}$ is the most probable molecular speed based on the reference temperature T_0 . For small deviations from equilibrium, the choice of an appropriate reference equilibrium is straightforward but necessary. If deviations from the reference equilibrium are large, either due to strong nonlinearity in the problem or an inappropriate choice of reference equilibrium, the simulation method becomes less efficient than DSMC due to the large number of particles required to simulate the deviation from equilibrium.

Particle methods, such as DSMC, typically solve the Boltzmann equation by applying a splitting scheme,² in which molecular motion is simulated as a series of collisionless advection and collision steps of length Δt . In such a scheme, the collisionless advection step integrates

$$\frac{\partial f}{\partial t} + \mathbf{c} \cdot \frac{\partial f}{\partial \mathbf{r}} = 0 \quad (5)$$

by simply advecting particles for a time step Δt , while the collision step integrates

$$\frac{\partial f}{\partial t} = \left[\frac{df}{dt} \right]_{\text{coll}} \quad (6)$$

by changing the distribution by an amount of $[df/dt]_{\text{coll}} \Delta t$. Spatial discretization is introduced by treating collisions as spatially homogeneous within (small) computational cells of volume $\mathcal{V}_{\text{cell}}$.

Our approach retains this basic structure although it must be noted that since computational particles represent the deviation from equilibrium, they may be positive or negative, depending on the sign of the deviation from equilibrium at the location in phase space where they reside. As in other particle schemes [12], in the interest of computational efficiency, each *computational* deviational particle represents an *effective number* N_{eff} of physical deviational particles. Below we discuss the two main steps in more detail.

3.1 Collision Step. The variance-reduced form of Eq. (6) can be written as

$$\left[\frac{df}{dt} \right]_{\text{coll}} = \frac{1}{\tau} (f^{\text{loc}} - F) - \frac{1}{\tau} f^d \quad (7)$$

Within each computational cell, we integrate Eq. (7) using a two-part process. This integration requires local (cell) values of various quantities, denoted here by hats, which are updated every time step by sampling the instantaneous state of the gas.

In the first part, we remove a random sample of particles by deleting particles with probability $\Delta t / \hat{\tau}$ to satisfy

$$\tilde{f}^d(t + \Delta t) = \hat{f}^d(t) - \frac{\Delta t}{\hat{\tau}} \hat{f}^d(t) \quad (8)$$

In our implementation, this is achieved through an acceptance-rejection process, which can also treat the case $\hat{\tau} = \hat{\tau}(\mathbf{c})$.

In the second part, we create a set of positive and negative particles (using an acceptance-rejection process) to satisfy

$$\hat{f}^d(t + \Delta t) = \tilde{f}^d(t + \Delta t) + \frac{1}{\hat{\tau}} [\hat{f}^{\text{loc}}(t) - F] \Delta t \quad (9)$$

This step can be achieved by the following procedure. Let c_c be a (positive) value such that $\hat{f}^{\text{loc}}(\mathbf{c}) - F(\mathbf{c})$ is negligible for $\|\mathbf{c}\|_1 > c_c$, where $\|\cdot\|_1$ is an L^1 -norm. Furthermore, let Δ_{max} bound $|\hat{f}^{\text{loc}}(\mathbf{c}) - F(\mathbf{c})|$ from above. Then, repeat \mathcal{N}_c times:

1. Generate uniformly distributed, random velocity vectors \mathbf{c} with $\|\mathbf{c}\|_1 < c_c$.
2. If $|\hat{f}^{\text{loc}}(\mathbf{c}) - F(\mathbf{c})| > \mathcal{R} \Delta_{\text{max}}$, create a particle with velocity \mathbf{c} at a randomly chosen position within the cell and sign $\text{sgn}[\hat{f}^{\text{loc}}(\mathbf{c}) - F(\mathbf{c})]$. Here, \mathcal{R} is a random number uniformly distributed on $[0, 1]$.

To find \mathcal{N}_c , we note that the number of particles (of all velocities and signs) that should be generated in a cell to obtain the proper change in the distribution function is

$$\frac{\Delta t}{N_{\text{eff}} \hat{\tau}} \int_{\mathcal{V}_{\text{cell}}} \int_{\mathbf{R}^3} \frac{|\hat{f}^{\text{loc}} - F|}{\tau} d^3 \mathbf{c} d^3 \mathbf{r} = \frac{\Delta t \mathcal{V}_{\text{cell}}}{N_{\text{eff}} \hat{\tau}} \int_{\mathbf{R}^3} |\hat{f}^{\text{loc}} - F| d^3 \mathbf{c} \quad (10)$$

where $\mathcal{V}_{\text{cell}}$ is the cell volume. The (expected) total number of particles ultimately generated by the above algorithm is

¹Within the rarefied gas dynamics literature, the relaxation-time approximation is known as the BGK model [20].

²Note that a symmetrized algorithm typically provides higher-order accuracy. See Refs. [8,9] and references therein.

$$\mathcal{N}_c = \frac{\int_{\mathbf{R}^3} |f^{\text{loc}} - F| d^3\mathbf{c}}{\Delta_{\text{max}} 8c_c^3} \quad (11)$$

By equating the above two expressions, we obtain $\mathcal{N}_c = 8\Delta t \Delta_{\text{max}} \mathcal{V}_{\text{cell}} c_c^3 / (\hat{\tau} N_{\text{eff}})$.

3.2 Advection Step. It can be easily verified that when the underlying equilibrium distribution is not a function of space or time, as is the case here,

$$\frac{\partial f}{\partial t} + \mathbf{c} \cdot \frac{\partial f}{\partial \mathbf{r}} = \frac{\partial f^d}{\partial t} + \mathbf{c} \cdot \frac{\partial f^d}{\partial \mathbf{r}} \quad (12)$$

and thus the advection step for deviational particles is identical to that of physical particles.

Boundary condition implementation, however, is slightly more complex because the mass flux to system boundaries includes contributions from deviational particles as well as the underlying equilibrium distribution. Our implementation is discussed in more detail below.

3.2.1 Boundary Condition Implementation. Here, we extend previous work on diffuse boundary conditions to the more general case of the Maxwell accommodation model with accommodation coefficient α . According to this model, a fraction α of the molecules impacting the boundary are accommodated (diffusely reflected), while the remaining particles are specularly reflected.

Let \mathbf{u}_b and c_b represent the boundary velocity and the most probable speed based on the boundary temperature, respectively. Let us assume, without loss of generality, that the boundary is parallel to the y - z plane and that the gas lies to the right ($x > 0$) of the wall. For simplicity, let us also assume that the boundary does not move in the direction normal to its plane; i.e., the x -component of \mathbf{u}_b is zero. Under these conditions, the Maxwell boundary condition can be written [26] as

$$f(c_x, c_y, c_z) = (1 - \alpha)f(-c_x, c_y, c_z) + \alpha n_b \phi^b(c_x, c_y, c_z), \quad c_x > 0 \quad (13)$$

where in order to simplify the notation we have suppressed the space and time dependence of the distribution function. Here, $\phi^b(c_x, c_y, c_z) = (\pi c_b^2)^{-3/2} \exp(-\|\mathbf{c} - \mathbf{u}_b\|^2 / c_b^2)$; the quantity n_b is determined by mass conservation at the wall, namely,

$$\int_{c_x < 0} c_x f d^3\mathbf{c} = -n_b \int_{c_x > 0} c_x \phi^b d^3\mathbf{c} \quad (14)$$

Equation (13) can be written as

$$f^d(c_x, c_y, c_z) = (1 - \alpha)f^d(-c_x, c_y, c_z) + \alpha[n_b \phi^b - F](c_x, c_y, c_z), \quad c_x > 0 \quad (15)$$

The algorithm used here for evaluating n_b considers deviational particles and the flux of particles due to the underlying equilibrium distribution $f^e \equiv F$ separately. More specifically, by introducing $n_b = n_b^e + n_b^d$ in Eq. (15), we obtain

$$f^d(c_x, c_y, c_z) = (1 - \alpha)f^d(-c_x, c_y, c_z) + \alpha n_b^d \phi^b(c_x, c_y, c_z) + \alpha[n_b^e \phi^b(c_x, c_y, c_z) - F(c_x, c_y, c_z)], \quad c_x > 0 \quad (16)$$

Using a probabilistic interpretation, this boundary condition may be implemented as follows: deviational particles striking the boundary are specularly reflected with probability $(1 - \alpha)$ or diffusely reflected with probability α . The fraction of deviational particles diffusely reflected (corresponding to n_b^d) can be treated using an algorithm similar to DSMC; i.e., particles striking the wall may be sent back to the computational domain drawn from the appropriate fluxal distribution (here, $c_x \phi^b, c_x > 0$). One impor-

tant difference, however, is that only the *net* number of deviational particles is sent back into the domain since pairs of positive and negative particles correspond to zero net mass flux and can be cancelled, i.e.,

$$n_b^d \int_{c_x > 0} c_x \phi^b d^3\mathbf{c} = - \int_{c_x < 0} c_x f^d d^3\mathbf{c} \quad (17)$$

Equation (16) reveals a third contribution to the deviational population, namely, $\alpha[n_b^e \phi^b - F]$. This contribution is associated with the molecular flux incident upon the wall due to the underlying equilibrium distribution; n_b^e is determined from

$$n_b^e \int_{c_x > 0} c_x \phi^b d^3\mathbf{c} = - \int_{c_x < 0} c_x F d^3\mathbf{c} \quad (18)$$

As shown in Refs. [16,18], this case can be treated by creating deviational particles from the distribution $c_x[n_b^e \phi^b - F]$, $c_x > 0$. The number of particles per unit wall surface area generated in a time step is

$$\mathcal{F} = \frac{\alpha \Delta t}{N_{\text{eff}}} \int_{c_x > 0} c_x |n_b^e \phi^b - F| d^3\mathbf{c} \quad (19)$$

Let M_{max} bound the integrand in Eq. (19) from above, c_a be a (positive) value such that the integrand is negligible for $\|\mathbf{c}\|_1 > c_a$, and A be the surface area of the boundary. The requisite number of particles is generated by repeating $\mathcal{N}_b = 4AM_{\text{max}}c_a^3\alpha\Delta t/N_{\text{eff}}$ times:

1. Generate uniformly distributed, random velocity vectors \mathbf{c} such that $\|\mathbf{c}\|_1 < c_a$ and $c_x > 0$.
2. If $c_x |n_b^e \phi^b(\mathbf{c}) - F(\mathbf{c})| > \mathcal{R}M_{\text{max}}$, create a particle with velocity \mathbf{c} and sign $\text{sgn}[n_b^e \phi^b(\mathbf{c}) - F(\mathbf{c})]$. Generated particles are advected for a random fraction of a time step.

4 Results and Discussion

We have performed extensive validations and performance evaluations of the proposed method using a variety of test cases. Here, we present some representative transient and steady-state results involving heat exchange between two infinite, parallel walls at different temperatures (T_0 and $T_1 = T_0 + \Delta T$ where $\Delta T = \varepsilon T_0$) and a distance L apart in the x direction. The Knudsen number is defined as $k = c_0 \tau_0 / L$, where τ_0 is the collision time at the reference (absolute equilibrium) condition.

We start by discussing the variance reduction achieved by the present method. Validation is discussed in the following section.

4.1 Relative Statistical Uncertainty. As stated above and as shown in Refs. [11,16,18], deviational methods such as the one presented here exhibit statistical uncertainties that scale with the local deviation from equilibrium, thus allowing the simulation of arbitrarily low deviations from equilibrium at a cost that is independent of this deviation. Here, we demonstrate this feature by studying the statistical uncertainty of the temperature in a problem involving heat transfer.

Figure 1 shows the relative statistical uncertainty in the temperature ($\sigma_T / \Delta T = \sigma_T / (\varepsilon T_0)$) as a function of ε for steady-state heat exchange between the two walls ($k = 1, T_0 = 273$ K, $\alpha = 1$); σ_T is defined as the standard deviation in the temperature measured in two computational cells in the middle of the computational domain, each containing approximately $N = 950$ particles. Our results are compared with those from a representative nondeviational method, namely, DSMC. The DSMC performance is calculated from the theoretical result of Ref. [15] obtained using equilibrium statistical mechanics (assuming small deviation from equilibrium). We also performed DSMC simulations (of the relaxation-time model) to verify that this theoretical result remains accurate for $\varepsilon \geq 0.1$. The figure shows that this is indeed the case, provided that in the equilibrium result [15],

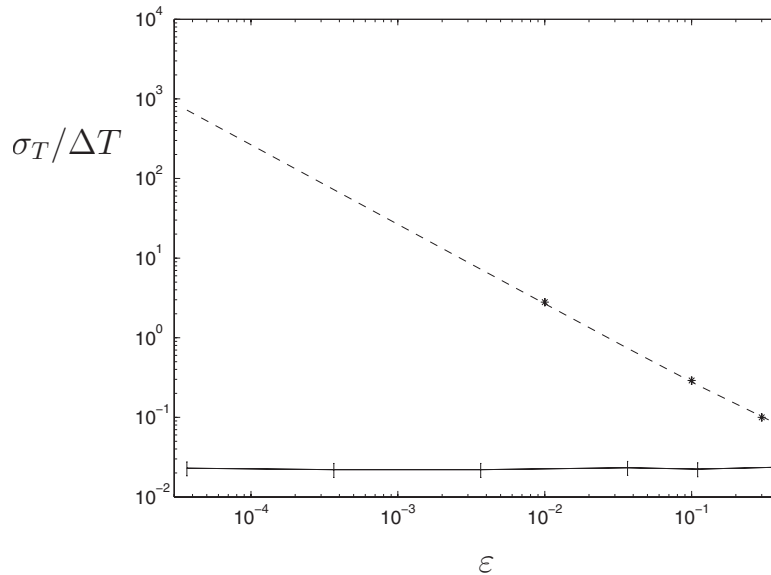


Fig. 1 The relative statistical uncertainty in temperature, $\sigma_T/\Delta T$, as a function of ε for steady-state heat exchange between two parallel plates at different temperatures with $k=1$, $\alpha=1$, and $T_0=273$ K. Simulation results (symbols with error bars on solid line) are presented and compared with the theoretical prediction [15] for DSMC (dashed line), which serves as a canonical case of a nondeviational method. Stars show actual DSMC results verifying that equilibrium theory is reliable up to at least $\varepsilon \approx 0.3$.

$$\sigma_T = \frac{T_0}{\sqrt{1.5N}} \quad (20)$$

T_0 is interpreted as the *local* temperature value.

Figure 1 also shows that for $\varepsilon \leq 0.3$ the relative statistical uncertainty of the deviational method proposed here remains essentially independent of ε , in sharp contrast to “nondeviational” methods. Moreover, the variance reduction achieved is such that significant computational savings are expected for $\varepsilon \leq 0.1$, particularly when considering that the cost savings scale with the square of the relative statistical uncertainty (since statistical noise decreases with the square root of the number of samples).

4.2 Validation. Figure 2 shows a comparison between the

numerical solution of the linearized ($\varepsilon \ll 1$) relaxation-time model of the Boltzmann equation [27] and our simulation results for the heat flux between the two walls, q , for the case $\alpha=1$. The figure compares the heat flux normalized by the free-molecular (ballistic) value, $|q_{fm}(\alpha)| = \alpha \varepsilon P_0 c_0 / [\sqrt{\pi}(2-\alpha)]$, as a function of k ; here, $P_0 = n_0 k_B T_0$ is the equilibrium gas pressure. The agreement between the two results is excellent.

Figure 3 shows a comparison for $\alpha=0.826$, one of the few cases for which numerical results for $\alpha \neq 1$ are readily available [28]. The agreement is again excellent.

Figure 4 shows a comparison between our simulation results and an analytical solution [29] of the linearized collisionless Boltzmann equation for oscillatory variation in the boundary tempera-

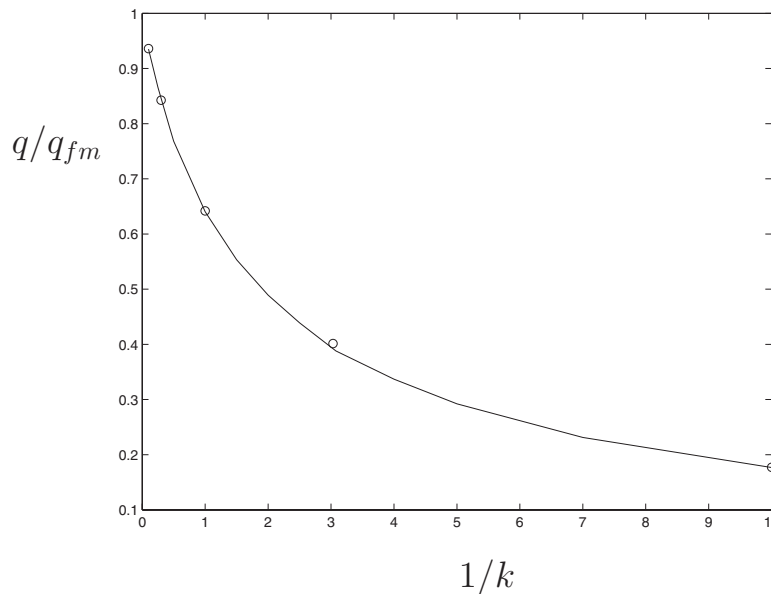


Fig. 2 Comparison between the numerical solution of the linearized Boltzmann equation by Bassanini et al. [27] (solid line) and simulation results (circles) for the heat flux between two parallel, infinite, fully accommodating walls. Some numerical solution data for $k > 1$ have been transcribed from Ref. [20].

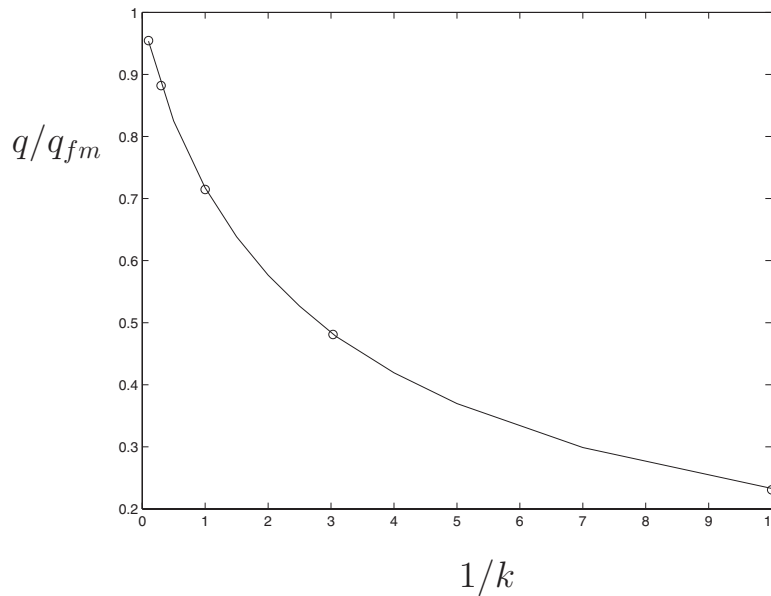


Fig. 3 Comparison between the numerical solution of the linearized Boltzmann equation by Bassanini et al. [28] (solid line) and simulation results (circles) for the heat flux between two parallel, infinite walls with $\alpha=0.826$

ture, i.e., $T_1=T_0(1+\varepsilon \sin \omega t)$, $\varepsilon \ll 1$, at a frequency ω that is large compared with the inverse acoustic (ballistic) system time scale ($\omega L/c_0 \gg 1$). The theoretical solution shows [29] that for sufficiently large frequencies, the hydrodynamic fields decay away from the wall proportionally to $\exp[-(\omega \delta_w/c_0)^{2/3}]$, where δ_w is the distance from the wall; in other words, “ballistic bounded layers” are formed (in contrast to Stokes layers, which are a result of diffusive transport). As a result, provided ω is sufficiently large, the collisionless description remains valid for systems of arbitrarily large size. Figure 4 shows a comparison between the theoretical results [29] and the simulation for $k=1$, $\alpha=1$, and $\omega L/c_0=40\pi$ for the density, flow velocity normal to the wall, temperature, and heat flux. The analytical solution is based on an asymptotic expansion valid for $\omega \delta_w/c_0 \gg 1$ [29]; thus, it is not

valid in small regions close to the wall where the above condition is not satisfied. Our results show that sufficiently far from the wall, the agreement between theory and simulation is excellent.

As shown above, although the computational advantage of the method presented here compared with nondeviational methods increases as the deviation from equilibrium decreases, the amount of variance reduction achieved is such that considerable computational savings are obtained even when the deviation from equilibrium is not small. Below, we present a comparison between our results and DSMC simulations of the relaxation-time model in this latter regime. Specifically, we simulate an impulsive heating problem where at time $t=0$ the temperature of the wall at $x=-L/2$ jumps from T_0 to $T_0+\Delta T$; the gas is initially in equilibrium at temperature T_0 , and both walls are fully accommodating ($\alpha=1$).

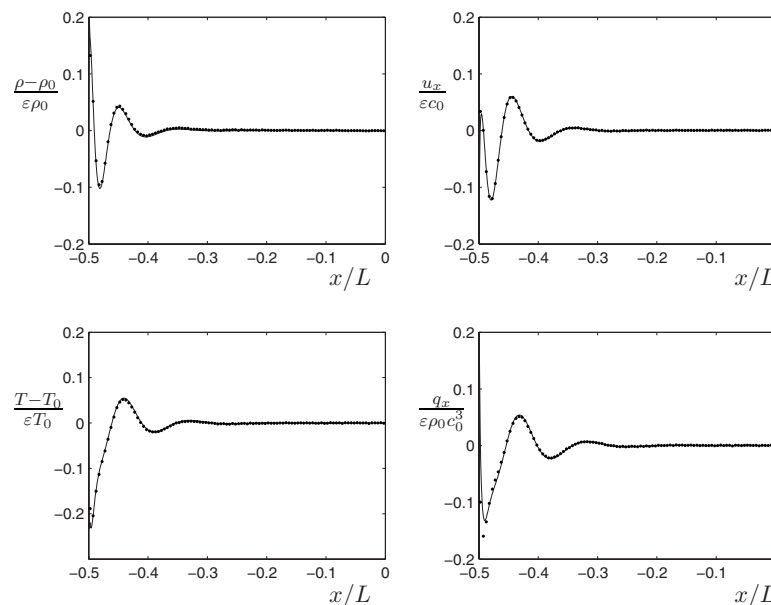


Fig. 4 Comparison between the proposed method (dots) and the theoretical results of Ref. [29] (solid lines) for $\omega L/c_0=40\pi$, $k=1$, $\alpha=1$, and $\varepsilon=0.02$. Here, $\rho_0=m n_0$.

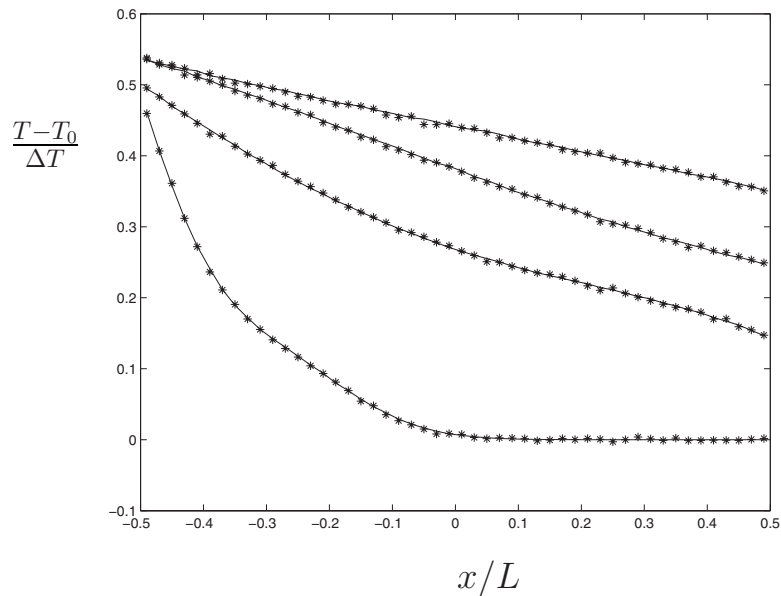


Fig. 5 Impulsive heating problem for $\varepsilon=0.1$ and $k=10$ at $t=0.02\tau_0$, $0.1\tau_0$, $0.2\tau_0$, and $0.4\tau_0$. The solid line denotes the present method, and stars denote DSMC results.

Figures 5–7 show a comparison between the two solutions for the transient evolution of the temperature field for $\varepsilon=0.1$ for $k=10$, $k=1$, and $k=0.1$, respectively. Figure 8 shows a comparison for $k=1$ and $\varepsilon=0.3$. This value of ε , which for $T_0=273$ K corresponds to $\Delta T=81.9$ K, places the deviation from equilibrium into the early nonlinear regime (previous work [5] shows that weakly nonlinear effects appear at $\varepsilon \approx 0.05$). The agreement between the two simulation approaches is excellent in all cases.

Although computational performance is always implementation dependent, an indication of the speedup achieved by the proposed method can be obtained by considering the following CPU times for calculations achieving a relative statistical uncertainty of 5% in the heat flux for $\varepsilon=0.01$: A transient variance-reduced calculation to time $t=2\tau_0$ at $k=0.1$ requires approximately 600 s on one core of a 3.0 GHz Intel Core 2 Quad processor; a calculation to

$t=0.2\tau_0$ at $k=10$ requires approximately 40 s. In contrast, with all discretization parameters the same (and thus similar memory usage), DSMC requires approximately 150,000 s to reach the same final time ($t=2\tau_0$) at $k=0.1$ and 65,000 s for $k=10$ ($t=0.2\tau_0$). The CPU times for other values of ε can be estimated by noting that for small ε , these times are independent of ε for the proposed method, while for DSMC they scale approximately as ε^{-2} . In steady-state problems—where continuous sampling after steady state is reached can be performed—the speedup will in general be smaller because in the low-variance calculations the time to reach steady state becomes an appreciable part of the total simulation time.

4.3 A Comment on Linear Conditions. The algorithm described in this paper imposes no restrictions on the magnitude of

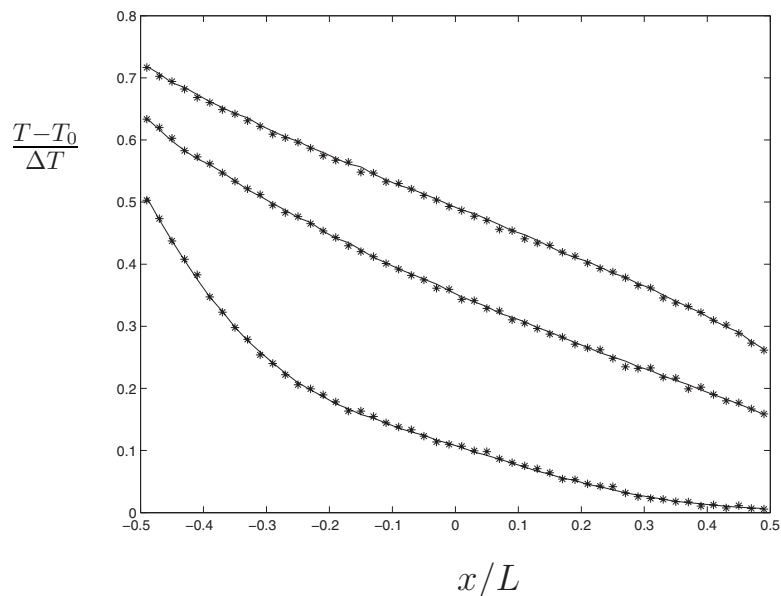


Fig. 6 Impulsive heating problem for $\varepsilon=0.1$ and $k=1$ at $t=0.4\tau_0$, $1.6\tau_0$, and $8\tau_0$. The solid line denotes the present method, and stars denote DSMC results.

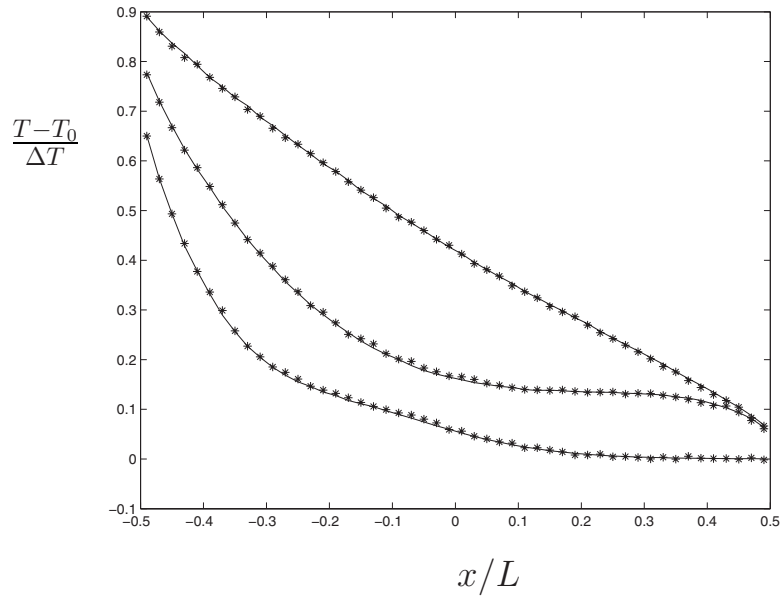


Fig. 7 Impulsive heating problem for $\varepsilon=0.1$ and $k=0.1$ at $t=4\tau_0$, $12\tau_0$, and $40\tau_0$. The solid line denotes the present method, and stars denote DSMC results.

f^d , although as discussed above, the deviational approach becomes significantly more efficient than traditional approaches when f^d is small. If f^d is sufficiently small for linearization to be appropriate, under some conditions, significant gains in computational efficiency can be achieved by considering the following. Under linear conditions, we can write

$$f^{\text{loc}} - F = F \left[\psi + 2 \frac{\hat{\mathbf{c}} \cdot \mathbf{u}_{\text{loc}}}{c_0} + \left(\hat{\mathbf{c}}^2 - \frac{3}{2} \right) \theta \right] \quad (21)$$

where $\psi = n_{\text{loc}}/n_0 - 1$, $\hat{\mathbf{c}} = \mathbf{c}/c_0$, and $\theta = T_{\text{loc}}/T_0 - 1$. This representation can be very useful for improving the computational efficiency of update (Eq. (9)). For example, for isothermal constant density flows, particles may be generated from a combination of a normal distribution and analytic inversion of the cumulative distribution function, which is significantly more efficient than acceptance-

rejection. Alternatively, Eq. (21) provides a means of obtaining bounds for $|f^{\text{loc}} - F|$, i.e., Δ_{max} , and thus reducing the number of rejections if the acceptance-rejection route is followed.

5 Conclusions

We have presented an efficient variance-reduced particle method for solving the Boltzmann equation in the relaxation-time approximation. The method combines simplicity with a number of desirable properties associated with particle methods, such as robust capture of traveling discontinuities in the distribution function and efficient collision operator evaluation using importance sampling [11], without the high relative statistical uncertainty associated with traditional particle methods in low-signal problems.

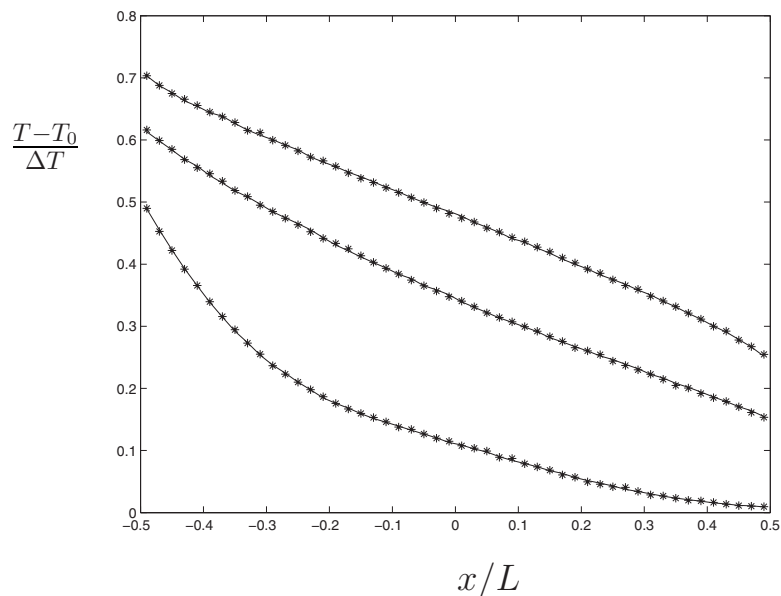


Fig. 8 Impulsive heating problem for $\varepsilon=0.3$ and $k=1$ at $t=0.4\tau_0$, $1.6\tau_0$, and $8\tau_0$. The solid line denotes the present method and stars denote DSMC results.

In particular, as shown above, the method presented here can capture arbitrarily small deviations from equilibrium at a cost that is independent of the deviation from equilibrium.

Future work will concentrate on further improving the efficiency of deviational methods. Recent work [30] shows that the ratio-of-uniforms method [31] can yield significant efficiency improvements in sampling distributions, while simulating the deviation from a spatially variable equilibrium distribution reduces the number of particles required to achieve the same statistical uncertainty.

Acknowledgment

This work was supported by the Singapore-MIT Alliance under the HPCES program.

Nomenclature

A	= surface area of the boundary
a	= acceleration due to an external field
c	= molecular velocity vector
f	= single-particle distribution function
F	= absolute equilibrium distribution
k	= Knudsen number ($=c_0\tau_0/L$)
k_B	= Boltzmann's constant
L	= plate separation
m	= molecular mass
M_{\max}	= upper bound on the difference between fluxal distributions
n	= number density
N	= number of particles
N_{eff}	= effective number of physical deviational particles per computational particle
\mathcal{N}	= number of trial particles
P	= pressure
q	= heat flux
r	= position vector in physical space
\mathcal{R}	= random number uniformly distributed on $[0,1]$
t	= time
T	= temperature
u	= flow velocity vector
$\mathcal{V}_{\text{cell}}$	= cell volume

Greek

α	= accommodation coefficient
δ_w	= distance from the wall
Δ_{\max}	= upper bound on the difference between distributions
ε	= dimensionless temperature difference ($=\Delta T/T_0$)
θ	= dimensionless temperature ($=T_{\text{loc}}/T_0-1$)
τ	= relaxation time
σ	= standard deviation
ϕ	= probability distribution function
ω	= oscillation frequency
ψ	= dimensionless density ($=n_{\text{loc}}/n_0-1$)

Subscripts and Superscripts

b	= boundary
c	= collision
d	= deviational
e	= equilibrium
fm	= free molecular
loc	= local
0	= absolute equilibrium

References

- [1] Chen, G., 2005, *Nanoscale Energy Transport and Conversion*, Oxford University Press, New York.
- [2] Majumdar, A., 1993, "Microscale Heat Conduction in Dielectric Thin Films," *ASME J. Heat Transfer*, **115**, pp. 7–16.
- [3] Chen, G., 2002, "Ballistic-Diffusive Equations for Transient Heat Conduction From Nano to Macroscales," *ASME J. Heat Transfer*, **124**, pp. 320–328.
- [4] Haji-Sheikh, A., Minkowycz, W. J., and Sparrow, E. M., 2002, "Certain Anomalies in the Analysis of Hyperbolic Heat Conduction," *ASME J. Heat Transfer*, **124**, pp. 307–319.
- [5] Manela, A., and Hadjiconstantinou, N. G., 2007, "On the Motion Induced in a Gas Confined in a Small-Scale Gap Due to Instantaneous Heating," *J. Fluid Mech.*, **593**, pp. 453–462.
- [6] Hadjiconstantinou, N. G., 2002, "Constant-Wall-Temperature Nusselt Number in Micro and Nano Channels," *ASME J. Heat Transfer*, **124**, pp. 356–364.
- [7] Hadjiconstantinou, N. G., 2003, "Dissipation in Small Scale Gaseous Flows," *ASME J. Heat Transfer*, **125**, pp. 944–947.
- [8] Hadjiconstantinou, N. G., 2006, "The Limits of Navier-Stokes Theory and Kinetic Extensions for Describing Small-Scale Gaseous Hydrodynamics," *Phys. Fluids*, **18**, p. 111301.
- [9] Hadjiconstantinou, N. G., 2000, "Analysis of Discretization in the Direct Simulation Monte Carlo," *Phys. Fluids*, **12**, pp. 2634–2638.
- [10] Frangi, A., Frezzotti, A., and Lorenzani, S., 2007, "On the Application of the BGK Kinetic Model to the Analysis of Gas-Structure Interactions in MEMS," *Comput. Struct.*, **85**, pp. 810–817.
- [11] Baker, L. L., and Hadjiconstantinou, N. G., 2005, "Variance Reduction for Monte Carlo Solutions of the Boltzmann Equation," *Phys. Fluids*, **17**, p. 051703.
- [12] Bird, G. A., 1994, *Molecular Gas Dynamics and the Direct Simulation of Gas Flows*, Clarendon, Oxford.
- [13] Peterson, R. B., 1994, "Direct Simulation of Phonon-Mediated Heat Transfer in a Debye Crystal," *ASME J. Heat Transfer*, **116**, pp. 815–822.
- [14] Mazumder, S., and Majumdar, A., 2001, "Monte Carlo Study of Phonon Transport in Solid Thin Films Including Dispersion and Polarization," *ASME J. Heat Transfer*, **123**, pp. 749–759.
- [15] Hadjiconstantinou, N. G., Garcia, A. L., Bazant, M. Z., and He, G., 2003, "Statistical Error in Particle Simulations of Hydrodynamic Phenomena," *J. Comput. Phys.*, **187**, pp. 274–297.
- [16] Baker, L. L., and Hadjiconstantinou, N. G., 2008, "Variance-Reduced Particle Methods for Solving the Boltzmann Equation," *J. Comput. Theor. Nanosci.*, **5**, pp. 165–174.
- [17] Homolle, T. M. M., and Hadjiconstantinou, N. G., 2007, "Low-Variance Deviation Simulation Monte Carlo," *Phys. Fluids*, **19**, p. 041701.
- [18] Homolle, T. M. M., and Hadjiconstantinou, N. G., 2007, "A Low-Variance Deviation Simulation Monte Carlo for the Boltzmann Equation," *J. Comput. Phys.*, **226**, pp. 2341–2358.
- [19] Cercignani, C., 1990, *Mathematical Methods in Kinetic Theory*, Plenum, New York.
- [20] Cercignani, C., 1988, *The Boltzmann Equation and Its Applications*, Springer-Verlag, New York.
- [21] Gurevich, V. L., 1986, *Transport in Phonon Systems*, North-Holland, New York.
- [22] Lundstrom, M., 2000, *Fundamentals of Carrier Transport*, 2nd ed., Cambridge University Press, Cambridge.
- [23] Davidson, B., and Sykes, J. B., 1957, *Neutron Transport Theory*, Clarendon, Oxford.
- [24] Modest, M. F., 2003, *Radiative Heat Transfer*, 2nd ed., Academic, New York.
- [25] Baker, L. L., and Hadjiconstantinou, N. G., 2008, "Variance Reduced Monte Carlo Solutions of the Boltzmann Equation for Low-Speed Gas Flows: A Discontinuous Galerkin Formulation," *Int. J. Numer. Methods Fluids*, **58**, pp. 381–402.
- [26] Sone, Y., 2002, *Kinetic Theory and Fluid Dynamics*, Birkhauser, Boston.
- [27] Bassanini, P., Cercignani, C., and Pagani, C. D., 1967, "Comparison of Kinetic Theory Analyses of Linearized Heat Transfer Between Parallel Plates," *Int. J. Heat Mass Transfer*, **10**, pp. 447–460.
- [28] Bassanini, P., Cercignani, C., and Pagani, C. D., 1968, "Influence of the Accommodation Coefficient on the Heat Transfer in a Rarefied Gas," *Int. J. Heat Mass Transfer*, **11**, pp. 1359–1369.
- [29] Manela, A., and Hadjiconstantinou, N. G., 2008, "Gas Motion Induced by Unsteady Boundary Heating in a Small-Scale Slab," *Phys. Fluids*, **20**, p. 117104.
- [30] Radtke, G. A., and Hadjiconstantinou, N. G., 2009, "Variance-Reduced Particle Simulation of the Boltzmann Transport Equation in the Relaxation-Time Approximation," *Phys. Rev. E*, **79**, p. 056711.
- [31] Wakefield, J. C., Gelfand, A. E., and Smith, A. F. M., 1991, "Efficient Generation of Random Variables via the Ratio-of-Uniforms Method," *Stat. Comput.*, **1**, pp. 129–133.

Magnus Fischer
Laboratory of Thermodynamics in Emerging
Technologies,
Institute of Energy Technology,
Department of Mechanical and Process
Engineering,
ETH Zürich,
8092 Zürich, Switzerland

Damir Juric
Laboratoire d'Informatique pour la Mécanique et
les Sciences de l'Ingénieur (LIMSI),
Centre National de la Recherche Scientifique
(CNRS),
UPR 3251, BP 133,
91403 Orsay Cedex, France

Dimos Poulikakos¹
Laboratory of Thermodynamics in Emerging
Technologies,
Institute of Energy Technology,
Department of Mechanical and Process
Engineering,
ETH Zürich,
8092 Zürich, Switzerland
e-mail: dimos.poulikakos@ethz.ch

Large Convective Heat Transfer Enhancement in Microchannels With a Train of Coflowing Immiscible or Colloidal Droplets

We show that heat transfer in microchannels can be considerably augmented by introducing droplets or slugs of an immiscible liquid into the main fluid flow. We numerically investigate the influence of differently shaped colloidal or simply pure immiscible droplets to the main liquid flow on the thermal transport in microchannels. Results of parametric studies on the influence of all major factors connected to microchannel heat transfer are presented. The effect of induced Marangoni flow at the liquid interfaces is also taken into account and quantified. The calculation of the multiphase, multispecies flow problem is performed, applying a front tracking method, extended to account for nanoparticle transport in the suspended phase when relevant. This study reveals that the use of a second suspended liquid (with or without nanoparticles) is an efficient way to significantly increase the thermal performance without unacceptably large pressure losses. In the case of slug-train coflow, the Nusselt number can be increased by as much as 400% compared with single liquid flow. [DOI: 10.1115/1.4002031]

Keywords: nanofluid, colloidal suspensions, thermal transport, Marangoni effect, droplet-laden flow, segmented flow, immiscible fluids

1 Introduction

Thermal management of microelectronic devices becomes more important and challenging as size is reduced and power density (converted to heat) increases. The demand of fast removal of the produced heat in microscale devices such as microprocessors or even microfuel cells stimulates growing research activities in the field of liquid cooling [1–4]. Among various techniques to improve the cooling performance in microchannels, we mention two promising approaches.

One employs engineered fluids, such as colloids consisting of a base fluid in which solid particles of sizes of 10–50 nm are dissolved. The thermal conductivity of such “nanofluids” can be significantly improved compared with the base fluid at concentrations of a few percent per volume, but at the expense of a corresponding increase in viscosity. Depending on particle size and concentration, the effective thermal conductivity of those fluids can be increased by as much as 10–40% [5,6] although the degree of improvement and the reasons behind it are still issues of debate [7]. For example, Lee et al. [6] reported in their study a 10% heat transfer enhancement using a suspension of Al_2O_3 particles of 38 nm in diameter at a concentration of 4.5% in distilled water. For detailed reviews on the thermal transport connected to nanofluids, see Keblinski et al. [8], Wang and Mujumdar [9], Yu et al. [10], and Buongiorno et al. [11].

Another option to improve cooling exploits the fact that the heat removal rate from a microchannel wall in organized bubble flows is higher than in single phase flows. In the presence of immersed bubbles, the thermal transport is augmented by a blockage effect in front of the bubbles and recirculation in their wake. Lakehal et al. [12] and Fukagata et al. [13] showed numerically that in the case of gas-liquid flow, the heat transfer is three to four

times higher than in pure water flow. Recently, a numerical study by Urbant et al. [14] on liquid-liquid flow indicated a similar trend. The number of experimental studies on heat transfer augmentation in two-liquid flows but also on two-phase gas-liquid flows in microchannels is limited. For example, Monde and Mitsutake [15] reported experiments on enhanced heat transfer in bubbly flow through small scale channels.

The present work aims at taking advantage of both the above-mentioned approaches by introducing immiscible pure or colloidal droplets into the liquid flow in a microchannel. In addition to a significant increase in the cooling performance, this approach is expected to result in a decrease in the undesirable pressure drop associated with the colloidal suspensions (nanofluids). The effect of noncolloidal droplets is also investigated.

Spherical or elongated nanofluid droplets are introduced at the entrance region of the channel into the base fluid. The flow around the droplets develops as they travel further downstream. There exist different methods to experimentally establish liquid-liquid droplet-laden flows. Those are, for example, flow or hydrodynamic focusing techniques [16,17], T- and Y-junctions [18–20], or concentric injection [21]. Cubaud and Mason [17] used a flow focusing device to produce liquid emulsions in a 100 μm wide microchannel. They reported on different flow patterns based on the capillary number of each fluid. The flow parameters and channel sizes in the presented study are in the range of the abovementioned experiments.

The goal of this paper is to numerically investigate all important aspects related to immiscible and colloidal droplet-laden two-fluid flow through heated microchannels. Through parametric studies, we assess the influence of different flow conditions (e.g., velocity and radius), liquid systems of water in oil and oil in water emulsions, and the presence of nanoparticles on the cooling performance of the channel. This is reported by the calculated local and overall Nusselt number. The model presented includes all relevant thermophysical phenomena such as Marangoni effects

¹Corresponding author.

Contributed by the Heat Transfer Division of ASME for publication in the JOURNAL OF HEAT TRANSFER. Manuscript received November 30, 2009; final manuscript received May 3, 2010; published online August 13, 2010. Assoc. Editor: Satish G. Kandlikar.

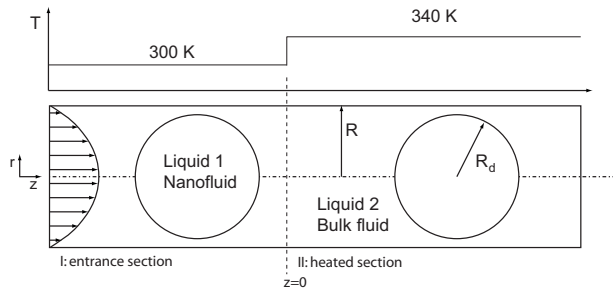


Fig. 1 The physical system under consideration. In the isothermal section of the microchannel, the droplets (liquid 1) are immersed into the base fluid (liquid 2).

caused by variable surface tension due to temperature gradients at the liquid-liquid interface as well as nanoparticle motion within the droplet.

A two component mixture model is applied to account for the convective and diffusive nanoparticle transport within the nanofluid droplet [22,23]. This model includes thermophoresis due to temperature gradients and Brownian diffusion, which are the major slip mechanisms causing nanoparticle transport relative to the embedding liquid.

In order to keep track of the interface between the droplets and the base fluid, a front tracking method is employed [24]. There exist several methods for dealing with two-phase flows, such as volume of fluid [25], level set [26], phase field [27], front tracking [28], or lattice Boltzmann methods [29,30]. Lakehal et al. [12] and Fukagata et al. [13], for example, employed a level set approach to calculate thermal two-phase flow in microchannels. Urbant et al. [14] used the volume of fluid method, although by applying interfacial tension values of only 5 mN m^{-1} .

Rather high interfacial tension values (40 mN m^{-1}) resulting in capillary numbers of $O(10^{-4})$ as well as high viscosity ratios in our simulation dictate the need for an accurate and reliable algorithm for calculating the interfacial forces. The accurate calculation of surface tension force becomes a major issue especially in flows, where capillary forces are the dominant physical mechanism [31]. In a conventional volume of fluid methods applying the continuous surface force (CSF) model [32] can lead to nonphysical, spurious currents [31]. In front tracking, spurious currents remain a rather small issue. However, to further suppress those numerical artifacts and to be able to calculate at even smaller capillary numbers, we apply a hybrid surface tension calculation method [24]. In this method, the solution of the interface curvature is based on the classical Lagrangian front tracking approach, and the surface tension force is calculated based on the Eulerian approach used in the level set and volume of fluid methods.

In the following section, the physical model and the governing transport equations for multiphase flow as well as an additional equation describing the convective and diffusive transport of nanoparticles in the colloid are introduced. The solution procedure and dimensionless groups relevant for thermal transport in microchannels are presented in Sec. 3. Results of the calculations as well as parametric studies on the heat transfer can be found in Sec. 4, followed by concluding remarks in Sec. 5.

2 Problem Definition

The microchannel under investigation is presented in Fig. 1. Liquid droplets of different sizes and elongation are immersed into the base fluid at the entrance region. The droplets are immersed by changing the physical properties in the circular region enclosed by the droplet surface. In the first part of the channel, the flow around the droplets develops as they are moving with the base fluid further downstream. The interface between the droplet and its surrounding liquid is freely deformable. Once the flow field is fully developed, the droplets enter the “thermal section” in

the second part of the channel. Here, the channel wall is heated, and we investigate the heat transfer to the two fluid flow. For a single fluid, the flow through the cylindrical channel would follow the well known Graetz problem of a thermally developing and hydrodynamically fully developed laminar flow [33]. To conserve computational time, we set the boundary conditions at the inlet to a fully developed Hagen–Poiseuille flow profile. The temperature distribution along the channel wall follows a step function. In the first isothermal section, the wall temperature is equal to the temperature of the liquid, and after six channel radii it is increased to 340 K and is kept at this value thereafter. The length of the channel is 26 radii in order to capture all phenomena present in the thermal entrance region.

The fluid in the droplets is either pure silicone oil, water, or a nanofluid consisting of nanoparticles and a solvent, in our case either polyalphaolefine (PAO) or water. The droplets are surrounded by the bulk fluid, which is, depending on the liquid within the droplet, either pure water or silicone oil. In the following, the fluid inside the droplets will be denoted as liquid 1 and the bulk fluid as liquid 2. The channel diameter is varied between 0.1 mm and 1 mm, and the initial radius of the droplets was chosen to be 0.8 channel radii. In case of slug flow, the initial radius of the cylindrical part of the elongated droplets was set to 0.95 channel radii. The initial distance between two subsequent droplets was set equal to 3.7 channel radii for spherical droplets and 2.5–3 channel radii for elongated droplets. The mean velocity in the channel ranges from 1 cm/s to 10 cm/s. These values are in the same range as reported in experiments of liquid-liquid flow [16–21]. The resulting Reynolds numbers ($Re_i = v_0 \rho_i R_0 / \mu_i$) between 1.0×10^{-2} and 100 indicate the purely laminar regime of the fluid flow. The strong influence of surface tension on the flow can be seen by the Weber number ($We_i = \rho_i R_0 v_0^2 / \sigma_0$) being as low as $1.1 \times 10^{-4} - 1.9 \times 10^{-1}$. The Peclet number ($Pe_i = Re_i Pr_i$) varies between 3.5 and 700.

The problem is solved using one set of continuity equations for the entire domain both inside and outside the droplets and is modeled as 2D axisymmetric. Both liquids are treated as incompressible with no external body forces as the influence of gravity can be regarded as negligible. This is justified by the fact that the Bond number is well below unity ($\Delta \rho g R_0^2 / \sigma \ll 1$).

With the abovementioned assumptions, the continuity and Navier–Stokes equations for the entire physical domain read

$$\nabla \cdot \mathbf{v} = 0 \quad (1)$$

$$\rho \left[\frac{\partial \mathbf{v}}{\partial t} + \mathbf{v} \cdot \nabla \mathbf{v} \right] = -\nabla p + \nabla \cdot \mu [\nabla \mathbf{v} + \nabla \mathbf{v}^T] + \mathbf{F} \quad (2)$$

where ρ and μ are the density and viscosity of the liquids. The last term in Eq. (2) accounts for the interfacial tension force, which can be calculated as

$$\mathbf{F} = \int_{S'(t)} (\sigma \kappa \mathbf{n} + \nabla_s \sigma) \delta(\mathbf{x} - \mathbf{x}') dS \quad (3)$$

In Eq. (3), σ and κ denote the temperature-dependent interfacial tension and the curvature of the freely deformable interface. \mathbf{n} is the normal to the interface, ∇_s is the tangential gradient operator and the Dirac distribution, $\delta(\mathbf{x} - \mathbf{x}')$ localizes the effects of the surface tension to the interface, and $S'(t)$ is defined by \mathbf{x}' . Contrary to the CSF method, the calculated curvature κ is related to the actual physical curvature of the Lagrangian interface [24]. The interfacial tension is calculated, assuming a linear dependence on temperature:

$$\sigma(T) = \sigma_0 + \sigma_T T \quad (4)$$

where σ_0 denotes the interfacial tension at a given temperature T_0 and $\sigma_T = -d\sigma/dT$ is the temperature coefficient.

The nanoparticle continuity and energy equations are derived from Buongiorno [22]. Here, the mixture of nanoparticles and its solvent is treated as a single phase, and the nanofluid is considered to be a dilute mixture. Brownian diffusion and thermophoresis, which is the particle motion under the influence of a thermal gradient, are the only relevant slip mechanisms for nanoparticle transport in laminar flow. They are incorporated into the nanoparticle transport equation as follows:

$$\frac{\partial \phi}{\partial t} + \mathbf{v} \cdot \nabla \phi = \nabla \cdot \left[D_B \nabla \phi + D_T \frac{\nabla T}{T} \right] \quad (5)$$

where ϕ denotes the particle volume fraction. Brownian diffusion and thermophoresis are described by the first and second terms on the right hand side, respectively. D_B and D_T are the Brownian and the temperature-dependent thermal diffusion coefficient, respectively. In the nanofluid, the coefficients can be calculated as [22]

$$D_B = \frac{k_B T}{3\pi\mu d_p}, \quad D_T = \beta \frac{\mu}{\rho} \phi \quad (6)$$

where k_B denotes Boltzmann's constant and β is a proportionality factor. In the bulk fluid (liquid 2), both diffusion coefficients are set to zero.

In the presence of nanoparticles, the energy equation takes the form

$$\rho c \left[\frac{\partial T}{\partial t} + \mathbf{v} \cdot \nabla T \right] = \nabla \cdot k \nabla T + \rho_p c_p \left[D_B \nabla \phi \cdot \nabla T + D_T \frac{\nabla T \cdot \nabla T}{T} \right] \quad (7)$$

Here, ρ_p and c_p are the nanoparticle density and specific heat. The entire term in brackets on the right hand side accounts for thermal transport due to particle motion. An order of magnitude analysis reveals that this term is negligible, and the energy equation becomes identical to the one of a pure fluid [22]. From this follows that the nanoparticles affect the heat transfer in the nanofluid only by their influence on the thermophysical properties.

The spatial distribution of the property fields in the entire physical domain can be calculated using the indicator function I . The calculation of I is presented in Ref. [24]. This function is 1 inside the droplet and zero in the bulk fluid. For example, for the density field it follows that

$$\rho(\mathbf{x}, t) = \rho_2 + (\rho_1 - \rho_2)I(\mathbf{x}, t) \quad (8)$$

where ρ_1 and ρ_2 are the densities of the nanofluid and the bulk fluid, respectively. The dynamic viscosity, thermal conductivity, and specific heat can be determined using the same approach. The spatial distribution of the diffusion coefficients is calculated using the same approach. By setting the diffusion coefficients in liquid 2 identical to zero and following Eq. (8), one obtains

$$D_B(\mathbf{x}, t) = D_{B,1}I(\mathbf{x}, t) \quad (9)$$

$$D_T(\mathbf{x}, t) = D_{T,1}I(\mathbf{x}, t)$$

The property field varies not only between the two liquids but also within the nanofluid (liquid 1) as it is a function of particle concentration. The density and specific heat of the nanofluid can be calculated using standard mixture laws [34]:

$$\rho_1 = \phi \rho_p + (1 - \phi) \rho_s \quad (10)$$

$$c_1 = \frac{\phi c_p \rho_p + (1 - \phi) c_s \rho_s}{\rho_1}$$

ρ_s and ρ_p denote the density of the solvent and the particles, respectively. There is still a lack of accurate theoretical models for the prediction of the viscosity and thermal conductivity of nanofluids. From measurements by Pak and Cho [35], the following correlations for the viscosity and thermal conductivity of alumina nanoparticles dissolved in water can be derived [22]:

$$\mu_1 = \mu_s(1 + 39.11\phi + 533.9\phi^2) \quad (11)$$

$$k_1 = k_s(1 + 7.47\phi) \quad (12)$$

For alumina particles in PAO, the viscosity and thermal conductivity can be correlated as follows [36]:

$$\mu_1 = \mu_s(1 + 18.8\phi) \quad (13)$$

$$k_1 = k_s(1 + 4.97\phi) \quad (14)$$

3 Numerical Solution

In order to facilitate the numerical simulation and to investigate the influence of the different characteristic groups, the following dimensionless scales are introduced:

$$\mathbf{u} = \frac{\mathbf{v}}{v_0}, \quad \Phi = \frac{\phi}{\phi_0}, \quad \theta = \frac{T - T_0}{\Delta T} \quad (15)$$

$$\varphi = \frac{p}{\rho_2 v_0^2}, \quad x = \frac{r}{R_0}, \quad \tau = t \frac{v_0}{R_0}$$

where v_0 , ϕ_0 , R_0 , T_0 , and ΔT are the mean velocity at the inlet of the channel, the initial nanoparticle concentration in the nanofluid, the channel radius, the initial temperature, and the temperature scale, respectively. With those transformations, the governing Eqs. (1), (2), (5), and (7) read

$$\nabla \cdot \mathbf{u} = 0 \quad (16)$$

$$\frac{\partial \mathbf{u}}{\partial \tau} + \mathbf{u} \cdot \nabla \mathbf{u} = -\frac{1}{\rho^*} \nabla \varphi + \frac{1}{\rho^* \text{Re}_2} \nabla \cdot \mu^* [\nabla \mathbf{u} + \nabla \mathbf{u}^T] + \frac{\mathbf{F}}{\rho^* \text{We}_2} \quad (17)$$

$$\frac{\partial \Phi}{\partial \tau} + \mathbf{u} \cdot \nabla \Phi = \frac{1}{\text{Re}_2 \text{Sc}_2} \left[\nabla \cdot I \nabla \Phi + \nabla \cdot \frac{I}{N_{BT}} \nabla \theta \right] \quad (18)$$

$$\frac{\partial \theta}{\partial \tau} + \mathbf{u} \cdot \nabla \theta = \frac{1}{\text{Re}_2 \text{Pr}_2} \frac{1}{\rho^* c^*} \nabla \cdot k^* \nabla \theta \quad (19)$$

The physical properties in Eqs. (16)–(18) are brought in dimensionless form with the values of the continuous phase (liquid 2). For both phases (liquids 1 and 2), we introduced the following dimensionless groups: the Reynolds, Schmidt, Prandtl, and Weber numbers as well as N_{BT} , which is the characteristic number for thermophoretic particle motion,

$$\text{Re}_i = \frac{v_0 \rho_i R_0}{\mu_i}, \quad \text{Sc}_i = \frac{\mu_i}{\rho_i D_B}, \quad \text{Pr}_i = \frac{c_i \mu_i}{k_i} \quad (20)$$

$$\text{We}_i = \frac{\rho_i R_0 v_0^2}{\sigma_0}, \quad N_{BT} = \frac{\rho_i D_B T_0}{\beta \mu_i \Delta T}$$

Two additional dimensionless numbers are used later on. These are the capillary number and the Peclet number:

$$\text{Ca}_i = \frac{v_0 \mu_i}{\sigma_0}, \quad \text{Pe}_i = \frac{\rho_i v_0 c_i R_0}{k_i} \quad (21)$$

The problem is solved by means of a finite difference scheme with uniform grid spacing on a staggered mesh. The diffusive terms are approximated using second order central differences. For the convective terms, a second order essentially nonoscillating (ENO) scheme is applied [37]. In this scheme, the discretization of the convective terms is a mixture of an upwind and a central differencing scheme depending on the properties of the flow in a computational cell. A second order implicit scheme is used for the temporal discretization. For the solution of the transport equations, the biconjugate gradient stabilized algorithm (BiCGStab) is applied [38]. The convergence criterion on the maximal residuals

Table 1 Physical properties of the liquids and the Al₂O₃ nanoparticles used in the calculations. ρ , μ , k , and c are the density, dynamic viscosity, thermal conductivity, and specific heat.

Fluid/solid	ρ (kg m ⁻³)	μ (Pa s)	k (W m ⁻¹ K ⁻¹)	c (J kg ⁻¹ K ⁻¹)	Ref.
Water	1.0 × 10 ³	1.0 × 10 ⁻³	6.0 × 10 ⁻¹	4.2 × 10 ³	-
Silicone oil (5 cS)	9.1 × 10 ²	4.6 × 10 ⁻³	1.2 × 10 ⁻¹	1.5 × 10 ³	[40]
PAO	8.0 × 10 ²	5.0 × 10 ⁻³	1.3 × 10 ⁻¹	2.3 × 10 ³	[41]
Al ₂ O ₃	4.0 × 10 ³	-	4.0 × 10 ¹	7.7 × 10 ²	[42]

was set to 1.0×10^{-7} . Grid independence of the solution of the temperature, velocity, and pressure field as well as the mean droplet velocities was ensured in parametric studies, resulting in an optimal number of 30×990 grid cells. In order to save computational costs, the time step size was varied between 1.0×10^{-4} and 1.0×10^{-2} during the calculations.

A detailed description of the numerical schemes connected to the front tracking method can be found in Ref. [24]. The front tracking program and numerical algorithms used herein were previously thoroughly validated in different numerical studies [24,39].

4 Results and Discussion

The heat transfer in the fluid was investigated for different flow conditions and fluid systems. The fluids used in this study are water, 5 cS silicone oil, and PAO. The nanofluid in the droplet is a mixture of Al₂O₃ nanoparticles suspended in either water or PAO. The initial volumetric concentration of particles in the solvent is 3%. The fluid properties used herein are presented in Table 1.

Interfacial tension values of the water-silicone oil system were estimated based on the model of Girifalco and Good [43] combined with literature values of the pure and combined phases [44,40]. This results in an interfacial tension of 38 mN m⁻¹ at 300 K and a temperature coefficient σ_T of 0.06 mN m⁻¹ K⁻¹. Due to the lack of clear data for interfacial tension, the same values were chosen for water-PAO as well. Reliable data do not exist for the interfacial tension between nanofluids of Al₂O₃ particles and water or silicone, to the best of our knowledge. However, Murshed et al. measured experimentally the temperature-dependent interfacial tension of TiO₂-water nanofluids in oil [45]. In their study, they reported a significantly reduced interfacial tension in the presence of nanoparticles. Following their results, we reduced the interfacial tension in the presence of nanoparticles by 25%.

We identified the Reynolds number, the capillary number ($Ca_i = We_i / Re_i$), and the Peclet number ($Pe_i = Re_i Pr_i$) in both liquids as well as the viscosity ratio μ_1 / μ_2 as being the relevant dimensionless groups, which determine the thermal transport in microchannels. The heat transfer can be expressed in terms of the local Nusselt number in the axial direction, which is defined as

$$Nu_z = \frac{2R_0 q|_{wall,z}}{k(T_b - T_{wall,z})} = \frac{2 \partial \theta / \partial x|_{wall,z}}{(\theta_{wall,z} - \theta_b)} \quad (22)$$

R_0 , T_b , and θ_b are the pipe radius and the dimensional and dimensionless local bulk mean temperatures, respectively. The local bulk mean temperature can be calculated in accordance with Ref. [46] as

$$\theta_b = \frac{\int_0^1 \rho^* c^* u_z \theta dx}{\int_0^1 \rho^* c^* u_z dx} \quad (23)$$

In Eq. (23), all fluid properties as well as the temperature and the axial velocity are a function of the radial position. The calculated

local Nusselt number for single liquid flow can be validated with an approximated solution of the Graetz problem. In the case of constant wall temperature, the Nusselt number in the early part of the thermal entrance region can be approximated as [47]

$$Nu = 1.357 \left(Pe \frac{R_0}{z} \right)^{1/3} \quad (24)$$

The calculated results and the Nusselt number obtained from Eq. (24) are plotted in Fig. 2, showing good agreement. Slight differences at the entrance region are caused by the fact that the approximated solution, Eq. (24), is obtained by neglecting axial diffusion and by linearizing the velocity near the wall.

The local Nusselt number in the axial direction for a point in time along with the temperature distribution for a flow of nanofluid droplets (PAO and Al₂O₃ particles) in water is depicted in Fig. 2 as well. Here, the mean inlet velocity v_0 was set to 10 cm/s, and the channel radius was 500 μ m. This results in a Reynolds number of 50 and a capillary number of 3.6×10^{-3} in the bulk fluid. Compared with single liquid flow, the Nusselt number is significantly higher in the present two-liquid flow arrangement.

In the presence of liquid droplets, the local Nusselt number exhibits two peaks: in the bulk liquid in front of the droplet and in the rear of the droplet. The droplets move 1.2 times faster than the bulk fluid. Thus, a recirculation zone develops between the droplets. In the wake of the droplets, the Nusselt number decays, as cold fluid is pulled toward the tail. In front of the droplets, a blockage effect occurs, and hot fluid is transported from the wall toward the center of the channel. In this region, the Nusselt number increases and exhibits the maximum value of 12. The second, lower peak in the rear of the droplets is caused by slight recirculation within the droplet, as shown in Fig. 3.

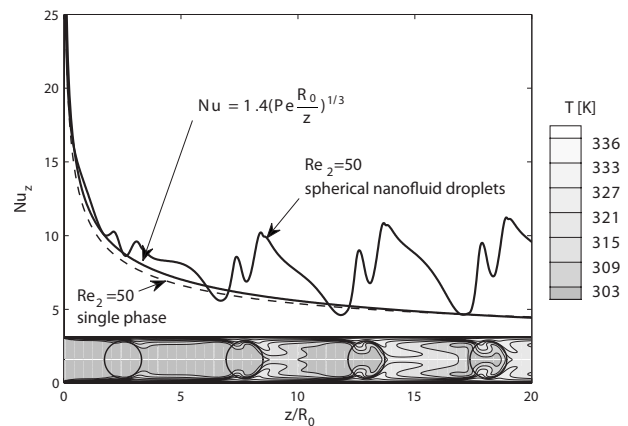


Fig. 2 Local Nusselt number and temperature field in the axial direction for liquid-liquid flow with spherical droplets. The liquids used are water as the base fluid (liquid 1) and PAO and Al₂O₃ nanoparticles as the suspended liquid (liquid 2). The dashed line compares to the Nusselt number of a single liquid flow of water. The solid line shows the approximate solution for the Nusselt number (Eq. (24)).

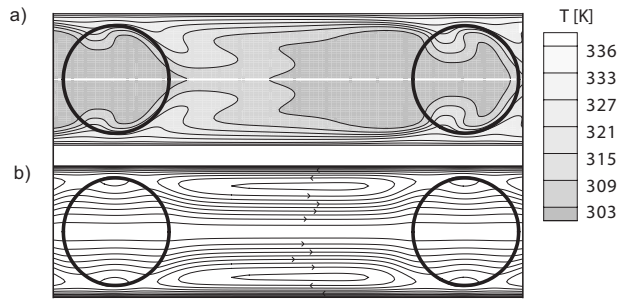


Fig. 3 (a) Temperature field and (b) streamlines in a moving reference frame for nanofluid droplet-laden flow. The liquids used are water as the base fluid (liquid 1) and PAO and Al_2O_3 nanoparticles as the suspended liquid (liquid 2).

To explore the influence of the recirculation on the wall thermal layer, streamlines and the temperature distribution of both cases are depicted in Fig. 3. The wall temperature was set to 340 K. Dark areas represent lower temperature values. The streamlines are plotted in a reference frame moving with the fluid flow (Fig. 3(b)). In Fig. 3(a), it can be seen that the wall thermal layer is affected at two distinct positions. In front of the droplet, hot fluid from the wall is dragged with the circulating flow toward the center of the channel. Here, the circulating flow between the two droplets, indicated by the velocity vectors, affects the thermal transport. Within the droplet, the recirculation is less pronounced. However, the wall thermal layer is disturbed in the rear of the droplets, where convective transport away from the channel wall takes place.

The Nusselt number can be further increased by establishing an elongated droplet or slug flow in the channel (Fig. 4). As in the previous case, the liquids are chosen to be water (main flow) and a nanofluid of PAO and Al_2O_3 . The velocity and the channel radius are the same as in Figs. 2 and 3. Compared with the case with only spherical droplets, a further rise of the Nusselt number can be detected. The Nusselt number triples compared with single liquid flow. Peak values are as high as 25. Due to the higher blockage effect, the recirculation inside and between the slugs is more pronounced. The profile exhibits again two peaks in front and in the wake of the slugs, where the wall thermal layer is affected. The decreased heat transfer within the droplets is a reason of the lower specific heat and thermal conductivity of the nanofluid compared with the aqueous bulk fluid.

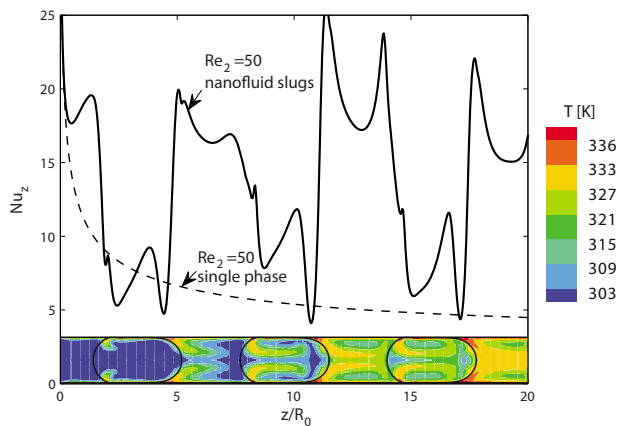


Fig. 4 Local Nusselt number and the temperature field in the axial direction for liquid-liquid flow with elongated droplets. The liquids used are water as the base fluid (liquid 1) and PAO and Al_2O_3 nanoparticles as the suspended liquid (liquid 2). The dashed line compares to the Nusselt number of a single liquid flow of water.

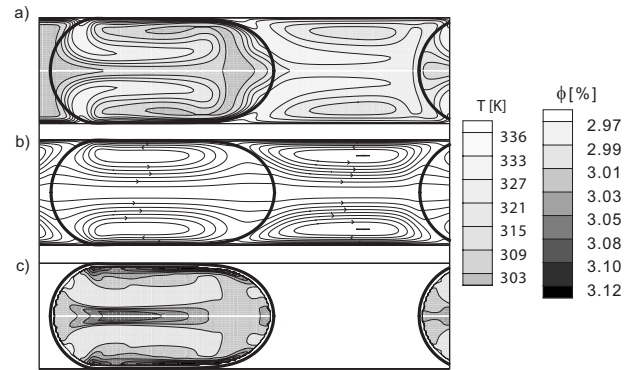


Fig. 5 (a) Temperature field), (b) streamlines in a moving reference frame, and (c) the particle concentration for liquid slug flow. The liquids used are water as the base fluid (liquid 1) and PAO and Al_2O_3 nanoparticles as the suspended liquid (liquid 2).

In slug flow, vortices within and between the droplets are more pronounced (Fig. 5(b)). The wall thermal layer is affected at the same positions as in the case of spherical droplets (Fig. 5(a)). However, the convective thermal transport is noticeably higher. The particle distribution within the slugs is depicted in Fig. 5(c). High particle concentrations are illustrated by dark colors. It can be seen that the particles accumulate at two areas, close to the interface at the channel wall and in a small band at the centerline of the droplet. The distribution of the particle concentration exhibits the same swirly pattern as the temperature field. This indicates that the particles are transported in a convective manner along the fluid flow in the elongated droplet. Due to the predominantly convective transport, the particles are transported toward the interface close to the hot channel wall. At the center of the droplet, a second effect can be identified: Here, the particles experience a thermophoretic force, pushing them toward the region of the centerline where they accumulate due to the lower fluid temperature. Since concentration gradients are smoothed out by the counteracting Brownian diffusion, both effects are rather small. Depending on the position of the slug, the particle concentration is only changed by 0.5–5%.

The influence of varying Reynolds numbers on the heat transfer is shown in Fig. 6, where the local Nusselt number, averaged over time, Nu_z in the axial direction for different flow conditions is

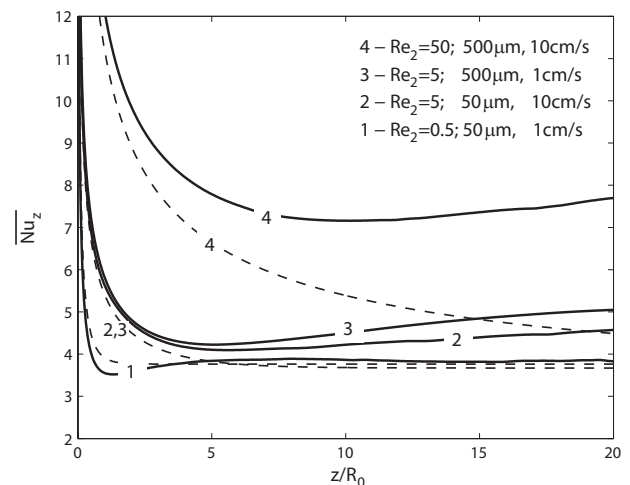


Fig. 6 Temporally averaged Nusselt number for different channel radii and velocities. The liquid in the droplet (liquid 1) is 5 cS silicone oil. It is surrounded by water (liquid 2). The dashed lines indicate the solution for aqueous single liquid flow.

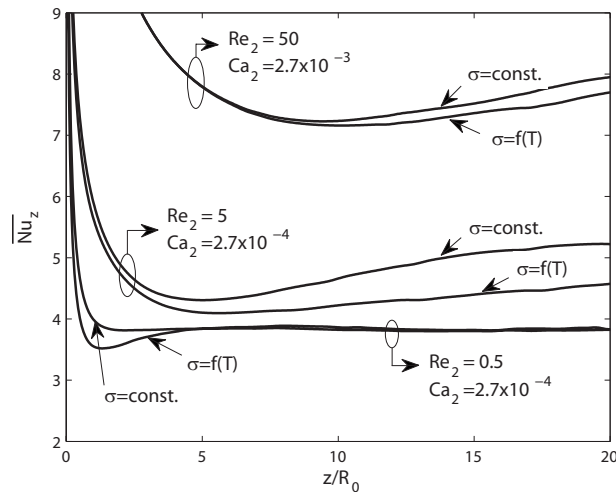


Fig. 7 Nusselt number distribution for different cases with constant surface tension ($\sigma = \sigma_0$) compared with calculations, where the Marangoni effect is included ($\sigma = f(T)$). The liquid in the droplet (liquid 1) is 5 cS silicone oil, surrounded by water (liquid 2).

depicted. The Nusselt number is averaged over the time period, a train of ten droplets needs to move through the channel. After the first droplet has left the channel, a quasi-steady-state has been reached. For the cases shown here, the liquid within the droplets is 5 cS silicone oil surrounded by water. The mean inlet velocity and the channel radius are varied between 1 cm/s and 10 cm/s and 50 μm and 500 μm , respectively. Compared with single liquid flow (dashed lines), a higher cooling performance can be detected for all cases. At high Reynolds numbers ($Re_2 = 50$), the Nusselt number nearly doubles. Also, for lower Reynolds numbers, a significant augmentation can be detected. Cases 2 and 3 reveal that not only the Reynolds and Peclet numbers have an influence on the heat transfer performance of the microchannel. Both the Peclet and Reynolds numbers are identical in these cases ($Re_2 = 5$, $Pe_2 = 35$). Different capillary numbers ($Ca_2 = 2.7 \times 10^{-4}$ for case 2; $Ca_2 = 2.7 \times 10^{-3}$ for case 3) show that the influence of the surface tension cannot automatically be neglected in micro scale heat transfer devices. For cases 2–4, the Nusselt number increases until the end of the channel ($z/R_0 = 20$). This nonmonotonic behavior is caused by the fact that the droplet flow affects the thermal wall layer. As will be seen later, this effect is even stronger for slug flow (Fig. 10). For low Reynolds numbers, $Re_2 = 0.5$ in the bulk fluid and $Re_1 = 0.1$ in the droplet, the profile exhibits an initial dent at the thermal entrance region, case 1 in Fig. 6. This dent can be explained by Marangoni effects. The initially high surface tension gradients, along the interface between the liquids at the entrance region, result in a Marangoni force. This force acts against the circulating flow at the interface of the droplets, as fluid is pushed toward regions with lower temperature. The low capillary numbers for the droplet ($Ca_1 = 1.2 \times 10^{-3}$) and the bulk fluid ($Ca_2 = 2.7 \times 10^{-4}$) emphasize this strong influence of surface tension Marangoni forces.

For higher Reynolds numbers, the Marangoni effect cannot be neglected either. This can be seen in Fig. 7, where calculations applying constant interfacial tension are compared with runs with temperature-dependent interfacial tension. The latter are identical to cases 1, 3, and 4 in Fig. 6. For all Reynolds number regimes, the Nusselt number is higher when constant interfacial tension is assumed. It follows that the Marangoni effect, i.e., the dependency of interfacial tension on temperature, decreases the heat transfer performance of microchannel two-liquid flow. The Marangoni force resulting from temperature gradients at the interface counteracts the swirling motion of the fluid flow.

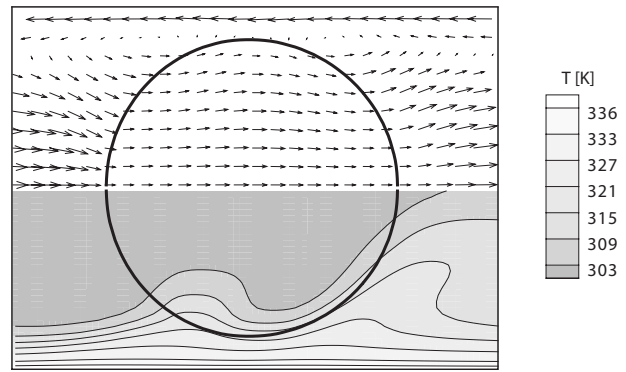


Fig. 8 Velocity vectors in a moving reference frame (top) and temperature field (bottom) around a single spherical droplet

This effect can be explained with the help of Fig. 8. The temperature gradient near the channel centerline in front and at the rear of the droplet results in a variation of the temperature-dependent surface tension (bottom half of Fig. 8). At both ends of the droplet, the gradient in surface tension causes a Marangoni force at the interface, which directs fluid toward the centerline of the channel. In front of the droplet, this force aids the rotational motion of the fluid outside the droplet (indicated by the velocity vectors in the top half of Fig. 8). However, in the rear of the droplet, a steeper temperature gradient results in a higher Marangoni force counteracting the rotational motion of the surrounding fluid toward the channel wall. The net result of both effects is a decreased rotational motion of the fluid in between two sequential droplets. For moderate Reynolds numbers of 5, this effect is rather high; here, the Nusselt number change is 13%. For Reynolds numbers of 50, a 4% change can still be detected. In the case of low Reynolds numbers ($Re_2 = 0.5$), the temperature gradients decrease already after four to five radii. Therefore, the Marangoni force only plays a role at the very beginning of the entrance region. In all cases, shown here the Nusselt number remains significantly higher than that of single liquid flow.

The positive influence of nanoparticles on the heat transfer performance in microchannels is shown in Fig. 9. In Fig. 9(a), the bulk fluid is 5 cS silicone oil, in which spherical water droplets are immersed. In Fig. 9(b), similar results are shown for slugs of polyalphaolefine in water. In both cases, the Reynolds numbers are chosen to vary between 5 and 50. To assess the influence of nanoparticles, Al_2O_3 particles are suspended into the droplet liquid. In Fig. 9(a), it can be seen that in the presence of nanoparticles, the local Nusselt number increases by 3–5% compared with the case of pure fluids. Here, the augmentation effect of nanoparticles increases for higher Reynolds numbers. As already mentioned earlier, the surface tension of nanofluids is smaller compared with pure fluids. This results in somewhat higher capillary numbers, supporting the effect of nanoparticles on the heat transfer. To further investigate this phenomenon, we performed calculations, where the surface tension was kept the same (Fig. 9(b)). Here, the Nusselt number only increases by 1.5% in the presence of nanoparticles. It can be concluded that the nanoparticles mainly improve the thermal transport by lowering the effective interfacial tension of the droplets. The positive effect caused by increased thermal properties, such as thermal conductivity or specific heat, is marginal.

The peaks in the profiles of the temporally averaged Nusselt number in Fig. 9(b) are caused by the strong impact of slug flow on the thermal wall layer. First, when entering the heated section of the channel, the colder slug pushes the hot liquid of the wall thermal layer away. Due to the strong recirculation within and between subsequent slugs, hot liquid is transported toward the centerline of the flow. At the same time, cold fluid from the centerline region flows toward the hot wall, causing steep temperature

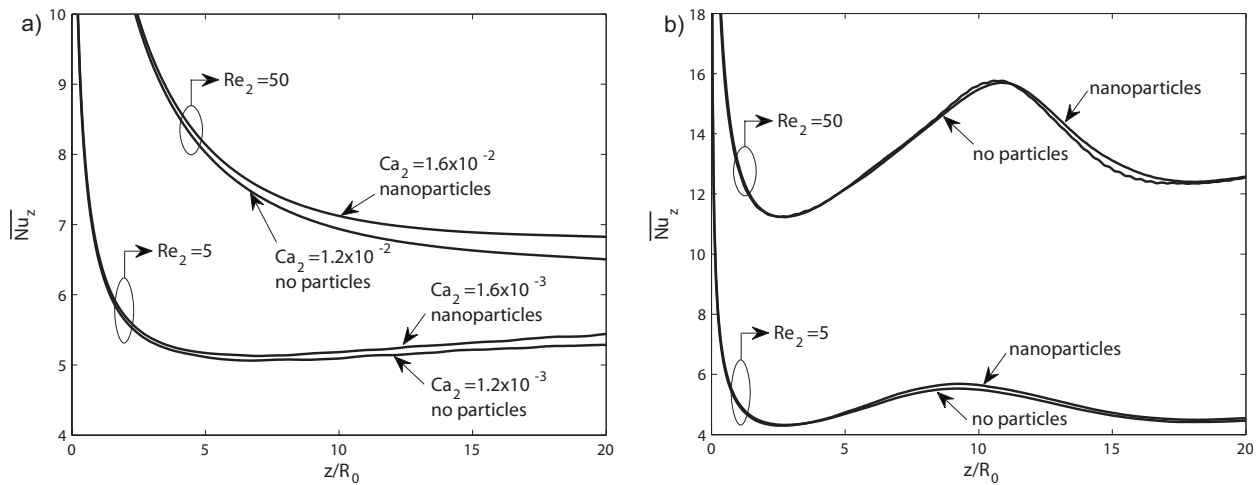


Fig. 9 The effect of nanoparticles on the temporally averaged local Nusselt number. In (a), the carrier liquid (liquid 2) is 5 cS silicone oil, and the liquid in the droplets (liquid 1) is water with and without nanoparticles. In (b), similar results are shown for slug flow, where the carrier liquid (liquid 1) is water and the liquid in the droplet (liquid 2) is PAO with and without nanoparticles.

gradients at the channel wall. This effect goes on until the first warm fluid particle in the vortex reaches the wall again (Fig. 4). This is the case after the slug has covered a distance of 11 radii. After this position, the temperature gradient (and the Nusselt number) decreases.

This can be seen in Fig. 10, where the absolute value of the temporally averaged heat flux q and the temporally averaged mean bulk temperature (Eq. (23)) are plotted. The heat flux shows a slightly decreasing plateau between $z/R_0=3$ and $z/R_0=11$, which is caused by the near constant temperature gradient $(dT/dr)_{wall,z}$ at the wall. After $z/R_0=11$, the temperature gradients and, in turn, the heat flux decrease. The bulk mean temperature T_b is constantly increasing, while the heat flux is nearly constant in the first part of the heated section. As a result, the Nusselt number (Eq. (22)) increases as well between $z/R_0=3$ and $z/R_0=11$, exhibiting a peak value at $z/R_0=11$, as can be seen in Fig. 9(b).

Another possibility for considerably increasing the thermal performance of the microchannel flow is to use droplets of higher viscosity, as is shown in Fig. 11. Here, the viscosity of the droplets is changed by using different types of silicone oil. The bulk fluid is water. The viscosity of the oil is 0.5 cS, 5 cS, or 50 cS. This results in viscosity ratios μ_1/μ_2 of 0.5, 4.6 and 46 for high viscous silicone oils. It can be seen that the Nusselt number strongly

depends on the viscosity ratio of the two phases. In the case of higher Reynolds numbers of the bulk fluid ($Re_2=50$), the influence is particularly strong. Here, the Nusselt number more than doubles compared with single liquid flow. For low Reynolds ($Re_2=0.5$), the influence is lower, but high viscosity ratios still increase the heat transfer performance of the liquid-liquid flow by 5%. High viscosity droplets move slower compared with droplets with low viscosity. The velocity of the less viscous droplets is 1.4 times higher than the mean velocity of the carrier liquid. Highly viscous droplets move only 1.2 times faster than the bulk fluid. However, due to the high viscosity ratio between the two liquids, the circulating motion of the fluid is significantly increased. As will be seen later, this results in a slightly increased pressure drop (Fig. 13).

From previous research on gas-liquid flow, it is known that the heat transfer of slug flow is considerably higher compared with bubbly flow [12]. In two-liquid flow, similar results can be obtained, as shown in Fig. 12. Here, the temporally averaged Nusselt number distribution is shown for differently shaped droplets. In Fig. 12(a), results are presented for droplets of 5 cS silicone oil; in Fig. 12(b), polyalphaolefine and Al_2O_3 nanoparticles are used. In both cases, the base fluid is water. For both liquid configurations,

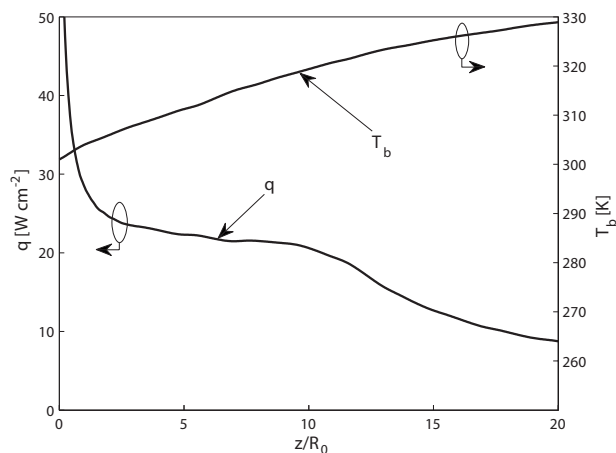


Fig. 10 Bulk mean temperature T_b and the absolute value of the heat flux from the wall $q|_{wall,z} = -k(dT/dr)_{wall,z}$ in axial direction, as defined by Eqs. (22) and (23)

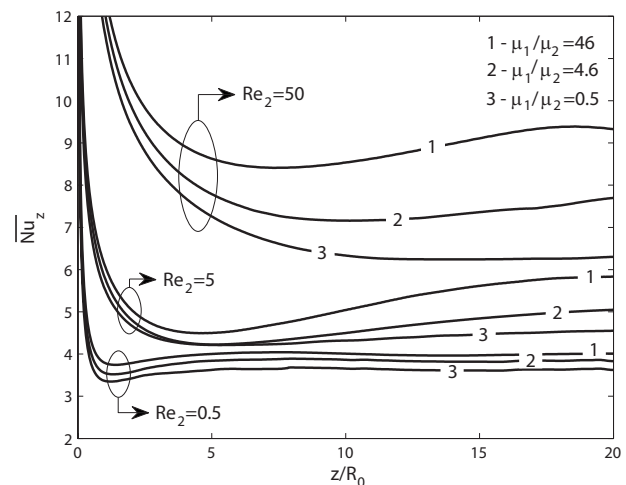


Fig. 11 Temporally averaged Nusselt number distribution for different viscosity ratios μ_1/μ_2 and Reynolds numbers of the bulk fluid (liquid 2) Re_2

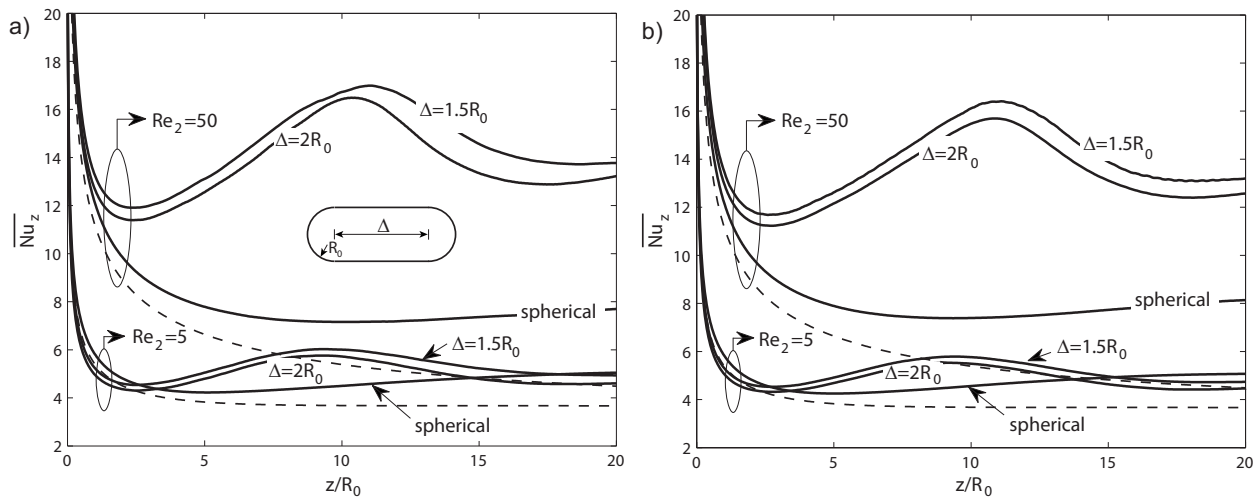


Fig. 12 Temporally averaged Nusselt number distribution for differently shaped droplets. The fluids used for the droplet liquid (liquid 1) are (a) 5 cS silicone oil and (b) nanofluid of PAO and Al_2O_3 particles. In both cases, the base fluid (liquid 2) is water. The dashed line compares to the Nusselt number of single liquid aqueous flow.

the heat transfer is strongly increased in the case when the Reynolds number is 50. Peak values of 17 for the Nusselt number can be achieved when the elongation of the slug is $1.5R_0$. For longer slugs ($2R_0$), the Nusselt number drops again as the amount of the suspended liquid (liquid 1) increases. The thermal properties of the suspension liquid are less adequate for thermal transport compared with the surrounding water. For low Reynolds numbers ($Re_2=5$), the influence of capillary forces is higher compared with viscous forces, resulting in a minor influence of the droplet shape.

The increase in thermal transport in slug flow is mainly caused by stronger recirculation between and within the slugs, which is in turn caused by the velocity difference between slugs and the carrier liquid. In slug flow, the mean velocity of the bulk fluid experiences a further drop. It follows that the increase in heat transfer in slug flow is achieved at the expense of a higher pressure drop. In the present study, the pressure drop along the channel triples for slug flow compared with spherical droplet-laden flow, as shown in Fig. 13.

In Fig. 13, the mean Nusselt number over the nondimensional pressure drop ($\zeta = \Delta p / 0.5 \rho_2 v_0^2$), normalized by the pressure drop of a single liquid ζ_0 (water), is depicted for two different scenarios. The Nusselt number is averaged over the length of the heated section of the channel and the time period needed so that ten subsequent droplets move through the channel. In Fig. 13(a), we compare the friction losses of differently shaped droplets of different liquids. It can be seen that the heat transfer in slug flow is considerably higher compared with single liquid flow (the increase in the Nusselt number is nearly 400%). The best cooling performance is obtained for slugs of 5 cS silicone oil. Here, the Nusselt number is 15 for a channel with a radius of $500 \mu m$ ($Re_2=50$). However, higher Nusselt numbers in slug flow are strongly connected to an increased pressure drop, which triples for slug flow compared with spherical droplet flow. Figure 13(a) reveals that the pressure drop further increases in the presence of nanoparticles, even though the positive effect of nanoparticles on

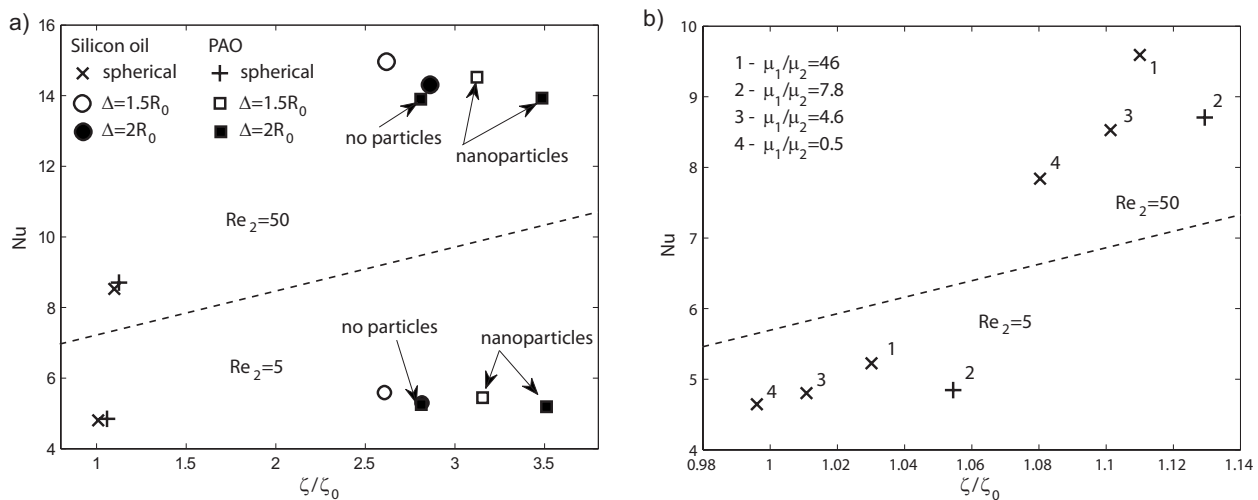


Fig. 13 Temporally and spatially averaged Nusselt number versus pressure drop normalized by the pressure drop of one liquid water flow. (a) Nusselt number for differently shaped droplets, with and without nanoparticles. The liquids of the droplet (liquid 1) as well as their elongation (Δ) are given in the legend. (b) Nusselt number for spherical droplets with different viscosity ratios μ_1/μ_2 . In (b), the liquids (liquid 1) are either PAO (+) or silicone oil (x). The dashed line separates high Reynolds number flow ($Re_2=50$) from lower Reynolds number flow ($Re_2=5$). In all cases shown here the base liquid (liquid 2) is water.

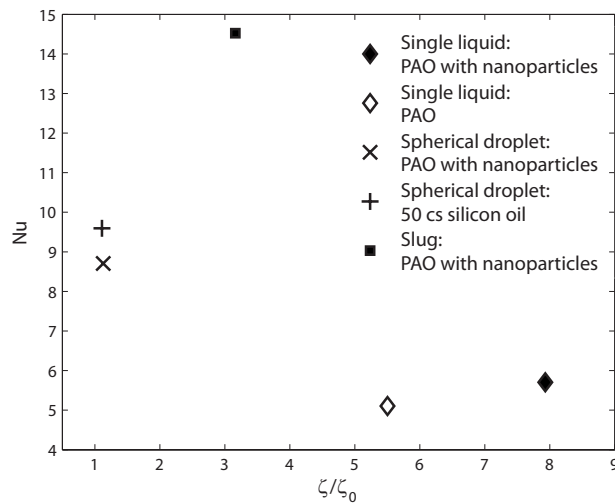


Fig. 14 Nusselt number versus pressure drop normalized by the pressure drop of one liquid flow (water)

the thermal performance is minor. Another possibility for increasing the thermal performance of a microchannel is to use higher viscosity droplets. Figure 13(b) shows that the Nusselt number can be increased to 9.6 when using 50 cS silicone oil ($\mu_1/\mu_2 = 46$) as the droplet liquid. The pressure drop increases by only 11% compared with a single fluid, whereas the Nusselt number more than doubles. Again, in Fig. 13, it can be seen that the use of a nanofluid (PAO with nanoparticles) increases the Nusselt number at the expense of a significant pressure drop increase.

To further elaborate on the effect of nanoparticles on the friction losses, the Nusselt number of single and two-liquid flow is plotted in Fig. 14. As expected, Fig. 14 reveals that suspended nanoparticles in single liquid flow of PAO increase the Nusselt number by nearly 12%. However, when using pure PAO as a coolant liquid, the pressure drop is augmented by a factor of 5.5 compared with the case when the cooling liquid is water. This is caused by the higher viscosity of PAO. In the presence of nanoparticles, the pressure drop rises even further by as much as 44%. By comparing to the results of a spherical droplet or slug flow, it can be seen that the use of a second suspended liquid (with and without nanoparticles) is an efficient way to increase the thermal performance without unacceptable pressure losses. Moreover, using nanofluids as an immiscible suspended liquid in a two-liquid flow configuration instead of a one liquid flow of nanofluids eliminates the unwanted fouling effect, which is present in every particle laden flow [48].

5 Conclusion

The thermal transport of liquid-liquid flow through microchannels was investigated for different flow conditions. A comprehensive model was presented, combining nanoparticle transport and nanofluidic heat transfer with a front tracking algorithm to capture multiphase flow and interfacial effects.

With thorough parametric studies, we elaborated on the strong effect of interfacial tension on the radial heat transfer in micro-scale devices. We observed that the influence of surface tension strongly affects the thermal transport mechanisms present in low Reynolds number flow. It was shown that the Marangoni effect decreases the heat transfer performance of microchannel two-liquid segmented flow. The Marangoni force resulting from temperature gradients at the interface counteracts the swirling motion of the fluid flow. Depending on the flow conditions, the Nusselt number decreases by as much as 13%.

A positive effect of nanoparticles on the heat transfer performance in microchannels was detected. However, this effect was rather small. In the presence of nanoparticles, the thermal trans-

port was increased by only 3–5%. This is mainly caused by the fact that nanoparticles lower the effective interfacial tension of the fluids. Lower surface tension results in a higher capillary number, which supports the marginal effect of increased thermal properties of the nanofluid on the heat transfer.

Another possibility for increasing the thermal performance of two-liquid segmented flow is to increase the flow rate of the suspended liquid. The Nusselt number considerably increases in the presence of slug flow compared with the flow of spherical droplets. This effect is primarily dominant for higher Reynolds numbers ($Re=50$). Here, the best performance was detected for 5 cS silicone oil, where the Nusselt number reached the value of 15. For lower Reynolds numbers ($Re=5$), the increase in thermal transport is less pronounced. The mean velocity of the bulk fluid experiences a further drop in slug flow. It can be seen that the increase in heat transfer in slug flow is generally achieved at the expense of a higher pressure drop. When the two effects need to be considered together, desirable operation regimes can be designed.

The most promising approach to considerably increase the thermal performance of microchannel flow with a moderate increase in friction losses is to use droplets of higher viscosity. We showed the strong influence of the viscosity ratio between the two liquids on the Nusselt number. In the case of higher Reynolds numbers, the influence is particularly strong. Here, for a viscosity ratio of 50, the Nusselt number more than doubles compared with single liquid flow. In this case, the pressure drop increases by only 11%. For low Reynolds numbers, the influence of the viscosity is lower, but high viscosity ratios still increase the thermal transport within the flow. In the case of nanofluids, the segmented “droplet train” approach showed clear advantages over forced convection of only the nanofluid in the microchannel.

Acknowledgment

We kindly acknowledge Werner Escher from IBM Zurich Research Laboratory for providing data on the properties of polyalphaolefine-nanoparticle solutions.

Nomenclature

c	= heat capacity ($J\ kg^{-1}\ K^{-1}$)
D_B	= Brownian diffusion coefficient ($m^2\ s^{-1}$)
D_T	= thermal diffusion coefficient ($m^2\ s^{-1}$)
\mathbf{F}	= interfacial tension force per unit volume ($N\ m^{-3}$)
k	= thermal conductivity ($W\ m^{-1}\ K^{-1}$)
p, φ	= pressure (Pa)
q	= wall heat flux ($W\ m^{-2}$)
r, x	= radial coordinate (m)
x'	= interface coordinate (m)
R_0	= channel radius (m)
S'	= surface of the interface
ΔT	= temperature scale (K)
T	= temperature (K)
t	= time (s)
\mathbf{v}, \mathbf{u}	= velocity vector ($m\ s^{-1}$)
z	= axial coordinate (m)

Greek Symbols

σ	= surface tension ($N\ m^{-1}$)
σ_T	= temperature coefficient ($N\ m^{-1}\ K^{-1}$)
θ	= temperature
μ	= dynamic viscosity ($kg\ m^{-1}\ s^{-1}$)
ρ	= density ($kg\ m^{-3}$)
τ	= time
κ	= curvature of the interface (m^{-1})
ϕ, Φ	= volumetric fraction

Subscripts

- b = bulk
- 1 = liquid 1: droplet liquid
- 2 = liquid 2: base liquid
- 0 = initial

Superscripts

- * = dimensionless physical properties

References

- [1] Escher, W., Michel, B., and Poulikakos, D., 2009, "Efficiency of Optimized Bifurcating Tree-Like and Parallel Microchannel Networks in the Cooling of Electronics," *Int. J. Heat Mass Transfer*, **52**(5–6), pp. 1421–1430.
- [2] Senn, S. M., and Poulikakos, D., 2004, "Laminar Mixing, Heat Transfer and Pressure Drop in Tree-Like Microchannel Nets and Their Application for Thermal Management in Polymer Electrolyte Fuel Cells," *J. Power Sources*, **130**(1–2), pp. 178–191.
- [3] Senn, S. M., and Poulikakos, D., 2004, "Polymer Electrolyte Fuel Cells With Porous Materials as Fluid Distributors and Comparisons With Traditional Channeled Systems," *ASME J. Heat Transfer*, **126**(3), pp. 410–418.
- [4] Senn, S. M., and Poulikakos, D., 2004, "Tree Network Channels as Fluid Distributors Constructing Double-Staircase Polymer Electrolyte Fuel Cells," *J. Appl. Phys.*, **96**(1), pp. 842–852.
- [5] Koblinski, P., Phillpot, S. R., Choi, S. U. S., and Eastman, J. A., 2002, "Mechanisms of Heat Flow in Suspensions of Nano-Sized Particles (Nanofluids)," *Int. J. Heat Mass Transfer*, **45**(4), pp. 855–863.
- [6] Lee, S., Choi, S. U. S., Li, S., and Eastman, J. A., 1999, "Measuring Thermal Conductivity of Fluids Containing Oxide Nanoparticles," *ASME J. Heat Transfer*, **121**(2), pp. 280–289.
- [7] Shalkevich, N., Escher, W., Buergi, T., Michel, B., Si-Ahmed, L., and Poulikakos, D., 2010, "On the Thermal Conductivity of Gold Nanoparticle Colloids," *Langmuir*, **26**(2), pp. 663–670.
- [8] Koblinski, P., Eastman, J. A., and Cahill, D. G., 2005, "Nanofluids for Thermal Transport," *Mater. Today*, **8**(6), pp. 36–44.
- [9] Wang, X. Q., and Mujumdar, A. S., 2007, "Heat Transfer Characteristics of Nanofluids: A Review," *Int. J. Therm. Sci.*, **46**(1), pp. 1–19.
- [10] Yu, W., France, D. M., Roubort, J. L., and Choi, S. U. S., 2008, "Review and Comparison of Nanofluid Thermal Conductivity and Heat Transfer Enhancement," *Heat Transfer Eng.*, **29**(5), pp. 432–460.
- [11] Buongiorno, J., Venerus, D. C., Prabhat, N., McKrell, T., Townsend, J., Christianson, R., Tolmachev, Y. V., Koblinski, P., Hu, L.-w., Alvarado, J. L., Bang, I. C., Bishnoi, S. W., Bonetti, M., Botz, F., Cecere, A., Chang, Y., Chen, G., Chen, H., Chung, S. J., Chyu, M. K., Das, S. K., Di Paola, R., Ding, Y., Dubois, F., Dzido, G., Eapen, J., Escher, W., Fufschilling, D., Galand, Q., Gao, J., Gharagozloo, P. E., Goodson, K. E., Gutierrez, J. G., Hong, H., Horton, M., Hwang, K. S., Iorio, C. S., Jang, S. P., Jarzelski, A. B., Jiang, Y., Jin, L., Kabelac, S., Kamath, A., Kedzierski, M. A., Kieng, L. G., Kim, C., Kim, J.-H., Kim, S., Lee, S. H., Leong, K. C., Manna, I., Michel, B., Ni, R., Patel, H. E., Philip, J., Poulikakos, D., Reynaud, C., Savino, R., Singh, P. K., Song, P., Sundararajan, T., Timofeeva, E., Triticak, T., Turanov, A. N., Van Vaerenbergh, S., Wen, D., Witharana, S., Yang, C., Yeh, W.-H., Zhao, X.-Z., and Zhou, S.-Q., 2009, "A Benchmark Study on the Thermal Conductivity of Nanofluids," *J. Appl. Phys.*, **106**(9), pp. 094312.
- [12] Lakehal, D., Larrignon, G., and Narayanan, C., 2008, "Computational Heat Transfer and Two-Phase Flow Topology in Miniature Tubes," *Microfluid. Nanofluid.*, **4**(4), pp. 261–271.
- [13] Fukagata, K., Kasagi, N., Ua-arayaporn, P., and Himeno, T., 2005, "Numerical Simulation of Gas-Liquid Two-Phase Flow and Convective Heat Transfer in a Micro Tube," *International Conference on Heat Transfer and Fluid Flow in Microscale*, Elsevier Science, Barga, Italy, pp. 72–82.
- [14] Urbant, P., Leshansky, A., and Halupovich, Y., 2008, "On the Forced Convective Heat Transport in a Droplet-Laden Flow in Microchannels," *Microfluid. Nanofluid.*, **4**(6), pp. 533–542.
- [15] Monde, M., and Mitsutake, Y., 1995, "Enhancement of Heat Transfer Due to Bubbles Passing Through a Narrow Vertical Rectangular Channel (Change in Heat Transfer Along Flow)," *Heat Mass Transfer*, **31**(1–2), pp. 77–82.
- [16] Joanicot, M., and Ajdari, A., 2005, "Applied Physics-Droplet Control for Microfluidics," *Science*, **309**(5736), pp. 887–888.
- [17] Cubaud, T., and Mason, T. G., 2008, "Capillary Threads and Viscous Droplets in Square Microchannels," *Phys. Fluids*, **20**(5), p. 053302.
- [18] Xu, J. H., Li, S. W., Tan, J., Wang, Y. J., and Luo, G. S., 2006, "Controllable Preparation of Monodisperse O/W and W/O Emulsions in the Same Microfluidic Device," *Langmuir*, **22**(19), pp. 7943–7946.
- [19] Zhao, Y. C., Chen, G. W., and Yuan, Q., 2006, "Liquid-Liquid Two-Phase Flow Patterns in a Rectangular Microchannel," *AIChE J.*, **52**(12), pp. 4052–4060.
- [20] Dessimoz, A. L., Cavin, L., Renken, A., and Kiwi-Minsker, L., 2008, "Liquid-Liquid Two-Phase Flow Patterns and Mass Transfer Characteristics in Rectangular Glass Microreactors," *Chem. Eng. Sci.*, **63**(16), pp. 4035–4044.
- [21] Cramer, C., Fischer, P., and Windhab, E. J., 2004, "Drop Formation in a Co-Flowing Ambient Fluid," *Chem. Eng. Sci.*, **59**(15), pp. 3045–3058.
- [22] Buongiorno, J., 2006, "Convective Transport in Nanofluids," *ASME J. Heat Transfer*, **128**(3), pp. 240–250.
- [23] Fischer, M., Dietzel, M., and Poulikakos, D., 2009, "Thermally Enhanced Solubility for the Shrinking of a Nanoink Droplet in a Surrounding Liquid," *Int. J. Heat Mass Transfer*, **52**(1–2), pp. 222–231.
- [24] Shin, S., Abdel-Khalik, S. I., Daru, V., and Juric, D., 2005, "Accurate Representation of Surface Tension Using the Level Contour Reconstruction Method," *J. Comput. Phys.*, **203**(2), pp. 493–516.
- [25] Hirt, C. W., and Nichols, B. D., 1981, "Volume of Fluid (VOF) Method for the Dynamics of Free Boundaries," *J. Comput. Phys.*, **39**(1), pp. 201–225.
- [26] Sussman, M., Smereka, P., and Osher, S., 1994, "A Level Set Approach for Computing Solutions to Incompressible 2-Phase Flow," *J. Comput. Phys.*, **114**(1), pp. 146–159.
- [27] Jamet, D., Lebaigue, O., Coutris, N., and Delhay, J. M., 2001, "The Second Gradient Method for the Direct Numerical Simulation of Liquid-Vapor Flows With Phase Change," *J. Comput. Phys.*, **169**(2), pp. 624–651.
- [28] Tryggvason, G., Bunner, B., Esmaeili, A., Juric, D., Al-Rawahi, N., Tauber, W., Han, J., Nas, S., and Jan, Y. J., 2001, "A Front-Tracking Method for the Computations of Multiphase Flow," *J. Comput. Phys.*, **169**(2), pp. 708–759.
- [29] Gupta, A., and Kumar, R., 2009, "Effect of Geometry on Droplet Formation in the Squeezing Regime in a Microfluidic T-Junction," *Microfluid. Nanofluid.*, **8**, pp. 799–812.
- [30] Gupta, A., Murshed, S. M. S., and Kumar, R., 2009, "Droplet Formation and Stability of Flows in a Microfluidic T-Junction," *Appl. Phys. Lett.*, **94**(16), p. 164107.
- [31] Renardy, Y., and Renardy, M., 2002, "Prost: A Parabolic Reconstruction of Surface Tension for the Volume-of-Fluid Method," *J. Comput. Phys.*, **183**(2), pp. 400–421.
- [32] Brackbill, J. U., Kothe, D. B., and Zemach, C., 1992, "A Continuum Method for Modeling Surface-Tension," *J. Comput. Phys.*, **100**(2), pp. 335–354.
- [33] Graetz, L., 1883, "Ueber Die Waermeleitungsfaehigkeit Von Flussigkeiten (On the Thermal Conductivity of Liquids), Part 1," *Ann. Phys. Chem.*, **18**, pp. 79–94.
- [34] Eastman, J. A., Phillpot, S. R., Choi, S. U. S., and Koblinski, P., 2004, "Thermal Transport in Nanofluids," *Annu. Rev. Mater. Res.*, **34**(1), pp. 219–246.
- [35] Pak, B. C., and Cho, Y. I., 1998, "Hydrodynamic and Heat Transfer Study of Dispersed Fluids With Submicron Metallic Oxide Particles," *Exp. Heat Transfer*, **11**(2), pp. 151–170.
- [36] Escher, W., 2009, private communication.
- [37] Shu, C.-W., and Osher, S., 1989, "Efficient Implementation of Essentially Non-Oscillatory Shock-Capturing Schemes, II," *J. Comput. Phys.*, **83**(1), pp. 32–78.
- [38] Fletcher, C. A. J., 1991, *Computational Techniques for Fluid Dynamics*, Springer-Verlag, Berlin.
- [39] Shin, S., Abdel-Khalik, S. I., and Juric, D., 2005, "Direct Three-Dimensional Numerical Simulation of Nucleate Boiling Using the Level Contour Reconstruction Method," *Int. J. Multiphase Flow*, **31**(10–11), pp. 1231–1242.
- [40] Lajeunesse, E., and Homsy, G. M., 2003, "Thermocapillary Migration of Long Bubbles in Polygonal Tubes. II. Experiments," *Phys. Fluids*, **15**(2), pp. 308–314.
- [41] Mohapatra, S. C. and Loikits, D., 2005, "Advances in Liquid Coolant Technologies for Electronics Cooling," 21st Annual IEEE Semiconductor Thermal Measurement and Management Symposium, IEEE, San Jose, CA, pp. 354–360.
- [42] Velagapudi, V., Konijeti, R. K., and Aduru, C. S. K., 2008, "Empirical Correlations to Predict Thermophysical and Heat Transfer Characteristics of Nanofluids," *J. Therm. Sci.*, **12**(2), pp. 27–37.
- [43] Girifalco, L. A., and Good, R. J., 1957, "A Theory for the Estimation of Surface and Interfacial Energies. I. Derivation and Application to Interfacial Tension," *J. Phys. Chem.*, **61**(7), pp. 904–909.
- [44] Svitova, T., Theodoly, O., Christiano, S., Hill, R. M., and Radke, C. J., 2002, "Wetting Behavior of Silicone Oils on Solid Substrates Immersed in Aqueous Electrolyte Solutions," *Langmuir*, **18**(18), pp. 6821–6829.
- [45] Murshed, S. M. S., Tan, S. H., and Nguyen, N. T., 2008, "Temperature Dependence of Interfacial Properties and Viscosity of Nanofluids for Droplet-Based Microfluidics," *J. Phys. D: Appl. Phys.*, **41**(8), pp. 085502.
- [46] Eckert, E. R. G., and Drake, R. M., 1959, *Heat and Mass Transfer, Part A*, McGraw-Hill, New York.
- [47] Deen, W. M., 1998, *Analysis of Transport Phenomena*, Oxford University Press, Oxford.
- [48] Perry, J., and Kandlikar, S., 2008, "Fouling and Its Mitigation in Silicon Microchannels Used for IC Chip Cooling," *Microfluid. Nanofluid.*, **5**(3), pp. 357–371.

Numerical Analysis of Interaction Between Inertial and Thermosolutal Buoyancy Forces on Convective Heat Transfer in a Lid-Driven Cavity

D. Senthil kumar
Research Scholar

K. Murugesan¹
Assistant Professor
e-mail: krimufme@iitr.ernet.in

Akhilesh Gupta
Professor

Department of Mechanical and Industrial
Engineering,
Indian Institute of Technology Roorkee,
Roorkee 247 667, India

In this paper, results on double diffusive mixed convection in a lid-driven cavity are discussed in detail with a focus on the effect of interaction between fluid inertial force and thermosolutal buoyancy forces on convective heat and mass transfer. The governing equations for the mathematical model of the problem consist of vorticity transport equation, velocity Poisson equations, energy equation and solutal concentration equation. Numerical solution for the field variables are obtained by solving the governing equations using Galerkin's weighted residual finite element method. The interaction effects on convective heat and mass transfer are analyzed by simultaneously varying the characteristic parameters, $0.1 < Ri < 5$, $100 < Re < 1000$, and buoyancy ratio (N), $-10 < N < 10$. In the presence of strong thermosolutal buoyancy forces, the increase in fluid inertial force does not make significant change in convective heat and mass transfer when the thermal buoyancy force is smaller than the fluid inertial force. The fluid inertial force enhances the heat and mass transfer only when the thermal buoyancy force is either of the same magnitude or greater than that of the fluid inertial force. The presence of aiding solutal buoyancy force enhances convective heat transfer only when Ri becomes greater than unity but at higher buoyancy ratios, the rate of increase in heat transfer decreases for $Re = 400$ and increases for $Re = 800$. No significant change in heat transfer is observed due to aiding solutal buoyancy force for $Ri \leq 1$ irrespective of the Reynolds number. [DOI: 10.1115/1.4002029]

Keywords: thermosolutal buoyancy forces, lid-driven cavity, velocity-vorticity equations, mixed convection

1 Introduction

The study of mixed convective heat and solute transport phenomena find importance in wide engineering applications such as atmospheric fluid convection, oceanography, nuclear waste disposal, drying chamber, chemical vapor deposition, crystal growth, plasma spray coating, etc. In applications such as nuclear waste disposal facilities, the primary interest will be the study of thermal energy transport in the presence of solute transport whereas the study of solute transport in the presence of heat transfer becomes important in the analysis of crystal growth, plasma spray coating problems. In all the above applied problems apart from the fluid inertial forces, the fluid momentum balance is also shared by the significant contribution of thermosolutal buoyancy forces generated as a result of temperature and species concentration gradients. When the fluid momentum balance consists of fluid inertial force derived from an external source and thermosolutal buoyancy forces then the resulting convective phenomenon is called double diffusive mixed convection. If the fluid momentum balance is achieved purely by thermosolutal buoyancy forces without externally derived fluid inertial force, then the phenomenon is called double diffusive natural convection. The mechanism behind fluid flow, heat and mass transfer in double diffusive natural convection has been well understood for enclosure problems [1–3] because in

such problems only the solutal buoyancy force is superimposed on the well established natural convection heat transfer problems. In contrast, thermosolutal buoyancy driven mixed convection problems give rise to complex flow situations, which in turn significantly affect the convective heat and mass transfer phenomena. When both thermal and solutal concentration gradients exist in a system, then the resulting density gradients may act in the same direction or in the opposite directions because the volumetric thermal expansion coefficient is always negative whereas the volumetric solutal expansion coefficient may be positive or negative depending upon the relation between density and species concentration.

In the absence of solutal buoyancy force, the mixed convective heat transfer with only thermal buoyancy force is characterized by Richardson number, defined as Gr_T/Re^2 and the Reynolds number for a given Prandtl number fluid. In this case, the fluid momentum conservation is tightly coupled with the fluid energy conservation. For a fixed value of Gr_T with increase in Reynolds number, the contribution from thermal buoyancy force to the fluid momentum balance becomes insignificant and the vice versa is expected at high value of Gr_T for a fixed Reynolds number. Although the physical mechanism behind mixed convection heat transfer phenomena is well understood [4,5], the situation is not straight forward in the presence of solutal buoyancy force. The solutal buoyancy force can be represented by defining solutal Grashof number Gr_S similar to thermal Grashof number Gr_T . In order to take into account the relative importance of solutal buoyancy force along with thermal buoyancy force, a buoyancy ratio is defined (as the

¹Corresponding author.

Contributed by Heat Transfer Division of ASME for publication in the JOURNAL OF HEAT TRANSFER. Manuscript received August 19, 2009; final manuscript received May 3, 2010; published online August 13, 2010. Assoc. Editor: Jayathi Murthy.

ratio of solutal buoyancy force to thermal buoyancy force) and used along with the well established Richardson number. In double diffusive mixed convection problems, the fluid flow pattern that affects the convective heat and mass transfer is mainly guided by the interaction between the fluid inertial force and thermosolutal buoyancy forces. Available literature on double diffusive mixed convection problems has focused only for specific flow situations without going into the details about the interaction between these forces, which are rigidly coupled in the fluid momentum balance. While studying direct condensation of solvent from a binary mixture in a double lid-driven cavity, Alleborn et al. [6] considered only thermal buoyancy force in the fluid momentum balance by decoupling the solutal conservation equation and reported flow instabilities at low Reynolds number. Al-Amiri et al. [7] found enhanced convective heat and mass transfer in a lid-driven cavity at low Richardson number because of the dominance of forced convection mechanism. Although they noted the expected increase in mass transfer for an increase in Lewis number, the effect of Lewis number was found to be insignificant at low Richardson number.

Recently, Maiti et al. [8] reported results on double diffusive natural and mixed convections in a square cavity by solving the problem with and without lid movement, respectively. By considering both positive and negative thermal and solutal volumetric expansion coefficients, they analyzed aiding and opposing flows for four different configurations obtained using the combinations of expansion coefficients and boundary conditions. Their focus was on the study of effect of stable and unstable stratification on convective heat and mass transfer and observed increase in average heat and mass transfer with increase in thermal/solutal gradients under unstable stratified conditions and they observed the opposite behavior under stable stratified conditions. Senthil kumar et al. [9] studied the buoyancy ratio effect in a geometrically complex lid-driven cavity, and they observed poor convective heat and mass transfer in the cavity because of the opposing thermal and solutal buoyancy forces. In the works detailed by Maiti et al. [8] and the results of the study by Senthil kumar et al. [9] are reported only for the variation in one of the characteristic parameters, Re, Ri and buoyancy ratio by keeping other parameters constant. However, the mechanism behind the interaction between the fluid inertial force and thermosolutal buoyancy forces can be understood only by analyzing the problem with simultaneous variations of Richardson number or Gr_T , Reynolds number, and buoyancy ratio.

In the present research paper an attempt is made for a detailed study on the interaction between the fluid inertial forces with thermosolutal buoyancy forces by considering simultaneous variations of the following parameters: $100 \leq Re \leq 1000$, $0.1 \leq Ri \leq 5$, and $-10 \leq N \leq 10$. The main focus of the work is to highlight the interaction effects on convective heat and mass transfer represented by Nusselt and Sherwood numbers. The governing equations for the present work consist of velocity Poisson equations, vorticity transport equation, energy, and species conservation equations. These coupled and nonlinear equations are solved numerically using Galerkin's weighted residual finite element method.

2 Problem Description

A two-dimensional square cavity of height H with adiabatic and impermeable side vertical walls, as shown in Fig. 1, is considered for the present study. An incompressible binary fluid is assumed to be the working fluid in the cavity, which is driven by the top wall moving with a uniform velocity U_0 . The bottom wall of the cavity is maintained at high temperature T_h and high species concentration C_h whereas the top lid is subjected to low temperature T_c and low concentration C_c . Such a configuration can be considered as simulating a real problem of continuous removal of pollutants generated at the bottom wall by the moving top lid. With the assumption of constant thermophysical properties Boussinesq approximation is employed only for the buoyancy force terms for

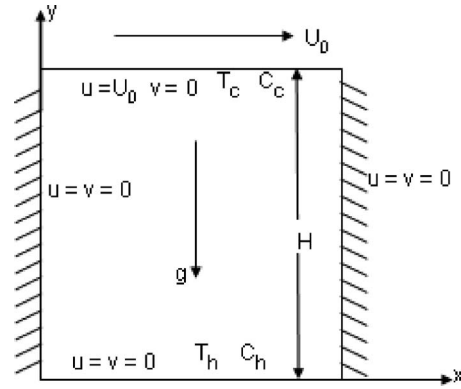


Fig. 1 Schematic diagram of the problem

small linear variation of density due to temperature and solutal concentration variations at constant pressure and it can be expressed as $\rho = \rho_0 [1 - \beta_T(T - T_c) - \beta_C(C - C_c)]$, where ρ_0 is a characteristic density, and β_T and β_C are volumetric thermal expansion coefficient and volumetric solutal concentration expansion coefficient, respectively. In general volumetric thermal expansion coefficient, β_T is always positive whereas the volumetric solutal concentration expansion coefficient β_C may be either positive for augmenting thermal and solutal buoyancy forces or negative for opposing buoyancy forces. The flow is assumed to be two-dimensional, steady, and laminar. Radiation, Soret, and Duffour effects are neglected in this study.

2.1 Governing Equations. Double diffusive mixed convection is governed by equations that represent conservation of mass, momentum, energy and solutal concentration. As the main focus of the analysis is on convective heat and mass transfer, the problem can be analyzed using governing equations in velocity-vorticity form without involving the pressure term. Following are the governing equations used in the present simulation and these equations have been obtained based on the detailed derivations discussed in Ref. [9].

Vorticity transport equation

$$\frac{\partial \zeta}{\partial \tau} + (\mathbf{V} \cdot \nabla) \zeta = \frac{1}{Re} \nabla^2 \zeta + Ri \left(\frac{\partial \theta}{\partial X} + N \frac{\partial \Phi}{\partial X} \right) \quad (1)$$

Velocity Poisson equations

$$\nabla^2 \mathbf{V} = -\nabla \times \zeta \quad (2)$$

Energy equation

$$\frac{\partial \theta}{\partial \tau} + \mathbf{V} \cdot \nabla \theta = \frac{1}{Re Pr} \nabla^2 \theta \quad (3)$$

Solutal concentration equation

$$\frac{\partial \Phi}{\partial \tau} + \mathbf{V} \cdot \nabla \Phi = \frac{1}{Re Sc} \nabla^2 \Phi \quad (4)$$

where

$$\zeta = \frac{\partial V}{\partial X} - \frac{\partial U}{\partial Y} \quad \text{and} \quad \mathbf{V} = (U, V)$$

and the nondimensional variables are defined as $(X, Y) = (x, y)/H$, $(U, V) = (u, v)/U_0$, $P = p/\rho U_0^2$, $\tau = U_0 t/H$, $\theta = T - T_c/\Delta T$, and $\Phi = C - C_c/\Delta C$ where $\Delta T = T_h - T_c$ and $\Delta C = C_h - C_c$ and the nondimensional parameters are $Re = U_0 H/\nu$, $Ri = Gr_T/Re^2$, $Pr = \nu/\alpha$.

$$\text{Gr}_T = \frac{g\beta_T\Delta TH^3}{\nu^2}, \quad \text{Gr}_S = \frac{g\beta_C\Delta CH^3}{\nu^2}, \quad \text{Sc} = \frac{\nu}{D},$$

$$\text{and } N = \frac{\beta_C\Delta C}{\beta_T\Delta T} \quad (5)$$

The Richardson number signifies the relative importance of thermal buoyancy force and inertial force of the fluid medium. The buoyancy ratio N in Eq. (1) reveals the relative strength of thermal and solutal buoyancy forces in the buoyancy driven flow field.

2.2 Initial and Boundary Conditions. The initial conditions are: At $\tau=0$ the field variables are

$$U = V = \zeta = \theta = \Phi = 0 \quad (6)$$

The boundary conditions for $\tau > 0$ are summarized as follows:

(i) at the top wall $U = 1, \quad V = 0, \quad \theta = \Phi = 0, \quad \zeta = \nabla \times \mathbf{V}$

(ii) at side walls $U = V = 0, \quad \frac{\partial \theta}{\partial X} = \frac{\partial \Phi}{\partial X} = 0, \quad \zeta = \nabla \times \mathbf{V}$

(iii) at the bottom wall $U = V = 0, \quad \theta = \Phi = 1, \quad \zeta = \nabla \times \mathbf{V}$ (7)

Vorticity boundary values are computed using a second order-accurate Taylor series expansion scheme. The convective heat and mass transfer along the bottom wall of the cavity are calculated in terms of average Nusselt and Sherwood numbers defined as follows:

$$\text{Nu}_{\text{av}} = \frac{1}{H} \int_0^H \left(U\theta - \frac{\partial \theta}{\partial Y} \right) dX \quad (8)$$

$$\text{Sh}_{\text{av}} = \frac{1}{H} \int_0^H \left(U\Phi - \frac{\partial \Phi}{\partial Y} \right) dX \quad (9)$$

3 Numerical Solution Procedure

The governing Eqs. (1)–(4) representing flow field, temperature and solutal concentration fields are solved using the initial and boundary conditions given by Eqs. (6) and (7). Global matrix-free Galerkin's weighted residual finite element method [10] has been employed to solve the governing equations for velocity, vorticity, temperature, and solutal concentration fields. Since the governing equations are coupled and nonlinear an iterative computational procedure is followed in the numerical solution scheme. The computational domain is discretized using four node bilinear isoparametric elements and Gaussian quadrature formula has been used to integrate the matrices obtained as a result of finite element procedure. The time derivatives are discretized using second order-accurate Crank–Nicolson scheme. Conjugate gradient iterative solver is employed for the solution of the final nodal equations. The solution field for velocity, vorticity, temperature and concentration is assumed to be converged for the time step “ $n+1$ ” when the error between two consecutive iterations “ q ” and “ $q+1$ ” for any primary variable is satisfied as follows: Λ

$$\sum_{j=1}^{\text{nnode}} \left(\frac{(|\Lambda_j^{q+1}| - |\Lambda_j^q|)}{\text{nnode}} \right) \leq 10^{-5}$$

where “nnode” is the total number of grid points in the computational domain. The unsteady state governing equations are being solved only as a false-transient device to get the steady state solutions.

4 Results and Discussion

4.1 Mesh Sensitivity and Validation Results. In order to make sure that the proposed computational algorithm is indepen-

Table 1 Mesh sensitivity test

Mesh No.	Mesh size	Average Nusselt number (Nu_{av}) at the bottom wall	Error (%)
I	41×41	7.7807	2.25
II	51×51	7.9604	0.0796
III	61×61	7.9664	
IV	71×71	7.9695	0.0388

dent of the computational mesh, a mesh sensitivity test has been conducted using four different structured meshes of size 41×41 , 51×51 , 61×61 , and 71×71 obtained using transfinite interpolation technique. Table 1 shows the comparison results for the average Nusselt number (Nu_{av}) at the bottom wall of the cavity for the above meshes at $\text{Re}=1000$, $\text{Ri}=0.1$, $\text{Le}=1$, and $N=1$. As seen from the table the error in Nu_{av} between two consecutive meshes continues to decrease with refinement of mesh. Since the variation in Nu_{av} is observed only in the third decimal point, the mesh 51×51 is selected for further computations in this work.

To validate the present code, double diffusive mixed convection in a lid-driven square cavity problem solved by Al-Amiri et al. [7] was considered. In this problem, the vertical walls of the cavity are assumed to be adiabatic and impermeable. The temperature and solutal concentration gradients are imposed on the cavity walls in the vertical direction. Figures 2(a) and 2(b) show the comparisons of U-velocity and temperature distributions along the vertical mid plane of the cavity between the results obtained in the present work and by Al-Amiri et al. [7] for $\text{Re}=500$, $\text{Gr}_T=\text{Gr}_S=100$, and $\text{Le}=2$. Our predicted results for velocity and temperature distributions show good agreement with the results of Al-Amiri et al. [7]. In order to make sure that our algorithm works well for variation in other parameter as well, variation in average Nusselt number with buoyancy ratio is computed and compared with the results of Al-Amiri et al. [7] for $\text{Re}=100$, $\text{Ri}=0.01$, and $\text{Le}=1$, as depicted in Fig. 2(c). The above figure indicates that our results show close agreement with the results of Al-Amiri et al. [7]. Thus, it is verified that the proposed numerical algorithm is validated for mesh sensitivity and reliability of results for double diffusive mixed convection problems. A detailed analysis of results obtained for the variation of different characteristic parameters is discussed in the following sections.

4.2 Streamline Distributions. Simulation results are obtained to study the variation of Nusselt and Sherwood numbers for simultaneous variations of Re , Ri , and N values. The dominance of fluid inertial force compared with viscous force of the fluid is represented by the magnitude of Re , whereas the relative strength of thermal buoyancy force over the inertial force of the fluid is denoted by the value of Ri . Buoyancy ratio N is used along with Re and Ri to bring the effect of solutal buoyancy force. Instead of Ri and N , other nondimensional numbers, Gr_T and Gr_S also can be used along with Re . In the present work Ri is preferred because the mixed convection due to thermal buoyancy force is generally explained using Ri . Hence, by varying Re , Ri , and N , one can study the effect of variations of inertial force, thermal and solutal buoyancy forces in the fluid medium. From the boundary conditions depicted in Fig. 1 one can easily understand that for positive values of N , the density near the hot and high concentration bottom wall will be less compared with the density near the cold and low concentration upper moving wall. Hence the lighter fluid moves from the bottom wall toward the top wall, thus, setting up an upward buoyancy force. For negative values of N , the density due to temperature gradient at the hot wall will be lower than that of the upper cold wall, whereas the density due to solutal concentration gradient at the high concentration bottom wall will be higher than that of the upper low concentration wall. Thus the

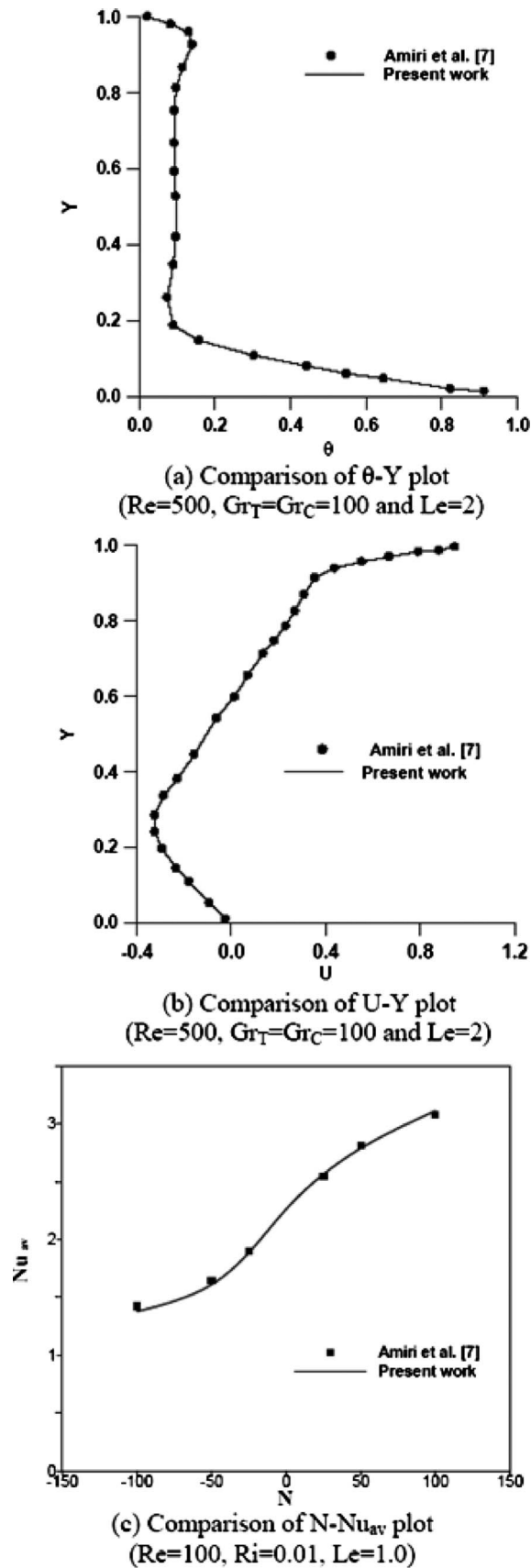


Fig. 2 Validation results

heavier fluid due to concentration gradient will oppose the upward movement of the lighter fluid due to temperature gradient, resulting in thermal and solutal buoyancy forces opposing each other.

Figure 3 illustrates the variation of streamline patterns for the variation of Ri for three values, 0.5, 1, and 3 at five different values of N , -10, -3, 1, 3, and 10 at $Re=100$ and $Le=1$. Since Re is fixed, increase in Ri will indicate an increase in thermal buoyancy force. Referring to Fig. 3(a) one can notice that for $N=1$ a flow field with single fluid core and a small eddy at the right bottom corner is formed. In this case the thermal and solutal buoyancy forces are equal and aid each other. The fluid momentum from the moving top wall has to reach the bottom wall for the convective heat transfer to take place from bottom wall toward the cold top wall. This flow regime represents a favorable situation for the fluid momentum transport from top to bottom wall of the cavity. As the value of N decreases in the negative direction, the high density gained due to increase in solutal buoyancy force encourages the formation of a secondary fluid circulation as observed for $N=-3$ and three fluid cells are observed when N is decreased to -10. Formation of these additional fluid cells will retard the fluid momentum transport and hence the heat transfer. The situation becomes reversed when N is increased to 3 and 10. Although a secondary fluid cell is also formed at $N=10$ due to the aiding nature of thermosolutal buoyancy forces the situation aids in fluid momentum transport from moving top wall to the bottom wall. With increase in Richardson number to 1, the streamline pattern almost exhibit very similar behavior as observed for $Ri=0.1$, except some difference in the size of the secondary cells observed for $N=-10$, -3, and 10. When Ri is increased to 3, the buoyancy force plays a major role compared with the inertial force of the fluid. From Fig. 3(c) one can observe that the formation of three fluid cores is advanced at $N=-3$ itself and a secondary fluid core is formed at all positive values of N . Increase in Ri and increase in positive value of N denotes the dominance of thermal and solutal buoyancy forces over the fixed inertial force of the fluid and hence the fluid momentum is dominated only by these two buoyancy forces. It will be interesting to observe how these phenomena will get modified when Re is varied.

Figure 4 depicts the variation in streamline patterns obtained for five values of Ri , 0.1, 0.5, 1, 3, and 5 at three values of Re , 300, 600, and 1000 at $N=1$. Under this situation the thermal and solutal buoyancy forces are equal to each other. At $Ri=0.1$ a distinct recirculation bubble is noted to be formed at the right bottom corner of the cavity for all the three Reynolds numbers. It is interesting to observe that this bubble grows in size with increase in Ri and Re . For a given Reynolds number increase in Ri results in increase in bubble size as depicted in Fig. 4(a), whereas the interfacial velocity gradients between the two bubbles vary significantly with increase in Reynolds number. Furthermore, it should not be missed to notice the generation of secondary vortex at the left bottom corner of the cavity with increase in Reynolds number and with increase in Ri beyond 1. With increase in both Ri and Re one can easily visualize that both thermal buoyancy force and inertial force of the fluid medium increases. The fluid momentum from the top moving plate has to reach the fluid closer to the hot bottom wall of the cavity so that convective heat transport takes place. In the present case thermal and solutal buoyancy forces are assumed to be equal to each other. The influence of solutal buoyancy force over and above the thermal and inertial force of the fluid can be understood by varying N along with Ri and Re as will be discussed in the later part of this paper.

4.3 Temperature and Concentration Contours. Convective heat and solute transport can be easily visualized by capturing the temperature and concentration contours in the flow field because it is the temperature and concentration gradients that will drive the heat and concentration transports into the fluid medium. Figure 5 depicts the temperature (concentration) contours for the variation of N and Ri for $Re=100$ at $Le=1$. The temperature varies from 1

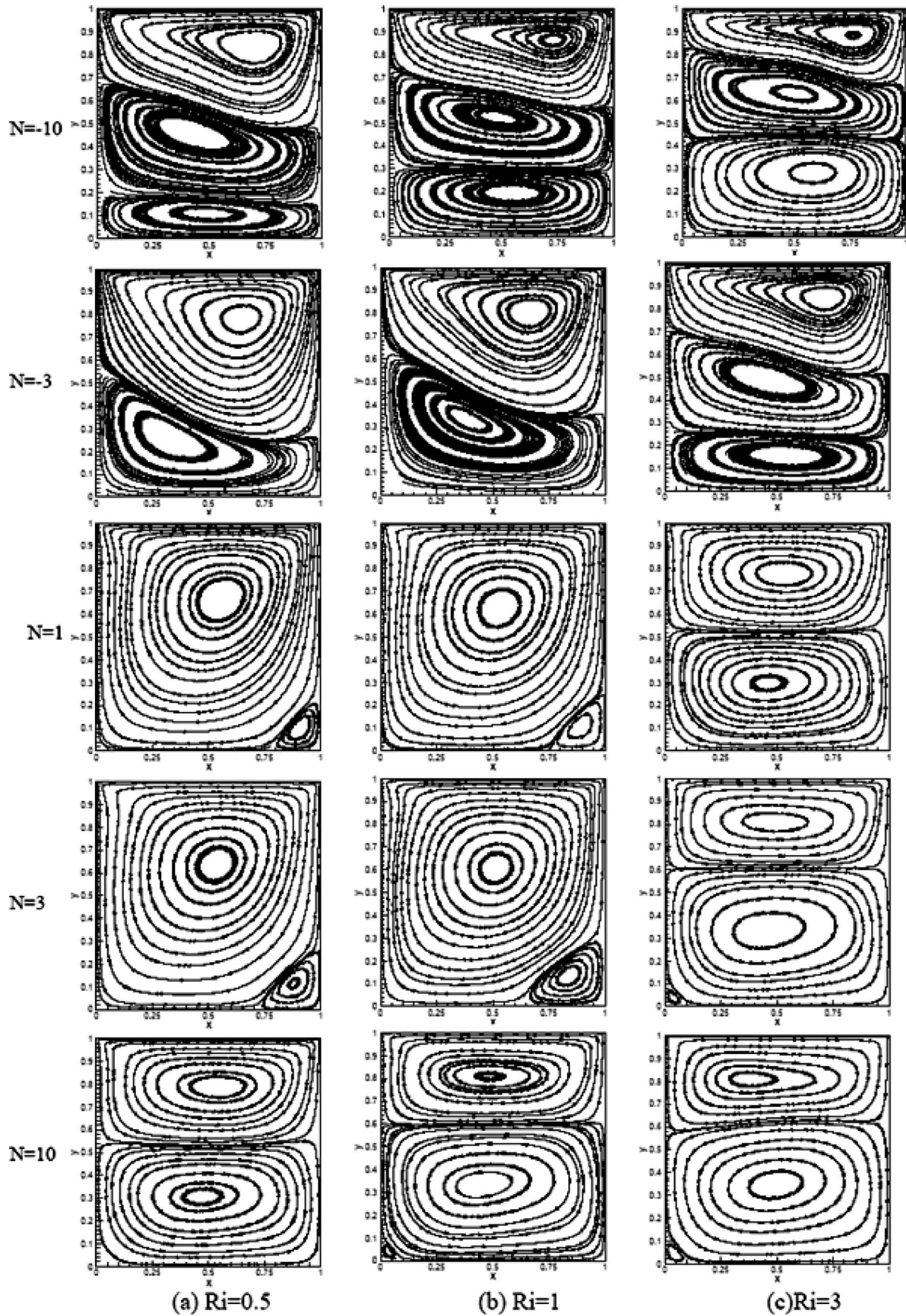


Fig. 3 Streamline patterns for the effect of buoyancy forces for different Ri at $Re=100$ and $Le=1$

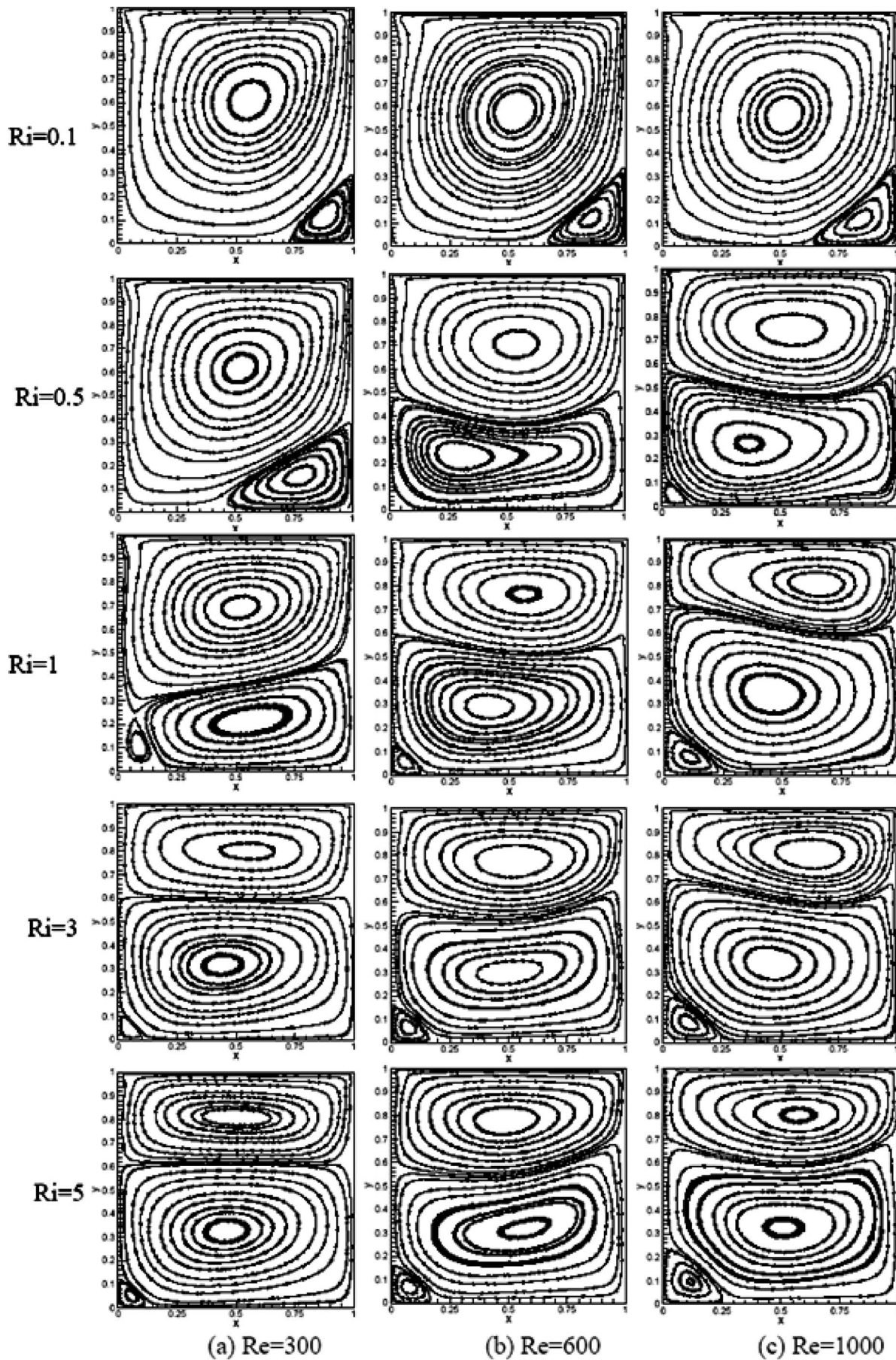


Fig. 4 Streamline patterns for the effect of Ri for different Re at $Le=N=1$

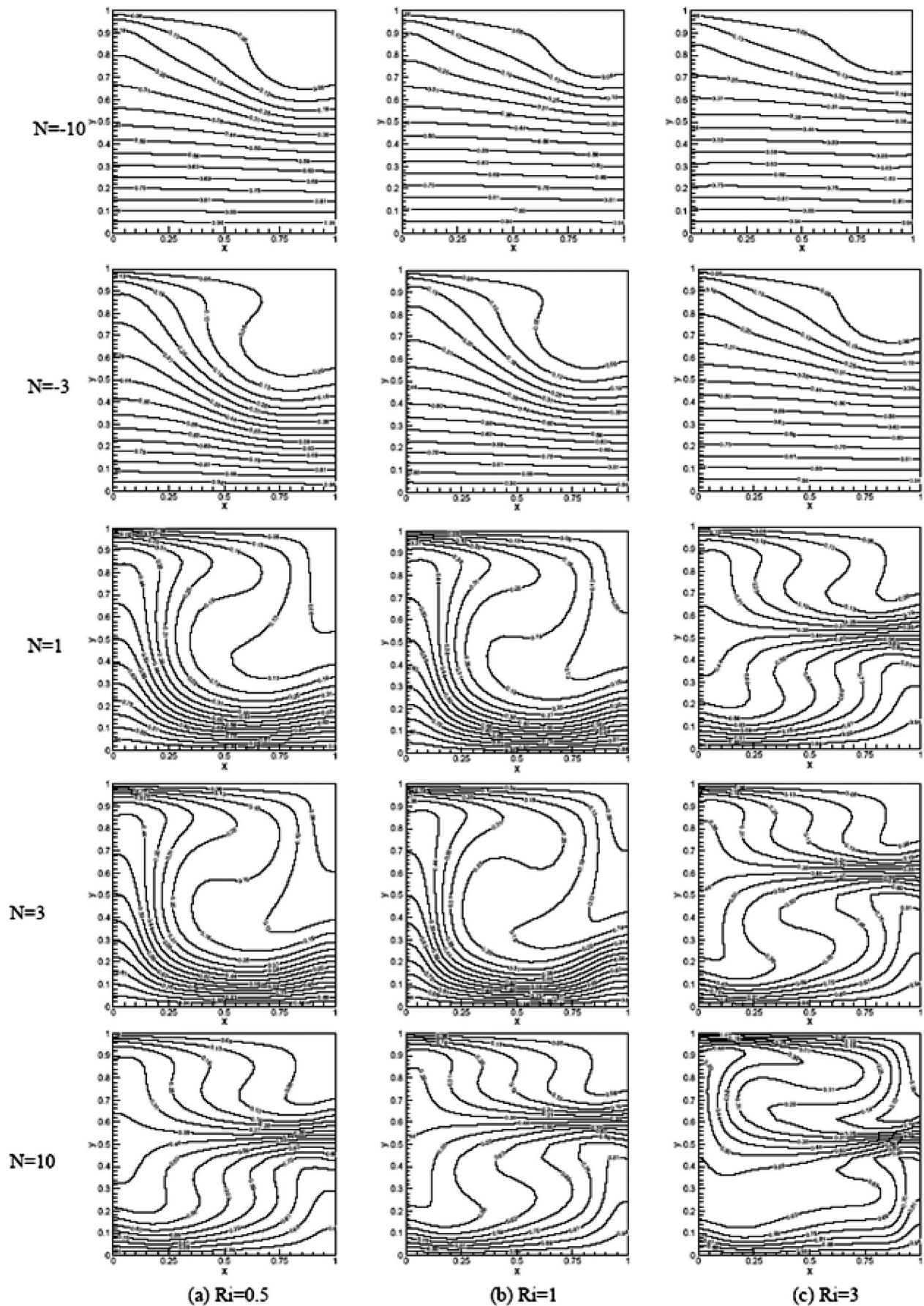


Fig. 5 Temperature and concentration contours for the effect of buoyancy forces for different Ri at $Re=100$ and $Le=1$

at the bottom hot wall to 0 at the top cold wall and become normal to the vertical side walls due to adiabatic boundary conditions. When N becomes negative the thermal and solutal buoyancy forces oppose each other and hence the heavier fluid settled closer to the hot bottom wall of the cavity will not encourage fluid convection, thus the heat transfer takes place purely by diffusion. These trends can be easily observed from the smooth linear variation of temperature depicted in Fig. 5 for $N=-10$ and -3 . As N becomes positive and increases in magnitude to 3, the fluid circulation inside the cavity increases giving rise to steep temperature gradients as observed in Fig. 5(a). This phenomenon is enhanced with increase in Ri from 0.5 to 1 as observed in four figures for $N=1$ and 3 for $Ri=0.5$ and 1 in Figs. 5(a) and 5(b). With increase in temperature gradients, the Nusselt number is expected to increase due to enhanced convective heat transfer. The trend changes with increase in N or Ri resulting in the formation of a secondary fluid core. Formation of secondary bubble is noticed at $Ri=3$ for $N=1$ and this tendency is advanced with increase in N to 10 at $Ri=0.5$ itself. Since both the thermal and solutal buoyancy forces aid each other and the magnitude of solutal buoyancy force is ten times that of the thermal buoyancy force a secondary fluid bubble is formed in the cavity enhancing the heat transfer. Although the secondary bubble is formed at $Ri=0.5$ for $N=10$, the size of this secondary bubble increases only with increase in Ri as noticed in Figs. 5(b) and 5(c). It is worth to compare this behavior with the growth of the secondary bubble formed at the right bottom corner with increase in N and Ri , as already observed in Fig. 3. The temperature gradient at the interface of the primary and secondary bubbles increases with increase in N and Ri and it should be remembered that this increase has resulted purely from the thermosolutal buoyancy forces since $Re=100$ is kept constant. For $N=1$, the effect of variation in Ri at different Reynolds numbers on temperature contours are illustrated in Fig. 6. For $Ri=0.1$, as the Reynolds number is increased from 300 to 1000, the temperature field intensity near the boundary walls of the cavity increases due to the increase in size of the fluid core at the center of the cavity as observed from Figs. 6(a)–6(c). As Reynolds number increases the fluid inertial force increases and, hence, the fluid momentum is able to reach the bottom wall of the cavity, which is hot and the temperature gradient adjacent to the wall cavity increases due to increased momentum transport closer to the boundary walls. The recirculatory flow pattern obtained as a result of end wall effect, will give rise to a central fluid core. The presence of a secondary bubble at the right bottom corner of the cavity alters the temperature distribution near that region as clearly noticed in Fig. 6(c) at $Ri=0.1$. When Ri and Re are increased, this secondary bubble grows in size and this results in setting up of temperature gradients at the interface of the primary and secondary bubbles. With increase in Ri the secondary bubble size increases but the temperature gradients at the interface becomes steeper only with increase in Re as noticed in Fig. 6, specifically for $Ri=3$ and 5 at $Re=300, 600,$ and 1000. The increase in thermal buoyancy force influences the growth of the secondary fluid whereas increase in Re favors the setting up of steep velocity gradients at the interface of the bubbles and hence the temperature gradients. Thus the formation of secondary bubble has allowed the transport of heat from the bottom hot wall to other parts of the cavity.

4.4 Nusselt and Sherwood Numbers. The effect of thermosolutal buoyancy forces on convective heat and mass transfer is analyzed at different Reynolds number to understand the transport mechanisms. The results are presented in the form of average Nusselt number, computed along the hot bottom wall of the cavity. Initially, the variation in average Nusselt (Sherwood) number (because $Le=1$) with Re and N is studied at $Ri=0.1$ and then this will be extended at different Richardson numbers as well. Figure 7 depicts the average Nusselt number plots for variations in N at different Reynolds numbers. At negative buoyancy ratio the heavy

fluid occupies the bottom side of the cavity and hence the fluid circulation is minimized, thus this situation gives rise to pure diffusion process. Hence it can be noted from the above figure that irrespective of the value of the Reynolds number, the average Nusselt number always becomes minimum although this minimum value increases in magnitude with increase in Reynolds number. In general, the average Nusselt number increases with increase in Reynolds number as observed in the above figure with significant increase being noted for $Re=800$ and 1000. At Reynolds number greater than 100, there is a steep rise and drop in Nusselt number when the buoyancy ratio varies from -5 to 5 and the rise being maximum for $Re=1000$. According to the boundary conditions assumed in the present test problem negative values of buoyancy ratio indicate that the thermal and solutal buoyancy forces oppose each other and the vice versa is followed for the case of positive values of buoyancy ratio. As the value of N is increased from -5 to 5, the dominance of opposing solutal buoyancy force decreases and becomes zero at $N=0$ and, hence, the upward acting thermal buoyancy force aids in transporting fluid momentum gained as a result of increase in Reynolds number. At $Re=100$, the fluid inertial force is not significant and hence the fluid behaves like a stagnant fluid without much fluid momentum transport but once the Reynolds number value is increased the fluid momentum transport is enhanced. It should be noted that the thermal buoyancy force is not significant because $Ri=0.1$ only and hence a rise is observed only when the opposing solutal buoyancy force decreases or becomes zero. When N is increased from 0 to 5 there is a transition period during which a secondary fluid bubble is being generated inside the cavity. Until this secondary cavity gets established itself in fluid momentum transport, the convective heat transfer decreases slightly and once the bubble is well established the convective heat transfer increases, as depicted by the continuous rise in the average Nusselt number.

The simulation study has been extended to higher Richardson number. Figure 8 shows the average Nusselt number variation plotted against N at different values of Ri and Re . At lower value of Re (Fig. 8(a)), that is at $Re=100$, the average Nusselt number continues to increase at $Ri=0.1$. However, for $Ri=0.5, 1$ and 3, a steep rise in the average Nusselt number is observed for the variation of N from -2.5 to 2.5 and reaches a maximum value at $N=2.5$ for $Ri=1$ followed by 0.5 and 3. When a sharp decrease in Nusselt number is observed for $Ri=0.5$ and 1 for the variation of N from 2.5 to 5, the Nusselt number continues to remain constant for $Ri=3$. This demonstrates that at lower Reynolds number aiding solutal buoyancy force enhances convective heat transfer only when the thermal buoyancy force is equal to fluid inertial force. Figures 8(b) and 8(c) depict the effect of Ri on Nusselt number variations for $Re=400$ and 800, respectively. The Nusselt number continues to increase as N varies from -10 to 0 with $Ri=0.1$ taking the lead followed by $Ri=3, 0.5,$ and 1 for both $Re=400$ and 800. Beyond $N=0$, the aiding thermosolutal buoyancy forces increase the convective heat transfer for $Ri=0.5, 1,$ and 3 at $Re=400$. At $Ri=0.1$ the Nusselt number decreases slightly and then increases as seen from Fig. 8(b). When Re is increased to 800 the Nusselt number drops a little and then increases for $Ri=0.5$ and 0.1, whereas it remains constant for $Ri=0.5$ and increases continuously for $Ri=3$ as noticed in Fig. 8(c). The increase in Nusselt number becomes more significant as Ri is increased from 0.1 to 3 because the aiding solutal buoyancy force enhances the convective heat transfer along with the thermal buoyancy force. It is understood from streamline distributions that with increase in Ri and Re there will be an increase in thermal and inertial forces, which will result in enhanced convective heat transfer. When these two forces are supported by the aiding solutal buoyancy force, a significant increase in convective heat transfer is observed as demonstrated by the results shown in Fig. 8.

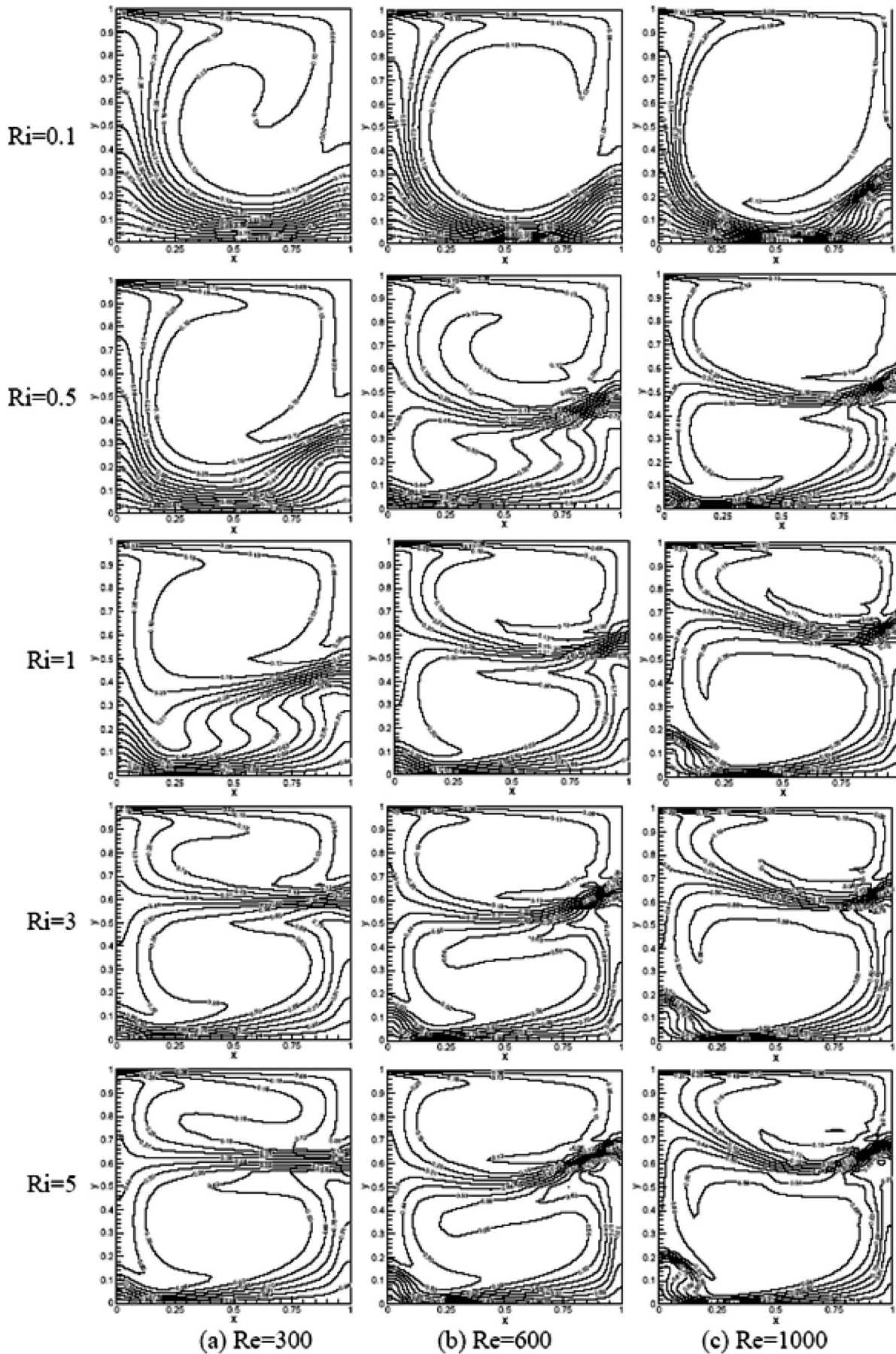


Fig. 6 Temperature and concentration contours for the effect of Ri for different Re at $Le=N=1$

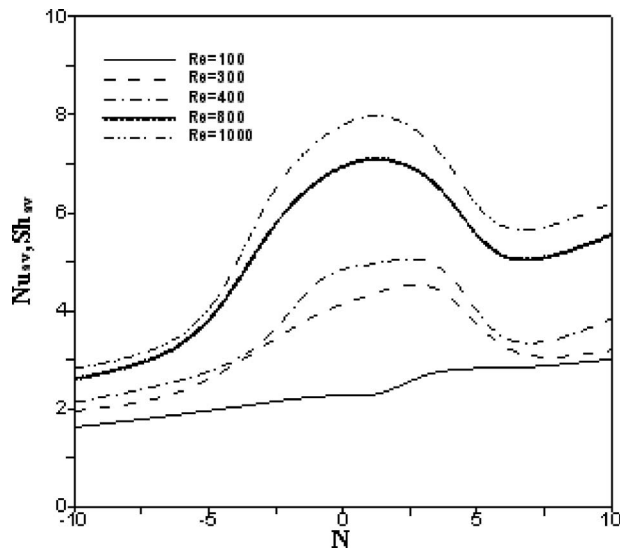


Fig. 7 Effect of buoyancy force and Reynolds number on average Nusselt number for $Ri=0.1$ and $Le=1$

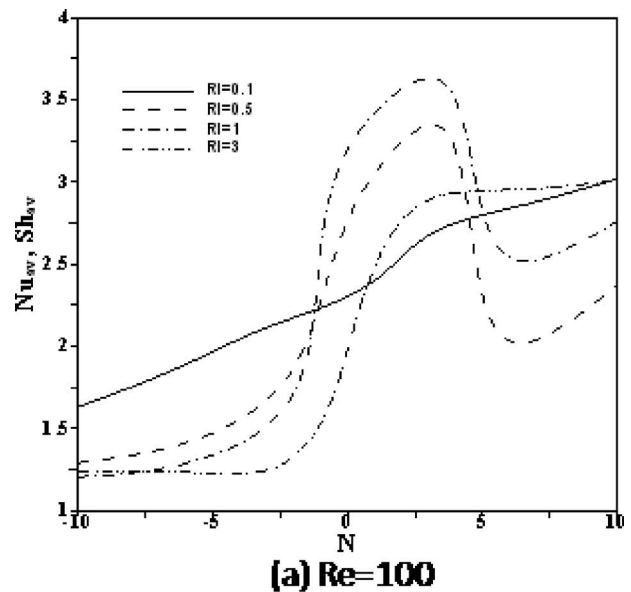
5 Conclusions

The interaction between fluid inertial force and thermosolutal buoyancy forces on convective heat transfer in a lid-driven square cavity has been studied in detail using velocity-vorticity form of Navier–Stokes equations. Simulation results have been obtained for simultaneous variations of Ri , Re , and N in the range, $0.1 < Ri < 5$, $100 < Re < 1000$ and $-10 < N < 10$. As the thermosolutal buoyancy forces change from opposing mode to aiding mode the following observations have been made.

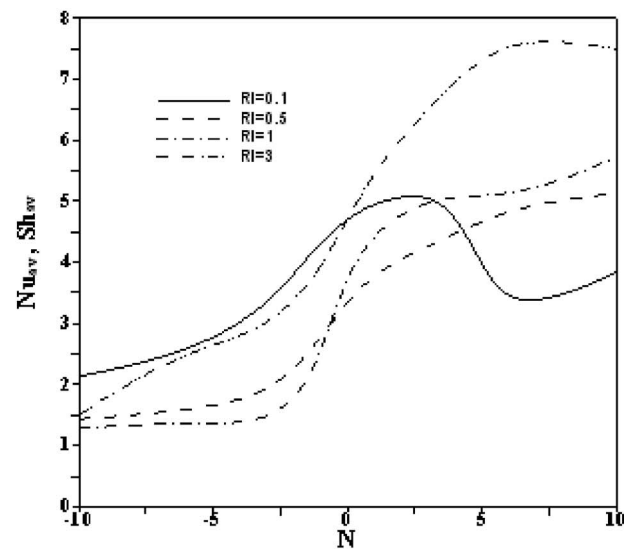
- At lower Reynolds number ($Re=100$), for $Ri=0.5$ and 1 , there is a sharp rise and drop in Nusselt number at the transition of the buoyancy forces closer to $N=0$.
- At higher Reynolds numbers ($Re=400$ and 800), there is a continuous rise in Nusselt number and this behavior is observed for all the Richardson numbers except for $Ri=1$ at $Re=800$ where the Nusselt number decreases and then starts increasing.
- Maximum rise in the Nusselt number is observed only for $Ri=3$ for all Reynolds numbers except for $Re=100$, where the maximum value is noted at $Ri=1$.
- At lower value of Ri ($Ri=0.1$) there is a continuous increase in Nusselt number for $Re=100$. When Re is increased to 400 and 800 , there is a rise and drop in Nusselt number closer to $N=0$.
- The increase in Ri and Re gives rise to increase in Nusselt number. At $Ri=3$ due to the aiding solutal buoyancy force the Nusselt number has increased by 54.6% for $Re=400$ and by 67% for $Re=800$ as N is varied from 0 to 10 , taking the Nusselt number value at $N=0$ as the reference for a given Reynolds number at $Ri=3$.

Nomenclature

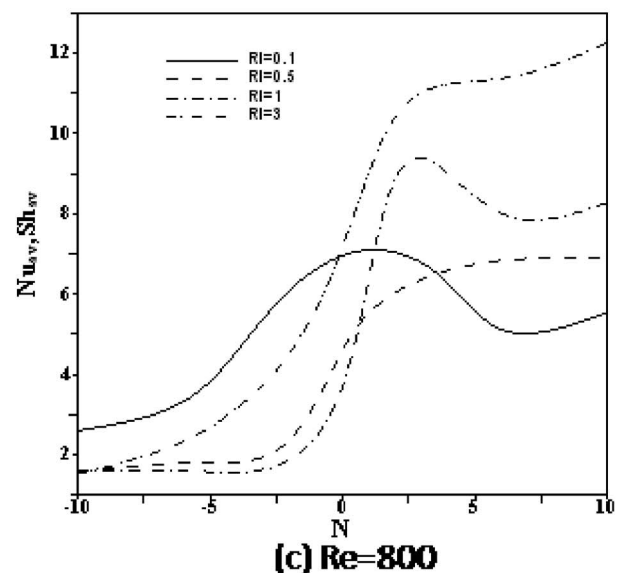
- C = species concentration
 D = binary diffusion coefficient
 g = gravitational acceleration
 Gr_S = Grashof number due to mass diffusion
 Gr_T = Grashof number due to thermal diffusion
 H = height of the cavity
 Le = Lewis number
 N = buoyancy ratio
 Nu = local Nusselt number
 p = pressure



(a) $Re=100$



(b) $Re=400$



(c) $Re=800$

Fig. 8 Effect of buoyancy forces on hot wall average Nusselt number for Reynolds number variation

P = nondimensional pressure
 Pr = Prandtl number
 Re = Reynolds number
 Ri = Richardson number
 Sc = Schmidt number
 Sh = local Sherwood number
 t = time
 T = temperature
 u, v = horizontal and vertical velocity components
 U, V = Nondimensional velocity components
 U_0 = lid velocity
 x, y = horizontal and vertical coordinates
 X, Y = Nondimensional coordinates

Greek Symbols

α = thermal diffusivity
 β_C = concentration volumetric expansion coefficient
 β_T = thermal volumetric expansion coefficient
 μ = dynamic viscosity
 ν = kinematic viscosity
 Φ = Nondimensional species concentration
 θ = Nondimensional temperature
 ρ = density
 τ = Nondimensional time
 ω = vorticity
 ζ = Nondimensional vorticity

Subscripts

c = cold

h = hot
 av = average

References

- [1] Gebhart, B., and Pera, L., 1971, "The Nature of Vertical Natural Convection Flows Resulting From the Combined Buoyancy Effects of Thermal and Mass Diffusion," *Int. J. Heat Mass Transfer*, **14**, pp. 2025–2050.
- [2] Pera, L., and Gebhart, B., 1972, "Natural Convection Flows Adjacent to Horizontal Surfaces Resulting From the Combined Buoyancy Effects of Thermal and Mass Diffusion," *Int. J. Heat Mass Transfer*, **15**, pp. 269–278.
- [3] Ostrach, S., 1980, "Natural Convection With Combined Driving Forces," *PCH, PhysicoChem. Hydrodyn.*, **1**, pp. 233–247.
- [4] Aydm, O., 1999, "Aiding and Opposing Mechanisms of Mixed Convection in a Shear and Buoyancy-Driven Cavity," *Int. Commun. Heat Mass Transfer*, **26**(7), pp. 1019–1028.
- [5] Mansour, R. B., and Viskanta, R., 1994, "Shear-Opposed Mixed-Convection Flow and Heat Transfer in a Narrow Vertical Cavity," *Int. J. Heat Fluid Flow*, **15**(6), pp. 462–469.
- [6] Alleborn, N., Raszillier, H., and Durst, F., 1999, "Lid-Driven Cavity With Heat and Mass Transport," *Int. J. Heat Mass Transfer*, **42**, pp. 833–853.
- [7] Al-Amiri, A. M., Khanafer, K. M., and Pop, I., 2007, "Numerical Simulation of Combined Thermal and Mass Transport in a Square Lid-Driven Cavity," *Int. J. Therm. Sci.*, **46**, pp. 662–671.
- [8] Maiti, D. K., Gupta, A. S., and Bhattacharyya, S., 2008, "Stable/Unstable Stratification in Thermosolutal Convection in a Square Cavity," *ASME J. Heat Transfer*, **130**, p. 122001.
- [9] Senthil kumar, D., Murugesan, K., and Thomas, H. R., 2008, "Numerical Simulation of Double Diffusive Mixed Convection in a Lid-Driven Square Cavity Using Velocity-Vorticity Formulation," *Numer. Heat Transfer, Part A*, **54**, pp. 837–865.
- [10] Murugesan, K., Lo, D. C., Young, D. L., Fan, C. M., and Chen, C. W., 2006, "Global Matrix-Free Finite-Element Scheme for Natural Convection in a Square Cavity With Step Blockage," *Numer. Heat Transfer, Part B*, **50**, pp. 353–373.

Scale-Up and Generalization of Horizontal-Base Pin-Fin Heat Sinks in Natural Convection and Radiation

D. Sahray
G. Ziskind
R. Letan

Department of Mechanical Engineering,
Heat Transfer Laboratory,
Ben-Gurion University of the Negev,
P.O. Box 653,
Beer-Sheva 84105, Israel

This paper provides further insight in heat transfer from horizontal-base pin fin heat-sinks in free convection of air. The main objective is to assess the effect of base size, and this with regard to the effects of fin height and fin population density studied in a previous work (Sahray, D., et al., 2010, "Study and Optimization of Horizontal-Base Pin-Fin Heat Sinks in Natural Convection and Radiation," ASME J. Heat Transfer, 132(012503), pp. 1–13). To this end, experimental and numerical investigations are performed with sinks of different base sizes. The sinks are made of aluminum, with no contact resistance between the base and the fins, and are heated using foil electrical heaters. In the corresponding numerical study, the sinks and their environment are modeled using the FLUENT 6.3 software. In the experiments, sink bases of $100 \times 100 \text{ mm}^2$ and $200 \times 200 \text{ mm}^2$ are used, while in the numerical study sinks of $50 \times 50 \text{ mm}^2$ are investigated, too. In addition to the sinks with exposed, free edges (Sahray, D., et al., 2010, "Study and Optimization of Horizontal-Base Pin-Fin Heat Sinks in Natural Convection and Radiation," ASME J. Heat Transfer, 132(012503), pp. 1–13), the same sinks are explored also with their edges blocked. This is done in order to exclude the edge effect, thus making it possible to estimate heat transfer from a sink of an "infinite" base size. Heat-transfer enhancement due to the fins is assessed quantitatively and analyzed for various base sizes and fin heights. The effect of fin location in the array on its contribution to the heat-transfer rate from the sink is analyzed. By decoupling convection from radiation, a dimensional analysis of the results for natural convection is attempted. Interdependence of the base size and fin height effects on the heat transfer is demonstrated. A correlation that encompasses all the cases studied herein is obtained, in which the Nusselt number depends on the Rayleigh number, which uses the "clear" spacing between fins as the characteristic length, and on the dimensions of the fins and the base. [DOI: 10.1115/1.4002032]

Keywords: pin fin, natural convection, scale-up, correlation

1 Introduction

In a recent paper [1], heat transfer by free convection and radiation from horizontal-base pin-fin heat-sinks, exposed to ambient at their perimeters, has been studied experimentally and numerically. The effects of fin height and fin population density on the performance of the sinks have been investigated at various heat inputs. The findings of Sahray et al. [1] agree quantitatively with the important results for pin-fin heat-sinks in natural convection [2], in particular, concerning additivity of natural convection and radiation and existence of optimum fin population, contributing to the literature on pin-fin sinks' performance in natural convection and radiation at various orientations [3–7].

It has been found in Ref. [1] that heat-transfer enhancement by fins increases up to a certain fin population density, and then decreases, demonstrating an optimum array at various fin heights. The results also showed that in horizontal-base pin-fin heat-sinks, the outer rows, which are exposed to free flow of ambient air, contribute the major part of the total heat transfer to the surroundings. Thus, an individual outer-row fin contributes much more than an inner fin.

The free convection contribution to the combined heat transfer has been decoupled from that of radiation, and generalization of

the results has been achieved defining the Nusselt and Rayleigh numbers based on the clear spacing between the fins, $\delta = S - W$, where S and W are the fin pitch and width, respectively:

$$\text{Nu}_\delta = \frac{h_c \delta}{k} \quad (1)$$

$$\text{Ra}_\delta = \frac{g \beta \Delta T \delta^3}{\nu^2} \text{Pr} \quad (2)$$

where h_c is the mean convective heat-transfer coefficient, calculated as the mean heat flux by convection only, divided by the temperature difference between the sink and the ambient, ΔT ; k is the thermal conductivity of air, β is the volumetric expansion coefficient, ν is the kinematic viscosity, and Pr is the Prandtl number. The heat flux was calculated using the total exposed area of the sink, namely, the sum of the base and fin-side areas. For the three different fin heights explored in Ref. [1], the results were approximated by curves that follow the same relation:

$$\text{Nu}_\delta = C \text{Ra}_\delta^{1/2} \left\{ 1 - \exp \left[- \frac{7000}{\text{Ra}_\delta} \right] \right\}^{1/3} \quad (3)$$

where the constant C was determined using a statistical analysis. The remarkable similarity of the curves for different heights indicated that it was possible to obtain a more general correlation, which was also demonstrated using the ratio of the fin height to its width, H/W .

Contributed by the Heat Transfer Division of ASME for publication in the JOURNAL OF HEAT TRANSFER. Manuscript received March 23, 2010; final manuscript received May 27, 2010; published online August 13, 2010. Assoc. Editor: He-Ping Tan.

While the analysis presented in Ref. [1] indicated the general role of fin height and fin population density in sink performance when the outside perimeter of the fins was exposed to the ambient, it was limited to the results obtained for the same base size, $100 \times 100 \text{ mm}^2$, in all cases explored. Thus, the effect of the base size on the sink performance has not been addressed at all. It was conjectured that a larger or smaller heat sink would perform in a similar manner only if the flow field remains similar, i.e., air enters from the sink edges, moves toward its center, and then flows up. On the other hand, as the base size increases, the flow field may change drastically, featuring, for instance, air inflow from above at the inner parts of the sink. As a result, the sink thermal performance would differ from that reported in Ref. [1]. Actually, this problem is of significant practical importance, being related to a broader question of sink scale-up.

The present study aims at further generalization of the results obtained in Ref. [1], to include pin-fin heat-sinks with a horizontal base of an *arbitrary* size. This is done by two different approaches, termed direct and indirect, as presented below:

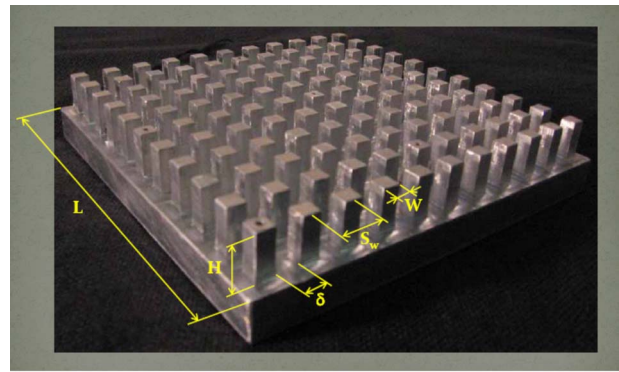
1. *Direct approach.* Heat sinks with various base sizes are studied both experimentally ($200 \times 200 \text{ mm}^2$ and $100 \times 100 \text{ mm}^2$ [8]) and numerically ($50 \times 50 \text{ mm}^2$ and $200 \times 200 \text{ mm}^2$ in addition to $100 \times 100 \text{ mm}^2$ [9]). While this approach is obvious, it has one serious limitation: The validity of the results does not extend beyond the largest sink actually explored. This fact impairs the ability to predict behavior of scaled-up sinks.
2. *Indirect approach.* The same heat-sinks are explored when their edges are blocked, i.e., air is not allowed to enter the sink from its sides. This approach, suggested in Ref. [10] and developed in Refs. [8,9,11], assumes that blocking the sink edges reduces air inflow from its sides. Thus, the flow is characterized by multiple entrances/exits at the top of the sink, as if the sink base were of an infinite size.

In the present work, all the heat-sinks explored in Ref. [1], as well as all the additional sinks introduced above, are studied also with the blocked edges [8,9]. The numerical model, which reconstructs meticulously the physical one, is validated versus the experimental results. Detailed analysis is done of the contributions of fin rows and individual fins to the total heat transfer from the sink, as related to the air flow patterns. The contributions of free convection and radiation are decoupled, and the results for free convection are generalized and correlated through a dimensional analysis.

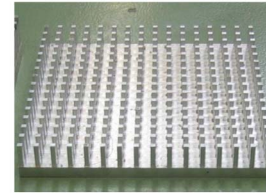
2 Physical and Numerical Models

Physical model. The experimental model has been extensively described in Ref. [1]; thus only the essential details are given here. The model consists of a pin-fin heat sink and insulation, both enclosed in a relatively large box open from above. The heat-sinks, examples of which are shown in Fig. 1, are made of aluminum 6061 blocks by machining, in order to exclude any contact resistance between the base and the fins. The base dimensions, $L \times L$, are $100 \times 100 \text{ mm}^2$ (Fig. 1(a)) and $200 \times 200 \text{ mm}^2$ (Fig. 1(b)), and its thickness is 10 mm. The fin cross section, $W \times W$, is $4 \times 4 \text{ mm}^2$ in all cases, whereas the fin height, H , is 10 mm, 20 mm, or 30 mm. As the number of fins in the sink varies, different values of fin pitch, S , and interfin “clear” spacing, δ , are obtained.

From below, an electrical foil heater is attached to the base. The heater is pressed to the base by an additional aluminum plate. The plate dimensions are identical to those of the base, and its thickness is 5 mm. The insulation is made of expanded polystyrene (EPS) and has the thermal conductivity of $k_{\text{ins}} = 0.034 \text{ W/m K}$ according to the manufacturer’s data. The insulation thickness is about 135 mm under the sink. Following the discussion above, the sink can be enclosed in the insulation in two different ways, as shown in Fig. 2:



a.



b.

Fig. 1 Examples of pin-fin heat-sinks used in the present study: (a) 100 mm sink with dimensions and (b) 200 mm sink

1. Regular installation, where the upper surface of the base is mounted flush with the upper surface of the insulation, which does not touch the fins, thus allowing horizontal flow of air from the edges to the fin array.
2. Modified installation [11], in which fin *tips* of the sink are mounted flush with the upper surface of the insulation. In the latter case, the horizontal distance between the fin outward surface and the insulation is equal to half the distance between the neighboring fins in the array. Thus, in the latter case, referred to as “blocked edges,” the influence of the edges is expected to be reduced or neutralized.

Table 1 summarizes the cases explored experimentally. Actually, all 11 sinks of $L=100 \text{ mm}$ [1] are now explored with blocked edges. In addition, three sinks of $L=200 \text{ mm}$ and various fin heights, manufactured for this study, are explored with both free and blocked edges [8,9].

The power inputs explored in the present study varied in the range from 4 W to 16 W for the sinks of $L=100 \text{ mm}$ and, proportionally, from 16 W to 64 W for the sinks of $L=200 \text{ mm}$. The upper limit has been set in order to keep the heaters at the temperatures below 100°C . The temperature of the sink, T_w , is monitored during the experiments, using eight T-type thermocouples installed at various locations inside the base and fins. Additional thermocouples monitor temperatures in the insulation, between the sink and the bottom, and the ambient temperature. All thermocouples are connected to a Fluke Hydra data acquisition unit. As reported in Ref. [1], the uncertainties were estimated using the

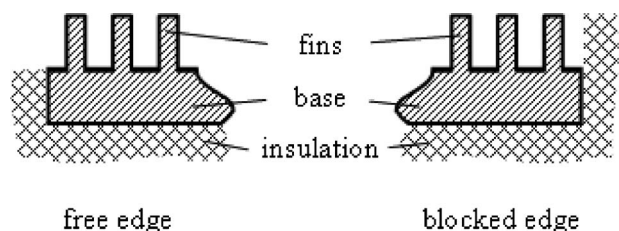


Fig. 2 Free and blocked edges

Table 1 Summary of the experimental cases, with free and blocked edges

Fin height H (mm)	Base size L (mm)	Array, fins	Pitch S (mm)	Pitch to width ratio, S/W
10	100 ^a	8×8=64	14	3.5
		9×9=81	12	3.0
		11×11=121	10	2.5
		16×16=256	6	1.5
	200	16×16=256	14	3.5
20	100 ^a	7×7=49	16	4.0
		8×8=64	14	3.5
		9×9=81	12	3.0
		11×11=121	10	2.5
	200	16×16=256	14	3.5
30	100 ^a	7×7=49	16	4.0
		8×8=64	14	3.5
		9×9=81	12	3.0
		16×16=256	14	3.5
	200	16×16=256	14	3.5

^aThese sinks were explored in Ref. [1] with free edges.

method of Kline and McClintock [12] as being within $\pm 0.3^\circ\text{C}$ and $\pm 0.3\text{ W}$ for the temperature difference, $\Delta T = T_w - T_\infty$, and the input power, $q = UI$, respectively.

Numerical model. As discussed in Ref. [1], the numerical model follows, in a most complete and detailed manner, the features and dimensions of the physical model, carefully reconstructing the physical prototype. Thus, the dimensions of the heat-sinks, including individual fins, as well as of the insulation and outer box, are exactly the same as in the experiments. The material properties used in the simulations are based on aluminum 6061, expanded polystyrene, and Perspex for the heat-sinks, insulation, and outer box, respectively [1].

While 14 different heat-sinks are explored in the experiments [8] and “reproduced” in the simulation [9], the total number of sinks explored numerically reaches 72, as summarized in Table 2: for each fin height, nine sinks are explored for the bases of $L = 100\text{ mm}$ and $L = 200\text{ mm}$ each, while for an additional base size of $L = 50\text{ mm}$ six sinks are explored. For each of the sinks, simulation is performed both for the free and blocked edges, thus bringing the overall number of cases to 144, of which 27 (the base of $L = 100\text{ mm}$ with free edges) have been considered previously.

Table 2 Summary of the numerical cases, with free and blocked edges

Fin height H (mm)	Base size L (mm)	Array, fins	Pitch S (mm)	Pitch to width ratio, S/W
10, 20, 30	50	3×3=9	23	5.75
		4×4=16	15	3.75
		5×5=25	11	2.75
		6×6=36	9	2.25
		7×7=49	7	1.75
		8×8=64	6	1.50
	100 ^a	6×6=36	19	4.75
		7×7=49	16	4.00
		8×8=64	14	3.43
		9×9=81	12	3.00
		10×10=100	10	2.50
		11×11=121	9	2.25
		12×12=144	8	2.00
		14×14=196	7	1.75
		16×16=256	6	1.50
		200	12×12=144	17
	13×13=169	16	4.00	
	14×14=196	15	3.75	
	15×15=225	14	3.50	
	16×16=256	13	3.25	
	17×17=289	12	3.00	
	18×18=324	11	2.75	
20×20=400	10	2.50		
22×22=484	9	2.25		

^aThese sinks were explored in Ref. [1] with free edges.

The full geometry is numerically simulated in every case. Typically, five different power inputs are considered for each sink.

In the simulations, the basic conservation equations of continuity, momentum, and energy are solved numerically, using the FLUENT 6.3 software. The velocity fields, temperature distributions in the air (convection), temperature distributions in the heat sink and insulation (conduction), and radiation exchange between various components are modeled simultaneously. Accordingly, the appropriate boundary conditions are used. For the momentum equation (air) no-penetration and no-slip are assumed at all the solid boundaries (exposed sink and insulation surfaces, box inner walls), with the pressure boundary condition $p' = 0$ imposed at the upper boundary of the system. Following Ref. [1], boundary conditions for the energy equation are based on the experimental parameters:

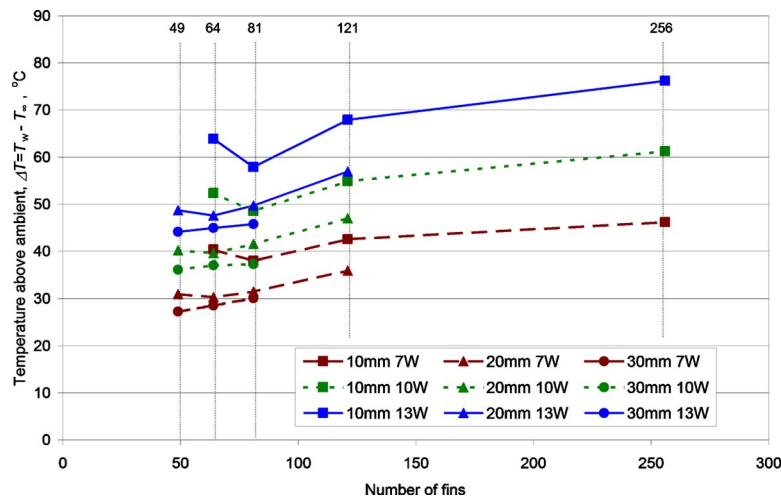
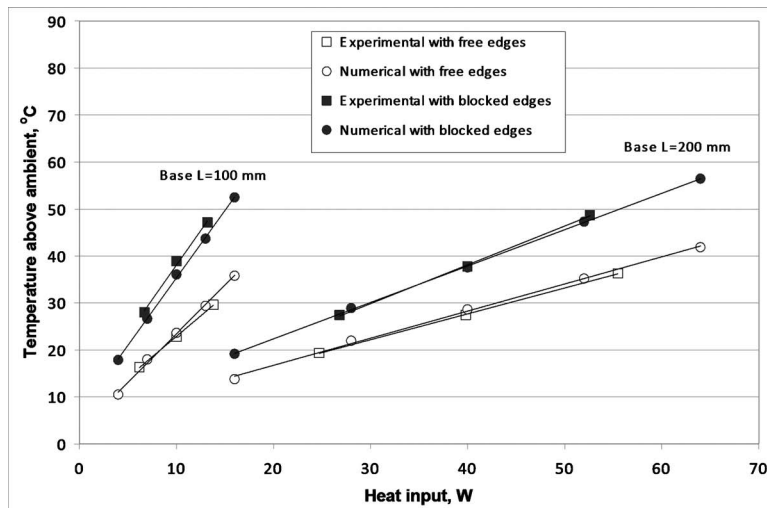
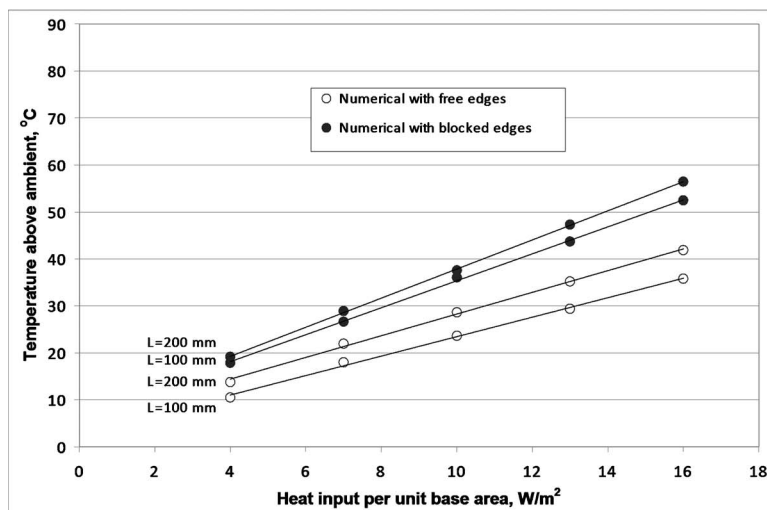


Fig. 3 Summary of the experimental results for the sinks of Table 1 at various heat inputs, $L = 100\text{ mm}$ and blocked edges



a.



b.

Fig. 4 Additional experimental results and validation of the numerical results at $H=30$ mm: (a) comparison for 100 mm and 200 mm sinks with free and blocked edges and (b) comparison for 100 mm and 200 mm sinks at the same heat input per unit base area

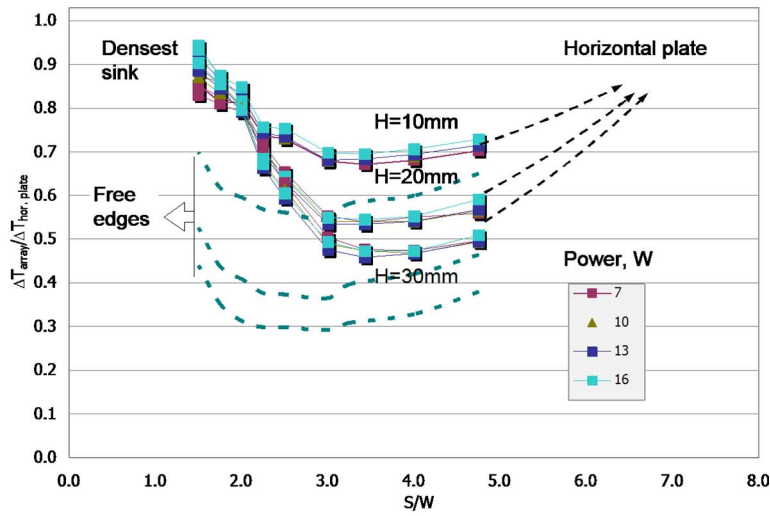
the heat input to the heat sink is set as in the corresponding experiment, whereas beyond the boundaries of the domain, the ambient temperature is assigned. Surface-to-surface radiation inside the system and from the system to the surroundings is taken into account through a so-called discrete transfer radiation model (DTRM). Following the analysis [1], the sink emissivity was set to be $\varepsilon=0.45$ in all cases. The overall rate of change of the internal energy of the air, as well as the overall heat input/output at any boundary, served to ensure the overall energy balance of the system.

It was discussed in Ref. [1] that some instability could be expected in the system, as is typical for natural convection caused by heating from below. However, no significant difference in the flow field was predicted by the numerical solution when the sink edges were free. The results for the sinks with blocked edges also do not show a significant variation in the average sink temperature. On the other hand, it appears that the actual flow field is essentially time dependent when the edges are blocked. For this reason, a time-dependent form of the conservation equations was also used.

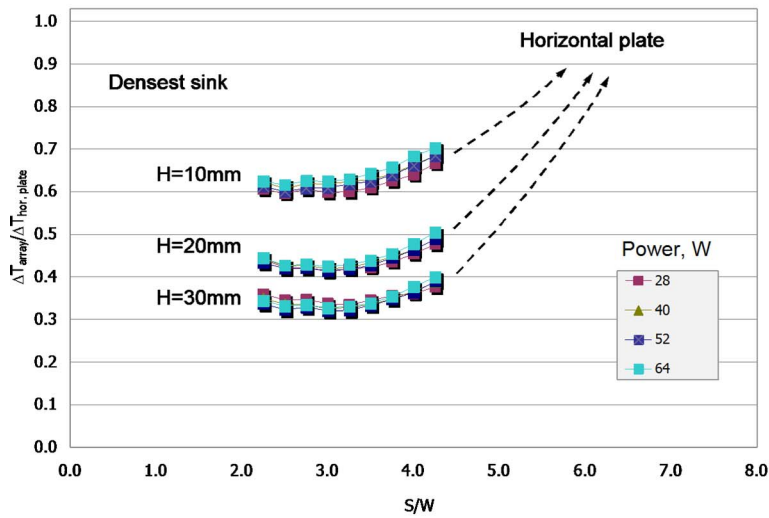
The technical details of the numerical model, including the domain size, and grid size and structure were discussed in Ref. [1]. Here we note that the grid depended on the base size, fin height, and fin population density, reaching about 8.5×10^6 elements for the largest and densest heat sink explored. Therefore, extensive computing resources were required. The authors were allowed access to an especially assembled workstation featuring the Intel(R) Core(TM)2 Quad CPU at 2.66 GHz processors and 8.00 Gbyte RAM. Still, a typical simulation could take up to 40 h.

3 Results and Discussion

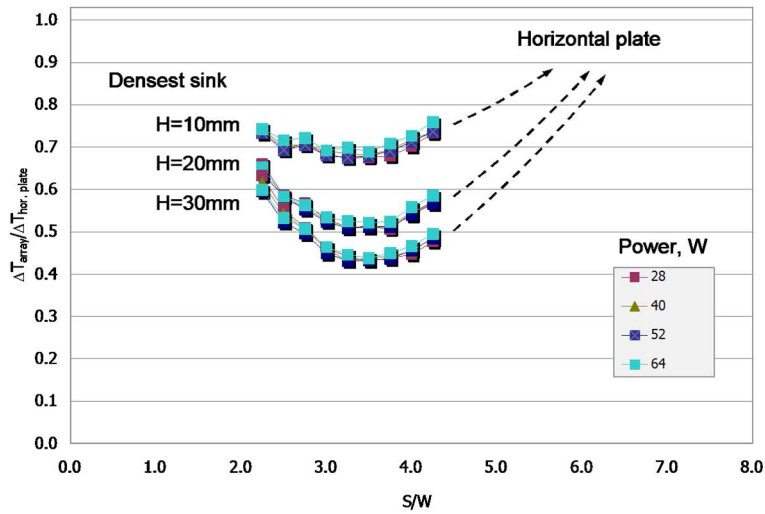
Figure 3 shows a summary of the experimental results for all 11 arrays of $L=100$ mm with blocked edges [10,11]. The temperature difference between the sink and the surroundings, $\Delta T=T_w-T_\infty$, serves as the dependent variable, shown as the function of the fin population, while the fin height and the heat input serve as parameters. One can see, as expected, the arrays with higher fins perform at lower temperature at the same number of fins for any



a.

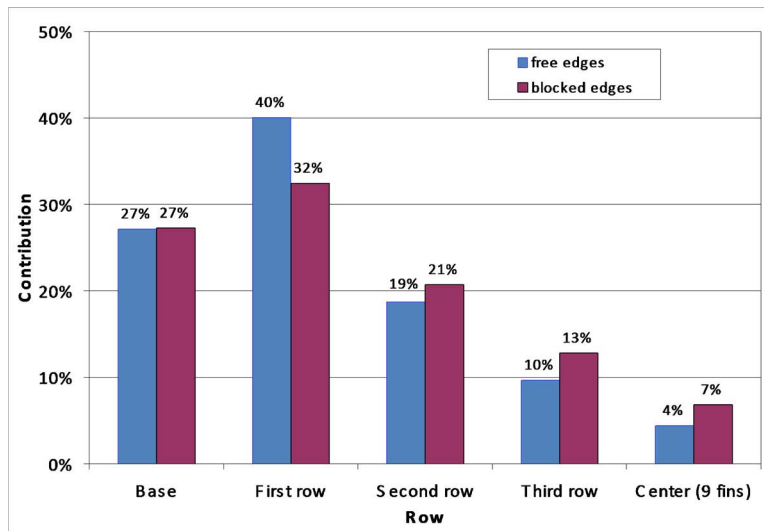


b.

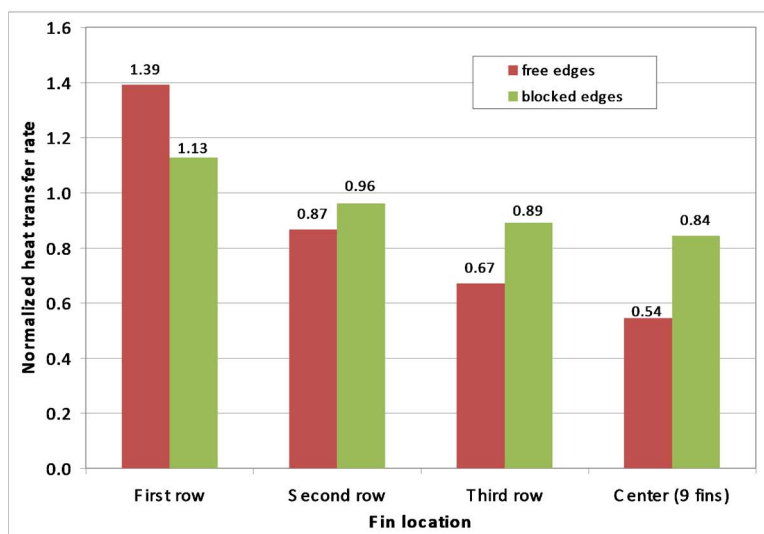


c.

Fig. 5 Normalized numerical results and optimum for different fin arrays: (a) 100 mm sinks with blocked edges (results for free edges are reproduced [1]), (b) 200 mm sinks with free edges, and (c) 200 mm sinks with blocked edges



a.



b.

Fig. 6 Contribution of different rows and individual fins to the total heat output of a sink with 81 fins, of $L=100$ mm and $H=10$ mm: (a) different rows and (b) individual fins

given heat input. Also, the effect of the fin population density is obviously not monotonic. However, it is different from the results for the same sinks with free edges [1], where the optimum fin population was the same for different fin heights. Figure 3 shows that for the fin height of $H=10$ mm the sink temperature is always lower at the same heat input when the array consists of 81 fins, like in Ref. [1]. However, the sink of 64 fins generally outperforms both the denser and “looser” sinks for the fin height of $H=20$ mm, whereas at the fin height of $H=30$ mm, the sink of 49 fins gives the best performance. Thus, one can see that the optimum population continues to exist when the edges are blocked, but it becomes looser when the fin height increases. This result is obviously connected to the patterns of air penetration from the top into the sink with blocked edges.

Figure 4 shows an example of the experimental and numerical results for the fin height of 30 mm and the base sizes of 100 mm and 200 mm [8,9], i.e., the latter is the largest sink explored in the present study. Figure 4(a) shows a very good agreement between the experiments and simulations in all four presented cases, with the assumed emissivity of $\varepsilon=0.45$ [1]. Actually, Fig. 4(a) provides additional validation of the numerical approach, going beyond the

results of Ref. [1] both for different base sizes and blocked edges. We note that the results for blocked edges are characterized by higher temperatures at otherwise identical conditions. Figure 4(b) shows the results in terms of the heat input per unit base area, bringing the results for $L=100$ mm and $L=200$ mm to a common denominator. The results show that the sinks of $L=100$ mm perform better than the sinks of $L=200$ mm. However, the difference due to sink size is much smaller when the sink edges are blocked. The results of Fig. 4 indeed confirm that the smaller the size of the base, the more pronounced the edge effect, reflecting the increasing ratio of the sink perimeter to the base area.

Examples of the optima, as defined from the numerical calculations, are presented in a normalized form in Fig. 5, where the fin pitch, S , normalized with the fin width, W , serves as the independent variable. The dependent variable is the normalized temperature, defined as the temperature above the ambient for the heat sink, ΔT_{array} , divided by the temperature above ambient for the flat plate, $\Delta T_{\text{hor.plate}}$, at the same heat input. The results for different heat inputs practically coincide at the same fin height when the normalized representation is used, both for the sinks of L

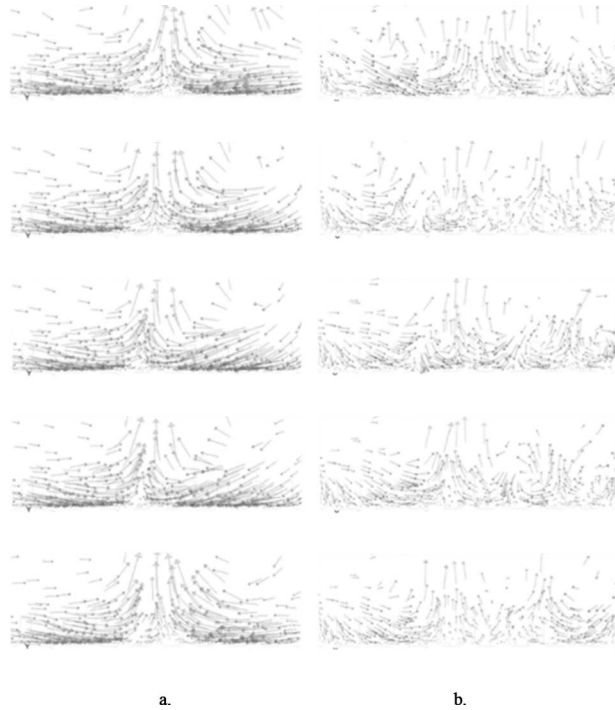


Fig. 7 Simulated transient flow fields of the sink with 81 fins, of $L=100$ and $H=10$ mm: (a) free edges and (b) blocked edges

$=100$ mm with blocked edges in Fig. 5(a), where the results for the same sink with free edges [1] are also shown schematically, and the sinks of $L=200$ mm with free and blocked edges in Fig. 5(b) and 5(c), respectively. It may be concluded, therefore, that the analysis suggested in Ref. [1], where only the sinks of $L=100$ mm with free edges were studied, is rather universal. The results prove again that (1) for a horizontal-base pin fin heat sink, there exists an optimum fin population, which yields a maximum of the combined-mode heat-transfer rate for a given base area at a given temperature difference, and (2) for a sink with given base and fin dimensions, the optimal fin population is practically independent of the temperature difference with the surroundings [1,2]. It is worth to note that when the sink edges are blocked, the performance of densely populated sinks tends to approach that of a horizontal plate. This result may be related to weak air penetration from above into the sink. Also, it is worth to note that the differences between the sinks of the same size with free and blocked edges are less significant when the base size increases.

As shown in Ref. [1], the temperature of the sink base and fins is essentially uniform, but the local heat flux from the base and the fins is highly nonuniform, varying from the periphery to the center and from one fin to another. The present results reveal significant differences between the sinks with free and blocked edges. Figure 6 provides an insight in the heat-transfer distribution between different fins in the sink, showing the time-averaged (180 s) relative contributions of various fins to the total convection-radiation heat loss from the sink. In Fig. 6(a), examples of the results are presented for “rows” of the array of $9 \times 9 = 81$ fins for $L=100$ mm and $H=10$ mm. It is essential to note that the rows are defined in the following manner: the “first row” denotes all the fins located at the outside perimeter of the sink, the “second row” means the next row inside, and so on. For instance, for the presented sink of $9 \times 9 = 81$ fins, this means that the rows from first to third count 32, 24, and 16 fins, respectively, whereas remaining 9 fins are in the center. One can see from Fig. 6(a) that the contributions of various rows are more uniform when the edges are blocked. The heat-transfer rate per an individual fin in the row is shown in Fig.

6(b). The results are presented in a normalized form: the heat-transfer rate per fin in a given row is divided by the average heat-transfer rate per fin in the sink.

The results of Fig. 6(b) show that unlike the sink with free edges, the contribution of individual fins to the total heat transfer from a sink with blocked edges is much more uniform. This situation obviously results from a rather different flow field, as shown in Fig. 7, for five consecutive seconds in each case. The heat sink is the same as in Fig. 6, namely, $L=100$ mm with $9 \times 9 = 81$ fins of $H=10$ mm. The typical flow patterns for both cases are shown for the vertical plane located 6 mm off the plane of symmetry of the sink. This is done in order to present the flow in the passages between the in-line fins shown at the background. When the edges are free, the cool air flows into the sink mostly from the sides, and the flow is essentially time independent, resembling, in general, an “inverse” stagnation flow from the sides toward and up the vertical axis of symmetry. When the edges are blocked, the flow is time dependent, with multiple shifting entrances and exits from above.

4 Dimensional Analysis of Natural Convection

Following Sparrow and Vemuri [2], it was shown in Ref. [1] that natural convection may be decoupled from radiation and analyzed separately. It has been demonstrated that for a sink with free edges, generalization is possible, as discussed above in connection with Eqs. (1)–(3). In Ref. [1], there was an extensive body of results for the sinks with the same base and free edges. Herein, two extra groups of results are added, namely, for the sinks with a smaller and a larger base size having free edges, and for the sinks of different sizes with blocked edges.

For the sinks with free edges, the analysis essentially follows that introduced in Ref. [1] and summarized above in Eqs. (1)–(3). Indeed, Fig. 8 shows that an excellent generalization is obtained separately for different fin heights, H , and base sizes, L , in the form of Eq. (3). The only adaptable parameter is the constant C , which was determined using a statistical analysis. The best fit for the cases with heights $H=10$, 20 mm and 30 mm and bases of $L=50$, 100, and 200 mm yielded the values of C and R^2 shown in Table 3.

One can see that for any given fin height, the Nusselt number decreases with an increase in the base dimensions. On the other hand, for any given base dimensions, the Nusselt number increases when the fin height increases. These trends suggest looking for a generalization, which is based on the dimensionless group L/H , in the form

$$C \sim f\left(\frac{H}{W}\right) \left\{ 1 + A_2 \exp\left(-A_3 \frac{L}{H}\right) \right\} \quad (4)$$

where A_2 and A_3 are constants yet to be determined. Here, an additional dimensionless group, H/W , is introduced in order to account for the fact that for large L the expression in figure brackets vanishes, while some effect of fin height must remain. In particular, for the heights of 10 mm, 20 mm, and 30 mm explored in the present study, it appears that the following form reflects the results:

$$f\left(\frac{H}{W}\right) = \left\{ 1 - \exp\left(-\frac{H}{W}\right) \right\} \quad (5)$$

This means that a certain increase in the Nusselt number occurs when the fin height increases, but this increase is much less pronounced at greater heights. For instance, in the present study the expression in figure brackets in Eq. (5) yields about 0.92 for $H=10$ mm, while the results for $H=20$ mm and $H=30$ mm are almost equal to each other and very close to unity.

Substitution of Eqs. (4) and (5) into Eq. (3) yields the following general relation:

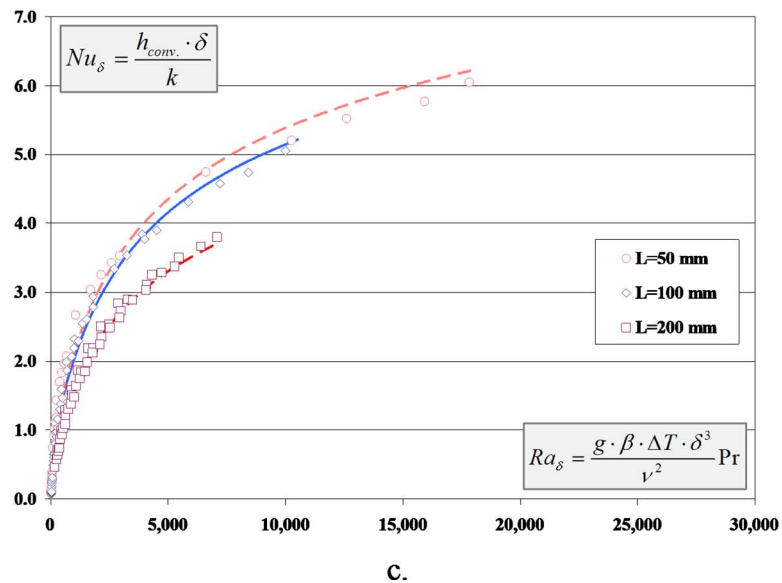
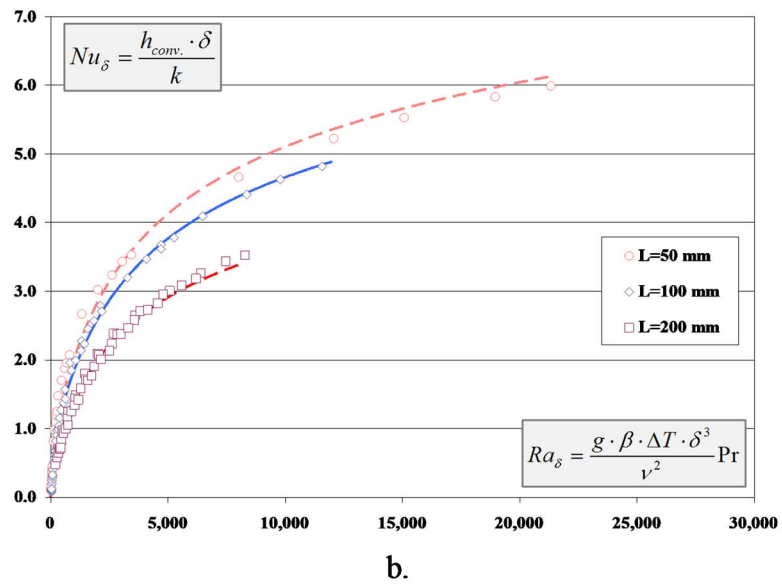
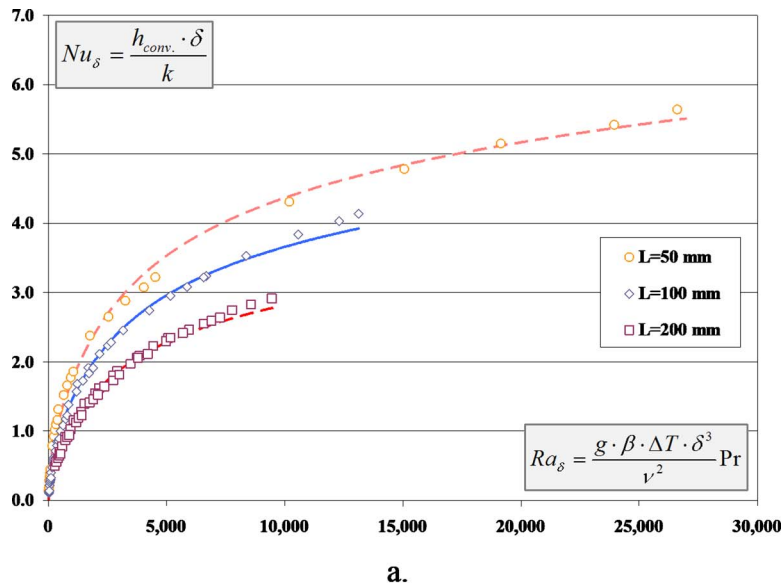


Fig. 8 Nusselt number versus Rayleigh number for different base sizes and fin heights with free edges: (a) $H=10$ mm, (b) $H=20$ mm, and (c) $H=30$ mm

Table 3 Coefficients C (with R^2 in parentheses) for various cases with free edges

	H (mm), L (mm)		
	10	20	30
50	0.05487(0.99645)	0.06417(0.99052)	0.06768(0.98644)
100	0.04597(0.99417)	0.05857(0.99283)	0.06465(0.98912)
200	0.03542(0.98959)	0.04524(0.98711)	0.05136(0.98430)

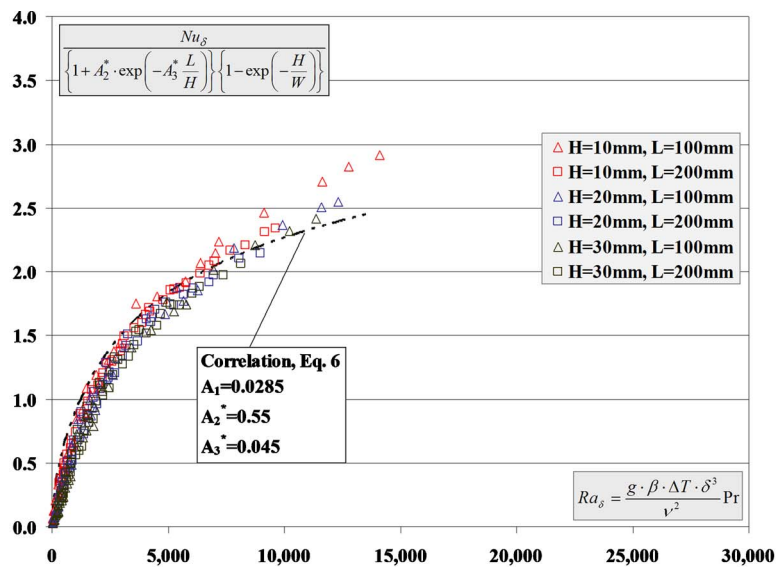
$$Nu_{\delta} = A_1 \left\{ 1 - \exp\left(-\frac{H}{W}\right) \right\} \left\{ 1 + A_2 \exp\left(-A_3 \frac{L}{H}\right) \right\} Ra_{\delta}^{1/2} \times \left\{ 1 - \exp\left[-\frac{7000}{Ra_{\delta}}\right] \right\}^{1/3} \quad (6)$$

where A_1 is an additional constant. Thus, the Nusselt number appears to depend on the Rayleigh number (in the same way as

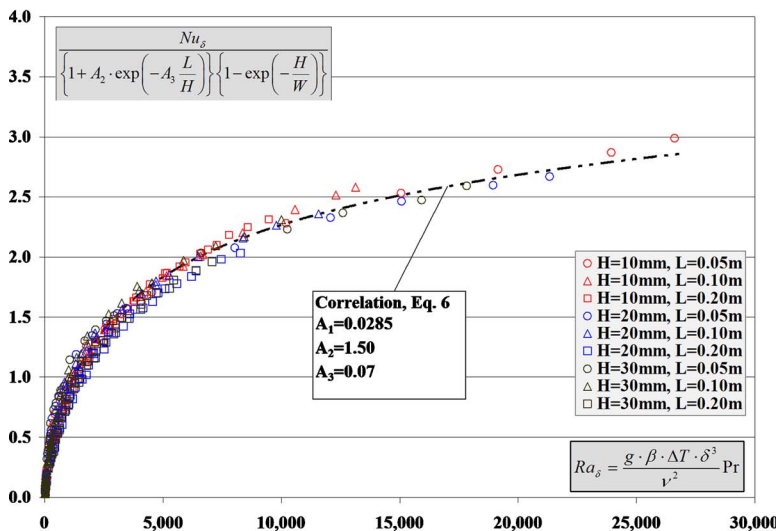
defined in Ref. [1]), on two additional dimensionless groups that reflect a full geometry of the sink, L/H and H/W , and also on constants A_1 , A_2 , and A_3 .

It appears that when L/H increases, the Nusselt number for any given Rayleigh number and H/W ratio is determined by the value of coefficient A_1 . Thus, it is desirable to estimate A_1 as accurately as possible. It is obvious that one way to do this is to use a statistical analysis, which would yield A_1 , A_2 , and A_3 . This would correspond to the direct approach introduced in Sec. 2

The values of C in Table 3 indicate, however, that it is impossible to have a reliable direct guess about how the Nusselt number changes when the sink size is beyond the bases actually studied. For this reason, we believe that it is essential to estimate A_1 using the indirect approach also introduced above. This is possible because for any given L , the Nusselt number for a sink with blocked edges is lower than that for the same sink with free edges. The results show that the difference between the two diminishes as L increases, since the flow fields become more similar to each other.



a.



b.

Fig. 9 Generalized results and overall correlation: (a) blocked edges and (b) free edges

Thus, it is obvious that the Nusselt number for blocked edges represents the lowest limit for the free edges' case.

It turns out that the results for blocked edges, excluding those for $L=50$ mm where no multiple vortices are formed, can be predicted fairly accurately. The same correlation is used, in the form of Eq. (6), with the following coefficients: $A_1=0.0285$, $A_2^*=0.55$, and $A_3^*=0.045$. The latter two coefficients have asterisks in order to underline that they are applied to the results for blocked edges, as shown in Fig. 9(a). Coefficient A_1 , however, must be the same for both free and blocked edges, since the performance of the former approaches that of the latter when the sink size, L , increases at the same fin height. Figure 9(b) shows a complete convergence of the results for all cases explored with free edges, and also an excellent agreement with the suggested correlation, Eq. (6), with $A_1=0.0285$, $A_2=1.50$, and $A_3=0.07$. This outcome is quite remarkable, considering the fact that the cases explored included three different base sizes, three different fin heights, and up to nine different fin population densities, i.e., a total of 72 geometrical cases with five different heat inputs in each.

The obtained correlation is valid for the horizontal-base heat-sinks with rectangular pin fins. As discussed above, it appears that the analysis suggested herein will remain valid even for very large base sizes. As for the fin height, the full similarity obtained for $H=10$ mm to $H=30$ mm indicates that the analysis may be extended to higher fins, as long as the fin efficiency remains close to unity. We note that as the fin width, W , is the only geometry parameter that did not vary in the present study, the values of constants included in the correlation may depend on such additional dimensionless group as W/S .

5 Conclusions

Heat transfer by free convection and radiation from horizontal-base pin-fin heat-sinks has been studied experimentally and numerically. The sinks had various fin population densities, fin heights, and base sizes. The study has focused on the effect of base size, thus aiming at the generalization of free convection attempted earlier.

In order to obtain generalization, heat-sinks with free and blocked edges were studied. The heat-sinks with blocked edges were used to model large sinks, which are less affected by their perimeter. It was demonstrated that, indeed, when the edges are blocked, air flow to the sink changes: Rather than moving from the edges to the center and up, it is characterized by multiple inflows from above, as expected when the base is very large.

Generalization of the results for free convection, decoupled from radiation contribution, has been achieved for all cases explored in the work, based on the Rayleigh and Nusselt numbers, defined for the "clear" spacing between the fins as the characteristic length, and the geometrical parameters of the sink. A correlation of the results, suggested in this study, makes it possible to design horizontal-base pin-fin heat-sinks in a broad range of base sizes, fin heights, and fin population densities.

Nomenclature

A = coefficient
 C = coefficient

g = gravitational acceleration (m/s^2)
 h_c = mean convective heat-transfer coefficient ($W/m^2 K$)
 H = fin height (m)
 I = electric current (A)
 k = thermal conductivity ($W/m K$)
 L = base length (m)
 Nu = Nusselt number
 Pr = Prandtl number
 q = power, heat-transfer rate (W)
 Ra = Rayleigh number
 S = pitch (m)
 T = temperature (K or $^{\circ}C$)
 U = voltage (V)
 W = fin width (m)

Greek Letters

β = volumetric expansion coefficient ($1/K$)
 δ = "clear" spacing between fins (m)
 Δ = difference
 ε = emissivity

Subscripts

c = convective
 inf = infinite size
 ins = insulation
 w = wall
 ∞ = ambient

References

- [1] Sahray, D., Shmueli, H., Ziskind, G., and Letan, R., 2010, "Study and Optimization of Horizontal-Base Pin-Fin Heat Sinks in Natural Convection and Radiation," *ASME J. Heat Transfer*, **132**(012503), pp. 1–13.
- [2] Sparrow, E. M., and Vemuri, S. B., 1986, "Orientation Effects on Natural Convection/Radiation Heat Transfer From Pin-Fin Arrays," *Int. J. Heat Mass Transfer*, **29**, pp. 359–368.
- [3] Zografos, A. I., and Sunderland, J. E., 1990, "Natural Convection From Pin Fins," *Exp. Therm. Fluid Sci.*, **3**, pp. 440–449.
- [4] Zografos, A. I., and Sunderland, J. E., 1990, "Numerical Simulation of Natural Convection From Pin-Fin Arrays," *ASME HTD-Vol. 157*, pp. 55–66.
- [5] Aihara, T., Maruyama, S., and Kobayakawa, S., 1990, "Free Convective/Radiative Heat Transfer From Pin-Fin Arrays With a Vertical Base Plate (General Representation of Heat Transfer Performance)," *Int. J. Heat Mass Transfer*, **33**, pp. 1223–1232.
- [6] Fisher, T. S., and Torrance, K. E., 1998, "Free Convection Limits for Pin-Fin Cooling," *ASME J. Heat Transfer*, **120**, pp. 633–640.
- [7] Huang, R.-T., Sheu, W.-J., and Wang, C.-C., 2008, "Orientation Effect on Natural Convective Performance of Square Pin Fin Heat Sinks," *Int. J. Heat Mass Transfer*, **51**, pp. 2368–2376.
- [8] Elmakaes, O., and Oren, Z., 2008, "Effect of Geometry on Heat Transfer From a Pin-Fin Array," Heat Transfer Laboratory, Department of Mechanical Engineering, Ben-Gurion University of the Negev, Graduation Project 08-38.
- [9] Sahray, D., 2010, "Analysis of Natural Convection and Radiation from Pin-Fin Heat Sinks With Horizontal Base," M.Sc. thesis, Ben-Gurion University of the Negev, Israel.
- [10] Sahray, D., Magril, R., Dubovsky, V., Ziskind, G., and Letan, R., 2007, "Study of Horizontal-Base Pin-Fin Heat Sinks in Natural Convection," *Proceedings of the ASME InterPACK '07*, Vancouver, Canada, Jul. 8–12.
- [11] Sahray, D., Shmueli, H., Segal, N., Ziskind, G., and Letan, R., 2008, "Pin-Fin Heat Sink With Horizontal Base and Blocked Edges," *Proceedings of the ASME 2008 Summer Heat Transfer Conference*, Jacksonville, FL, Aug. 10–14.
- [12] Kline, S. J., and McClintock, F. A., 1953, "Describing Uncertainties in Single-Sample Experiments," *Mech. Eng. (Am. Soc. Mech. Eng.)*, **75**, pp. 3–8.

Vadasz Number Influence on Vibration in a Rotating Porous Layer Placed Far Away From the Axis of Rotation

S. Govender

Corporate Specialist, Gas Turbines
Adjunct Professor
Generation Business Engineering,
ESKOM Holdings Ltd.,
Maxwell Drive,
Sunninghill,
Johannesburg 2000, South Africa;
School of Mechanical Engineering,
University of Kwa-Zulu Natal,
King George V Avenue,
Durban 4001, South Africa

*We consider vibration effects on the classical Rayleigh–Be’nard problem and the classical Vadasz (1994, “Stability of Free Convection in a Narrow Porous Layer Subject to Rotation,” *Int. Commun. Heat Mass Transfer*, **21**, pp. 881–890) problem, which includes rotation of a vertical porous layer about the z -axis. In particular, we focus on the influence of the Vadasz number on vibration for small to moderate and large Vadasz numbers. For small to moderate Vadasz numbers, we develop an analogy between the Vadasz problem (Vadasz, 1994, “Stability of Free Convection in a Narrow Porous Layer Subject to Rotation,” *Int. Commun. Heat Mass Transfer*, **21**, pp. 881–890) placed far away from the axis of rotation and classical Rayleigh–Be’nard problem, both of which include the effects of vibration. It is shown here that the stability criteria are identical to the Rayleigh–Be’nard problem with vibration when $g^* = \omega^2 X_0^*$. The analysis for the large Vadasz number scaling indicates that a frozen time approximation is appropriate where the effect of vibration is modeled as small variations in the Rayleigh number definition. [DOI: 10.1115/1.4002036]*

Keywords: gravity modulation, porous media, natural convection, Rayleigh number, Froude number

1 Introduction

The classical Rayleigh–Be’nard problem has been exhaustively studied for both pure fluids and porous domains with and without rotation. Comprehensive reviews are provided by Nield and Bejan [1] for saturated porous media, which is the porous equivalent of the work of Chandrasekar [2]. Vadasz [3] provided a detailed analysis of rotational effects on convection in porous media in the absence of gravity. This original work was later extended to include the effects of offsetting the porous layer along the x -axis and was detailed in Vadasz [4].

Later, Vadasz and Govender [5,6] included the effects of gravity in this analysis. In principle, the effects of gravity are passive when considering convection in a vertical rotating porous layer, and the key finding was that the vertical component of the wave number is identically zero, implying that the streamlines are constrained to the x - y plane. Govender [7] later reconfirmed this result in his investigation of an alternate orientation of the Vadasz [8] study and clearly showed that convection rolls are the only permissible convection mode.

As is the case with rotation, time-dependent body forces may occur in systems with density gradients subjected to vibrations. The influence of vibrations on thermal convection depends on the orientation of the time-dependent acceleration with respect to the thermal stratification. Much work has been done for pure fluids for a vertically modulated fluid layer with constant vertical stratification, i.e., modulated Rayleigh–Be’nard convection by Gresho and Sani [9], Wadih and Roux [10], Christov and Homsy [11], and Hirata et al. [12].

Govender [13,14] provided stability analyses for convection in gravity modulated porous layers heated from below and above. In addition, Govender [15] provided a weak nonlinear analysis of

convection in a gravity modulated porous layer. Bardan and Mojtabi [16] and Pedramrazi et al. [17] also contributed to the existing body of knowledge in this field and provided a very interesting distinction between the direct and averaged solution techniques, the latter being for large vibration frequencies. The latter technique is shown to be deficient in recovering the transition from synchronous to subharmonic solutions while the former method was demonstrated by Govender [18] to achieve a clear transition from synchronous to subharmonic modes. Kuznetsov [19] also extended the body of knowledge in this field by investigating bioconvection in the presence of gravity modulation.

The objective of the current work is to illustrate the controlling effect of the Vadasz number on the stability of convection in a vibrating vertical rotating porous layer placed far away from the axis of rotation for small to moderate and large Vadasz numbers. For the small to moderate Vadasz number scaling, we will develop an analogy between the classical Vadasz [3] study (when placed far away from the axis of rotation) and the Rayleigh–Be’nard problem, including the effects of vibration. In this study, we consider a vertical vibrating porous layer placed far away from the axis of rotation and will, henceforth, neglect gravitational effects, as it was shown by Govender [7], to play a passive role in the stability of convection. Furthermore, we adopt the direct solution technique in this analysis. A separate analysis for large Vadasz numbers will also be undertaken to determine the stability criteria.

2 Problem Formulation

A tall fluid saturated porous layer placed far away from the axis of rotation and subjected to vibration is presented in Fig. 1(a). The porous layer is constrained between two rigid vertical plates spaced a distance L^* apart and oscillates parallel to the centrifugal force in the horizontal direction. In addition, the Darcy law is extended to include the time derivative, while the Boussinesq approximation is applied to account for the effects of the density

Contributed by the Heat Transfer Division of ASME for publication in the JOURNAL OF HEAT TRANSFER. Manuscript received April 9, 2010; final manuscript received June 7, 2010; published online August 13, 2010. Assoc. Editor: Peter Vadasz.

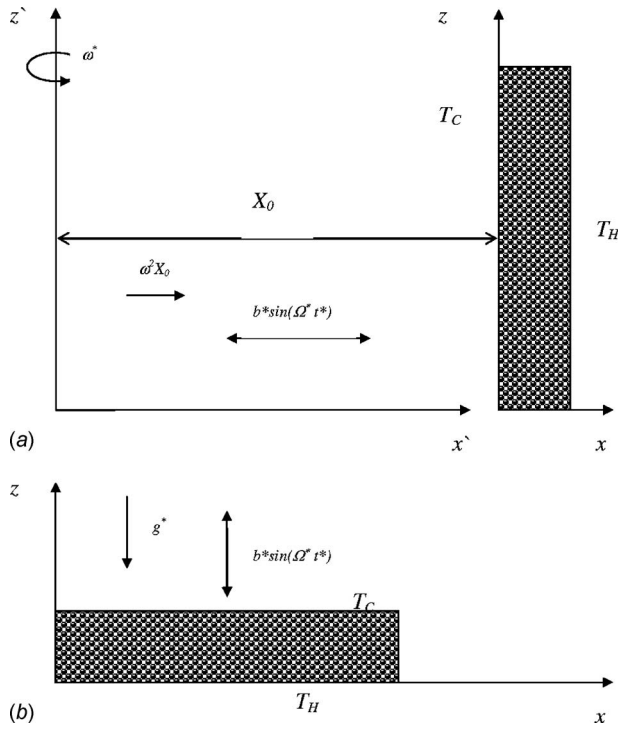


Fig. 1 (a) The offset vertical rotating porous layer to vibration and (b) the horizontal porous layer subjected to gravity modulation

variations. Based on the above, the following system of dimensional equations for continuity, momentum, and energy is proposed:

$$\nabla^* \cdot \mathbf{V}^* = 0 \quad (1)$$

$$\mathbf{V}^* = \frac{k^*}{\mu^*} \left[-\nabla^* p^* - (\rho^* - \rho_c^*) (\omega^{*2} X_0^* + b^* \Omega^{*2} \sin(\Omega^* t^*)) \hat{e}_x - \frac{\rho_c^*}{\phi} \frac{\partial \mathbf{V}^*}{\partial t^*} \right] \quad (2)$$

$$\frac{\partial T^*}{\partial t^*} + \mathbf{V}^* \cdot \nabla T^* = \lambda^{*2} \nabla^{*2} T^* \quad (3)$$

The entities λ^*/L^* , $\mu^*\lambda^*/k_c^*$, and $\Delta T = T_H - T_C$ are used to scale the filtration velocity components (u^*, v^*, w^*), reduced pressure (p^*), and temperature variations $T^* - T_C$ where λ^* is the thermal diffusivity, μ^* is the viscosity, and k_c^* is the characteristic permeability associated with the porous matrix. The length of the porous layer L^* is used to scale the spatial directions and offset distance as follows: $x = x^*/L^*$, $y = y^*/L^*$, $z = z^*/L^*$, and $X_0 = X_0^*/L^*$. The time variable is scaled using L^{*2}/λ^* , and the density variation is related to the temperature according to $\rho^* = \rho_c^*(1 + \beta^* \Delta T_c T)$, where β^* is the thermal expansion coefficient. Subjecting Eqs. (1)–(3) to the dimensional analysis, the following system of dimensionless equations results:

$$\nabla \cdot \mathbf{V} = 0 \quad (4)$$

$$\left(\frac{1}{\text{Va}} \frac{\partial}{\partial t} + 1 \right) \mathbf{V} = -\nabla p - \text{Ra}_{\omega 0} (1 + \delta_{\omega} \sin(\Omega t)) T \hat{e}_x \quad (5)$$

$$\frac{\partial T}{\partial t} + \mathbf{V} \cdot \nabla T = \nabla^2 T \quad (6)$$

The symbols \mathbf{V} , T , and p represent the dimensionless filtration velocity vector, temperature, and reduced pressure, respectively, and \hat{e}_x is a unit vector in the x -direction. In Eq. (5), Ω is the scaled

frequency defined as $\Omega = \omega^* L^{*2} / \lambda_{*}$, while the nondimensional amplitude δ is defined as $\delta_{\omega} = \kappa \text{Fr}_{\omega} \Omega^2$, where $\kappa = b^*/L^*$ and Fr_{ω} is the modified Froude number defined as $\text{Fr}_{\omega} = \lambda^{*2} / ((\omega^{*2} X_0^*) / L^{*3})$. The parameter Va is the Vadasz number, first proposed by Straughan [20], and includes the Prandtl and Darcy numbers as well as the porosity of the porous domain and is defined as $\text{Va} = \phi \text{Pr} / \text{Da}$, where $\text{Pr} = \nu^*/\lambda^*$ is the Prandtl number, $\text{Da} = k_{c^*} / L^{*2}$ is the Darcy number, ϕ is the porosity, and ν^* stands for the kinematic viscosity of the fluid. It is only through this combined dimensionless group that the Prandtl number affects the flow in the porous media (see Vadasz [8] for a full discussion on the numerical values that Pr can assume in a typical porous medium). In Eq. (5), one also observes the Rayleigh number $\text{Ra}_{\omega 0}$ defined as $\text{Ra}_{\omega 0} = \beta^* \Delta T \omega^{*2} X_0^* k_c^* / (\lambda^* \nu^*)$. As all boundaries are rigid, the solution must follow the impermeability conditions there, i.e., $\mathbf{V} \cdot \hat{e}_n = 0$ on the boundaries, where \hat{e}_n is a unit vector normal to the boundary. The temperature boundary conditions are $T = 0$ at $x = 0$, $T = 1$ at $x = 1$, and $\nabla T \cdot \hat{e}_n = 0$ on all other walls representing the insulation condition on these walls. The partial differential Eqs. (4)–(6) form a nonlinear coupled system, which, together with the corresponding boundary conditions, accepts a basic motionless solution with a parabolic pressure distribution. The solutions for the basic temperature and flow field are given as $T_B = x$ and $\mathbf{V}_B = 0$. To provide a nontrivial solution to the system, it is convenient to apply the curl operator ($\nabla \times$) twice on Eq. (5), consider the solenoidal velocity field, Eq. (4), and consider only the horizontal x -component of the result, yielding

$$\left(\frac{1}{\text{Va}} \frac{\partial}{\partial t} + 1 \right) \nabla^2 u + \text{Ra}_{\omega 0} (1 + \delta_{\omega} \sin(\Omega t)) \nabla^2 T \quad (7)$$

The vertical Laplacian operator in Eq. (7) is defined as $\nabla_v^2 = (\partial^2 / \partial y^2 + \partial^2 / \partial z^2)$.

3 Linear Stability Analysis

The linear stability analysis will adopt the direct solution technique as opposed to the nondirect technique adopted by Pedramrazi et al. [17] and Kuznetsov [19]. As the Mathieu charts will ultimately be used to determine the stability criteria, there will be a degree of error in reading off the charts, but the trends will be qualitatively correct. The basic motionless solution is $\mathbf{V}_B = 0$ and $T_B = x$. Assuming small perturbations around the basic solution in the form $\mathbf{V} = \mathbf{V}_B + \mathbf{V}'$ and $T = T_B + T'$ and linearizing Eqs. (6) and (7) yields the following linear system:

$$\left(\frac{1}{\text{Va}} \frac{\partial}{\partial t} + 1 \right) \nabla^2 u' + \text{Ra}_{\omega 0} (1 + \delta_{\omega} \sin(\Omega t)) \nabla_v^2 T' = 0 \quad (8)$$

$$\left(\frac{\partial}{\partial t} - \nabla^2 \right) T' + u' = 0 \quad (9)$$

where u' is the perturbation to the horizontal component of the filtration velocity. The boundary conditions in the x -direction required for solving Eqs. (5) and (6) are $u' = T' = 0$ at $x = 0$ and $x = 1$. In the z -direction, $\partial T' / \partial z = 0$ at $z = 0$ and $z = L$. We may uncouple Eqs. (8) and (9) by eliminating u' to provide one equation for the temperature perturbation in the form

$$\left(\frac{1}{\text{Va}} \frac{\partial}{\partial t} + 1 \right) \nabla^2 \left(\nabla^2 - \frac{\partial}{\partial t} \right) + \text{Ra}_{\omega 0} (1 + \delta_{\omega} \sin(\Omega t)) \nabla_v^2 T' = 0 \quad (10)$$

Assuming an expansion into normal modes in the y - and z -directions and a time-dependent amplitude $\theta(t)$ of the form

$$T' = \theta(t) \exp[i(s_y y + s_z z)] \sin(\pi x) \quad (11)$$

where $s^2 = s_y^2 + s_z^2$. Substituting Eq. (11) into Eq. (10) provides an ordinary differential equation for the amplitude $\theta(t)$,

$$\frac{1}{\gamma} \frac{d^2 \theta}{dt^2} + 2\psi \frac{d\theta}{dt} - F(\alpha)[(\tilde{R}_\omega - \tilde{R}_0) + \tilde{R}_\omega \delta_\omega \sin(\Omega t)]\theta = 0 \quad (12)$$

where $\alpha = s^2/\pi^2$, $\gamma = Va/\pi^2$, and $\tilde{R}_\omega = Ra_{\omega 0}/\pi^2$. In Eq. (9), $2\psi = \pi^2((\alpha+1)/\gamma+1)$, $F(\alpha) = \pi^4\alpha/(\alpha+1)$, and \tilde{R}_0 is the characteristic Rayleigh number defined as $\tilde{R}_0 = (\alpha+1)^2/\alpha$, which represents both the unmodulated characteristic gravitational and rotational Rayleigh numbers. Incidentally, when the porous layer is placed far away from the axis of rotation (without vibration), the stability criteria is identical to the Rayleigh–Be’nard stability criteria.

3.1 Small to Moderate Vadasz Number Scaling. For this scenario, we shall use the definition $\gamma_{SM} = Va_{SM}/\pi^2$ to represent small to moderate Vadasz numbers; thus, Eq. (12) may be rewritten as

$$\frac{1}{\gamma_{SM}} \frac{d^2 \theta}{dt^2} + 2\psi \frac{d\theta}{dt} - F(\alpha)[(\tilde{R}_\omega - \tilde{R}_0) + \tilde{R}_\omega \delta_\omega \sin(\Omega t)]\theta = 0 \quad (13)$$

For small to moderate Vadasz numbers, the second order time derivative in Eq. (13) is retained. Typically, when considering binary alloy systems, one would encounter Vadasz numbers in the small to moderate range (Vadasz [8]). The direct solution technique using Mathieu functions may be employed, and by using the transformation $t = (\pi/2 + 2\tau)/\Omega$, Eq. (13) may be cast into the canonical form of the Mathieu equation, as outlined by McLachlan [21], as follows:

$$\frac{d^2 X}{d\tau^2} + [a - 2q \cos(2\tau)]X = 0 \quad (14)$$

The sign in front of “2q” could be positive or negative with no effect on the solution. The solution to Eq. (14) follows the form $\theta = X \exp(-p\tau)$, where X is a periodic function with a period of π or 2π and p is a characteristic exponent, which is a complex number and is a function of a and q , respectively. In this paper, the definitions for a , q , and p are obtained upon transforming Eq. (13) to the canonical form (14) and are defined as

$$\frac{2}{\sqrt{-a}} \Big|_\omega = \frac{\Omega}{[F(\alpha)\gamma_{SM}(\tilde{R}_\omega - \eta)]^{1/2}} \quad (15)$$

$$\frac{1}{2}q \Big|_\omega = F(\alpha)\gamma_{SM}\tilde{R}_\omega\kappa Fr_\omega \quad (16)$$

$$\sigma = -2\psi/\Omega \quad (17)$$

where η is a parameter defined as

$$\eta = -R_o \frac{(\alpha+1-\gamma)^2}{4\gamma_{SM}(\alpha+1)} \quad (18)$$

where subscript ω refers to the case with rotation. When $\sigma=0$, the solution to Eq. (14) is defined in terms of Mathieu functions such that for each Mathieu function, there exists a relation between a and q (McLachlan [21]). Recalling the results from Govender [18] for a horizontal porous layer subjected to gravity modulation (Fig. 1(b)), we may present the definitions for a and q as follows:

$$\frac{2}{\sqrt{-a}} \Big|_g = \frac{\Omega}{[F(\alpha)\gamma_{SM}(\tilde{R}_g - \eta)]^{1/2}} \quad (19)$$

$$\frac{1}{2}q \Big|_g = F(\alpha)\gamma_{SM}\tilde{R}_g\kappa Fr_g \quad (20)$$

where subscript g refers to the case with gravity, Fr_g is the modified Froude number defined as $Fr_g = \lambda^{*2}/(g^*L^{*3})$, and $\tilde{R}_g = Ra_g/\pi^2$ is the scaled gravity referenced Rayleigh number where $Ra_g = \beta^* \Delta T \omega^{*2} g^* L^*/(\lambda^* \nu^*)$.

In developing the analogy, we set

$$\frac{2}{\sqrt{-a}} \Big|_g = \frac{2}{\sqrt{-a}} \Big|_\omega \quad \text{and} \quad \frac{1}{2}q \Big|_g = \frac{1}{2}q \Big|_\omega \quad (21)$$

which results in the following relations:

$$\tilde{R}_g = \tilde{R}_\omega = \eta + \frac{\tilde{R}_o - \eta}{\xi^2} \quad \text{and} \quad Fr_g = Fr_\omega \quad (22)$$

where $\xi = \sigma/\sqrt{-a}$ (Govender [13]). So from the results of Eq. (22) and the definitions of the modified Froude numbers, we obtain

$$\omega^* = \sqrt{g^*/X_0^*} \quad (23)$$

In principle, for $g^* = 9.81 \text{ m/s}^2$ and for large offset distances, the rotational speeds that are derived from Eq. (23) are small in magnitude. In other words, the results indicate that a horizontal gravity modulated porous layer is analogous to a slow rotating vertical porous layer placed far away from the axis of rotation.

The stability results presented by Govender [18] are applicable to the system of Eqs. (15)–(18) so an analysis will not be repeated here, but the overall conclusion that vibration stabilizes convection is applicable to the rotating offset system presented in Fig. 1(a). Besides the useful analogy derived in Eq. (23), it is observed that for the systems presented in Fig. 1, the effects of vibration on the stability of convection are only significant when the Vadasz number lies in the small to moderate range.

3.2 Large Vadasz Number Scaling. For this scenario, we shall use the definition $\gamma_L = Va_L/\pi^2$ to represent large Vadasz numbers; thus, Eq. (14) may be rewritten as follows, with the definitions for a and q included:

$$\frac{\Omega^2}{\gamma_L} \frac{d^2 X}{d\tau^2} - F(\alpha)[4(\tilde{R}_\omega - \eta) + \tilde{R}_\omega \delta_\omega \cos(2\tau)]X = 0 \quad (24)$$

For large Vadasz numbers, the influence of the second order time derivative in Eq. (24) becomes negligible when $\Omega^2/\gamma_L < 1$. As a result, for moderate (note large) frequencies and large Vadasz numbers, Eq. (12) may be reduced to

$$\frac{d\theta}{dt} - \pi^2 \frac{\alpha}{\alpha+1} [\tilde{R}_\omega(t) - \tilde{R}_0]\theta = 0 \quad (25)$$

where $\tilde{R}_\omega(t) = \tilde{R}_\omega(1 + \delta_\omega \sin(\Omega t))$. Directly solving Eq. (25) yields

$$\theta = C e^{\pi^2[\alpha/(\alpha+1)][\sigma_L t - \kappa Fr_\omega \Omega \cos(\Omega t)]} \quad (26)$$

where $\sigma_L = \tilde{R}_\omega - \tilde{R}_0$. For marginal stability, $\sigma_L = 0$, which implies that $\tilde{R}_\omega = \tilde{R}_0$. This condition can only be met if $\Omega = 0$, thus implying that the form of the solution given by Eq. (26) must be $\theta(t) = C \exp[\pi^2(\alpha/(\alpha+1))\sigma_L t]$. Substituting this result in Eq. (11) and setting $\Omega = 0$ in Eq. (10) would allow the author to arrive at the result $\tilde{R}_\omega = \tilde{R}_0$, which clearly illustrates that for large Vadasz numbers, vibration has no effect on the stability of convection.

4 Conclusion

In the current work, we demonstrate the important influence of the Vadasz number on the stability of convection with vibration for the systems presented in Fig. 1. Adopting the direct solution technique, we firstly develop an analogy between the classical Vadasz [3] problem (placed far away from the axis of rotation) and the classical Rayleigh–Be’nard problem, including gravity modulation for small to moderate Vadasz number scaling. We neglect gravity as it was shown by Govender [7] to play a passive role in the stability of convection. The analogy developed shows that the gravity modulated horizontal porous layer is analogous to a slow rotating vertical porous layer placed far away from the axis of rotation. The stability criteria are then shown to be identical to the horizontal gravity modulated porous layer.

For the large Vadasz number scaling, we demonstrate that the stability criteria for marginal stability is identical to the nonvibrating offset rotating porous layer.

In summary, the magnitude of the Vadasz number influences the retention or removal of the second order time derivative, which is shown to dictate the influence of the vibration on the stability criteria. Small to moderate Vadasz numbers allow for vibration to affect the stability criteria, while large Vadasz numbers render the effects of vibration as being negligible on the stability criteria. This is an important observation that future researchers need to be cognizant of when developing the momentum equation to include vibration especially if their area of focus will be for a system that displays large Vadasz numbers.

Nomenclature

Latin Symbols

- a = variable in canonical form of Mathieu equation
 b^* = vibration amplitude
 Da = Darcy number, equals k_{0^*}/L_*
 \hat{e}_x = unit vector in the x -direction
 \hat{e}_y = unit vector in the y -direction
 \hat{e}_z = unit vector in the z -direction
 Fr_g = gravity based Froude number, equals $Fr_g = \lambda^{*2}/(g^*L^{*3})$
 Fr_ω = rotation based Froude number
 g^* = gravitational acceleration
 H^* = height of porous layer
 k_* = permeability of the porous matrix
 H = the front aspect ratio of the porous layer, equals H^*/L_*
 L_* = the length of the porous layer
 p = dimensionless reduced pressure
 q = variable in canonical form of Mathieu equation
 Pr = Prandtl number, equals ν^*/λ_*
 V = dimensionless filtration velocity vector, equals $u\hat{e}_x + v\hat{e}_y + w\hat{e}_z$
 Va = Vadasz number, equals $\phi Pr/Da$
 Ra_g = gravity based Rayleigh number, equals $Ra_g = \beta^* \Delta T g^* k_c^* L^* / (\lambda^* \nu^*)$
 $Ra_{\omega 0}$ = rotation based Rayleigh number, equals $Ra_{\omega 0} = \beta^* \Delta T \omega^{*2} X_0^* k_c^* L^* / (\lambda^* \nu^*)$
 \tilde{R}_g = scaled gravity based Rayleigh number, equals Ra_g / π^2
 \tilde{R}_ω = scaled rotation based Rayleigh number, equals $Ra_{\omega 0} / \pi^2$
 s = convection wave number
 t_* = dimensional time
 T = dimensionless temperature, equals $(T_* - T_C)/(T_H - T_C)$
 T_C = coldest wall temperature
 T_H = hottest wall temperature
 u = horizontal x component of the filtration velocity
 v = horizontal y component of the filtration velocity
 w = vertical z component of the filtration velocity
 x = horizontal length coordinate
 y = horizontal width coordinate
 z = vertical coordinate

Greek Symbols

- α = a parameter related to the wave number, equals s^2 / π^2
 β_* = thermal expansion coefficient

- δ_g = gravity based vibration amplitude, equals $\kappa Fr_g \Omega^2$
 δ_ω = rotation based vibration amplitude, equals $\kappa Fr_\omega \Omega^2$
 ΔT_C = characteristic temperature difference
 ϕ = porosity
 γ = equals Va / π^2
 κ = equals b^* / L_*
 λ_* = effective thermal diffusivity
 μ_* = fluid dynamic viscosity
 ρ = fluid density
 σ = Mathieu exponent
 ω_* = rotation frequency
 Ω^* = vibration frequency
 Ω = scaled vibration frequency, equals $\omega_* L_*^2 / \lambda_*$
 ν_* = fluid kinematic viscosity
 ξ = scaled exponent, equals $\sigma / \sqrt{-a}$

Subscripts

- * = dimensional values
 c = characteristic
 cr = critical values
 C = related to cold wall
 H = related to hot wall
 o = related to unmodulated quantities
 SM = small to moderate values
 L = large values

Over

- \sim = scaled quantities

References

- [1] Nield, D. A., and Bejan, A., 1995, *Convection in Porous Media*, Wiley, New York.
- [2] Chandrasekar, S., 1961, *Hydrodynamic and Hydromagnetic Stability*, Oxford University Press, London, UK.
- [3] Vadasz, P., 1994, "Stability of Free Convection in a Narrow Porous Layer Subject to Rotation," *Int. Commun. Heat Mass Transfer*, **21**, pp. 881–890.
- [4] Vadasz, P., 1996, "Convection and Stability in a Rotating Porous Layer With Alternating Direction of the Centrifugal Body Force," *Int. J. Heat Mass Transfer*, **39**(8), pp. 1639–1647.
- [5] Vadasz, P., and Govender, S., 1998, "Two-Dimensional Convection Induced by Gravity and Centrifugal Forces in a Rotating Porous Layer Far Away From the Axis of Rotation," *Int. J. Rotating Mach.*, **4**(2), pp. 73–90.
- [6] Vadasz, P., and Govender, S., 2001, "Stability and Stationary Convection Induced by Gravity and Centrifugal Forces in a Rotating Porous Layer Distant From the Axis of Rotation," *Int. J. Eng. Sci.*, **39**, pp. 715–732.
- [7] Govender, S., 2003, "Oscillatory Convection Induced by Gravity and Centrifugal Forces in a Rotating Porous Layer Distant From the Axis of Rotation," *Int. J. Eng. Sci.*, **41**(6), pp. 539–545.
- [8] Vadasz, P., 1998, "Coriolis Effect on Gravity-Driven Convection in a Rotating Porous Layer Heated From Below," *J. Fluid Mech.*, **376**, pp. 351–375.
- [9] Gresho, P. M., and Sani, R. L., 1970, "The Effects of Gravity Modulation on the Stability of a Heated Fluid Layer," *J. Fluid Mech.*, **40**, pp. 783–806.
- [10] Wadih, M., and Roux, B., 1988, "Natural Convection in a Long Vertical Cylinder Under Gravity Modulation," *J. Fluid Mech.*, **193**, pp. 391–415.
- [11] Christov, C. I., and Homsy, G. M., 2001, "Nonlinear Dynamics of Two-Dimensional Convection in a Vertically Stratified Slot With and Without Gravity Modulation," *J. Fluid Mech.*, **430**, pp. 335–360.
- [12] Hirata, K., Sasaki, T., and Tanigawa, H., 2001, "Vibrational Effect on Convection in a Square Cavity at Zero Gravity," *J. Fluid Mech.*, **455**, pp. 327–344.
- [13] Govender, S., 2004, "Stability of Convection in a Gravity Modulated Porous Layer Heated From Below," *Transp. Porous Media*, **57**(1), pp. 113–123.
- [14] Govender, S., 2005, "Destabilising a Fluid Saturated Gravity Modulated Porous Layer Heated From Above," *Transp. Porous Media*, **59**(2), pp. 215–225.
- [15] Govender, S., 2005, "Weak Non-Linear Analysis of Convection in a Gravity Modulated Porous Layer," *Transp. Porous Media*, **60**(1), pp. 33–42.
- [16] Bardan, G., and Mojtabi, A., 2000, "On the Horton–Rogers–Lapwood Convective Instability With Vertical Vibration," *Phys. Fluids*, **12**, pp. 2723–2731.
- [17] Pedramrazi, Y., Maliwan, K., Charrier–Mojtabi, M. C., and Mojtabi, A., 2005, "Influence of Vibration on the Onset of Thermoconvection in Porous Medium," *Handbook of Porous Media*, Marcel Dekker, New York, pp. 321–370.

- [18] Govender, S., 2005, "Linear Stability and Convection in a Gravity Modulated Porous Layer Heated From Below: Transition From Synchronous to Subharmonic Solution," *Transp. Porous Media*, **59**(2), pp. 227–238.
- [19] Kuznetsov, A. V., 2006, "Linear Stability Analysis of the Effect of Vertical Vibration on Bioconvection in a Horizontal Porous Layer of Finite Depth," *J. Porous Media*, **9**, pp. 597–608.
- [20] Straughan, B., 2000, "A Sharp Nonlinear Stability Threshold in Rotating Porous Convection," *Proc. R. Soc. London, Ser. A*, **457**, pp. 87–93.
- [21] McLachlan, N. W., 1964, *Theory and Application of Mathieu Functions*, Dover, New York.

Radiation and Conduction in an Isotropic Scattering Rectangular Medium With One Semitransparent and Diffusely Reflecting Boundary

Jian-Feng Luo¹

Associate Professor
National University of Defense Technology,
410073 Changsha, P.R. China
e-mail: luo_jianfeng@yahoo.com

Hong-Liang Yi

Associate Professor
Harbin Institute of Technology,
150001 Harbin, P.R. China
e-mail: hongliang_yi@yahoo.com.cn

Sheng-Li Chang

Professor
National University of Defense Technology,
410073 Changsha, P.R. China

He-Ping Tan¹

Professor
Harbin Institute of Technology,
150001 Harbin, P.R. China
e-mail: tanheping@hit.edu.cn

Using the ray tracing-node analyzing method, the 2D transient coupled radiative and conductive heat transfer in a rectangular semitransparent medium is investigated. The rectangular medium has one semitransparent and diffuse boundary (the other three boundaries are black) and is isotropically scattering. The transient differential energy equation is discretized by the fully implicit finite difference method, and the radiative source term of the energy equation is expressed by the radiative transfer coefficients (RTCs). The integrality and reciprocity relationships of the RTCs without considering scattering for the 2D physical model are discovered, which are much different from those for the 1D case. When solving the isotropic scattering RTCs, the RTCs without considering scattering are normalized at first, and then the normalized RTCs are used to trace the energy scattered by control volumes. Finally, the isotropic scattering RTCs are solved by reverse calculation. The Patankar's linearization method is used to linearize the radiative source term and the opaque boundary conditions, and the boundary conditions are dealt with an additional source term method. The alternating direction implicit method is applied to solve the nominal linearized equations. The effects of scattering albedo, extinction coefficient, refractive index, etc., on transient coupled heat transfer are studied. The study shows that when the extinction coefficient is so small, the increase in scattering albedo can intensify the cooling of the three black surfaces of the rectangular medium. [DOI: 10.1115/1.4002030]

Keywords: ray tracing-node analyzing method, 2D rectangular semitransparent medium, diffuse reflectivity, transient, radiation

1 Introduction

Radiative heat transfer, coupled with other heat transfer modes in semitransparent media, has a broad engineering application background, such as heat insulating techniques for the protection of aeroengines [1], thermal analysis of multilayer optical windows for spacecraft applications [2], and the manufacture of glass and its application in high temperature environment [3]. Almost all of the engineering applications belong to the multidimensional problem, such as heat transfer in boilers, furnaces, and combustion chambers, wherein temperatures are very high and radiation plays an important role in heat transfer. Therefore, developing research on multidimensional transient coupled heat transfer is of practical importance.

The remote action of radiation often implies taking into account the whole thermal system, which requires us to solve the radiative transfer equation (RTE) to obtain the temperature distributions. Since an exact analytical solution to the highly nonlinear integrodifferential RTE is nearly impossible to find, many numerical methods have been developed. Compared with the 1D case, the complex geometry of a multidimensional physical model increases the difficulties to solve the RTE. Hollands [4] explored a new Fredholm integral equation solver to problems in thermal radiation. Using a discrete transfer method (DTM) based on unstructured

triangular meshes, Feldheim and Lybaert [5] studied radiative transfer in 2D complex-shaped geometries, and the ray effect of this method is analyzed. Using a new finite volume method (FVM) to solve the RTE and using the parallel hierarchical adaptive multilevel code to solve the energy equation, Asllanaj et al. studied the pure radiative heat transfer [6] and transient coupled radiative-conductive heat transfer [7] in 2D complex-shaped media. Ravishankar et al. [8] investigated the method of spherical harmonics for an approximate solution of the RTE in participating media. Using the ray-tracing technique to calculate the radiative source and the alternating direction implicit (ADI) method to solve the energy equation, Dez et al. [9] studied steady-state coupled radiative and conductive heat transfer in an axisymmetric semitransparent medium. Using the finite element method (FEM) combined with the iterative technique, Furmanski and Banaszek [10] studied transient coupled radiative and conductive heat transfer in a 2D rectangular scattering medium. Widmer [11] investigated the sparse finite element method (SFEM) for solving the RTE in a nonscattering medium. Becker et al. [12] studied the angular dependency of the even-parity equation of radiative transfer by the FEM. Using the zonal method, Hitti et al. [13] studied 3D transient radiation and conduction heat transfer occurring inside thin glass sheets undergoing high temperature processing. Using the method of "subtraction of singularity" to solve the radiative integral transfer equation, Altaç and Tekkalmaz [14] gave a benchmark solution of radiative transfer equation for 3D rectangular homogeneous media.

Mishra et al. [15,16] and Mishra and Roy [17] also conducted a deep investigation on transient coupled radiative and conductive

¹Corresponding authors.

Contributed by the Heat Transfer Division of ASME for publication in the JOURNAL OF HEAT TRANSFER. Manuscript received October 16, 2009; final manuscript received June 11, 2010; published online August 13, 2010. Assoc. Editor: He-Ping Tan.

heat transfer in a rectangular medium. Using the collapsed dimension method (CDM) to compute the RTE and the lattice Boltzmann method (LBM) and FVM to solve the energy equation, they [15] studied transient coupled radiative and conductive heat in a 2D rectangular medium. Reference [16] studied the effect of thermal conductivity of the medium varying linearly with temperature on transient coupled radiative and conductive heat transfer. Using FVM to compute the RTE and LBM and FVM to compute the energy equation, Mishra and Roy [17] studied transient coupled radiative and conductive heat transfer in a rectangular isotropically scattering medium.

Recently, many researchers draw much attention to the control volume finite element method (CVFEM). Rouse et al. [18,19] validated the CVFEM for solving 2D radiative heat transfer in a rectangular or complex-shaped enclosure. Ben Salah et al. [20] also used this method for the treatment of radiative heat transfer in 2D media. Recently, Grissa et al. [21] extended this method to the solution of 3D radiative transfer in emitting, absorbing, and scattering media.

The discrete ordinate method (DOM) is a very popular method for studying radiative transfer because the fundamental advantage of this method is that numerical equation can be easily derived and expanded to higher order approximations to increase the accuracy. As early as 1991, using DOM to solve the RTE, Kim and Baek [22] studied steady-state coupled radiative and conductive heat transfer in a 2D anisotropically scattering rectangular medium. Using this method, Sakami et al. [23] studied steady-state coupled radiative and conductive heat transfer in a 2D scattering enclosure of arbitrary geometry. Vaillon et al. [24] thought that the extension of the DOM to a curvilinear system was only limited to cylindrical and spherical coordinates, so they extended this method to the study of the radiative transfer in general curvilinear coordinates. Also, using this method, Liu and Tan [25] studied the transient coupled radiative-conductive heat transfer in a 2D semitransparent cylinder medium with a black boundary surface under pulse irradiation on one end of the cylinder. Cheong and Song [26] modified DOM as the discrete ordinate interpolation method (DOIM) and applied DOIM to 2D geometry. Three years later, Cha and Song [27] expanded DOIM to 3D unstructured grid systems with a gray medium, and recently Kim et al. [28] further applied this method to the study of radiative heat transfer with real particle and gas radiative properties. In allusion to the manufacturing and processing of glass, Lee and Viskanta [29] studied coupled radiation and conduction in a rectangular glass medium and compared the DOM with the Rosseland diffusion approximation method for solving the RTE.

The ray tracing-node analyzing method (RTNAM), which was first developed by Tan [30], is also an effective method for studying radiative transfer. In the past, this method has been mainly used to study 1D transient coupled radiative and conductive heat transfer in a parallel plane single layer [31] or a composite [32] medium. The advantage of this method is that it can avoid ray effect and false scattering because when solving the RTCs the radiative intensity does not need to be discretized along the coordinates, and the solid angle also does not need to be discretized but is integrated directly. Therefore, this method has high accuracy. In addition, this method can be easily used to solve the radiative transfer problem in a 1D multilayer composite having semitransparent and specular interfaces [32], and up to now, we have not found this problem to be solved by other methods, such as the DOM and FVM.

Recently, we [33] extended the RTNAM to study 2D transient coupled radiative and conductive heat transfer in an isotropic scattering rectangular medium with four black boundaries. Based on Ref. [33], the main purpose of this paper is to further extend this method to the study of transient coupled heat transfer in an absorbing, isotropic scattering rectangular medium with one semitransparent and diffusely reflecting boundary (the other three boundaries being opaque and black). Radiative energy will be

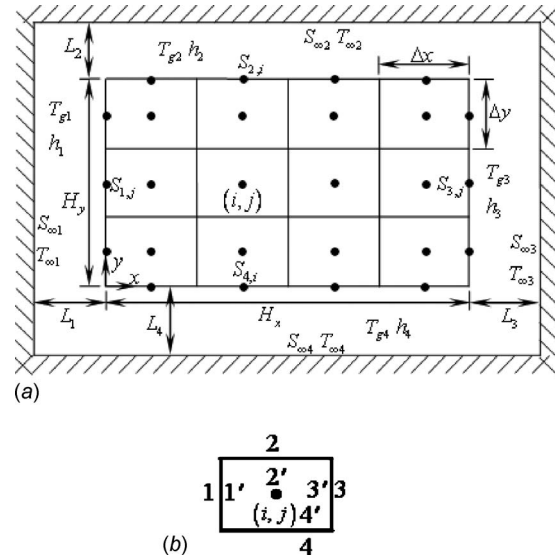


Fig. 1 Physical model of 2D coupled heat transfer in a rectangular medium with one semitransparent diffuse boundary: (a) physical model and (b) control volume $V_{(i,j)}$

reflected and transmitted when it reaches the semitransparent boundary, and total reflection will occur therein when the incident angle is greater than the critical angle. Therefore, the problem becomes more complex. Furthermore, we will deduce the isotropic scattering RTCs and reveal the characteristics of this deductive process.

2 Physical Model and Determination of Reflectivity

The physical model of the present study is shown in Fig. 1. The rectangular enclosure bounded by S_1 , S_2 , S_3 , and S_4 is a semitransparent medium, which is surrounded by black surroundings represented by $S_{\infty 1}$, $S_{\infty 2}$, $S_{\infty 3}$, and $S_{\infty 4}$. The space between the black surroundings and the surfaces of the rectangular medium is full of air, which can exchange convective heat energy with the surfaces of the rectangular medium. Assume S_2 to be semitransparent and diffusely reflecting and the other three surfaces to be opaque and black. The rectangular semitransparent medium not only absorbs radiative energy but also isotropically scatters. The absorption coefficient α , extinction coefficient κ , and refractive index n of the selective medium are expressed with a series of rectangular spectral band models. The total number of spectral bands is NB, and subscript k denotes the k th spectral band.

The reflectivity of S_2 is determined as follows. As pointed out by Siegel [34], although the interface is not optically smooth, it is assumed that each bit of roughness acts as a smooth facet so that the reflectivity can be obtained from Fresnel's reflective law for a nonabsorbing dielectric medium. When the radiation passing into a medium of a higher refractive index $n_h (=n)$ from a medium of a smaller refractive index n_s ($n_s=1$, the refractive index of the fluid medium of the environment), by integrating the reflected energy over all incident directions, the reflectivity ρ_{sh} of the interface is [34]

$$\rho_{sh} = \frac{1}{2} + \frac{(3n' + 1)(n' - 1)}{6(n' + 1)^2} + \frac{n'^2(n'^2 - 1)^2}{(n'^2 + 1)^3} \ln\left(\frac{n' - 1}{n' + 1}\right) - \frac{2n'^3(n'^2 + 2n' - 1)}{(n'^2 + 1)(n'^4 - 1)} + \frac{8n'^4(n'^4 + 1)}{(n'^2 + 1)(n'^4 - 1)^2} \ln(n') \quad (1a)$$

where $n' = n_h/n_s$. When incidence from the reverse direction, meanwhile considering the effect of total reflection, the reflectivity ρ_{hs} of the interface is [34]

$$\rho_{hs} = 1 - 1/n^2(1 - \rho_{sh}) \quad (1b)$$

3 Governing Equation and Radiative Source Term

As shown in Fig. 1, for the inner node (i, j) ($1 < i < M$ and $1 < j < N$), using the finite difference method and the implicit scheme in time, the discretized form of the 2D transient energy balance differential equation is written as [33]

$$\begin{aligned} \rho c [T_{(i,j)}^{m+1} - T_{(i,j)}^m] / \Delta t = & k [T_{(i+1,j)}^{m+1} - T_{(i,j)}^{m+1}] / \Delta x^2 - k [T_{(i,j)}^{m+1} - T_{(i-1,j)}^{m+1}] / \Delta x^2 \\ & + k [T_{(i,j+1)}^{m+1} - T_{(i,j)}^{m+1}] / \Delta y^2 - k [T_{(i,j)}^{m+1} \\ & - T_{(i,j-1)}^{m+1}] / \Delta y^2 + \Phi_{(i,j)}^{r,m+1} / (\Delta x \Delta y) \end{aligned} \quad (2)$$

where superscript m means the m th time step. The term $\Phi_{(i,j)}^r$ is the radiative heat source term for control volume $V_{(i,j)}$. In terms of RTCs, $\Phi_{(i,j)}^r$ can be expressed as [33]

$$\begin{aligned} \Phi_{(i,j)}^r = & \frac{\sigma}{\pi} \sum_{k=1}^{NB} \left\{ \sum_{m=1}^N n_k^2 [[S_{1,m} V_{(i,j)}]_k A_{k,T_{S_{1,m}}} T_{S_{1,m}}^4 \right. \\ & - [V_{(i,j)} S_{1,m}]_k A_{k,T_{(i,j)}} T_{(i,j)}^4 + \sum_{m=1}^N n_k^2 [[S_{3,m} V_{(i,j)}]_k A_{k,T_{S_{3,m}}} T_{S_{3,m}}^4 \\ & - [V_{(i,j)} S_{3,m}]_k A_{k,T_{(i,j)}} T_{(i,j)}^4 + \sum_{l=1}^M n_k^2 [[S_{4,l} V_{(i,j)}]_k A_{k,T_{S_{4,l}}} T_{S_{4,l}}^4 \\ & - [V_{(i,j)} S_{4,l}]_k A_{k,T_{(i,j)}} T_{(i,j)}^4 + \left. \left[\sum_{l=1}^3 [S_{\infty l} V_{(i,j)}]_k A_{k,T_{S_{\infty l}}} T_{S_{\infty l}}^4 \right. \right. \\ & \left. \left. - n_k^2 [V_{(i,j)} S_{\infty}]_k A_{k,T_{(i,j)}} T_{(i,j)}^4 \right] \right\} \\ & + \sum_{l=1}^M \sum_{m=1}^N n_k^2 [[V_{(l,m)} V_{(i,j)}]_k A_{k,T_{(l,m)}} T_{(l,m)}^4 \\ & - [V_{(i,j)} V_{(l,m)}]_k A_{k,T_{(i,j)}} T_{(i,j)}^4 \end{aligned} \quad (3)$$

where $[V_{(l,m)} V_{(i,j)}]_k$, etc., are the RTCs for isotropic scattering media. $[V_{(l,m)} V_{(i,j)}]_k$ means the part of radiative energy absorbed by $V_{(i,j)}$ to that emitted from $V_{(l,m)}$ in the k th spectral band for isotropic scattering media, and the meanings of the other RTCs are similar to that of $[V_{(l,m)} V_{(i,j)}]_k$. On the right-hand side of Eq. (3), the first term denotes the net radiative energy transferred to the control volume $V_{(i,j)}$ by all the black surface elements $S_{1,m}$, and the meanings of the second and third terms are similar to that of the first one. The fourth term means the net radiative energy transferred to the control volume $V_{(i,j)}$ by all the black environment surfaces. The fifth term means the net radiative energy transferred to the control volume $V_{(i,j)}$ by all the control volumes.

4 Boundary Condition

4.1 Opaque Boundary Condition. S_1 , S_3 , and S_4 are opaque surfaces, wherein there is an energy balance of radiation, conduction, and convection. For example, the discretized boundary condition for the opaque element $S_{3,j}$ is

$$2k(T_{(M,j)} - T_{S_{3,j}}) \Delta y / \Delta x + (q_{S_{3,j}}^r - q_{S_{3,j} \rightarrow S_{\infty}}^r) = h_3(T_{S_{3,j}} - T_{g3}) \Delta y \quad (4)$$

where $q_{S_{3,j}}^r$ is the net radiative energy transferred to $S_{3,j}$ by all the control volumes, all the inner surface elements $S_{1,j}$ ($j=1-N$) and $S_{4,i}$ ($i=1-M$), and the black surroundings $S_{\infty 1}$, $S_{\infty 2}$, and $S_{\infty 3}$

$$\begin{aligned} q_{S_{3,j}}^r = & \frac{\sigma}{\pi} \sum_{k=1}^{NB} \left\{ \sum_{m=1}^N n_k^2 [[S_{1,m} S_{3,j}]_k A_{k,T_{S_{1,m}}} T_{S_{1,m}}^4 - [S_{3,j} S_{1,m}]_k A_{k,T_{S_{3,j}}} T_{S_{3,j}}^4] \right. \\ & + \sum_{l=1}^M n_k^2 [[S_{4,l} S_{3,j}]_k A_{k,T_{S_{4,l}}} T_{S_{4,l}}^4 - [S_{3,j} S_{4,l}]_k A_{k,T_{S_{3,j}}} T_{S_{3,j}}^4] \\ & + \left. \left[\sum_{j=1}^3 [S_{\infty j} S_{3,j}]_k A_{k,T_{S_{\infty j}}} T_{S_{\infty j}}^4 - n_k^2 [S_{3,j} S_{\infty}]_k A_{k,T_{S_{3,j}}} T_{S_{3,j}}^4 \right] \right\} \\ & + \sum_{l=1}^M \sum_{m=1}^N n_k^2 [[V_{(l,m)} S_{3,j}]_k A_{k,T_{(l,m)}} T_{(l,m)}^4 \\ & - [S_{3,j} V_{(l,m)}]_k A_{k,T_{S_{3,j}}} T_{S_{3,j}}^4 \end{aligned} \quad (5)$$

The term $q_{S_{3,j} \rightarrow S_{\infty}}^r$ in Eq. (4) is the net radiative energy transferred to S_{∞} by $S_{3,j}$,

$$q_{S_{3,j} \rightarrow S_{\infty}}^r = \sigma T_{S_{3,j}}^4 \Delta y - C_{S_{3,j}} \quad (6a)$$

$$\begin{aligned} C_{S_{3,j}} = & \frac{2\sigma T_{\infty 2}^4}{\pi} \int_0^{L_3} dx \int_0^{\pi/2} d\varphi \int_{\arctg[(L_3-x)/(H_y-j\Delta y+L_2)\cos\varphi]}^{\arctg[(L_3-x)/(H_y-j\Delta y+L_2)\cos\varphi]} \\ & \times \cos\theta \sin\theta d\theta \\ & + \frac{2\sigma T_{\infty 4}^4}{\pi} \int_0^{L_3} dx \int_0^{\pi/2} d\varphi \int_{\arctg[(L_3-x)/(H_y-(j-1)\Delta y+L_2)\cos\varphi]}^{\arctg[(L_3-x)/(j\Delta y-L_4+L_4)\cos\varphi]} \\ & \times \cos\theta \sin\theta d\theta + \frac{2\sigma T_{\infty 3}^4}{\pi} \int_0^{L_2+H_y-j\Delta y} dx \int_0^{\pi/2} \\ & \times d\varphi \int_{\arctg(x/L_3 \cos\varphi)}^{\arctg((x+\Delta y)/L_3 \cos\varphi)} \cos\theta \sin\theta d\theta \\ & + \frac{2\sigma T_{\infty 3}^4}{\pi} \int_0^{L_4+(j-1)\Delta y} dx \int_0^{\pi/2} d\varphi \int_{\arctg(x/L_3 \cos\varphi)}^{\arctg((x+\Delta y)/L_3 \cos\varphi)} \\ & \times \cos\theta \sin\theta d\theta \\ & + \frac{4\sigma T_{\infty 3}^4}{\pi} \int_0^{\Delta y} dx \int_0^{\pi/2} d\varphi \int_0^{\arctg(x/L_3 \cos\varphi)} \cos\theta \sin\theta d\theta \end{aligned} \quad (6b)$$

where the term $\sigma T_{S_{3,j}}^4 \Delta y$ means the radiative energy transferred to S_{∞} by $S_{3,j}$, and $C_{S_{3,j}}$ means the radiative energy transferred to $S_{3,j}$ by the black surroundings. For simplicity, the deduction of Eq. (6b) is omitted.

4.2 Semitransparent Boundary Condition. Surface S_2 is semitransparent. For the reason that the semitransparent surface does not absorb radiative energy, there is only energy balance of conduction and convection at S_2 . The discretized boundary condition for $S_{2,i}$ is

$$2k_{(i,N)}(T_{(i,N)} - T_{S_{2,i}}) / \Delta y = h_2(T_{S_{2,i}} - T_{g2}) \quad (7)$$

5 Deduction of the RTCs Without Considering Scattering

Before solving the RTCs for isotropic scattering media, the RTCs without considering scattering must be solved first. In a scattering medium, the radiative intensity I is attenuated in accordance with Bouguer's law, $Ie^{-\kappa_k l}$, where $\kappa_k = \alpha_k + \sigma_k$ and l is the

distance that the radiative intensity passes through the media. The RTCs without considering scattering are expressed with round brackets, such as $(V_{(l,m)}V_{(i,j)})_k$, etc.

5.1 Deduction of the RTCs of Control Volumes Versus the Other Elements. For the RTCs of control volume vs the other elements, five RTCs, such as $(V_{(i,j)}S_{1,l})_k$, $(V_{(i,j)}S_{3,l})_k$, $(V_{(i,j)}S_{4,m})_k$, $(V_{(i,j)}V_{(l,m)})_k$, and $(V_{(i,j)}S_{\infty})_k$, needed to be deduced. We take $(V_{(i,j)}S_{1,l})_k$ as an example to illustrate the deduction. For convenience of deduction, the four interfaces of each control volume are defined, as shown in Fig. 1(b), and the outside of interface n of $V_{(i,j)}$ is expressed as $V_{(i,j)}^n$, while the inside of interface n of $V_{(i,j)}$ is expressed as $V_{(i,j)}^{n'}$ ($n=1-4$).

5.1.1 Expression of RTC $(V_{(i,j)}S_{1,l})_k$. The RTC $(V_{(i,j)}S_{1,l})_k$ can be expressed as

$$(V_{(i,j)}S_{1,l})_k = \sum_{n=1}^4 f_{V_{(i,j)}^n}^{S_{1,l},k} - \sum_{n=1}^4 f_{V_{(i,j)}^{n'}}^{S_{1,l},k} \quad (8)$$

where $f_{V_{(i,j)}^n}^{S_{1,l},k}$ (or $f_{V_{(i,j)}^{n'}}^{S_{1,l},k}$) means the radiative energy absorbed by $S_{1,l}$, emitted by $V_{(i,j)}^n$ (or $V_{(i,j)}^{n'}$) at the k th spectral band over the whole hemispherical space.

The radiative energy will be reflected when it arrives at S_2 . So, each of the functions $f_{V_{(i,j)}^n}^{S_{1,l},k}$ (or $f_{V_{(i,j)}^{n'}}^{S_{1,l},k}$) includes two parts: (1) $f1_{V_{(i,j)}^n}^{S_{1,l},k}$ (or $f1_{V_{(i,j)}^{n'}}^{S_{1,l},k}$), the radiative energy directly absorbed by $S_{1,l}$

(not being reflected by S_2), emitted by $V_{(i,j)}^n$ (or $V_{(i,j)}^{n'}$) at the k th spectral band over the whole hemispherical space, and (2) $f2_{V_{(i,j)}^n}^{S_{1,l},k}$ (or $f2_{V_{(i,j)}^{n'}}^{S_{1,l},k}$), the radiative energy absorbed by $S_{1,l}$ after being reflected by S_2 , emitted by $V_{(i,j)}^n$ (or $V_{(i,j)}^{n'}$) at the k th spectral band over the whole hemispherical space. Therefore, the functions $f_{V_{(i,j)}^n}^{S_{1,l},k}$ and $f_{V_{(i,j)}^{n'}}^{S_{1,l},k}$ can be expressed as

$$f_{V_{(i,j)}^n}^{S_{1,l},k} = f1_{V_{(i,j)}^n}^{S_{1,l},k} + f2_{V_{(i,j)}^n}^{S_{1,l},k} \quad (n=1-4) \quad (9a)$$

$$f_{V_{(i,j)}^{n'}}^{S_{1,l},k} = f1_{V_{(i,j)}^{n'}}^{S_{1,l},k} + f2_{V_{(i,j)}^{n'}}^{S_{1,l},k} \quad (n=1-4) \quad (9b)$$

In the following, we take $f_{V_{(i,j)}^2}^{S_{1,l},k}$ as an example to illustrate the deduction of $f_{V_{(i,j)}^n}^{S_{1,l},k}$ and $f_{V_{(i,j)}^{n'}}^{S_{1,l},k}$, and for this case, there is

$$f_{V_{(i,j)}^2}^{S_{1,l},k} = f1_{V_{(i,j)}^2}^{S_{1,l},k} + f2_{V_{(i,j)}^2}^{S_{1,l},k} \quad (10)$$

The two terms on the right-hand side of the above equation will be solved in the following.

5.1.2 Determination of the Function $f1_{V_{(i,j)}^2}^{S_{1,l},k}$. In terms of the basic principle law of radiative transfer, for element $V_{(i,j)}^2$ we can deduce

$$f1_{V_{(i,j)}^2}^{S_{1,l},k} = \begin{cases} 2 \int_{(i-1)\Delta x}^{i\Delta x} dx \int_0^{\pi/2} d\varphi \int_{\arctg(x/(l-1)\Delta y \cos \varphi)}^{\arctg(x/(l-1)\Delta y \cos \varphi)} \exp\left(-\frac{x\kappa}{\sin \theta \cos \varphi}\right) \cos \theta \sin \theta d\theta & (l > j \text{ and } l \neq j+1) \\ 2 \int_{(i-1)\Delta x}^{i\Delta x} dx \int_0^{\pi/2} d\varphi \int_{\arctg(x/(l-j)\Delta y \cos \varphi)}^{\arctg(x/(l-j)\Delta y \cos \varphi)} \exp\left(-\frac{x\kappa}{\sin \theta \cos \varphi}\right) \cos \theta \sin \theta d\theta & (j > j \text{ and } l = j+1) \\ 0 & (l \leq j) \end{cases} \quad (11)$$

For simplicity, the detailed deduction of Eq. (11) is omitted here. In the following, we mainly analyze the deduction of $f2_{V_{(i,j)}^2}^{S_{1,l},k}$.

5.1.3 Determination of the Function $f2_{V_{(i,j)}^2}^{S_{1,l},k}$

5.1.3.1 Determination of the REQTFSE. Before solving the function $f2_{V_{(i,j)}^2}^{S_{1,l},k}$, we must first solve the radiative energy quotient transfer function of surface element (REQTFSE), which is used to trace the reflected and transmitted radiative energies.

As shown in Fig. 1, the length H_x of S_2 is divided into M equal parts, called surface elements, and from left to right the l th surface element is denoted as $S_{2,l}$. Define $f_{S_{2,l}}^X$ as the REQTFSE, i.e., the quotient of the radiative energy absorbed by element X (superscript of $f_{S_{2,l}}^X$) to that emitted downward by the inner surface of $S_{2,l}$ (subscript of $f_{S_{2,l}}^X$), where X represents $V_{(i,j)}$, $S_{1,j}$, $S_{3,j}$, or $S_{4,j}$, so there are four REQTFSEs: $f_{S_{2,l}}^{V(i,j)}$, $f_{S_{2,l}}^{S_{1,j}}$, $f_{S_{2,l}}^{S_{3,j}}$, and $f_{S_{2,l}}^{S_{4,m}}$, which are used to trace the reflected and transmitted radiative energy from $S_{2,l}$. Here, take $f_{S_{2,l}}^{S_{1,j}}$ as an example to illustrate their expressions. According to the principles of radiative heat transfer, we have

$$f_{S_{2,l}}^{S_{1,j}} = \begin{cases} \frac{2}{\pi \Delta x} \int_{(l-1)\Delta x}^{l\Delta x} dx \int_0^{\pi/2} d\varphi \int_{\arctg(x/(N-l)\Delta y \cos \varphi)}^{\arctg(x/(N-l)\Delta y \cos \varphi)} \exp\left(-\frac{x\kappa}{\sin \theta \cos \varphi}\right) \cos \theta \sin \theta d\theta & (l \neq N) \\ \frac{2}{\pi \Delta x} \int_{(l-1)\Delta x}^{l\Delta x} dx \int_0^{\pi/2} d\varphi \int_{\arctg(x/(N-l+1)\Delta y \cos \varphi)}^{\arctg(x/(N-l+1)\Delta y \cos \varphi)} \exp\left(-\frac{x\kappa}{\sin \theta \cos \varphi}\right) \cos \theta \sin \theta d\theta & (l = N) \end{cases} \quad (12)$$

On the right-hand side of Eq. (12), the denominator term $\pi \Delta x$ means the total energy emitted by $S_{2,l}$ over the whole hemispherical space. The remaining part means the radiative energy absorbed by $S_{1,l}$ and emitted downward by $S_{2,l}$, and this part of radiative

energy is divided by $\pi \Delta x$ to get the quotient of the radiative energy absorbed by $S_{1,l}$ to that emitted by $S_{2,l}$ over the whole hemispherical space. So, there is $0 < f_{S_{2,l}}^{S_{1,j}} < 1$. The function $f_{S_{2,l}}^{S_{1,j}}$ is independent of spectral properties. The expressions of the other

REQTFSEs can also be deduced, and for simplicity, these expressions are not given here.

5.1.3.2 Determination of the RTFCVISE. Define $f_{V_{(i,j)}^n}^{S_{2,I}^{2,I}}$ ($n = 1-4$) as the radiative transfer function for control volume interface versus surface element (RTFCVISE), i.e., the radiative energy arriving at $S_{2,I}$ and emitted by $V_{(i,j)}^n$ at the k th spectral band.

$$f_{V_{(i,j)}^n}^{S_{2,I}^{2,I}} = \begin{cases} 2 \int_{(i-1)\Delta x}^{i\Delta x} dx \int_0^{\pi/2} d\varphi \int_{\arctg(x-I\Delta x)/(M-j)\Delta y \cos \varphi}^{\arctg(x-(I-1)\Delta x)/(M-j)\Delta y \cos \varphi} \exp\left[\frac{(M-j)\Delta y}{\cos \theta}\right] \sin \theta \cos \theta d\theta & (I < i) \\ 4 \int_{(i-1)\Delta x}^{i\Delta x} dx \int_0^{\pi/2} d\varphi \int_0^{\arctg(x-(I-1)\Delta x)/(M-j)\Delta y \cos \varphi} \exp\left[\frac{(M-j)\Delta y}{\cos \theta}\right] \sin \theta \cos \theta d\theta & (I = i) \\ 2 \int_{(i-1)\Delta x}^{i\Delta x} dx \int_0^{\pi/2} d\varphi \int_{\arctg(I\Delta x-x)/(M-j)\Delta y \cos \varphi}^{\arctg((I-1)\Delta x-x)/(M-j)\Delta y \cos \varphi} \exp\left[\frac{(M-j)\Delta y}{\cos \theta}\right] \sin \theta \cos \theta d\theta & (I > i) \end{cases} \quad (13)$$

For simplicity, the deduction of Eq. (13) is omitted, and the expressions of the other functions $f_{V_{(i,j)}^1}^{S_{2,I}^{2,I}}$, $f_{V_{(i,j)}^2}^{S_{2,I}^{2,I}}$, and $f_{V_{(i,j)}^3}^{S_{2,I}^{2,I}}$ ($=0$) are not given here.

5.1.3.3 Determination of the function $f_{V_{(i,j)}^4}^{S_{2,I}^{2,I}}$. Based on the two functions $f_{S_{2,I}}^{S_{1,I}}$ and $f_{V_{(i,j)}^2}^{S_{2,I}^{2,I}}$ solved as above, the function $f_{V_{(i,j)}^4}^{S_{2,I}^{2,I}}$ can be deduced. The energy emitted at the k th spectral band by $V_{(i,j)}^2$ and arriving at $S_{2,I}$ is denoted by $f_{V_{(i,j)}^2}^{S_{2,I}^{2,I}}$, and part $f_{V_{(i,j)}^2}^{S_{2,I}^{2,I}} \rho_{hs,k}$ of this energy is reflected by $S_{2,I}$. The reflected energy $f_{V_{(i,j)}^2}^{S_{2,I}^{2,I}} \rho_{hs,k}$ can be considered as that diffusely emitted by $S_{2,I}$, and as a result, quotient $f_{S_{2,I}}^{S_{1,I}}$ of $f_{V_{(i,j)}^2}^{S_{2,I}^{2,I}} \rho_{hs,k}$ is absorbed by $S_{1,I}$. So, after being reflected by all the surface elements of S_2 , the total energy absorbed by $S_{1,I}$ is

$$f_{V_{(i,j)}^4}^{S_{2,I}^{2,I}} = \sum_{l=1}^M f_{V_{(i,j)}^2}^{S_{2,I}^{2,I}} \rho_{hs,k} f_{S_{2,I}}^{S_{1,I}} \quad (14)$$

Substitution of Eqs. (11) and (14) into Eq. (10) yields $f_{V_{(i,j)}^4}^{S_{2,I}^{2,I}}$.

5.1.3.4 Deduction of the RTC $(V_{(i,j)}S_{1,I})_k$. By a similar deduction as above, we can solve the other functions $f_{V_{(i,j)}^1}^{S_{1,I}^{1,I}}$, $f_{V_{(i,j)}^2}^{S_{1,I}^{1,I}}$, $f_{V_{(i,j)}^3}^{S_{1,I}^{1,I}}$ ($=0$), $f_{V_{(i,j)}^4}^{S_{1,I}^{1,I}}$, $f_{V_{(i,j)}^1}^{S_{2,I}^{2,I}}$, and $f_{V_{(i,j)}^2}^{S_{2,I}^{2,I}}$. Therefore, we have

$$f_{V_{(i,j)}^1}^{S_{1,I}^{1,I}} = f_{V_{(i,j)}^1}^{S_{1,I}^{1,I}} + f_{V_{(i,j)}^2}^{S_{1,I}^{1,I}} \quad (15a)$$

$$f_{V_{(i,j)}^2}^{S_{1,I}^{1,I}} = f_{V_{(i,j)}^2}^{S_{1,I}^{1,I}} + f_{V_{(i,j)}^3}^{S_{1,I}^{1,I}} \quad (15b)$$

$$f_{V_{(i,j)}^3}^{S_{1,I}^{1,I}} = f_{V_{(i,j)}^3}^{S_{1,I}^{1,I}} + f_{V_{(i,j)}^4}^{S_{1,I}^{1,I}} \quad (15c)$$

Using the following relationship, the functions $f_{V_{(i,j)}^n}^{S_{1,I}^{1,I}}$ ($n=1-4$) can be deduced:

$$\begin{aligned} f_{V_{(i,j)}^1}^{S_{1,I}^{1,I}} &= f_{V_{(i-1,j)}^1}^{S_{1,I}^{1,I}}, & f_{V_{(i,j)}^2}^{S_{1,I}^{1,I}} &= f_{V_{(i,j+1)}^2}^{S_{1,I}^{1,I}}, & f_{V_{(i,j)}^3}^{S_{1,I}^{1,I}} &= f_{V_{(i+1,j)}^3}^{S_{1,I}^{1,I}}, & f_{V_{(i,j)}^4}^{S_{1,I}^{1,I}} &= f_{V_{(i,j)}^4}^{S_{1,I}^{1,I}} \\ &= f_{V_{(i,j-1)}^1}^{S_{1,I}^{1,I}} \end{aligned} \quad (16)$$

Thus, substitution of Eqs. (10), (15), and (16) into Eq. (8) gives

The position of $S_{2,I}$ relative to $V_{(i,j)}^2$ has three conditions: (1) $S_{2,I}$ located in the top-left direction of $V_{(i,j)}^2$ ($I < i$); (2) $S_{2,I}$ located directly upon $V_{(i,j)}^2$ ($I = i$); and (3) $S_{2,I}$ located in the top-right direction of interface 2 ($I > i$). Therefore, the expression of function $f_{V_{(i,j)}^2}^{S_{2,I}^{2,I}}$ has three different types:

$(V_{(i,j)}S_{1,I})_k$.

Deductions of the other RTCs $(V_{(i,j)}S_{3,I})_k$, $(V_{(i,j)}S_{4,m})_k$, $(V_{(i,j)}V_{(l,m)})_k$, and $(V_{(i,j)}S_{\infty})_k$ are similar to the above, and for simplicity, the detailed deductions are not given here.

5.2 Deduction of the RTCs for the Black Surroundings Versus Other Elements. As shown in Fig. 1, the radiative energy emitted by the black surroundings $S_{\infty 1}$ and $S_{\infty 3}$ with the length of L_2 and the whole $S_{\infty 2}$ can pass through S_2 and is absorbed by all the control volumes and inner surfaces of all the surface elements. So, the RTCs $(S_{\infty a}V_{(i,j)})_k$ and $(S_{\infty a}S_{b,l})_k$ (where $a=1-3$ and $b=1, 3$, and 4) should be solved.

Function $q_{S_{\infty a}^k}^{S_{2,I}^{2,I}}$ is defined as the radiative energy arriving at $S_{2,I}$ and emitted by $S_{\infty a}$ at the k th spectral band over the whole hemispherical space, and according to the principles of radiative heat transfer, the expression of $q_{S_{\infty a}^k}^{S_{2,I}^{2,I}}$ can be obtained. For example, for $S_{\infty 2}$, we have

$$\begin{aligned} q_{S_{\infty 2}^k}^{S_{2,I}^{2,I}} &= \frac{2\sigma T_{\infty 2}^4}{\pi} \int_0^{L_1+(I-1)\Delta x} dx \int_0^{\pi/2} d\varphi \int_{\arctg(x/L_2 \cos \varphi)}^{\arctg((x+\Delta x)/L_2 \cos \varphi)} \cos \theta \sin \theta d\theta \\ &+ \frac{2\sigma T_{\infty 2}^4}{\pi} \int_0^{L_3+H_x-(I-1)\Delta x} dx \int_0^{\pi/2} d\varphi \int_{\arctg(x/L_2 \cos \varphi)}^{\arctg((x+\Delta x)/L_2 \cos \varphi)} \cos \theta \sin \theta d\theta \\ &+ \frac{4\sigma T_{\infty 2}^4}{\pi} \int_0^{\Delta x} dx \int_0^{\pi/2} d\varphi \int_0^{\arctg(x/L_2 \cos \varphi)} \cos \theta \sin \theta d\theta \end{aligned} \quad (17)$$

For simplicity, the expressions of $q_{S_{\infty 1}^k}^{S_{2,I}^{2,I}}$ and $q_{S_{\infty 3}^k}^{S_{2,I}^{2,I}}$ are not given here.

Part $\gamma_{sh,k}$ ($=1-\rho_{sh,k}$, transmittivity) of the radiative energy $q_{S_{\infty a}^k}^{S_{2,I}^{2,I}}$ transmits $S_{2,I}$ and enters the rectangular medium. Then, the function $f_{V_{(i,j)}^n}^{S_{2,I}^{2,I}}$ is used to trace the transmitted energy to get the part absorbed by $V_{(i,j)}$, and then adding up all the part of the energy absorbed by $V_{(i,j)}$, we can solve the RTC $(S_{\infty a}V_{(i,j)})_k$. Therefore, analyzing as above, we have

$$(S_{\infty a} V_{(i,j)})_k = \sum_{l=1}^M q_{S_{\infty a},k}^{S_{2,l}} \gamma_{sh,k} f_{S_{2,l}}^{V_{(i,j)}} \quad (a=1-3) \quad (18)$$

The function $f_{S_{2,l}}^{V_{(i,j)}}$ is the REQTFSE. Its expression is similar to Eq. (12) and, for simplicity, not given here.

In addition, the RTC $(S_{\infty a} S_{b,l})_k$ can be expressed as

$$(S_{\infty a} S_{b,l})_k = \sum_{l=1}^M q_{S_{\infty a},k}^{S_{2,l}} \gamma_{sh,k} f_{S_{2,l}}^{S_{b,l}} \quad (a=1-3 \text{ and } b=1, 3, \text{ and } 4) \quad (19)$$

where $f_{S_{2,l}}^{S_{b,l}}$ is the REQTFSE, as shown in Eq. (12).

5.3 Reciprocity and Integrality Relationships of the RTCs

5.3.1 Reciprocity Relationships of the RTCs. In our calculation, we validate the following reciprocity and integrality relationships of the RTCs. The RTCs have the following reciprocity relationships:

- (1) reciprocity relationships for control volume versus control volume, control volume versus black surface element, and black surface element versus black surface element

$$\begin{aligned} (V_{(i,j)} V_{(l,m)})_k &= (V_{(l,m)} V_{(i,j)})_k, \quad (S_{1,j} V_{(i,j)})_k \\ &= (V_{(i,j)} S_{1,j})_k, \quad (S_{1,j} S_{3,j})_k = (S_{3,j} S_{1,j})_k \end{aligned} \quad (20a)$$

$$\begin{aligned} (S_{4,i} V_{(i,j)})_k &= (V_{(i,j)} S_{4,i})_k, \quad (S_{3,j} S_{4,i})_k \\ &= (S_{4,i} S_{3,j})_k, \quad (S_{3,j} V_{(i,j)})_k = (V_{(i,j)} S_{3,j})_k \\ (S_{1,j} S_{4,i})_k &= (S_{4,i} S_{1,j})_k \end{aligned}$$

- (2) reciprocity relationships for control volumes versus black surroundings and black surface elements versus black surroundings

$$\begin{aligned} \frac{\gamma_{hs,k}}{\gamma_{sh,k}} \sum_{a=1}^3 (S_{\infty a} V_{(i,j)})_k &= (V_{(i,j)} S_{\infty})_k, \quad \frac{\gamma_{hs,k}}{\gamma_{sh,k}} \sum_{a=1}^3 (S_{\infty a} S_{b,i})_k \\ &= (S_{b,i} S_{\infty})_k \quad (b=1,3,4) \end{aligned} \quad (20b)$$

Equation (20b) is a very interesting relationship, which is quite different from the 1D case. Equation (20b) makes the reciprocity relationships of the RTCs of the RTNAM more consummate in theory.

5.3.2 Integrality Relationships of the RTCs. The RTCs have the following integrality relationships:

$$\begin{aligned} \sum_{l=1}^M \sum_{m=1}^N (V_{(i,j)} V_{(l,m)})_k + \sum_{j=1}^N [(V_{(i,j)} S_{1,j})_k + (V_{(i,j)} S_{3,j})_k] \\ + \sum_{i=1}^M (V_{(i,j)} S_{4,i})_k + (V_{(i,j)} S_{\infty})_k = 4\pi\kappa_k \Delta x \Delta y \end{aligned} \quad (21a)$$

$$\begin{aligned} \sum_{l=1}^M \sum_{m=1}^N (S_{1,j} V_{(l,m)})_k + \sum_{i=1}^M (S_{1,j} S_{4,i})_k + \sum_{J=1}^N [(S_{1,j} S_{1,J})_k + (S_{1,j} S_{3,J})_k] \\ + (S_{1,j} S_{\infty})_k = \pi \Delta y \end{aligned} \quad (21b)$$

$$\begin{aligned} \sum_{l=1}^M \sum_{m=1}^N (S_{3,j} V_{(l,m)})_k + \sum_{i=1}^M (S_{3,j} S_{4,i})_k + \sum_{J=1}^N [(S_{3,j} S_{3,J})_k + (S_{3,j} S_{1,J})_k] \\ + (S_{3,j} S_{\infty})_k = \pi \Delta y \end{aligned} \quad (21c)$$

Table 1 Reciprocity relationships for control volume versus control volume, control volume versus black surface element, and black surface element versus black surface element

RTC <i>a</i>		RTC <i>b</i>		Relative error: $\frac{a-b}{a}$ (%)
1	$(V_{(5,9)} V_{(6,3)}) = 0.00001279$	$(V_{(6,3)} V_{(5,9)}) = 0.00001279$		0.000
2	$(S_{1,5} V_{(4,6)}) = 0.00051663$	$(V_{(4,6)} S_{1,5}) = 0.00051672$		-0.016
3	$(S_{3,4} V_{(7,6)}) = 0.00035734$	$(V_{(7,6)} S_{3,4}) = 0.00035729$		-0.014
4	$(S_{1,3} S_{3,5}) = 0.00480056$	$(S_{3,5} S_{1,3}) = 0.00480055$		0.000
5	$(S_{4,5} V_{(7,8)}) = 0.00028290$	$(V_{(7,8)} S_{4,5}) = 0.00028280$		0.036
6	$(S_{3,9} S_{4,7}) = 0.00350465$	$(S_{4,7} S_{3,9}) = 0.00350463$		0.000
7	$(S_{1,2} S_{4,5}) = 0.00433689$	$(S_{4,5} S_{1,2}) = 0.00433682$		0.002

$$\begin{aligned} \sum_{l=1}^M \sum_{m=1}^N (S_{4,i} V_{(l,m)})_k + \sum_{j=1}^N [(S_{4,i} S_{1,j})_k + (S_{4,i} S_{3,j})_k] + \sum_{l=1}^M (S_{4,i} S_{4,l})_k \\ + (S_{4,i} S_{\infty})_k = \pi \Delta x \end{aligned} \quad (21d)$$

$$\begin{aligned} \sum_{l=1}^M \sum_{m=1}^N (S_{\infty a} V_{(l,m)})_k + \sum_{j=1}^N [(S_{\infty a} S_{1,j})_k + (S_{\infty a} S_{3,j})_k] + \sum_{l=1}^M (S_{\infty a} S_{4,l})_k \\ = \sum_{l=1}^M q_{S_{\infty a},k}^{S_{2,l}} \gamma_{sh,k} \quad (a=1-3) \end{aligned} \quad (21e)$$

In Eq. (21e), the term $q_{S_{\infty a},k}^{S_{2,l}}$ is the radiative energy arriving at $S_{2,l}$ and emitted by $S_{\infty a}$ ($a=1-3$), as shown in Eq. (17).

5.3.3 Validation of the Reciprocity and Integrality Relationships for the RTCs. Equations (20) and (21) are used to validate the correctness of the RTCs. In the following, we use an example to validate these relationships. The parameters used are $H_x=H_y=0.5$ m, $M=N=11$, $\kappa=0.5$ m⁻¹, $n=2$, and $L_i=1$ ($i=1-4$). The medium is supposed to be gray, and for the gray medium, subscript k is omitted.

The results of the validation for the reciprocity relationships of the RTCs are shown in Tables 1 and 2. As shown in the two tables, the relative errors are very small. Therefore, Eq. (20) is correct.

The integrality relationships of the RTCs, Eq. (21), are also well satisfied. For example, for control volume $V_{(3,5)}$, the value of the term on the left-hand side of Eq. (21a) is 0.01298179, and the value of the term on the right-hand side is $4\pi\kappa\Delta x\Delta y=0.01298179$.

6 Determination of the RTCs Considering Isotropic Scattering

6.1 Normalization of the RTCs Without Considering Scattering. For absorbing and isotropically scattering media, a part of the radiative energy represented by RTCs without considering scattering, such as $(V_{(i,j)} V_{(l,m)})_k$, etc., is absorbed, and the rest is scattered. According to the physical mechanism of radiative transfer in scattering media, the part of the radiative energy scattered by control volumes must be redistributed. Before that, the RTCs for the absorbing media deduced above should be normalized according to Eq. (21). That is,

$$\begin{aligned} (V_{(i,j)} A)_k^* &= (V_{(i,j)} A)_k / (4\kappa_k \Delta x \Delta y) \\ (S_{u,j} A)_k^* &= (S_{u,j} A)_k / (\pi \Delta y) \quad (u=1 \text{ or } 3) \\ (S_{4,m} A)_k^* &= (S_{4,m} A)_k / (\pi \Delta x) \end{aligned} \quad (22)$$

Table 2 Reciprocity relationships for control volumes versus black environment and black surface elements versus black environment

RTC of black environment versus other elements				Value A	Value B	Relative error: $\frac{A-B}{A}$ (%)
1	$(S_{\infty 1} S_{1,5})$ 0.00252512	$(S_{\infty 2} S_{1,5})$ 0.01783137	$(S_{\infty 3} S_{1,5})$ 0.00255812	0.00572866	$\frac{\gamma_{hs} \sum_{l=1}^3 (S_{\infty a} S_{1,5})}{\gamma_{sh a} \sum_{l=1}^3 (S_{\infty} S_{1,5})}$ 0.00572637	0.040
2	$(S_{\infty 1} S_{3,8})$ 0.00370446	$(S_{\infty 2} S_{3,8})$ 0.02747183	$(S_{\infty 3} S_{3,8})$ 0.00414014	0.00882911	$\frac{\gamma_{hs} \sum_{l=1}^3 (S_{\infty a} S_{3,8})}{\gamma_{sh a} \sum_{l=1}^3 (S_{\infty} S_{3,8})}$ 0.00882562	0.040
3	$(S_{\infty 1} S_{4,7})$ 0.00262120	$(S_{\infty 2} S_{4,7})$ 0.02539136	$(S_{\infty 3} S_{4,7})$ 0.00284198	0.00493673	$\frac{\gamma_{hs} \sum_{l=1}^3 (S_{\infty a} S_{4,7})}{\gamma_{sh a} \sum_{l=1}^3 (S_{\infty} S_{4,7})}$ 0.00493657	0.003
4	$(S_{\infty 1} V_{(5,8)})$ 0.00034035	$(S_{\infty 2} V_{(5,8)})$ 0.00232269	$(S_{\infty 3} V_{(5,8)})$ 0.00032116	0.00074605	$\frac{\gamma_{hs} \sum_{l=1}^3 (S_{\infty a} V_{(5,8)})}{\gamma_{sh a} \sum_{l=1}^3 (S_{\infty} V_{(5,8)})}$ 0.00074575	0.040

$$(S_{\infty a} B)_k^* = (S_{\infty a} B)_k \left(\sum_{l=1}^M q_{S_{\infty a} k}^{S_{2,l}} \gamma_{sh,k} \right) \quad (a = 1, 2, \text{ or } 3)$$

where the asterisk denotes normalized RTCs, A represents the elements $S_{v,m}$ ($v=1, 3, \text{ or } 4$), $V_{(l,m)}$, and S_{∞} , and B represents the elements $S_{v,m}$ ($v=1, 3, \text{ or } 4$) and $V_{(l,m)}$. The value of each normalized RTC is greater than zero and less than 1. From Eq. (22), we can see that the normalization of the RTC $(S_{\infty a} B)_k$ is quite different from that of the 1D case.

6.2 Determination of the RTCs Considering Isotropic Scattering. The RTC $[V_{(i,j)} S_{\infty}]_k$ is taken as an example to illustrate the deductive process. For convenience, in the following, the subscript k is omitted, and subscript a and A are introduced to denote the absorption quotient. Notice that only the medium scatterers radiation and the surfaces do not. Isotropic scattering effects can be considered as follows.

- (1) At first, the energy quotient directly absorbed by S_{∞} to that emitted by $V_{(i,j)}$ is

$$[V_{(i,j)} S_{\infty}]_a^{*1st} = (V_{(i,j)} S_{\infty})^* \quad (23)$$

- (2) After the first tracing of the scattered energy, the energy quotient scattered by all control volumes to that emitted by $V_{(i,j)}$ is $\sum_{l_1=1}^M \sum_{m_1=1}^N (V_{(i,j)} V_{(l_1, m_1)})^* \omega$, which is homogeneously distributed over the whole spherical space and can be considered equivalent to that isotropically emitted by the control volume $V_{(l_1, m_1)}$. This tracing of the scattered energy causes the portion

$$[V_{(i,j)} S_{\infty}]_a^{*1st} = \sum_{l_1=1}^M \sum_{m_1=1}^N (V_{(i,j)} V_{(l_1, m_1)})^* \omega (V_{(l_1, m_1)} S_{\infty})^* \quad (24)$$

to be absorbed by S_{∞}

$$[V_{(i,j)} S_{\infty}]_a^{*2nd} = [V_{(i,j)} S_{\infty}]_a^{*1st} + [V_{(i,j)} S_{\infty}]_a^{*1st} \quad (25)$$

- (3) Part $\sum_{l_2=1}^M \sum_{m_2=1}^N [(V_{(i,j)} V_{(l_2, m_2)})^* \omega \sum_{l_1=1}^M \sum_{m_1=1}^N (V_{(l_2, m_2)} V_{(l_1, m_1)})^* \omega]$ of the scattered energy $\sum_{l_1=1}^M \sum_{m_1=1}^N (V_{(i,j)} V_{(l_1, m_1)})^* \omega$, derived in step (2), is scattered again, which causes some of the radiative energy, emitted by $V_{(i,j)}$, to be absorbed by S_{∞} once more. Thus, the second tracing of the scattered energy causes the portion

$$[V_{(i,j)} S_{\infty}]_a^{*2nd} = \sum_{l_2=1}^M \sum_{m_2=1}^N \left[(V_{(i,j)} V_{(l_2, m_2)})^* \omega \sum_{l_1=1}^M \sum_{m_1=1}^N (V_{(l_2, m_2)} \times V_{(l_1, m_1)})^* \omega (V_{(l_1, m_1)} S_{\infty})^* \right] \quad (26a)$$

to be absorbed by S_{∞} . Equation (26a) can be rewritten as

$$[V_{(i,j)} S_{\infty}]_a^{*2nd} = \sum_{l_2=1}^M \sum_{m_2=1}^N [(V_{(i,j)} V_{(l_2, m_2)})^* \omega [V_{(l_2, m_2)} S_{\infty}]_a^{*1st}] \quad (26b)$$

where $[V_{(l_2, m_2)} S_{\infty}]_a^{*1st}$ can be calculated from Eq. (24) by replacing $V_{(i,j)}$ with $V_{(l_2, m_2)}$. Therefore, after the second tracing of the scattered energy, we have

$$[V_{(i,j)} S_{\infty}]_a^{*3rd} = [V_{(i,j)} S_{\infty}]_a^{*2nd} + [V_{(i,j)} S_{\infty}]_a^{*2nd} \quad (27)$$

- (4) The scattered energy $\sum_{l_2=1}^M \sum_{m_2=1}^N [(V_{(i,j)} V_{(l_2, m_2)})^* \omega \sum_{l_1=1}^M \sum_{m_1=1}^N (V_{(l_2, m_2)} V_{(l_1, m_1)})^* \omega]$, derived in step (3), will be scattered again, which causes part of the radiative energy to be absorbed by S_{∞} for the third tracing of the scattered energy.
- (5) The rest are deduced by analogy, and after the $(n-1)$ th tracing of the scattered energy, if all the control volumes satisfy the following inequality

$$\left| 1 - \sum_{m=1}^N \{ [V_{(i,j)} S_{1,m}]_a^{*nth} + [V_{(i,j)} S_{3,m}]_a^{*nth} \} - \sum_{l=1}^M [V_{(i,j)} S_{4,l}]_a^{*nth} - [V_{(i,j)} S_{\infty}]_a^{*nth} - \sum_{l=1}^M \sum_{m=1}^N [V_{(i,j)} V_{(l,m)}]_a^{*nth} \right| < 10^{-6} \quad (28)$$

the calculation is finished. Then, we have

$$[V_{(i,j)} S_{\infty}]_a^{*nth} = [V_{(i,j)} S_{\infty}]_a^{*(n-1)th} + [V_{(i,j)} S_{\infty}]_a^{*(n-1)th} \quad (29a)$$

where

$$[V_{(i,j)}S_{\infty}]_A^{*(n-1)\text{th}} = \sum_{l_{n-1}=1}^M \sum_{m_{n-1}=1}^N [(V_{(i,j)}V_{(l_{n-1},m_{n-1})})^* \times \omega[V_{(l_{n-1},m_{n-1})}S_{\infty}]_A^{*(n-2)\text{th}}] \quad (29b)$$

From Eq. (29b), we can see that $[V_{(i,j)}S_{\infty}]_A^{*(n-1)\text{th}}$ can be iteratively calculated.

Finally, $[V_{(i,j)}S_{\infty}]$ can be calculated from the inverse calculation:

$$[V_{(i,j)}S_{\infty}] = 4\kappa(1 - \omega)\Delta x\Delta y[V_{(i,j)}S_{\infty}]_a^{*n\text{th}} \quad (30)$$

The deduction of the other isotropic scattering RTCs is similar to above.

7 Solution to the Temperature Field

As we know, the radiative source term and opaque boundary condition are nonlinear functions of temperatures at all nodes, as shown in Eqs. (3)–(5), (6a), and (6b), so we should first linearize them using Patankar's linearization method. Readers can refer to Ref. [35] to get more details about the linearization of the radiative source term and opaque boundary condition, and for simplicity, we do not discuss it here.

In this paper, the additional source method is used to eliminate the unknown temperatures at boundary nodes [35]. Moreover, the ADI method is used to solve the linearized equations. Readers can refer to Ref. [35] for more information about the numerical method of this paper.

8 Results and Discussion

Using the Intel FORTRAN compiler, the following calculation has been performed on a Dell PowerEdge 2900 server, 1.6 GHz dual-core processor with 8 Gbyte random access memory (RAM), which is installed with a Linux operating system.

In the following, the steady state is supposed to be reached when the temperatures of all nodes between the m th and $(m+1)$ th steps satisfy $|T_{(i,j)}^{m+1} - T_{(i,j)}^m| < 10^{-4}$. For the m th time step, if the temperatures of all nodes between the n th iteration calculation and the $(n+1)$ th one satisfy $|T_{(i,j)}^{m,n+1} - T_{(i,j)}^{m,n}| < 10^{-4}$, the convergent solution is reached.

8.1 Validation of This Paper. We cannot compare our results with other published data to validate the correctness of this paper because we have not found a physical model similar to ours. Thus, we mainly validate the correctness of the radiative heat transfer model developed in this paper from the following two aspects. First, the RTCs satisfy the reciprocity and integrality relationships, as shown in Eqs. (20) and (21), which proves that the RTCs are correct. Second, supposing the length along the x -axis direction of the rectangular medium is much bigger than that along the y -axis direction, the 2D physical model can be approximately simplified as a 1D one; therefore, the results of this paper can be compared with those of the 1D physical model of our own to validate the correctness of the 2D physical model developed in this paper.

The calculating parameters are $L_r=1$ m, $T_r=1000$ K, $T_0=1000$ K, $H_x^*=12$, $H_y^*=1$, $M \times N=69 \times 30$, $N'=0.3$, $n=2$, $\kappa=2$ m⁻¹, $\omega=0.95$, $L_1=L_2=L_3=L_4=10^{-3}$ m, $T_{gi}=1000$ K ($i=1-4$), $T_{\infty 2}=1500$ K, $T_{\infty 1}=T_{\infty 3}=T_{\infty 4}=1000$ K, $h_1=h_2/2=h_3=h_4=100$ W m⁻² K⁻¹, $\Delta t_1^*=0.002$, $\Delta t_2^*=0.007$, and $\Delta t_3^*=1$, and the medium is supposed to be gray. The length of the rectangular medium along the x -axis direction is 12 times bigger than that along the y -axis direction, so the 2D physical model is approximately simplified to a 1D one. The results are shown in Fig. 2. The solid lines are the results of the 2D physical model approximately simplified to a 1D one, and the dashed lines are the results of our former precise 1D model. From the figure, we can see that the temperature distributions along the centerline $x^*=6$ agree very

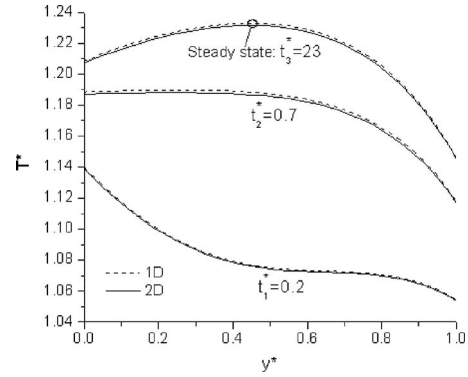


Fig. 2 Validation of this paper

well with those of the 1D model. This partially proves that the 2D radiative heat transfer model with a semitransparent and diffuse surface developed by the RTNAM is correct.

8.2 Transient Cooling of the Rectangular Medium. The calculating parameters are taken as $\omega=0.9$, $L_r=1$ m, $T_r=1000$ K, $T_0=1500$ K, $N'=0.1$, $n=1.5$, $\kappa=1$ m⁻¹, $H_x^*=1.2$, $H_y^*=1$, $T_{\infty 1}=T_{\infty 3}=T_{\infty 4}=1500$ K, $T_{\infty 2}=500$ K, $h_1=h_2=h_3=h_4=100$ W m⁻² K⁻¹, $T_{gi}=1500$ K, and $L_i^*=2$ ($i=1-4$). The medium is supposed to be gray. From the calculating parameters, we can see that the 2D rectangular medium is cooled by the $S_{\infty 2}$ having a lower temperature.

In the following simulation, we just give transient results at $t_1^*=0.03$, $t_2^*=0.1$, and steady state. The time steps are chosen as $\Delta t_1^*=0.006$, $\Delta t_2^*=0.002$, and $\Delta t_3^*=10$. With the above calculating parameters, the temperature distribution is shown in Fig. 3. In Fig. 3(c), the solid lines, dashed lines, and dotted lines correspond to $M \times N=47 \times 43$, $M \times N=59 \times 55$, and $M \times N=37 \times 33$, respectively, and as shown in the figure the three sorts of lines are almost superposed with each other, which means that the results of the three kinds of mesh division are almost the same. So, in the following we chose $M \times N=47 \times 43$ to determine the meshes, and with this mesh division the calculating time for Figs. 3(a) and 3(b) is about 47 h.

As a result of the semitransparent surface S_2 , the inner regions of media can exchange radiative energy with $S_{\infty 2}$ through S_2 . As shown in Fig. 3, at the beginning of the transients, S_1 , S_3 , and S_4 are cooled more rapidly than the inner regions because they have a higher emissivity, and the extinction coefficient is small so that in the medium the attenuation of thermal radiation emitted from the three inner surfaces becomes very weak. As a result, the temperature profile is concave downward. The closer to S_2 the regions are, the stronger the radiative cooling effect of the regions is, and the lower the temperatures therein are. In addition, the convective heating of the surrounding fluid on S_2 causes the temperatures of S_2 to rise. Therefore, maximum temperatures appear in the medium. The boundary conditions at S_2 and S_4 are different, as shown in Eqs. (4) and (7). Heat conduction at S_2 has a significant effect on temperature distributions of the medium. At steady state, S_4 has the lowest temperature because it is furthest away from S_2 , and the convective heating coupled with conduction at S_2 has the smallest effect on S_4 .

8.3 Effect of Scattering Albedo on Temperature Distributions. Keeping the other parameters of Fig. 3 unchanged, effects of $\omega=0.98$ on temperature distributions are shown in Fig. 4. The absorption coefficient decreases when the scattering albedo increases, which weakens the emitting ability of the medium. Therefore, at the beginning of the transients, the radiative cooling of the central regions of the medium slows down. The weakened cooling of the regions close to S_2 increases the temperature of S_2 .

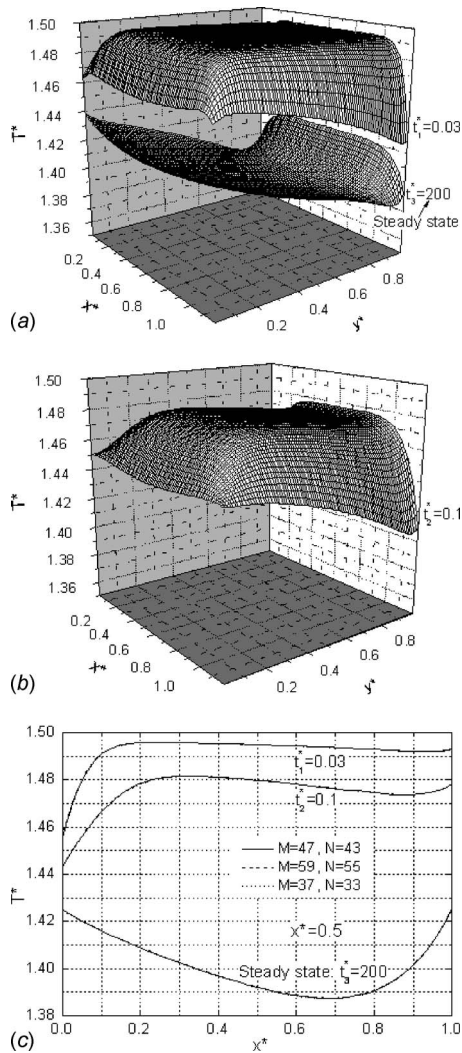


Fig. 3 Transient cooling of the rectangular medium: (a) $\xi_1 = 0.03$ and steady state and (b) $\xi_2 = 0.1$. (c) Temperature distributions along vertical centerline.

The radiative energy emitted by the inner surfaces of the three black surfaces and transferred to S_∞ includes two parts: One is directly transferred to S_∞ , and the other is transferred to S_∞ by scattering. The increase in scattering albedo intensifies the radiative cooling effect of S_∞ on S_1 , S_3 , and S_4 caused by scattering. The calculating time is about 48 h.

8.4 Effects of Conduction-Radiation Parameter on Temperature Distributions. Keeping the other parameters of Fig. 3 unchanged, the effects of $N' = 1$ on temperature distributions are shown in Fig. 5. The heat transfer ability of the medium is intensified as the conduction-radiation parameter increases. Therefore, the temperatures distribute more homogeneously in the medium, and the temperature profiles of the medium close to the three black surfaces are not steep any more. The calculating time is about 48 h.

9 Conclusions

This paper studies 2D transient coupled heat transfer in a rectangular isotropic scattering medium using the RTNAM. The rectangular medium has one semitransparent and diffusely reflecting boundary, and the other three boundaries are opaque and black. Radiative energy will be reflected and transmitted by the semitransparent boundary, which makes this problem complex, and a

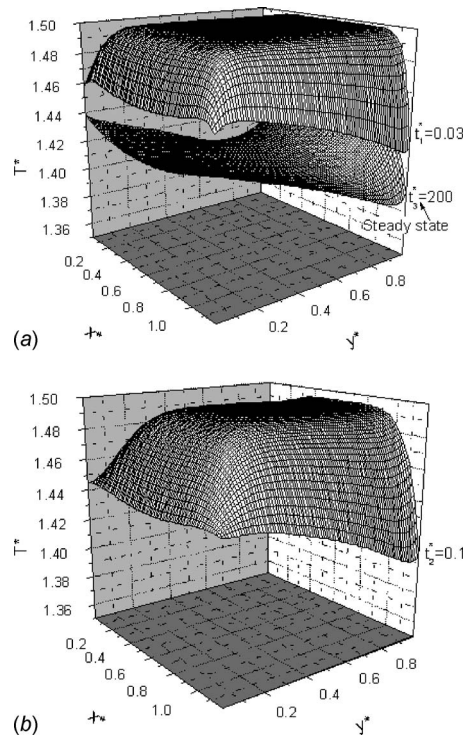


Fig. 4 Effect of scattering albedo on temperature distributions: (a) $\xi_1 = 0.03$ and steady state and (b) $\xi_2 = 0.1$

proper method is developed here to solve this problem; that is, the radiative energy reflected and transmitted by the semitransparent boundary is successfully traced. The diffuse reflectivity of the semitransparent surface is determined by assuming that each bit of roughness acts as a smooth facet so that Fresnel's reflective law and Snell's refractive law can be used.

Transient differential energy equation is discretized using the fully implicit finite difference method. The effect of thermal radiation on heat transfer is considered as a radiative source term expressed by the RTCs. For the RTCs without considering scattering, the integrality and reciprocity relationships of this 2D physical model are found, which are quite different from those of the 1D physical model. The RTCs without considering scattering are normalized according to their integrality relationships, and then the normalized RTCs are used to trace the radiative energy scattered by the medium. Finally, the RTCs considering isotropic scattering are solved through reverse calculation. Patankar's linearization method is used to linearize the radiative source term and the opaque boundary conditions, and the boundary conditions

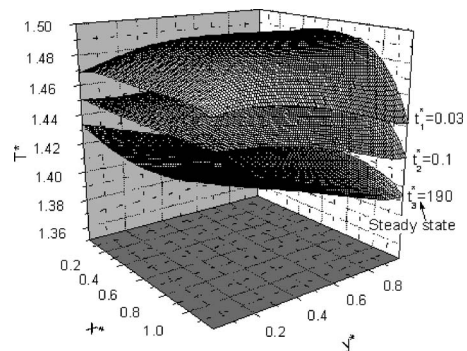


Fig. 5 Effects of conduction-radiation parameter on temperature distributions

are dealt with an additional source term method. The ADI method is applied to solve the nominal linear equations to obtain the temperature distributions within the medium. The correctness of this paper is validated.

The effects of scattering albedo and conduction-radiation parameter on temperature distributions are investigated. From the above analysis, we can draw the following conclusions:

- (1) When the extinction coefficient is so small, the increase in scattering albedo can intensify the cooling of the three black surfaces of the rectangular medium.
- (2) When the conduction-radiation parameter increases, the temperature distributions within the medium become more homogeneous, and the temperature profiles within the medium close to the three black surfaces are not steep any more.

Acknowledgment

This research is supported by the Foundation for the Author of National Excellent Doctoral Dissertation of China (Grant No. 200438), the National Natural Science Foundation of China (Grant No. 50806018), and the key project of the National Natural Science Foundation of China (Grant No. 50930007).

Nomenclature

- $A_{k,T} = \int_{\Delta\lambda_k} I_{\lambda,b}(T) d\lambda / (\sigma T^4)$, where $I_{\lambda,b}(T)$ Planck's law λ is the wavelength and subscript k means the k th spectral band
- H_x = length of the rectangular medium (Fig. 1), m
 H_x^* = dimensionless length of the rectangular medium, H_x/L_r
- H_y = width of the rectangular medium (Fig. 1), m
 H_y^* = dimensionless width of the rectangular medium, H_y/L_r
- h_i = convective heat transfer coefficients at surfaces S_i , where $i=1-4$, $W m^{-2} K^{-1}$
- (i,j) = node in medium, where i and j are the integral coordinates of each node along the x and y directions (Fig. 1), respectively
- k = thermal conductivity of the medium, $W m^{-1} K^{-1}$
- L_i = distance from surface S_i to black surrounding surface $S_{\infty i}$, where $i=1-4$, m
- L_r = reference distance, m
- M = integer parameter, used to divide H_x into M equal parts
- N = integer parameter, used to divide H_y into N equal parts
- N' = conduction-radiation parameter of medium, $k/(4\sigma T_r^3 L_r)$
- n = refractive index of the medium n th interface of control volume
- NB = total number of spectral bands
- $S_{\infty i}$ = black surface representing the surroundings (Fig. 1), where $i=1-4$
- S_{∞} = enclosed black surroundings composed of $S_{\infty 1}$, $S_{\infty 2}$, $S_{\infty 3}$, and $S_{\infty 4}$
- S_i = boundary surface (Fig. 1), where $i=1-4$
- $S_{i,j}$ = boundary node j on surface S_i
- T = absolute temperature, K
- T_0 = uniform initial temperature, K
- T_r = reference temperature, K
- T^* = dimensionless temperature, T/T_r
- $T_{S_{i,j}}$ = temperature of boundary node j on surface S_i , where $i=1-4$, K
- $T_{\infty i}$ = temperature of black surrounding surface $S_{\infty i}$ (Fig. 1), where $i=1-4$, K

- T_{gi} = gas temperature for convection at surface S_i , where $i=1-4$, K
- t_i = i th physical time, s
- t_i^* = i th dimensionless time, $4\sigma T_r^3 t_i / (\rho c L_r)$
- $V_{(i,j)}$ = control volume corresponding to node (i,j)
- $V_{(i,j)}^n$ = outside of interface n of $V_{(i,j)}$, where $n=1-4$
- $V_{(i,j)}^{n'}$ = inside of interface n of $V_{(i,j)}$, where $n=1-4$
- x = x coordinate, m
- x^* = dimensionless coordinate, x/L_r
- y = y coordinate, m
- y^* = dimensionless coordinate, y/L_r
- Δx = length of each control volume, H_x/M , m
- Δy = width of each control volume, H_y/N , m
- Δt_i = interval for time t_i , s
- Δt_i^* = dimensionless time interval for time t_i^*

Greek Letters

- α_k = k th spectral band absorption coefficient of medium, m^{-1}
- γ_k = k th spectral band diffuse transmittivity, $1-\rho_k$
- κ_k = k th spectral band extinction coefficient of medium, $\kappa_k = \alpha_k + \sigma_k$, m^{-1}
- ρ_k = k th spectral band diffuse reflectivity
- ρc = specific heat capacity of medium, $J m^{-3} K^{-1}$
- σ = Stefan-Boltzmann constant, $5.6696 \times 10^{-8} W m^{-2} K^{-4}$
- σ_k = k th spectral band scattering coefficient of medium, m^{-1}
- ω_k = k th spectral band scattering albedo of medium, σ_k / κ_k

References

- [1] Siegel, R., 1999, "Transient Thermal Analysis of a Translucent Thermal Barrier Coating on a Metal Wall," ASME J. Heat Transfer, **121**, pp. 478-481.
- [2] Luo, J.-F., Yi, H.-L., and Tan, H.-P., 2008, "Thermal Analysis of Optical Windows for Spacecraft Application," J. Thermophys. Heat Transfer, **22**(2), pp. 296-301.
- [3] Lee, K. H., and Viskanta, R., 1999, "Comparison of the Diffusion Approximation and the Discrete Ordinates Method for the Investigation of Heat Transfer in Glass," Glass Sci. Technol., (Offenbach, Ger.), **72**, pp. 254-265.
- [4] Hollands, K. G. T., 2010, "The Simplified-Fredholm Integral Equation Solver and Its Use in Thermal Radiation," ASME J. Heat Transfer, **132**, p. 023401.
- [5] Feldheim, V., and Lybaert, P., 2004, "Solution of Radiative Heat Transfer Problem With the Discrete Transfer Method Applied to Triangular Meshes," J. Comput. Appl. Math., **168**, pp. 179-190.
- [6] Asllanaj, F., Feldheim, V., and Lybaert, P., 2007, "Solution of Radiative Heat Transfer in 2-D Geometries by a Modified Finite-Volume Method Based on a Cell Vertex Scheme Using Unstructured Triangular Meshes," Numer. Heat Transfer, Part B, **51**, pp. 97-119.
- [7] Asllanaj, F., Parent, G., and Jeandel, G., 2007, "Transient Radiation and Conduction Heat Transfer in a Gray Absorbing-Emitting Medium Applied on Two-Dimensional Complex-Shaped Domains," Numer. Heat Transfer, Part B, **52**, pp. 179-200.
- [8] Ravishankar, M., Mazumder, S., and Kumar, A., 2010, "Finite-Volume Formulation and Solution of the P_3 Equations of Radiative Transfer on Unstructured Meshes," ASME J. Heat Transfer, **132**, p. 023402.
- [9] Dez, V. L., Vaillon, R., Lemonnier, D., and Lallemand, M., 2000, "Conductive-Radiative Coupling in an Absorbing-Emitting Axisymmetric Medium," J. Quant. Spectrosc. Radiat. Transf., **65**, pp. 787-803.
- [10] Furmanski, P., and Banaszek, J., 2004, "Finite Element Analysis of Concurrent Radiation and Conduction in Participating Media," J. Quant. Spectrosc. Radiat. Transf., **84**, pp. 563-573.
- [11] Widmer, G., 2010, "An Efficient Sparse Finite Element Solver for the Radiative Transfer Equation," ASME J. Heat Transfer, **132**, p. 023403.
- [12] Becker, R., Koch, R., Bauer, H.-J., and Modest, M. F., 2010, "A Finite Element Treatment of the Angular Dependency of the Even-Parity Equation of Radiative Transfer," ASME J. Heat Transfer, **132**, p. 023404.
- [13] Hitti, G. E., Nemer, M., and Khoury, K. E., 2010, "Transient Radiation and Conduction Heat Transfer in Glass Sheets by the Thin Layer Approximation," ASME J. Heat Transfer, **132**, p. 023506.
- [14] Altaç, Z., and Tekkalmaz, M., 2008, "Benchmark Solution of Radiative Transfer Equation for Three-Dimensional Rectangular Homogeneous Media," J. Quant. Spectrosc. Radiat. Transf., **109**, pp. 587-607.
- [15] Mishra, S. C., Lankadasu, A., and Beronov, K. N., 2005, "Application of the Lattice Boltzmann Method for Solving the Energy Equation of a 2-D Transient

- Conduction-Radiation Problem." *Int. J. Heat Mass Transfer*, **48**, pp. 3648–3659.
- [16] Mishra, S. C., Talukdar, P., Trimis, D., and Durst, F., 2005, "Two-Dimensional Transient Conduction and Radiation Heat Transfer With Temperature Dependent Thermal Conductivity," *Int. Commun. Heat Mass Transfer*, **32**, pp. 305–314.
- [17] Mishra, S. C., and Roy, H. K., 2007, "Solving Transient Conduction and Radiation Heat Transfer Problems Using the Lattice Boltzmann Method and the Finite Volume Method," *J. Comput. Phys.*, **223**, pp. 89–107.
- [18] Rouse, D. R., Gautier, G., and Sacadura, J. F., 2000, "Numerical Prediction of Two-Dimensional Conduction, Convection, and Radiation Heat Transfer I. Formulation," *Int. J. Therm. Sci.*, **39**, pp. 315–331.
- [19] Rouse, D. R., Gautier, G., and Sacadura, J. F., 2000, "Numerical Prediction of Two-Dimensional Conduction, Convection, and Radiation Heat Transfer. II. Validation," *Int. J. Therm. Sci.*, **39**, pp. 332–353.
- [20] Ben Salah, M., Askri, F., Rouse, D. R., and Ben Nasrallah, S., 2005, "Control Volume Finite Element Method for Radiation," *J. Quant. Spectrosc. Radiat. Transf.*, **92**, pp. 9–30.
- [21] Grissa, H., Askri, F., Ben Salah, M., and Ben Nasrallah, S., 2007, "Three-Dimensional Radiative Transfer Modeling Using the Control Volume Finite Element Method," *J. Quant. Spectrosc. Radiat. Transf.*, **105**, pp. 388–404.
- [22] Kim, T. Y., and Baek, S. W., 1991, "Analysis of Combined Conductive and Radiative Heat Transfer in a Two-Dimensional Rectangular Enclosure Using the Discrete Ordinates Method," *Int. J. Heat Mass Transfer*, **34**(9), pp. 2265–2273.
- [23] Sakami, M., Charette, A., and Dez, V. L., 1996, "Application of the Discrete Ordinates Method to Combined Conductive and Radiative Heat Transfer in a 2-D Complex Geometry," *J. Quant. Spectrosc. Radiat. Transf.*, **56**(4), pp. 517–533.
- [24] Vaillon, R., Lallemand, M., and Lemonnier, D., 1996, "Radiative Heat Transfer in Orthogonal Curvilinear Coordinates Using the Discrete Ordinate Method," *J. Quant. Spectrosc. Radiat. Transf.*, **55**(1), pp. 7–17.
- [25] Liu, L.-H., and Tan, H.-P., 2001, "Transient Radiation and Conduction in a Two Dimensional Participating Cylinder Subjected to a Pulse Irradiation," *Int. J. Therm. Sci.*, **40**, pp. 877–889.
- [26] Cheong, K. B., and Song, T. H., 1997, "An Alternative Discrete Ordinates Method With Interpolation and Source Differencing for Two-Dimensional Radiative Transfer Problem," *Numer. Heat Transfer, Part B*, **32**, pp. 107–125.
- [27] Cha, H., and Song, T. H., 2000, "Discrete Ordinates Interpolation Method Applied to Irregular Three-Dimensional Geometries," *ASME J. Heat Transfer*, **122**, pp. 823–827.
- [28] Kim, K., Lee, E., and Song, T. H., 2008, "Discrete Ordinates Interpolation Method for Radiative Heat Transfer Problem in Three-Dimensional Enclosures Filled With Non-Gray or Scattering Medium," *J. Quant. Spectrosc. Radiat. Transf.*, **109**, pp. 2579–2589.
- [29] Lee, K. H., and Viskanta, R., 2001, "Two-Dimensional Combined Conduction and Radiation Heat Transfer: Comparison of the Discrete Ordinate Method and the Diffusion Approximation," *Numer. Heat Transfer, Part A*, **39**, pp. 205–225.
- [30] Tan, H.-P., 1988, "Transfert Couplé Rayonnement-Conduction Instationnaire Dans Les Milieux Semi-Transparents à Frontières Opaques ou Naturelles Soumis à des Conditions de Température et de Flux," Ph.D. thesis, Université de Poitiers, France.
- [31] Tan, H.-P., Ruan, L.-M., Xia, X.-L., Yu, Q.-Z., and Tong, T.-W., 1999, "Transient Coupled Radiative and Conductive Heat Transfer in an Absorbing, Emitting and Scattering Medium," *Int. J. Heat Mass Transfer*, **42**, pp. 2967–2980.
- [32] Luo, J.-F., Tan, H.-P., Ruan, L.-M., and Tong, T. W., 2003, "Refractive Index Effects on Heat Transfer in Multilayer Scattering Composite," *J. Thermophys. Heat Transfer*, **17**(3), pp. 407–419.
- [33] Luo, J.-F., Chang, S.-L., Yang, J.-K., and Yang, J.-C., 2009, "Conduction and Radiation in a Rectangular Isotropic Scattering Medium With Black Surfaces by the RTNAM," *Int. J. Heat Mass Transfer*, **52**, pp. 5064–5071.
- [34] Siegel, R., 1993, "Variable Refractive Index Effects on Radiation in Semitransparent Scattering Multilayered Regions," *J. Thermophys. Heat Transfer*, **7**(4), pp. 624–630.
- [35] Luo, J.-F., and Shen, X., 2009, "Numerical Method of the Ray Tracing-Node Analysing Method for Solving 2-D Coupled Heat Transfer in a Rectangular Medium," *Numer. Heat Transfer, Part A*, **55**, pp. 465–486.

Thermohydraulic Study of a Flat Plate Heat Pipe by Means of Confocal Microscopy: Application to a 2D Capillary Structure

Stéphane Lips

e-mail: stephane.lips@insa-lyon.fr

Frédéric Lefèvre

e-mail: frederic.lefevre@insa-lyon.fr

Jocelyn Bonjour

e-mail: jocelyn.bonjour@insa-lyon.fr

Université de Lyon, CNRS,
INSA-Lyon, CETHIL, UMR 5008,
F-69621, Villeurbanne, France,
Université Lyon 1, F-69622, France

Thermal and hydrodynamic experimental results of a flat plate heat pipe (FPHP) are presented. The capillary structure is made of crossed grooves machined in a copper plate. The shape of the liquid-vapor interface in this type of capillary structure—that can also be viewed as an array of posts—is studied theoretically and experimentally. A confocal microscope is used to visualize the liquid-vapor interface and thus the capillary pressure field in the system. These hydrodynamic measurements, coupled to temperature measurements on the FPHP wall, are used to estimate the permeability and the equivalent thermal conductivity of the capillary structure filled with methanol or FC72. These parameters are obtained from a comparison between the experimental data and an analytical model. Finally, the model is used to compare the draining capability of crossed grooves with that of longitudinal grooves. [DOI: 10.1115/1.4001930]

Keywords: flat plate heat pipe, crossed grooves, 2D capillary structure, confocal microscopy, meniscus

1 Introduction

Thermal management of high heat flux devices is an important issue for a number of industrial applications. For instance, local hot spots in electronic components can reduce their life time and thus high efficiency cooling systems are required. Flat plate heat pipes (FPHPs) are passive devices that are able to transfer high heat fluxes with small temperature gradients. They are particularly adapted for the cooling of electronic components [1] and are increasingly used in notebook PCs [2]. They can also be used in others applications such as the cooling of fuel cells [3,4].

Thermal and hydrodynamic performance of FPHP depend on the system geometry and, particularly, on the capillary structure geometry. The most studied capillary structures are made of longitudinal grooves. In this configuration, the liquid flow is 1D and, thus, heat sources and heat sinks have to be well located otherwise some grooves cannot be useful. Few papers deal with capillary structures made of crossed grooves. However, crossed grooves are well adapted to electronic cooling because electronic components can be located anywhere on the system due 2D liquid flows inside the capillary structure.

Shen et al. [5] tested a silicon FPHP with crossed grooves machined with a diamond saw. Their width and depth are both equal to 75 μm . Benson et al. [6] studied a FPHP with crossed grooves of same dimensions and a wick structure made of crosses realized by deep plasma etching technique. Gromoll [7] realized a FPHP with an original capillary structure that consists of pyramids with a height of 320 μm . Avenas et al. [8] machined a FPHP with crossed grooves by plasma etching. Grooves are 80 μm wide and 100 μm deep. Ivanova et al. [9] tested a circular FPHP where the capillary structure is made of radial grooves connected in the center by small hexagonal posts.

FPHP tested in Refs. [5–9] are made of silicon. These studies are limited to temperature measurements, obtained by IR ther-

mography [8,9] or by local temperature measurements under heat sink and heat source [5–7]. Lefèvre et al. [10] tested a silicon capillary structure similar to that of Ivanova et al. [9]. Radial grooves are connected in the center of the FPHP by small square posts. They measured both the temperature field from the center to the periphery of the FPHP by means of nine thermocouples and the meniscus curvature radii in the grooves by means of confocal microscopy. The confocal microscope was not useful to visualize the crossed grooves in the center because the pins were too small. This experimental technique was already used in Refs. [3,4] to validate hydrodynamic and thermal models of FPHP made of longitudinal grooves or to understand the effects of the filling ratio and the vapor space height on the performance of a FPHP [11].

Numerical models for longitudinal grooves are based on Young–Laplace law and on the balance equations [3,4,9,12–14]. A similar approach is not possible for 2D capillary structure because the liquid-vapor interface has a 3D shape. Thus, numerical models of this type of capillary structure are based on Darcy's law and on the balance equations. Huang and Liu [15] and Qin and Liu [16] developed an analytical model based on the Darcy's law to calculate both the pressure and the velocity fields in the capillary structure of a FPHP with several heat sources and heat sinks. Zhu and Vafai [17] and Zuo and North [18] presented numerical models based on the same laws. In 2006, Lefèvre and Lallemand [19] improved the analytical model of Qin and Liu [16] by taking into account the 2D vapor flow inside the FPHP and the 3D temperature field in the wall. The capillary structure is assumed to be a porous medium, whose characteristics are the permeability and the equivalent thermal conductivity. This model has been validated in 2008 by Revellin et al. [20] with the experimental results of a FPHP with longitudinal grooves tested by Rullière et al. [3]. Nevertheless, the experimental results presented in literature are not sufficient to validate this model in 2D conditions.

In this paper, we present an experimental study of a copper FPHP with a capillary structure made of crossed grooves. The shape of the liquid-vapor interface is theoretically studied and measured by confocal microscopy. Thermocouples are located on

Contributed by the Heat Transfer Division of ASME for publication in the JOURNAL OF HEAT TRANSFER. Manuscript received December 10, 2009; final manuscript received April 28, 2010; published online August 13, 2010. Assoc. Editor: Louis C. Chow.

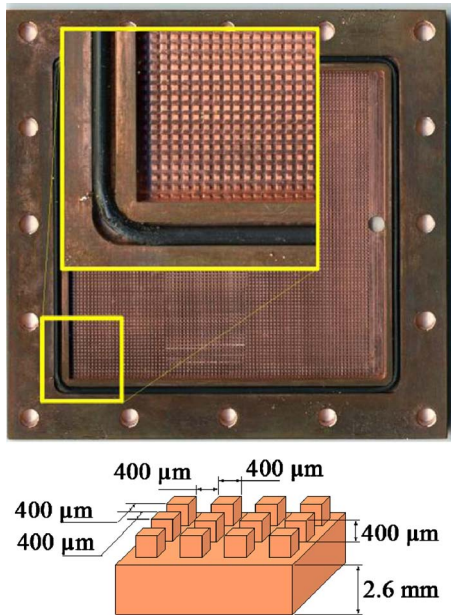


Fig. 1 Schematic of the capillary structure

the surface to measure the 2D temperature field. The experimental results are compared with the analytical model of Lefèvre and Lallemand [19].

2 Experimental Set-Up

The experimental set-up is based on an experimental test bench already presented in previous papers [3,10,11,21]. The FPHP is realized by sealing a transparent plate on the capillary structure to allow confocal microscopy measurements. The capillary structure, of dimensions $72 \times 68 \text{ mm}^2$, is shown in Fig. 1. It is made of 85×90 crossed microgrooves, machined in a copper plate. Each groove has a square cross-section ($400 \times 400 \mu\text{m}^2$). The distance between two grooves is equal to $400 \mu\text{m}$. The wall thickness under the grooves is equal to 2.6 mm .

The vapor space thickness h_v is equal to 1.6 mm . A filling copper pipe closed by a valve is sealed on the copper plate at the level of the condenser. The heat source is located on the copper wall. It is a thick resistor film of dimensions $20 \times 20 \text{ mm}^2$ supplied by a dc power supply. Its resistance is approximately equal to 0.2Ω . Electric power is obtained by measuring the voltage drop across the heating resistor and the current by means of a calibrated resistance. Thus, the uncertainty due to the power measurement is negligible. The heat sink is a water heat exchanger of dimensions $15 \times 72 \text{ mm}^2$. The water flow rate is constant and the inlet temperature is controlled by means of a thermostatic bath. Two series of nine calibrated thermistors (uncertainty lower than 0.2 K) are located along the FPHP wall. They are fixed with silver lacquer in small grooves that were machined in the wall in order to reduce the contact resistance (Fig. 2). The value of their resistance is recorded by a Keithley 2700 multimeter.

The FPHP is thermally insulated during thermal tests. Before thermal tests, the FPHP has to be degassed and filled. In order to promote surface wetting, the copper plate is first cleaned. The FPHP and the working fluid are degassed carefully to eliminate the noncondensable gases. The method of evacuating the noncondensable gases from the working fluid is based on the fluid solidification under vacuum. The fluid contained in a heated vessel vaporizes, releases noncondensable gases and solidifies in a second vessel dipped into liquid nitrogen. The noncondensable gases are evacuated by vacuum pumps. The FPHP is degassed by heating during vacuum pumping at 10^{-5} mbar .

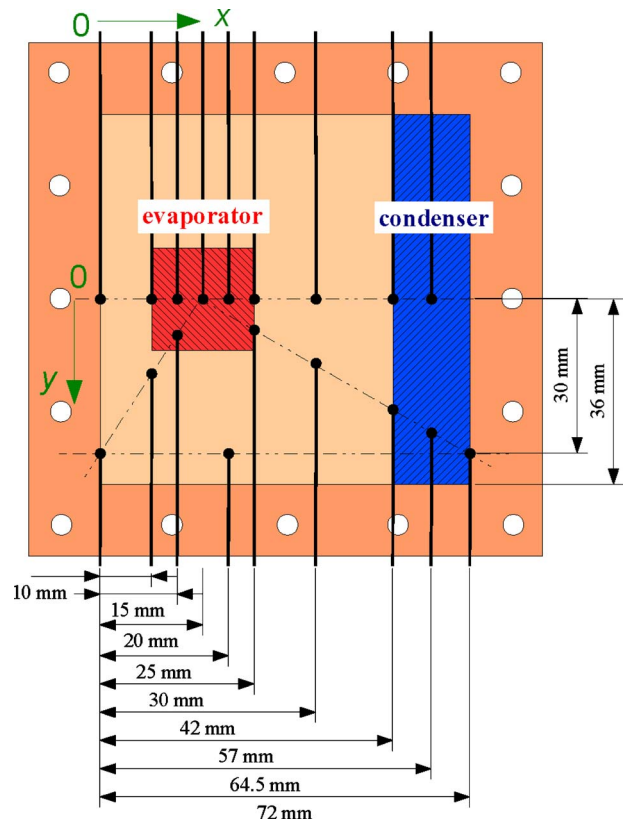


Fig. 2 Thermistor location on the copper plate

A confocal microscope is used to measure the meniscus curvature radius in the grooves, the FPHP being in horizontal orientation. The confocal microscope is a STIL Micromesure 2 system. The optical sensor has a nominal measuring range of $350 \mu\text{m}$. The working distance is about 13 mm . The maximum measuring angle for specular reflection is equal to 27.4 deg . The optical sensor velocity is about 1 mm s^{-1} , which is fast enough for not thermally disturbing the measurement. More details about the use of confocal microscopy for the study of FPHP are available in Refs. [3,10,11,21].

3 Shape of the Liquid-Vapor Interface in Crossed Grooves

The shape of the liquid-vapor interface has a huge impact on the thermal and hydrodynamic performance of FPHP. Indeed, the cross-section of the liquid channel and the capillary pressure in each point of the system depend on this shape. The thermal resistance of the FPHP is also directly linked to the liquid film thickness in the capillary structure. In longitudinal grooves, the shape of the liquid-vapor interface can be considered as locally cylindrical. This is not the case in crossed grooves and a specific study is required to determine the properties of the menisci in this configuration. In this section, a theoretical analysis of the shape of the liquid-vapor interface in crossed grooves is presented.

3.1 Liquid-Vapor Interface Modeling: Theoretical Value of the Maximum Capillary Pressure. The vapor and liquid pressures (respectively, P_v and P_l) are linked to the surface curvature H by the Young-Laplace equation.

$$P_{\text{cap}} = P_v - P_l = 2\sigma H \quad (1)$$

where P_{cap} is the capillary pressure and σ is the surface tension of the fluid.

The maximum capillary pressure that a capillary structure can sustain depends on the maximum curvature of the liquid-vapor

interface. It is an important parameter for FPHP operation because it is linked to the maximum heat flux that the system can transfer before the evaporator dries out. In longitudinal grooves, the liquid-vapor interface can be determined by only one curvature radius. Assuming that the cross-section of the interface is a circle, the maximum interface curvature is given by simple geometric considerations.

$$H_{\max} = \frac{\cos \theta}{l_g} \quad (2)$$

$$H = \frac{\left[1 + \left(\frac{\partial z}{\partial y}\right)^2\right] \left(\frac{\partial^2 z}{\partial x^2}\right) - 2 \left(\frac{\partial z}{\partial x}\right) \left(\frac{\partial z}{\partial y}\right) \left(\frac{\partial^2 z}{\partial x \partial y}\right) + \left[1 + \left(\frac{\partial z}{\partial x}\right)^2\right] \left(\frac{\partial^2 z}{\partial y^2}\right)}{2 \left[1 + \left(\frac{\partial z}{\partial x}\right)^2 + \left(\frac{\partial z}{\partial y}\right)^2\right]^{3/2}} \quad (3)$$

where x and y are the coordinates in the plane of the capillary structure (Fig. 2). H depends on the amount of liquid in the grooves. It can be either positive or negative. In this last case, the volume of liquid is greater than that of the grooves.

Equation (3) can be rewritten as

$$2HA_1 = A_2 \left(\frac{\partial^2 z}{\partial x^2}\right) + A_3 + A_4 \left(\frac{\partial^2 z}{\partial y^2}\right) \quad (4)$$

with $A_1 = [1 + (\partial z / \partial x)^2 + (\partial z / \partial y)^2]^{3/2}$, $A_2 = 1 + (\partial z / \partial y)^2$, $A_3 = -2(\partial z / \partial x)(\partial z / \partial y)(\partial^2 z / \partial x \partial y)$, and $A_4 = 1 + (\partial z / \partial x)^2$.

The surface is calculated using a rectangular mesh with a variable step-size discretization (Fig. 3). Using the finite-difference method and notations defined in Fig. 3, it is possible to express the coordinate $z_{i,j}$ of a point as a function of its neighbors for a given surface curvature H .

$$z_{i,j} = \frac{A_2 \left(\frac{z_{i+1,j} + z_{i-1,j}}{\Delta x_{i+1/2} \Delta x_{i-1/2}}\right) + A_3 + A_4 \left(\frac{z_{i,j+1} + z_{i,j-1}}{\Delta y_{j+1/2} \Delta y_{j-1/2}}\right) - 2HA_1}{\left(\frac{2A_2}{\Delta x_{i+1/2} \Delta x_{i-1/2}} + \frac{2A_4}{\Delta y_{j+1/2} \Delta y_{j-1/2}}\right)} \quad (5)$$

The central finite-difference scheme is used to calculate the derivatives in parameters A_1 – A_4 .

We consider symmetric boundary conditions at the symmetry axis of the capillary structure. At the junction between the wall and the meniscus, the boundary condition depends on the angle α between the meniscus and the vertical wall (x - z or y - z plane). For low H , the meniscus is hung to the top of the posts and α can be

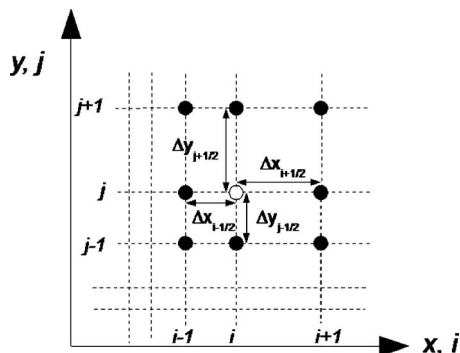


Fig. 3 Scheme of the variable step-size

where θ is the liquid-wall contact angle and l_g is the groove width.

For crossed grooves, the calculation of the maximum interface curvature is not simple because the shape of the interface is 3D. Thus, a model of the liquid-vapor interface has to be developed in this configuration.

The liquid is assumed to be in equilibrium with the vapor and motionless. Gravitational forces are neglected. Thus, the shape of the liquid-vapor interface is only due to capillary forces. In these conditions, the surface curvature is constant and can be expressed in cartesian coordinates as

different from the liquid-wall contact angle θ . For high values of H , this condition is not verified on all the edge and a part of the meniscus moves locally downward the vertical wall. For this part of the meniscus, α is supposed to be equal to θ . When α is equal to θ all over the liquid-wall junction, the maximum value of the curvature H_{\max} is reached, which corresponds to the maximum capillary pressure.

As Eq. (5) is not linear, an iterative method is used. The interface is supposed to be plain initially. At each step, the new coordinates of the surface are calculated and boundary conditions on the edge are modified by calculating the new value of α , which depends on the surface shape calculated with Eq. (5).

$$|\cos \alpha| = \frac{\left|\frac{\partial z}{\partial y}\right|}{\sqrt{1 + \left(\frac{\partial z}{\partial x}\right)^2 + \left(\frac{\partial z}{\partial y}\right)^2}} \quad (6)$$

Iterations are stopped when the maximum relative difference between the desired and calculated surface curvature is lower than 10^{-3} .

Figure 4 presents the calculated shape for the capillary structure presented in Sec. 2 and for two surface curvatures $H=1700 \text{ m}^{-1}$ and $H=2000 \text{ m}^{-1}$. The contact angle θ is equal to 30 deg. The liquid-vapor interface has a saddle shape. Case (a) corresponds to the maximal surface curvature for which the meniscus remains attached to the edge of the posts. Case (b) corresponds to the surface curvature H_{\max} for which the capillary pressure is maximum. In that case, the meniscus is attached to the top of the posts at a single point located in the middle of the edge. The difference of capillary pressure between case (a) and case (b) is equal to 15%, which is not negligible.

For a given capillary structure, the maximum surface curvature depends on the liquid wall contact angle. Figure 5 presents the maximum surface curvature as a function of θ for crossed grooves and longitudinal grooves of same cross-section. The maximum surface curvatures are very close whatever the contact angle. As a result, we can conclude that the maximum capillary pressure in crossed grooves is similar to that in longitudinal grooves.

3.2 Experimental Visualization. Confocal microscopy is used to measure the liquid-vapor interface in the capillary structure (Fig. 6). The top of the pins is not homogeneous because of the copper roughness. The liquid-vapor interface is smoother and has a saddle shape, very close to that simulated numerically.

As the measure of the confocal microscope is punctual, the surface measurement is obtained by moving the FPHP with a

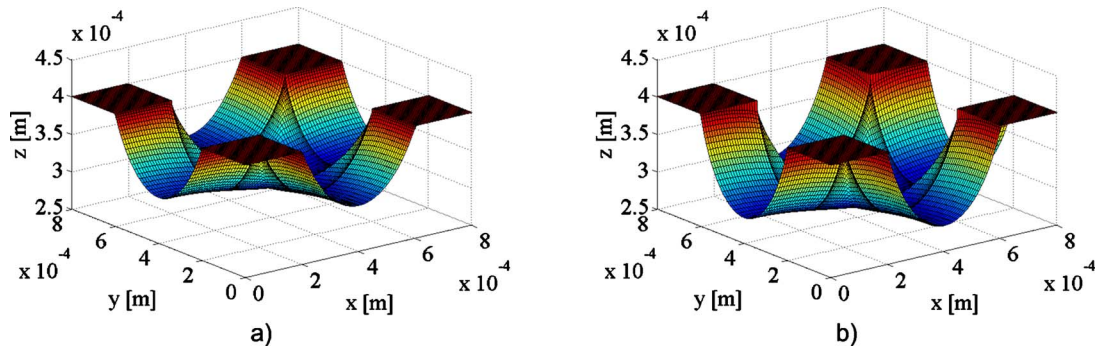


Fig. 4 Shape of the liquid-vapor interface: (a) $H=1700 \text{ m}^{-1}$ and (b) $H=2000 \text{ m}^{-1}$

motorized table in x and y directions. The acquisition time depends on the size of the surface to be scanned and on the spatial sampling interval. In the example of Fig. 6, a surface of $1 \times 1 \text{ mm}^2$ is observed with a sampling interval of $10 \mu\text{m}$ while the FPHP is in nonworking conditions. The acquisition time for this measurement is about one minute but for the entire surface of the FPHP, the measurement would last 12 days. Thus, in working conditions, it is necessary to increase the sampling interval and to scan only a part of the FPHP. The measurement is easier in longitudinal grooves because it is not necessary to measure a surface but only a profile of the meniscus perpendicularly to the grooves. Once the meniscus is measured, it has to be analyzed to calculate the curvature all over the FPHP. In longitudinal grooves, the curvature is obtained by fitting a circle in a profile measurement. Here, the analysis is more complicated.

The most intuitive method is to identify the curvature of the interface by means of the numerical model (Eq. (5)). However, this method is not applicable in our configuration because the shape of the posts is not regular due to the milling technique (Fig. 7). As the shape of the liquid-vapor interface is strongly dependant on the shape of the posts, the identification of the surface curvature by means of the numerical model is not possible. This method would be useful in the case of a very regular capillary

structure such as those machined in silicon [10].

In this study, the surface curvature is calculated at each point using Eq. (3) with finite-difference approximation. As this equation is very sensitive to the measurement noise, the value of the curvature is averaged on an area of $240 \times 240 \mu\text{m}^2$ where the grooves intersect. A sampling interval of $30 \mu\text{m}$ has been chosen, which leads to reasonable acquisition time and measurement uncertainties.

3.3 Validation of the Experimental Method. In order to validate the experimental method, the measurements have been made in nonworking conditions while the FPHP was tilted. In such conditions, the evolution of the capillary pressure is theoretically equal to the evolution of the hydrostatic pressure in the liquid.

$$\frac{dP_{\text{cap}}}{dx} = \rho_l g \sin(\beta - \beta') \quad (7)$$

where β is the angle between the FPHP and the horizontal and β' is a correction of β . Indeed, as the menisci in the upper part of the system are deeper than those in the lower part, the angle β' between the line formed by the bottom of the menisci in the grooves and the line formed by the top of the posts has to be taken into account (Fig. 8). Figure 9 presents the evolution of the capillary pressure measured for the FPHP filled with methanol and with FC72 with an inclination angle with respect to the horizontal β equal to 5 deg and 2.5 deg, respectively. The uncertainty on the angle is equal to 0.1 deg. β' is equal to 0.09 ± 0.02 deg for methanol and to 0.25 ± 0.02 deg for FC72. In Fig. 9, solid lines are the theoretical evolution of the capillary pressure. A good agreement is observed between experimental and theoretical results, which validates our experimental method. The accuracy of the method is evaluated to be of the order of 1 Pa.

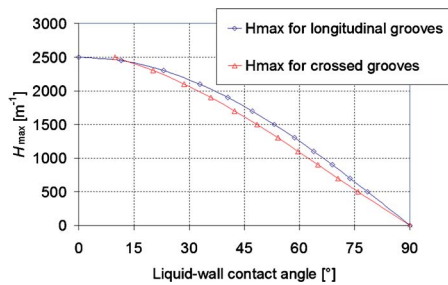


Fig. 5 Maximum surface curvature in crossed grooves and longitudinal grooves

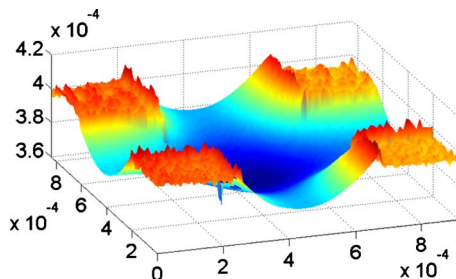


Fig. 6 Experimental visualization of the liquid vapor-interface in crossed grooves (dimensions in m)

4 Experimental Results and Comparison With an Analytical Model

4.1 Determination of the Optimum Filling Ratio. The optimum amount of liquid in the system is determined experimentally.

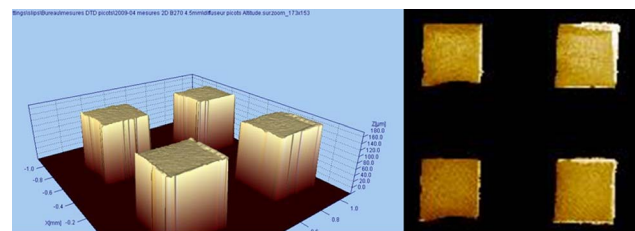


Fig. 7 Visualization of the shape of the posts by confocal microscopy

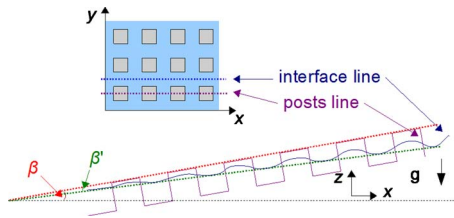


Fig. 8 Correction of the inclination angle of the FPHP

The flat heat pipe is tested in horizontal orientation with a heat flux q equal to 6 W cm^{-2} at the heat source and a cold source temperature T_{cond} fixed to 40°C . Methanol is used as working fluid. Figure 10 presents the temperature field in the FPHP for different filling ratios f_r (i.e., the ratio between the liquid volume and the internal volume of the FPHP). The temperature fields were reconstructed from linear interpolations between the local temperature measurements given by the thermistors, whose location is recalled on Fig. 10 by black dots.

Figure 11 presents the evolution of the thermal resistance R_{th} versus the filling ratio. The thermal resistance is the ratio between the maximum temperature difference measured in the FPHP and the heat input: $R_{\text{th}} = (T_{\text{max}} - T_{\text{min}}) / Q$. The best thermal performance is observed for f_r in the range of 8–13%, which correspond to liquid volumes between 60% and 100% of the total volume of the grooves. For a filling ratio lower than 8%, R_{th} increases abruptly. On the contrary, the increase in R_{th} with f_r is relatively smooth at

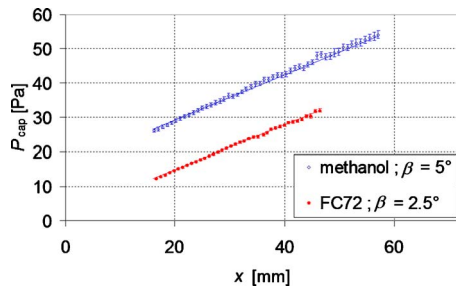


Fig. 9 Comparison between experimental and theoretical results

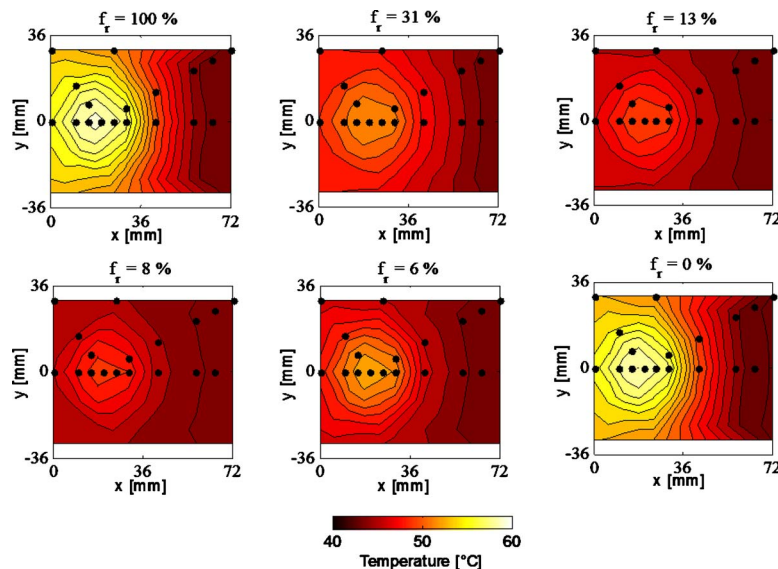


Fig. 10 Temperature measurements in the FPHP for different filling ratio ($q = 6 \text{ W cm}^{-2}$; $T_{\text{cond}} = 40^\circ\text{C}$)

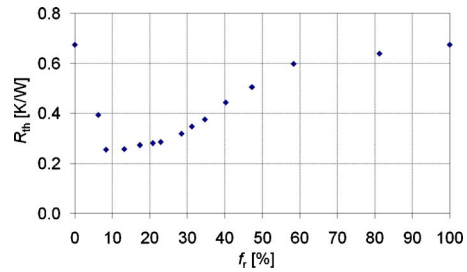


Fig. 11 Thermal resistance of the FPHP ($q = 6 \text{ W cm}^{-2}$; $T_{\text{cond}} = 40^\circ\text{C}$)

least between $f_r = 13\%$ and $f_r = 20\%$. A filling ratio of 12% is chosen to characterize the performance of the FPHP in the next sections.

4.2 Temperature and Meniscus Curvature Measurements.

The temperature field in the FPHP wall has been recorded for different heat fluxes and for two working fluids (FC72 and methanol). The thermostatic bath temperature is constant and equal to 40°C for measurements with methanol and 30°C for measurements with FC72. The estimated 2D temperature fields obtained by interpolation between thermistor measurements are presented in Fig. 12 for methanol and in Fig. 13 for FC72. Isotherms are plotted every 1°C . For methanol, the thermal resistances of the FPHP are equal to 0.35 K/W and 0.36 K/W for $q = 2 \text{ W/cm}^2$ and $q = 4 \text{ W/cm}^2$, respectively. For FC72, their values reach 0.61 K/W and 0.56 K/W , respectively, in the same conditions.

The capillary pressure field in the FPHP has been measured by confocal microscopy in the same experimental conditions. For methanol, the capillary pressure variation is about 2 Pa between the heat source and the heat sink for a heat flux of 4 W/cm^2 . This variation is similar in magnitude to the experimental noise (about 1 Pa). This small variation is due to the low mass flow in the grooves. Experimentally, it is not possible to perform measurements at heat fluxes higher than 4 W/cm^2 : Indeed, beyond this heat flux, nucleate boiling develops in the evaporator. This phenomenon was already observed and described in a previous article [22] dedicated to the study of a capillary structure made of longitudinal grooves. It has to be noticed that the FPHP still works with higher heat fluxes but bubbles prevent observations, which are the

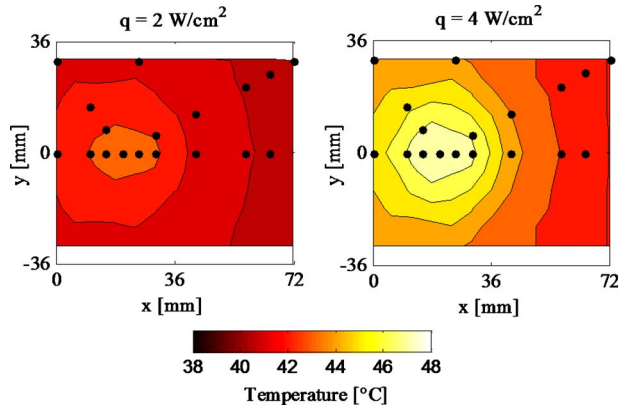


Fig. 12 Temperature field in the FPHP (methanol: $f_r=12\%$ and $T_{\text{cond}}=40^\circ\text{C}$)

goal of the present article.

FC72 has been chosen as working fluid in order to increase the measurement sensibility in spite of its low thermal performance. Indeed FC72 has a smaller latent heat of vaporization and a smaller surface tension than methanol. As a result, for a given heat flux, the liquid flow in the grooves is higher with FC72 than with methanol. Moreover, for a given capillary pressure variation, the meniscus curvature variation is higher, which increases the measurement accuracy. Figure 14 presents the evolution of the capillary pressure in the middle of the FPHP ($y=0$ mm) for different heat fluxes. It has to be noticed that the capillary pressure is not constant for a heat flux of 0 W. This indicates that the FPHP is slightly inclined ($\beta=0.08$ deg). In the next section, this inclination angle is taken into account.

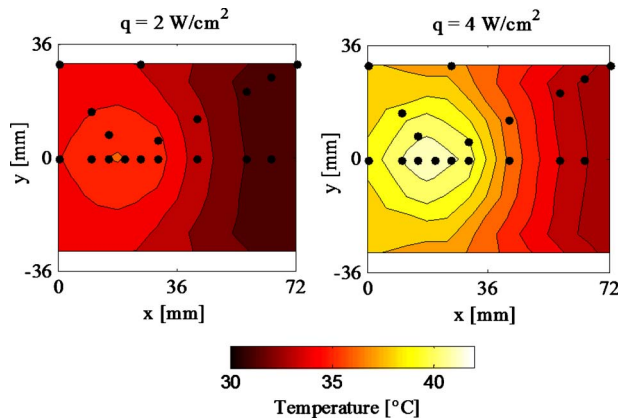


Fig. 13 Temperature field in the FPHP (FC72: $f_r=12\%$ and $T_{\text{cond}}=40^\circ\text{C}$)

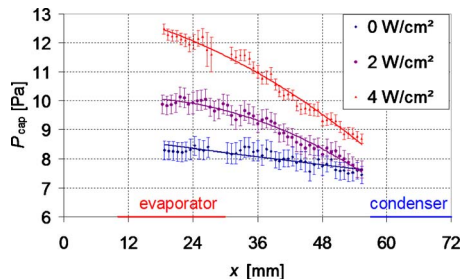


Fig. 14 Capillary pressure for the FPHP filled with FC72

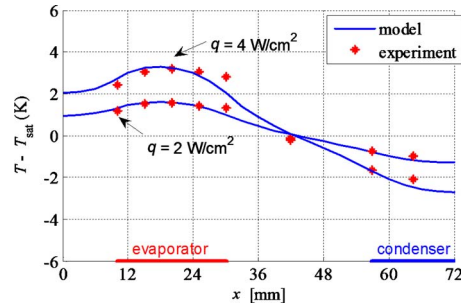


Fig. 15 Measured and calculated temperatures along line $y=0$ mm (methanol)

4.3 Comparison With an Analytical Model

4.3.1 Model Equations. The experimental results are compared with the analytical model developed by Lefèvre and Lallemand [19]. This model couples a 3D thermal model of the FPHP wall with a 2D hydrodynamic model of the liquid and vapor flows inside the FPHP.

The temperature field in the wall can be expressed by Fourier's series.

$$T - T_{\text{sat}} = \sum_{m=1}^{\infty} B_{m0}(z) \cos(m\pi x) + \sum_{n=1}^{\infty} B_{0n}(z) \cos(n\pi y) + \sum_{m=1}^{\infty} \sum_{n=1}^{\infty} B_{mn}(z) \cos(m\pi x) \cos(n\pi y) \quad (8)$$

where T_{sat} is the saturation temperature. B_{m0} , B_{0n} , and B_{mn} depend on the location and on the heat transfer rate of the heat sources. The equivalent conductivity of the capillary structure is introduced in order to take into account phase change by evaporation or condensation.

Once the temperature field is calculated, it is possible to calculate the evaporation and condensation mass flow rates at each point of the system. A 2D hydrodynamic model, based on Darcy's law and on mass balances, is used to calculate the liquid and vapor velocities in the capillary structure and in the vapor channel, and the liquid and vapor pressure fields in the system. For the liquid, the pressure field is obtained by Fourier's series.

$$P_l = \frac{\mu_l}{Kh_{lv}\rho_l h_g} \sum_{m=1}^{\infty} C_{m0} \cos(m\pi x) + \sum_{n=1}^{\infty} C_{0n} \cos(n\pi y) + \sum_{m=1}^{\infty} \sum_{n=1}^{\infty} C_{mn} \cos(n\pi y) \quad (9)$$

where K is the permeability of the capillary structure, μ_l is the dynamic viscosity, and h_{lv} is the latent heat of vaporization of the liquid. C_{m0} , C_{0n} , and C_{mn} are calculated from the thermal model. The boundary conditions are a zero velocity at the extremities of the FPHP in x and y directions. A similar expression can be obtained for the vapor flow. More details about the model are given in Refs. [19,20].

4.3.2 Comparison of the Experimental Results With the Thermal Model. For longitudinal grooves, mathematical expressions can be found to calculate the equivalent conductivity of the capillary structure [20,23]. For crossed grooves, such expressions are not available in literature. Thus, this parameter is fitted by comparison between the experimental results and the model. In order to limit boundary effects, thermistors located at the edge of the FPHP are not taken into account. Figures 15 and 16 present the comparison of the measured and modeled temperature profiles along the line $y=0$ mm for different heat fluxes and for both

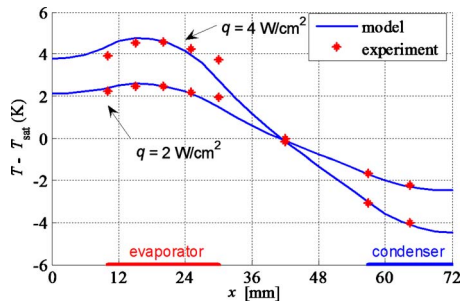


Fig. 16 Measured and calculated temperatures along line $y=0$ mm (FC72)

working fluids (the saturation temperature is determined by comparison with numerical results). The equivalent conductivity is equal to 1.19 W/m K and 1.08 W/m K with methanol for heat fluxes equal to 2 W/cm² and 4 W/cm², respectively. With FC72, the equivalent conductivity is equal to 0.16 W/m K and 0.26 W/m K in the same conditions. The thermal performance obtained with methanol is better than that obtained with FC72, which is mainly due to the low latent heat of vaporization and the low thermal conductivity of FC72.

4.3.3 Comparison of the Experimental Results With the Hydrodynamic Model. Once the temperature field is calculated, it is used to calculate the mass flow rate of evaporation and condensation at each point of the FPHP and, thus, the velocity and pressure fields in the vapor and liquid channels. As for the equivalent thermal conductivity, no expression is available in literature to calculate the permeability of crossed grooves. Nevertheless, such an expression can be found for longitudinal grooves [23].

$$K_{\text{longitudinal grooves}} = \frac{D_h^2 \varphi}{2f\text{Re}_l} \quad (10)$$

where φ is the porosity of the capillary structure, $D_h = 4l_g h_g / (2h_g + l_g)$ is the hydraulic diameter of the grooves, and $f\text{Re}_l$ is the product of the friction factor by the Reynolds number, which is also called the Poiseuille number. It can be calculated with the Shah and London correlation [23].

$$f\text{Re}_l = 24(1 - 1.3553c_{\min} + 1.9467c_{\min}^2 - 1.7012c_{\min}^3 + 0.9564c_{\min}^4 - 0.2537c_{\min}^5) \quad (11)$$

with $c_{\min} = \min(2h_g/l_g, l_g/2h_g)$.

Let us introduce the nondimensional permeability K^* , which is the ratio between the permeability of crossed grooves and the permeability of longitudinal grooves of same dimensions.

$$K^* = \frac{K_{\text{crossed grooves}}}{K_{\text{longitudinal grooves}}} \quad (12)$$

In Figs. 17 and 18, we compare our experimental results with the model using three different values of K^* ($K^*=0.75$, $K^*=1$, and $K^*=1.25$). The profile of the capillary pressure is presented for two heat fluxes (2 W/cm² and 4 W/cm²). To the extent of experimental uncertainties, experimental and numerical results are in a reasonable agreement for K^* ranging from 0.75 to 1.25. Therefore, the permeability of crossed grooves is found to be close to that of longitudinal grooves in our experiments. It is not possible to increase the accuracy of identification of K^* with this experimental test bench because of the development of nucleate boiling for heat fluxes higher than 4 W/cm². In order to increase the capillary pressure variation, a FPHP with a higher surface should be realized (especially a higher evaporator surface) to increase the pressure variation inside the capillary structure with heat fluxes lower than the onset of nucleate boiling.

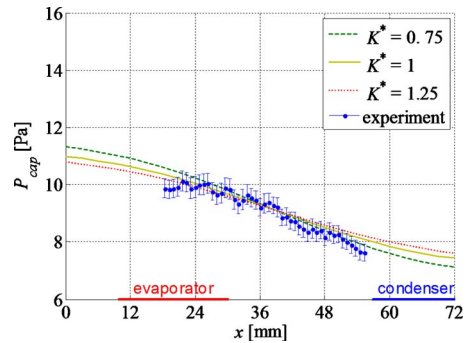


Fig. 17 Capillary pressure for the FPHP filled with FC72 ($q=2$ W/cm²)

4.4 Comparison Between Longitudinal and Crossed Grooves. The analytical model of Lefèvre and Lallemand [19] can be modified to take into account a FPHP with longitudinal grooves. The thermal model is not changed. Thus, heat diffusion occurs in the wall, which allows for evaporation in grooves that are not above the heat source. The hydrodynamic model has been modified to allow liquid redistribution at the extremity of the condenser. Instead of a zero velocity condition, a constant pressure is imposed along the line $x=72$ mm. Thus, the mass balance is verified.

Numerical simulations have been performed considering longitudinal and crossed grooves in the same conditions as the experiments with FC72. In both cases, the relative permeability K^* of the capillary structure is supposed to be equal to 1 and the equivalent thermal conductivity is supposed to be equal to 0.26 W/m K.

Velocity fields obtained from simulations are plotted in Fig. 19 for $q=4$ W/cm². In crossed grooves (case (a)), the whole capillary structure is useful for the liquid flow in the system. In longitudinal grooves (case (b)), the liquid is mainly drained by the grooves under the heat source. The other grooves work less and only because of heat conduction in the FPHP wall. As a consequence, for the same heat flux, the velocity in the central grooves and, thus, the pressure drops, are higher for the 1D capillary structure than for crossed grooves.

The calculated liquid pressure profile in the middle line of the FPHP ($y=0$ mm) for both capillary structures is presented in Fig. 20. It has to be noticed that the pressure drop presented for crossed grooves slightly differs from that presented in Fig. 18 because the FPHP is supposed to be perfectly horizontal while an angle of 0.08 deg is taken into account in the comparison with experimental results. In this configuration, the pressure drop in longitudinal grooves is approximately 1.6 times higher than in crossed grooves. By considering a liquid-wall contact angle equal to zero, the capillary limit of the FPHP is equal to 140 W with

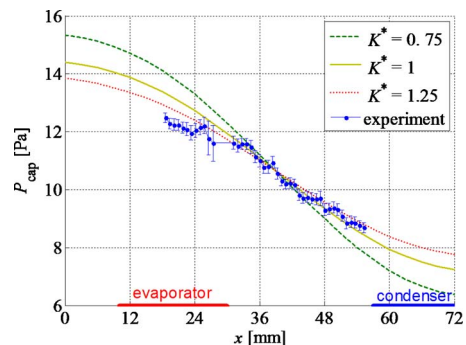


Fig. 18 Capillary pressure for the FPHP filled with FC72 ($q=4$ W/cm²)

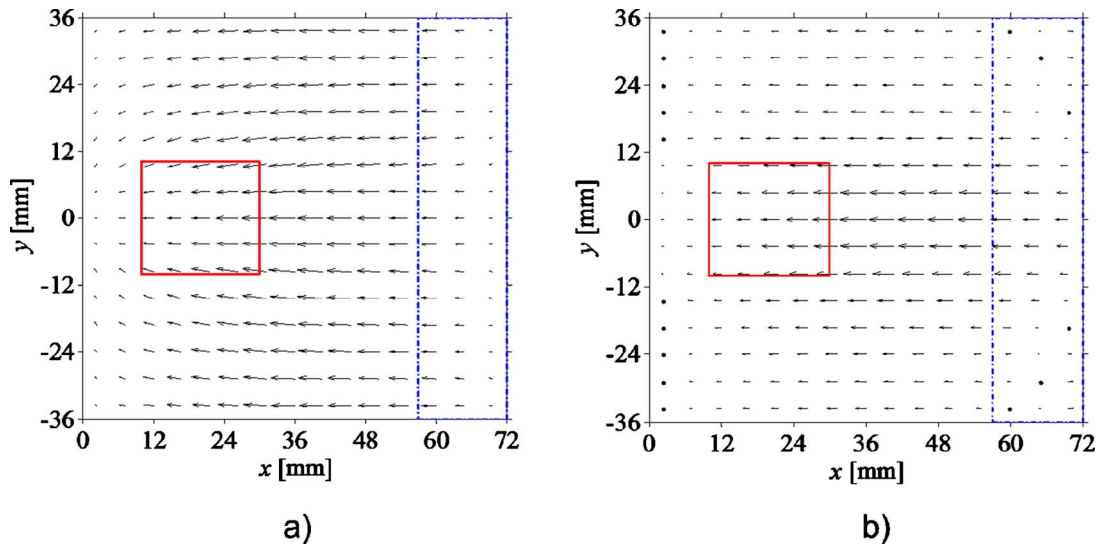


Fig. 19 Numerical comparison between 1D and 2D capillary structures: (a) Liquid velocity field for crossed grooves and (b) liquid velocity field for longitudinal grooves

crossed grooves and only 85 W for longitudinal grooves. These values definitively show the advantage of a 2D capillary structure compared with a 1D capillary structure in such a configuration.

5 Conclusion

A flat plate heat pipe made of copper and having a capillary structure made of crossed grooves has been designed, built and characterized experimentally. The shape of the liquid-vapor interface has been studied theoretically. It appears that the maximum capillary pressure that such a capillary structure can sustain is close to that of longitudinal grooves of same dimensions. A confocal microscope has been used to visualize the liquid-vapor interface and to determine the capillary pressure in the grooves. The FPHP has been tested with methanol and FC72. The comparison with coupled thermal and hydrodynamic models permits to determine the permeability and the equivalent thermal conductivity of the capillary structure. For capillary flows developing in such FPHP, the permeability of the capillary structure made of crossed grooves has been found to be close to that of longitudinal grooves with same dimensions. When several heat sources and sinks are located on a FPHP or when the sources do not fully cover the width of the FPHP, crossed grooves perform better than longitudinal grooves because the whole capillary structure is used to drain the liquid from the condenser to the evaporator. Such a study could also be performed for other capillary structures, such as metallic meshes or sintered metal powder, in order to create an

experimental database for both the equivalent thermal conductivity and the permeability. Indeed, these parameters are not always well referenced in literature.

Acknowledgment

This work was supported by the GIP-ANR in the frame of the nonthematic project "INTENSIFILM" N° Contract No. ANR-06-BLAN-0119-03.

Nomenclature

- A_1, A_2, A_4 = numerical parameters
- A_3 = numerical parameter, m^{-1}
- B_{0m}, B_{0n}, B_{mn} = Fourier coefficients for T
- C_{0m}, C_{0n}, C_{mn} = Fourier coefficients for P
- c_{min} = minimum aspect ratio
- D_h = hydraulic diameter, m
- f = friction factor
- f_r = filling ratio
- g = gravitational acceleration, $m\ s^{-2}$
- h = height, m
- h_{lv} = latent heat of vaporization, $J\ kg^{-1}$
- H = curvature, m^{-1}
- K = permeability, m^2
- K^* = nondimensional permeability
- l = width, m
- P = pressure, Pa
- q = heat flux, $W\ m^{-2}$
- Q = heat transfer rate, W
- Re = Reynolds number
- R_{th} = thermal resistance, $K\ W^{-1}$
- T = temperature, K
- x, y, z = coordinates, m

Greek Symbols

- α = meniscus angle with pin vertical walls
- β = angle with horizontal
- β' = correction angle
- θ = liquid-wall contact angle
- μ = dynamic viscosity, $Pa\ s$
- ρ = density, $kg\ m^{-3}$
- σ = surface tension, $N\ m^{-1}$
- φ = porosity

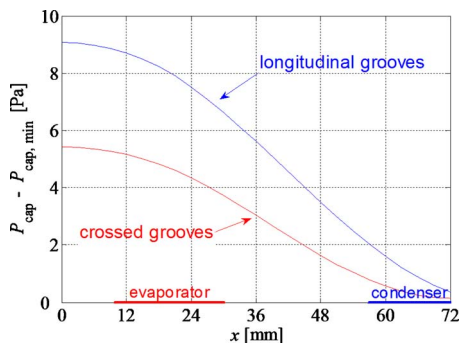


Fig. 20 Capillary pressure along line $y=0$ mm

Subscripts

cond = condenser
cap = capillary
g = grooves
l = liquid
max = maximum
sat = saturation
v = vapor

References

- [1] Lallemand, M., and Lefèvre, F., 2004, "Micro/Mini Heat Pipes for the Cooling of Electronic Devices," Thirteenth International Heat Pipe Conference, Shanghai, China, pp. 12–22.
- [2] Groll, M., Schneider, M., Sartre, V., Zaghoudi, M. C., and Lallemand, M., 1998, "Thermal Control of Electronic Equipment by Heat Pipes," *Rev. Gen. Therm.*, **37**, pp. 323–352.
- [3] Rullière, R., Lefèvre, F., and Lallemand, M., 2007, "Prediction of the Maximum Heat Transfer Capability of Two-Phase Heat Spreaders—Experimental Validation," *Int. J. Heat Mass Transfer*, **50**, pp. 1255–1262.
- [4] Lefèvre, F., Rullière, R., Pandraud, G., and Lallemand, M., 2008, "Prediction of the Temperature Field in Flat Plate Heat Pipes With Micro-Grooves—Experimental Validation," *Int. J. Heat Mass Transfer*, **51**, pp. 4083–4094.
- [5] Shen, D. S., Mitchell, R. T., Dobranich, D., Adkins, D. R., and Tuck, M. R., 1995, "Micro Heat Spreader Enhanced Heat Transfer in MCMs," IEEE MCMC'95 Conference, Santa Cruz, pp. 189–194.
- [6] Benson, D. A., Mitchell, R. T., Tuck, M. R., Palmer, D. W., and Peterson, G. P., 1998, "Ultrahigh-Capacity Micromachined Heat Spreaders," *Microscale Thermophys. Eng.*, **2**, pp. 21–30.
- [7] Gromoll, B., 1998, "Micro Cooling Systems for High Density Packaging," *Rev. Gen. Therm.*, **37**, pp. 781–787.
- [8] Avenas, Y., Ivanova, M., Schaeffer, C., Perret, R., and Sanchez, J.-L., 2003, "Etude et réalisation de caloducs à réseau capillaire à picots carrés pour le refroidissement en électronique," Congrès Français de Thermique, SFT, Grenoble, Jun. 3–6, pp. 913–918.
- [9] Ivanova, M., Lai, A., Gillot, C., Sillon, N., Shaeffer, C., Lefèvre, F., Lallemand, M., and Fournier, E., 2006, "Design, Fabrication and Test of Silicon Heat Pipes With Radial Microcapillary Grooves," ITherm 2006, San Diego, May 30–Jun. 2.
- [10] Lefèvre, F., Rullière, R., Lips, S., and Bonjour, J., 2010, "Confocal Microscopy Applied to Capillary Film Measurements in a Radial Flat Plate Heat Pipe Made of Silicon," *ASME J. Heat Transfer*, **132**, p. 031502.
- [11] Lips, S., Lefèvre, F., and Bonjour, J., 2010, "Combined Effects of the Filling Ratio and the Vapour Space Thickness on the Performance of a Flat Plate Heat Pipe," *Int. J. Heat Mass Transfer*, **53**, pp. 694–702.
- [12] Longtin, J. P., Badran, B., and Gerner, F. M., 1994, "A One-Dimensional Model of a Micro Heat Pipe During Steady-State Operation," *ASME J. Heat Transfer*, **116**, pp. 709–715.
- [13] Launay, S., Sartre, V., Mantelli, M. B. H., de Paiva, K. V., and Lallemand, M., 2004, "Investigation of a Wire Plate Micro Heat Pipe Array," *Int. J. Therm. Sci.*, **43**, pp. 499–507.
- [14] Wang, Y. X., and Peterson, G. P., 2002, "Analysis of Wire-Bonded Micro Heat Pipe Arrays," *J. Thermophysics Heat Transfer*, **16**, pp. 346–355.
- [15] Huang, X. Y., and Liu, C. Y., 1996, "The Pressure and Velocity Fields in the Wick Structure of a Localized Heated Heat Flat Plate Heat Pipe," *Int. J. Heat Mass Transfer*, **39**, pp. 1325–1330.
- [16] Qin, W., and Liu, C. Y., 1997, "Liquid Flow in the Anisotropic Wick Structure of a Flat Plate Heat Pipe Under Block-Heating Condition," *Appl. Therm. Eng.*, **17**, pp. 339–349.
- [17] Zhu, N., and Vafai, K., 1998, "Vapor and Liquid Flow in a Asymmetrical Flat Plate Heat Pipe: A Three Dimensional Analytical and Numerical Investigation," *Int. J. Heat Mass Transfer*, **41**, pp. 159–174.
- [18] Zuo, Z. J., and North, M. T., 1999, "Improved Heat Pipe Performance Using Graded Wick Structures," Eleventh IHPC Musachinoshi-Tokyo, Vol. 2, pp. 80–84.
- [19] Lefèvre, F., and Lallemand, M., 2006, "Coupled Thermal and Hydrodynamic Models of Flat Micro Heat Pipes for the Cooling of Multiple Electronic Components," *Int. J. Heat Mass Transfer*, **49**, pp. 1375–1383.
- [20] Revellin, R., Rullière, R., Lefèvre, F., and Bonjour, J., 2009, "Experimental Validation of an Analytical Model for Predicting the Thermal and Hydrodynamic Capabilities of Flat Micro Heat Pipes," *Appl. Therm. Eng.*, **29**, pp. 1114–1122.
- [21] Lips, S., Lefèvre, F., and Bonjour, J., 2009, "Thermal and Hydrodynamic Study of a Flat Plate Heat Pipe," Experimental Heat Transfer, Fluid Mechanics and Thermodynamics ExHFT-7, Krakow, Poland, Jun. 28–Jul. 03.
- [22] Lips, S., Lefèvre, F., and Bonjour, J., 2009, "Nucleate Boiling in a Flat Grooved Heat Pipe," *Int. J. Therm. Sci.*, **48**, pp. 1273–1278.
- [23] Faghri, A., 1995, *Heat Pipe Science and Technology*, Taylor & Francis, London.

Effect of Rotation on Heat/Mass Transfer for an Impingement/Effusion Cooling System

Sung Kook Hong

Korea Institute of Energy Research,
Daejeon 305-343, Korea

Dong Hyun Lee

Hyung Hee Cho¹

e-mail: hhcho@yonsei.ac.kr

Department of Mechanical Engineering,
Yonsei University,
Seoul 120-749, Korea

In the present study, the effects of the rotating direction on heat/mass transfer in an impingement/effusion cooling system were investigated. The experiments were carried out with three different jet orientations relative to the axis of rotation and two plate spacing. For high H/d with an orthogonal jet orientation, low and nonuniform heat/mass transfer occurred between the effusion holes since the impinging jet was deflected by the Coriolis force. For a small H/d , the jet deflection effect was diminished, and rotation enhanced the heat/mass transfer in the stagnation region. [DOI: 10.1115/1.4002146]

Keywords: impingement/effusion cooling, gas turbine, heat transfer, Coriolis force, rotation

1 Introduction

Recent increase in turbine inlet temperatures necessitates more efficient cooling of the rotor blades, as well as stationary guide vanes and combustor liners. To attain this, impingement/effusion cooling could be incorporated into the rotor blades. However, there have been relatively few studies of rotating impingement/effusion cooling systems.

Epstein et al. [1] first investigated the heat transfer characteristics of an impinging jet in the leading edge of a turbine blade. They found that rotation reduces heat transfer and changes the heat transfer distributions. Aronstein [2] studied rotating impinging jet flow using flow visualization in a rotating water tank. He observed that the main jet flow and vortex structure are dependent on the injecting jet orientation. Iacovides et al. [3] studied impinging jets under the ultimate rotational conditions, with $Ro=0.18$, and obtained the Nusselt number for the impinging surface. More detailed measurements were performed by Hong et al. [4,5]. They reported that local heat/mass transfer is altered by the jet orientation relative to the rotating axis.

However, there is little data for accurately predicting the detailed heat transfer distribution on a rotating blade with effusion holes. Such information is required for a better blade design in order to prevent hot spots. In the present study, the local heat/mass transfer characteristics of a rotating impingement/effusion cooling system are investigated in terms of various parameters, such as jet orientation and H/d .

¹Corresponding author.

Manuscript received October 12, 2009; final manuscript received July 7, 2010; published online August 13, 2010. Assoc. Editor: Wei Tong.

2 Experimental Apparatus and Procedure

Figure 1(a) shows the schematics of the test duct. The details of the rotating facility are described in Ref. [6]. The diameters of the injection and effusion holes were 5 mm. The length and width of the test duct were 280×50 mm², and the height of the test duct was varied from 10 mm to 30 mm (H/d from 2.0 to 6.0). The injection plate had 16 (2×8) injection holes, and 8 (1×8) effusion holes were positioned on the effusion plate. The ratio of hole spacing to hole diameter (P_{hole}/d) was 4.0 in the spanwise direction and was 6.0 in the streamwise direction.

All the rotation tests were carried out at a fixed Ro number of 0.032 (560 rpm) and a jet Reynolds number of 3000. To investigate the effect of jet orientation, three different orientations were considered, as shown schematically in Fig. 1(b). These three orientations are referred to as axial, leading, and trailing orientations, respectively [4,5].

Mass transfer coefficients were calculated from the sublimation depth, naphthalene vapor density, and solid naphthalene density. The details of the measuring procedure are discussed in an earlier study [7]. The Sherwood number was used to present the heat/mass transfer results and can be expressed as

$$Sh = h_m d / D_{\text{naph}} \quad (1)$$

The uncertainty of the Sherwood numbers was within $\pm 8.7\%$ over the entire operating range of measurement [8].

3 Results and Discussion

Figure 2 shows the Sh distributions on the effusion plates with $H/d=6$. The white dotted circles represent the positions of the injection holes and the concentric solid-line circles denote effusion holes. For the stationary case, the local Sh peak region, caused by wall jet interaction, appeared at $z/d=0.0$. Interaction regions also occurred at $x/d=3, 9, 15$, etc., but the Sh levels were lower than those at $z/d=0.0$ due to weakened wall jet strength resulting from large hole-to-hole spacing. Figure 2(b) shows the Sh distributions with the axial orientation. The regions of wall jet interaction (e.g., at $x/d=21.0$) deviated slightly from the centers of the effusion holes due to rotation, as depicted schematically in Fig. 3. The flow was discharged into the effusion holes in the counterclockwise direction, and the wall jets were deflected in the clockwise direction following impingement. Therefore, the wall jet interaction regions at $z/d=2$ were moved slightly to the left side, while those at $z/d=-2$ were shifted to the right side. At the same time, the Sh distributions at the right end of the duct were shifted somewhat to the right side due to the blocked side wall effect. The Sh levels were slightly higher than those of the stationary case over the whole region since flow mixing was enhanced by rotation.

Both the leading and trailing orientations exhibited a periodic heat transfer pattern. With the leading orientation, the stagnation region was shifted downstream by ld . Moreover, a low heat transfer area was generated behind the effusion holes since most of the wall jet flow was deflected into the downstream effusion holes, leaving the opposite region (the upstream effusion holes) relatively untouched by the wall jets. The trailing orientation showed an inverse Sh pattern compared with the leading orientation due to the effect of the Coriolis force on the diametrically opposite jet flow.

The local Sh distributions at $z/d=-2.0$ and 0.0 are shown in Fig. 4. For the leading (trailing) orientation, the stagnation peak at $z/d=-2.0$ was shifted downstream (upstream) by ld from the projected centers of the injection holes (at $x/d=12, 18$, and 24). The peak value was slightly lower than that of the stationary case. There were two possible reasons for this: The reduced jet flow momentum caused by jet deflection and the deflected wall jets in the upstream region affect the overall injected jet flow (in other words, the crossflow effect). On the whole, asymmetrical Sh values were obtained because of the deflected flow.

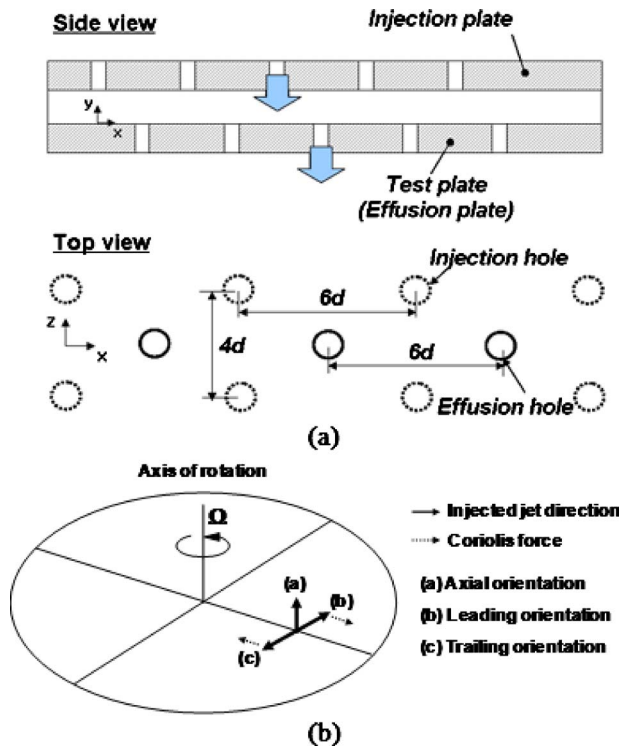


Fig. 1 Schematic view of (a) test duct and (b) jet orientation

At $z/d=0.0$, the stationary case and the axial orientation case had high Sh values in the middle region due to wall jet interaction. The Sh values increased slightly at both edges of the effusion holes due to discharged flow acceleration [9]. For the leading and trailing orientations, a high Sh value was observed at one edge of the effusion holes because of the deflected wall jet interaction and the one-sided flow acceleration. Overall heat transfer was decreased by 20%, and large heat transfer variation occurred on account of the deflected wall jets compared with the stationary or the axial orientation cases.

Figure 5 shows Sh contours for the impingement/effusion cooling system with $H/d=2.0$. The overall Sh distributions of the rotating cases were similar to those of the stationary case, al-

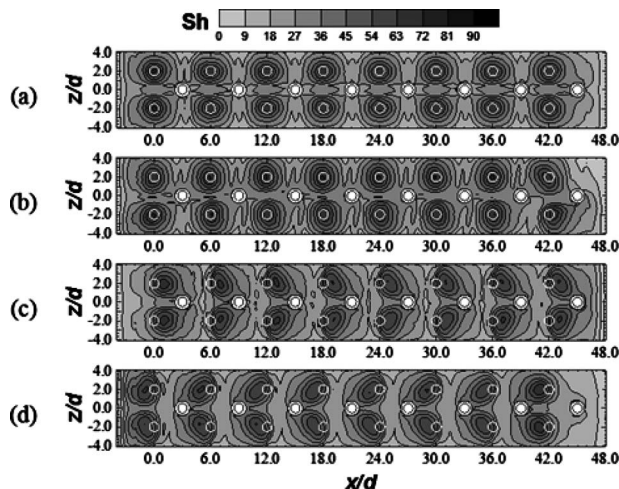


Fig. 2 Contour plots of the Sh for (a) stationary case, (b) axial orientation, (c) leading orientation, and (d) trailing orientation with $H/d=6.0$

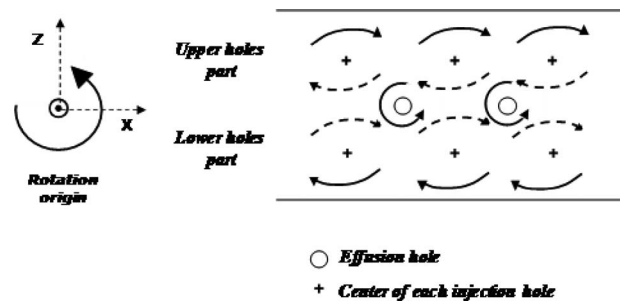


Fig. 3 Expected flow behavior of impingement/effusion cooling with axial orientation

though the Sh level in the stagnation region was higher in the rotating cases than in the stationary case. Figure 6 shows the local Sh values along the line $z/d=-2.0$. For the stationary case, the first peak was at a distance of $0.5d$ from the stagnation point due to stagnation flow acceleration [10]. For the axial orientation, the Sh value in the stagnation region was 15% higher than that in the stationary case. This was primarily on account of the jet-spreading phenomenon [6]. When the jet direction was parallel to the axis of rotation, the main axial velocity component of the jet was not affected. However, the radial velocity was influenced by the Coriolis force. When the jet began to spread in the radial direction while moving downstream, the Coriolis force generated a swirl flow for the radial velocity component of each jet. The turbulence of the jet core was greater than that of the stationary jet. Consequently, the heat transfer increased in the stagnation region.

For the leading and trailing orientations, a high Sh value was observed in the stagnation region. This was possibly due to the increased turbulence caused by rotation. The overall Sh distributions were shifted slightly upstream or downstream, depending on the jet orientation, due to the weak Coriolis force that accompanied a small gap distance.

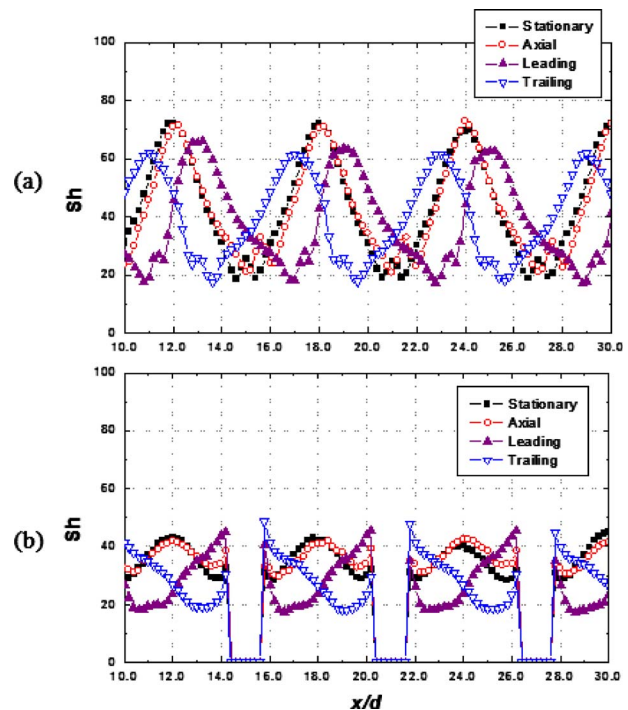


Fig. 4 Local plots of the Sh for (a) $z/d=-2.0$ and (b) $z/d=0.0$ with $H/d=6.0$

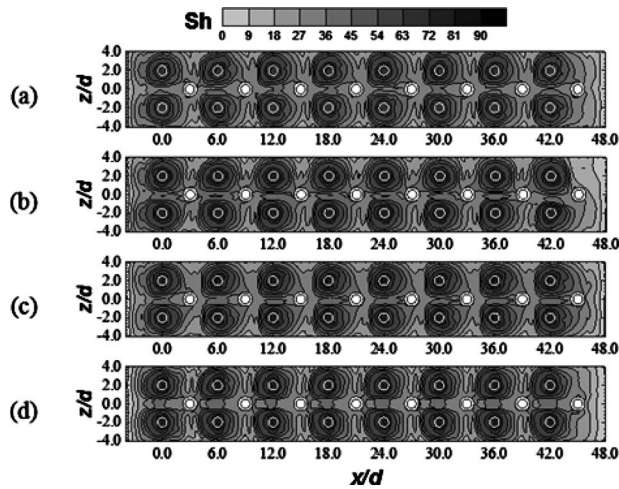


Fig. 5 Contour plots of the Sh for (a) stationary case, (b) axial orientation, (c) leading orientation, and (d) trailing orientation with $H/d=2.0$

As indicated by the previous results (Figs. 2 and 5) with an orthogonal orientation, the Sh distributions for the smaller H/d were relatively unchanged compared with the larger gap distance ($H/d=6$). This was because the jet deflection was considerably decreased until the jet flow reached the target surface. The results show that a large gap distance (H/d) produced a locally low heat transfer area and reduced the uniformity of the heat transfer. A small gap distance is therefore recommended when the jet direction is orthogonal to the axis of rotation.

4 Conclusions

In the present study, the effects of rotation on heat/mass transfer were investigated for an impingement/effusion cooling system. The results are summarized below.

1. The axial orientation had Sh distributions similar to the stationary case. On the other hand, for the leading and trailing orientations and high H/d , the Sh distributions were deflected, and a local low heat transfer area was generated between the effusion holes due to jet deflection by the Coriolis force.
2. A smaller value of H/d reduced the jet deflection effect, and the Sh distributions for the rotating cases were similar to those of the stationary case. For small H/d , rotation enhanced the flow mixing in the stagnation region, producing a 10–15% Sh augmentation compared with the stationary case.

Acknowledgment

This work was supported by the Power Generation and Electricity Delivery of the Korea Institute of Energy Technology Evaluation and Planning (KETEP) grant funded by the Korean Ministry of Knowledge Economy and the Yonsei University Research Fund of 2009.

Nomenclature

d = injection and effusion hole diameter

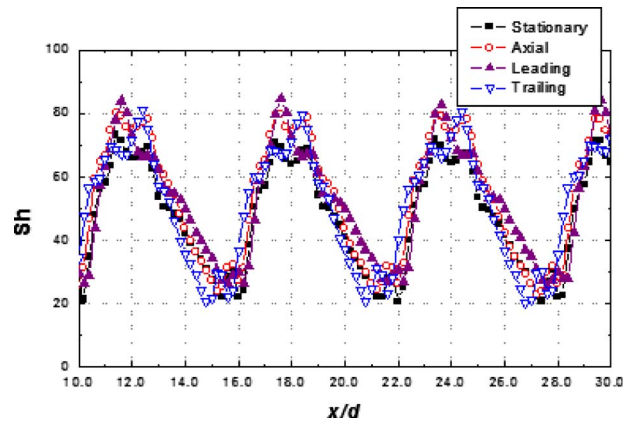


Fig. 6 Local plots of the Sh for various rotating cases of impingement/effusion cooling along $z/d=-2.0$ at $H/d=2.0$

D_{naph} = mass diffusion coefficient of naphthalene vapor in air

H = gap distance between the injection hole and the target surface

h_m = local mass transfer coefficient, Eq. (1)

P_{hole} = pitch of the injection holes at the injection plate

Re = Reynolds number based on hole diameter and the average velocity in the jet hole

Ro = rotation number based on hole diameter and the average velocity in the jet hole, $\Omega d/v_i$

Sh = Sherwood number based on the hole diameter, Eq. (1)

x, z = distance from the center of an effusion hole

Ω = rotational velocity

References

- [1] Epstein, A. H., Kerrebrock, J. L., Koo, J. J., and Preiser, U. Z., 1987, "Rotational Effects on Impingement Cooling," *Proceedings of the First International Symposium on Transport Phenomena*, Hemisphere, Washington, D.C., pp. 86–102.
- [2] Aronstein, D. C., 1994, "Effects of Rotation on Impinging Jets for Turbine Cooling," Ph.D. thesis, University of Washington, Washington, D.C.
- [3] Iacovides, H., Kounadis, D., Launder, B. E., Li, J., and Xu, Z., 2005, "Experimental Study of the Flow and Thermal Development of a Row of Cooling Jets Impinging on a Rotating Concave Surface," *ASME J. Turbomach.*, **127**(1), pp. 222–229.
- [4] Hong, S. K., Lee, D. H., and Cho, H. H., 2010, "Local Heat/Mass Transfer Measurements on Effusion Plates in Impingement/Effusion Cooling With Rotation," *Int. J. Heat Mass Transfer*, **53**(7–8), pp. 1373–1379.
- [5] Hong, S. K., Lee, D. H., and Cho, H. H., 2009, "Heat/Mass Transfer in Rotating Impingement/Effusion Cooling With Rib Turbulators," *Int. J. Heat Mass Transfer*, **52**(13–14), pp. 3109–3117.
- [6] Hong, S. K., Lee, D. H., and Cho, H. H., 2008, "Heat/Mass Transfer Measurement on Concave Surface in Rotating Jet Impingement," *J. Mech. Sci. Technol.*, **22**(10), pp. 1952–1958.
- [7] Rhee, D. H., Choi, J. H., and Cho, H. H., 2003, "Flow and Heat (Mass) Transfer Characteristics in an Impingement/Effusion Cooling System With Crossflow," *ASME J. Turbomach.*, **125**(1), pp. 74–82.
- [8] Hong, S. K., Lee, D. H., and Cho, H. H., 2009, "Effect of Jet Direction on Heat/Mass Transfer of Rotating Impingement Jet," *Appl. Therm. Eng.*, **29**(14–15), pp. 2914–2920.
- [9] Goldstein, R. J., Cho, H. H., and Jabbari, M. Y., 1997, "Effect of Plenum Crossflow on Heat (Mass) Transfer Near and Within the Entrance of Film Cooling Holes," *ASME J. Turbomach.*, **119**(4), pp. 761–769.
- [10] Cho, H. H., and Rhee, D. H., 2001, "Local Heat/Mass Transfer Measurement on the Effusion Plate in Impingement/Effusion Cooling System," *ASME J. Turbomach.*, **123**(3), pp. 601–608.

A Four-Step Fixed-Grid Method for 1D Stefan Problems

M. Tadi

Department of Mechanical Engineering,
University of Colorado at Denver,
Campus Box 112,
P.O. Box 173364,
Denver, CO 80217-3364
e-mail: mohsen.tadi@ucdenver.edu

This note is concerned with a fixed-grid finite difference method for the solution of one-dimensional free boundary problems. The method solves for the field variables and the location of the boundary in separate steps. As a result of this decoupling, the nonlinear part of the algorithm involves only a scalar unknown, which is the location of the moving boundary. A number of examples are used to study the applicability of the method. The method is particularly useful for moving boundary problems with various conditions at the front. [DOI: 10.1115/1.4002148]

Keywords: Stefan problems, parabolic systems

1 Introduction

In this note, we consider a numerical method for 1D moving boundary problems. This problem appears in a large number of applications including melting and solidification, chemical depositions, and flow through porous media. The literature on the numerical solution of this class of problems are vast. Here, we refer the reader to Refs. [1–3]. In addition, a number of methods have also been reviewed in Refs. [4,5]. Recent results for particular free boundary problems appearing in various applications also include a method based on approximate solution [6], perturbation method [7], and boundary element method [8].

The purpose of this note is to formulate a fixed-grid finite difference method for 1D moving boundary problems. Compared with a variable mesh method, it is easier to extend a fixed-grid method to higher dimensions, which will be considered in a future work. The present algorithm is composed of an explicit first-order accurate and an implicit second-order accurate formulations. As a result, the algorithm is only first-order accurate in time. The order of the accuracy in space can be improved if needed. The algorithm introduces a decoupling, which separates the solution step for the field variables and the location of the front. As a result, the nonlinear part of the algorithm involves a scalar unknown only. Section 2 introduces the method in details for a two-phase problem. Section 3 studies the stability issues and Sec. 4 introduces a number of examples.

2 A Two-Phase Stefan Problem

For simplicity, consider a one-dimensional melting of a solid with constant thermal properties and without sources and sinks. Assume that the variables $u(t,x)$ and $v(t,x)$ denote the material temperature in the liquid and solid phase, respectively. The two-phase moving boundary problem is given by

$$\begin{aligned} u_t = u_{xx}, \quad x \in [0:s(t)], \quad u(0,x) = f_0(x) > 0, \\ x \in [0:s(0)], \quad u(t,0) = f_1(t) \end{aligned} \quad (1)$$

$$\begin{aligned} v_t = v_{xx}, \quad x \in [s(t):\infty], \quad v(0,x) = g_0(x) < 0, \\ x \in [s(0):\infty], \quad v(t,\infty) = g_1(t) \end{aligned} \quad (2)$$

The moving boundary $s(t)$ is subject to a phase change condition given by

$$u(t,s(t)) = v(t,s(t)) = 0, \quad \frac{ds}{dt} = v_x(t,s(t)) - u_x(t,s(t)) \quad (3)$$

where, for simplicity, various physical parameters are set equal to one. Assume that the temperature distribution and the front location is known at a time $t_n = n\Delta t$. Also, assume that the domain is divided into m equal intervals. Consider a finite difference mesh given in Fig. 1 and assume that the front is at location $s(n\Delta T) = s(t_n)$, which is known to be between the nodes k and $k+1$. The interest is to find the temperature distribution at time interval $(n+1)$ and the location of the front, i.e., δ . Also, denote the two distances τ_1 and τ_2 , which will be used later. Note that both τ_1 and τ_2 are larger than Δx by design. Also, $(\tau_1 + \tau_2 = 3\Delta x)$ for all times. As the time marching proceeds, the front moves, and as a result, the nodes that enclose the front change. Since the mesh consists of equal fixed intervals, it is quite easy to identify the nodes, just before and just after the front. Figure 1 also shows two local variables η and ξ , which will be used later. The present algorithm consists of the following four steps.

Step I. Approximate the field equation, Eq. (1), at location $(n, k-1)$, using an explicit finite difference formulation given by

$$\begin{aligned} u_{k-1}^{n+1} &= u_{k-1}^n + \Delta t u_{xx}|_{k-1} \\ u_{xx}|_{k-1} &= \frac{6\Delta x}{(\Delta x + \tau_1)(2\Delta x + \tau_1)} \frac{-u_{k-1}}{\tau_1} + \frac{(4\Delta x - 2\tau_1)}{\Delta x(\Delta x + \tau_1)} \frac{(u_{k-2} - u_{k-1})}{\Delta x} \\ &\quad + \frac{(2\tau_1 - 2\Delta x)}{\Delta x(2\Delta x + \tau_1)} \frac{(u_{k-3} - u_{k-1})}{2\Delta x} \end{aligned} \quad (4)$$

The above approximation uses the field variables at $[n, (k-3)], [n, (k-2)], [n, (k-1)]$, and at the front $u(t_n, s(t_n)) = 0$ to obtain a four point central differencing expression for the second derivative centered at the node $[n, (k-1)]$. Also, approximate the field equation, Eq. (2), at location $[n, (k+2)]$, using an explicit finite difference formulation given by

$$\begin{aligned} v_{k+2}^{n+1} &= v_{k+2}^n + \Delta t v_{xx}|_{k+2} \\ v_{xx}|_{k+2} &= \frac{6\Delta x^2 + 4\tau_2\Delta x + \tau_2^2}{\Delta x(\Delta x + \tau_2)(2\Delta x + \tau_2)} \frac{-v_{k+2}}{\tau_2} + \frac{(4\Delta x - 2\tau_2)}{\Delta x(\Delta x + \tau_2)} \frac{(v_{k+3} - v_{k+2})}{\Delta x} \\ &\quad - \frac{(2\Delta x - 2\tau_2)}{\Delta x(2\Delta x + \tau_2)} \frac{(v_{k+4} - v_{k+2})}{2\Delta x} \end{aligned} \quad (5)$$

Again, the above formulation uses the field variables at $v(t_n, s(t_n)) = 0, [n, (k+2)], [n, (k+3)],$ and $[n, (k+4)]$ to obtain a four point central differencing expression for the second derivative at the node $(n, k+2)$. Since both τ_1 and τ_2 are larger than Δx , the orders of accuracy for these formulations are given by $(\Delta t, \Delta x^2)$. We will discuss the stability requirements at a latter time.

Step II. Treat the values of u_{k-1}^{n+1} and v_{k+2}^{n+1} as Dirichlet boundary conditions at $x = (k-1)\Delta x$ and $x = s(n\Delta t) + \tau_2$ and use Crank–Nicolson method to solve for the temperature distributions at both sides of the front at time interval $(n+1)$. For $\lambda = \Delta t / \Delta x^2$, these approximations are given by

$$-\frac{\lambda}{2} u_{i-1}^{n+1} + (1 + \lambda) u_i^{n+1} - \frac{\lambda}{2} u_{i+1}^{n+1} = u_i^n + \frac{\Delta t}{2} u_{xx,i}^n, \quad 1 \leq i \leq k-2 \quad (6)$$

Contributed by the Heat Transfer Division of ASME for publication in the JOURNAL OF HEAT TRANSFER. Manuscript received January 2, 2010; final manuscript received July 7, 2010; published online August 16, 2010. Assoc. Editor: Oronzio Manca.

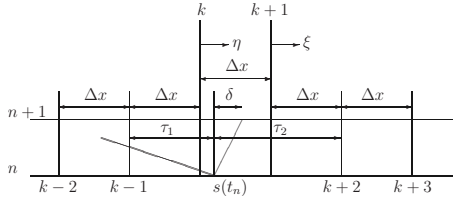


Fig. 1 Finite difference mesh close to the interface

$$-\frac{\lambda}{2}v_{i-1}^{n+1} + (1 + \lambda)v_i^{n+1} - \frac{\lambda}{2}v_{i+1}^{n+1} = v_i^n + \frac{\Delta t}{2}v_{xx,i}^n, \quad k+3 \leq i \leq m-1 \quad (7)$$

This step also make use of the given boundary conditions at $x=0$ and $x=\infty$. Note that after this step, the field variables u_k^{n+1} and v_{k+1}^{n+1} are still unknown. They are computed in the step IV using two quadratic interpolating functions.

Step III. Use the values of the field variables at $(n+1)$ and obtain one-sided first derivatives at the interface. These first derivatives are given by

$$u_x|_{x=s(t=(n+1)\Delta t)} = \frac{\tau_1 + \delta}{\Delta x(\tau_1 + \Delta x + \delta)}u_{k-2}^{n+1} - \frac{\tau_1 + \Delta x + \delta}{(\tau_1 + \delta)\Delta x}u_{k-1}^{n+1} \quad (8)$$

$$v_x|_{x=s(t=(n+1)\Delta t)} = \frac{\tau_2 - \delta + \Delta x}{(\tau_2 - \delta)\Delta x}v_{k+2}^{n+1} - \frac{\tau_2 - \delta}{\Delta x(\Delta x + \tau_2 - \delta)}v_{k+3}^{n+1} \quad (9)$$

where the fact that the temperature is zero at the interface is used. Using the above first derivatives, the implicit treatment of the condition at the boundary leads to a nonlinear scalar equation for δ given by

$$\frac{ds}{dt} = \frac{\delta}{\Delta t} = u_x|_{x=s(t=(n+1)\Delta t)} - v_x|_{x=s(t=(n+1)\Delta t)} \quad (10)$$

The above interface condition is a scalar nonlinear equation for the movement of the interface δ .

Step IV. Use the computed field variables at time step $(n+1)$ and the given value of the field at the front and interpolate for the field variables at the nodes just before and just after the front, i.e., u_k^{n+1} and v_{k+1}^{n+1} . The front location is computed in step III. The field variables u_{k-1}^{n+1} , u_{k-2}^{n+1} , v_{k+2}^{n+1} , and v_{k+3}^{n+1} are computed in step II. Using these values, the field variables at u_k^{n+1} and v_{k+1}^{n+1} can be computed using a quadratic interpolation function. This step is accomplished by assuming a quadratic polynomial for the field variable centered at location u_k^{n+1} given by

$$u(\eta) = u^{n+1}|_{x \text{ around } k} = c_1\eta^2 + c_2\eta + c_3, \quad \eta = x - (k-1)\Delta x, \quad (11)$$

where the local variable η is shown in Fig. 1. Note that $u(\eta=0) = u_k^{n+1}$. The constants c_1-c_3 can be computed using the three conditions

$$u(-\Delta x) = u_{k-1}^{n+1}, \quad u(-2\Delta x) = u_{k-2}^{n+1}, \quad u(\tau_1 - \Delta x + \delta) = 0. \quad (12)$$

Also, note that the condition, $u(\tau_1 - \Delta x + \delta) = 0$, is the given boundary condition at the front. Similarly, a quadratic polynomial centered around v_{k+1}^{n+1} can be used to obtain the field variable at v_{k+1}^{n+1} .

The above four steps can be applied for the next time interval after solving for the movement of the front δ and the field variables at time interval $(n+1)$ including the nodes adjacent to the front.

The first derivatives that appear in Eqs. (8) and (9), and the interpolations for the field variables u_k^{n+1} and v_{k+1}^{n+1} , can be accomplished using third-order polynomials, if more accuracy in space is needed.

3 Stability Studies

The proposed method is composed of four different steps, one of which is the numerical solution of a nonlinear scalar equation. For this problem, it is not possible to use local Fourier analysis [9] to derive definitive sufficient conditions for stability of the scheme. This is due to the nonlinearity and, in addition, the fact that the computational domain is changing. It is however possible to show that Fourier analysis suggests a region of stability for the numerical scheme.

It is helpful to note that while the front location is enclosed by the nodes k and $k+1$, the values of the field variables at k and $k+1$ are not used in the computation of the field variables or the front location. These values are used once the front moves across the node $(k+1)$.

Consider the explicit finite difference formulation given in Eq. (4) in step I. This explicit formulation is used to obtain a Dirichlet boundary condition for the time interval $(n+1)$ after which an implicit Crank–Nicolson is used in step II. The explicit formulation is given in Eq. (4). The implicit formulation in step II is given in Eq. (6), and for, $i=(k-2)$, simplifies to

$$u_{k-2}^{n+1} - u_{k-2}^n = \frac{1}{2}\lambda(u_{k-3}^{n+1} - 2u_{k-2}^{n+1} + u_{k-1}^{n+1}) + \frac{1}{2}\lambda(u_{k-3}^n - 2u_{k-2}^n + u_{k-1}^n) \quad (13)$$

where $\lambda = \Delta t / \Delta x^2$. One can now replace the value of u_{k-1}^{n+1} with the explicit formulation given in Eq. (4), which leads to

$$u_{k-2}^{n+1} - \frac{1}{2}\lambda u_{k-3}^{n+1} + \lambda u_{k-2}^{n+1} = u_{k-2}^n + \frac{1}{2}\lambda(u_{k-3}^n - 2u_{k-2}^n + u_{k-1}^n) + \frac{1}{2}\lambda u_{k-1}^n + \lambda^2 \left[\frac{-3}{\sigma(\sigma+1)(\sigma+2)}u_{k-1}^n + \frac{2-\sigma}{\sigma+1}u_{k-2}^n - u_{k-1}^n + \frac{\sigma-1}{2(\sigma+2)}(u_{k-3}^n - u_{k-1}^n) \right], \quad (14)$$

where $\sigma = \tau_1 / \Delta x$. The value of τ_1 , which appears in the second derivative in the above approximation, is bounded between Δx and $2\Delta x$, i.e., $\Delta x \leq \tau_1 < 2\Delta x$. In other words

$$1 \leq \sigma = \frac{\tau_1}{\Delta x} < 2 \quad (15)$$

It is now possible to consider a Fourier component given by $u_{k-2}^n = \psi^n e^{j\ell x_{k-2}}$ and investigate the condition for the amplitude to remain bounded. Substituting the above relation into Eq. (14) leads to

$$\left[1 + \lambda - \frac{1}{2}\lambda e^{-j\ell \Delta x} \right] \psi^{n+1} = \left[1 - \lambda + \frac{1}{2}\lambda(e^{-j\ell \Delta x} + e^{j\ell \Delta x}) + \frac{1}{2}\lambda e^{j\ell \Delta x} \right] \psi^n + \lambda^2 \left[\frac{-3}{\sigma(\sigma+1)(\sigma+2)} e^{j\ell \Delta x} + \frac{2-\sigma}{\sigma+1} (1 - e^{j\ell \Delta x}) + \frac{\sigma-1}{2(\sigma+2)} (e^{-j\ell \Delta x} - e^{j\ell \Delta x}) \right] \psi^n. \quad (16)$$

The above equation describes the behavior of the amplitude of the error. It is in the form $A\psi^{n+1} = B\psi^n$, where both coefficients A and B are complex. For stability, we need to have $|A| \geq |B|$. To identify

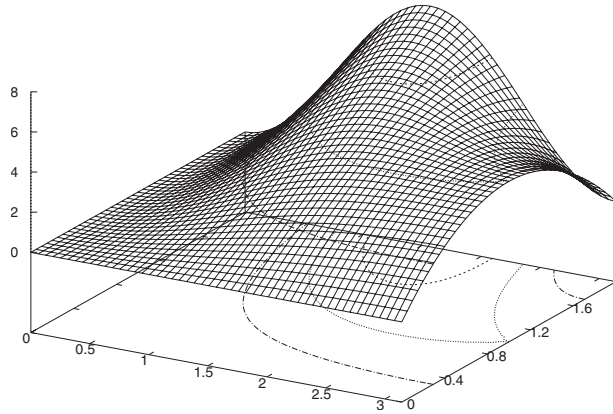


Fig. 2 The region of stability for the explicit-implicit mesh at $(k-2, n+1)$ just before the front for $\sigma=1$. The function is positive for $\lambda \leq 2$. The x axis is $\lambda \Delta x$ with the range $[0, 3.2]$. The y axis is λ with the range $[0, 1.8]$. The z axis is the function $f(\lambda, \ell \Delta x)$.

the region of stability, it is possible to simply compute and plot the function

$$f(\lambda, \ell \Delta x) = |A|^2 - |B|^2 \quad (17)$$

and look for the region where the quantity is positive. To account for the variable τ_1 , one can plot the above function for different values of σ within $[1; 2]$. Figure 2 shows the variation of $f(\lambda, \ell \Delta x)$ as functions of $\ell \Delta x$ and λ for $\sigma=1$. Figure 2 shows that the amplitude of the error remains bounded for $\lambda < 2$. This range for λ is also valid for other values of σ , i.e., $1 < \sigma < 2$.

It is also important to note that this condition is not an exact sufficient condition for the stability. The above analysis simply suggests a region of numerical stability, which will be confirmed with a number of numerical examples.

4 Numerical Example

4.1 Example 1. We first consider a one-phase Stefan problem, which has an exact solution. Consider melting of a certain material occupying the half space $x > 0$ that is initially at its freezing temperature. The governing equation in terms of the dimensionless temperature is given by

$$u_t = u_{xx}, \quad 0 < x < s(t), \quad t > 0 \quad (18)$$

subject to the initial and boundary conditions

$$s(0) = 0, \quad u(0, x) = 0, \quad u(0, t) = 1 \quad (19)$$

In addition, the condition at the free boundary is given by

$$T(s(t), t) = 0, \quad \frac{ds}{dt} = -u_x|_{x=s(t)} \quad (20)$$

The above problem has the exact solution given by

$$u(t, x) = 1 - \frac{\operatorname{erf}\left(\frac{x}{2\sqrt{t}}\right)}{\operatorname{erf}(\gamma)}, \quad s(t) = 2\gamma\sqrt{t} \quad (21)$$

where γ satisfies the equation

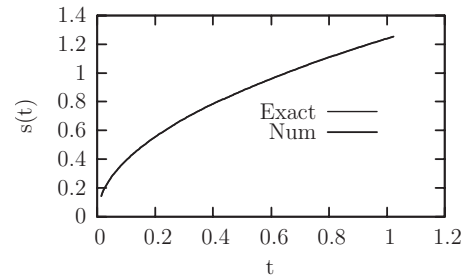


Fig. 3 The location of the front for example 1. The figure compares the exact solution to the numerical result.

$$\sqrt{\pi} \gamma \operatorname{erf}(\gamma) e^{\gamma^2} = 1 \quad (22)$$

The initial condition for this problem makes it necessary to start the numerical simulation at a time larger than zero. Assume that at the initial time, the front is located at $s(t_0) = 0.14358$. Once the initial time is specified, it is also possible to provide the initial temperature profile for the present algorithm. Figure 3 presents the location of the front and compares it to the exact solution. Table 1 compares these two values at specific time instances. The present method can produce very accurate results. The mesh size for this case is $\Delta x = 0.01$ and the time step size is $\Delta t = 0.00009$. For this mesh, the scheme can produce stable numerical results for $\Delta t \leq 0.00018$, which is also very close to the limit suggested by the stability analysis.

4.2 Example 2. We next consider a two-phase Stefan problem for which an exact solution exists [10]. For this case, it is possible to have a nonzero initial domain. The exact solution corresponds to the case in which the domain extends to infinity in both directions $x \in [-\infty; \infty]$. The variable $s(t)$ is the location of the front, which is initially located at the origin, i.e., $s(0) = 0$. The mathematical model is given by

$$u_t = u_{xx}, \quad x \in [-\infty; s(t)], \quad u(0, x) = 1, \quad x \in [-\infty; 0] \quad (23)$$

$$v_t = v_{xx}, \quad x \in [s(t); \infty], \quad v(0, x) = -1, \quad x \in [0; \infty] \quad (24)$$

The moving boundary $s(t)$ is subject to a phase change condition given by

$$u(t, s(t)) = v(t, s(t)) = 0, \quad \frac{ds}{dt} = \theta v_x(t, s(t)) - u_x(t, s(t)) \quad (25)$$

For $\theta = 1/2$, the exact solution for the location of the front is given by $s(t) = 2\beta\sqrt{t}$ where β is the solution of a nonlinear algebraic equation. For the data in this example, β is given by $\beta = 0.14522$.

It is possible to approximate the infinite domain by considering the region $x \in [-3; 3]$. The domain $[-3; 3]$ is divided into 140 equal intervals. Figure 4 compares the exact location of the front for this example to the result obtained using the present method. The time interval is fixed at $\Delta t = 0.0001$. This choice for the time interval satisfies stability condition obtained in Sec. 2.

4.3 Example 3. We next consider a two-phase Florin problem [10] for which we also have exact solution. For this problem the condition at the front is given by

Table 1 Accuracy of the numerical method for example 1

Time	0.18	0.36	0.54	0.81	0.999
Numerical	0.52609	0.74403	0.91126	1.1161	1.2395
Exact	0.52614	0.74407	0.91130	1.1161	1.2395
% Error	0.0092	0.0056	0.0042	0.0007	0.00001

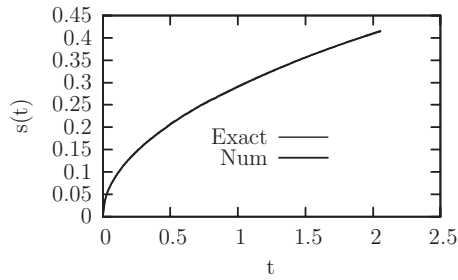


Fig. 4 The location of the front for example 2. The figure compares the exact solution to the numerical result. At $t=2$ the numerical solution is $s(2)=0.4095$, whereas the exact solution is $s(2)=0.4107$.

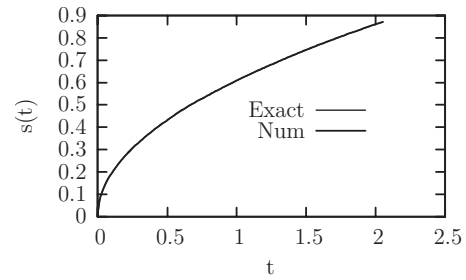


Fig. 5 The location of the front for the example 3. The figure compares the exact solution to the numerical result. At $t=2$ the numerical solution is $s(2)=0.8628$, whereas the exact solution is $s(2)=0.8614$.

$$u(t, s(t)) = v(t, s(t)) = 0, \quad \theta v_x(t, s(t)) = u_x(t, s(t)) \quad (26)$$

where the location of the front appears in an implicit way. The present method can still be applied. The exact solution for the location of the front is given by $s(t) = 2\beta\sqrt{t}$ where again β is the solution of a nonlinear algebraic equation. For $\theta = 1/2$, β is given by $\beta = 0.30457$

Figure 5 shows the location of the front as a function of time. It compares the exact solution to the numerical method obtained using the present method. The numerical mesh is the same as the one used in example 2. Increasing the number of intervals or reducing the time step size does not significantly improve the accuracy of the method. This is in part due to the nature of the formulation at the vicinity of the front.

5 Conclusion

In this note we presented a simple method for 1D moving boundary problems. The method is a fixed-grid finite difference method that solves for the location of the moving boundary and the field variables in separate steps. This decoupling leads to a significant simplification. Since the method uses a fixed grid, it can be extended to higher dimensions, which will be taken up in a future work.

References

- [1] Crank, J., 1984, *Free and Moving Boundary Problems*, Oxford University Press, New York.
- [2] Hill, J. M., 1987, *One-Dimensional Stefan Problems*, Longman, New York.
- [3] Sethian, J., 1996, *Level Set Methods and Fast Marching Methods*, Cambridge University Press, New York.
- [4] Javierre, E., Vuik, C., Vermolen, F. J., and Van Der Zwaag, S., 2006, "A Comparison of Numerical Methods for One-Dimensional Stefan Problems," *J. Comput. Appl. Math.*, **192**, pp. 445–459.
- [5] Mitchell, S. L., and Vynnycky, M., 2009, "Finite-Difference Methods With Increased Accuracy and Correct Initialization for One-Dimensional Stefan Problems," *Appl. Math. Comput.*, **215**, pp. 1609–1621.
- [6] Crepeau, J., and Siahpush, A., 2008, "Approximate Solutions to the Stefan Problems With Internal Heat Generation," *Heat Mass Transfer*, **44**, pp. 787–794.
- [7] Caldwell, J., and Kwan, Y. Y., 2003, "On the Perturbation Method for the Stefan Problem With Time-Dependent Boundary Conditions," *Int. J. Heat Mass Transfer*, **46**, pp. 1497–1501.
- [8] Chantasirawan, S., Johansson, B. T., and Lesnic, D., 2009, "The Method of Fundamental Solution for Free Surface Stefan Problems," *Eng. Anal. Boundary Elem.*, **33**, pp. 529–538.
- [9] Morton, K. W., and Mayers, D. F., 1994, *Numerical Solution of Partial Differential Equations*, Cambridge University Press, New York.
- [10] Bizhanova, G. I., 2006, "Exact Solutions of One-Dimensional Two-Phase Free Boundary Problems for Parabolic Equations," *J. Math. Sci. (N.Y.)*, **136**(2), pp. 3672–3681.